Development of a Laser Test Range for the Italian Air Force

Airborne Laser Systems Performance Prediction, Safety Analysis, Flight Testing and Operational Training

submitted by

Roberto Sabatini

To the University of Cranfield
as a thesis for the degree of Doctor of Philosophy
in the Department of Aerospace, Power and Sensors

December 2003

This thesis is available for library use on the understanding that it is copyright material and that no quotation from this thesis be published without acknowledgement.

I certify that all the material in this thesis which is not my own work has been identified and that no material is included for which a degree has previously been conferred upon me.

"Hinc Per Aethram Alam

Temptat Icari

Progenies"

PREFACE

It was the beginning of 1994 when Lt.Col. Giuseppe Arpaia (Chief of the Armament and Avionics Department, and successively Technical Director of RSV) asked me to undertake a study aimed at defining a reliable method for predicting and evaluating the performance of airborne laser designation systems. At that time, I was a young and recently qualified Flight Test Engineer with a little professional experience and only two years spent at "Reparto Saperimentale di Volo" (RSV), which is the Italian Air Force Official Flight Test Centre. The study was necessary for planning the initial test activities with the Convertible Laser Designation Pod (CLDP) and GBU-16 Laser Guided Bombs (LGB's) on the Italian TORNADO-IDS aircraft, which were to be carried out at the Cazaux test range in France and at the Sardinia test/training range (Poligono Interforze del Salto di Quirra - PISQ), in Italy, during 1994 and 1995.

During the CLDP flight test campaigns, it was also understood that investigation of eye-safety issues was very crucial for test/training mission planning, and that an adequate level of knowledge had to be acquired in that area, before introducing into service the CLDP system (for performing, in fully safe conditions, the necessary flight squadrons training activities). I was therefore asked by the RSV Technical Director to undertake a safety case study for the CLDP employment at the Sardinia test range.

In October 1995 I became the program manager for CLDP test activities on the Italian TORNADO-IDS aircraft and, shortly after, I was nominated responsible for the integration of CLDP on the AM-X ground attack aircraft.

Between 1996 and 1997, I was involved in the test activities of three different Ground Laser Target Designator (GLTD) systems, with the aim of issuing technical recommendations for the Italian Air Force, Army and Navy procurement branches.

In 1997, during a meeting at the Italian Air Staff, Lt.Col. Pasquale D'Amore asked me: "Would it be feasible to upgrade the Sardinia test range adding new facilities for carrying out safe and effective experimental and training activities with laser systems and laser guided weapons?". Convinced about the importance of having a laser test and training range in Italy (the PISQ has one of the largest controlled ground range

areas in Europe), I contacted various government, industrial and academic institutions in Italy and abroad, and started to convince myself about the technical feasibility of the task. Therefore, with a few technical elements and the braveness of a "visionary" young engineer, I presented my ideas to the Technical Director and to the Chief of the Armament and Avionics Department at RSV. After various contacts with the Air Staff in Rome, which formally tasked RSV for the activity, I started a proper "feasibility study".

I worked one year to verifying the technical issues and setting the requirements for upgrading the Sardinia test/training range. The final proposal issued by RSV was very well received by the Air Staff and, after a few more steps, a dedicated research and development program was financed by the Air Force Logistic Command.

At the beginning of 1998 the PILASTER (PISQ LASer Test and Evaluation Range) development program was launched. I was nominated program manager and technical responsible for the activity, and was in that period that I first met Dr Mark Richardson at the Royal Military College of Science in Shrivenham, during the "Guided Weapons Technology Short Course" which I attended in that year.

During my permanence at Shrivenham, I had the opportunity to illustrate my ideas to Dr Mark Richardson, and he suggested me to undertake a part-time PhD at RMCS. After solving some funding issues, in 1999 I formally started my research studies at RMCS and Dr Mark Richardson was my supervisor.

This thesis contains the results of my last five years of research (I only omitted unnecessary or classified information). Particularly, I described all research work performed for designing, developing and testing the PILASTER test/training range. This included the design of new range instrumentation and facilities, development of innovative methods for military systems performance prediction/evaluation and determination of eye-safety requirements for employment of ground and airborne laser systems at the PILASTER range (during both experimental and training activities), together with extensive laboratory, ground and flight test activities with state-of-the-art ground/airborne laser systems and laser guided weapons.

ACKNOWLEDGEMENTS

I would like to express my deepest gratitude to Dr Mark Richardson, my supervisor during this research. His great competence and experience, his sense of humour, and his incredible "human touch" will never be forgotten... and sorely missed from Italy.

I would like to tank Gen. Carlo Landi (former RSV Commander, PISQ Commander and now CSV Commander) and Col. Giovanni Fantuzzi (Commander of RSV) for strongly supporting the PILASTER project since its earliest stages.
I would also like to tank Col. Pierluigi Mancini (Italian Air Force Logistic Command) for his friendship and the great help he gave to me at the early stages of my flight test engineering carrier.
Great tanks go to Lt.Col. Giuseppe Arpaia, Lt.Col. Flavio Guercio, Lt.Col. Giuseppe Gallarato (RSV Technical Department) and Lt.Col. Pasquale D'Amore (Italian Air Staff) for supporting my ideas, giving suggestions and encouraging my work since the beginning of this project.

Many thanks go to the technical personnel of Marconi-Selenia Communications and LOT-Oriel, for their support to the PILASTER program, and for sharing with me the difficulties of life in the Sardinian "desert" of Perdasdefogu.

Thanks also go to my colleagues of RSV for their qualified technical advise and for keeping me entertained with good conversation, humour and occasional diversions to the Officer's Club.

Finally, I wish to thank my wife Janete ("La mia bimba"). Her constant love, her patience and her continuous support, encouraged me during the many days and long nights spent writing my thesis, and gave me the motivation to complete this ambitious project. She made it possible and... worthwhile.

SUMMARY OF THESIS

This thesis describes the research work performed for designing, developing and testing a new laser test and training range for the Italian Air Force. This includes the design of new range instrumentation and facilities, development of innovative methods for military systems performance prediction/evaluation and determination of eye-safety requirements for employment of ground and airborne laser systems at the laser range (during both experimental and training activities), and extensive laboratory, ground and flight test activities with state-of-the-art ground/airborne laser systems and laser guided weapons.

Between 1997 and 1998 the Italian Air Force Official Flight Test Centre (ItAF-OTC) set the requirements for upgrading the PISQ test/training range (Poligono Interforze del Salto di Quirra – Sardinia – Italy), adding new facilities for carrying out safe training and experimental activities with airborne and ground laser systems, together with LGW delivery tests. According to these initial requirements, the PILASTER (**PI**SQ **LAS**er **T**est and **E**valuation **R**ange) research and development program was divided in two different phases. The aim of the first phase of the program (1999-2002) was to provide an initial operational capability for carrying out, in fully safe conditions, ground tests and flight experimental activities (with related measurements and semi-automated data analysis), required for performance evaluation of military laser systems. The successive phase of the program (still ongoing) is aimed to implementing the PILASTER full operational capability, required for performing all laser test/training activities, including all mission planning and fully-automated post-mission data analysis tasks (2002-2004).

Implementation of suitable mathematical models for laser systems performance analysis (i.e., atmospheric propagation, mission geometry, target back-scattering, etc.) is an essential requirement of the PILASTER program, due to the need for 'realistic' simulation and mission planning, together with reliable post-mission data analysis at the

range. Very important is also the definition of eye-safety criteria and procedures, since most of current laser systems operate in the near infrared, with considerable risk for the naked human eye.

In this research, present laser technology status and future technology trends are investigated, with particular emphasis for the systems now in service or under development for the Italian Air Force. These include the *Thompson* Convertible Laser Designation Pod (CLDP), The *ELOP* Portable Laser Designator (PLD) system, Laser Guided Bombs (e.g., PAVEWAY II, PAVEWAY III and Lizard), and the *Marconi-Selenia* Laser Obstacle Avoidance System (LOAS) for helicopters. Furthermore, suitable mathematical models for ground/airborne laser systems performance analysis and mission planning are presented, together with innovative methods for evaluating the hazards associated with the use of ground and airborne laser systems at the PILASTER range.

Particularly, after describing the technical requirements and design characteristics of the PILASTER range instrumentation, safety issues of state-of-the-art ground/airborne laser systems are thoroughly investigated, in order to identify operational procedures and limitations for the safe employment of such equipment at the PILASTER range during execution of both test and training missions. Furthermore, various mathematical algorithms are presented, developed for the PILASTER simulation and mission planning tools, that allow a complete verification of laser-safety for ground and airborne laser systems.

Extensive laboratory, ground and flight experimental activities is performed with both ground and airborne laser systems in order to test the various PILASTER laser range systems and to validate/refine the models developed for systems performance analysis and simulation. Furthermore, the LOAS system is tested both on the ground and in flight, in order to assess the system obstacle detection performance in various weather conditions, and the efficiency of the algorithms developed for obstacle classification and trajectory optimisation.

Finally, the requirements for both tactical and test/training mission planning are determined, and dedicated simulation tools are presented for aircraft flight profile optimisation in both operational and test/training missions, including programs for calculation of ground laser safety areas and aircraft flight profile restrictions for both test and training missions.

LIST OF MY PUBLICATIONS

- R. Sabatini. "Tactical Laser Systems Performance Prediction in Various Weather Conditions". Paper presented at the 1st Symposium of the NATO-RTO SET Panel (organised by the former AGARD-SPP Panel) titled "E-O Propagation, Signature and System Performance Under Adverse Meteorological Conditions Considering Out-of-Area Operations", held at the Italian Air Force Academy, Naples (Italy), 16-19 March 1998.

- R. Sabatini. "Tactiacal Laser Systems Performance Prediction, Simulation and Flight Testing". Paper presented at the 10th Annual Symposium of the Society of Flight Test Engineers - European Chapter: "Quality of Flight Test", held at Linköping (Sweden), 14-17 June 1998.

- R. Sabatini. "High Precision DGPS and DGPS/INS Positioning for Flight Testing". Paper presented at the 6th Saint Petersburg International Conference on Integrated Navigation Systems (Central Scientific and Research Institute of Russia "Elektropribor"/NATO-RTO SCI Panel), held at Saint Petersburg (Russia), 24-26 May 1999.

- F. Guercio, R. Sabatini and S. Vignola. "Eye-safety Analysis of Tactical Laser Systems". Paper presented at the 11th Symposium of the Society of Flight Test Engineers - European Chapter, held at Delft Technical University (The Netherlands), 21-23 June 1999.

- R. Sabatini. "DGPS and DGPS/INS Trajectography for Flight Testing". Paper presented at the 11th Symposium of the Society of Flight Test Engineers - European Chapter, held at Delft Technical University (The Netherlands), 21-23 June 1999.

- R. Sabatini, F. Guercio and S. Vignola. "Airborne Laser Systems Performance Analysis and Mission Planning". Paper presented at the NATO RTO-SCI Panel Conference on "Advanced Mission Management and System Integration Technologies for Improved Tactical Operations", held at Scuola di Guerra Aerea, Florence (Italy), 27-29 September 1999.

- R. Sabatini, F. Guercio, G. Campo and A. Marciante. "Laser Guided Bombs and Convertible Designation Pod Integration on Italian TORNADO-IDS". Paper presented at the 31st Annual Symposium of the Society of Flight Test Engineers "Flight Test in the New Millennium", held at Turin (Italy), 18-22 September 2000.

- R. Sabatini. "MB-339CD Aircraft Development. COTS Integration in a Modern Avionics Architecture". Paper presented at the NATO RTO-SCI Panel Conference on "Strategies to Mitigate Obsolescence in Defence Systems Using Commercial Components", held at Budapest (Hungary), 23-25 October 2000;

- R. Sabatini and M. A. Richardson. "System Integration and Flight Testing of a Laser Designation Pod and Laser-guided Bombs on the Italian Interdiction Strike Aircraft". Paper published on the *Journal of Battlefield Technology* (Volume 4 – Number 2) in July 2001;

- R. Sabatini, F. Guercio, G. Campo and A. Marciante. "Simulation and Flight Testing for Integration of a Laser Designation Pod and Laser Guided Bombs on Italian TORNADO-IDS". Paper presented at the NATO RTO-SCI Panel Symposium on "Integration of Simulation with System Testing", held at Toulouse (France), 22-24 October 2001.

- R. Sabatini, E. Roviaro and M. Cottalasso. "Development of a Laser Collision Avoidance System for Helicopters: Obstacle Detection/Classification and Calculation of Alternative Flight Paths". Paper presented at the Symposium "Complementarity of Ladar and Radar", organised by the Sensors & Electronics Technology Panel (SET) of the NATO-RTO, held at Prague (Czech Republic), 22-23 April 2002.

- R. Sabatini, E. Roviaro and M. Cottalasso. "Development of a LADAR system FOR Helicopter Nap-of-the-Earth Flying: Performance Prediction, Simulation and Flight Testing". Paper presented at the Symposium "Emerging Military Capabilities Enabled by Advances in Navigation Sensors", organised by the Sensors & Electronics Technology Panel (SET) of the NATO-RTO. Istanbul (Turkey), 14-16 October 2002.

- R. Sabatini. "Aircraft Autonomous Integrity Augmentation for High Precision Differential GPS Applications". Paper to be presented at the Symposium "Emerging Military Capabilities Enabled by Advances in Navigation Sensors", organised by the Sensors & Electronics Technology Panel (SET) of the NATO-RTO. Istanbul (Turkey), 14-16 October 2002.

- R. Sabatini and M.A. Richardson. "A New Approach to Eye-Safety Analysis for Airborne Laser Systems Flight Test and Training Operations". Paper published on the *Journal of Optics and Laser Technology* (JOLT 796) in November 2002.

CONTENTS

Chapter 3: LASER SYSTEMS RANGE PERFORMANCE

Chapter 4: PILASTER GENERAL REQUIREMENTS

Chapter 5: PILASTER SYSTEMS DESIGN

Chapter 6: SYSTEMS EYE-SAFETY ANALYSIS

Chapter 7: LABORATORY EXPERIMENTAL ACTIVITY

Chapter 8: GROUND EXPERIMENTAL ACTIVITIES

Chapter 9: FLIGHT TEST ACTIVITIES

Chapter 10: MISSION ANALYSIS AND SIMULATION

Chapter 11: CONCLUSIONS AND FURTHER WORK

APPENDIXES

LIST OF FIGURES

Chapter 2

Chapter 3

LIST OF TABLES

Chapter 7

Chapter 8

Chapter 1

INTRODUCTION

1.1 Background

Technological development in the realm of optronics have led to innovative concepts in the mission management of current and next generation ground attack aircraft. Particularly, tactical systems including Laser Range Finders (LRF's), Laser Radars (LADAR's) and Laser Target Designators (LTD's) are used today by most military forces in the world and new promising laser technologies are being explored. Most laser systems are active devices that operate in a manner very similar to microwave radars but at much higher frequencies (e.g., LADAR and LRF). Other devices (e.g., LTD and beam-rider) are used to precisely direct Laser Guided Weapons (LGW's) against ground targets. A combination of both functions is often encountered in modern integrated airborne navigation-attack systems. Compared to similar microwave devices, the higher frequency of laser systems has the beneficial effect of smaller components and remarkable angular resolution values. On the other hand, laser systems performance are much more sensitive to the vagaries of the atmosphere and are thus generally restricted to shorter ranges than microwave systems.

For the accomplishment of aircraft operational tasks with LDT/LGW systems, it is important to optimise flight profiles in both self-designation and co-operative attack missions, allowing stand-off operations and safe escape manoeuvres. This can be achieved by a careful mission planning (i.e., modelling and simulation), taking into account all elements playing a significant role. These elements obviously include weather conditions (i.e., laser beam atmospheric propagation), target characteristics

(e.g., reflectance, shape, dimensions, etc.), and aircraft-target relative geometry during the attack (i.e., LTD/LGW tactics).
Similarly, for flight experimental and training activities with laser systems and LGW's it is important to take into account the tactics of employment of the systems/weapons in different operational scenarios and to verify their performances in realistic operational and environmental conditions at the ranges. Also important for test/training purposes is the definition of laser safety criteria, since most systems currently in service operate in the near infrared with considerable risk for the naked human eye.

Eye-safe technology is also being applied to airborne laser systems. Promising applications that are now receiving a growing attention include LADAR systems for obstacle warning in low-level flight missions. This kind of systems are particularly attractive for helicopter applications. Essential steps in the development of such systems are obviously laser beam propagation analysis in various weather conditions, definition of the obstacle detection performances and implementation of suitable obstacle classification and prioritisation algorithms.

Since the beginning of the 90's, the Italian Air Force Official Flight Test Centre (RSV) has conducted various test programs with LGW's, and LTD/LRF systems for both airborne and ground applications. In some cases, the activities had to be carried out in foreign test ranges, equipped with ground instrumentation sufficient for some measurement tasks (e.g., determination of laser systems pointing accuracy), but not fulfilling the RSV test requirements. Particularly, in many cases, laser spot data gathering and post-mission data analysis were very limited, considerably reducing the scope of the experimental activities and often increasing the time and money required to complete the flight test campaigns. Furthermore, once the various laser systems were introduced into service, there was a growing need for an effective training at the ranges, with adequate real-time data acquisition and post-mission data analysis tools.

Therefore, between 1997 and 1998 the Italian Air Force set the requirements for upgrading the PISQ test/training range (Poligono Interforze del Salto di Quirra –

Sardinia – Italy), adding new facilities for carrying out safe training and experimental activities with airborne and ground laser systems, together with LGW delivery tests.
According to the initial requirements, the PILASTER (**PI**SQ **LAS**er **T**est and **E**valuation **R**ange) research and development program was divided in two different phases. The aim of the first phase of the program (1999-2002) was to provide an initial operational capability for carrying out, in fully safe conditions, ground tests and flight experimental activities (with related measurements and semi-automated data analysis), required for performance evaluation of military laser systems. The successive phase of the program (now ongoing) is aimed to implementing the PILASTER full operational capability, required for performing all laser test/training activities, including all mission planning and fully-automated post-mission data analysis tasks.

1.2 Aim of Research

The main objective of this research is to design, develop and test a new laser range for the training and experimental activities required by the Italian Air Force. This includes the design of new range instrumentation and facilities, development of innovative methods for military systems performance prediction/evaluation, determination of eye-safety requirements for employment of ground and airborne laser systems at the range both during experimental and training activities, and extensive laboratory, ground and flight test activities with state-of-the-art ground/airborne laser systems and weapons.

1.3 Outline of Research

This thesis describes the research work performed for designing, developing and testing the PILASTER laser range for the Italian Air Force. This paragraph gives an outline of the format of this thesis.

Chapter 2 describes some of the airborne laser systems fundamental concepts more relevant to this research and gives an overview of the main applications encountered in

the operational field. Particularly, chapter 2 reviews current laser technology status and future technology trends, with particular emphasis for the systems now in service or under development for the Italian Air Force. These include the Convertible Laser Designation Pod (CLDP), various types of LGB's and the *Marconi-Selenia Communications* Laser Obstacle Avoidance System (LOAS) for helicopters. More detailed information about the relevant laser technologies, and further discussion about the various airborne systems applications, are presented in Appendix A.

Chapter 3 discusses the key elements of laser systems performance analysis, with the aim of introducing the mathematical models required for operational mission planning and simulation. Particularly, suitable forms of the laser range equation are developed, for determining the performance of ground and airborne laser systems under specific conditions and with various types of targets. Furthermore, an outline is presented of the laser beam atmospheric propagation models used for PILASTER test/training operations (i.e., mission planning, safety studies and performance analysis) with ground/airborne laser systems. Finally, chapter 3 discusses target reflection properties, and presents the operational considerations necessary for laser systems performance analysis (i.e., target/spot size, system error sources and effects, mission geometry, etc.). More detailed information about the various laser systems performance issues are given in the Appendixes B, C and D. Particularly, a discussion of laser systems range and detection performances is presented in Appendix B, fundamentals of laser beam propagation physics are given in Appendix C, and laser reflection properties are discussed in Appendix D.

The PILASTER test/training range requirements are described in chapter 4. Particularly, the laser range concept of operation is illustrated, and the general systems requirements set in 1998 for the PILASTER program are presented. These include requirements for both training and experimental activities, with a conceptual definition of the systems necessary both in the range operational area (i.e., targets, sensors, area-networks, etc.), and in the remote control-room.

Detailed information about the PILASTER design and technical characteristics, progressively refined during the various implementation phases of the program, are presented in chapter 5. Particularly, the PILASTER Sensor Tracking and Measurement Unit (STU) and remote Monitoring and Control Station Unit (MSU) systems design is presented. The PILASTER STU system allows accurate measurement on the ground (i.e., targets locations) of various important laser parameters (i.e., beam pointing accuracy, energy received at the target location, spot geometry on the target, etc.). These information are recorded at the STU and passed, through the range local and wireless area networks (LAN/WAN) to the MSU placed in the remote control-room. All information required for real-time mission management (i.e., eye-safety verification and test/training operations) are then displayed and recorded, in suitable formats, at the PILASTER MSU.

The methods developed for evaluating the hazards associated with the use of ground and airborne laser systems, are presented in chapter 6. Particularly, safety issues of state-of-the-art Nd :YAG target designators are thoroughly investigated, in order to identify operational procedures and limitations for the employment of such equipment at the PILASTER range during execution of both test and training missions.
Various mathematical algorithms are presented, developed for the PILASTER simulation and mission planning tools, that allow a complete verification of laser-safety for ground and airborne laser systems.

In order to optimise the employment of the systems in service (e.g., LTD's and LGW's), as well as for developing new systems (e.g., PILASTER sensors, LOAS), and fully defining test/training range requirements, it was essential to perform a number of experiments. Some of these experiments, such as determination of LGW seeker detection thresholds, PILASTER sensors selection/calibration and measurements of target materials reflection properties, were conveniently performed in a laboratory facility. Other important measurements and tests were performed during appropriate field and flight test sessions.

Chapter 7 describes the laboratory experimental activities carried out during this research. These include:

- Determination of LGW Seekers Detection Thresholds;
- Measurements of Surface/Paints Reflection Properties (PILASTER targets);
- PILASTER Sensors Testing and Calibration;
- LOAS Laser System Testing;
- Test of Laser Protection Filters (Cinetheodolites, Ground Personnel and Aircrew).

Particularly, the specific test aims, test methods (i.e., instrumentation requirements, details of measures performed, etc.) and test results, are presented in this chapter.

Ground experiments performed during this research are described in chapter 8. These include NIR laser beam atmospheric propagation measurements, LTD/LRF pointing accuracy tests, systems harmonisation and performance evaluation trials of the STU and Differential GPS (DGPS) components of the PILASTER system. Furthermore, dedicated ground trials were performed on the LOAS system in order to assess its detection performance (in various weather conditions), and to verify the reliability of its obstacle classification algorithms. The various test objectives and procedures, instrumentation employed and methods of analysis are described in chapter 8, together with results of the ground experimental activities.

Chapter 9 describes the flight test activities performed during this research and gives indications about further activities planned for the future. Flight test activities performed as part of the PILASTER development project, included the following:

- Propagation Measurements in Oblique Air-to-ground Paths;
- CLDP Pointing Accuracy Measurements (TORNADO-IDS);
- CLDP FLIR Systems Flight Testing (TORNADO-IDS);
- MB-3339C DGPS Flight Trials;
- TORNADO-IDS DGPS Flight Trials;
- LOAS Preliminary Flight Trials on the NH-300 Helicopter;
- LOAS Final Flight Trials on the AB-212 Helicopter.

Particularly, the PILASTER STU and MSU systems were tested during their employment in real air-to-ground missions (both with and without deliveries of guided weapons). With the PILASTER systems in their operational configuration, atmospheric extinction measurements were performed with typical air-to-ground mission geometries (i.e., oblique laser paths), and the correction factors for the ESLM sea-level atmospheric propagation models were determined in these conditions. CLDP pointing accuracy (from geometric and energy spot measurements) was also determined during the TORNADO-IDS flight test campaign and CLDP FLIR systems tests were performed with various aircraft-target geometries.

The DGPS test activities were performed with the aim of selecting a suitable Position Reference System for both experimental and training activities (i.e., real-time and post-flight mission trajectory data analysis). Furthermore, the aircraft envelope limitations associated with the use of airborne GPS systems were determined.

The LOAS flight test activities were carried out in order to verify the functionality of the system in a representative operational environment (i.e., system detection performance in various weather conditions and with various obstacle scenarios), and to assess the efficiency of the LOAS obstacle classification/prioritisation algorithms.

Chapter 10 is dedicated to the simulation tools developed during the PILASTER program for systems eye-safety and performance analysis. The mathematical models developed during the research were incorporated in the PILASTER simulation tools, allowing definition of test/training mission constraints and operational feasibility, together with post-mission data analysis. The assumptions adopted for implementation of the various algorithms in the PILASTER simulation/analysis programs are presented in this chapter, together with results of some relevant simulation tasks performed.

Finally, chapter 11 summarises the main achievements of this research and outlines suggestions for further work.

Chapter 2

LASER SYSTEMS OVERVIEW

2.1 General

Since the early days of laser technology, many countries supported large laser R&D budgets which leaded to a rich diversity of systems, ranging from 'laboratory' systems demonstrating the latest non-linear optical technology to eye-safe, low cost laser-ranging binoculars. Traditionally, military interests in laser systems has been concentrated in four general areas: Laser Rangefinders (LRF's) and Target Designators (LTD's), Laser Radars (LADAR's), Laser Communication Systems (LCS's), and Directed Energy Weapons (DEW's). The nature of the interest in laser technology is, for a considerable part, significantly dissimilar for the three military service branches, and this is mainly due to the different requirements (e.g., environmental, weight/size, performance, etc.) of systems to be used on land, at sea, and in the air. Although military lasers are significantly different from those which exist in the commercial world, commercial applications of military technologies are being also exploited.

Due to the aim of the present research, in this chapter we will review the fundamentals of the most popular of current airborne and ground tactical laser systems (i.e., LADAR/LRF and LTD), with particular emphasis for the systems currently in service or under development for the Italian Air Force. More detailed information about the relevant laser technologies, and a discussion of various airborne systems applications, is presented in Appendix A.

2.2 Laser Rangefinders and Target Designators

Range finding was the first military application of laser technology. Operational range finders were introduced into the armed forces as early as the mid-sixties, only five years after Theodore Maiman presented the first working laser. Since then, thousands and thousands of Laser Range Finders (LRF's) and Laser Target Designators (LTD's) have been delivered to the defence forces in many countries all over the world. Today, LRF's and LTD's are necessary parts of modern Weapon Aiming and Fire Control Systems.

The high radiance and narrow beamwidth of the laser makes it possible to determine distances with great accuracy. The accurate range and angle information provided by the LRF in modern Fire Control Systems (FCS's) is responsible for a major advance in the precision and effectiveness of weapons in battlefield conditions. Additionally, shrinking defence budgets make it more attractive for military organizations to upgrade existing systems rather than to procure new ones. Integration of a modern LRF in military platforms can provide major performance enhancement at modest cost, particularly compared to all-new systems. A variety of laser technologies have been applied to rangefinders and Neodymium-Yttrium Aluminium Garnet (Nd:YAG) LRF's, operating at a wavelength of 1064 nm and based on the principle of pulse time-of-flight measurement, are the state-of-the-art. The advent of inexpensive eye-safe systems in the military field offers both the opportunity for expanded training and new applications. LRF's operating at 1530-1550 nm, based on Er:fiber and Raman-shifted Nd:YAG lasers, may be used were eye-safety is fundamental. CO_2 eye-safe LRF's, operating at 10.6 μm, have been developed in many configurations and they can play a significant part in conjunction with passive thermal imaging systems and other multi-functional system applications.

Laser Target Designators (LTD's) and Laser Guided Weapons (LGW's) were developed in order to satisfy the military requirement for weapon systems (i.e., bombs and missiles) capable of pinpoint accuracy, especially when the target is relatively small and well defended. Until recently, there have only been two alternatives to deal with

this kind of situation: either get close enough to the target to make certain of a hit or use some kind of blanket bombing over a fairly large area. Closing in the target may be extremely dangerous and, if it is well defended, could lead to a high casualty rate. On the other hand, blanket bombing may not be effective in destroying the target or may require excessive amounts of ammunition. Furthermore, a concern particularly important in current conflict scenarios is the reduction of collateral damage. This has forced the military into the development of 'smart munitions' which easily pinpoint specific targets. The LTD is an essential element for the operation of these sophisticated weapon systems. For operation of LGW's or 'smart munitions', a coded laser beam from the LTD is directed at the target. The reflected pulses from the target are scattered in many directions. They are detected by the LGW (bomb or missile) target seeker, which is a sensor on the head of the LGW responding to the same code as in the beam. The missile/bomb, which normally is fired from a distant place (e.g., an aircraft), will thus home in on the target and destroy it.

From the description given, it appears evident that, with simple design modifications (e.g., specific laser coding), a LRF can serve admirably as a target designator and it has the added advantage of simultaneously providing slant range to the target.

A technical introduction to LRF, LTD and LGW systems is given in Appendix A. In the following paragraphs, we present an overview of the relevant technical characteristics of the systems in service with the Italian Air Force.

2.3 Italian Air Force LTD/LGB Systems

Since the beginning of the 90's, the Italian Air Force Flight Test Centre (RSV) has been involved in various activities related with laser guided weapons and designation systems for airborne and ground applications. Particularly, the *Thomson* Convertible Laser Designation Pod (CLDP) with both TV and IR capabilities have been integrated on TORNADO-IDS aircraft, together with Laser Guided Bombs (LGB) of various characteristics (PAVEWAY II and III), and a Ground Laser Target Designator (GLTD) has been also tested by RSV and introduced into service with Air Force Ground Troops (AGT) and Army Forward Air Controllers (FAC's). Other activities currently

ongoing, include integration of CLDP on the AM-X aircraft and of LIZARD LGB on the AM-X and TORNADO aircraft. Future activities include integration of a new generation Laser Designation Pod (LDP) on *Eurofighter* Typhoon, and enhanced PAVEWAY III (i.e., GPS aided laser guidance) on both TORNADO and Typhoon aircraft.

Figure 2-1. TORNADO PAVEWAY II Flight Trials.

The CLDP system is designed for day/night self-designation and cooperative attacks, and can also perform accurate navigation fixes (i.e., range finding). In the TORNADO-IDS integration scheme, CLDP is a non-jettisonable store and is carried on the forward section of the aircraft left shoulder pylon.

GBU-16 (PAVEWAY II) LGB is an MK-83 1000 pounds warhead, equipped with second generation modular electronics and mechanical assemblies designed to provide the weapon with a laser bang-to-bang guidance capability, for medium and high altitude attacks.

GBU-24 (PAVEWAY III) is the third generation of laser guided munitions, composed by a 2000 lbs warhead (MK-84/BLU-109) and a proportional-guidance system. Specifically designed to enhance low altitude delivery (hence the name LLLGB – Low Level Laser Guided Bomb), the weapon characteristics also greatly simplify medium and high altitude deliveries.

LIZARD is a medium-high altitude LGB with proportional guidance and a standard MK-82 (500 lbs) warhead, recently integrated on the AM-X aircraft. The LIZARD has physical characteristics (i.e., mass distribution, mechanical interfaces, etc.) identical to the OPHER IR Guided Bomb (IGB), previously in service with the Italian Air Force (this fact greatly simplified the activities required for LIZARD-aircraft integration).

In the following paragraphs, after a brief technical description of the CLDP and GLTD systems characteristics, relevant information is provided about LGB's currently in service with the Italian Air Force (i.e., GBU-16, GBU-24 and LIZARD).

2.3.1 CLDP Description

The Convertible laser Designation Pod (CLDP) is a system designed to provide the aircraft with day and night laser designation capability, for cooperative and self-designation attacks performed using laser-guided weapons. The pod is equipped with an internal designation laser operating at 1.064 μm (non-eyesafe region of the spectrum) and may be configured for day-time operation by using a television camera (TV) or for day/night operation by using an IR sensor (IR). The TV configuration may also provide daytime advantages in high humidity conditions. In its subsidiary role, the CLDP can also act as a sensor for navigation fixing including height fixing.

As shown in Fig. 2-2, both CLDP configurations consist primarily of two sections: an interchangeable front section containing a TV sensor head or IR sensor head, and a common body containing a central section and a rear cooling unit [1].

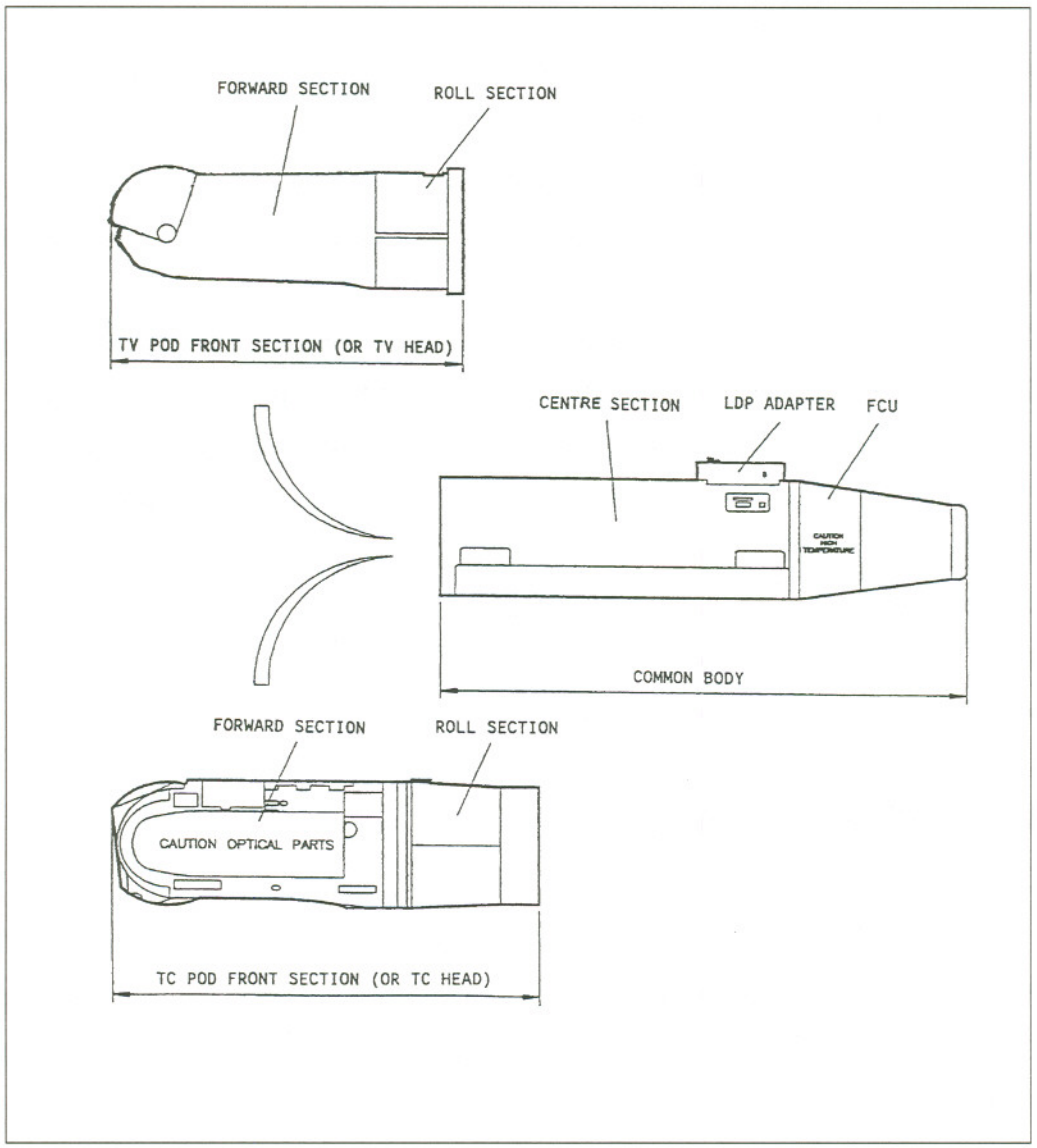

Figure 2-2. CLDP TV and IR configurations.

In the TORNADO-IDS integration scheme [2], the CLDP is a non-jettisonable store and is carried on the forward section of the aircraft left shoulder pylon (Fig. 2-3).

In conjunction with the Main Computer (MC), real time video with CLDP symbology is displayed on the aircraft TV/TAB navigator's displays, and the CLDP related symbology is displayed on the pilot's Head-Up Display (HUD).

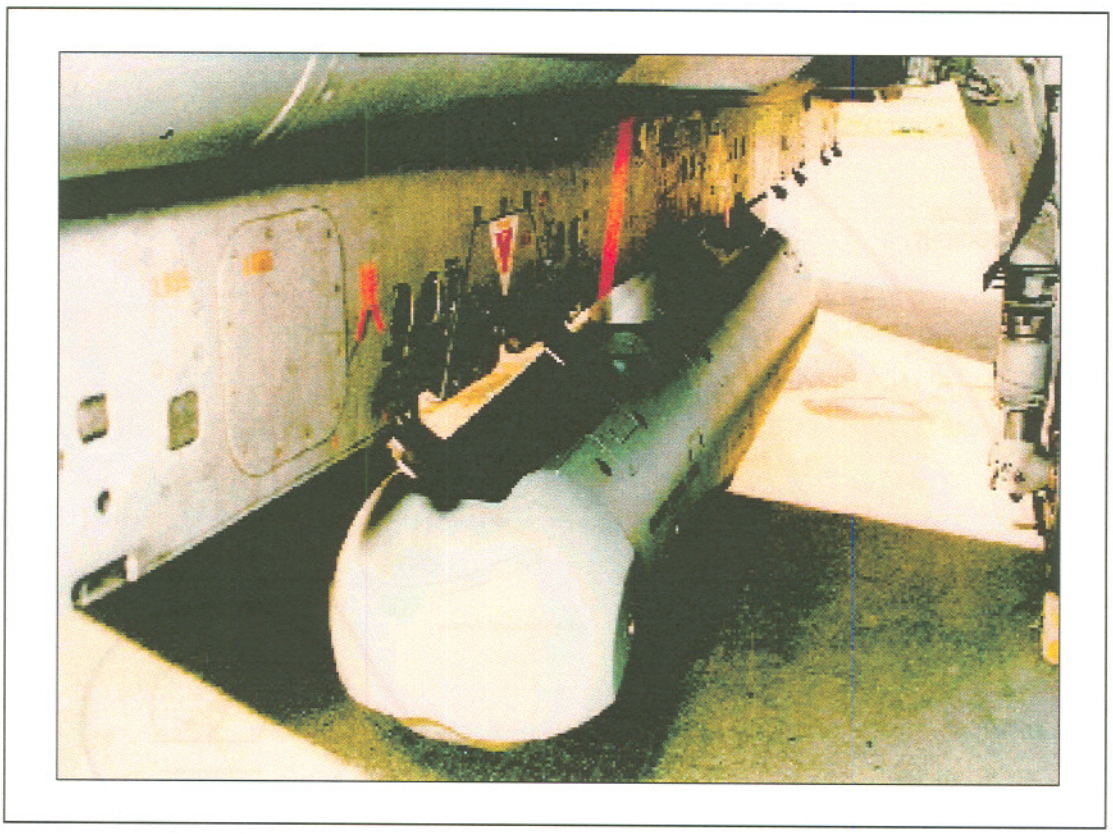

Figure 2-3. TORNADO-IDS CLDP installation.

An electrical adaptor installed on the back of the centre section provides the electrical interface between the CLDP and the aircraft. The adaptor interfaces with the MC via the aircraft Missile Control Unit (MCU), using a MIL-STD-1553B data bus.

TORNADO CLDP main functions are selected by the Weapon System Operator (WSO). Commands and controls are located in the TORNADO rear cockpit. Pod Line of Sight (LOS) controls are located both in front and rear cockpits (Fig. 2-4). The various CLDP functions (automatic or selectable by the crew) are described in the following sub-sections.

System Initialization. The pod is switched on via the CLDP control panel (CP) located in the rear cockpit (Fig. 2-4). The system executes a start-up sequence, checking CLDP internal equipment status. At the end of sequence the pod enters the stand-by mode.

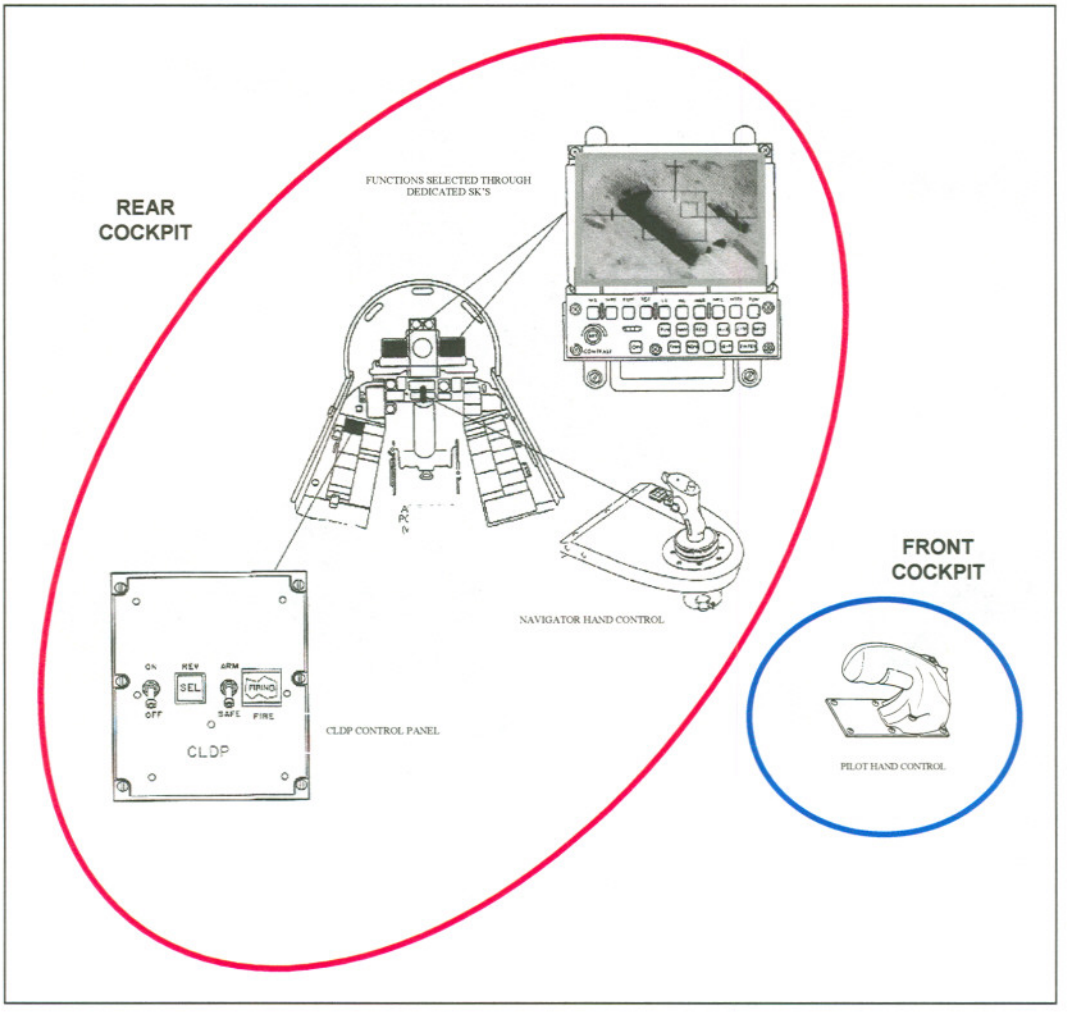

Figure 2-4. CLDP cockpit controls.

CLDP system Status Check. The system continuously checks the integrity of CLDP-aircraft communication, advising the crew of failure occurrences. If an internal equipment failure is detected by the system, a specific warning is shown on the WSO display (TV-TAB). Further advise of pod internal sub-system failure is also given to the WSO by mean of a dedicated TV-TAB CLDP format which can be recalled through a display "soft key".

Slave Modes. The CLDP LOS pointing is controlled through direction cosines calculated in the aircraft MC. Furthermore, pointing can be adjusted manually using the

Navigator or Pilot Hand Controls (NHC/PHC). The following Slave modes are available:

- *Slave-Slave.* The LOS points at the target or at a fix-point provided that the system is in Fixing or in Attack mode. In this mode the LOS pointing is fixed to the target virtual position.

- *Slave-Ground Stabilized.* LOS position can be adjusted via NHC inputs. In this mode the LOS is ground stabilized to the target position, taking into account the NHC demands.

- *Slave-Cage.* LOS points straight ahead in azimuth and 4° down in elevation.

- *Slave-Manual.* LOS direction can be controlled via NHC input. Starting in a Slave-Cage position (system in navigation mode), LOS pointing can be adjusted via NHC. In this mode LOS is not ground stabilized (no target/fix-point is recognized by the aircraft MC).

Track Modes. The pod enters in Track mode from Slave on WSO selection. With the Tracking mode selected, the pod does not consider the MC inputs in terms of LOS direction cosines but it maintains the LOS overlapped to the target by itself, using one of the two available sub-modes:

- *Tracking by Area Correlation (TAC).* CLDP performs a digital store of the whole video image which is then superimposed onto the actual live image. The correlation between the two images generates commands to move LOS consequently. However, LOS can be manually oriented provided that NHC is selected for CLDP use.

- *Tracking by Image Contrast (TIC).* CLDP performs a digital scan of the video image looking for an area of high contrast with the background. The CLDP will then correct LOS position over that area, focused to the video centred image. If the position is manually adjusted via NHC, then this function is disabled and the TAC mode is automatically re-selected.

Masking. CLDP LOS pointing is limited by aircraft masking effects (i.e., obscuration of the CLDP line-of-sight due to impingement of the aircraft body). The CLDP automatically prevents the laser from firing on aircraft structure and external stores. Together with aircraft profile (including stores), the masking function also takes into account the CLDP Blind Cone (CLDP rear). A pre-masking function is also available to warn the aircrew of the mask limit proximity.

Computed Rate Track (CRT). The CRT function is automatically selected whenever Tracking mode loses "good track" or at the occurrence of a mask impingement. In CRT mode the LOS is aimed to the target by CLDP computer using the aircraft velocity, attitude and slant-range to target information provided by the MC.

Pod/Aircraft Harmonization (P/A). The Pod/Aircraft (P/A) Harmonization procedure must be performed every time the pod is installed on aircraft. The procedure corrects the misalignment between the CLDP and the aircraft axes. Providing that the pod is in Track mode, this function can be performed through WSO and Pilot co-operation (Pilot method) or by WSO only (Navigator method). During the P/A Harmonization procedure, the misalignment in Z and Y rotation axes (vertical and transverse axis) is calculated by the system and stored in a pod not-volatile memory as delta-pilRh and delta-yaw angles to be added to the azimuth and elevation LOS pointing.

Video/laser Boresight (V/L). The V/L Boresight function is used to check the laser efficiency and to correct any laser/optical axis misalignment. This function is required to be executed before attack/fixing.

Reversionary. The Reversionary mode is automatically selected if the Weapon or Avionic Bus fails, the Weapon Bus is shut-down as result of MC failure or Re-cycle, or the MCU fails. When in Reversionary mode the pod is still capable of tracking and illuminating the target.

CLDP Target/Navigation Fixing. CLDP can be used as a sensor for navigation/target fixing purposes, in the following modes:

- *Plan Fixing* (no laser operation). CLDP LOS angular position and selected height sensor data are used to calculate the aircraft position with respect to target/fix-point.

- *Three Dimensional Fixing* (laser operation). Laser Range and LOS angular position are used to calculate aircraft position with respect to the target/fix-point.

Designation Attacks. The system allows for:

- *Self Designation Attacks*, in which the aircraft acts as illuminator for the own carried LGB's. The following bombing attack profiles can be performed during self-designation attacks:

  - GBU 16: Dive, Level, Loft.
  - GBU 24: Dive, Level.

- *Co-operative Designation Attacks*, in which the aircraft acts as the illuminator for partner(s) aircraft. Co-operative profiles can be chosen between:

  - NSTR (No Steering), in which aircraft is driven direct to over-fly the target.
  - STR (Steering), in which aircraft is driven to pass tangent to the Lethal Range (LR) according to pre-planned Heading Change (HC).

The laser can be operated by a pre-planned counter (Real Time or Count Down) or manually. Co-operative attack steering laws require that the attack is initiated respecting the aircraft to target minimum distance (break-off point not yet reached) and track angle error within the operational limits, as shown in Fig. 2-5. If one or both of these limits are exceeded, the aircraft will not respect proper steering and will not perform properly the expected turn or will not acquire the planned heading change.

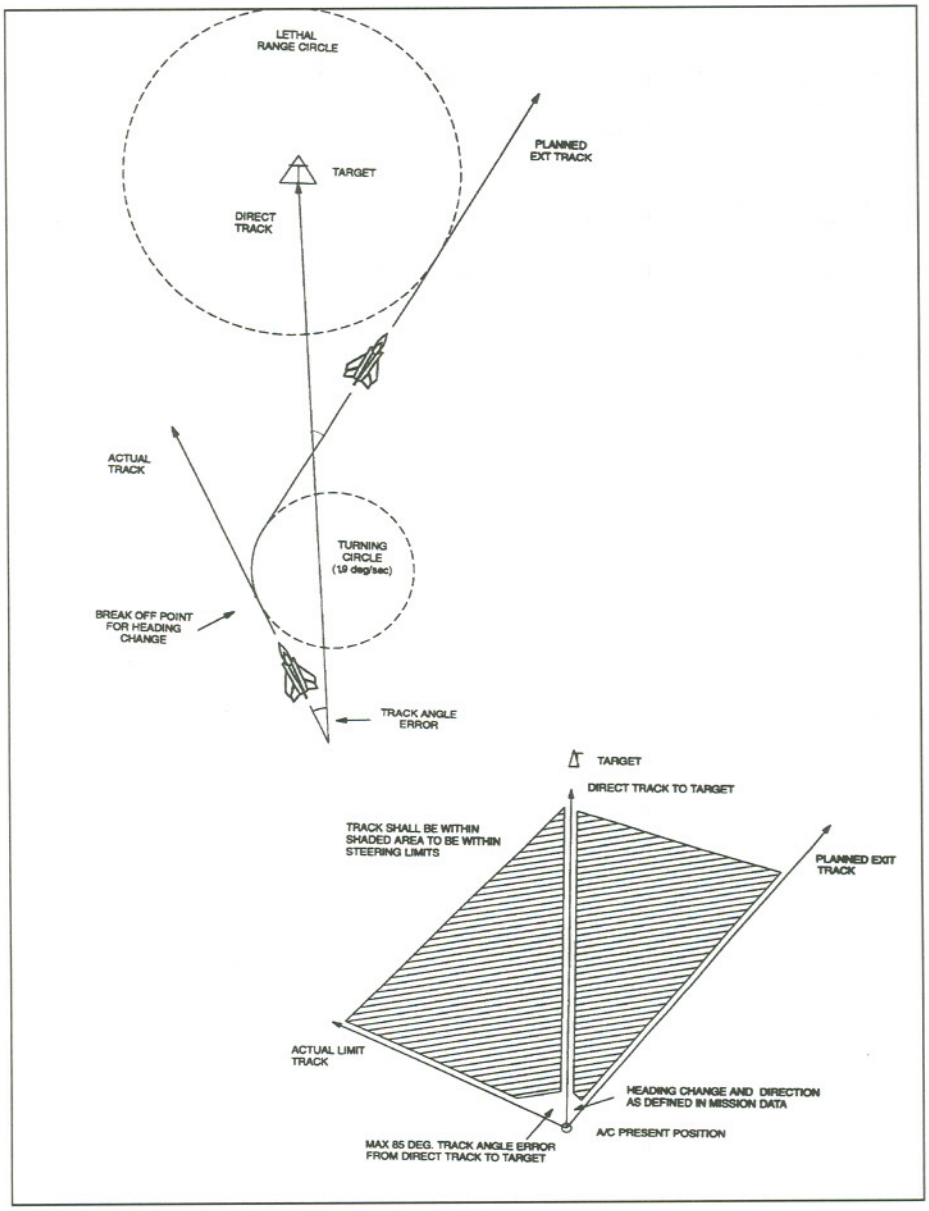

Figure 2-5. CLDP co-operative attack steering laws.

2.3.2 ELOP-GLTD System Characteristics

The ELOP-GLTD system, in service with the Italian Air Force, is designed for day-night operations with LGW's and is equipped with a Remote Control (RC) and a Tactical Computer (TC) where the distance, azimuth, elevation and WGS-84 geodetic

coordinates (obtained from a GPS) of the target are displayed. As shown in Fig. 2-6, the ELOP-GLTD system is constituted by the following main components [3]:

- Portable Laser Designator (PLD)
- Artillery Thermal Imager Module Long-Range (ARTIMLR)
- Traversing Unit (TU)
- Tactical Computer (TC)
- Computer Heater Battery
- Remote Control (Fire Switch)
- Tripod
- Battery Pack
- Communication Cable
- Power Cable

The system is based on the PLD. This unit enables viewing and acquisition of targets, designating them and measuring their range. Night vision is obtained by the ARTIMLR. The PLD and the ARTIMLR are attached to the TU, which allows the maneuvering of the system during the search for targets or their tracking, by easy change of azimuth and elevation angle. The TU is mounted on the Tripod, that allows setting up and leveling of the system on practically any terrain. The handheld TC is attached to the system components. The computer enables data processing, navigation and target coordinates assignment (it contains a GPS receiver). The computer is connected to a heater battery for extremely low temperature operation. The PLD is powered by an external power source (battery). The ARTIMLR is powered by an attached battery pack. The handheld TC is powered by internal batteries.
The ELOP-GLTD system functions are:

- Air strike support and laser designation.
- Range finding and artillery fire control.
- Acquisition and management of targets bank.
- Northing with a manual compass.
- Positioning and navigation using the internal GPS receiver.

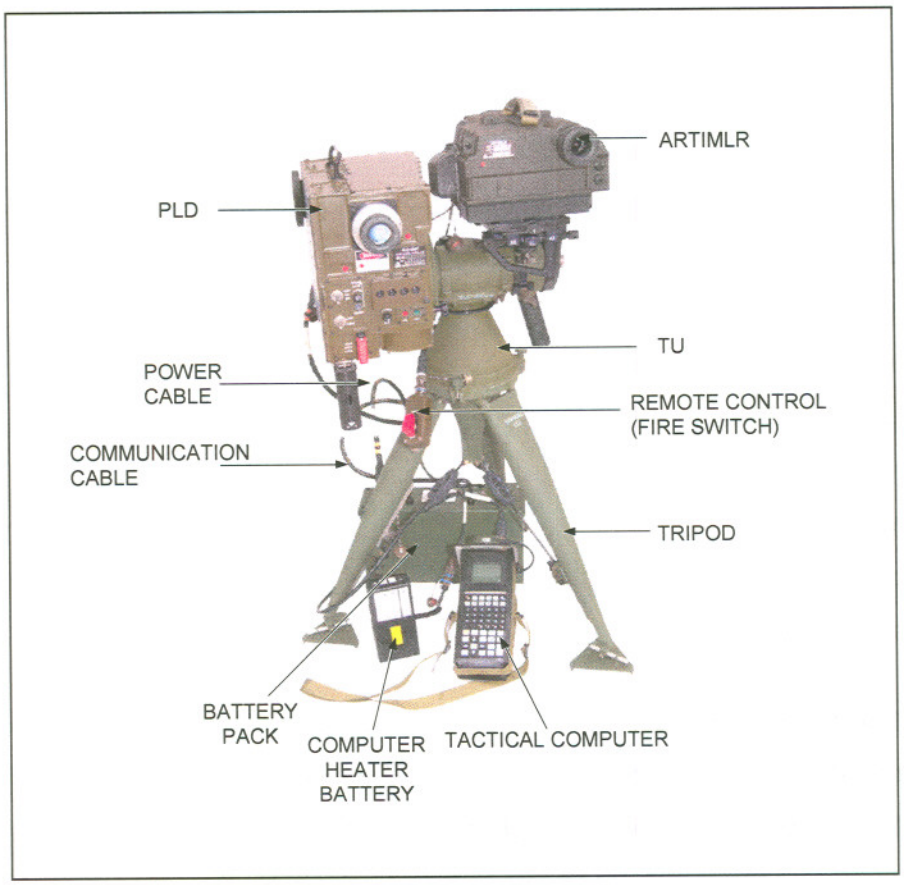

Figure 2-6. ELOP-GLTD system composition.

The ELOP-GLTD system can be carried by three soldiers and can be dismantled and reassembled easily and quickly under any field conditions. The main technical characteristics of the ELOP-GLTD system are listed below.

ELOP-GLTD System

- Azimuth Range 360°
- Elevation Range ±20°
- Tripod Weight 2.8 kg
- TU Weight 7 kg
- Battery Pack Weight 6.1 kg

PLD Designator

Transmitter

- Output Energy 130 mJ
- Beam Divergence 130 µRad (85% of output energy)
- Laser Beam/LOS Boresight 80 µrad
- Maximum Lasing Rate 20 PPS
- Coding PRF (NATO Code)

Range Receiver

- Range Discrimination 30 m
- Sensitivity 49 dB for a white diffusive target at 500 m
- Range Measurement 250 to 19990 m

Sight Performance

- Telescope Magnification ×13
- Field of View 5.5°
- Eye Protection 45 dB for 1.064 µm

ARTIMLR

Performance Characteristics

Spectral Sensitivity	8 µm - 10.5 µm
Fields of View (FOV) - Narrow (H x V) - Wide (H x V)	 2.1° x 1.3° ± 0.2° 7.3° x 4.5° ± 0.5°
FOV Change	Electrically activated
Focus Change	Electrically activated
Focus Range	200 m to infinity in the NFOV 50 m to infinity in the WFOV
Reticles	Electronically generated reticle with different patterns for WFOV and NFOV as shown in Fig. 2-7.
Operating Time	2 hours with Standard NiMH battery (continuous operation at room ambient temperature).

Table 2-1. ARTIMLR performance characteristics.

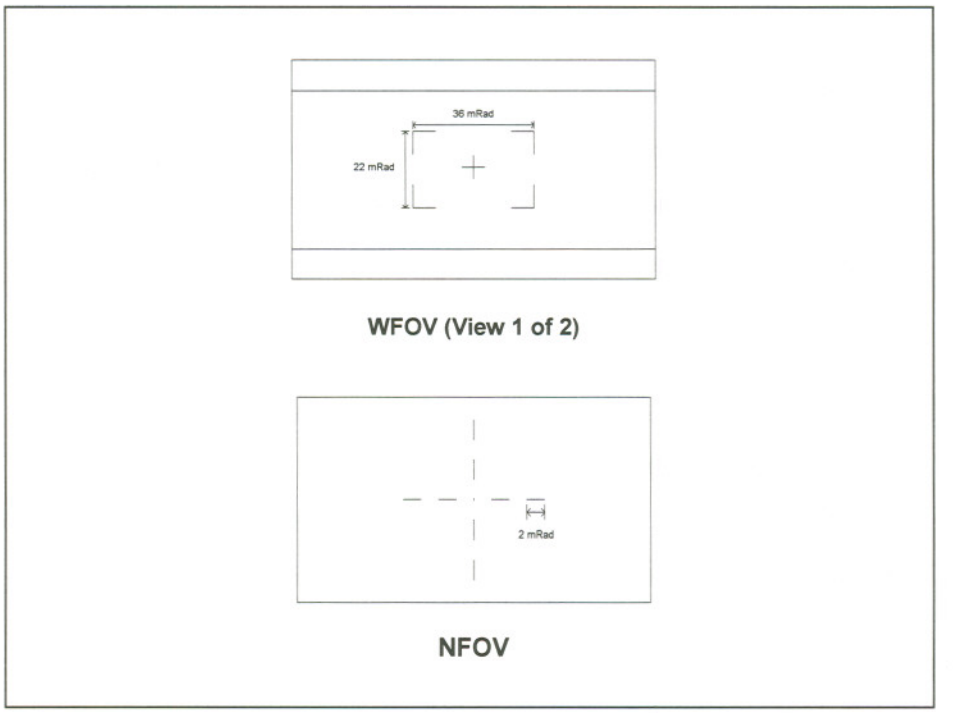

Figure 2-7. ARTIMLR reticle patterns - WFOV and NFOV.

2.3.3 GBU-16 (PAVEWAY II) Description

The GBU-16 (PAVEWAY II) laser Guided Bomb is an MK-83 1000 pound warhead, equipped with second generation modular electronics and mechanical assemblies designed to provide the weapon with the capability for laser terminal guidance [4]. Particularly, the GBU-16 consists of a forward Computer Control Group (CCG) including control canards and an aft wing assembly, attached to the MK-83 body (Fig. 2-8). The Detector Unit Housing (DUH) is mounted on the front section of the CCG and is free to gimbal (move laterally) in any direction, and is aerodynamically stabilised by the ringtail molded into the rear of the detector assembly housing. To a first approximation the detector is aligned with the velocity vector of the weapon. The detector senses laser energy reflected from an illuminated target. The detector output is amplified and converted into commands that are transmitted to the forward control fins (or canards).

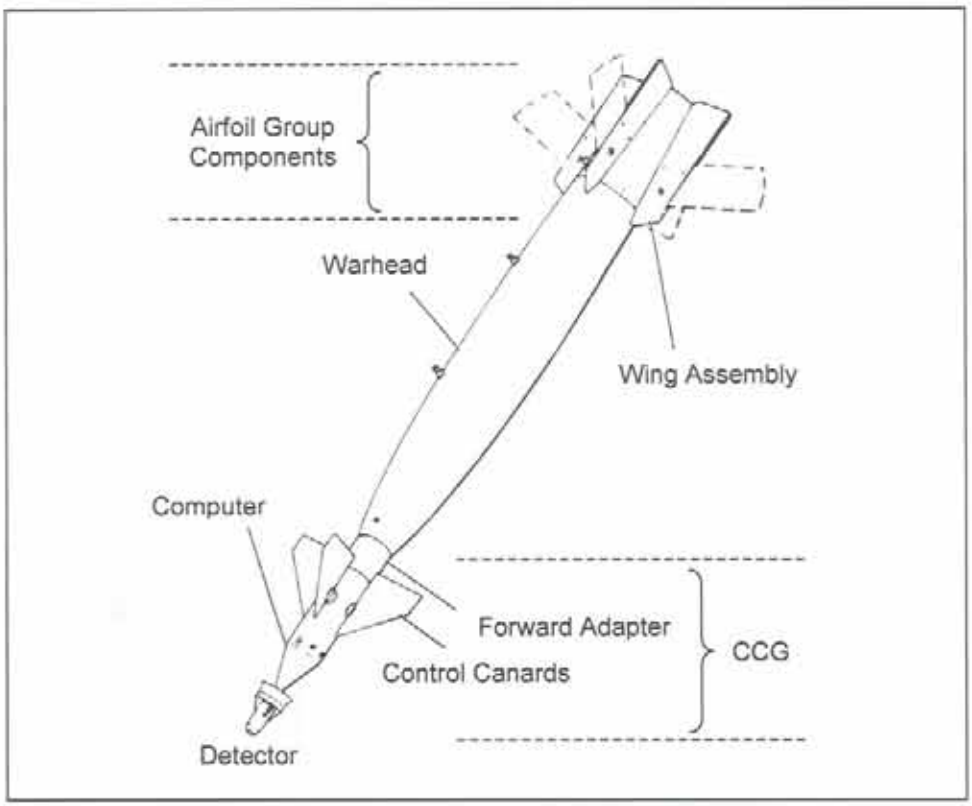

Figure 2-8. GBU-16 configuration.

GBU-16 guidance is provided by a "Bang-Bang" control. When the computer senses a position error, the control fins are driven to the limit of their travel by high-pressure gas, regardless of the magnitude of the error. Therefore, the control fins are either at the trail position or full deflection during guidance. The GBU-16 guidance system attempts to fly a straight-line trajectory from its present location to the illuminated target. At acquisition, the computer section of the guidance unit recognises the angular difference between its flight path (velocity vector) and the LOS from its present position to the illuminated target (guidance error angle). By adjusting the GBU-16 flight path to reduce the magnitude of this error, the weapon can be guided to the illuminated target.

The GBU-16 is designed for medium and high altitude attacks, performed both in level and dive conditions. Nevertheless, theoretically the bomb may be dropped in loft conditions, although the associated release envelope is narrowed and the delivery accuracy is degraded.

2.3.4 GBU-24 (PAVEWAY III) Description

The GBU-24 (PAVEWAY III) is the third generation of laser guided munitions that were developed during the Vietnam era. Specifically, designed to enhance low altitude delivery (hence the name LLLGB – Low Level laser Guided Bomb), the weapon characteristics also greatly simplify medium and high altitude deliveries [5]. The PAVEWAY III series of weapons consist of a nose mounted guidance unit and an aft wing assembly which can be mounted on various classes of warheads (see Fig. 2-9).

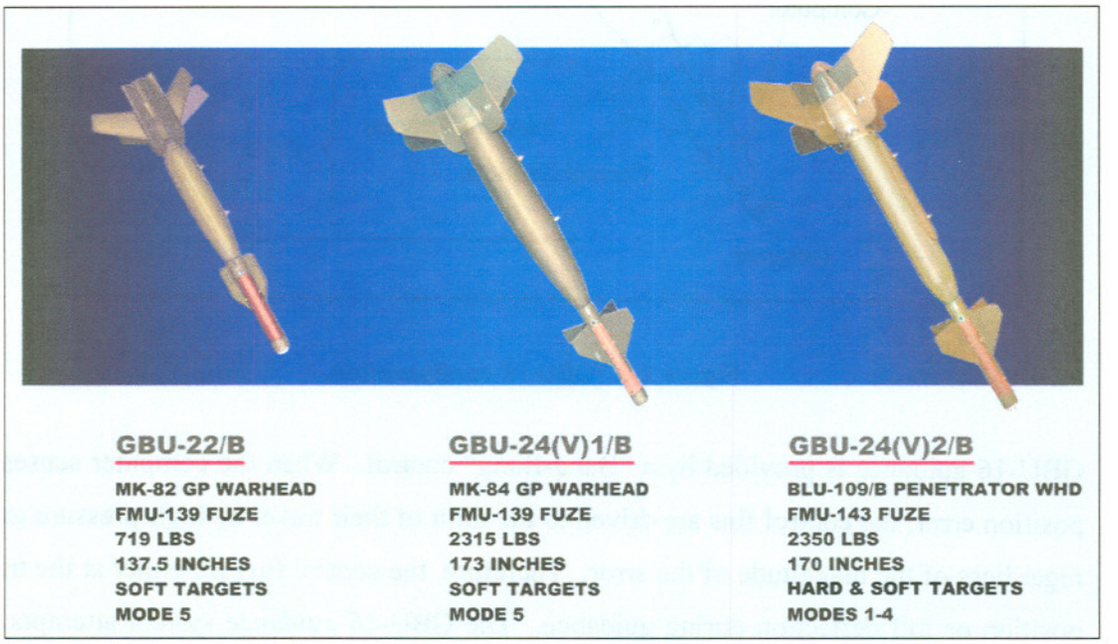

Figure 2-9. Paveway III family.

The Italian Air Force selected two 2000 pound bombs, namely the MK-84 (complete assembly GBU-24(V)1/B) and BLU-109 (complete assembly BGU-24(V)2/B) high penetration warhead. As in the case of PAVEWAY II, PAVEWAY III LGB is loaded, released, or jettisoned using the same ground equipment and aircraft systems used for employing conventional, unguided warheads. Operation is independent of the aircraft except for normal suspension and release functions. No electrical interface or aircraft

Appendix C

LASER BEAM PROPAGATION IN THE ATMOSPHERE

C.1 General

As briefly illustrated in chapter 3, the laser beam is attenuated as it propagates through the atmosphere, mainly due to absorption and scattering phenomena. In addition, the beam is often broadened, defocused, and may be deflected from its initial propagation direction. These atmospheric effects have important consequences for the use of lasers in weaponry, target designation, ranging, remote sensing, and all other applications that require transmission of laser through the atmosphere. The attenuation and amount of beam alteration depend on the wavelength of operation, the output power and the characteristics of the atmosphere. When the output power is low, the effects are linear in behaviour. That is, doubling the initial beam intensity results in a doubled intensity at every point along the propagation path. Absorption, scattering, and atmospheric turbulence are examples of linear effects. On the other hand, when the power is sufficiently high, new effects are observed that are characterised by non-linear relationships. Some important non-linear effects are thermal blooming, kinetic cooling, beam trapping, two-photon absorption, bleaching, and atmospheric breakdown, which, incidentally, fixes an upper limit on the intensity that can be transmitted. In both cases the effects can be significant and severely limit the usefulness of the beam.

C.2 Molecular Absorption and Scattering

Some features of the interaction of laser beams with the atmosphere are different than those encountered in routine practice with conventional optical systems. Most of these differences are the result of the interaction of the highly

monochromatic laser radiation with the fine structure of the atmosphere. Particularly, molecular absorption and scattering are the dominating attenuation phenomena, both of which are strongly wavelength dependent.

Conventional (passive) electro-optical systems typically operate over bandwidths that are large compared to the width of most molecular absorption lines. As a result, the response of passive systems is integrated over the entire band and the effects the fine structure of the atmosphere are averaged out. These effects, however, are most severe for (active) laser systems, that typically operate over long ranges and use a naturally occurring atmosphere gas as the laser gain medium. In these cases, there is an unavoidable coincidence of the laser line with an atmospheric absorption line.

The fine structure of the atmosphere can also have significantly different effects on the atmospheric transmission of the transmit and receive paths of an active system like a LRF or a LADAR. If the transmitter or the target is in motion, the *Doppler* effect will shift the carrier wavelength on transmission or reflection respectively. Particularly, a transmitted laser line, which normally does coincide with an atmospheric absorption line, can be *Doppler* shifted so that it experiences significantly higher attenuation. Although this is a rare occurrence, the system design of the laser system must consider the manner in which it will be used to ensure that such conditions are avoided.

C.2.1 Molecular Line Absorption

When we consider molecular absorption only, the fraction of monochromatic radiation transmitted (or the transmittance) is given by:

$$\tau(f) = e^{-\alpha(f)z} \tag{C.1}$$

were $\alpha(f)$ is the frequency-dependent absorption coefficient and z is the path length. Eq. (C.1) is valid when the absorption coefficient is constant for the entire path length z. To describe slant path propagation where $\alpha(f)$ is not a constant over the path length, one uses the more general expression:

$$\tau(f) = e^{-\int_0^l \sigma_a(f) N dr} \tag{C.2}$$

where $\sigma_a(f)$ is the absorption cross section, N is the number density of absorbing molecules, and the integration extends over the propagation range of length l.

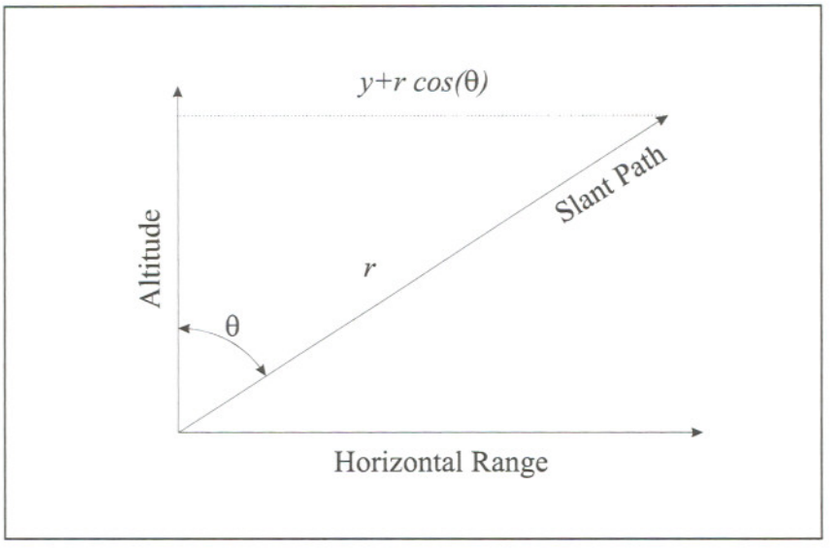

Figure C-1. Geometry of laser beam propagating along slant path.

The transmittance of the atmosphere for a laser beam propagating along the slant path shown in Fig. C-1 is then given by:

$$\tau(f) = e^{-\sec(\theta)\int_0^{y+r\cdot\cos(\theta)} N(y)\sigma_a(f,y)dy} \tag{C.3}$$

The ideal gas law may be used to express the integrand in eq. (C.3) in terms of the atmospheric pressure $p(y)$ at the altitude y and the fractional concentration $f(y)$. Thus, we have:

$$N(y) = f(y)\, p(y)/kT(y) \tag{C.4}$$

For an isothermal atmosphere and assuming that air is an ideal gas, the pressure as a function of the altitude can be shown to be given by the following expression:

$$p(y) = p_0 e^{-y/H} \tag{C.5}$$

where $H = kT/mg$ is customarily referred to as the scale height. The parameters $m=(\Sigma_j m_j N_j)/N$ and g are the average molecular mass and gravitational acceleration,

respectively. The scale height is the distance in which the pressure of an isothermal atmosphere of constant composition drops by a factor of e^{-1}. Eq. (C.4) does not apply to the ozone and water vapour concentrations. The amount of ozone is chiefly a function of the altitude only, while the amount of water vapour depends on the relative humidity.

If we next assume that the absorption cross section $\sigma_a(f)$ has a *Lorentz* line shape of line width Δf (i.e., collisions are the dominant line-broadening mechanism), then:

$$\Delta f = \Delta f_0 \left(\frac{p(y)}{p_0} \right)^{\sqrt{\frac{T_0}{T(y)}}} \tag{C.6}$$

The subscript 0 refers to a reference altitude. Because of the more numerous collisions of the absorbing molecules with N_2 and 0_2 molecules, the broadening pressure in eq. (C.6) is simply the total atmospheric pressure at the altitude of interest. The absorption cross section as a function of frequency and altitude may be expressed in the form:

$$\sigma_a(f,y) = \frac{S(y)\Delta f(y)}{2\pi\left[(f - f_0)^2 + \left(\frac{\Delta f(y)}{2} \right)^2 \right]} \tag{C.7}$$

The parameter $S(y)$ is called the line intensity or line strength and is given by:

$$S(y) = \int_{-\infty}^{\infty} \sigma_a(f,y)\,df \tag{C.8}$$

The total molecular absorption coefficient at the laser frequency f is found by summing over each molecular species present and the various allowed transitions that contribute to the total absorption coefficient. Therefore, we have:

$$\alpha(f) = \sum_i \sum_j \frac{S_{ij}(y)\Delta f_{ij}(y)N_j(y)}{2\pi\left[(f - f_{0,ij})^2 + \left(\frac{\Delta f_{ij}(y)}{2} \right)^2 \right]} \tag{C.9}$$

The subscript i refers to the *ith* line of the *jth* molecular species with the number density $N_j(y)$. For example, the He-Ne laser, in addition to the 0.6328 μm transition, can also be operated at 1.152276 μm. It turns out that the water vapour molecule has five absorption lines in this region; they are centred at 1.152277 μm, 1.152319 μm, 1.152373 μm, 1.152420 μm, and 1.152423 μm. The total absorption at the wavelength of the He-Ne laser is due to the sum of the absorption arising from each line.

The above example illustrates yet another important aspect of the interaction of laser radiation and the atmosphere. Since the line widths of lasers are typically very narrow (e.g., between 10^{-3} and about 2Å for gas lasers), the spectral absorption regions of interest are also very narrow. Experimentally this necessitates high resolution measurements, and the usual tables or spectral transmittance curves, that give average absorption over relatively wide bands are not strictly applicable to laser beam absorption. Fortunately, a large amount of high-resolution data is now available, together with moderate and high-resolution transmission codes (e.g., MODTRAN, HITRAN, etc.). Some of these will be described in later paragraphs of this appendix.

Because of the need for high-resolution data it is sometimes desirable to calculate the atmospheric absorption coefficient. Combining eqs. (C.3) and (C.9), the atmospheric transmittance at the frequency f is given by:

$$\tau(f) = e^{-\frac{\sec(\theta)}{2\pi}\int_0^{y=\infty}\sum_i\sum_j \frac{S_{ij}(y)\Delta f_{ij}(y)N_j(y)}{2\pi\left[(f-f_{0,ij})^2+\left(\frac{\Delta f_{ij}(y)}{2}\right)^2\right]}dy} \qquad \text{(C.10)}$$

This equation must be evaluated by analytic or numerical techniques. Obviously, any exact evaluation of eq. (C.10) is exceedingly difficult, if not impossible. Most calculations of this sort assume a model standard clear atmosphere and require estimates that are at times not much better than educated guesses. Nevertheless, attempts have been made to compile all known molecular absorption lines and theoretically calculate atmospheric absorption coefficients [1].

3.1.1 Continuum Absorption

In addition to molecular absorption by discrete absorption lines, there exists a slowly varying component of molecular absorption in the atmosphere caused mainly by molecular clusters. This absorption plays a fundamental role particularly in "window" regions where absorption by discrete lines is small. It is difficult to separate the cluster molecular absorption from absorption in the distant wings of strong discrete absorption lines. For practical reasons far wing absorption and cluster absorption are combined and called "continuum" absorption. In regions of more substantial line absorption, the problem reduces to that of deciding how far into the wings of each line to assume individual line contributions and how much of the experimentally observed absorption to model as "continuum". Various models have been developed for continuum absorption contributions in the various atmospheric windows. A comprehensive collection of these models is presented in Ref. [2]. However, it should be underlined that, because of the considerable lack of experimental data, related to the physical complexity of continuum absorption processes, there is still some uncertainty in the continuum contributions.

3.1.2 Atmospheric Scattering

Scattering in the second attenuation process that we describe. In this process there is no loss of energy but only a directional redistribution which may lead to a significant reduction in beam intensity for large path lengths. For example, on a clear day scattering reduces transmission in the visible spectrum to 20% for a 16 km path.

The physical size of the scatterer determines the type of scattering. Thus, air molecules that are typically several angstrom units in diameter (larger than electron but smaller than λ) lead to *Rayleigh* scattering, whereas the aerosols (comparable in size to λ) scatter light in accordance with the *Mie* theory. Furthermore, when the scatterers are relatively large (much larger than λ), such as the water droplets found in fog, clouds, rain, or snow, the scattering process is more properly described by diffraction theory.

3.1.2.1 Rayleigh Scattering

Rayleigh scattering is due to the displacement of bound electrons by the incident field. The process is schematically illustrated in Fig. C-2. The incident harmonic field induces a dipole in the molecule whose polarizability determines the displacement.

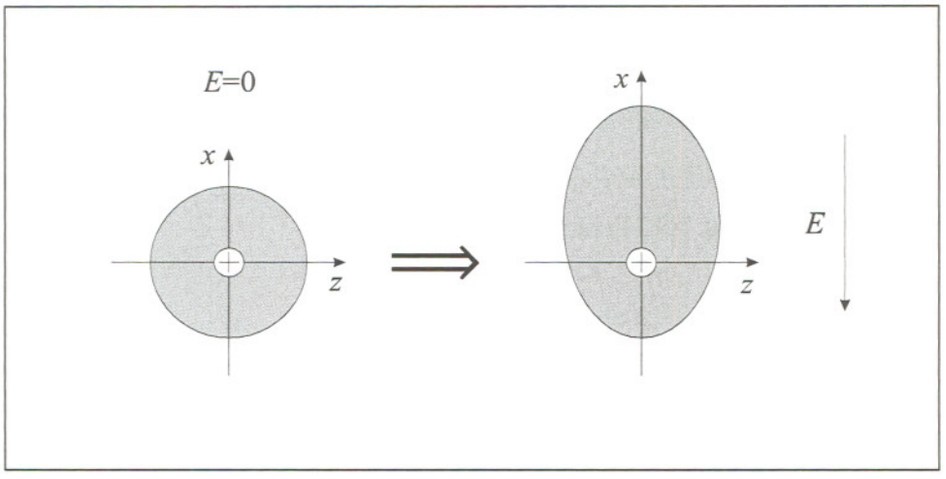

Figure C-2. Induced dipole in presence of applied harmonic field E.

The induced dipole oscillates at the same frequency as the incident and emits electromagnetic radiation whose spatial distribution is shown in Fig. C-3. This reradiated energy constitutes the scattered light.

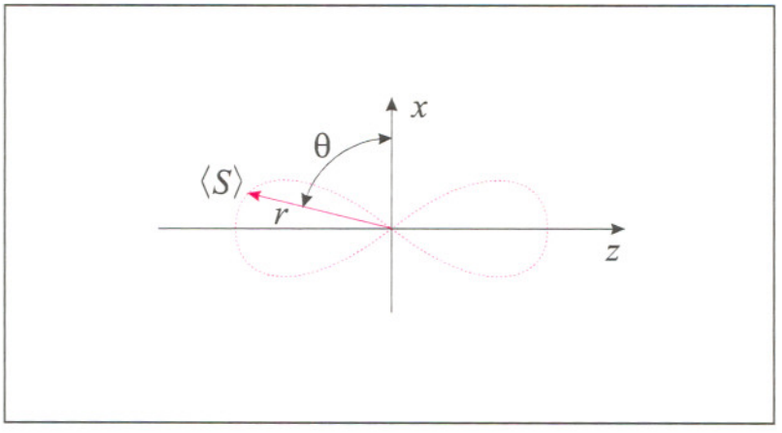

Figure C-3. Spatial distribution of radiated energy flux (S).

Using the laws of classical electrodynamics, it can be shown that the scattering cross-section of a single dipole radiator is given by [3]:

$$\sigma_s = \frac{\left(\frac{e^2}{m}\right)^2 \omega^4}{6\varepsilon_0^2 \pi c^4 \left[\left(\omega_0^2 - \omega^2\right)^2 + \left(\Gamma\omega\right)^2\right]} \tag{C.11}$$

where ω_0 is the natural frequency, e is the electron charge, ω is the applied frequency, and Γ is the damping coefficient. For the special case where the applied frequency ω is much lower than the natural frequency ω_0 and where the damping coefficient Γ is small, eq. (C.11) reduces to:

$$\sigma_s = \frac{\left(\frac{e^2}{m}\right)^2}{6\varepsilon_0^2 \pi c^4} \left(\frac{\omega}{\omega_0}\right)^4, \text{ for } \omega << \omega_0 \text{ and small } \Gamma \tag{C.12}$$

To generalize this result we need to multiply eq. (C.12) by the so-called oscillator strength f, which is defined as the effective number of electrons per molecule that oscillate at the natural frequency ω_0. The maximum value of the oscillator strength is equal to the total number of electrons in the molecule. Since the more tightly bound inner electrons usually cannot participate in the interaction, the oscillator strength is usually considerably smaller than this limit.

Thus the final expression for the scattering cross section takes the form:

$$\sigma_s = \frac{f \cdot e^4 \lambda_0^4}{6\pi\varepsilon_0^2 m^2 c^4} \frac{1}{\lambda^4} \tag{C.13}$$

which is the classical scattering formula developed by *Rayleigh*. In the visible and near-infrared region of the spectrum, the effect of this type of scattering is often many orders of magnitude larger than the molecular absorption. Beyond 1 μm, *Rayleigh* scattering is no longer important and, because of the λ^{-4} dependence, may be neglected.

3.1.2.2 Mie Scattering

Reyleigh scattering equations are based on the assumption that the wavelength of the laser beam was considerably longer than the radius a of the molecule (*i.e.,* $\lambda >> a$). This assumption permits to ignore the spatial variation of the electric field over the molecular charge distribution. Because of this assumption, the results obtained in the previous paragraph are not applicable when the scattering particles have radii that are comparable to the wavelength. *Gustav Mie*, a German meteorologist, was the first to study the scattering of electromagnetic waves by small dielectric spheres. The theory involved is quite complex but, as we are primarily concerned with the attenuation of laser beams, we will only use some of the more important results.

Mie scattering in the atmosphere is caused by the ever-present aerosol particles and by small water droplets. As can seen from Fig. C-4 [4], the attenuation in the spectral region from 0.3 μm to 4 μm due to this type of scattering far exceeds the attenuation due to both *Rayleigh* scattering and ozone absorption. This is in spite of the fact that aerosol particle concentrations are many orders of magnitude less than molecular concentrations.

Mie's scattering theory takes into account the size, shape, dielectric constant, and absorptivity of the particle. One important result of this theory is that particles with the same product of the particle radius a and propagation constant k have the same scattering properties. The product ka along with the refractive index difference Δn between the aerosol particle and the air determine all scattering characteristics.

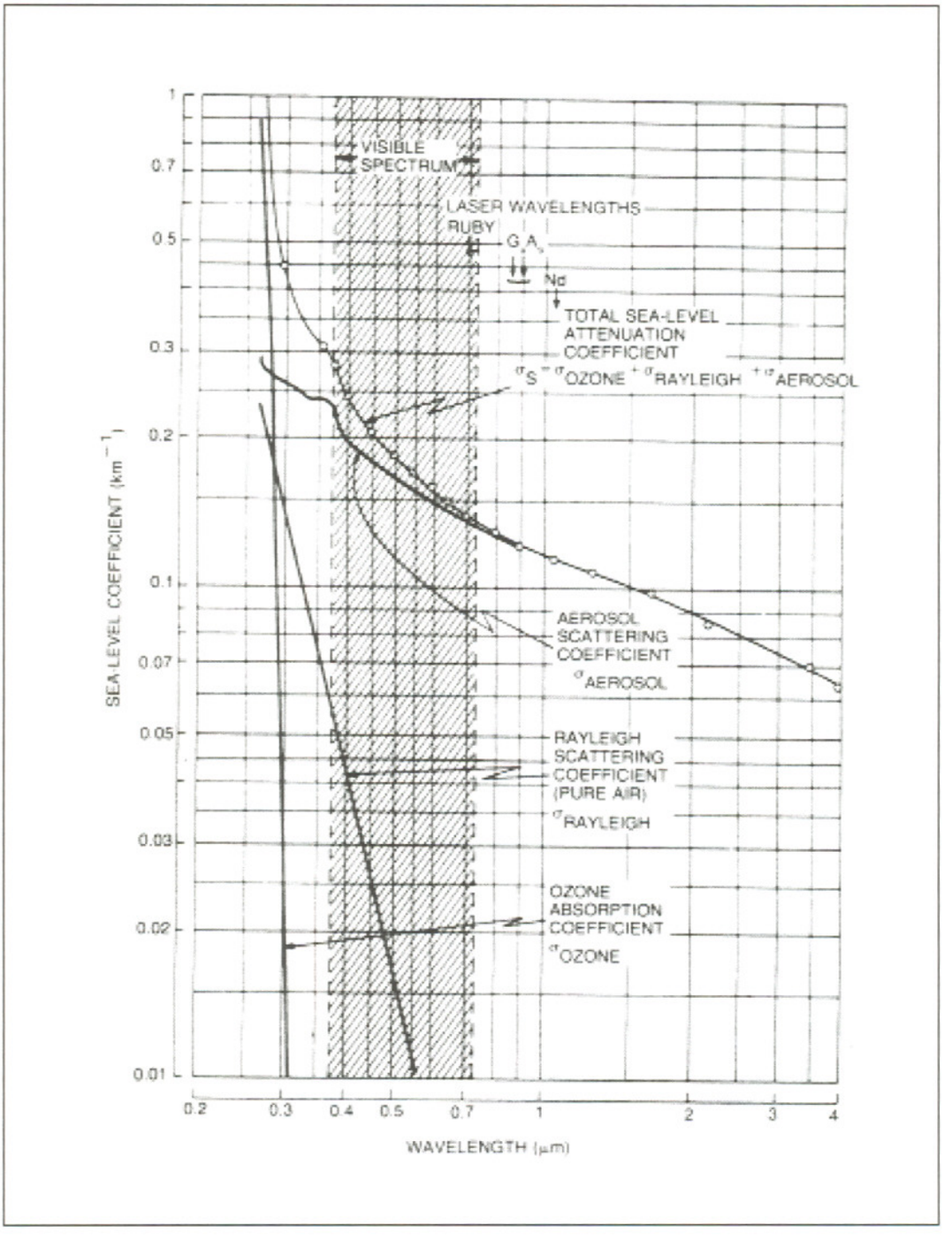

Figure C-4. Calculated atmospheric attenuation coefficient for horizontal transmission at sea-level in a model standard clear atmosphere.

To calculate the *Mie* attenuation coefficient we refer to the experiment illustrated in Fig. C-5 [3]. A monochromatic beam of light of cross-sectional area A and intensity I is incident on a cell of volume $V = Adz$ containing an aerosol with identical

spherical particles of radius a. The total cross section of the particles is $\sigma_T = NAdz\pi a^2$ if no one particle shields another particle. Because of absorption in addition to scattering, the effective attenuation cross section per particle is larger by the factor K, where K is the so-called attenuation factor and $K\pi a^2$ the attenuation cross section. If no absorption occurs the attenuation cross section is equal to the scattering cross section.

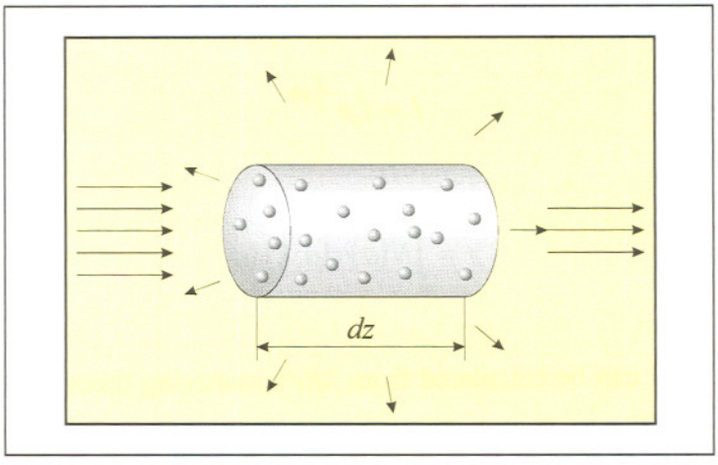

Figure C-5. Experiment to illustrate Mie scattering.

The fractional decrease in intensity of the monochromatic beam of light as it propagates through the cell shown in Fig. C-5 is then:

$$-\frac{dI}{I} = \frac{K\pi a^2 NAdz}{A} = N\sigma(a,\lambda)dz \qquad \text{(C.14)}$$

where $N\sigma(a,\lambda)$ is the *Mie* attenuation coefficient and $\sigma = K\pi a^2$ is the *Mie* attenuation cross section. Thus, the *Mie* attenuation coefficient is equal to the product of the number density N of aerosol particles and the extinction cross section. Since the energy removed is partly due to scattering and partly due to absorption by the particle, the attenuation factor K consists of a scattering and absorption term:

$$K(a,\lambda) = K_s + K_a \qquad \text{(C.15)}$$

Because a fraction of the scattered radiation is directed forward, the attenuation of the laser beam is in reality less than that predicted by a straightforward application of eq. (C.15).

More generally, for particles with a size distribution $N(a)$, where $N(a)da$ is the number of particles per unit volume within the range a to $a + da$, the fractional change in the beam intensity is:

$$-\frac{dI}{I} = dz\int_0^\infty N(a)\sigma(a,\lambda)da \tag{C.16}$$

Integration of eq. (C.16) yields:

$$I = I_0 e^{-\int \gamma dz} \tag{C.17}$$

where:

$$\gamma = \int_0^\infty N(a)\sigma(a,\lambda)da \tag{C.18}$$

The value of $K(a,\lambda)$ can be calculated from *Mie*'s scattering theory. A typical result for small water droplets having a refractive index $n = 1.33$ is shown in Fig. C-6 [3].

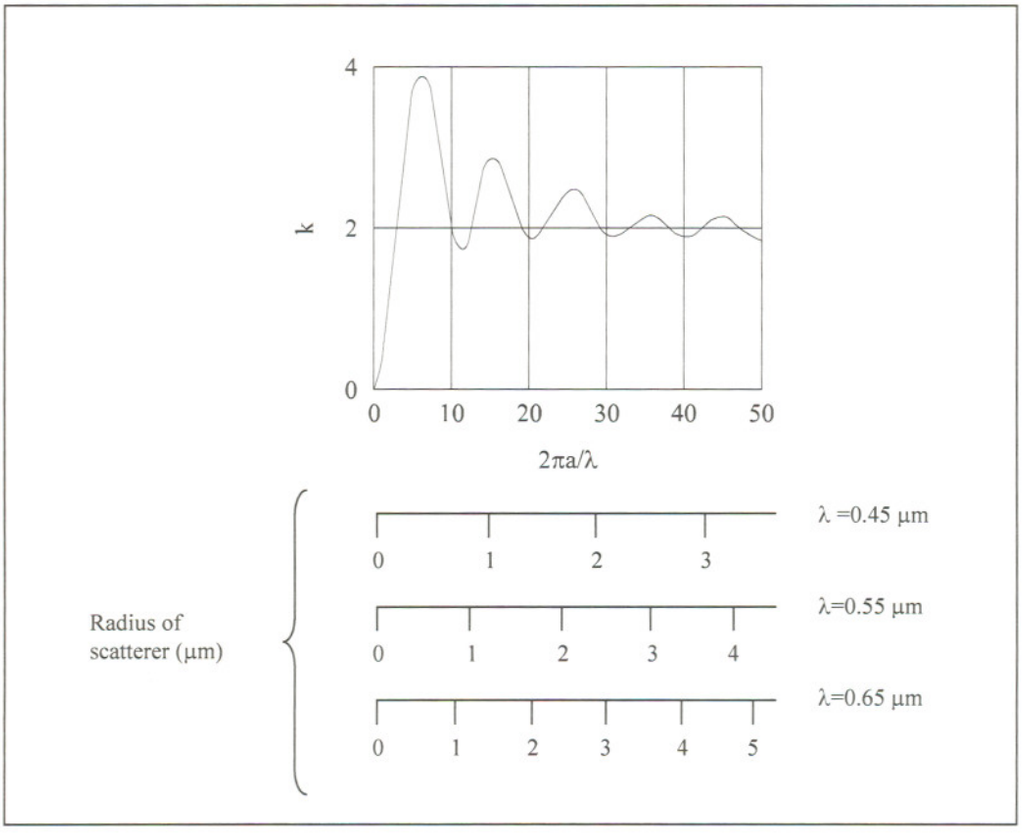

Figure C-6. Plot of the Mie attenuation factor K for water droplets with n = 1.33.

The results are important in connection with the propagation of radiation through haze, fog, and clouds. The curve exhibits a characteristic series of decreasing maxima and minima as the particle size increases. We note also that as the particle size increases, the attenuation becomes less dependent on wavelength. For large particle sizes the attenuation factor approaches $K = 2$, which means that the attenuation cross section of large obstacles is equal to twice its geometrical cross section, and the wavelength dependence has disappeared completely.

The three scales below the abscissa in Fig. C-6 indicate the radii of the particles in microns for three different wavelengths. For example, a water droplet of radius $a = 1\ \mu m$ has for the blue $\lambda, = 0.450$ μm) the attenuation factor $K = 2.38$; for green ($\lambda = 0.550\ \mu m$), $K = 1.78$; and for red ($\lambda = 0.650\ \mu m$), $K = 2.29$. In this case both blue and red light would scatter more than green light. lf the droplets had a radius of $0.7\ \mu m$, a beam of white light would appear blue after transmission, since the red spectral components will have been removed from the beam because of scattering. If the droplets radii were $0.4\ \mu m$, the situation would be reversed, with the scattered light being blue and the transmitted light red. Since generally aerosols vary considerably in size, light scattered by them will be white; this is why clouds are white or grey.

The theoretical aspects of *Mie* scattering are well understood. The difficulty arises when this theory is applied to an aerosol containing a variety of particle sizes and concentrations. Both of these quantities must be known before the atmospheric attenuation coefficient can be calculated. As might be expected, the particle size distribution and concentration vary widely, both geographically and temporally, at a given location. The aerosol particle size distribution also has been found to depend on both the relative humidity and wind velocity. Due to the condensation of water vapour onto the particles, the relative humidity also affects the effective refractive index of the aerosol particle. Accurate measurements of all these parameters is difficult, and the amount of reliable data is limited. From the available data, however, some particle size distributions have been obtained.

In propagation studies one generally assumes a two-component particle distribution, one for continental air and another for maritime air. Thus, the total aerosol particle size distribution of a given location is:

$$N(a) = Xn(a)_c + Xn(a)_m \tag{C.19}$$

where $N(a)$ is the total number of particles per unit volume per radii interval da. The factors X and Y represent the relative contributions of the continental and maritime aerosol particles, respectively; $n(a)_c$ and $n(a)_m$ are the corresponding size distributions. This two-component distribution applies to beam propagation over land as well as ocean, since aerosol particles of continental origin have been found in air masses over the middle of large oceans, and vice versa. If the aerosol particle size distribution and effective index of refraction of the particles are known, the scattering coefficient β is given by:

$$\beta(\lambda) = \pi \int_{a1}^{a2} N(a) K_s a^2 da \tag{C.20}$$

Eq. (C.20) has been evaluated for several different values of the relative humidity [5]. The results are presented in Fig. C-7, which also shows some measured values of the scattering coefficient in the spectral region extending from the visible to 2.5 μm. It is evident that they are in good agreement with the calculated values.

It is difficult to obtain reliable scattering coefficient data in the infrared because of the presence of both scattering and absorption. A measurement is generally confined to spectral regions where molecular absorption is known to be negligible (i.e., within atmospheric windows). The assumption is then made that the attenuation coefficient measured is equivalent to the scattering coefficient. A further assumption is that absorption by water droplets is negligibly small. This, however, is only appropriate in the visible region of the spectrum. For cloud droplets in the *5*- to *200-μm* diameter range, absorption rather than scattering is the predominant attenuation mechanism of *IR* radiation.

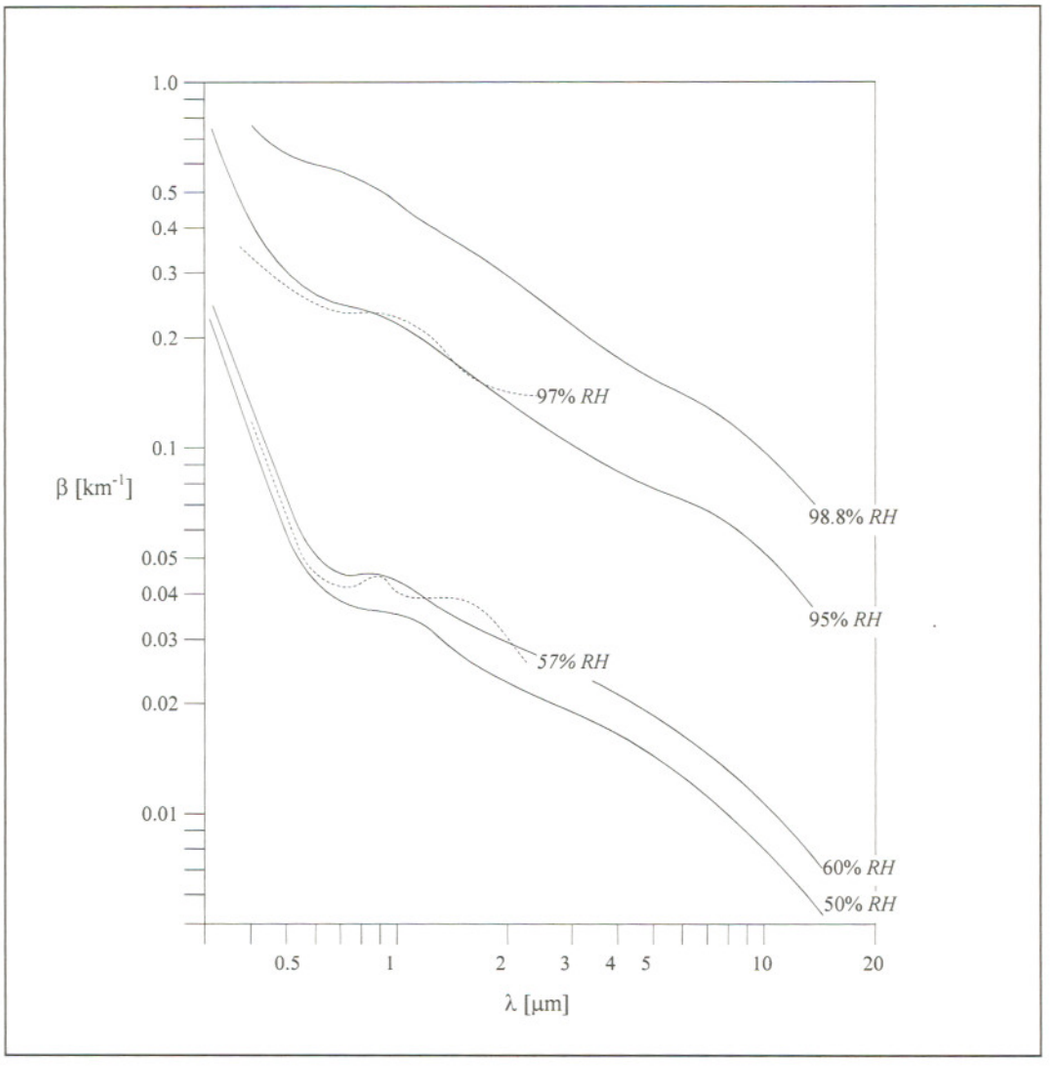

Figure C-7. Calculated and measured atmospheric aerosol scattering coefficients. All calculated values (solid curves) are for a 1.0:1.0 continental: maritime aerosol mixture. The dashed curves correspond to measured values. The relative humidity (RH) is as indicated.

3.2 Propagation Through Haze, Fog and Rain

The effects of precipitation (rain, fog, and snow) on the transmission of laser beams were studied extensively by Chu and Hogg [6]. A summary of their results is reproduced in Fig. C-8. The figure shows the attenuation coefficients for a typical dense fog and a representative shower for the wavelength range from 0.6 μm to 15 μm. For reference, the absorption of a layer of water containing the same amount of liquid water as the rain is also presented. For the wavelength range shown

in Fig. C-8 the attenuation by rain, which increases gradually from the visible region to the *IR* region, is considerably less than that for fog. For dense fogs, Chu and Hogg found that the attenuation at 10.6 μm can exceed 40 dB/km. It is interesting to note that attenuation by light fog at λ = 3.5 μm and λ = 10.6 μm is up to one order of magnitude less than at 0.63 μm (He-Ne laser), while attenuation of 0.63 μm wavelength radiation in rain is about 20%n less than at 3.5 μm.

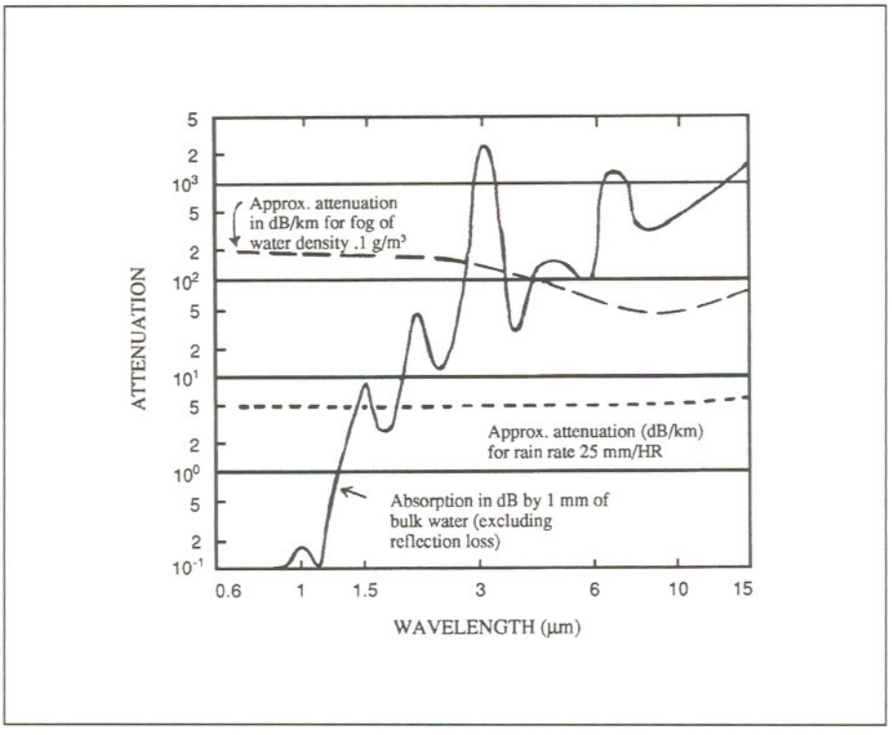

Figure C-8. Attenuation of infrared radiation due to rain (lower dashed curve) and fog (upper dashed curve). Absorption for a water layer containing the same amount of liquid water as the rain is represented by the solid curve.

The attenuation properties of snow seem to be between those of fog and rain [7].

In summary, laser beams suffer considerable attenuation while propagating through rain, fog, and snow. Penetration of laser beams through a dense fog is much more difficult than through a heavy rain. It is evident that the beam attenuation by precipitation is a dominant factor that must be considered when the feasibility of laser weapon systems, laser remote sensing, or open-air communication systems are to be determined.

3.3 Propagation Through Atmospheric Turbulence

Temperature fluctuations are introduced into the atmosphere by such relatively large-scale phenomena as convection from solar heating of the earth's surface and by wind shear. The turbulence energy is thus injected over scale sizes larger than some minimum value L_0, which is called the outer scale of turbulence. The corresponding wave number is $K_0=(2\pi/L_0)$. For wave numbers smaller than K_0, the form of the turbulence energy spectrum is determined by local surface terrain and weather conditions. Since conditions found at one point in the atmosphere usually differ from those that exist at another point, the turbulence is generally not bomogeneous and isotropic. Unfortunately, the only situation for which there is a well-developed atmospheric model is in the case of homogeneous isotropic turbulence, where the refractive index fluctuations are random due to well-mixed temperature fluctuations. Typical scale sizes for L_0 are about 100 m, or 0.2 times the height above the ground, whichever is less.

The inner scale of turbulence ℓ_0 marks the turbulence scale sizes at which viscous dissipation converts the turbulent energy into heat. Typically it is on the order of 1 mm near the ground to about 1 cm at the tropopause. The corresponding wave number is $K_m=(2\pi/\ell_0)$. The region between K_o and K_m is known as the inertial sub-range. The motion of the large turbulent eddies, or cells, causes the formation and transfer of energy to smaller eddies that transfer their energy to still smaller eddies. This process continues until viscous effects dominate and the turbulent energy of the smallest eddies is dissipated. The viscous dissipation begins at the spatial wave number K_m. Intuitively, $\ell = 2\pi/\mathrm{K}$ may be regarded as the size of the turbulent eddy, or cell. The turbulent inner and outer scales are by no means fixed, constant values, but possess dynamic vertical profiles that depend on such factors as temperature, pressure, humidity, and wind speed [3].

3.3.1 Refractive Index Structure Coefficient

The single most important parameter appearing in almost all equations that describe beam disturbances caused by turbulence is the refractive index structure coefficient C_n. It is governed by the pressure and temperature difference at two

points separated by the distance r (measured in centimetres) and may be approximated by [3]:

$$C_n = \left[79 \cdot 10^{-6} \frac{p}{T^2} \right] C_T \qquad \text{(C.21)}$$

Where the temperature structure parameter is:

$$C_T = \sqrt{\left\langle (T_1 + T_2)^2 \right\rangle} \frac{1}{\sqrt[3]{r}} \qquad \text{(C.22)}$$

The temperatures T, T_1, and T_2 are all in °K, and p is the atmospheric pressure in millibars. Typical values are: for strong turbulence, C_n = 5 x 10^{-7}; for intermediate turbulence, C_n = 4 x 10^{-8} ; and for weak turbulence, C_n = 8 x 10^{-9}. The structure parameter usually appears in the literature in the form C_n^2, which varies from about 10^{-17} $m^{-2/3}$ for extremely weak turbulence to 10^{-13} $rn^{-2/3}$ or more when the turbulence is strong. This latter value is usually observed near the ground in direct sunlight. Measurements of C_n with temperature sensors 1.6 m above the ground have shown that the minimum value of C_n, occurs about one to two hours before sunrise and after sunset. The peak values have been recorded around noon on sunny days.

All parameters in eq. (C.21) are a function of the altitude. Particularly, it appears evident that the structure parameter C_n decreases with altitude. Some approximate values are given in Table C-2 [3].

Height (Km)	C_n ($m^{-1/3}$) x 10^8
0.001	30
0.003	20
0.01	15
0.03	10
0.1	6
0.3	4
1.0	1
3.0	1

Table C-2. Typical values of C_n as a function of height.

Various models have been suggested to describe C_n^2 through the altitude (h) only. Most of these models can be condensed by the following general formula:

$$C_n^2(h) = C_{no}^2 h^{-b} \exp(-h/h') \tag{C.23}$$

where C_{no}^2, b and h' are the chosen parameters. Particularly, the following models can been found in the literature.

Fried's model [8]:

$b=1/3$

$h'=3200\ m$ ⇒ $C_n^2(h) = 4.22\times10^{-14} h^{-1/3} \exp(-h/3200)\ \mathrm{m}^{-2/3}$ (C.24)

$C_{no}^2 = 4.22\times10^{-14}\ \mathrm{m}^{-1/3}$

Brookner's model [9]:

$b=5/6$

$h'=320\ m$ ⇒ $C_n^2(h) = 3.6\times10^{-13} h^{-5/6} \exp(-h/320)\ \mathrm{m}^{-2/3}$ (C.25)

$C_{no}^2 = 3.6\times10^{-13}\ \mathrm{m}^{-1/6}$

Tatarski's model [10]:

$b=4/3$

$h'=\infty$ ⇒ $C_n^2(h) = 4.16\times10^{-13} h^{-4/3}\ \mathrm{m}^{-2/3}$ (C.26)

$C_{no}^2 = 4.16\times10^{-13}\ \mathrm{m}^{-2/3}$

Another model, accounting also for wind influence, is the ***Hufnagel's model*** presented below [11]:

$$C_n^2(h) = 2.7\times10^{-16}\left[2.2\times10^{-37} h^{10} (w/27)^2 \times \exp(-h/1000) + \exp(-h/1500)\right]\mathrm{m}^{-2/3} \tag{C.27}$$

In the *Hufnagel*'s model, the factor w is the average wind speed in the range of elevations from 5 to 20 km. All other models do not account for wind characteristics. Eq. (C.27) is actually a combination of two parts, each of which has the form of eq. (C.23). For the first part, b=-10, h'=1000 m, $C_{no}^2 = 5.94\times10^{-53}$ $m^{-32/3}$, and a weight factor $(w/27)^2$ is put into eq. (C.23). In the second part, b=0, h'=1500 m, $C_{no}^2 = 2.7\times10^{-16}$ $m^{-2/3}$. The *Hufnagel*'s model is only valid for the range of elevations from 3 km above the local ground level to 24 km above sea level.

The *Tatarski*'s model is a theoretical model while the other models are based on experimental measurements. All models have been checked under different weather conditions and measurements fields. *Tatarski*'s model appears to fit best for small altitudes, while the other models are more suited to higher altitudes [12]. It must be mentioned, however, that some $C_n^2(h)$ vertical profile measurements performed at night [13], indicate increases in $C_n^2(h)$ at altitudes on the order of 10 to 20 km. These results contradict the models presented in this section. The curves of $C_n^2(h)$ for all four models presented are shown in Fig. C-9 [12].

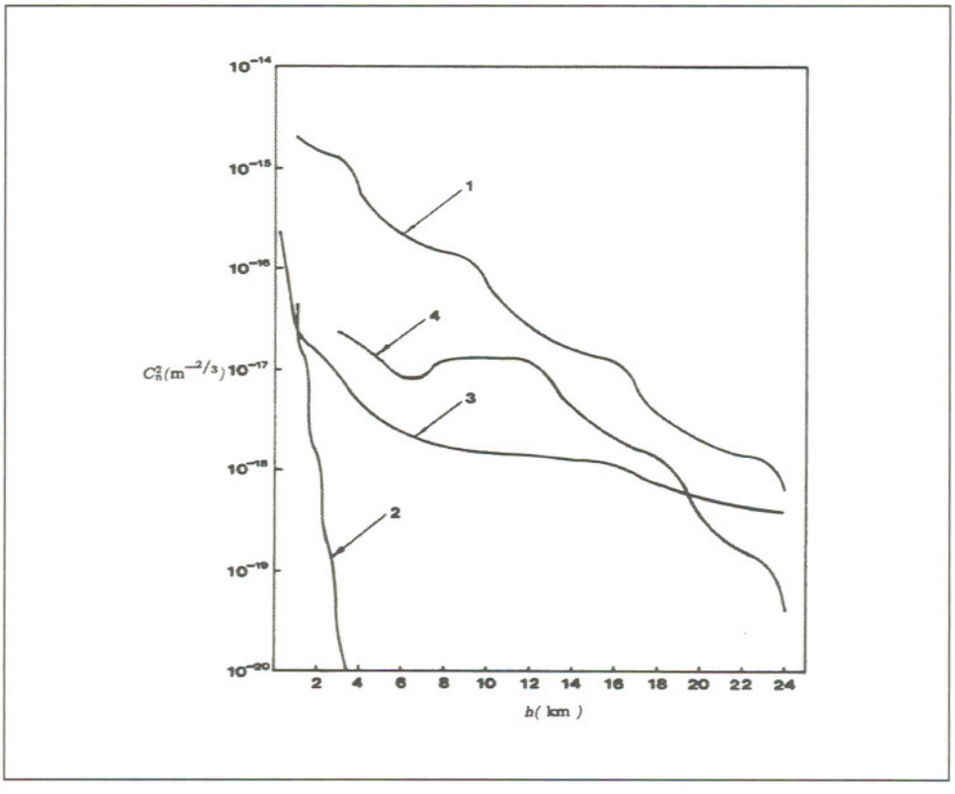

Figure C-9. Refractive index structure coefficient as a function of altitude. 1) Fried's model; 2) Brookner's model; 3) Tatarski's model; and 4) Hufnagel's model (assuming w = 18 m/s).

3.3.2 Turbulence Effects

Let us next consider the experiment shown in Fig. C-10 in which an expanded beam is transmitted through a region of atmospheric turbulence to a target where it is observed. The characteristics of the transmitter are determined by the output beam diameter d, the wavelength λ, and the focal length f of the beam expander. The turbulence present is described by outer and inner scale sizes as well as the refractive index structure coefficient C_n.

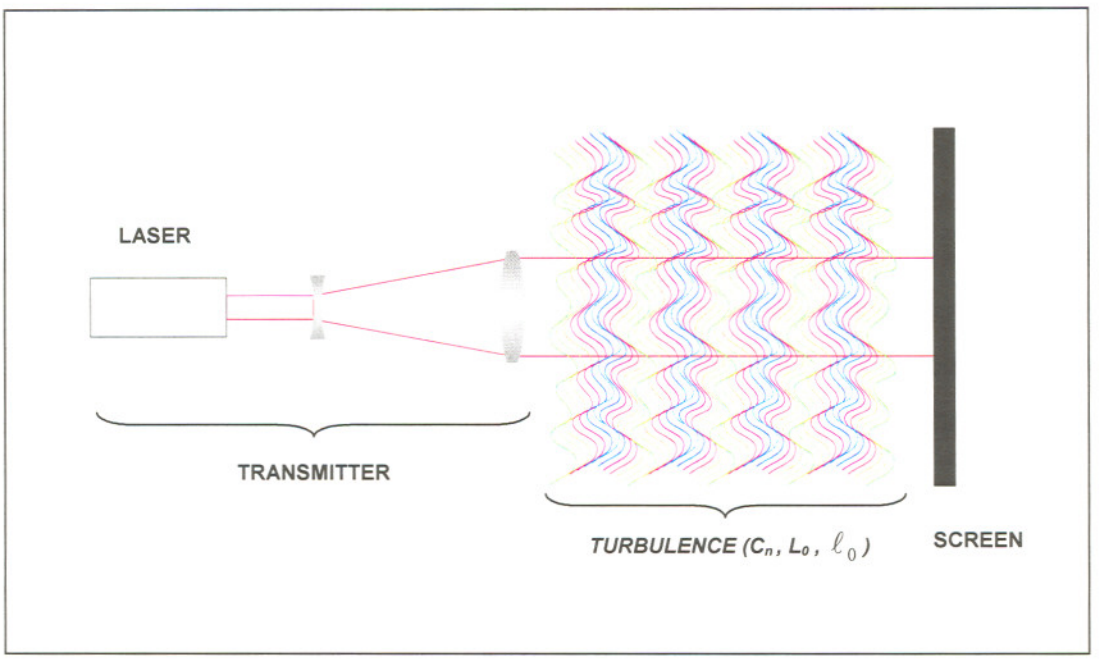

Figure C-10. Transmission of a laser beam through atmospheric turbulence. The region is characterized by the refractive index structure coefficient C_n, the outer scale L_0 and the inner scale ℓ_0.

Depending on the dominant turbulence scale size and beam diameter we can identify two cases that lead to different effects. For instance, if the scale sizes at all points along the beam path are larger than the beam diameter, the turbulence cells act as very weak lenses that deflect the beam as a whole in a random way, leaving the beam diameter essentially unaltered. This is shown schematically in Fig. C-11. The resulting beam displacement from the initial beam direction is known as "beam wander".

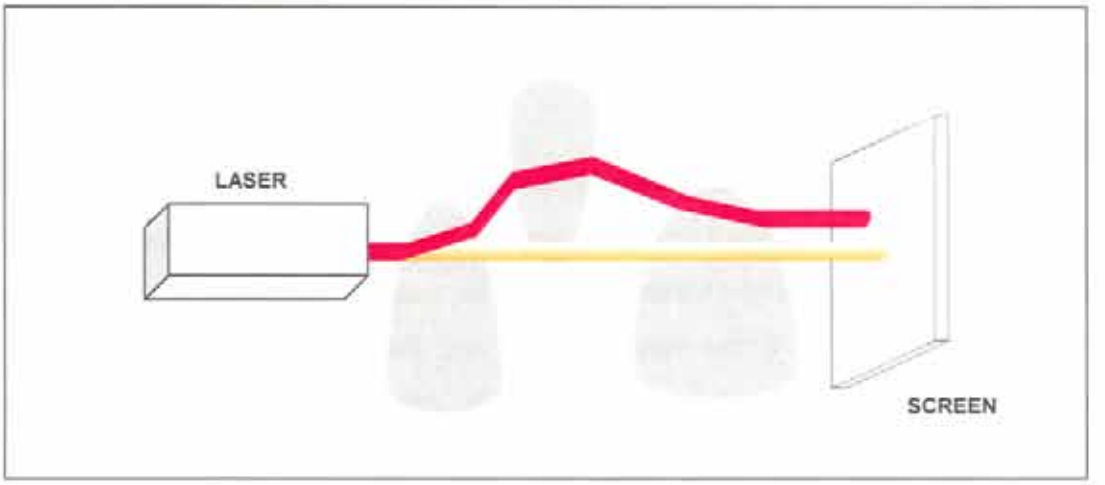

Figure C-11. Laser beam deflected by turbulence cells larger than the beam diameter.

When the scale sizes (or cell dimensions) are smaller than the diameter of the beam, diffraction and refraction of the beam takes place and the beam's intensity profile is smeared out and as a rule markedly distorted. This effect, schematically illustrated in Fig. C-12, is referred to as "beam breathing" and "scintillation". Depending on the characteristics of the turbulence and of the laser beam, both cases may be observed simultaneously.

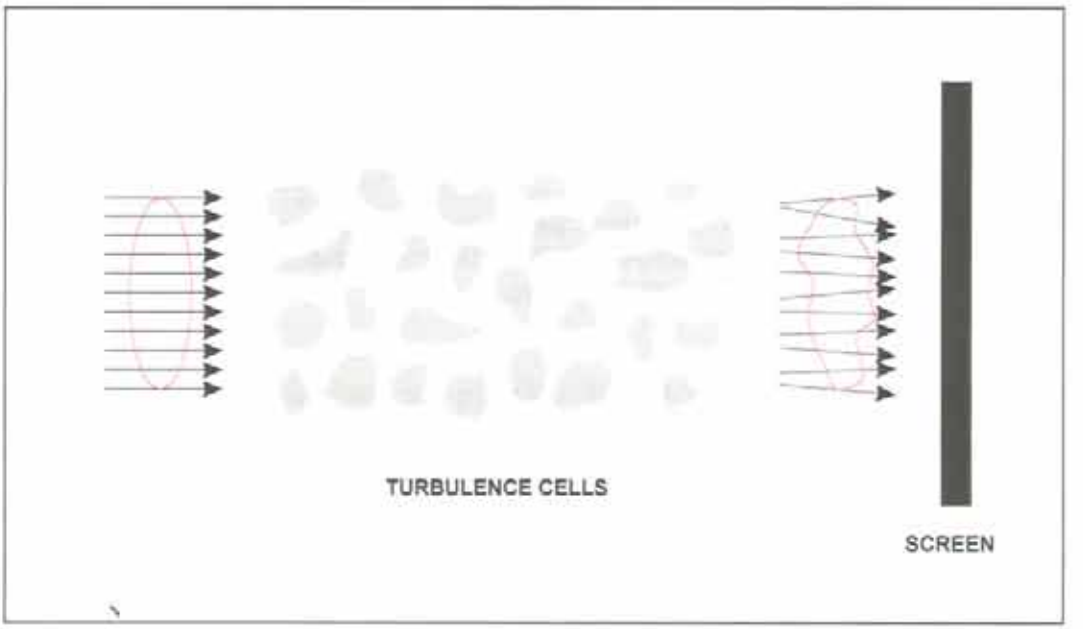

Figure C-12. The laser beam is broken up by turbulence cells smaller than the beam diameter.

3.3.2.1 Beam Wander

The term "beam wander" is used to describe the rapid displacement of the beam's spot on a screen a distance L from the laser. Since this effect is due to large turbulence scale sizes, a geometrical optics approach can be adopted. The analysis, however, is lengthy and for this reason we only present the results. Chiba [14] obtained the following expression for the radial variance of beam wander:

$$\sigma_r^2 = 1.90 \cdot C_n^2 \frac{L^3}{2w_0} \tag{C.28}$$

where w is the beam spot size at the transmitter, L is the screen distance from the laser and C_n is the index structure coefficient.

Sometimes it is more desirable to know the relationship between the radial variance σ_r^2 and the beam's wavelength λ. According to Weichel [3], we can rewrite the eq. (C.28) as:

$$\sigma_r^2 = 1.83 \cdot C_n^2 \sqrt[6]{\frac{L^{17}}{\lambda}} \tag{C.29}$$

where both λ and L are expressed in meters. Beam wander has been measured under varying conditions of transmitter configurations and turbulence strengths. In general, the results show that beam wander is to a very high degree independent of wavelength, as predicted by eq. (C.29) and closely follows an LC_n^2 relationship [3,14]. Beam wander becomes a major problem whenever a laser beam must remain on a specific target point for some time. It is possible, however, to negate wandering with the aid of a fast-tracking (a few Hertz) optical system. For communication systems it may be more practical to use sufficiently large apertures that will cover the entire range of the beam motion.

3.3.2.2 Beam Intensity Fluctuations

As illustrated before, the movement of small index-of-refraction inhomogeneities through the path of a beam causes random deflection and

interference between different portions of the wavefront, which can lead to an internal breaking up of the beam spot into smaller "hot spots". The resulting beam shape and energy distribution may be considerably different from the ones originated at the laser source. Various experiments performed have shown that the dominant size of the hot spots in the laser pattern observed on a screen distant L from the source is given approximately by $\sqrt{L\lambda}$ [15]. Bright patches of about 1 cm diameter are typical for $L \approx 1$ km. Because of the constantly changing pattern, a small detector placed in the beam will measure intensity fluctuations or scintillation. The temporal frequency of the intensity fluctuations recorded fixed point within the beam usually varies between 1 and 100 Hz. [16].

As already mentioned, beam intensity fluctuations are primarily produced by cells that are smaller than the beam diameter. As a result, diffraction plays an important role in scintillation. To illustrate this we refer to the turbulence conditions shown in Fig. C-13. If the small detector is omni-directional, the atmosphere will provide an effective acceptance angle for the receiver (shaded cone in Fig. C-13).

Radiation scattered from turbulence cells within the cone contribute to the field at the receiver, while radiation scattered from cells outside the cone will not. The cone angle θ is determined by a representative cell that forms the diffracting aperture and has an average diameter l. Thus, $\theta \cong \frac{\lambda}{l}$, and the largest cone angle is given by the smallest cell, so that:

$$\theta_{max} \cong \frac{\lambda}{l_0} \tag{C.30}$$

where l_0 is, as before, the inner scale of turbulence. The maximum width of the cone is, of course, determined by the beam diameter, and as long as this width ($L\theta$) is less than l_0, geometrical optics produces good results. Therefore, geometrical optics is valid as long as:

$$L\theta_{max} = \frac{L\lambda}{l_0} < l_0 \tag{C.31}$$

or

$$\sqrt{L\lambda} < l_0 \tag{C.32}$$

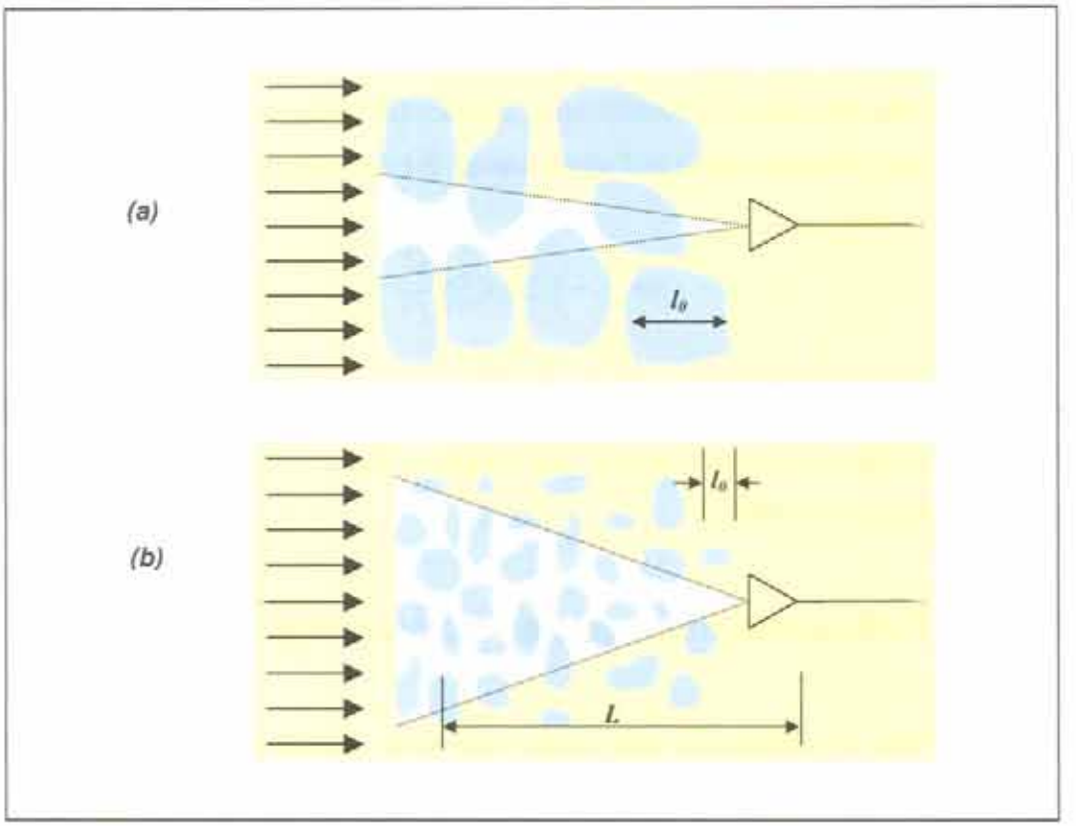

Figure C-13. Radiation scattered from turbulence cells inside the shaded region will contribute to the scattered field at the detector. (a) Geometrical optics is valid since the width of the cone is less than the dimension of a cell. (b) Diffraction effects become important when the width of the scattering cone includes many cells.

However, when $\sqrt{L\lambda} \geq l_0$, the scattering cone may contain many smaller cells [see Fig. C-13(b)], and as long as the detector area is less than the beam diameter the detector would record power fluctuations. Since the inner scale of turbulence may be as small as 0.5 cm, we see that for a range of $L \approx 1$ km and a wavelength $\lambda > 0.025$ μm, scintillation would be observed. It should be apparent that the power fluctuations can be smoothed out by increasing the detector aperture so that a number or statistically independent portions of the intensity pattern are received.

An important parameter in the analysis of scintillation is the logarithm of the instantaneous intensity $I(t)$, which is expressed as:

$$i(t) = ln\left(\frac{I(t)}{\langle I \rangle}\right) \tag{C.33}$$

where $< I >$ is the average intensity. Since *i(t)* has a *Gaussian* probability distribution, the strength of the scintillation is described in terms of the "log-intensity variance". For horizontal paths and plane waves, the variance of *i(t)* is given by:

$$\sigma_{i(t)}^2 = 1.23 \cdot C_n^2 \sqrt[6]{\frac{k^7}{L^{11}}} \tag{C.34}$$

where $k = 2\pi / \lambda$ is the propagation constant, L is the path length in metres, and C_n is the refractive index structure constant. For spherical waves the equation is the same, but the coefficient is 0.496.

3.3.2.3 Turbulence-Induced Beam Spreading

Due to turbulence the beam will also spread in size beyond the dimensions attributed to the usual diffraction spreading. According to the diffraction theory, a focused beam from a uniformly illuminated circular aperture of diameter d produces a radiation pattern in the focal plane whose diameter is:

$$d_0 = \frac{f\lambda}{d} \tag{C.35}$$

where f is the focal length of the optical system and λ the wavelength of the beam. The presence of atmospheric turbulence, however, prevents us from achieving diffraction-limited focal spot sizes. In practice the observed spot sizes are often twice as large as the spot sizes predicted by diffraction theory. This is shown in Fig. C-14 [16], where the diffraction-limited (ideal) beam diameter and the experimentally observed diameter are plotted against transmitter aperture.

The turbulence-induced beam spreading has been shown by Yura [17] to be given in the far field by:

$$a_t \cong \frac{2z}{k\rho_0} \tag{C.36}$$

where a_t is the distance from the z axis to where the relative mean irradiance is down by $1/e$, and:

$$\rho_0 = \frac{1}{\sqrt[5]{\left(0.545 \cdot k^2 C_n^2 z\right)^3}} \tag{C.37}$$

is a measure of the lateral coherence length of a spherical wave propagating through a medium containing homogeneous turbulence.

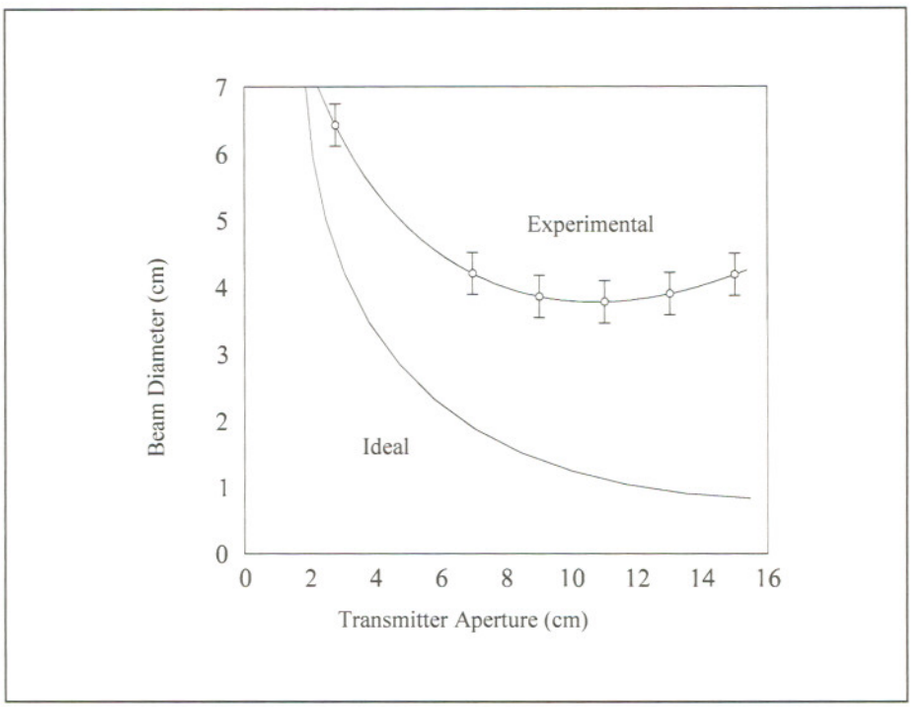

Figure C-14. Diameter of transmitted beam versus transmitter aperture. Transmitted beam diameter was taken as the distance between half power points. Path length 2 km. Exposure time 30 sec.

The expression for ρ_0 in eq. (C.37) is valid in the range $z_c \ll z \ll z_i$, where:

$$z_c = \frac{1}{0.4 \cdot k^2 C_n^2 \sqrt[3]{\left(\frac{L_0}{2\pi}\right)^5}} \tag{C.38}$$

and

$$z_i = \frac{1}{0.4 \cdot k^2 C_n^2 \sqrt[3]{l_0^5}} \tag{C.39}$$

The ranges z_c and z_i are the distances where the average field and lateral coherence length are down by *1/e* and equal to the inner scale of turbulence (l_0) respectively. As before, L_0 is the outer scale length of turbulence. For intermediate turbulence we find that $z_c \approx 1$ km and $z_i >> 10^3$ km. From these values we conclude that for most problems of interest, the path length z is within the limits defined by z_c and z_i. For path lengths where $z < z_c$, turbulence spreading is negligible because $\rho_0 \approx \infty$. At long ranges where $z > z_i$, the coherence length ρ_0 becomes:

$$\rho_0 = \frac{\sqrt[6]{l_0}}{0.76 \cdot C_n k \sqrt{z}} \tag{C.40}$$

Since $a_t = 2z/(k\rho_0)$, it can be seen that the turbulent beam spreading becomes wavelength independent. For most situations, however, turbulent beam spreading is wavelength dependent, and according to eqs. (C.36) and (C.37) is given by:

$$a_t = 2.01\sqrt[5]{\frac{C_n^6 z^8}{\lambda}} \tag{C.41}$$

This result shows that the dependence of turbulence-induced beam spreading on wavelength is small, being proportional to $\lambda^{-1/5}$. This is an important result because it implies an optimum wavelength for propagation in a turbulent atmosphere for a given aperture diameter, since beam spreading due to diffraction is proportional to the wavelength.

3.4 Astronomical Refraction

A laser beam propagating through the atmosphere whose refractive index (n) is a function of the altitude r will be bent into an arc of radius R, such that:

$$R^{-1} = \frac{1}{n(r)} \frac{dn}{dr} \tag{C.42}$$

or

$$\frac{d\theta}{dz} = \frac{1}{n(r)} \frac{dn}{dr} \tag{C.43}$$

where θ is the beam deflection angle and z is the path length through the atmosphere. Eq. (C.43), describes the propagation of a ray through a medium with a refractive index gradient. Since the atmospheric refractive index n decreases in magnitude with height r, dn/dr is negative, and therefore a negative beam curvature C (defined by $C = d\theta/dz$) means a downward bending of the beam. A specific expression for the dependence of the refractive index on the height is [3]:

$$\frac{dn}{dr} = 79\times10^{-6}\left(\frac{1}{T}\frac{dp}{dr} - \frac{p}{T^2}\frac{dT}{dr}\right) \tag{C.44}$$

When eq. (C.44) is substituted into eq. (C.43), and with $n(r) = 1$, the beam curvature C is:

$$C = 79\times10^{-6}\left(\frac{1}{T}\frac{dp}{dr} - \frac{p}{T^2}\frac{dT}{dr}\right) \tag{C.45}$$

At sea level, where the pressure and temperature normally are 1013.25 mbar and 293 °K, respectively, and the vertical gradient is -121 mbar/km, the beam curvature (in units of μrad/km) is related to the temperature lapse rate (in K/km) by:

$$C = -32.6 - 0.93\frac{dT}{dr} \tag{C.46}$$

The temperature lapse rate of a normal atmosphere is -6 °K/km. However, a considerably greater lapse rate can occur for short distances above a hot surface. This may produce an upward curvature (C > 0). Conversely, if the lapse rate becomes strongly positive, exceeding about 134 °K/km (this may happen above a very cold surface), the normal downward curvature of a ray may exceed the curvature of the earth's surface, which is 157 μrad/km.

Experimental measurements of atmospheric beam bending over a 24-hour period have shown a diurnal variation of about 30 μrad/km on a 15 km path [18]. In another experiment A. L. Buck [16] observed that in 30 min the beam of a He-Ne laser would drift vertically as much as 4 m at a distance of 10 km from the laser. Measurements such as these reveal that beam bending effects are generally slow and

can be corrected with a servomechanism or by manually adjusting the transmitter optics.

3.5 Non-linear Propagation

The propagation of a laser beam through atmospheric turbulence is a linear phenomenon in that the air is not affected by the beam. Strictly speaking, this is only true for beams of relatively low irradiance. As the beam's irradiance is increased, molecular absorption will lead to temperature gradients in the medium that in turn induce density and index-of-refraction changes. The final result is a medium whose optical properties have been altered. This phenomenon is non-linear, in that the beam's irradiance distribution leads to index-of-refraction changes, which in turn alter the beam's irradiance distribution, which alters the refractive index, etc.

3.5.1 Thermal Blooming

One effect that can be attributed to the beam-induced index-of-refraction change is a defocusing, or "blooming," of the beam. The divergence angle is considerably more than that due to diffraction alone. This thermo-optical effect is conceptually easy to explain (Fig. C-15). A high-irradiance CW beam with a *Gaussian* irradiance profile propagates through stationary air characterised initially (at $t = 0$) by a constant temperature T_0, density ρ_0, and index of refraction n_0. Upon absorption of laser photons by the air the energy is quickly released as heat, and the temperature of the air within the beam rises. The hot air near the centre of the beam axis expands radially outward (at the speed of sound). The expansion causes a decrease in the mass density, which in turn lowers the index of refraction near the beam's axis. The beam now undergoes a weak, but nevertheless observable, defocusing not unlike that which takes place when a beam is passed through a negative lens.

Various experiments carried out indicate that the blooming process is most significant during the first several hundred milliseconds. During this time the initially *Gaussian* irradiance distribution changes to one where the peak irradiance has an annular shape that moves radially outward toward the initial beam edge.

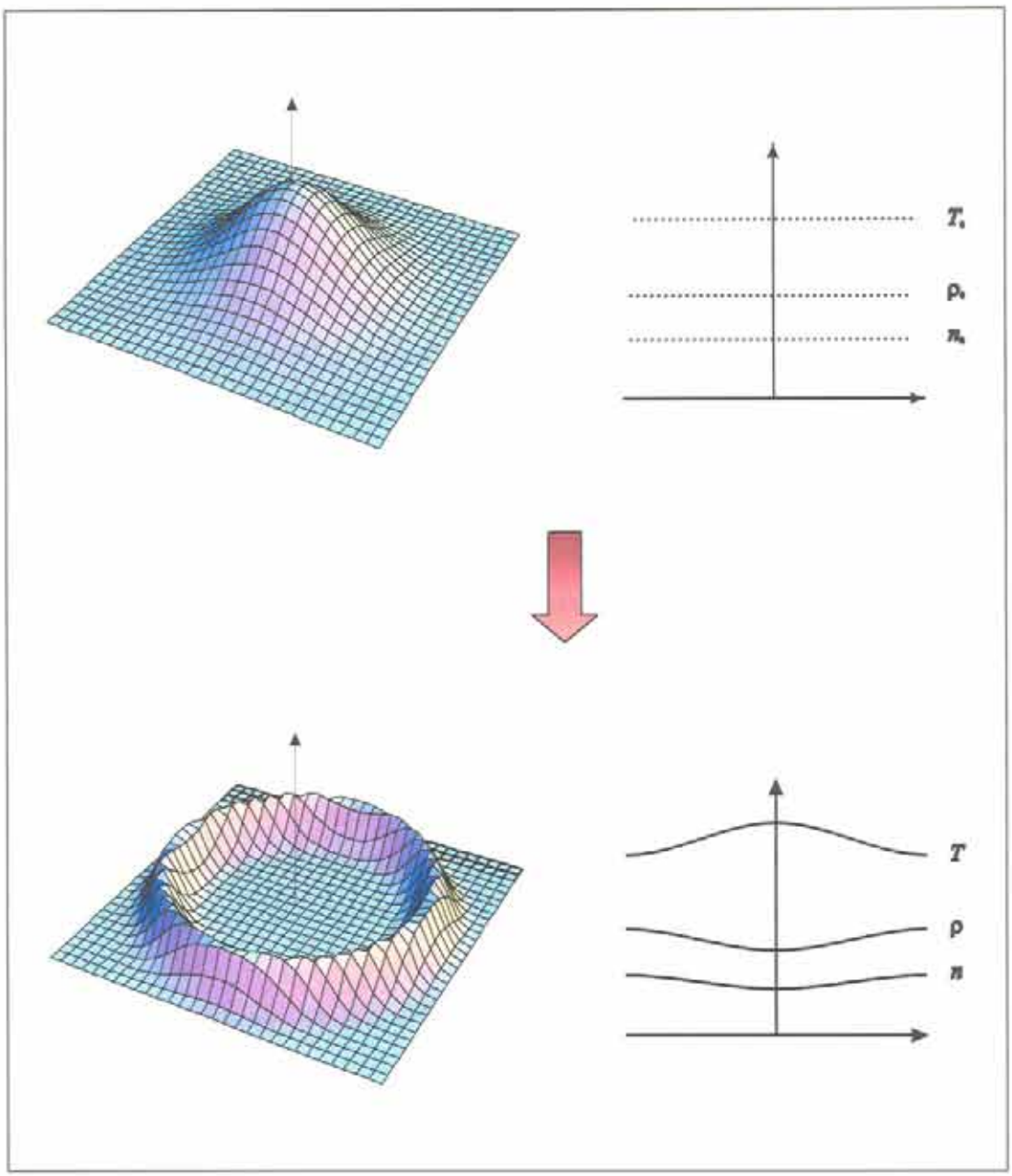

Figure C-15. Irradiance profile of an initially Gaussian CW beam propagating through stationary air that at t = 0 has a constant temperature T_0, density ρ_0, and index of refraction n_0.

The annular pattern next merges into a crescent-shaped irradiance distribution in which the region of peak intensity is refracted in the direction of the air flow. For instance, an apparent downward deflection of a laser beam is caused by the convective movement of the heated air through the beam. This behaviour can be understood qualitatively by considering the unit volume of air as it moves across the beam because of either natural convection or wind. As the parcel of air enters the beam it begins to absorb energy, and its temperature increases. This brings about a

flow of mass away from the unit volume at the speed of sound. This exodus of mass lowers the density and therefore the index of refraction. As a result the refractive index decreases from the upwind to the downwind side (or from the bottom to the top, in the case of convection) and the rays are refracted into the regions of higher refractive index (i.e., the laser beam bends into the flow of air).

At higher wind speeds, the parcel of absorbing air is moved through the beam so rapidly that very little energy is absorbed during its transit time. Density changes are thus very small, and consequently very little optical distortion occurs. The transit time of a parcel of air across the beam is a characteristic time that is of interest to the thermal blooming problem. For instance, at the beginning, when the time is less than the transit time, pure thermal blooming is the main source of optical distortion. For times that are long compared to the transit time, an initially *Gaussian* beam evolves into a steady-state, kidney-shaped irradiance pattern with its centre shifted into the wind direction.

Quantitative analyses of blooming may be found in the literature [3, 19]. In this appendix, a simple empirical approach is presented, giving the ratio R of the bloomed $I(B)$ to unbloomed $I(UB)$ peak irradiance. For this purpose, let us consider a laser beam with an initial *Gaussian* intensity distribution. If blooming occurs in the presence of wind, the intensity distribution will be altered. An example of "before" and "after" irradiance distribution is shown in Fig. C-16.

The empirical relationship giving the ratio R of the bloomed $I(B)$ to unbloomed $I(UB)$ peak irradiance, is the following [20]:

$$R = \frac{I(B)}{I(UB)} = \frac{1}{1 + 0.0625N^2} \tag{C.47}$$

where N, the thermal distortion parameter, is a dimensionless quantity that indicates the degree or strength of thermal distortion. Here N is given by:

$$N = N_0 \left[\frac{2}{z^2} \int_0^z \frac{a_0}{a(z')} dz' \int_0^{z'} \frac{a_0^2 v_0 \, exp(-\gamma z'')}{a^2(z'')v(z'')} dz'' \right] \tag{C.48}$$

where

$$N_0 = \frac{-n_T \alpha_m P z^2}{\pi d_0 v_0 c_p a_0^3} \tag{C.49}$$

- Determine the BRDF of various materials.

  Using the Laser Scatter-meter (LSM) designed and constructed during this research, further laboratory measurements of BRDF's can be performed with samples of various materials of tactical interest. This activity can also serve to built a BRDF data base which would very useful for tactical mission planning.

- Perform further flight tests with the LOAS system.

  Future flight tests will be performed at the PILASTER range in order to further assess the LOAS system performance (sensor and processing algorithms) in day/night with various weather/environmental conditions and to optimise the system human machine interfaces. Particularly, starting in June 2004, a dedicated flight test activity will be carried out in order to assess the LOAS system performances for future installation on the Italian NH-90 TTH/NFH helicopters. This activity will be conducted using an AB-412 test-bed helicopter, and will be addressed to the LOAS performance verification with various reference obstacle scenarios and in various weather conditions, and to very the validity of the Human Machine Interface (HMI) being developed for the Italian NH-90 helicopter.

THE END

APPENDIXES

Appendix A

INTRODUCTION TO AIRBORNE LASER SYSTEMS

A.1 Laser Range Finders

For many military applications, such as the delivery of unguided bombs and gunnery, it is essential to be able to measure range accurately. There are several ways in which this can be done. The traditional method, is to use an optical rangefinder. This either measures the angle subtended at a distant point by a fixed optical baseline, or measures the angle subtended at the operator by a target of known size. In airborne systems the problem is usually complicated by the continuously changing geometry between the aircraft and a point on the target, and the implied requirement for rapid measurement techniques. By using standard sensors within the aircraft system, the range between aircraft and ground targets can be estimated by knowing the altitude of the aircraft and the depression angle between the horizontal and a line to the target, or by measuring the rate of change of this angle and knowing the aircraft velocity. All these methods have limited accuracy and most of them are not easily integrated into any automated weapon system.

A more suitable technique used in conventional radar, is to transmit a pulse of radiation. After reflection and reception, the time of flight of the pulse is then measured. This is a direct measurement of range. Unfortunately, microwave radars suffer low performance at low grazing angles, which occurs at level flight at low altitudes. In addition to this, land targets are rarely isolated from other reflectors within the radar beam and these give rise to spurious returns which can lead to ranging errors in conventional radar.

To overcome these effects conventional radar systems require sophisticated transmission and return signal processing. Lasers, on the other hand, with their

narrow beams offer an immediate advantage with simpler signal processing and better target definition. They can also produce very short pulses which give excellent range resolution (ΔR). Range resolution is given by:

$$\Delta R = c\tau/2 \qquad \text{(A.1)}$$

where τ = pulse width. For example, a pulse width of 10 ns will give a range resolution of about 1.5 metres. A particularly demanding ranging application which has received considerable attention and which illustrates the advantages of laser ranging, is the measurement of range from a high speed low-level aircraft to a ground target. Fig. A-1 illustrates the obvious errors which can arise over undulating ground owing to the error in assessing the true aircraft to target height.

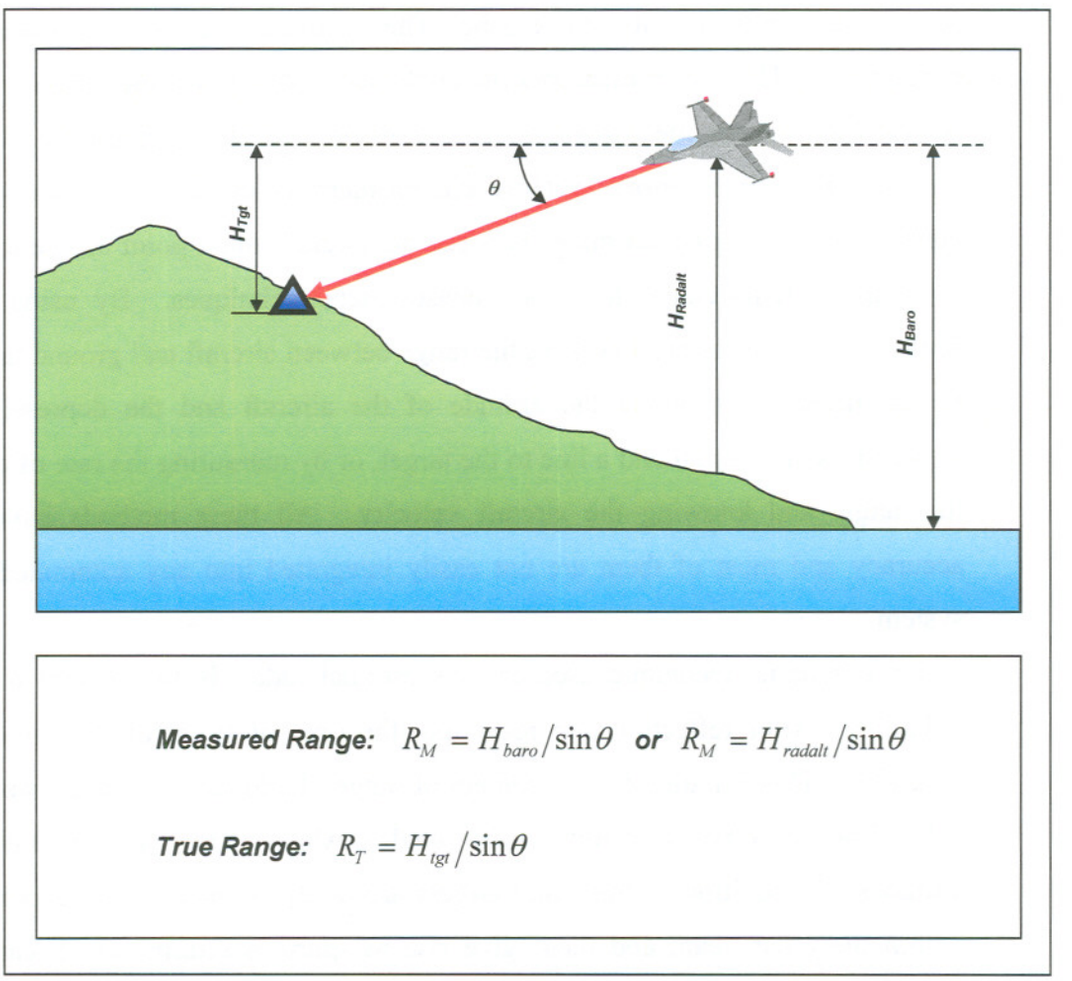

Figure A-1. Ranging error obtained by scaling aircraft height measurements.

The choice of laser and receiver for a system will depend, to a large extent, upon the application. Generally, for rangefinders, the most important parameter is the maximum range of operation. Laser Rangefinders (LRF's) usually operate at ranges between 7 and 15 km. A considerably large output power is required to operate much beyond this range. Early systems used ruby lasers but these have now been discontinued in favour of the higher efficiency pulsed Nd:YAG systems. With pulsed systems high output power, of the order of MW, is required since it is the peak power output of each pulse that determines the maximum range. The majority of LRF's, in operation at the present time, use an optically pumped Nd:YAG laser as the source of the transmitter power (λ = 1.064 μm), but eye-safe Er:glass (λ = 1.550 μm) and CO_2 (λ = 10.6 μm) laser systems are also being employed.

The architecture of a typical LRF system is shown in Fig. A-2 [1]. The transmitter is shown in Fig. A-2 (a) and contains an electro-optically Q-switched laser.

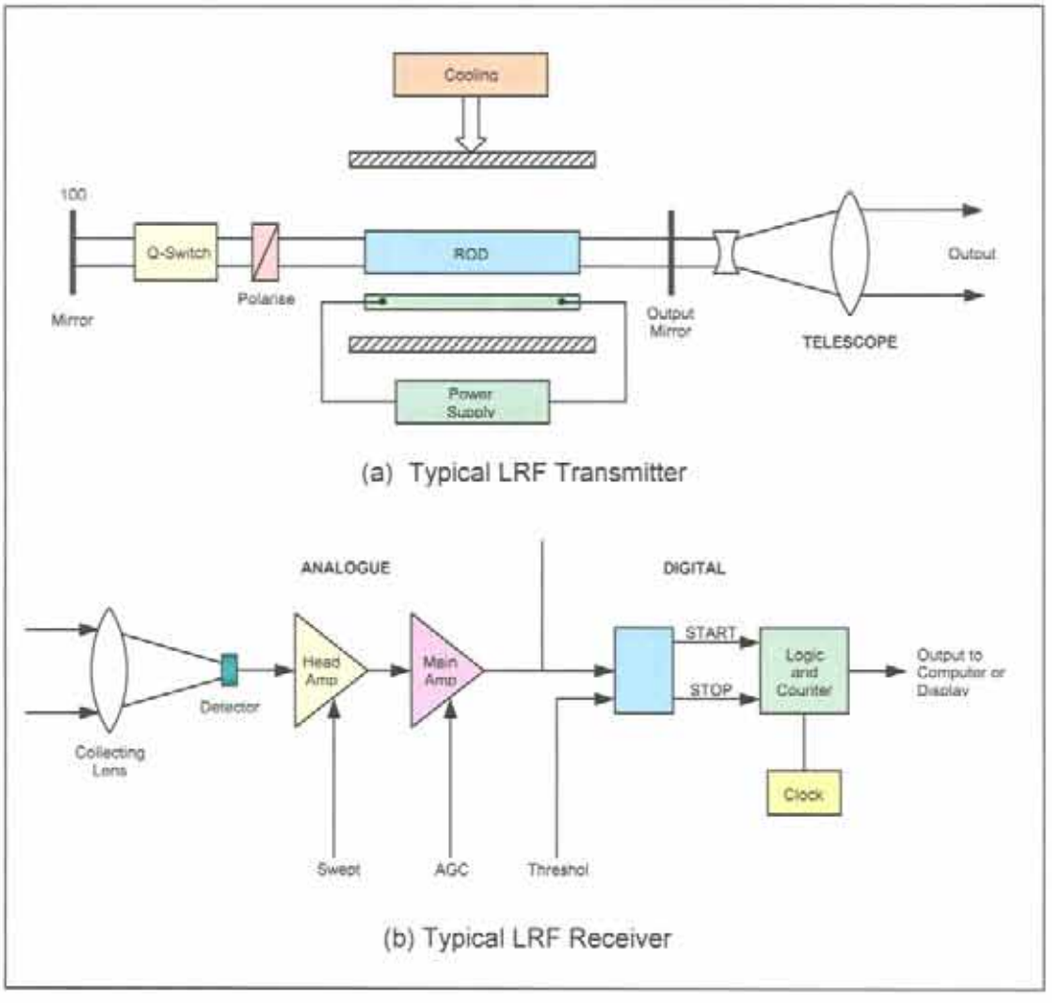

Figure A-2. Typical laser rangefinder architecture.

This type of laser can operate up to 50 pps and produce output pulses with about 10 MW peak power and pulse widths of only 10 to 15 ns. The beam divergence from the laser may be several milliradians and in order to obtain accurate target definition a simple collimating telescope has been added, which would reduce this to less that 1 mrad.

Figure A-2 (b) shows a typical LRF receiver system. The radiation scattered from the target is collected by the receiver which may be a conventional mirror or lens system. The field of view is restricted so that it only just encompasses the transmitted beam, in order to reduce unwanted signals from the natural illumination of the target area and also to improve the security of the overall system. The receiver could also incorporate a narrow pass-band spectral filter centred on the laser wavelength to further reduce the standing background signal which contributes to the overall system noise. The electronics for the receiver are shown in block diagram form and consist of two parts:

- an analogue section, which amplifies the return pulse whilst retaining its shape;
- a digital section, which performs logical timing processes and calculates the range.

Multiple pulse returns are obtained, either because the beam is scattered by the atmosphere, from foliage between the transmitter and target, or from radiation "spilling" over the target and hitting the background. In order to select the correct pulse, either first pulse or last pulse logic can be used. For air-to-ground operations atmospheric backscatter and sightline obscuration are the most likely problems and last pulse logic is favoured. After selection, the correct pulse is fed to a counting circuit which determines the time of transmit, and hence the range.

A.2 Target Designators and Guided Weapons

A Laser Target Designator (LTD) is an accurate pointing system which provides the pulsed laser source and the precision optics and stabilisation required to accurately shine a laser beam on a target. A Laser Guided Wepon (LGW) generates an electric signal (photons converted into electrons) when laser light is received at

the wavelength and with the pulse coding of the LTD system, consequently a portion of the laser light reflecting off of the target is "visible" to the weapon. This provides signals on which the LGW can "home" toward the target by actuating its aerodynamic surfaces. Obviously, the pointing accuracy of the laser is most important, as any laser error degrades the weapon accuracy. In many instances, a slightly modified LRF (pulse coding) serves admirably as a target designator, and it has the added advantage of simultaneously providing slant range to the target.
As already mentioned, the LGW (missile or bomb) does not follow the beam emitted by the designator (as with laser beam riders), but automatically tracks the signal reflected from the target. Currently, two different LGW guidance "strategies" are adopted:

- **Bang-bang guidance**, in which the LGW only senses a position error, and the control fins are driven to the limit of their travel (generally by high-pressure gas), regardless of the magnitude of the error (i.e., the control fins are either at the trail position or full deflection during guidance);

- **Proportional guidance,** in which the LGW seeker continuously tracks the maximum of the reflected laser energy and the LGW computer directs towards the target by actuating the weapon aerodynamic surfaces, giving commands proportional to the measured offset.

Dive, level and loft types of attacks are all possible with Laser Guided Bombs (LGB) and a variety of profiles would be available with airborne Laser Guided Missiles (LGM). In general, two main categories of attacks with LTD/LGW can be distinguished:

- **Self Designation Attacks**, in which the aircraft acts as illuminator for the own carried LGW and laser illumination is automatically controlled by the LTD, manually controlled by the Weapon System Operator (WSO), or by the aircraft computers (e.g., using a pre-planned counter to be chosen between various mutually exclusive possibilities). An example of a typical LGW Self Designation mission profile is reported in Figure A-3(a).

- **Co-operative Designation Attacks**, in which a ground Forward Air Controller (FAC) (or an aircraft) perform illumination with an LTD for the LGW carried by an(other) aircraft. Automatic steering functions are often implemented in co-operative profiles. In these cases, aircraft is forced to pass tangent to the Target Lethal Range (TLR) according to pre-planned steering laws. Also in this case, the laser can be operated by a pre-planned counter or manually. An example of a typical Co-operative mission profile is shown in Fig. A-3(b).

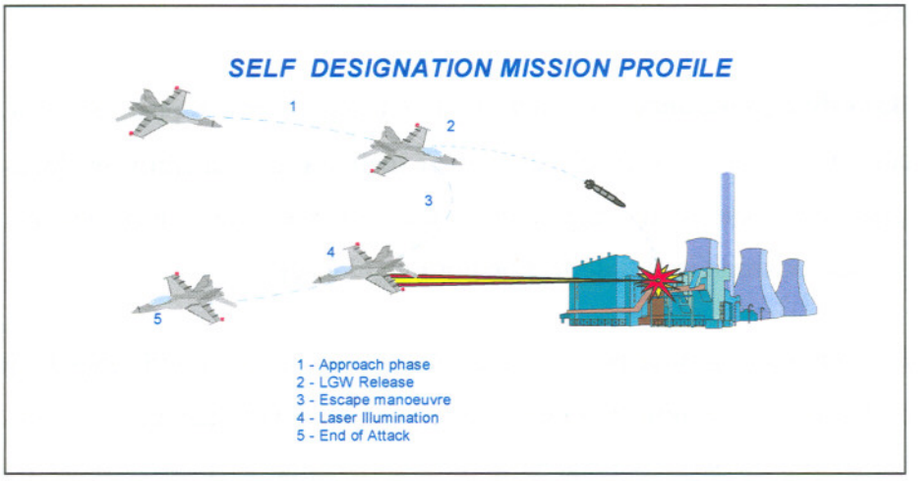

(a) Self Designation Attack.

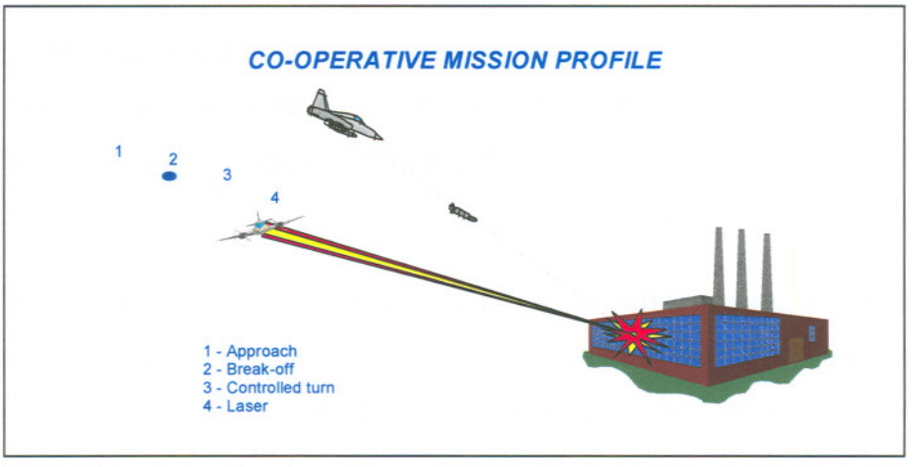

(b) Co-operative Attack.

Figure A-3. LTD/LGW Mission Profiles.

A.3 Laser Radars

Laser radars can be grouped according to the type of measurement made by the laser radar, the detection technique, the type of interferometer employed in a coherent laser radar (if appropriate), the modulation technique, the demodulation technique, the type of laser or the wavelength of operation, the function performed, the type of data collected, or the data format. In addition, laser radar can be classed as monostatic or bistatic, depending on whether it uses a single aperture to transmit and to receive or separate apertures. Some of these groupings are summarized in Table A-1 [2].

The name given to a particular system is seldom sufficient to completely identify what it does and is certainly not sufficient to identify how well it performs.

As can be seen in Table A-1, there are many types of laser radars. The variety found among laser radar systems is one of the primary reasons for their versatility. Unfortunately, it can also create some confusion. For example, wavelength-dependent technological limitations frequently prevent simple parametric extrapolation of performance from one type of system to another. These limitations can make routine performance at a one laser wavelength well beyond the state of the art (and possibly beyond fundamental physical limitations) at another wavelength. Extreme care must be exercised when extrapolating the performance of one type of laser radar to another.

The use of very wavelength specific technology and components represents a significant difference from passive optical systems or conventional radar systems. The availability of laser sources makes only a finite (and small) number of wavelengths practical alternatives for laser radars. Passive optics and conventional radars - Radio Frequency (RF) through Millimeter-Wave (MMW) - can select the wave band to optimise performance without major changes in technology. Laser radars often must change technologies completely (e.g., electrically pumped gas lasers versus optically pumped solid-state lasers) to effect even small changes in operating wavelength.

Types of Lasers (Typical)	Carrier Wavelength
$C0_2$	9.2 μm -- 11.2 μm
Er:YAG	2 μm
Raman Shifted Nd:YAG	1.54 μm
Nd:YAG	1,06 μm
GaAlAs	0.8 μm -- 0.904 μm
HeNe	0.63 μm
Frequency Doubled Nd:YAG	0.53 μm

Detection Technique	Interferometer Type	Modulation Technique
Direct Detection	Not Applicable	Pulsed Amplitude Modulation (AM)
Coherent Detection	Heterodyne Homodyne Offset Homodyne	Pulsed Amplitude Modulation (AM) Frequency Modulation (FM) Hybrid (AM/FM, Pulse Burst) None (CW)

Functions	Measurements
Tracking Moving Target Indication (MIT) Machine Vision Velocimetry Wind Shear Detection Target Identification Imaging Vibration Sensing	Amplitude (Reflectance) Range (Time delay) Velocity (Doppler Shift or differential range) Angular Position Vibration Spectra

Table A-1. Types of Laser Radars.

The concept of operation of a laser radar (LADAR) is identical to that of a conventional radar. Laser radar transmits a signal that is reflected by a target and then collected by the laser radar receiver. Range to the target is determined by measuring the round-trip time of the reflected light. Radial velocity of the target is measured by either determining the Doppler shift of the reflected light or by making two (or more) range measurements and calculating the rate of change of range.

In direct detection laser radar (Fig. A-4), the received optical energy is focused onto a photosensitive element that generates a voltage (or current) that is directly proportional to the optical power that strikes it. This process is identical to a conventional, passive optical receiver or to a typical laser rangefinder (described before).

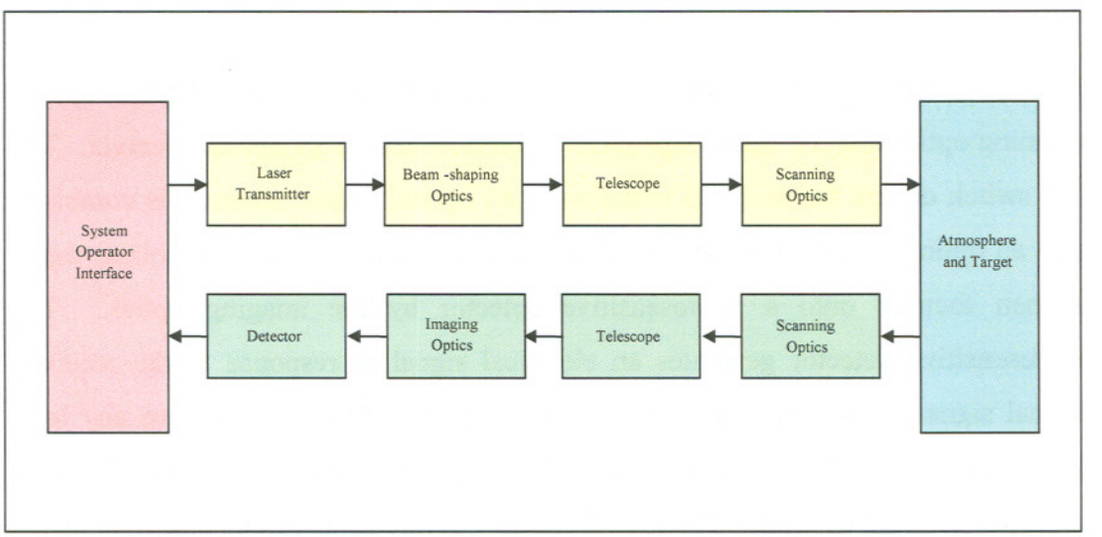

Figure A-4. Block diagram of a direct detection laser radar.

A block diagram, of a typical heterodyne (or coherent) detection laser radar is shown in Fig. A-5. An optical signal is generated by the transmitter laser. The divergence and beam diameter of this optical signal are then matched to the rest of the system by beam-shaping optics. This matching is optional because some systems are designed to operate with the unmodified transmitter laser beam. In a monostatic system, the transmitted laser signal enters a transmit-to-receive (T/R) switch. The T/R switch permits the laser radar transmitter and receiver to operate through a common optical aperture. The laser radar signal then enters the beam expander or output telescope and the scanning optics that direct the optical signal to the target.

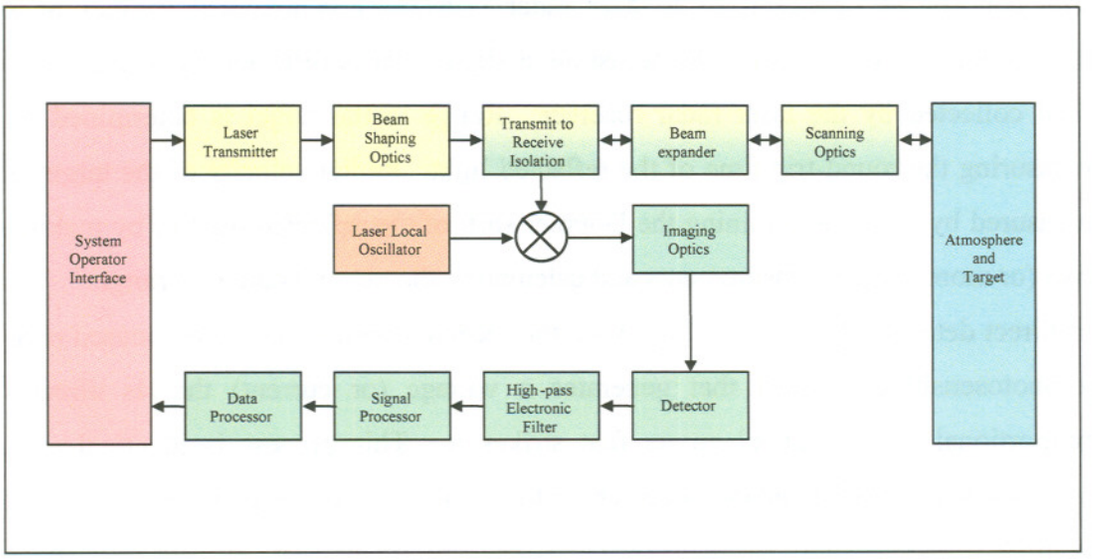

Figure A-5. Block diagram of a coherent detection laser radar.

In a monostatic system, radiation reflected from the target is collected by the scanning optics and the beam expander, which now acts as an optical receiver. The T/R switch directs the received radiation to an optical mixer, where it is combined with an optical reference signal, which is the local oscillator. The combined signal is then focused onto a photosensitive detector by the imaging optics. The photosensitive detector generates an electrical signal in response to the received optical signal. The electrical signal is then high-pass filtered to remove any low-frequency components, such as those from background sources and from the local oscillator-induced dc signal. The high frequency components of this electrical signal contain the target information obtained by the laser radar. Metric information is then extracted from the electrical signal by signal and data processors.

In a bistatic system, the T/R switch is omitted. A separate beam expander and scanning optics are then dedicated to the receiver. The remainder is identical to a monostatic system, as previously described.

An additional distinction, is between conventional heterodyne receivers - requiring a separate laser source to serve as the local oscillator - and homodyne receivers, in which part of the laser radiation from the transmitter source is also used as the local oscillator for the receiver. Furthermore, offset homodyne receivers have been constructed, in which the local oscillator beam portion is frequency shifted from the transmitter beam.

A.3.1 Airborne Laser Radar Applications

Possible airborne LADAR applications include the following:

- Aircraft guidance (obstacle avoidance and terrain following);
- Tactical imaging systems (surveillance and reconnaissance);
- Wind velocity measurement (clear air turbulence and severe storm sensor).

Some of these potential applications are described in the following paragraphs.

A.3.2 Airborne Surveillance and Reconnaissance

Laser systems offer several advantages over the standard photographic and microwave radar methods for airborne surveillance and reconnaissance, such as:

- the high optical resolution and small aperture associated with photographic systems can be made available during both night and day;

- passive beacons utilizing retro-reflection are extremely light and small, of the order of millimetres is size;

- by gating the receiver, the range to scene can be determined and foreground backscatter eliminated.

Line-scan systems use a narrow laser beam to scan the target area. The return energy is detected and then recorded in synchronism on a film or television monitor. Gated-TV systems flood the target area with a short pulse of radiation and use an image tube which can be switched on just before the arrival of the return energy. This allows a range determination and also helps to suppress false returns from haze or obstructions in the foreground. These systems can be used for night-time operation, relatively covert observations, and using a retro-reflector, for target identification, search and rescue, and landing aids.
In this section the use of lasers and their advantages in airborne surveillance and reconnaissance applications will be discussed.

A.3.2.1 Advantages of Laser Illumination

The short wavelength of laser radiation offers high resolution with extremely small size transmitting or receiving apertures. The diffraction-limited property of a laser allows concentration of the radiation in an area of diameter as small as one centimetre with a l0 cm aperture. Although this allows illumination of a very small target area, in practice one would normally use larger illumination areas. For cooperative targets, the optical wavelengths offer extremely efficient and lightweight passive beacons or retro-reflectors. Optical retro-reflectors focus the return signal into a very narrow beam and increase the target reflection. For example a triangular corner retro-reflector has a backscatter cross-section given by:

$$\sigma = \frac{4\pi a^4}{3\lambda^2} \qquad \text{(A.2)}$$

where a is the edge length. Thus a retro-reflector with a one centimetre edge length has an effective backscatter cross-section of approximately 400 m^2 at a wavelength of 10.6 μm. This is increased to approximately 4000 m^2 at a wavelength of 1.06 μm. This simple beacon capability is especially valuable for co-operative tracking, as a landing aid, for search and rescue operations, and in target identification.

A.3.2.2 Systems and Applications

There are two basic types of systems which utilize laser sources for obtaining images from an airborne platform. These systems implement line-scan and gated television modes. In the first method a narrow laser beam is scanned over the ground and the return radiation measured by a spectrally filtered optical detector on board the aircraft. In a gated TV system the whole scene is illuminated by a short pulse of laser radiation and the image recorded through a regular optical system except that the image tube is gated such that it only records the return optical image after a finite delay time, determined by the range to the target area.

The line-scan and gated-TV systems offer both complimentary and unique capabilities compared with normal photography or microwave radar. For example, compared to normal photography, the line-scan system can operate on a 24 hour

basis since it supplies its own source of illumination. Side-looking microwave radar also has a full-time capability and has a much larger area of coverage. However, the limiting resolution is far superior for laser systems, which is very important in certain applications. In the case of the gated-TV system, again the night-time capability has marked advantages over photography, and in addition, the gating facility allows penetration of haze when normal visibility is poor. All these attributes offer distinct advantages for many forms of reconnaissance, although the specific gains are dependent upon the mission.

Beyond the general advantages for obtaining photographic reconnaissance as well as tactical surveillance, the use of simple lightweight passive beacons offers several advantages in certain instances, such as: search and rescue operations, where a downed pilot is supplied with a tiny retro-reflector to aid in location; target identification, where suitable beacons may be used to identify friendly targets; and landing aids, where the retro-reflectors can act as markers for landing strips.

A.3.3 Obstacle Warning Systems

Lasers have also found applications in helping to solve the problems of very low level flight by military aircraft. Military aircraft adopt this low altitude mode of flight in order to enhance their war-zone penetration capability. However, flight at very low levels greatly increases the probability of striking the terrain or man-made obstacles such as wires, poles, towers or buildings.

Conventional radar has the capability to provide a terrain following mode; however, it is inadequate for development into a reliable obstacle warning system. Although microwave systems were the first to be investigated in an attempt to develop obstacle warning systems, these investigations revealed that such radars are not suitable for this application. The nature of the inadequacy is twofold:

- the resolution of microwave wavelengths results in a very low and insufficient energy density at the target (obstacle);

- at microwave frequencies much of the energy that is incident on the obstacle is reflected according to Snell's Law and therefore, unless the beam is incident on

the obstacle at very close to 90 degrees, the energy is reflected away from the receiver.

For a laser radar to be effective as a terrain following and obstacle avoidance system it must meet certain operational criteria of performance. These criteria in turn will dictate the system design.

A.3.3.1 Operational Requirements for an OWS

In order to achieve mission effectiveness in the present threat environment, Western military aircraft operations have focused on-terrain or nap-of-the-earth flying. This is the tactic of employing the aircraft in such a manner as to utilize the terrain profile to enhance survivability by degrading the enemy's ability to visually, optically or electronically detect or locate the aircraft. The radar is required to maintain the aircraft flight at a preset altitude above the terrain. Since the adoption of this philosophy, the incidence of obstacle strike accidents has grown. For an Obstacle Warning System (OWS) to be effective it must meet certain requirements. The first and most important requirement is reliable detection of all obstacles at almost all angles of incidence of radiation with a very high probability of detection and very low false alarm rate. By all obstacles, it is meant terrain masses, buildings, poles, towers, power cables and indeed any structure which may pose a hazard to low, fast flying aircraft.

The need for a high probability of detection is obvious since no obstacle must go undetected. A low false alarm rate is required to prevent spurious warnings that would cause the pilot to increase his altitude without real need, thus making him a better target.

Another operational requirement is the minimum detection range. This will depend upon the aircraft speed, climb angle capability (i.e., very different for helicopter and for airplane platforms), and pilot reaction time. As an example, for an airplane flying straight and level at 300 m/sec and allowing a reasonable pilot reaction time and aircraft response time of between five to ten seconds, detection ranges of about two to three kilometres are adequate. For helicopter applications, this range is generally reduced by an order of magnitude or more.

The system should, ideally, perform all of its required functions in all weather, day and night. In practice however, laser radiation is not capable of all weather operation and the best trade-off of system characteristics must be looked at.

A.3.4 Airborne Wind Velocity Measurements

Extreme wind turbulence is known as wind-shear and the most extreme form of wind-shear is known as a microburst. These phenomena have been blamed for several aircraft accidents in the past few years. The danger is in the fact that, if an aircraft flies into wind-shear at low altitudes without warning, it lacks the height to allow the pilot to compensate for the way the change in wind speed affects the aircraft flight path. Figure A-6 [3] illustrates the way the wind direction and speed change to push an aircraft off course.

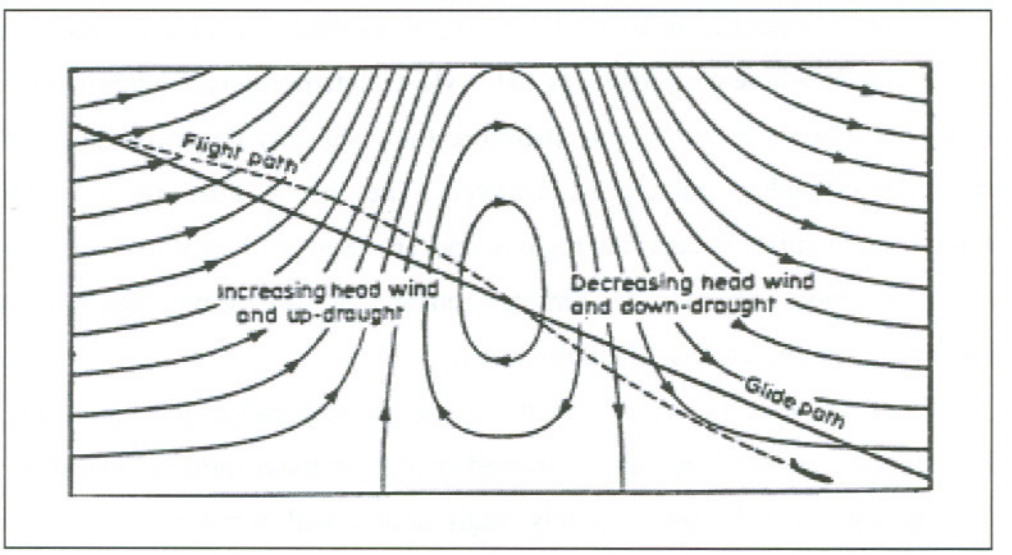

Figure A-6. The wind-shear problem.

Federal Aviation Administration Advisory Circulars in the United States provide guidance for pilots on low-level wind-shear and describe it as: "A change in wind direction and/or speed in a very short distance in the atmosphere". The circulars noted that, under certain conditions, the atmosphere is capable of producing some dramatic shears very close to the ground; for example wind direction changes of 180 degrees with speed changes of 50 knots or more within 200 ft of the ground have been observed.

A microburst lasts for a short period of time, about 15 minutes, and occurs over a distance of about three to four kilometres. Typically, the downdraft in a microburst could be travelling at between 2000 to 5000 ft/min. When flying through a microburst, the aircraft initially encounters a head wind which lifts it above its correct path. The pilot's natural reaction is to bring the aircraft back onto its correct path by, for example, reducing engine thrust. Within a few seconds the aircraft encounters a tail wind which will take the aircraft below its flight path. Now the aircraft needs more lift but the engine thrust has already been reduced and it will take the engine several seconds to respond to provide more power and thus produce the required lift. If the pilot is aware of the wind speed in front of the aircraft and has sufficient warning of impending wind-shear, it is possible for him to take the necessary corrective action.

Conventional Doppler radars have been experimented for many years endeavouring to study such atmospheric phenomena as convective cloud dynamics, boundary layer kinematics, and turbulence properties [4]. Most meteorological radars operate at wavelengths between 3 and 10 cm, therefore they can only detect particles of the order of a few hundred microns in diameter. They are of little use for studying atmospheric dynamics in clear-air regions and are used primarily to detect severe storms. A more appropriate remote sensor for providing clear-air wind measurements is coherent laser Doppler radar.

The methods of sensing wind velocity using a laser radar are based on the assumption that aerosols are fully entrained in the air mass motion caused by the wind. The laser provides an extremely bright source with a narrow spectral width which, when focused on an object, can give sufficient scattered radiation to permit measurement of very low velocities by means of heterodyne detection methods. This process is termed Laser Doppler Velocimetry (LDV).

Laser Doppler systems have been under research for some time and the main aim initially was to provide a system to make remote measurements of the wind so that very large changes (e.g., wind-shear) could be identified. Systems are now under development that can be fitted into the nose of an aircraft and can be used to measure the wind speed in front of the aircraft where it is unaffected by the airflow around the fuselage or wings. Furthermore, laser Doppler systems that can measure wind speed and wind changes accurately could prove useful in the design of an auto-

throttle system that would help to reduce the workload of the pilot. This system could be used on both military and civilian aircraft to improve safety, particularly during takeoffs and landings.

A.3.5 Multi-Sensor Systems

Laser radar, while being a powerful sensor for airborne applications, still has its limitations. As an obstacle warning or an attack sensor its range is degraded by adverse weather. When used for terrain flying, its narrow beamwidth does not allow wide coverage as does conventional radar; consequently, it can only be used as a backup system. However, as part of a multi-sensor system, laser radar could be very powerful. An example is the combination of a laser radar with a Forward Looking Infra-Red (FLIR) sensor in a single system. This solution offers night vision using the FLIR with the terrain flying and obstacle avoidance capabilities of the laser.

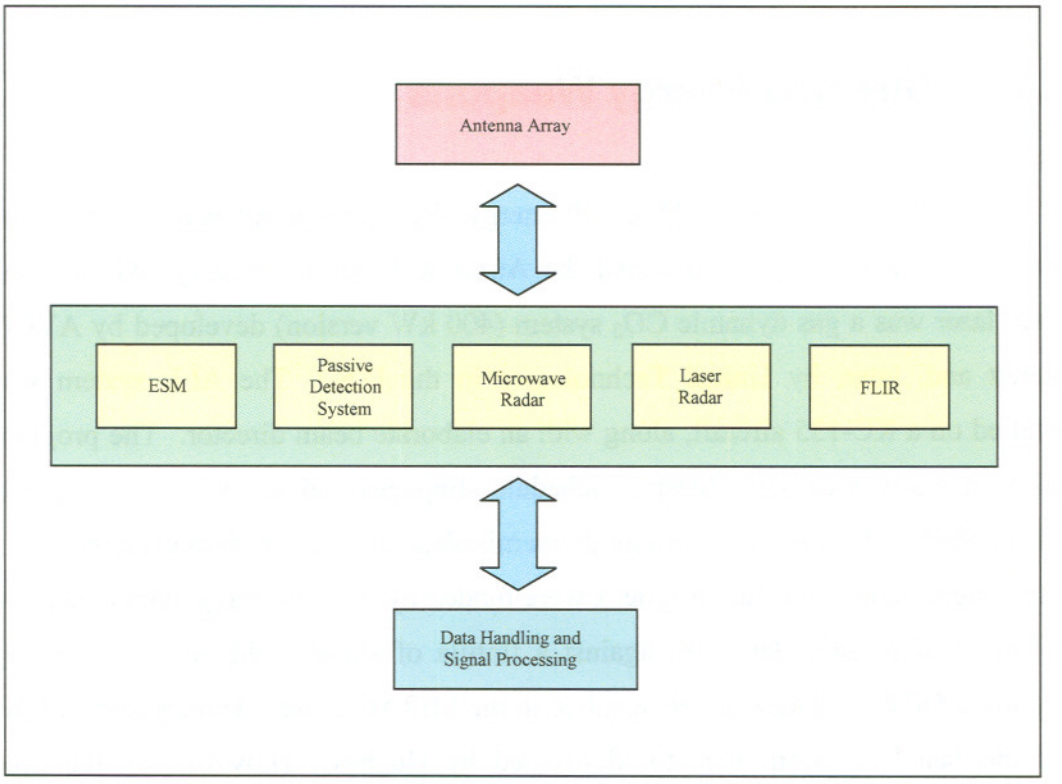

Figure A-7. Example of Multi-sensor System.

Fig. A-7 is an example of a combined radar and electronic surveillance system which could perform five different functions:

- passive listening, for gathering intelligence on other radar and transmissions over a wide frequency band;
- laser obstacle avoidance and terrain following for covert operation;
- primary radar for use in bad weather or as a cueing system for laser radar;
- passive detection for accurate determination of the bearing of jammers or other radars;
- real-time passive night vision.

The control of these functions would obviously involve complex computer processing which would respond to the various operational situations. Considerable research is currently underway addressing the problem of laser sensors integration in airborne integrated nav-attack, recognisance and electronic warfare systems.

A.4 Directed Energy Weapons

The first airborne Directed Energy Weapon (DEW) was tested in the mid-1970's, under a program called the Airborne Laser Laboratory (ALL). The tested laser was a gas dynamic CO_2 system (400 kW version) developed by AVCO Everett and, later, by United Technologies in the U.S.. The ALL system was installed on a KC-135 aircraft, along with an elaborate beam director. The program was technically successful (despite schedule slippages and an early missed shot), and the ability of the system to shoot down missiles in flight was demonstrated [5].
In the late seventies, further programs were funded by the U.S. Navy, convinced that the threat of missiles launched against a flotilla of ships could be minimised by shipborne DEW's. These efforts resulted in the MIRACL laser, developed by TRW, and the Sea Lite Beam Director developed by Hughes. However, by the time MIRACL was operational, shipborne antimissiles and guns proved to be a more attractive choice due to their lower cost and more mature technology. If DEW's were too expensive and complex for the defence of tactical assets, the logic followed

that they might be used to "take out" opponent's strategic military assets, such as satellites.

Although these early airborne and non-airborne applications did not reach the final operational stage, they served to develop several different laser technologies (primarily chemical and free electron lasers), which are now being used in current military developments and in a wide diversity of commercial applications.

An airborne laser DEW system is now being developed in the U.S.. The system, named ABL ("Air Borne Laser"), uses a high-energy laser mounted on a modified 747-400F aircraft to shoot down heater ballistic missiles in their boost phase. Particularly, a tracking laser beam illuminates the missile, and computers measure the distance and calculate its course and direction. After acquiring and locking onto the target, a second laser (with weapons-class strength) fires a 3- to 5-second burst from a turret located in the 747 nose. The missile is then destroyed over the launch area. A pictorial representation of the ABL operation concept is shown in Fig. A-8.

Figure A-8. ABL concept of operation.

The airborne laser fires a Chemical Oxygen Iodine Laser, or COIL, which was invented at Phillips Lab in 1977. The laser fuel consists of the same chemicals found in hair bleach and Drano (hydrogen peroxide and potassium hydroxide) which are then combined with chlorine gas and water. The laser operates at an infrared wavelength of 1.315 microns, which is invisible to the eye. By recycling chemicals, building with plastics and using a unique cooling process, the COIL team was able to

make the laser lighter and more efficient while, at the same time, increasing its power by 400 percent in five years. The flight-weighted ABL module is similar in performance and power levels to the multi-hundred kilowatt class COIL Baseline Demonstration Laser (BDL-2) module demonstrated by TRW in August 1996. As its name implies, though, it is lighter and more compact than the earlier version due to the integration of advanced aerospace materials into the design of critical hardware components. For the operational ABL system, several modules have been linked together in series to achieve ABL required megawatt-class power level.

Atmospheric turbulence, which weakens and scatters the laser's beam, is produced by fluctuations in air temperature (the same phenomenon that causes stars to twinkle). Adaptive optics relies on a deformable mirror, sometimes called a rubber mirror, to compensate for tilt and phase distortions in the atmosphere. The mirror has 341 actuators that change at a rate of about a 1,000 per second.

The Airborne Laser is a Major U.S. Defense Acquisition Program. Testing of the laser module has been completed. The Program Definition and Risk Reduction (PDRR) phase (detailed design, integration, and test) will culminate in a lethality demonstration in the year 2002. A follow-on Engineering Manufacturing and Development/Production (EMD) effort could then begin in the early 2003 time frame. A fleet of fully operational EMD systems is intended to satisfy Air Combat Command's boost-phase Theater Air Defense requirements. If all goes as planned, a fleet of seven ABLs should be flying operational missions by 2008.

Performance requirements for the Airborne Laser Weapons System are established by the operational scenarios and support requirements defined by the user, U.S. Air Combat Command, and by measured target vulnerability characteristics provided by the U.S. Air Force lethality and vulnerability community centred at the Phillips Laboratory. The ABL PDRR Program is supported by a robust technology insertion and risk reduction program to provide early confidence that scaling to EMD performance is feasible. The technology and concept design efforts provide key answers to the PDRR design effort in the areas of lethality, atmospheric characterization, beam control, aircraft systems integration, and environmental concerns. These efforts are the source of necessary data applied to exit criteria ensuring higher and higher levels of confidence are progressively reached at key milestones of the PDRR development.

A.5 Airborne Laser Data Links

Modern battlefield strategy is predicated on knowing where the enemy's (or potential enemy's) assets ore located and their operational capability. This vital information is constantly being gathered and updated by various ground, space, and airborne sensors. The requirement to send ever increasing amounts of tactical military information between sensor aircraft and information processing facilities has begun to press the limits of present airborne data links, even when data compression techniques are used. Therefore, utilization of optical data links is being considered as a possible solution.

The feasibility of laser airborne data links was demonstrated in the mid-80's by the U.S. Air Force Research Laboratory HAVE LACE (Laser Airborne Communications Experiment) Program. This program develop and tested two laser communications terminals that operated at 19.2 kilobits/sec. The terminals were tested using two KC-135 aircraft that nominally flew at 20,000 to 25,000 feet (ft) altitudes with separation distances out to 160 km. The most significant result of the HAVE LACE flights was the difficulty of initial signal acquisition between the two moving platforms, since it had to be performed manually. However, once signal acquisition was accomplished, tracking proved to be robust and communications performance was consistently measured at 10^{-6} bit error rate (BER) or better.

Since the HAVE LACE program, laser terminal development and data rates have improved dramatically. Therefore, various research programs have been undertaken in order to fully exploit the potentials of this technology, mainly for spaceborne and airborne applications. Another U.S. Air force program is currently ongoing to develop a wideband laser data link operating at 810 and 852 nm [6]. In September 1995, the program successfully ground demonstrated a 1.1 gigabit/second full duplex data link over a distance of 150 km (Hawaii Islands). Successively, the system used in the ground demonstration was redesigned and installed in two jet aircraft for flight demonstration at distances up to 500 km. The demonstration flights, performed in September 1998, were successful and proved the ability of the system to communicate in the upper atmosphere to 500 km with a BER of 10^{-6}. The tests also provided data on atmospheric attenuation and beam scintillation. Furthermore, data on the effects of aircraft airflow upon beam steering were also

collected. These data, and the information obtained from similar developments, are now being used for other laser communication development efforts (e.g., an air-to-space capability).

A.6 References

1. Hulme K.F., "CO2 Laser Heterodyne Rangefinders". Infrared Physics Vol. 25 (N° 1-2). 1985.
2. Kamerman G.W., "Laser Radar". ERIM-SPIE IR&EO Systems Handbook - Vol. 6 (Chapter 1). Second Printing. 1996.
3. Hardesty R.M., Elmore K. and Minisclou S., "The Anglo-French Compact Laser Radar Demonstrator Programme". AGARD-CP-563. 1995.
4. Grossman J., "The Airborne Laser Laboratory (ALL) Completes Successful Tests". International Defense Review - Vol. 116. 1983.
5. Gill R.A. and Feldmann R.J., "Development of a Wideband Airborne Laser Data Link". AGARD-CP-595. 1998.

Appendix B

LASER RANGE EQUATION AND SYSTEMS DETECTION PERFORMANCES

B.1 Laser Range Equation

Since the subject of our discussion is electromagnetic propagation, the microwave radar range equation also applies to laser systems [1]:

$$P_R = \frac{P_T G_T}{4\pi R^2} \times \frac{\sigma}{4\pi R^2} \times \frac{\pi D^2}{4} \times \tau_{atm} \tau_{sys} \qquad \text{(B.1)}$$

where:

P_R = received signal power (W);
P_T = transmitter power (W);
G_T = transmitter antenna gain;
α = transmitter beamwidth;
σ = effective target cross section (m^2);
K_a = aperture illumination constant;
R = system range to target (m);
λ = wavelength (m);
D = aperture diameter (m);
τ_{atm} = atmospheric transmission factor;
τ_{sys} = system transmission factor.

With laser systems [2], the transmitter antenna gain is substituted by the aperture gain, expressed by the ratio of the steradian solid angle of the transmitter beamwidth $(\alpha)^2$ to that of the solid angle of a sphere, which is equal to the relation:

$$G_T = 4\pi/\alpha^2 \tag{B.2}$$

For laser beamwidths on the order of 1 mrad, the typical aperture gain at laser wavelengths is about 70 dB. In the far field, we may also write the transmitter beamwidth as:

$$\alpha = K_a \lambda / D \tag{B.3}$$

Substituting the above expressions for transmitter aperture gain (B.2) and beamwidth (B.3), equation (B.1) becomes:

$$P_R = \frac{P_t \sigma D^4 \tau_{atm} \tau_{sys}}{16 R^4 \lambda^2 K_a^2} \quad \text{(in the far-field)} \tag{B.4}$$

Eq. (B.4), obtained from the standard radar range equation, applies only in the far field of the aperture. At typical microwave bands of λ = 1 to 10^{-3} m, the far-field distances are quite short, as shown in Fig. B-1. The far-field (*Fraunhofer*) region of an aperture is typically concerned with the distance $2D^2/\lambda$ to infinity; in this vicinity, the generalised range equation applies. In some cases, the far field distance occurs within the feed horn assembly of a microwave antenna. As illustrated by the figure, at λ = 1.064 μm (Nd:YAG laser), a 10 cm aperture has a far-field distance of approximately 20 km. As a result, it is not unusual to operate in the near-field of the optical systems; thus modifications to the range equation to account for near-field operation is required.
This near-field effect modifies the beamwidth such that:

$$\alpha = \sqrt{\left(\frac{K_a D}{R}\right)^2 + \left(\frac{K_a \lambda}{D}\right)^2} \tag{B.5}$$

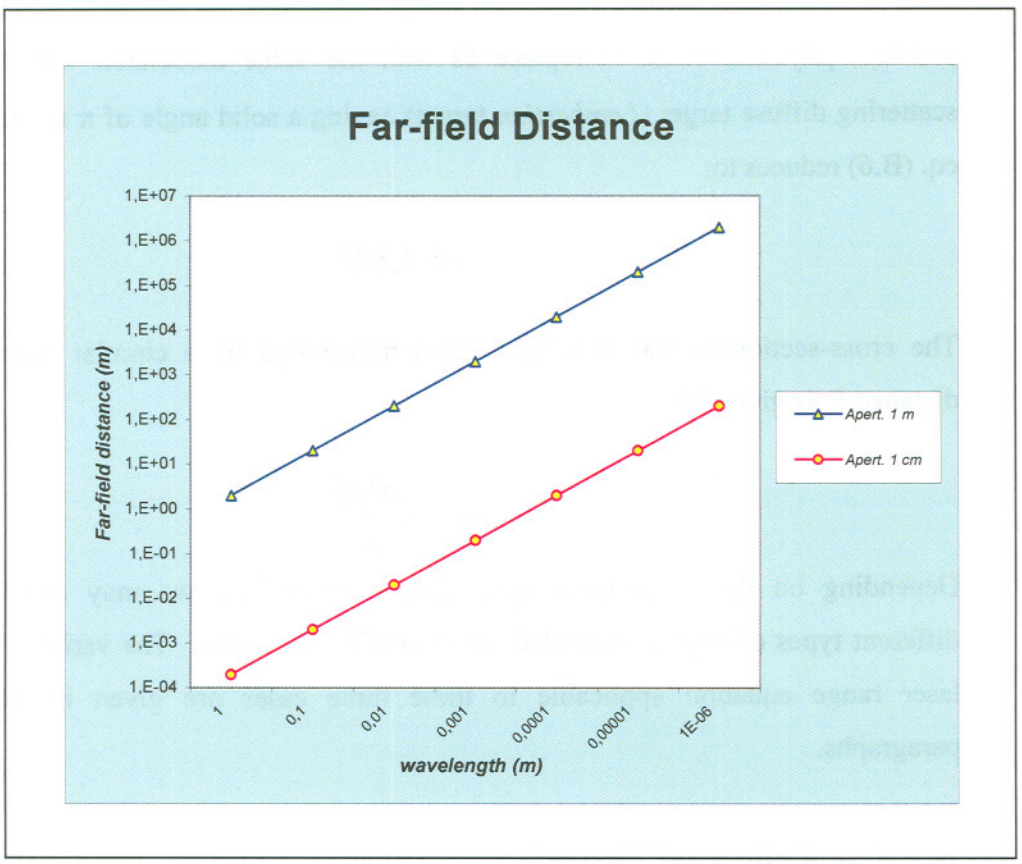

Figure B-1. Far-field distance versus λ for 1 m and 10 cm apertures.

B.2 Range Equation Dependence on Target Area

The effective target cross-section is defined as:

$$\sigma = \frac{4\pi}{\Omega}\rho dA \tag{B.6}$$

where:

Ω = scattering solid angle of target (sr);

ρ = target reflectivity;

dA = target area.

Both specular and diffuse reflection components may be considered. However, in practice, physicists tend to replace Ω with the value associated with the standard scattering diffuse target (*Lambertian* target) having a solid angle of π steradians. Thus, eq. (B.6) reduces to:

$$\sigma = 4\rho_T dA \tag{B.7}$$

The cross-sectional area of a laser beam transmitted by a circular aperture from a distance R, is given by:

$$dA = \frac{\pi R^2 \theta_T^2}{4} \tag{B.8}$$

Depending on the target-laser spot relative dimensions we may distinguish three different types of targets: extended, point and linear targets. The various forms of the laser range equation applicable to these three cases are given in the following paragraphs.

B.2.1 Extended Target

For an extended target (Fig. B-1), all incident radiation is involved in the reflection process. Thus, for an extended *Lambertian* target we have:

$$\sigma_{ext} = \pi\rho R^2 \theta_T^2 \tag{B.9}$$

Hence, using eq. (B.4), we have:

$$P_R = \frac{\pi P_T \rho D^2 \tau_{atm} \tau_{sys}}{16 R^2} \tag{B.10}$$

Therefore, with narrow laser beams, we may have an inverse range square dependency of the range performance obtained with a certain target, compared to the standard inverse fourth power of range dependency of microwave systems.

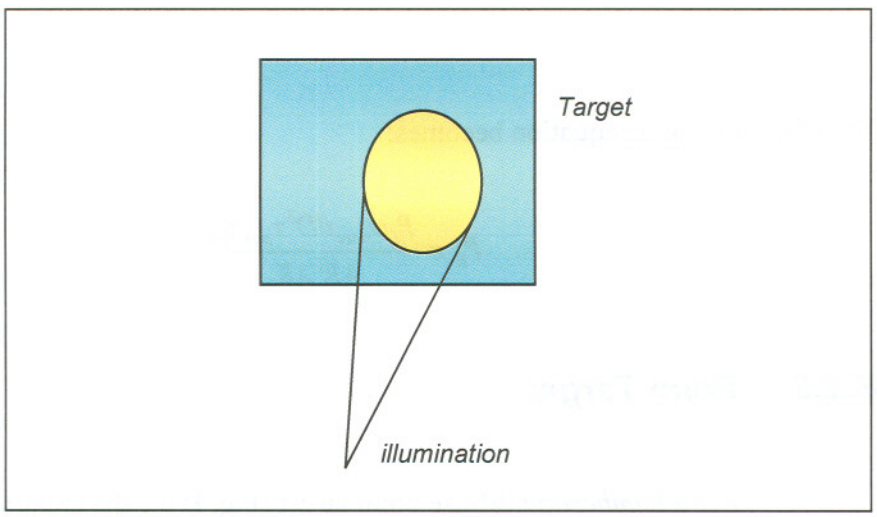

Figure B-2. Extended Target.

B.2.2 Linear Target

A linear target, such as a wire (Fig. B-3), can have a length larger than the illuminated area but a smaller width (d). For a typical diffuse (*Lambertian*) wire target, the target cross-section may be shown to be approximately:

$$\sigma_{wire} = 4\rho_{wire} R\theta d \tag{B.11}$$

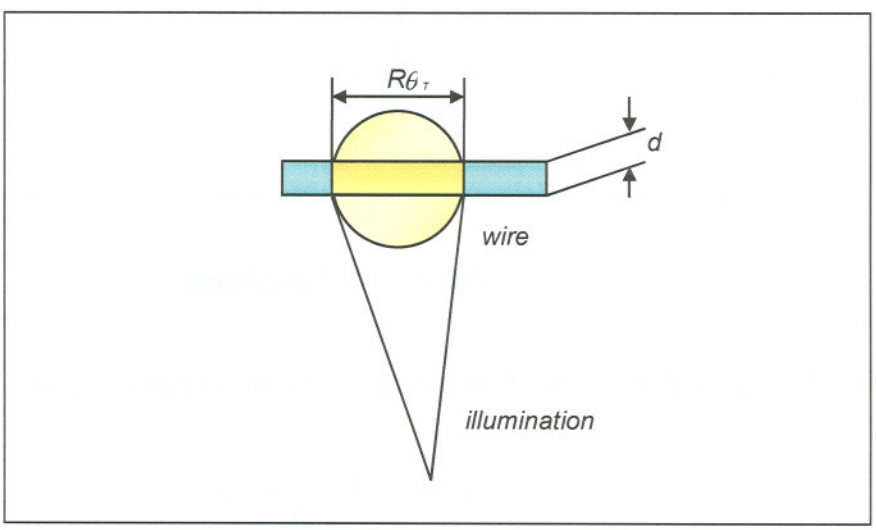

Figure B-3. Linear Target.

Therefore, the range equation becomes:

$$P_R = \frac{P_T \sigma_{wire} dD^3 \tau_{atm} \tau_{sys}}{4R^3 \lambda K_a} \tag{B.12}$$

B.2.3 Point Target

For a *Lambertian* diffuse point target (Fig. B-4), the cross section becomes:

$$\sigma_{pt} = 4\rho_T dA \tag{B.13}$$

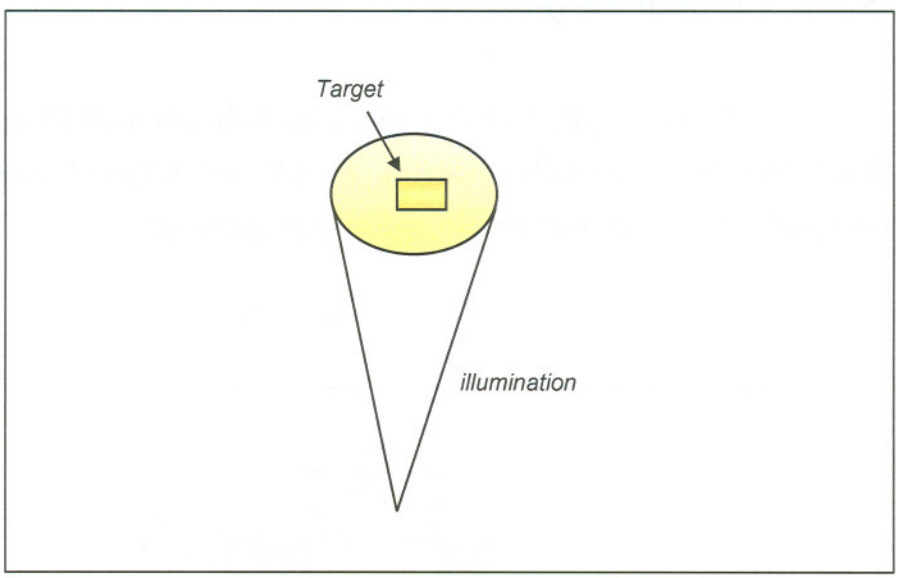

Figure B-4. Point Target.

Substituting the point target cross section in the range equation gives:

$$P_R = \frac{P_T \rho dAD^4}{4R^4 K_a^2 \lambda^2} \tau_{sys} \tau_{atm} \tag{B.14}$$

B.3 Receiver Detection Techniques

Fig. B-5 shows diagrams relative to incoherent detection (ID) and coherent detection (CD) receivers [2]. ID receivers at optical wavelengths are similar to video radiometers receivers (i.e., envelope detectors at microwave wavelengths). However, optical receivers have an additional term besides the signal term (P_{SIG}), the optical background power (P_{BK}) which is due to undesired signals such as sunlight, cloud reflections, flares, etc.. The received optical power, after suitable filtering, is applied to the optical detector. Square law detection then occurs, producing a video bandwidth electrical signal.

The coherent detection receiver is similar to the incoherent; however, a portion of the laser signal (f_o), is coupled to the optical detector via beamsplitters. As a result, the optical detector has the local oscillator power (P_{LO}) in addition to the received signal power (P_{SIG}), and the competing background terms (P_{BK}).

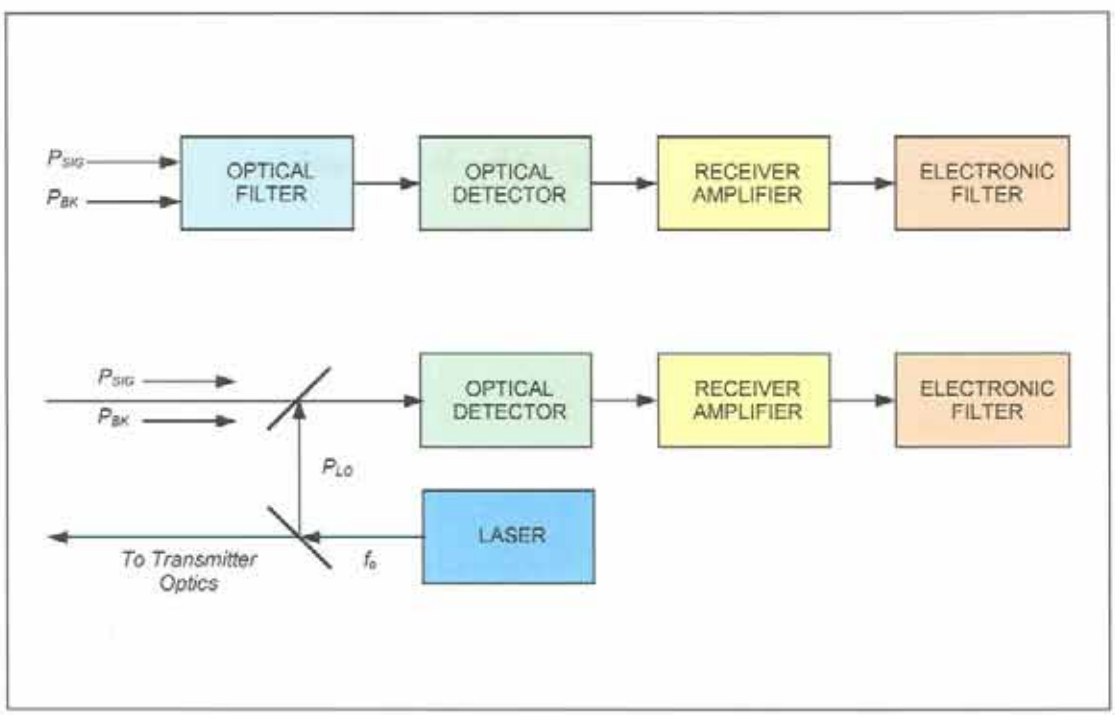

Figure B-5. Laser receiver systems.

B.4 Background Noise Terms

Noise terms in an optical receiver are not the same considered in the microwave receivers. Particularly, background noise in optical receivers includes reflections of signals from the earth, the sun, the atmosphere, clouds, or any other source that constitutes an undesired signal to the receiver. Signal-induced noise refers to the noise caused by the receiver signal itself coming into the detector. Also the received signal causes a noise to be generated. This noise is called quantum noise (*Poisson*) because it is induced by the signal when the signal exists.

The following equations are those associated with calculating the amount of background radiation that may be incident upon a receiver [2]:

Blackbody Radiation

$$P_{BB} = \frac{\varepsilon k T^4 \Delta\lambda \Omega_R A_R}{\pi} \eta_{SYS} \eta_{ATM} \tag{B.15}$$

Solar Backscatter

$$P_{SB} = k_t S_{IRR} \Delta\lambda \Omega_R \rho \eta_{SYS} A_R \tag{B.16}$$

Atmospheric Solar Scatter

$$P_{NS} = k_t S_{IRR} \Delta\lambda \Omega_R I_S \eta_{SYS} A_R \tag{B.17}$$

where:

ε = target emissivity;

ρ = target reflectivity;

T = temperature (°K);

$\Delta\lambda$ = optical badwidth (μm);

A_R = receiver area (m^2);

k_t = fraction of solar radiation penetrating Earth's atmosphere;

S_{IRR} = solar irradiance (W/m^2-μm);

I_S = atmospheric scatter coefficient;

η_{SYS} = system optical efficiency;

Ω_R = solid angle over which energy radiates from radiating body;

σ_T = Stefan-Boltzmann constant (5.67×10^{-12} W cm^{-2} °K^{-4}).

B.5 SNR Expression Development

In general, the signal-to-noise ratio (SNR) of a laser radar system can be expressed in the form [2]:

$$SNR = \frac{i_{SIG}^2}{i_{SN}^2 + i_{TH}^2 + i_{BK}^2 + i_{DK}^2 + i_{LO}^2} \tag{B.18}$$

where:

i_{SIG}^2 = mean square signal current;

i_{SN}^2 = mean square shot noise current;

i_{TH}^2 = mean square thermal noise current;

i_{BK}^2 = mean square background noise current;

i_{DK}^2 = mean square dark noise current;

i_{LO}^2 = mean square local oscillator noise current (CD systems only).

The mean squared background noise term may be expressed as:

$$i_{BK}^2 = 2qP_{BK}\rho_i B \tag{B.19}$$

where:

q = electron charge (1.602×10^{-19} Coulombs);

P_{BK} = background power (W);

ρ_i = current responsivity (A/W);

B = electronic bandwidth (Hz).

Shot noise is due to fluctuations in the detector output caused by the random arrival of signal photons. The mean square shot noise current is given by:

$$i_{SN}^2 = 2qP_{SIG}\rho_i BG^2 \tag{B.20}$$

where G is the detector gain.

In the absence of photons at the detector, there is a current flowing, termed the detector dark current (I_{DK}). The mean square dark current term in eq. (B.18) is given by:

$$i_{SN}^2 = 2qI_{DK}B \tag{B.21}$$

The thermal noise current term can be expressed as:

$$i_{TH}^2 = \frac{4kTBNF}{R_L} \tag{B.22}$$

where:

NF = receiver noise factor;

k = Boltzmann's constant (1.39×10^{-23} J/°K);

R_L = detector load resistance.

For coherent detection systems, assuming that a photovoltaic detector is employed, the local oscillator induced noise is given by:

$$i_{LO}^2 = 2qP_{LO}\rho_i B \tag{B.23}$$

where P_{LO} is the local oscillator power.

For a photoconductor detector, an additional noise term, called generation-recombination noise (i_{GR}^2), can arise:

$$i_{GR}^2 = 4q\rho_i(P_{LO} + P_{SIG})B \tag{B.24}$$

The signal current, for incoherent and coherent systems, is determined as:

$$i_{SIG} = \frac{\eta_D q P_{SIG} G}{hf} \quad \text{incoherent} \tag{B.25}$$

$$i_{SIG} = \frac{\eta_D q P_{SIG} G}{hf} \quad \text{coherent} \tag{B.26}$$

where η_D is the detector quantum efficiency.

B.6 Incoherent and Coherent Detection Comparison

Considering the various receiver noise and signal terms, two forms of the SNR equation can be obtained, for incoherent and coherent detection systems. These two equations are presented below [2].

Incoherent detection

$$SNR = \frac{\eta_D P_{LO} P_{SIG}}{hf\left[2B(P_{SIG} + P_{BK})\right] + K_i(P_{DK} + P_{TH})} \tag{B.27}$$

Coherent detection

$$SNR = \frac{\eta_D P_{LO} P_{SIG}}{hfB(P_{LO} + P_{SIG} + P_{BK}) + K_j(P_{DK} + P_{TH})} \tag{B.28}$$

where:

η_D = detector quantum efficiency;

h = Planck's constant (6.626×10^{-34});

f = transmission frequency;

B = electronic bandwidth;

P_{SIG} = received signal power;

P_{BK} = background power;

P_{DK} = equivalent dark current power = $A_d B/(D^*)^2$;

P_{TH} = equivalent receiver thermal noise = $\frac{4kTBNF}{R}$;

P_{LO} = reference local oscillator power;

k = Boltzmann's constant (1.39×10^{-23} J/°K);

T = receiver temperature (290 °K);

NF = receiver noise figure;

R_L = resistance;

K_i = η_d / ρ_i^2 ;

K_j = $hf/2qp$,

and:

ρ_i = detector current responsivity (A/W);

D^* = specific detectivity (cm-$Hz^{1/2}$/W);

A_d = detector area (cm^2);

q = electron charge (1.6×10^{-19} Coulombs).

The SNR for the incoherent system has the received signal power squared in its numerator, and has a summation of noise terms associated with the return signal, the background signal, the dark current, and the thermal noise of the receiver in the denominator. The returned signal power and the background power are included as noise sources in the detection process because of the random photon arrival rate (*Poisson* noise). In the coherent detection system, the local oscillator power is an additional source of noise (compared to the incoherent system), and the numerator is related to the product of the received signal power and the local oscillator power. The local oscillator power is very important in the detection process; here, it may be

increased so that it overwhelms all of the other noise sources. As a result, the local oscillator power in the denominator cancels out the local oscillator power in the numerator; the SNR is directly proportional to the received signal power, rather than to the received signal power squared (as with the incoherent system). Additionally, because the local oscillator power becomes the predominant noise source, the coherent detection system typically is background immune, since only signals that are phase coherent with the local oscillator are efficiently detected.

For coherent detection where the local oscillator power is increased to provide shot-noise-limited operation of the receiver, the SNR expression for coherent detection reduces to:

$$SNR = \frac{i_{SIG}^2}{i_N^2} = \frac{\eta_D P_{SIG}}{hfB} \quad \text{or} \quad SNR = \frac{\eta_D E_{SIG}}{hf} \tag{B.29}$$

where E_{SIG} is the received signal energy, B is the matched filter bandwidth ($B=1/T$) and SNR represents the number of detected photons if $\eta_D = 1$.

For a background noise-limited incoherent receiver, eq. (B.27) becomes:

$$SNR = \frac{\eta_D P_{SIG}^2}{2hfBP_{BK}} \tag{B.30}$$

Fig. B-6 [2], illustrates the reference transmitter power versus SNR relationship for coherent and incoherent detection laser radar systems using a 100-ns pulse width, with $\eta_D = 0.5$, $hf = 1.9 \times 10^{-20}$ Joules, $D^* = 2 \times 10^{10} \ \frac{cm\sqrt{Hz}}{W}$, $\sqrt{A_d} = 0.03$ cm, $\rho_i = 4$ A/W and $R = 1$ kΩ, at $\lambda = 10.6$ μm. It may be observed that as the SNR requirement increases, the transmitter power of the coherent system increases linearly, and that of the incoherent system increases as the square root. In the limit, incoherent detection systems approach the sensitivity of coherent systems for very large SNRs. For a typical SNR requirement of 100 (20 dB), the coherent system is seen to have a 30-dB increased sensitivity over that of an incoherent system.

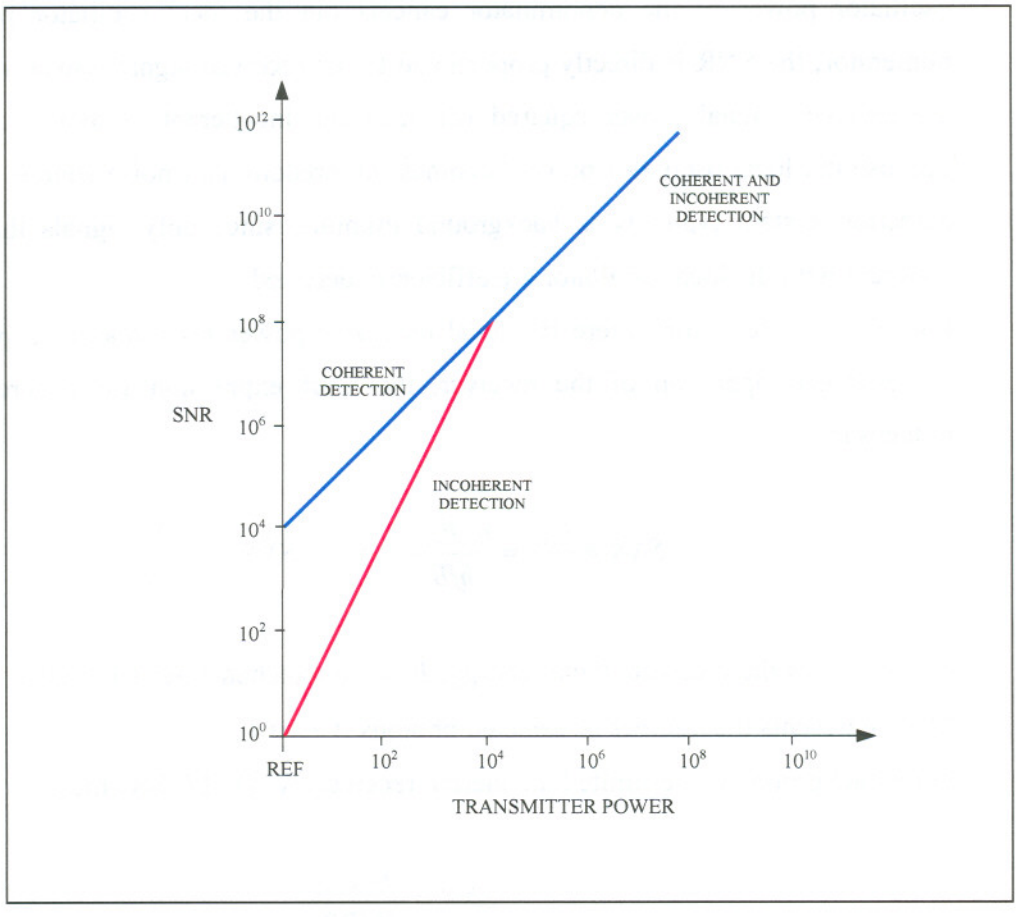

Figure B-6. Transmitter power versus SNR for coherent and incoherent detection.

B.7 References

1. Skolnik M.I., "Introduction to Radar Systems". McGraw-Hill (New York). 1980.
2. Jelalian A.V., "Laser Radar Systems". Artech House (Boston-London). 1992.

Examples of these results are shown in Fig. 9-37.

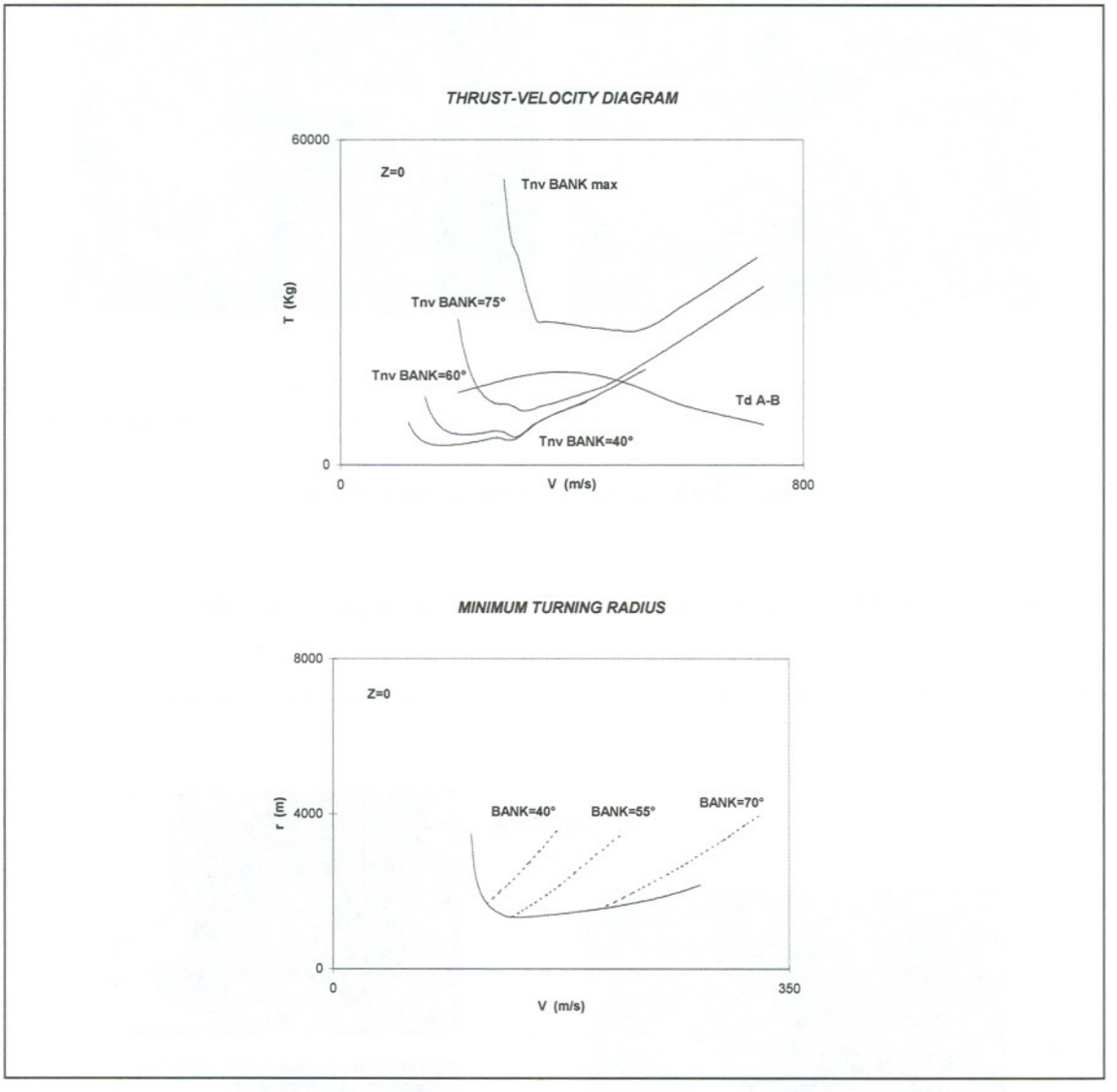

Fig. 9-37. Performance analysis results.

9.5 LOAS Flight Test Campaigns

LOAS system flight trials were performed using two different test platforms: NH-300 and AB-212 helicopters. Fig. 9-38 shows the LOAS prototype system used for the flight trials. Particularly, the LOAS sub-units are shown in Fig. 9-38(a), while the Sensor Head Unit (SHU) and pilot interface units are shown in Fig. 9-38(b).

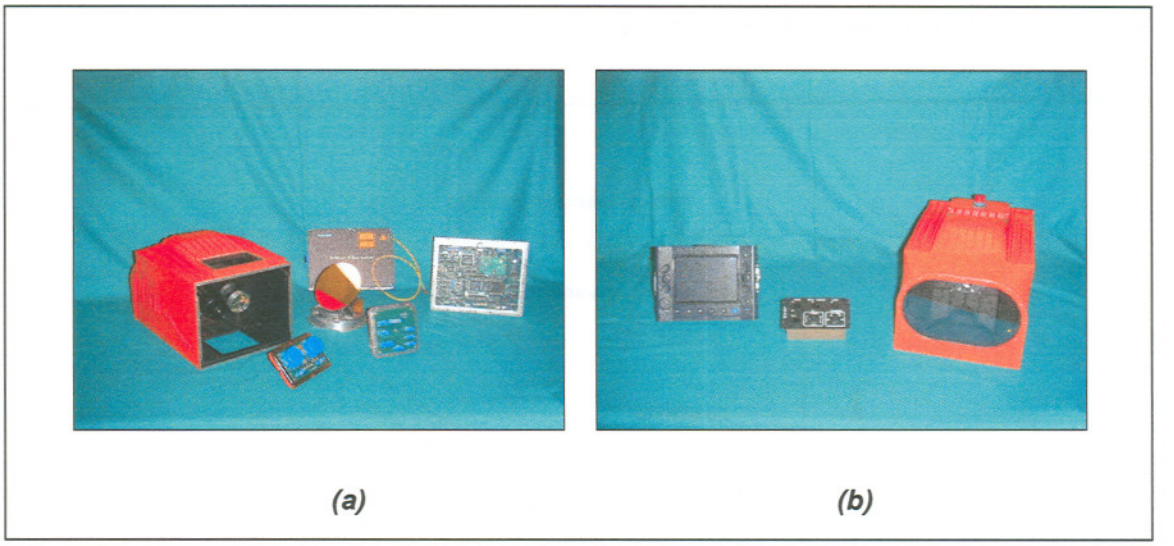

Figure 9-38. LOAS prototype used in the trials.

Fig. 9-39 shows the LOAS installed on the first test helicopter (NH-300).

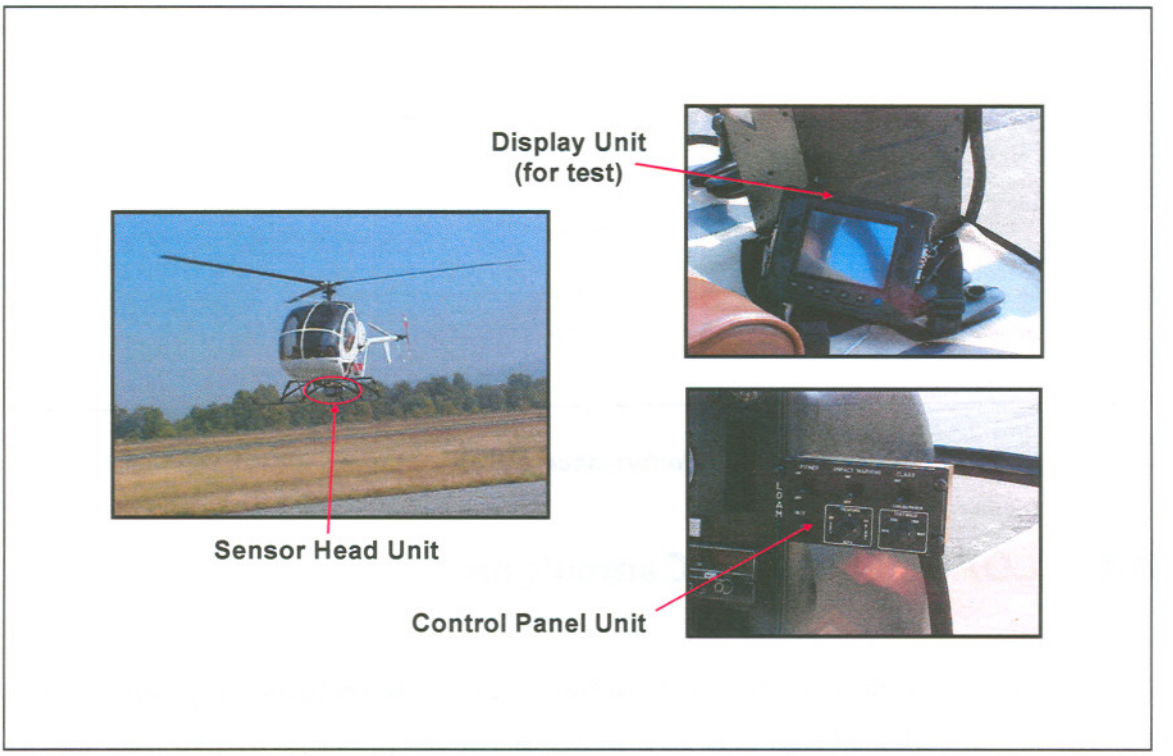

Figure 9-39. LOAS prototype units installed on the NH-300 helicopter.

Fig. 9-40 shows the LOAS SHU mounted on the second test helicopter (AB-212).

Figure 9-40. LOAS SHU installed on the AB-212 helicopter.

The Cockpit Display Unit (CDU) used for the AB-212 flight trials is shown in Figure 9-41(a). As shown in Figure 18-b, the LOAS CDU was installed in the center of the AB-212 glareshield, in order to be accessible to both pilot and co-pilot.

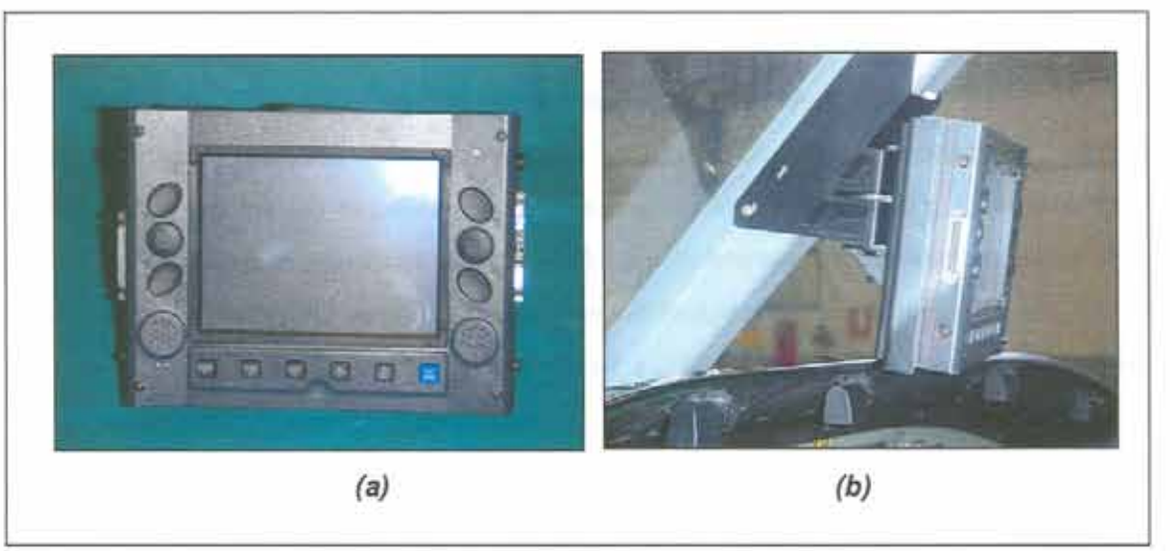

Figure 9-41. LOAS Display Unit installed on the AB-212 helicopter.

For the AB-212 test campaign, the LOAS Control Unit (LCU) was installed at the centre of the helicopter middle-consolle (in a position accessible to both pilot and co-pilot), as shown in Fig. 9-42.

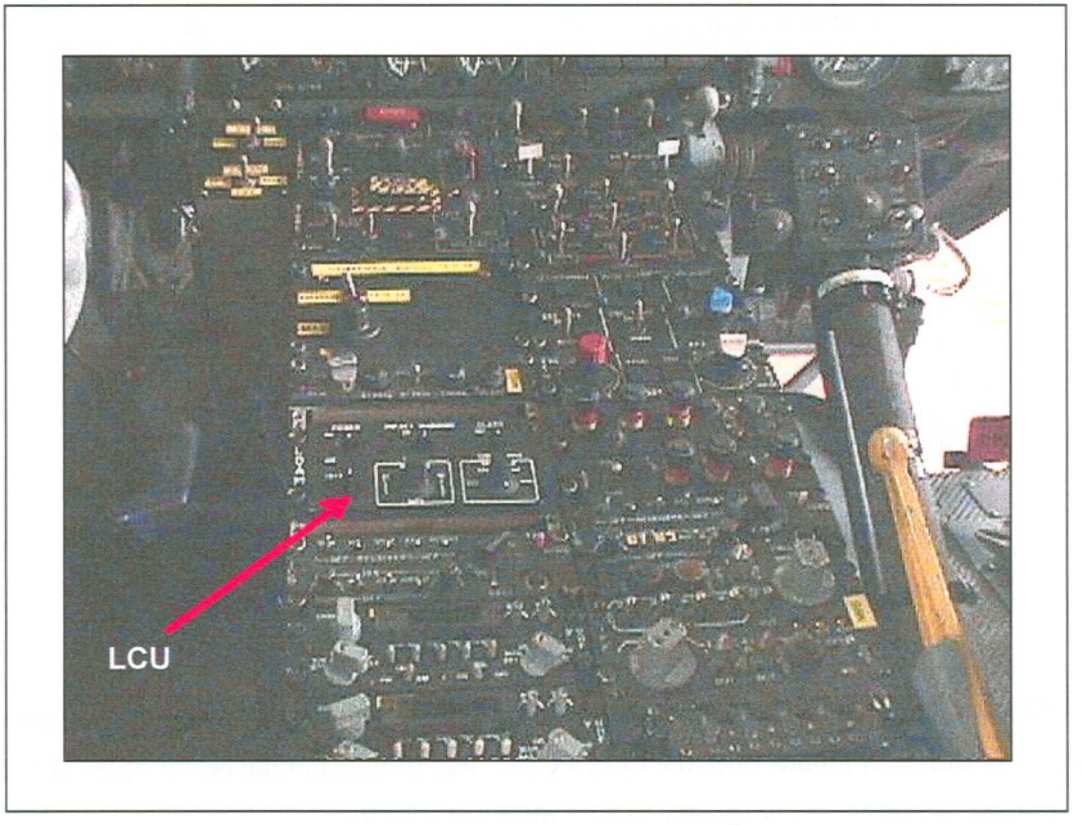

Figure 9-42. LOAS control unit installed on AB-212.

For the trials, various types of well characterised cables (with different sections and physical characteristics) where used, in conjunction with suitable sustaining poles. Furthermore, five different 'slices' of terrain were identified in the test range, useful for performing a dedicated assessment of the LOAS surface rendering capability. In order to obtain accurate geodetic coordinates of the terrain datum points, DGPS static surveys were performed at the range. Consequently, a 3-D reference grid was produced for comparison with the LOAS 3-D terrain profile data.

During the test flights, a flight test engineer operated a computer, linked to the LOAS system and displaying in real-time the 3-dimensional (3-D) images reconstructed using the LOAS data (Fig. 9-43). All images were recorded for the successive data analysis.

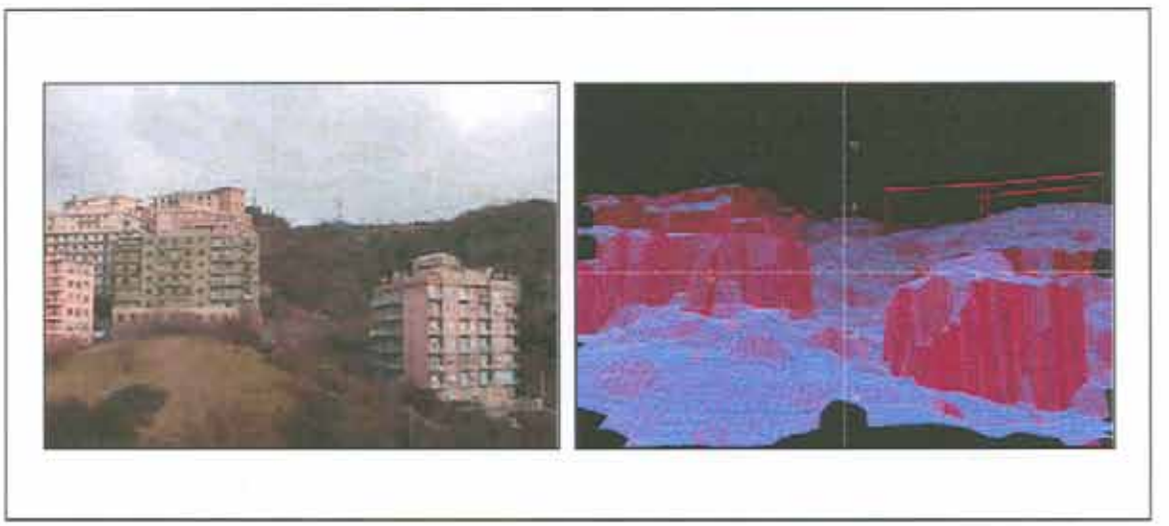

Figure 9-43. LOAS 3-D display format (flight test engineer).

The results of the test campaigns were very satisfactory. Particularly, the LOAS range performances were in accordance with the predictions obtained with mathematical models (see chapter 9). Furthermore, the basic LOAS detection/classification data processing algorithms were validated, although a fine tuning of some processing parameters was required. Furthermore, it was verified that the LOAS "History Function" and Impact Warning Function (IWF) were correctly implemented.

Future tests will be performed in order to further assess the LOAS system performance (sensor and processing algorithms) in day/night with various weather/environmental conditions and to optimise the system human machine interfaces. Particularly, starting in June 2004, a dedicated flight test activity will be carried out in order to assess the LOAS system performance for future installation on the Italian NH-90 TTH/NFH helicopters. This activity will be carried out using an AB-412 test-bed helicopter. The trials will be addressed to LOAS performance verification in various (reference) obstacle scenarios and with various weather conditions, and to very the validity of the Human Machine Interface (HMI) being developed for the NH-90 helicopter. A scheme relative to the current status of the LOAS customisation for Italian NH-90 helicopters (TTH and NFH versions) is shown in Fig. 9-44.

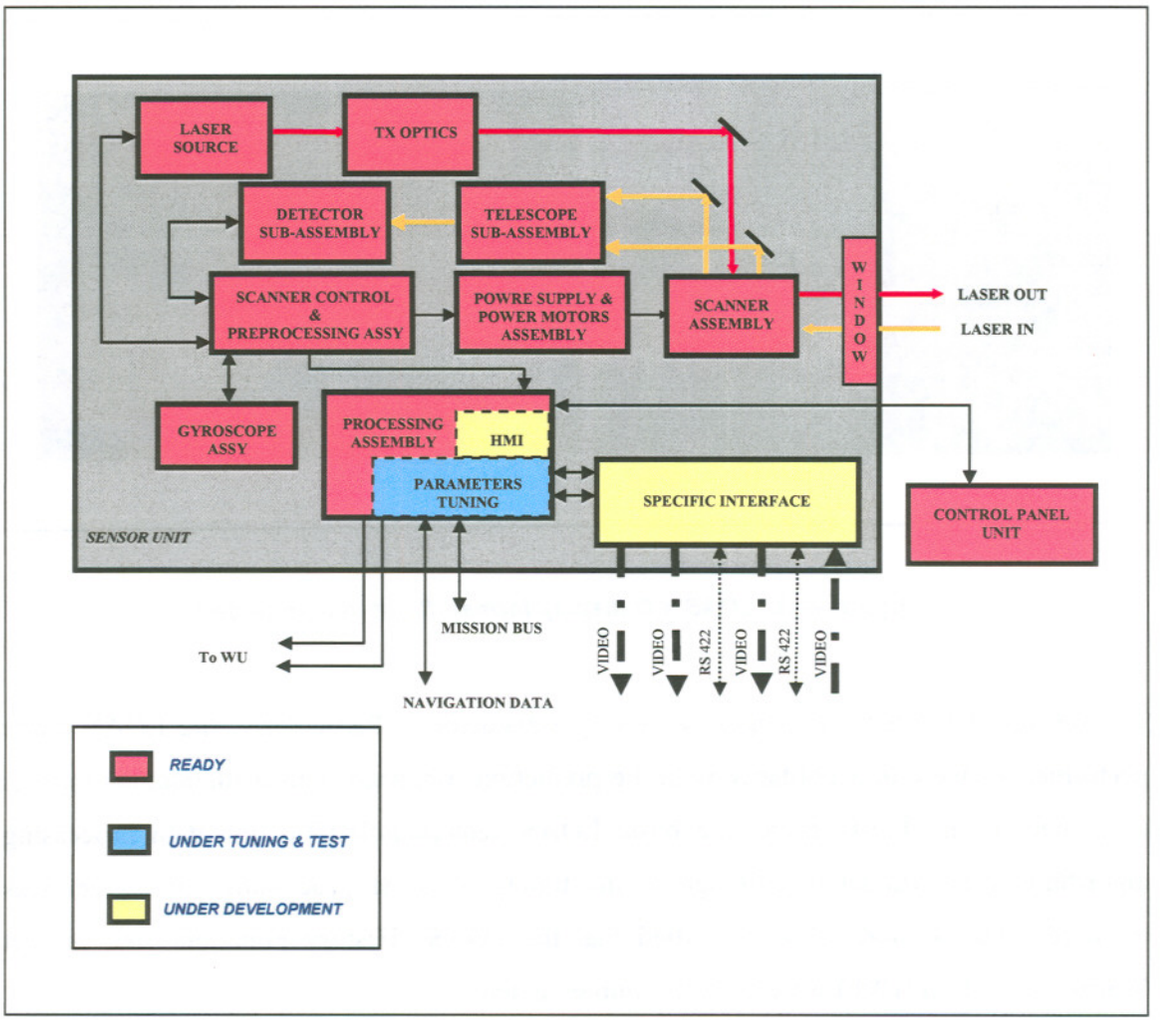

Figure 9-44. LOAS development status for the Italian NH-90 TTH and NFH helicopters.

9.6 References

1. Johnson J., "Analysis of Imaging Forming Systems". Proceedings of the Image Intensifier Symposium (pp. 249-273). Warfare Electrical Engineering Dept. - US Army Engineering Research and Development Laboratories (Ft. Belvoir, VA). 1958. This article was reprinted in "Selected Papers on Infrared Design", R.B. Johnson and W.L. Wolfe. SPIE Proceedings (Vol. 513, pp. 761-781). 1985.
2. Ratches J.A., "Static Performance Model for Thermal Imaging Systems". Optical Engineering Vol. 15(6) (pp. 525-530). 1976.

3. Howe J.D., "Electro-Optical Imaging SystemsPerformance Prediction". The Infrared and Electro-Optical Systems Handbook. Vol. 4 - Electro-Optical Systems Design, Analysis and Testing. Accetta J.S. and Shumaker D.L. eds. Published by the Environmental Research Institute of Michigan and SPIE Press. 1993.
4. Holst G.C., "Applying the Log-normal Distribution to Target Detection". Infrared Imaging Systems: Design, Analysis, Modeling and Testing III. Holst G.C. ed. SPIE Proceedings Vol. 1689 (pp. 213-216). 1992.
5. Schmieder D.E. and Weathersby M.R., "Detection Performance in Clutter with Variable Resolution". IEEE Transactions on Aerospace and Electronic Systems (Vol. AES-19(4), pp. 622-630). 1983.
6. Ratches J.A., Lawson W.R., Orbet L.P., Begemann R.J., Cassidy T.W., and Swenson J.M., "Night Vision Laboratory Static Performance Model for Thermal Viewing Systems". ECOM Report ECOM-7043 (Forth Monmouth, NJ). 1975.
7. Holst G.C., "Electro-Optical Imaging System Performance". SPIE Optical Engineering Press. Bellingham, Washington USA. 1995.
8. Parkinson B.W. and Spilker J.J., "Global Positioning System: Theory and Applications". AIAA Progress in Astronautics and Aeronautics (Vol. 163). 1996.

Chapter 10

MISSION ANALYSIS AND SIMULATION

10.1 General

This chapter is dedicated to the simulation tools developed during the PILASTER program, especially in the areas of eye-safety and system performance analysis. The theoretical and empirical models described in the previous chapters were used in the software programs, allowing a complete definition of test/training laser mission constraints and operational feasibility, together with post-mission data analysis. The assumptions adopted for implementation of the various mathematical algorithms in the PC simulation/analysis programs are presented in this chapter, together with results of some relevant simulation runs performed. The chapter closes with some concluding remarks.

10.2 Eye-safety Verification Programs

A discussion about the key-parameters considered for laser safety analysis was presented in chapter 6, together with description of the relevant geometric elements of typical ALS/GLS operational tasks, and an underline of the safety verification algorithms developed for the various cases. In this paragraph, we detail the various assumptions adopted for implementing two MATLAB^{TM} Eye-safety Verification Programs (EVP) for both ALS (A-EVP) and GLS (G-EVP) systems. Furthermore, the results of simulations are presented, relative to the ELOP PLD ground LTD and to a typical airborne LTD system (the Thompson CLTD

technical characteristics are not presented due to military classification), for operation at the PILASTER test range.

10.2.1 A-EVP and G-EVP Simulation Assumptions

The following assumptions were adopted for implementation of the A-EVP and G-EVP programs:

- **The reflecting surface (BZ) is perfectly planar**; this assumption is conservative in the case of convex surfaces laying within the BZ (these would in fact determine an increase of divergence with consequent reduction of the energy density at the observer location); while, in the case of concave surfaces, it is extremely improbable that their presence in the BZ can determine focusing (reduction of divergence) of the laser beam.

- **The laser beam reflection is totally specular**; this assumption is conservative from a safety point of view, because the energy density of a specularly reflected laser beam is always greater than in the real case. This is because reflection from any practical surface is always characterised by the co-hesitance of two components: a diffuse component and a specular component, each more or less important depending on the physical characteristics of the reflecting surface.

- **For the A-SVP the entire A-BZ is considered as a specular reflector**; this is a conservative assumption for eye-safetyu calculations. Moreover, considering the entire BZ as the actual reflector, the presence of any reflecting material inside the BZ is not relevant for safety (i.e., objects removal is not required within the BZ, but only evacuation of the ground personnel).

- **For the G-SVP the target surface is considered as a diffuse reflector**; this is a condition that was imposed when designing the PILASTER targets.

- **Atmospheric attenuation of the laser beam is not considered**; this assumption implies that the entire energy emitted by the LTD reaches the

observer location. This is obviously a conservative assumption, since atmospheric absorption and scattering effects are neglected.

- **The NOHD is calculated for direct vision of a Gaussian laser beam.** The assumption of direct vision is conservative, since the observer is assumed to look directly at the laser source, instead of a reflected beam; while a Gaussian distribution of the laser beam is applicable in practice for most ALS systems (e.g., Thompson CLDP).

- **Allowance is made for atmospheric scintillation effects**; this assumption is conservative as it implies, in the absence of C_n measurements, that $OHD_S = 2.662 \cdot NOHD$.

- **For the A-SVP a significant instability of the system LOS is considered.** Both in the TRACK and in the SLAVE modes of operation of the A-LTD, the point of itersectioin of the LOS with the ground is not fixed. Based on data relative to various real A-LTD systems, the maximum instability was assumed to be 20 m in SLAVE mode and 4 m in TRACK mode.

Moreover, it is considered that **no magnifying instruments are used** in the test range (i.e., the NOHD can be used instead of the EOHD). This is not properly an assumption, since a prohibition can be imposed by the range authorities (as long as cinetheodolites are not required; in which event proper filtering measures are essential).

10.2.2 A-EVP Airborne LTD Simulation

The probabilities of hazardous events during real missions, for a typical airborne laser target designator (A-LTD) are presented in Table 10-1 (see also Tables 6-1 and 6-2 in chapter 6). For completeness of information, a description of the missions listed in the table, is give below:

- **Ferry flight**, is a transfer mission in which the WSO does not use any of the LTD operating modes and the WSO control panel is in the SAFE position;

- **DRY attack**, is a simulated attack mission (without activation of the laser FIRE mode), carried out with the WSO control panel in the SAFE position;

- **HOT attack**, is a real attack mission (with or without actual bomb dropping), in which all operational modes of the LTD are used.

As indicated in Table 10-2, during HOT/DRY attacks carried out in the test range, it is essential that the target (either hard or soft) is visually acquired by the WSO and it is desirable that the clearance for firing the laser is obtained by a Laser Safety Officer, monitoring at a ground control station (connected with the aircraft trough an encrypted video telemetry system) the correct pointing of the system LOS.

MISSION	*Operative Conditions*	*LTD Modes*	*Hazard Probability*
Ferry Flight	N.A.	LTD ON/ Laser FIRE	$P_{SAFE \rightarrow FIRE}$= 7E-6
DRY Attack (in the range)	Controlled range target, visually acquired	LTD ON/ TRACK-SLAVE/ Laser SAFE	P_{ROT}*$P_{SAFE \rightarrow FIRE}$= 1.4E-9
HOT Attack (in the range)	Controlled range target, visually acquired	LTD ON/ TRACK-SLAVE/ Laser FIRE	P_{ROT}=2E-6
DRY Attack (outside range)	Target visually acquired	LTD ON/ Laser SAFE	$P_{SAFE \rightarrow FIRE}$=7E-4
HOT Attack (outside range)	NOT POSSIBLE IN ANY CONDITION		

Table 10-1. The probabilities of hazardous events during real missions.

Using the data in Table 10-2, relative to the main technical characteristics of a generic airborne laser target designator (A-LTD) system (technical data relative to the CLDP are not presented due to military classification), together with data already presented in Tables 6-1, 6-2 and 10-1 (relative to the same generic A-LTD), we give an example of a practical application of the EVP simulation program described in the previous paragraphs.

The MPE_P (i.e., MPE for a single pulse) is 0.05 J/m^2. Therefore, with the previously stated assumptions, the NOHD equates to 7679 m (i.e., about 25200 ft), and the OHD_S to 20426 m. This means that, in the absence of scintillation effects (i.e., low turbulence), the HA does not exist as long as the aircraft is flying at an altitude higher than 25200 ft (in case of turbulence, the required aircraft altitude exceeds the tangential altitude of any existing military aircraft!).

Wavelength	1064 nm
Beam Diameter	60 mm
Beam Divergence	0.2 mrad
Output Energy	100 mJ
Pulse Duration	10^{-9} sec
Pulse Repetition Rate	13 Hz
Max LOS Misalignment	SLAVE mode: 40 m TRACK mode: 4 m

Table 10-2. A-LTD design characteristics.

In order to carry out missions at lower altitudes, the hazard probabilities given in Table 10-1, have to be accepted. For instance, if the maximum acceptable risk level is associated with a probability of hazardous event of 1E-5, all missions can be carried out, with exception for DRY/HOT attacks outside the test range. If, however, the probability level is set to 1E-8, none of the missions is possible, with the exception of DRY attacks inside the test range.

Simulation results relative to the aircraft flight limitations during laser firing (i.e., minimum and maximum distance of the aircraft from the target) applicable to the PILASTER range with a maximum evacuation area of 4.3 km radius around the target location (A-EBZ), are shown in Fig. 10-1 and 10-2. The tolerance of the aircraft height is ±100ft. The ground-speed lower limit is 250 kts. It is underlined that no restrictions to the aircraft trajectory are applied in the horizontal plane.

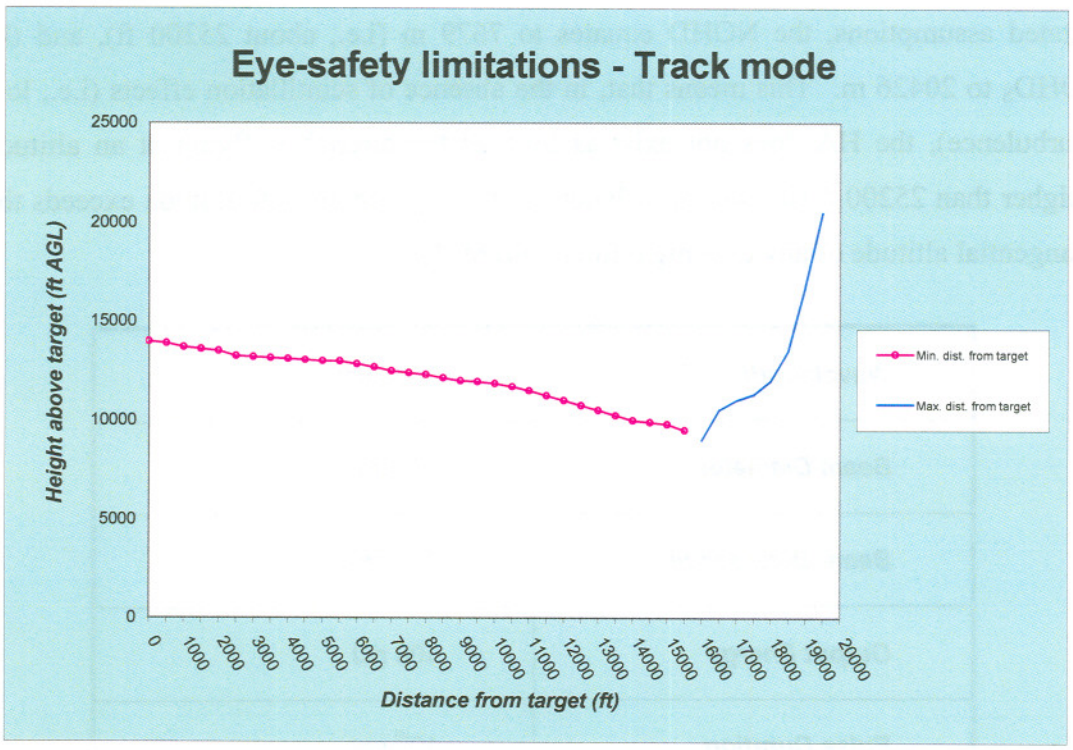

Figure 10-1. A-LTD TRACK mode simulation results.

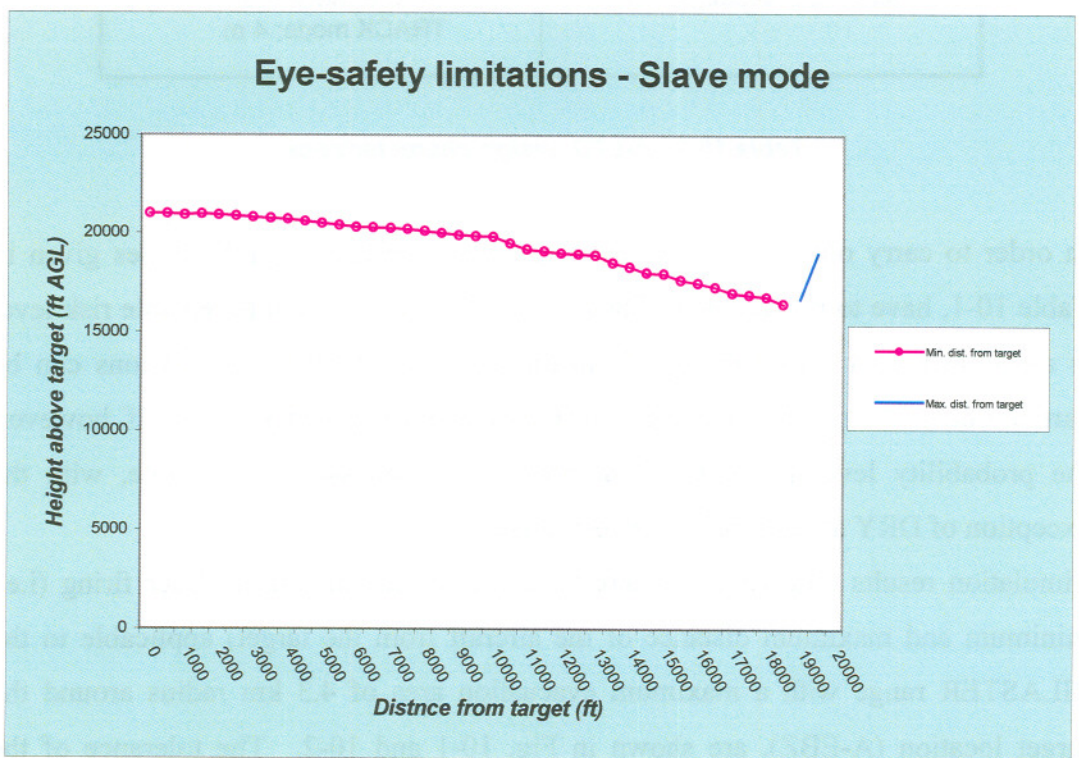

Figure 10-2. A-LTD SLAVE mode simulation results.

10.2.3 G-EVP ELOP-PLD Simulation Results

The ELOP-PLD Ground LTD (G-LTD) system technical characteristics relevant to eye-safety are listed in Table 10-3.

Parameter	Value
Wavelength	*1064 nm*
Output Energy	*130 mJ*
Beam Divergence	*130 μrad (80% of the output energy)*
Pulse Duration	*19 nsec*
Beam Output Diameter	*90 mm*
Maximum laser/LOS Misalignment	*80 μrad*
Laser PRF	*10 or 20 Hz*

Table 10-3. ELOP-PLD technical characheteristics.

Since the divergence was specified at 80% of total ouput energy, the *1/e* divergence required for safety calculations was obtained using the following equation:

$$\Phi_{1/e} = \Phi_{\eta}\sqrt{\frac{ln(1-0.632)}{ln(1-\eta)}} \tag{10.1}$$

where Φ_{η} is the given divergence (Φ_{η} = 0.13 mrad) and η is the relative percentage of total energy (i.e., $\eta = 0.8$). For the ELOP-PLD, we obtained $\Phi_{1/e} = 0.102$ mrad. The NOHD and OHDS calculated for PRF = 10Hz (used for LGB) and for various times of exposure (T_E), are shown in Fig. 10-3.

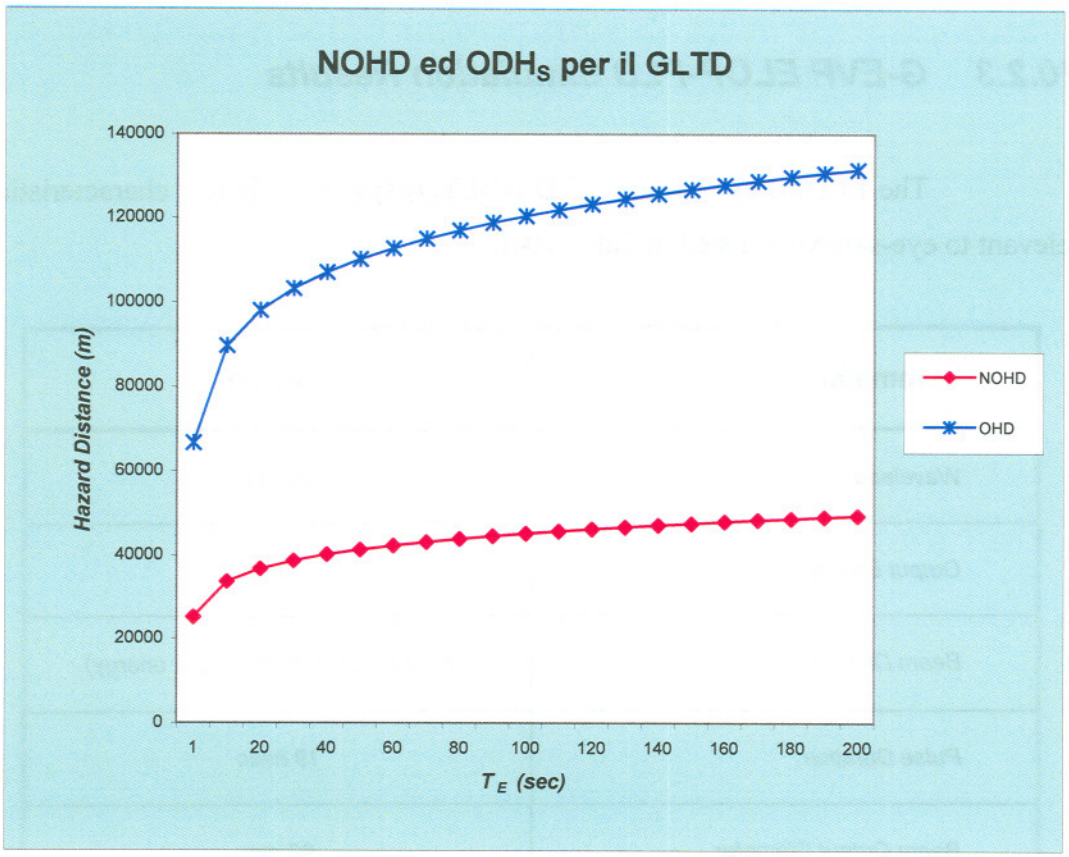

Figure 10-3. ELOP-PLD ocular hazard distances.

Taking into account the experimental results obtained during the ground experimental activities performed with the ELOP-PLD, together with temporary scintillation phenomena in the presence of high turbulence (i.e., $C_n \geq 2.43 \cdot 10^{-7}$), remarkable and very frequent spreading effects where observed, especially for long LTD-to-target slant ranges. In order to account for this in the ELOP-PLD eye safety calculations, the BZE described in chapter 6 (and not the NOHD) was calculated considering the maximum measured laser spot divergence (calculated from spot diameter measurements) geometric divergence of the ELOP-PLD systems (Φ_{eff} = 0.25 mrad) instead of the *1/e* divergence ($\Phi_{1/e}$ = 0.102 mrad).

Fig. 10-4 shows the curves relative to the maximum LTD-target slant-ranges admitted (with various horizontal incidence angles), calculated in accordance with the G-LTD safety verification procedure n° 1 described in chapter 6, considering various target surface dimensions. Particularly, the PILASTER permanent and modular targets dimensions have been considered (i.e., 10×10 m and 9.76×7.925 m

respectively), together with the PILASTER modular target square sections (i.e., dimensions of 7.32×7.32 m, 4.88×4.88 m and 2.44×2.44 m).

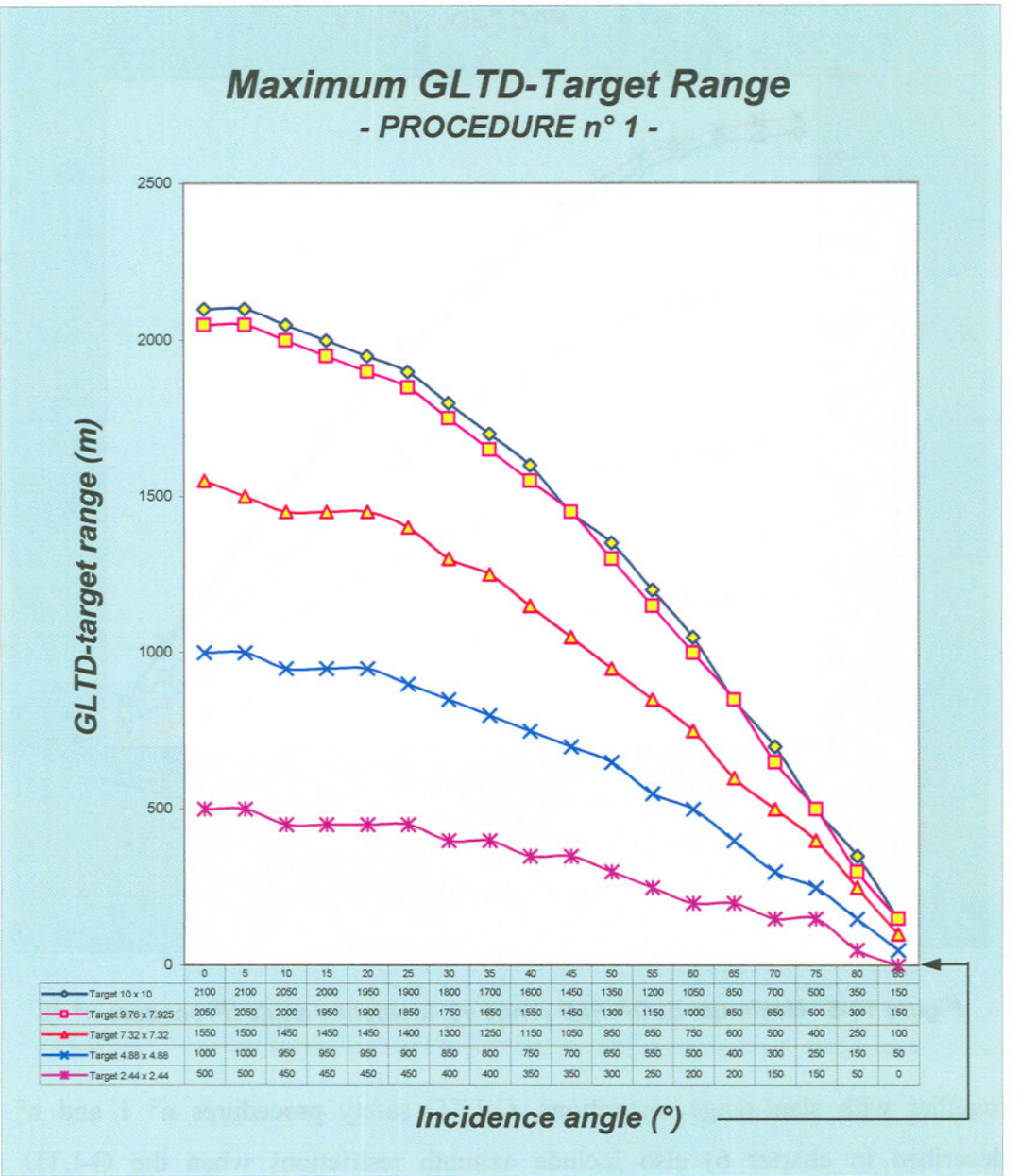

Figure 10-4. Maximum ELOP-PLD range vs. incidence angle (Procedure n° 1).

Fig. 10-5 shows the curves relative to the maximum LTD-target slant-ranges admitted (vs incidence angle), calculated in accordance with the G-LTD safety verification procedure n° 4 described in chapter 6 (i.e., PILASTER NIR-camera real-time monitoring), considering the various PILASTER targets dimensions.

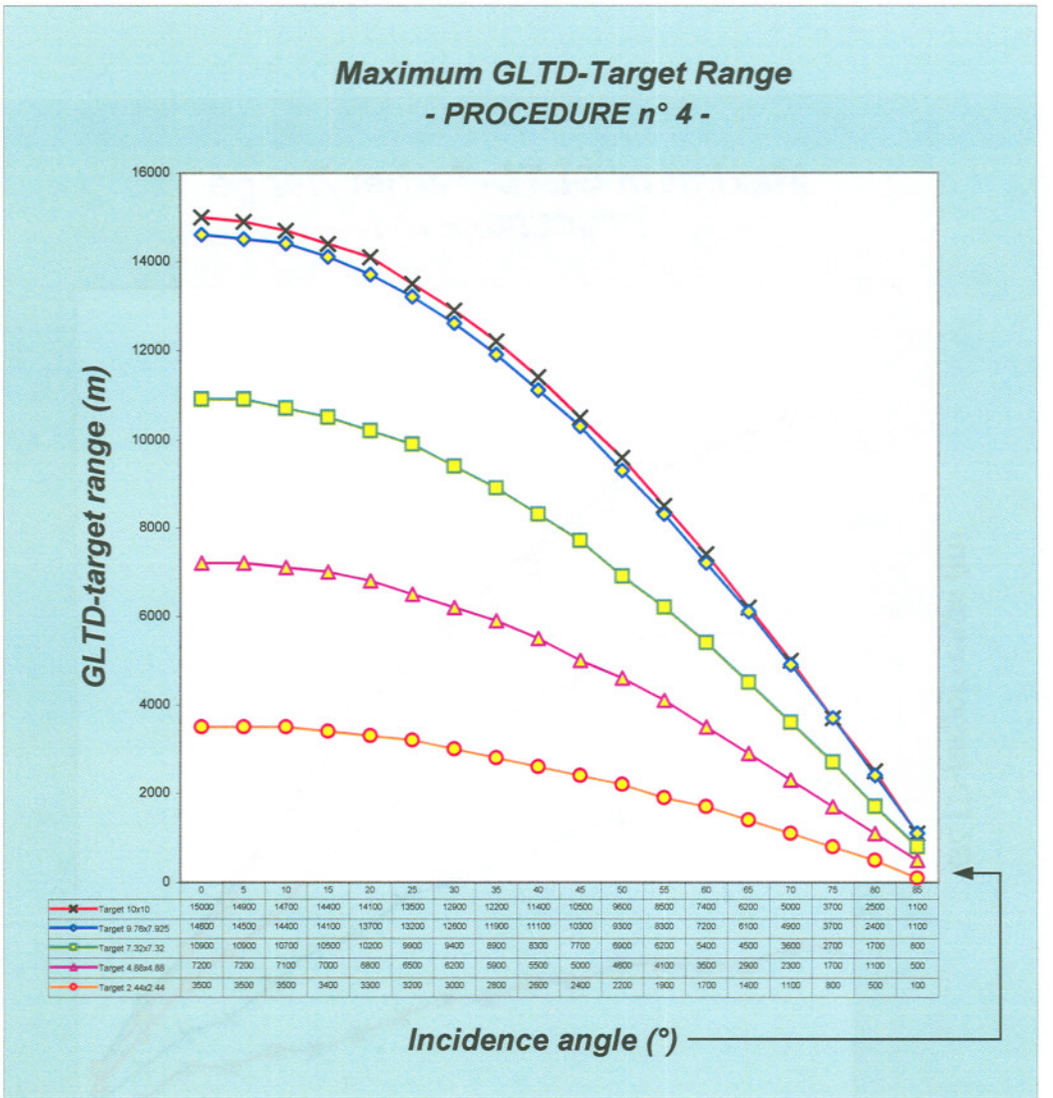

Figure 10-5. Maximum ELOP-PLD range vs. incidence angle (Procedure n° 4).

Together with slant-range restrictions, G-LTD safety procedures n° 1 and n° 4 (described in charter 6) also include azimuth restrictions when the G-LTD is positioned at an elevated location with respect to the target. Taking into account both slant-range and azimuth restrictions (knowing the maximum altitude difference h_{max} between the target and the G-LTD locations), the G-EVP program computed the PILASTER areas where laser firing with the ELOP-PLD was permitted (SPA). These areas, identified as Safe Positioning Areas (SPA), calculated with the G-EVP program for both procedure n° 1 and n° 4, are summarised in Fig. 10-6 and in the Tables 10-4 and 10-5.

ELOP-PLD SAFE POSITIONING AREAS

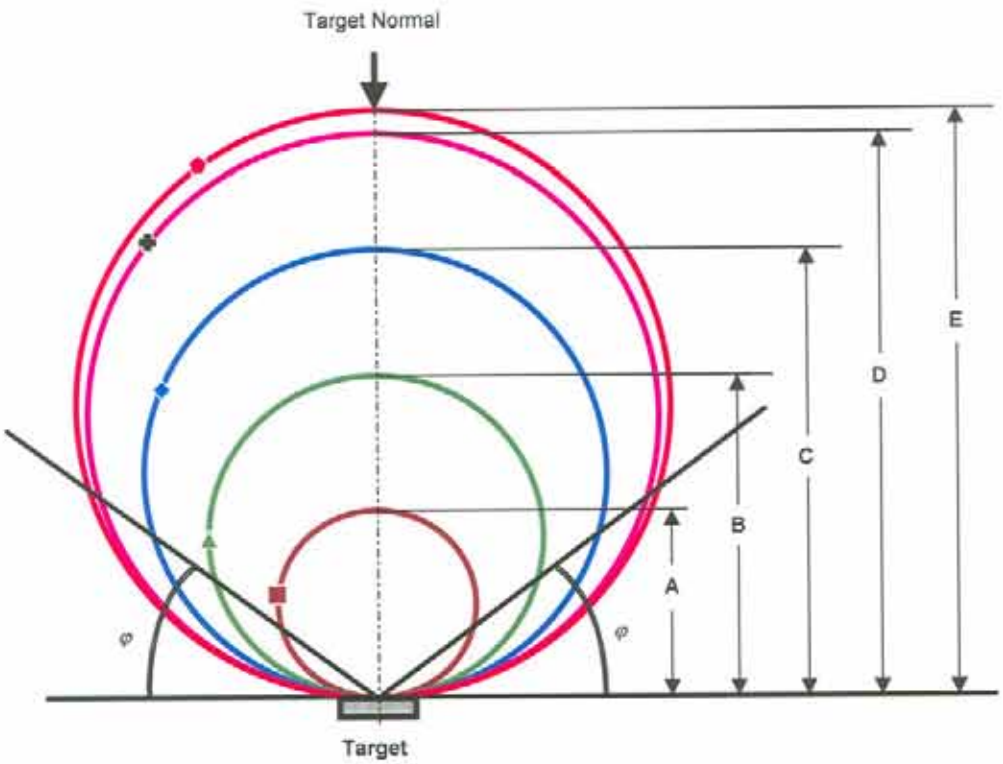

Symbols:

Target 10 ×10 m

Target 9.76 ×7.92 m

Target 7.32 ×7.32 m

Target 4.88 ×4.88 m

Target 2.44 ×2.44 m

THE ELOP-PLD SPA IS GIVEN BY THE CIRCLES (IN THE PILASTER RANGE), WITH THE RESTRICTIONS IN SYSTEM-TARGET RELATIVE ALTITUDE GIVEN BY h_{MAX} AND IN AZIMUTH GIVEN BY THE ANGLE φ

Procedure n° 1		*Procedure n° 4*	
A	500 m	A	3500 m
B	1000 m	B	7200 m
C	1550 m	C	10900 m
D	2050 m	D	14600 m
E	2100 m	E	15000 m

Figure 10-6. G-EVP output - safe positioning areas.

d (m)	h_{MAX} (m)	Procedure n° 4 - φ (°)				
		r_{MIN}=10 m	r_{MIN}=7.925 m	r_{MIN}=7.32 m	r_{MIN}=4.88 m	r_{MIN}=2.44 m
100	50	2	3	3	3	5
200	150	4	4	4	5	10
300	250	4	6	6	8	13
400	250	7	4	4	7	12
500	250	7	5	5	6	12
600	250	8	5	5	7	14
700	250	11	5	6	8	16
800	250	9	6	6	9	16
900	250	7	6	7	10	18
1000	250	8	7	7	10	19
1500	250	8	9	10	14	28
2000	250	10	12	13	18	37
2500	250	12	14	15	22	47
3000	250	13	17	18	27	60
3500	250	15	19	21	31	81
4000	250	17	22	23	36	n.a.
4500	250	19	24	26	40	n.a.
5000	250	21	27	29	45	n.a.
5500	250	23	29	32	51	n.a.
6000	250	25	32	35	58	n.a.
7000	250	30	38	42	76	n.a.
8000	250	34	44	49	n.a.	n.a.
9000	250	39	51	57	n.a.	n.a.
10000	250	43	59	68	n.a.	n.a.

n.a. = not available

Table 10-4. G-EVP output - azimuth limitations for procedure n° 4.

d (m)	h_{MAX} (m)	Procedure n° 1 - φ (°)				
		r_{MIN}=10 m	r_{MIN}=7.925 m	r_{MIN}=7.32 m	r_{MIN}=4.88 m	r_{MIN}=2.44 m
100	50	5	5	6	9	16
200	150	10	11	13	19	38
300	250	13	15	17	24	51
400	250	15	19	20	31	79
500	250	17	20	23	33	n.a.
600	250	18	23	25	38	n.a.
700	250	21	26	28	45	n.a.
800	250	23	29	32	52	n.a.
900	250	26	33	36	60	n.a.
1000	250	28	37	40	71	n.a.
1500	250	43	59	68	n.a.	n.a.
2000	250	63	n.a.	n.a.	n.a.	n.a.

n.a. = not available

Table 10-5. G-EVP output - azimuth limitations for procedure n° 1.

Some examples of ELOP-PLD safe positioning areas relative to the procedures n° 1 and n° 4, plotted on the PILASTER ground range map area are shown in the Figs. 10-7 through 10-10.

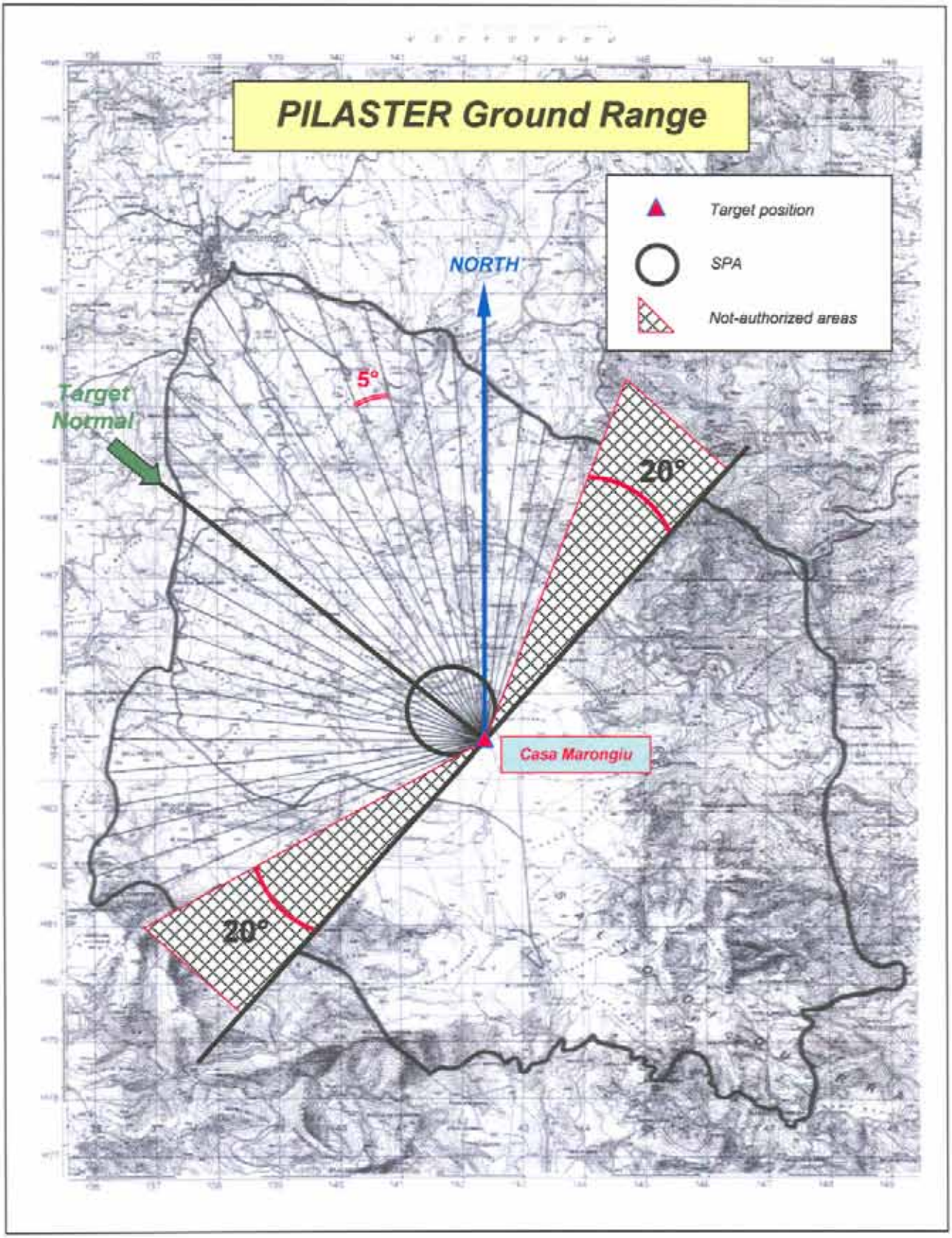

Figure 10-7. Procedure n° 1 – PILASTER SPA for r_{min} = 7.32 m, maximum PLD-target SR = 400 m and maximum relative altitude difference h_{max} = 250 m.

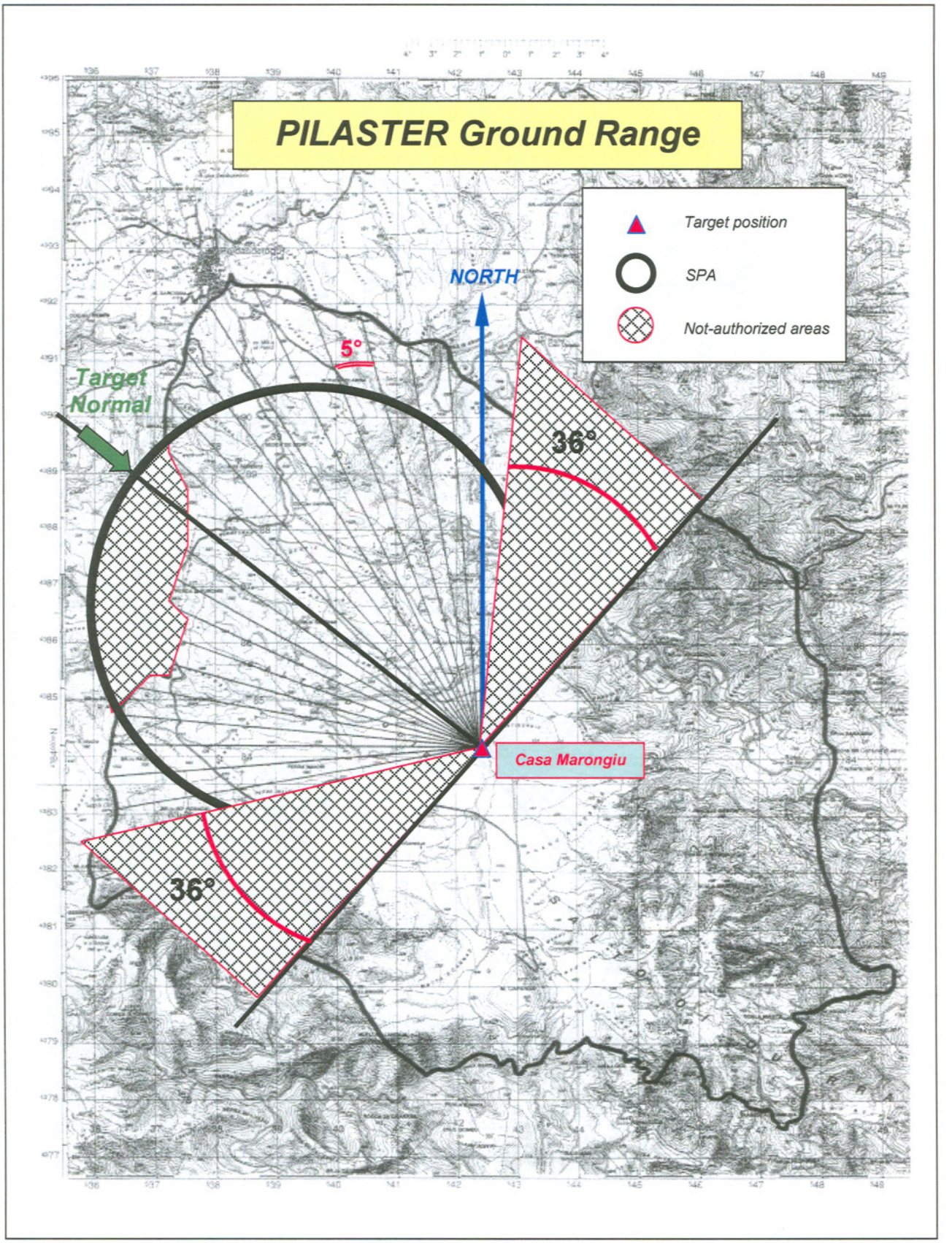

Figure 10-8. Procedure n° 4 – PILASTER SPA for r_{min} = 4.88 m, maximum PLD-target SR = 4 km and maximum relative altitude difference h_{max} = 250 m.

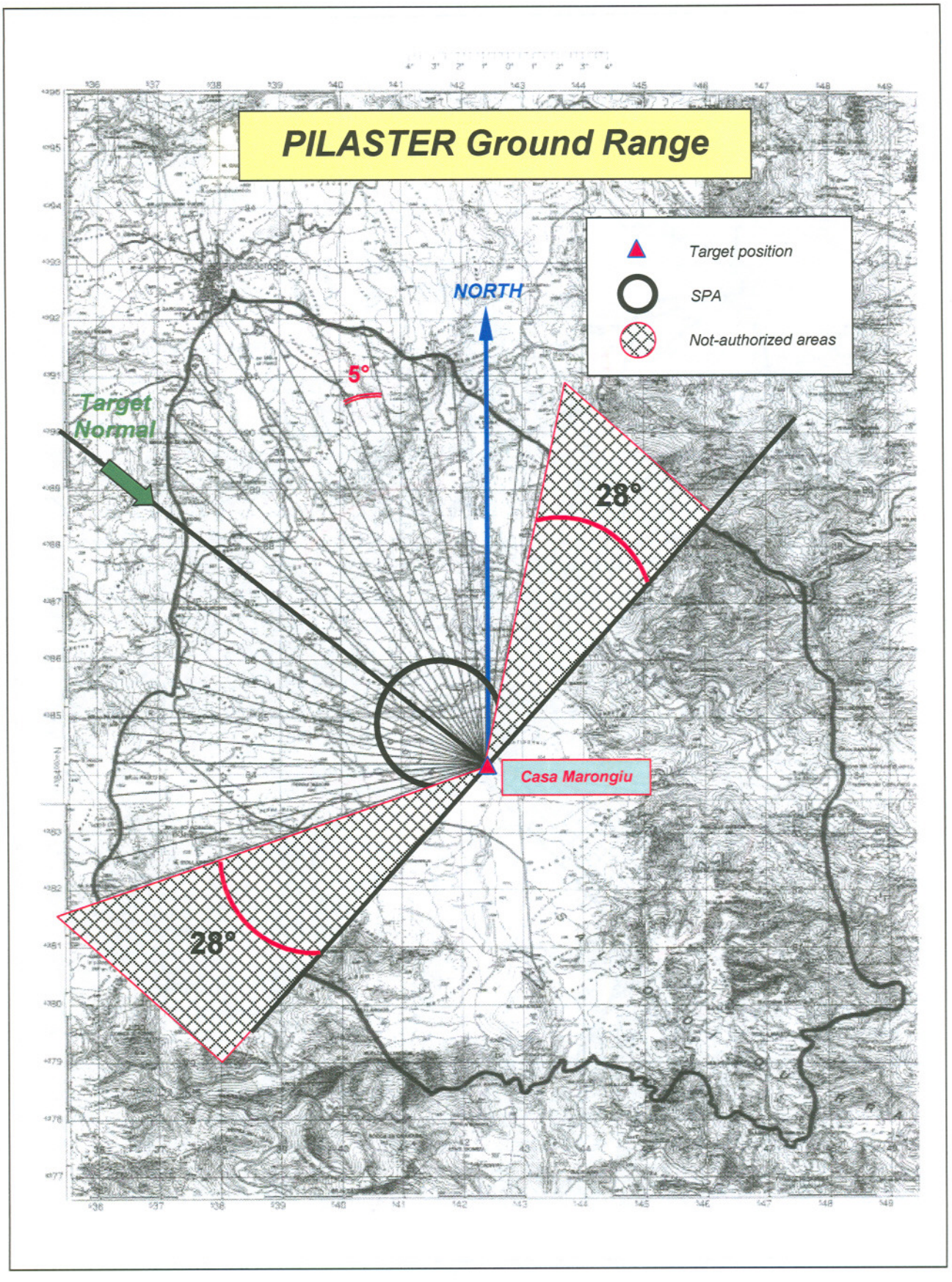

Figure 10-9. ***Procedure n° 1 – PILASTER SPA for r_{min} = 10 m, maximum PLD-target SR = 1 km and maximum relative altitude difference h_{max} = 250 m.***

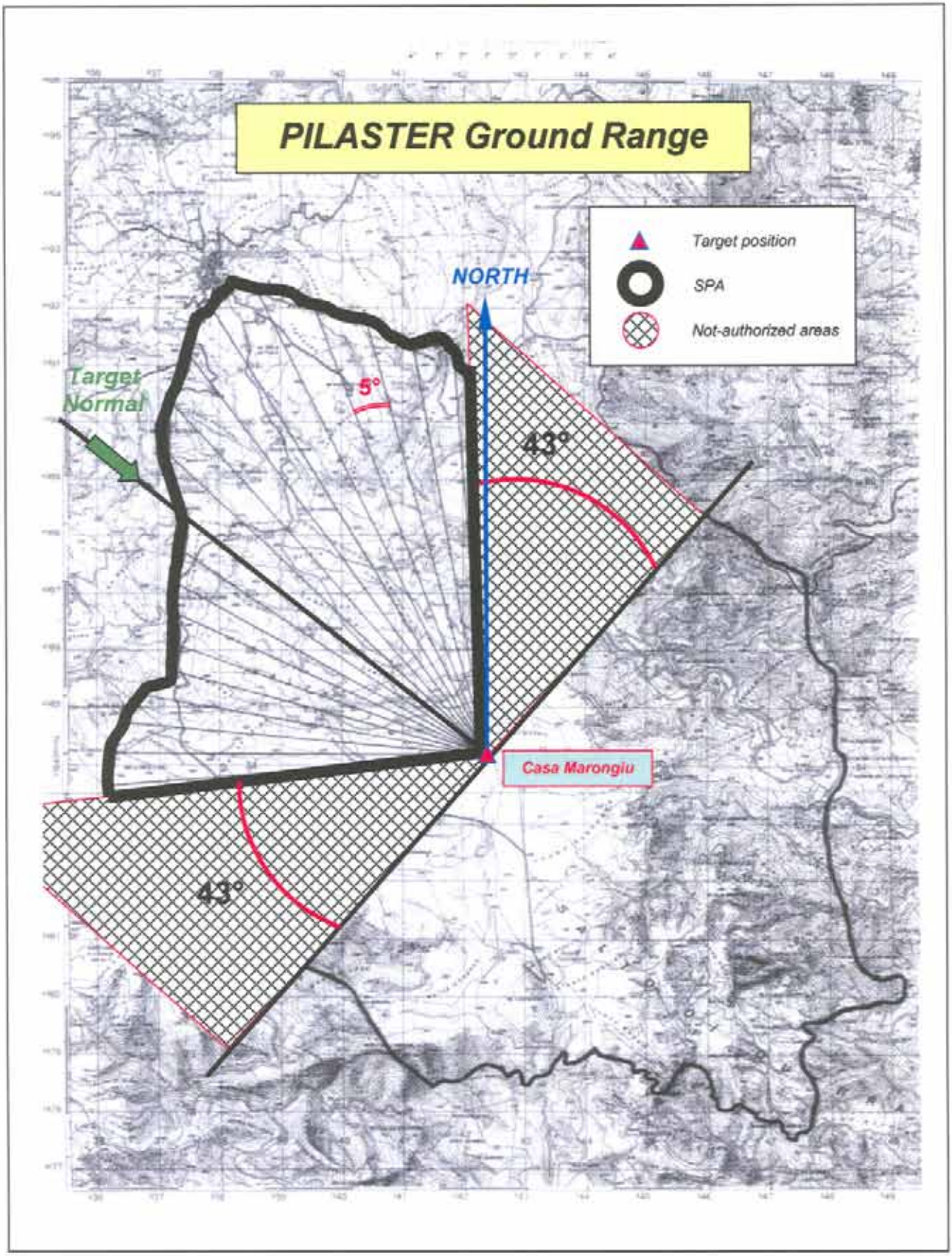

Figure 10-10. Procedure n° 4 – PILASTER SPA for r_{min} = 10 m, any PLD-target SR in the range area and maximum relative altitude difference h_{max} = 250 m.

10.3 Range Performance Prediction Program (RP3)

In the following paragraphs the Range Performance Prediction Program (RP3) is described. The RP3 program was implemented using the models described in chapter 3, with the corrections to the ESLM propagation model presented in the chapters 9 and 10. Future versions of the program will be refined with further experimental results (LPDB).

10.3.1 RP3 Simulation Assumptions

The following general assumptions have been adopted for implementation of the RP3 program:

- **The Elder-Strong-Langer-Middleton (ESLM) model is used** to calculate the atmospheric attenuation coefficient. Corrections are adopted according to the results presented in chapter 9 and 10;

- **The ESLM-LOWTRAN Model is used to calculate scattering due to rain**. Corrections are adopted according to the results presented in chapter 9;

- **The output laser beam is assumed Gaussian**. A realistic assumption for most LTD currently in service;

- **Diffraction, jitter and spreading are not considered**, assuming an average irradiance at the target also having a Gaussian distribution;

- **The target reflecting surface is assumed planar and extended**; this assumption is acceptable considering the relative dimensions of the laser beam and most targets of practical interest;

Furthermore, either the **target directional reflectivity** (diffuse and specular reflection components) computed from BRDF data or the **diffuse reflectivity component** can be used for RP3 performance calculations.

10.3.2 RP3 Simulation Results

With the assumptions described above, we calculated the range performance of a particular LTD/LGB combination, using the data given in Table 10-6. These data are referred to generic LTD and LGB systems operating at a wavelength of 1.064 μm.

LTD	
Beam Diameter	60 mm
Beam Divergence	0.2 mrad
Wavelength	1.064 μm
Pick Energy	100 mJ
Pulse Duration	10^{-8} sec

LGB	
FOV	18°
MDPD	3 $\mu W/m^2$

Table 10-6. LTD/LGB combination characteristics.

Using the RP3 program, we evaluated the performance of this particular LTD/LGB combination in a certain operational scenario, with different atmospheric conditions. Furthermore, with the same atmospheric conditions, we calculated the performance of the systems when used against target with different geometries (i.e., the maximum distance of the illuminating aircraft for an effective designation).

The curves shown in the Figs. 10-11 through 10-16 describe the range performance of the considered A-LTD/LGB combination, with different values of visibility (V) in the absence of rain. The RP3 input data included, together with parameters in Table 10-6, the relative humidity (RH) which was set to 100% at a temperature (T) of 30 °C, and the target reflectivity which was assumed to be 10% (with a purely *Lambertian* distribution).

In each graph, the range LTD-target is given as a function of the range LGB-target and a family of curves has been traced for different orientations of the target over the horizon (i.e., different values of the angles $Q_{t(MAX)}$ and $Q_{r(MAX)}$).

Using the curves it is possible to determine whether or not the attack can be performed with a certain estimated minimum illumination time. Given the weapon initial conditions (i.e., velocity and trajectory) before designation is initiated, it is possible to estimate the designation time, taking into account the time required by the LGW from these initial conditions to stabilise towards the target (i.e., guided weapon ballistics). If the guidance algorithms are unknown it is possible to roughly estimate the designation time by assuming a straight trajectory of the bomb towards the target and a velocity in the final portion of its drop correspondent to the maximum theoretical velocity of the weapon. With these assumptions, the minimum theoretical range LGB-target before designation can be plotted in the graphs and consequently the maximum range of the aircraft at the beginning of the designation is determined. Obviously, when this range is less than the Target Lethal Range (TLR), the attack can not be performed successfully.

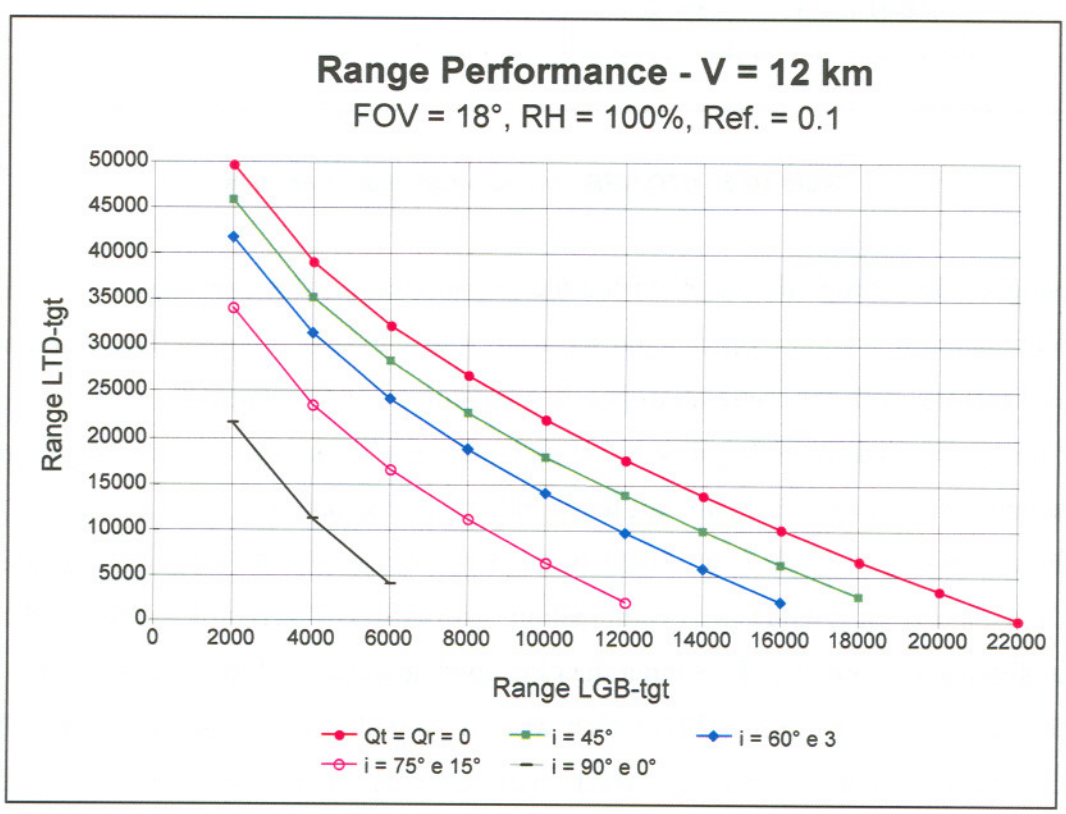

Figure 10-11. LTD/LGB range performance for V = 12 km.

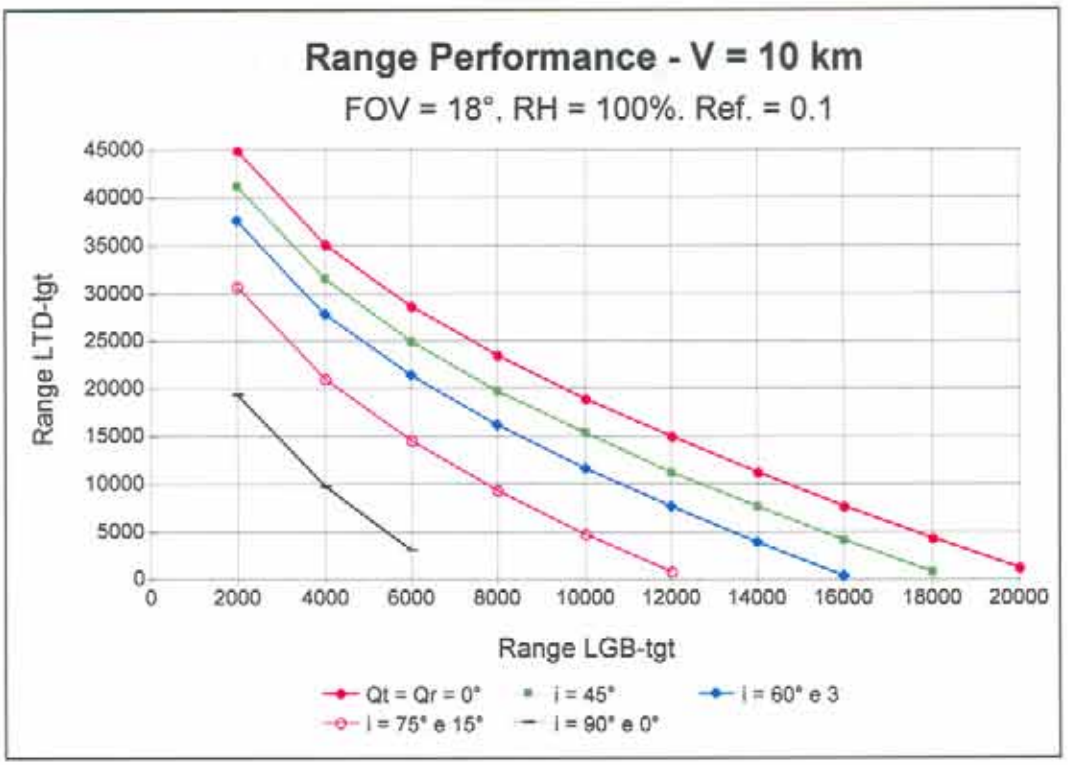

Fig. 10-12. LTD/LGB range performance for V = 10 km.

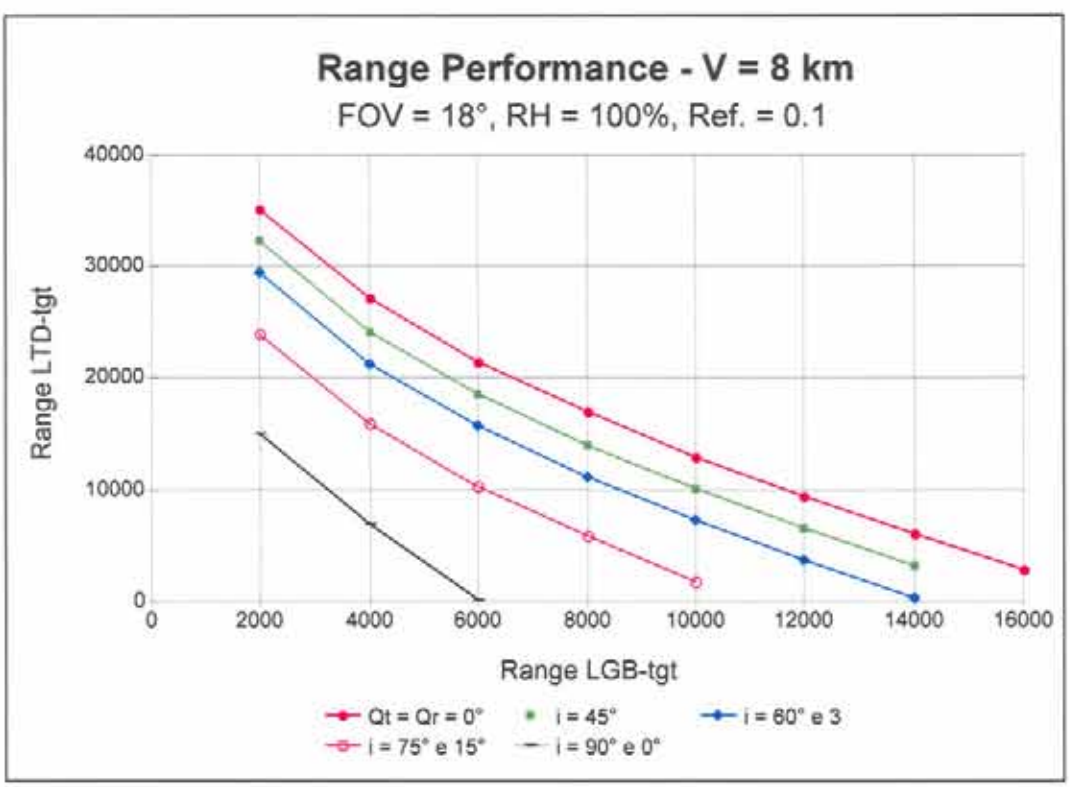

Fig. 10-13. LTD/LGB range performance for V = 8 km.

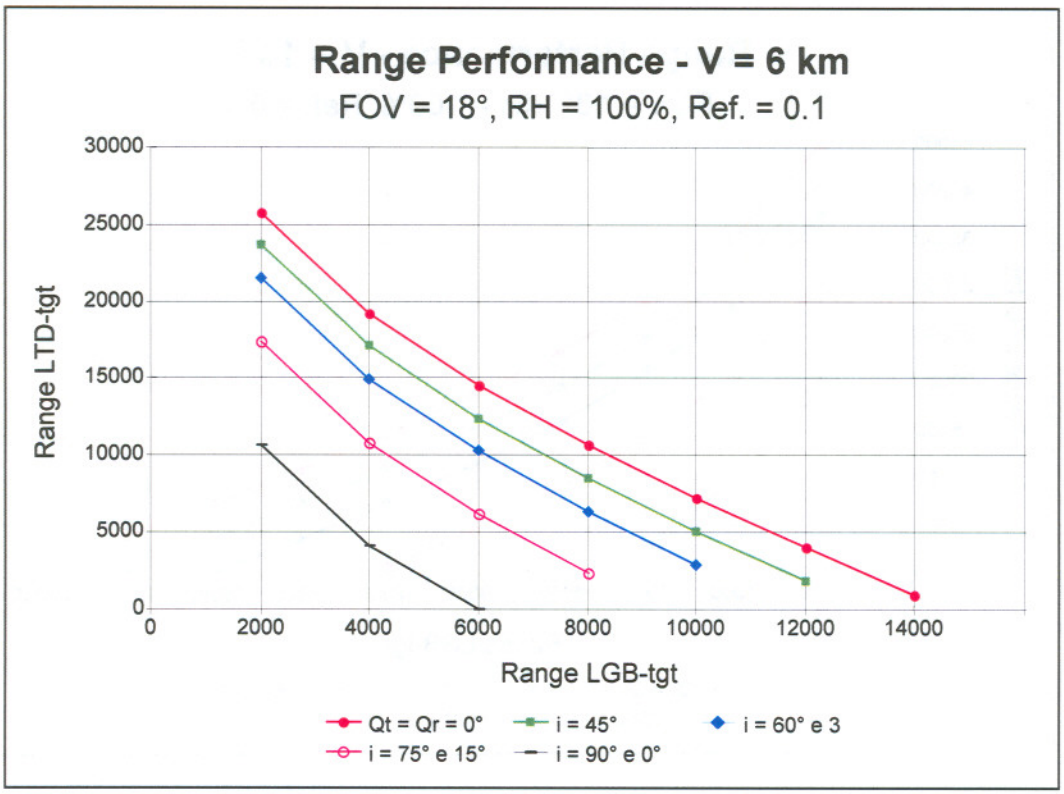

Fig. 10-14. LTD/LGB range performance for V = 6 km.

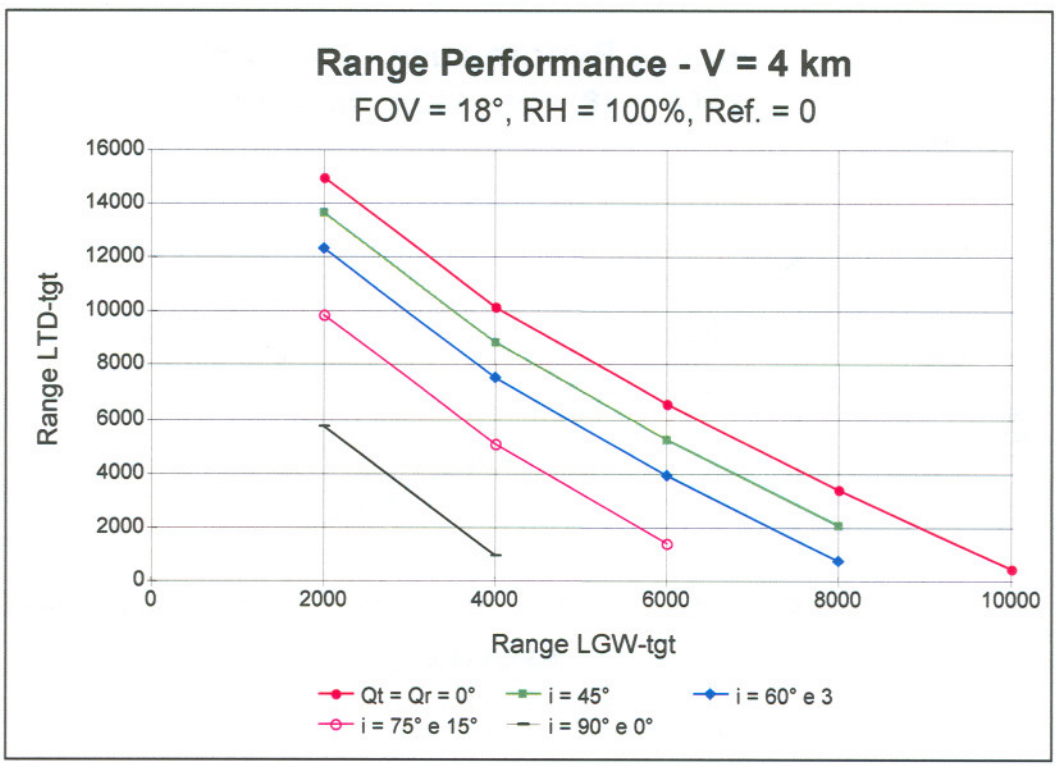

Fig. 10-15. LTD/LGB range performance for V = 4 km.

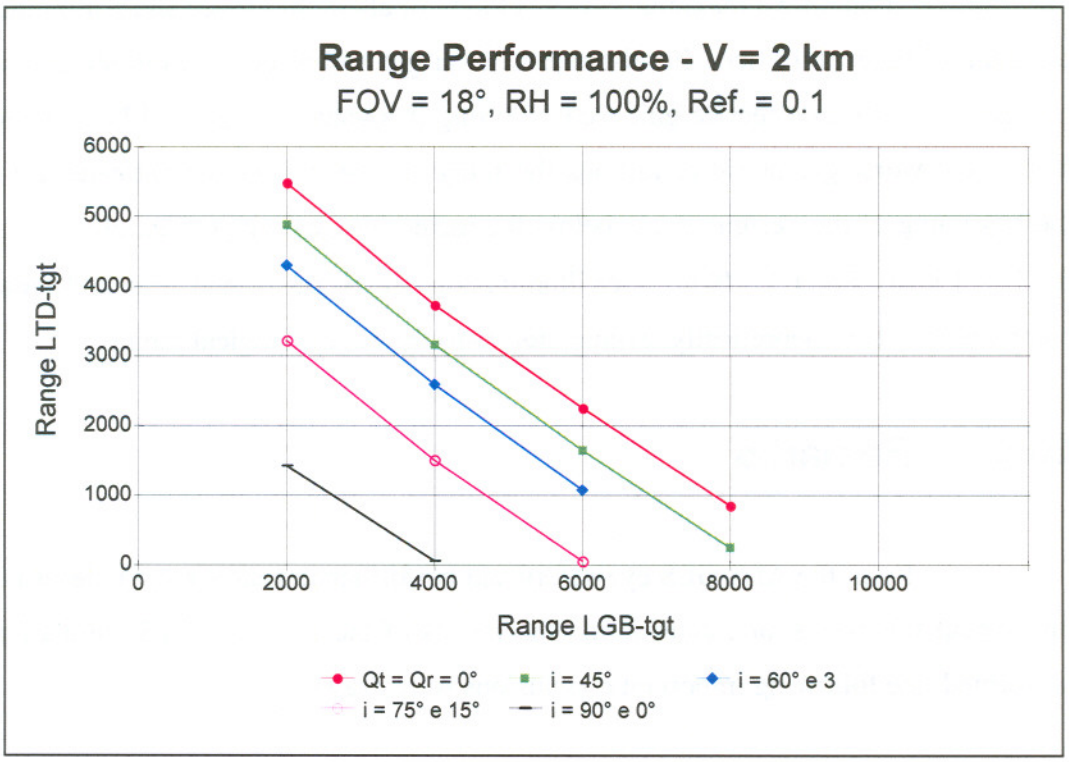

Fig. 10-16. LTD/LGB range performance for V = 2 km.

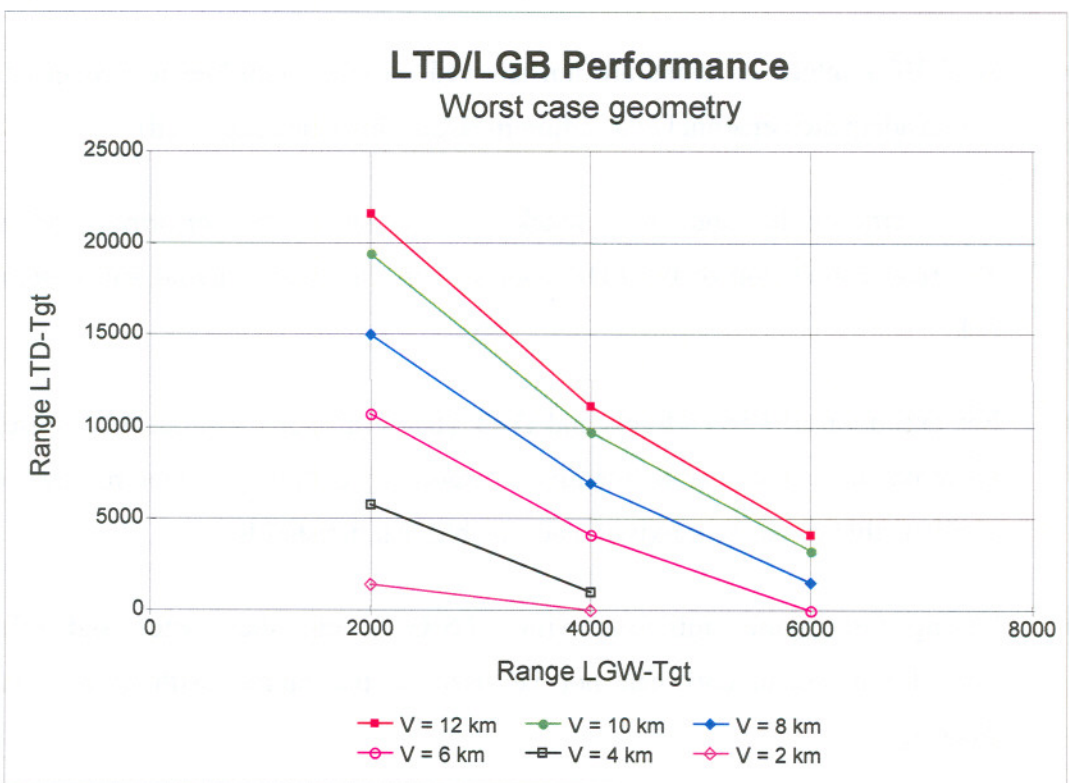

Figure 10-17. LTD/LGB range performance with worst case geometry.

For instance, assuming a maximum LGB velocity of about 800 ft/sec and a minimum designation time of 12 sec, the distance LGB-target before designation should not exceed 3 km, for an effective guidance. Plotting this value in Fig. 10-17, we notice that in the worst geometric conditions the range LTD-target (illuminator-target) at the beginning of the designation is below the meteorological range (i.e., about 2 km for $V = 4$ km). For $V \geq 10$km, laser illumination can be performed form a distance comparable to (or, theoretically, even grater than) the meteorological range.

10.4 Remarks

From the ALS/GLS eye-safety and performance analysis work described throughout this thesis, and considering the results of the EVP and RP3 simulations performed, the following important conclusions were drawn:

- Both for ALS and for GLS systems, it is essential to define the maximum acceptable risk thresholds (i.e., maximum admitted probabilities of inadvertent hazardous events), before test/training missions can be performed at the ranges.

- ALS HOT attack missions are not allowed outside controlled test ranges (in which adequate personnel evacuation measures have been adopted).

- ALS Ferry Flights and DRY attack missions should be performed without electrical connection of the LDP laser system, in order to avoid any possible risk.

- For execution of Ferry Flights and DRY attach missions with an ALS system powered, it is essential to identify a (national) authority, either military or civilian, able to set the maximum acceptable risk thresholds.

- During test/training missions with ALS/GLS, cine-theodolites and other magnifying instruments can not be used at the ranges without adequate filtering.

- With typical A-LTD/LGB combinations, in dry-air conditions and visibility greater than 4 km, laser illumination can be performed successfully with the A-

LTD carrying aircraft flying at a slant-range form the target not exceeding the meteorological range.

- With rain conditions, there is a considerable reduction of the range performance, limiting the operational use of most practical LTD/LGB combinations to the cases where the meteorological range is greater than 4 km.

10.5 ALS Mission Planning Program (ALS-MPP)

As discussed in the previous chapters, prediction of laser systems performance requires appropriate knowledge of target signatures (e.g., reflectivity, BRDF/LCS), background characteristics, atmospheric attenuation, hardware performance (e.g., detectors, pointing/tracking and FOV), mission geometry (e.g., masking, laser grazing angle, aircraft and target motion) and, in some cases, human operator performance (e.g., target search and acquisition with TV/FLIR aids, manual laser firing, etc.). Furthermore, for mission planning purposes, it is also important to take into account eye-safety issues (especially for test and training activities with ALS systems). The kernel of a *Java* simulation program for a complete analysis of ALS systems performance and mission planning (test/training an operational missions), were developed during this research. Particularly, the ALS-MPP kernel is composed of various classes, divided into three main groups: classes relative to the attack geometry and range performance model, classes relative to atmospheric laser beam propagation, and classes relative to the eye-safety analysis. The various classes were designed with the aim of developing a modular, flexible, and easily modifiable kernel. The kernel code with explanations of the various classes implemented, are presented in Appendix F.

10.5.1 Future Developments

The ALS-MPP input and output interfaces have not been finalised jet, although a process in currently ongoing for developing the program interfaces in accordance with ItAF Operational Squadrons requirements. The current status of the ALS-MPP input interface (I/P-I) is illustrated in the Figs. 10-18 through 10-23.

Currently, the I/P-I is composed by various data input panels and a global menu for managing the simulation. The first panel ('Meteo'), shown in Fig. 10-18, allows to input the relevant weather parameters (i.e., rain type, absolute humidity and visibility).

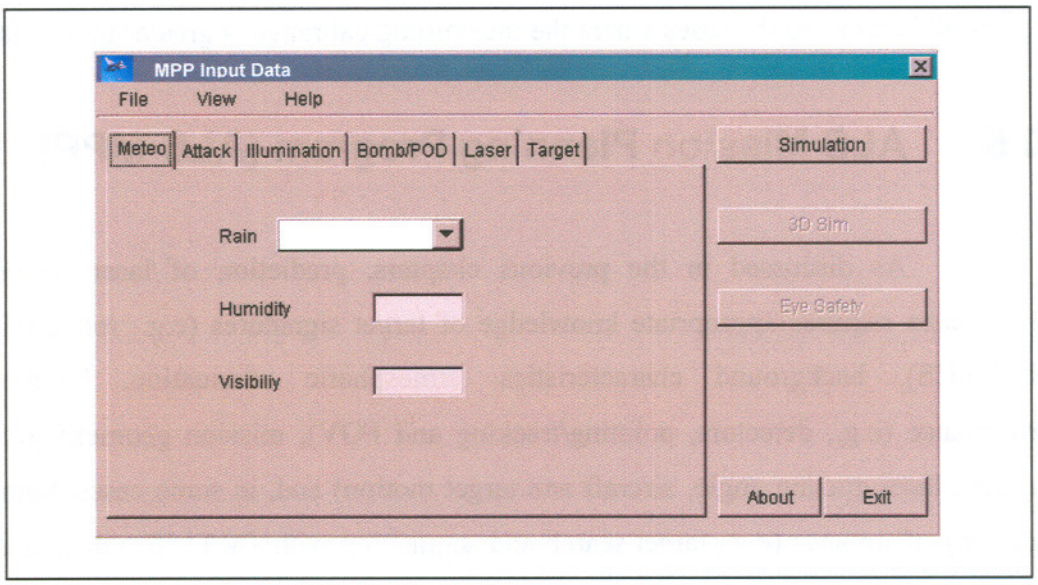

Figure 10-18. ALS-MPP I/P-I panel 'Meteo'.

The second panel ('Attack') is relative to the attack parameters (Fig. 10-19). The combined window (i.e., 'kind of attack') allows selection of 'dive', 'loft', or 'level' attack profiles. The sub-panels 'Altitude' and 'Preferred Directions' permit to input specific geometric constraints for the simulated mission.

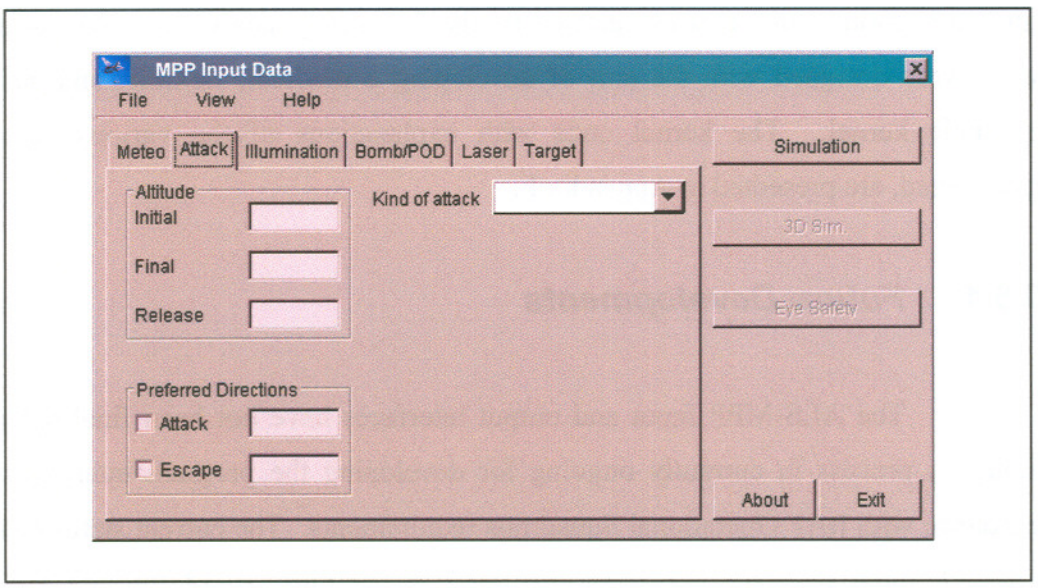

Figure 10-19. ALS-MPP I/P-I panel 'Attack'.

The panel 'Illumination' includes selection of the type of attack (i.e., self-designation or co-operative) and, in case of a co-operative attack, the desired trajectory of the 'spiker' aircraft (Fig. 10-20).

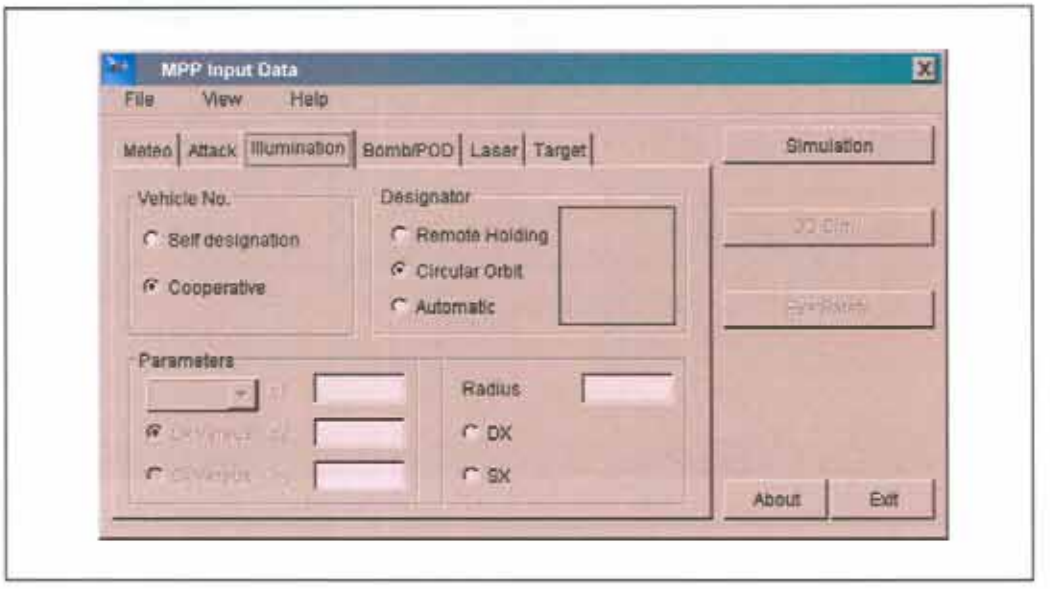

Figure 10-20. ALS-MPP I/P-I panel 'Illumination'.

The fourth panel ('Bomb/POD') allows definition of the LGB and A-LTD aircraft configurations, with automatic selection (from a dedicated library) of the relative masking matrixes (Fig. 10-21).

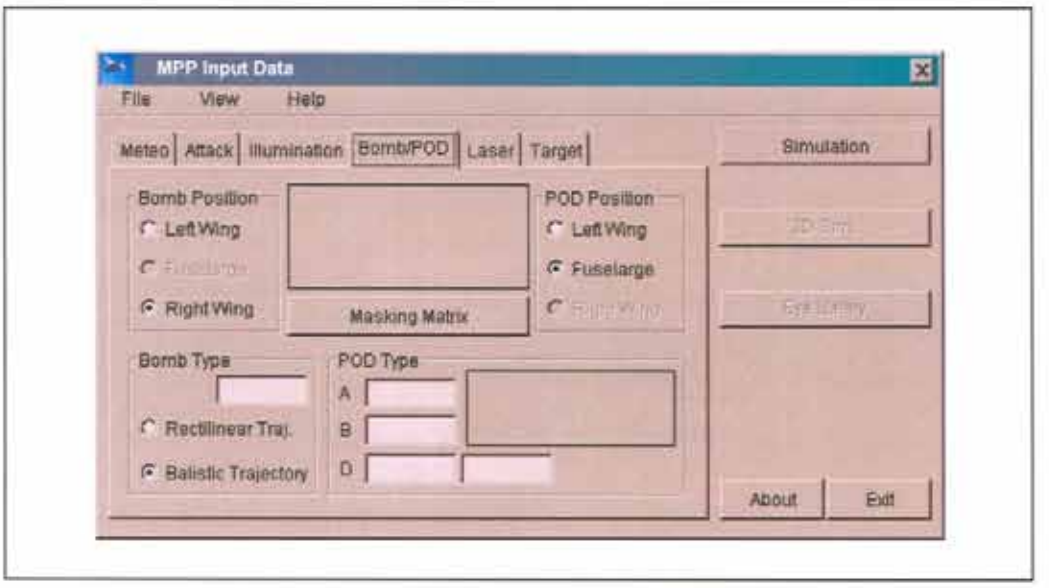

Figure 10-21. ALS-MPP I/P-I panel 'Bomb/POD'.

The panel 'Laser' is available for input of the relevant A-LTD laser parameters (Fig. 10-22).

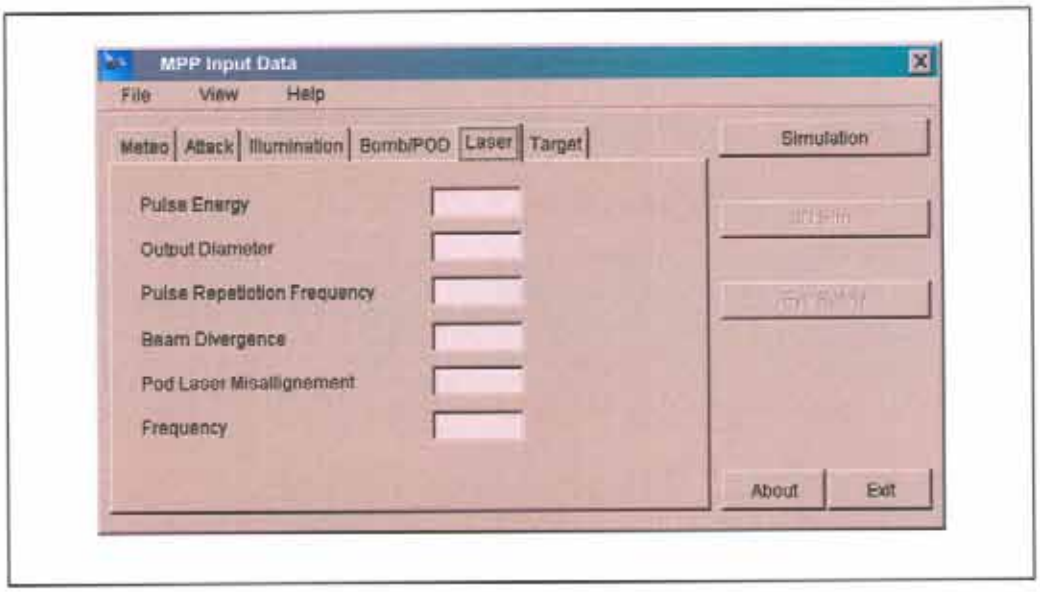

Figure 10-22. ALS-MPP I/P-I panel 'Laser'.

The last panel is dedicated to the target description in terms of position, orientation, dimensions and material. A combined window is also available for selection of the type of coordinates to be used. In the absence of accurate LCS or BRDF data, the program uses a library of diffuse reflectance data associated to the selectable target materials.

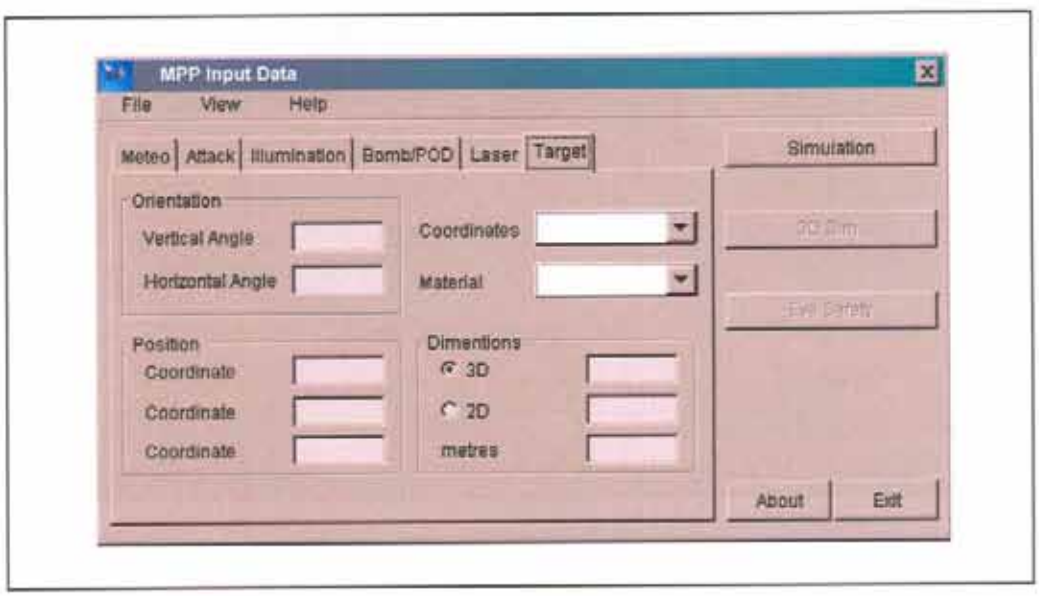

Figure 10-23. ALS-MPP I/P-I panel 'Target'.

Examples of the current ALS-MPP output interfaces (O/P-I) are illustrated in the Figs. 10-24 through 10-27.

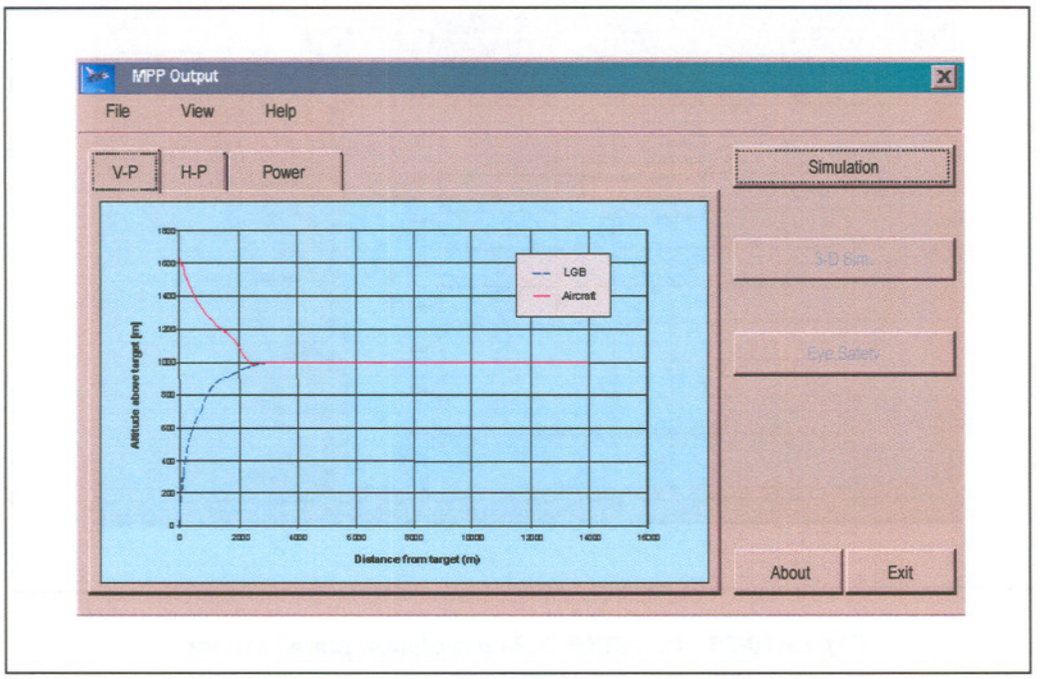

Figure 10-24. ALS-MPP simulation O/P-I 'Vertical Profile' (V-P).

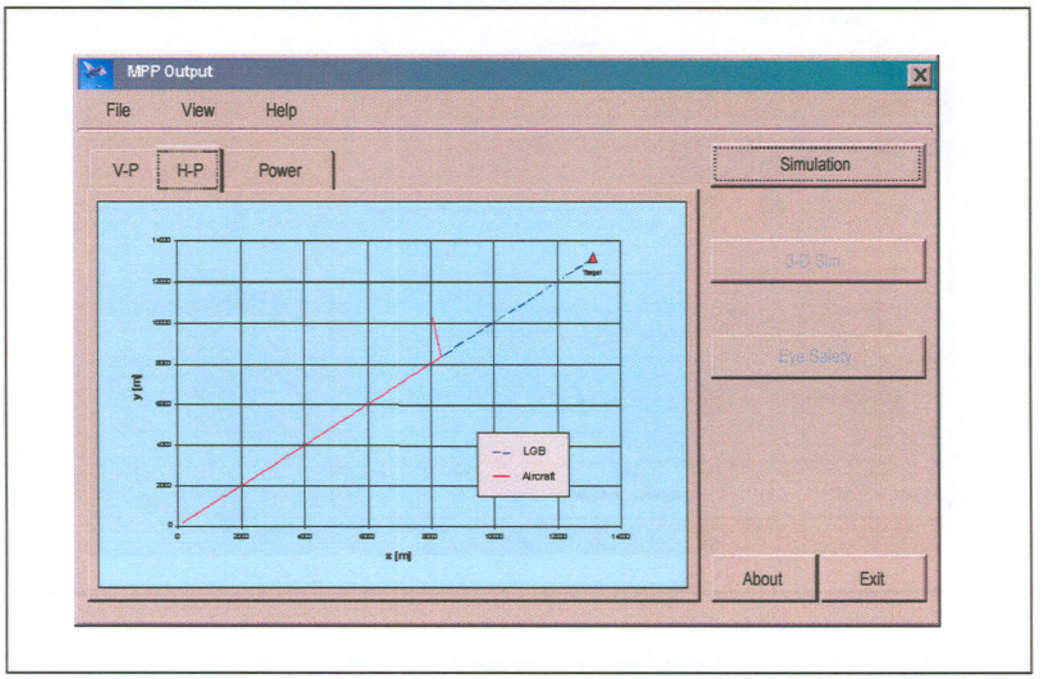

Figure 10-25. ALS-MPP simulation O/P-I 'Horizontal Profile' (H-P).

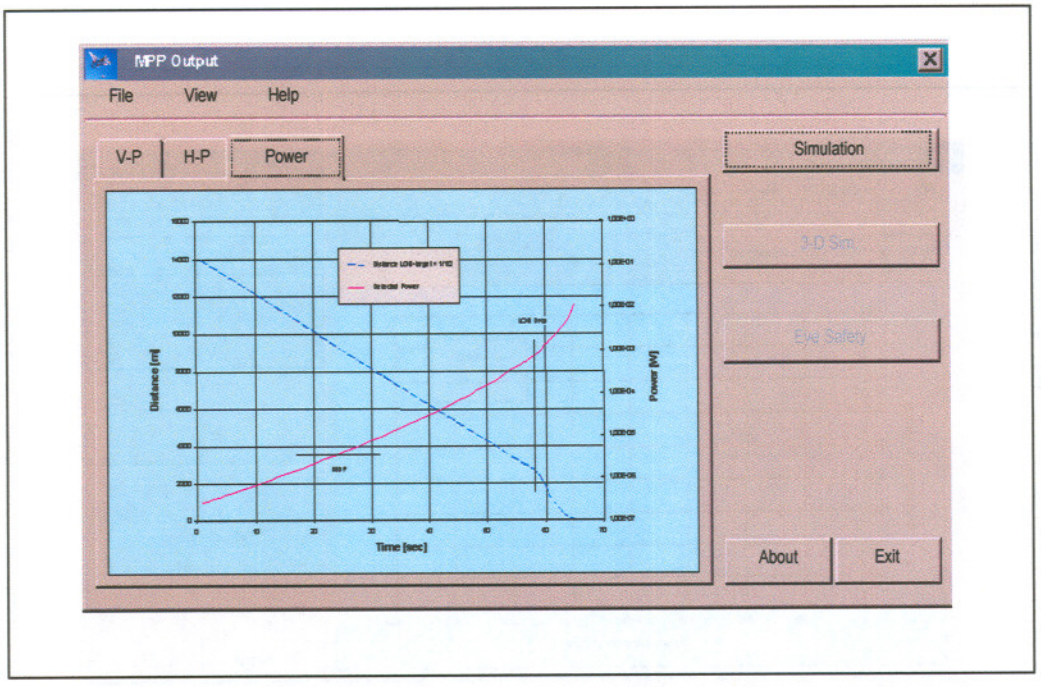

Figure 10-26. ALS-MPP O/P-I simulation panel 'Power'.

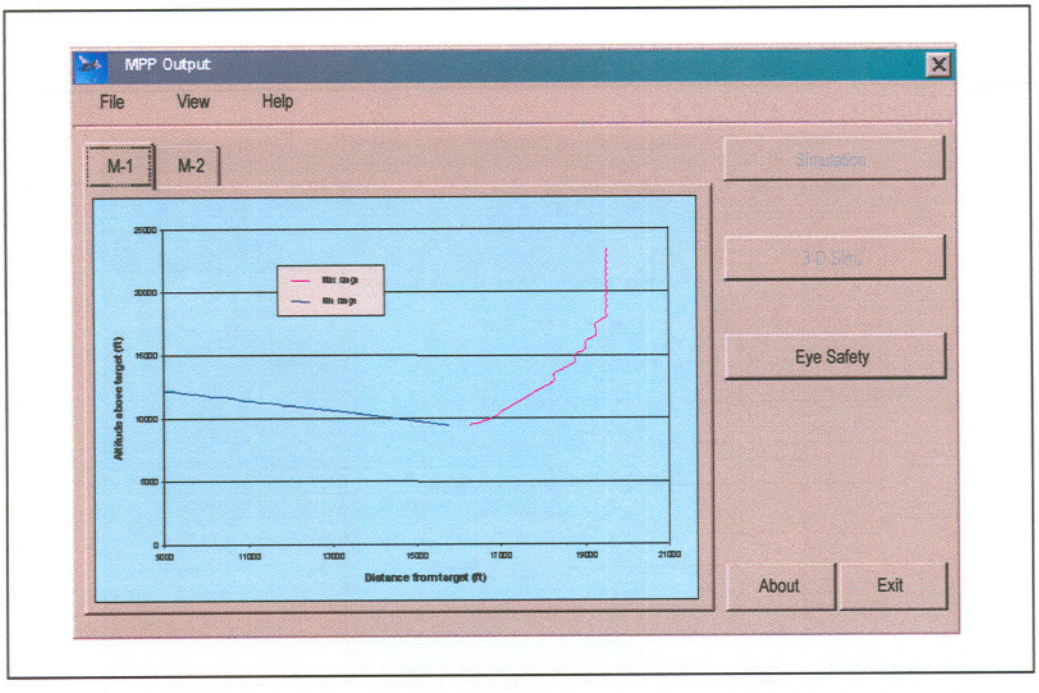

Figure 10-27. ALS-MPP eye-safety analysis O/P-I for 'Mode-1' (M-1).

Fig. 10-28 shows examples of the ALS-MPP 3-D visualisation tool, which is now being developed based on ItAF Operational Squadrons requirements .

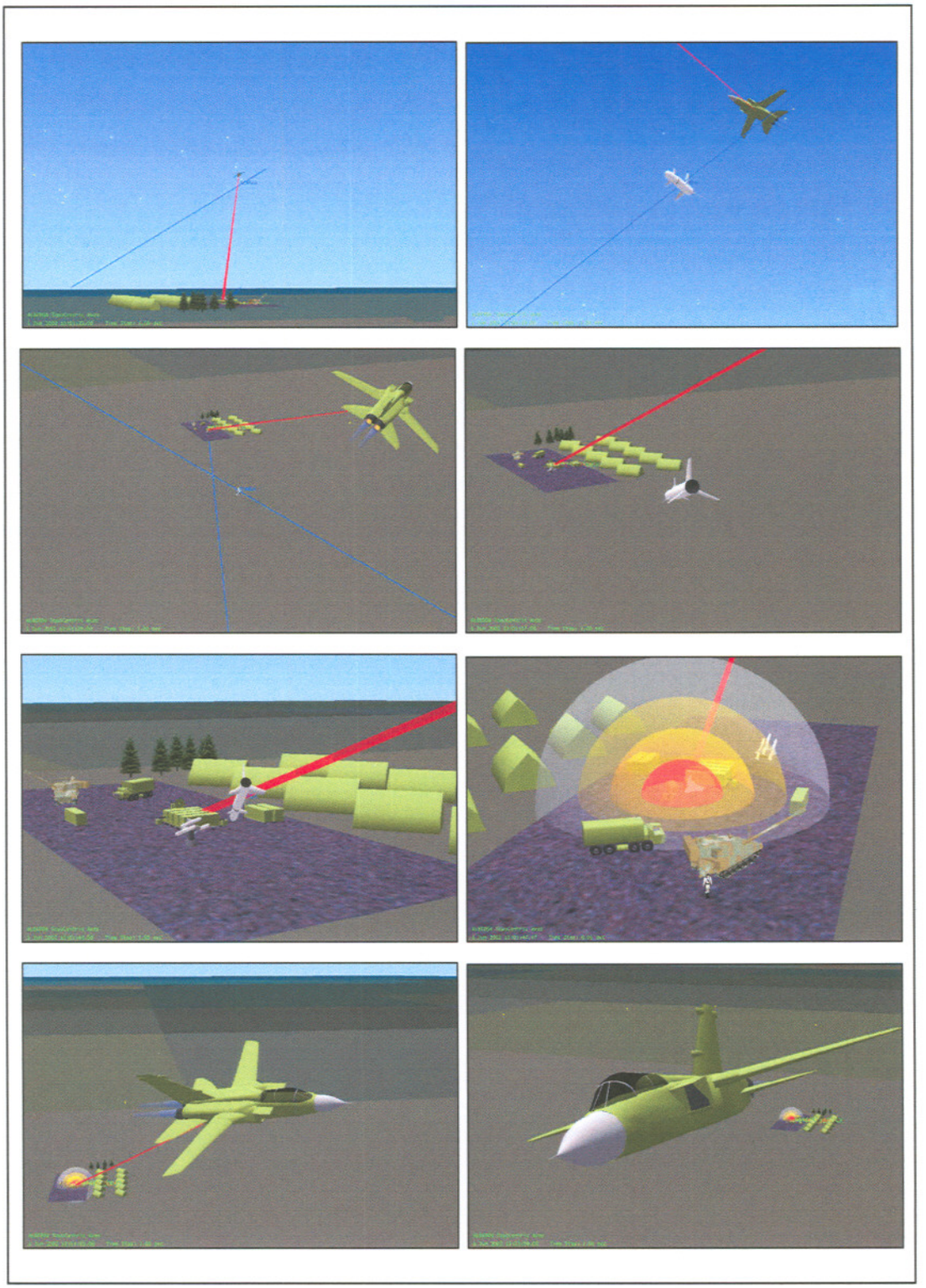

Figure 10-28. ALS-MPP 3-D simulation O/P-I.

Chapter 11

CONCLUSIONS AND FURTHER WORK

This thesis has described the research work performed for designing, developing and testing a new laser test and training range for the Italian Air Force. After the initial feasibility studies, the actual research work started back in 1998, when the Italian Air Force Official Flight Test Centre (ItAF-OTC) set the requirements for upgrading the PISQ test/training range (Poligono Interforze del Salto di Quirra – Sardinia – Italy), adding new facilities for carrying out safe training and experimental activities with airborne and ground laser systems, together with LGW delivery tests. According to these initial requirements, the PILASTER (**PI**SQ **LAS**er **T**est and **E**valuation **R**ange) development program was divided in two different phases. The aim of the first phase of the program (1999-2002) was to provide an initial operational capability for carrying out, in fully safe conditions, ground tests and flight experimental activities (with related measurements and semi-automated data analysis), required for performance evaluation of military laser systems. The successive phase of the program (now ongoing) is aimed to implementing the PILASTER full operational capability, required for performing all laser test/training activities, including all mission planning and fully-automated post-mission data analysis tasks.

11.1 Conclusions

The PILASTER program included the design of new range instrumentation and facilities, development of innovative methods for military systems performance prediction/evaluation and determination of eye-safety requirements for employment of ground and airborne laser systems at the laser range (during both experimental and training activities), together with extensive laboratory, ground and flight test activities with state-of-the-art ground/airborne laser systems and weapons.

In this research, present laser technology status and future technology trends were investigated, with particular emphasis for the systems now in service or under development for the Italian Air Force (i.e., the *Thompson* CLDP laser pod, the *ELOP* PLD system, PAVEWAY II, PAVEWAY III and Lizard LGB's, and the *Marconi-Selenia* LOAS system for helicopters). Due to the need for 'realistic' simulation and mission planning, together with reliable post-mission data analysis at the PILASTER range, various mathematical models were developed for ground/airborne laser systems performance analysis. These included:

- Suitable forms of the range equation for laser systems.
- Atmospheric laser beam propagation models.
- Laser scattering and target cross-section models.
- Air-to-ground missions geometric models.

The technical requirements of the PILASTER range instrumentation were defined. Particularly, these requirements included:

- PILASTER concept of operation.
- PILASTER flight/ground test requirements.
- PILASTER training requirements (real/simulated attacks).
- PILASTER systems requirements, including sensors/systems, real-time and post-processing data analysis, fixed and destroyable/recoverable targets, meteorological sensors, and remote control room requirements.
- PILASTER growth potentials.

Furthermore, the detailed design characteristics of the PILASTER Laser Tracking and Monitoring System (LTM) and targets were defined, including the following:

- PILASTER Laser Sensor Tracking and Measurement Unit (STU), constituted by IR/TV cameras, processing units, sensor arrays, LAN/WAN units, etc., located in proximity of the PILASTER targets.

- PILASTER Monitoring and Control Station Unit (MSU), composed by all systems required for real-time and post-processing data display, together with remote control of the STU systems (i.e., LAN/WAN units, MSU computer, GPS/FTI receivers, communication systems, etc.).
- PILASTER LTM functional modes (i.e., alignment/calibration mode, BITE mode, operational mode and data transfer mode).
- Weather monitoring equipment, including the sensors/systems required for measuring and recording relative humidity, pressure, temperature, state of turbulence, rainfall-rate, wind speed and wind direction.
- PILASTER DGPS based time and space position information (TSPI) system.
- Software for laser spot data tracking and analysis, including the PILASTER extinction measurement techniques.
- PILASTER Fast-recoverable Target (FRCT), Fixed Target (FXDT) and IR Reference Target (IREF).

Very important for the PILASTER development was also definition of eye-safety criteria and procedures, since most of current laser systems operate in the near infrared, with considerable risk for the naked human eye. Therefore, safety issues were deeply analysed in the light of the operational requirements for ground and airborne laser systems, and suitable algorithms/procedures were developed for calculation of ground laser safety areas and aircraft flight profile restrictions (airborne systems) for both test and training missions. These included the following:

- Models for Airborne Laser System (ALS) safety areas calculations: beam hazard area (A-BHA), buffer zone (A-BZ) and extended buffer zone (A-EBZ).
- Algorithms for accounting aircraft dynamics in A-EBZ calculations.
- Algorithms for determining aircraft envelope restrictions, with a certain predefined A-EBZ (evacuation area).
- Models for Ground Laser System (GLS) safety areas: beam hazard area (G-BHA), buffer zone (G-BZ) and extended buffer zone (G-EBZ).

- Models for calculating the effective G-BZ (BZE) with various GLS-target LOS geometries (horizontal and/or vertical misalignment).
- Procedures for GLS safety at the PILASTER range, also using the real-time information provided by the PILASTER LTM sensors and systems.

Extensive laboratory, ground and flight experimental activities were performed with both ground and airborne laser systems in order to test the various PILASTER laser range systems and to validate/refine the models developed for systems performance analysis and simulation. Furthermore, the LOAS system was tested both on the ground and in flight, in order to assess the system obstacle detection performance in various weather conditions, and the efficiency of the algorithms developed for obstacle classification and trajectory optimisation.

Laboratory experimental activities performed during this research included the following:

- Determination of LGW seekers detection thresholds.
- Measurements of surface/paints reflection properties.
- PILASTER sensors testing and calibration.
- LOAS laser system testing.
- Test of PILASTER protection filters and eye-wears (cinetheodolites, ground personnel and aircrew).

Determination of LGW seeker Minimum Detectable Power Density (MDPD) and measurements of surface reflection properties at laser wavelengths were essential for predicting realistic range performance of both ground and airborne laser systems, as well as for aircraft tactics (flight profile) optimisation, PILASTER range initial design activities (i.e., target-STU geometry, target characteristics, sensors optimisation, etc.), analysis of flight/ground test data and assessment of training exercises with laser systems.

Determination of materials/paints scattering properties included spectral reflectance and Bidirectional Reflectance Distribution Function (BRDF) measurements. The samples

for scattering measurements were selected in order to allow an appropriate choice of the paints to be used for the PILASTER targets, and also to gather useful data regarding the reflective properties of materials normally encountered in the operational employment of laser systems.

Ground experiments performed during this research included:

- Near Infrared (NIR) laser beam atmospheric propagation measurements (λ = 1064 nm and λ = 1550 nm);
- LTD/LRF systems pointing accuracy tests;
- Systems harmonisation and performance evaluation trials of the STU and (D)GPS components of the PILASTER system;
- Dedicated ground trials with the LOAS system in order to assess its detection performance (in various weather conditions), and to initially verify the reliability of the obstacle classification algorithms.

Flight test activities performed as part of the PILASTER development project, included the following:

- Propagation measurements in oblique air-to-ground paths (λ = 1064 nm);
- CLDP pointing accuracy measurements;
- CLDP laser beam diameter measurements for long air-to-ground paths.
- Differential GPS (DGPS) MB-3339C flight trials;
- DGPS TORNADO-IDS flight trials.
- LOAS preliminary trials on NH-300 helicopter;
- LOAS trials on AB-212 helicopter.

Particularly, the PILASTER systems were tested during ground and flight trials (including real air-to-ground missions), allowing sensors site calibration, progressive improvements of the STU and MSU hardware components and refinements of the data acquisition/analysis software tools.

Furthermore, with the PILASTER systems in their operational configuration, atmospheric extinction measurements were performed with the geometries typical of ground designation and air-to-ground missions (i.e., oblique laser paths), and correction factors for the ESLM atmospheric propagation models were determined in conditions of great operational significance and in various weather conditions (i.e., hazy, clear and rainy weather conditions). Pointing accuracies (from geometric and energy spot measurements) of various ground LRF/LTD systems and of the CLDP were determined, and laser spot distortion measurements were performed with the ELOP-PLD system.

The DGPS ground and flight test campaigns were performed with the aim of selecting a suitable Position Reference System for both experimental and training activities (i.e., real-time and post-flight mission trajectory data analysis). After comparative evaluation of various off-the-shelf systems, the ASHTECH XII receivers and the ASHTECH P-NAV software were selected for use at the PILASTER range. Furthermore, during the TORNADO-IDS flight test activity, the aircraft envelope limitations associated with the use of the ASHTECH XII airborne GPS (applicable during activities with airborne laser systems) were determined.

The LOAS ground and flight test activities allowed to verify the functionality of the system in a representative operational environment and to assess the system detection performance with various weather conditions/obstacles and the efficiency of the obstacle classification/prioritisation algorithms.

Finally, the general requirements for both tactical and test/training mission planning were determined, together with specific requirements for PILASTER test and training post-mission data analysis tasks. Particularly, taking into account the results of the various laboratory, field and flight experimental activities performed, the kernel algorithms of the PILASTER computer programs for ground/airborne laser systems performance prediction and eye-safety analysis were progressively refined. Furthermore, dedicated simulation tools were developed for aircraft flight profile and laser systems employment optimisation in both operational and test/training missions.

11.2 Further Work

Although the work done for this thesis has fully achieved the goals of designing the PILASTER range instrumentation and facilities, developing innovative methods for military systems performance prediction/evaluation and eye-safety analysis for ground/airborne laser systems at the laser range (during both experimental and training activities), and defining the requirements for both tactical and test/training mission planning, there is still a large amount of further work that will follow from this thesis. This section gives some directions for further work.

- Continue performing laser beam propagation tests.

  During the future PILASTER ground and flight experimental activities, NIR laser beam propagation effects will be investigated, with particular emphasis for the measurement of atmospheric extinction. Performing further tests in this area (with NIR lasers but also with MIR/FIR laser sources when available), is required in order to improve the reliability of the empirical models currently used for propagation analysis in both dry-air and rainy conditions (i.e., corrected ESLM models for absorption and scattering). Particularly, it is believed that a statistical approach, making use of the PILASTER Laser Propagation Data Base (LPDB), would be well suited for a progressive refinement of the ESLM models.

- Explore the effects of atmospheric turbulence.

  During the future PILASTER ground and flight experimental activities, the effects of turbulence on atmospheric laser beam propagation will be studied. Particularly, using horizontal and vertical turbulence (C_n), wind, temperature and humidity profiles, the effects of turbulence on horizontal and oblique/vertical paths propagation will be better understood and modelled.

- Improve mission planning and post-mission analysis tools.

  Based on the achievements of this research, the current phase of the PILASTER program (planned to be completed in May-June 2004) is aimed at implementing the range full operational capability, required for performing all laser test/training activities, including all mission planning and fully-automated post-mission data analysis tasks. During the forthcoming PILASTER experimental activities, the mission planning and post-mission analysis tools developed during this research, will be further tested and improved.

- Further investigate oblique and vertical path propagation.

  During this research, the CLDP/TORNADO-IDS flight trials were also used for obtaining experimental data regarding the variations of the attenuation coefficient at λ = 1064 nm as a function of altitude. Particularly, the decrease of atmospheric extinction was determined for various oblique slant-paths (i.e., ξ = 50°, 40°, 30° and 20°) and altitudes varying between 7000 and 22000 ft AGL. It must be considered, however, that the functions relative to the various grazing angles are representative of the experimental data trends only in the altitude intervals where the data were collected. Furthermore, the experimental flight sorties were carried out only in clear weather with similar values of the relevant meteorological parameters measured on the ground (i.e., visibility, relative humidity and temperature). Therefore, it is possible that using these functions beyond the respective altitude intervals and in different weather conditions may not provide reliable predictions of the attenuation coefficient.

  In order to obtain accurate and reliable predictions of the attenuation coefficient variations with altitude, required for performance data analysis and simulation purposes at the PILASTER range, it is essential to perform further flight trials, in appropriate meteorological and operational scenarios, including representative weather conditions and wider portions of the TORNADO-IDS/CLDP operational flight envelopes.

$$i_{TH} = \sqrt{4K_B \frac{T_k Bk}{R_L}} \tag{8.43}$$

$$i_{DK} = 0.5 \cdot 10^{-12} \tag{8.44}$$

$$i_{RA} = 1.5 \cdot 10^{-12} \tag{8.45}$$

where:

P_S = received solar power

P_h = amplifier gain

M_A = avalance multiplier

k = noise factor of the avalance photodiode

B = electronic bandwidth

K_B = Boltzmann constant (1.39×10^{-23} J/°K)

T_K = absolute temperature (°K)

R_L = amplifier load resistance

The following characteristics were defined for a 'wire type' obstacle according to LOAS operational requirements:

- *Diameter:* 5 mm ≤ D_W ≤ 70 mm
- *Shape:* twisted or round
- *Reflection:* Purely diffuse (Lambertian)
- *Reflectivity:* ≥ 20% ($\theta = 0$)

The reference environmental parameters were set as follows:

- *Visibility:* $V \geq 800$ m
- *Humidity:* $RH \leq 100\%$
- *Temperature:* $T \leq 50$ °C
- *Rain:* Light/Medium/Heavy
- *Background:* $P_B = 50$ W/m^2 sr μm

For calculation purposes, the $i_{SIG}\,(R,\theta)$ term in eq. (8.40), was modelled as:

$$i_{SIG} = \sqrt{\frac{P_T d_W \rho D_a{}^3 \eta e^{-2\gamma R}}{4R^3 \lambda} \cdot \frac{P_h}{K_a} \cdot \frac{1}{R_L}} \tag{8.46}$$

where:

P_T = transmitted power

P_h = amplifier gain

D_a = aperture diameter

K_a = aperture illumination constant = $sen(\theta)^{5.4}$

Results of range performance calculations performed with various visibilities and with all other parameters set to the worst case, are shown in Fig. 8-42.

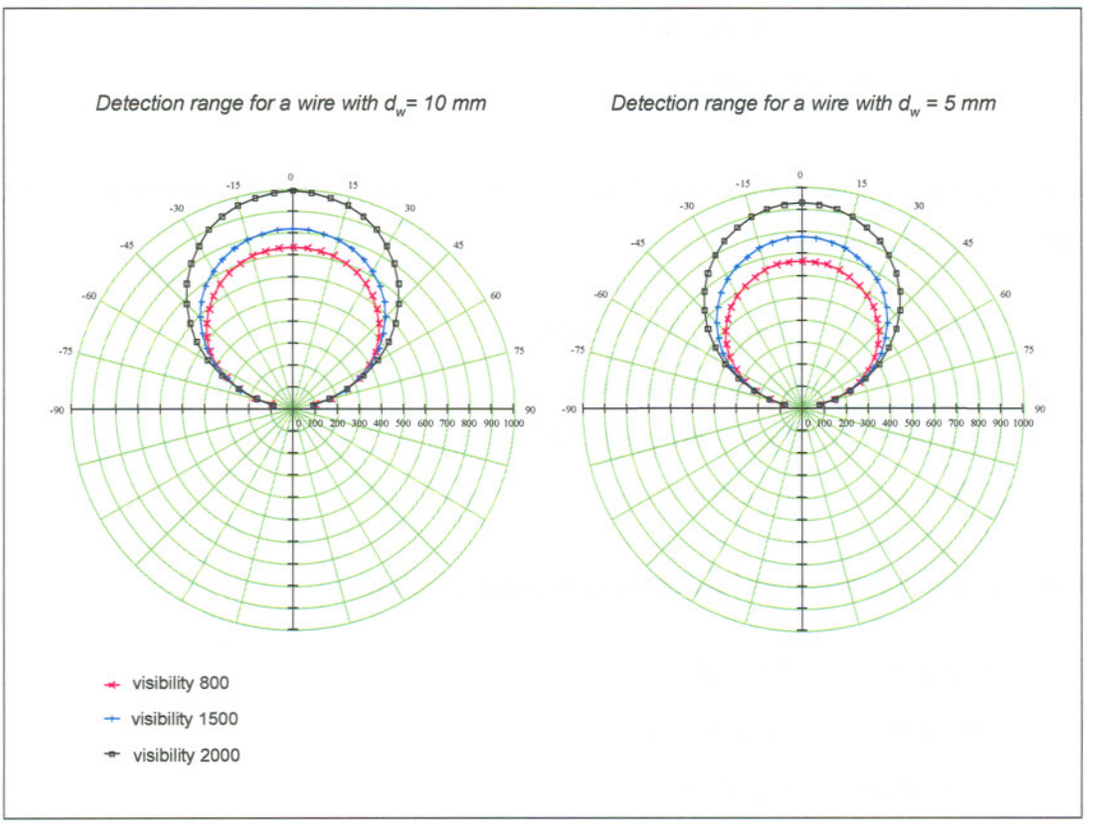

Figure 8-42. LOAS detection range performance with wires.

The false alarm probability was modelled by:

$$P_{fa} = \frac{1}{B \cdot T_{fa} \cdot \eta} \tag{8.47}$$

where:

B = receiver bandwidth

T_{fa} = mean time between false alarms

η = maximum useful range/maximum non ambiguous range

The mean time between false alarms corresponds to elementary electrical false alarms at the receiver level. The probability to have several false alarms on a straight line pattern is much lower. Statistically, these phenomena are described by the False Alarm Rate (FAR) and Detection Probability (P_d). If the noise and signal distributions are known, the SNR can be estimated and the corresponding DP and FAR can be determined. According to the Rice calculation [1], the average FAR for the LOAS system is given by:

$$\overline{FAR} = \frac{1}{2\tau\sqrt{3}} exp\left(-\frac{I_t^2}{2I_n^2}\right) \tag{8.48}$$

where:

τ = Electrical pulse length

l_t = Threshold current

l_n = Average noise current

The LOAS P_d is determined using pure *Gaussian* statistics [1, 2]:

$$P_d = \frac{1}{\sqrt{\pi}} \int_{\frac{I_t - I_n}{\sqrt{2}I_n}}^{\infty} exp\left(-\frac{i_n^2}{2I_n^2}\right) d\left(\frac{i_n}{\sqrt{2}I_n}\right) \tag{8.49}$$

I_n = average signal current

i_n = instantaneous noise current

The false alarm probability (P_{fa}) is given by:

$$P_{fa} = \tau \cdot \overline{FAR} \tag{8.50}$$

and the cumulative detection probability (P_D) is given by:

$$P_D = 1 - \sum_{i=0}^{m} C_M^i P_d^i (1 - P_d)^{M-i} \tag{8.51}$$

where:

M = number of possible detections

m = minimum number of detections required

To validate the LOAS performance models, ground tests were performed using a wire of known section and reflectivity (D_W = 2.5 cm and ρ = 40%), and with various weather conditions (i.e., clear weather with $10 \leq V \leq 15$ km, and light/medium/heavy rain). The scenario in which ground tests were performed is shown in Fig. 8-43.

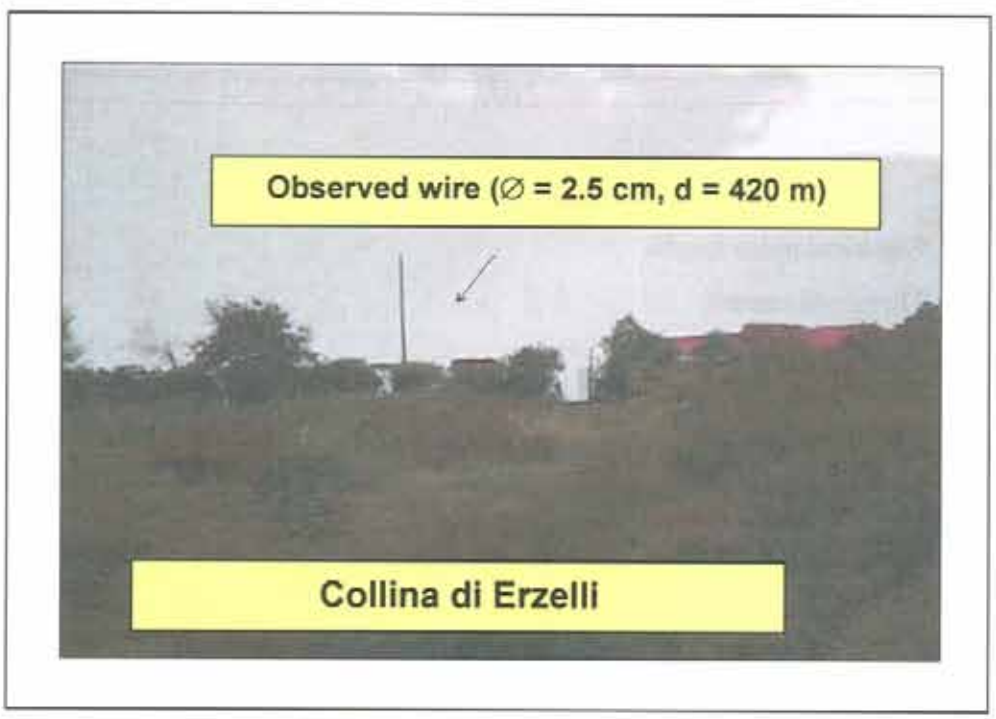

Figure 8-43. LOAS ground tests scenario.

The collected data sets showed that the returned signal power fluctuates independently from pulse to pulse according to a *Gaussian* distribution. The sets of data collected in clear and rainy weather conditions are shown in Fig. 8-44.

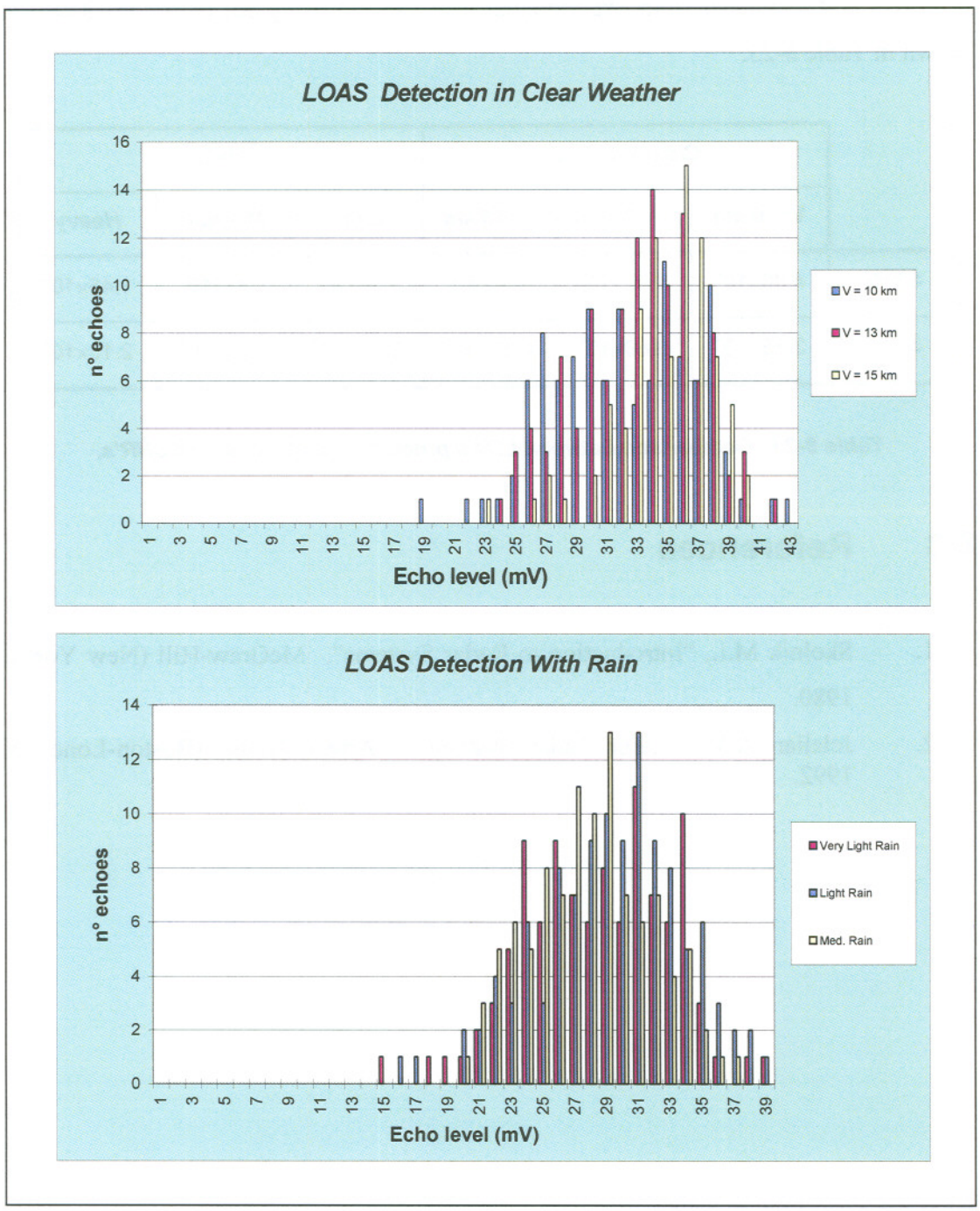

Figure 8-44. LOAS detection characteristics.

A comparison between the SNR predicted (SNR_P) using eq. (8.39) with γ calculated using the ESLM model (0.19 $km^{-1} \leq \gamma \leq$ 0.22 km^{-1} for clear weather and 1.23 $km^{-1} \leq \gamma \leq$ 2.94 km^{-1} for rainy conditions), assuming a background power of 10 Watt/m^2/sr/μm and ρ = 0.5, and estimated from experimental data (SNR_E) using eq. (8.40) to (8.46), is shown in Table 8-23.

	Clear Weather			*Rain*		
	V=10 km	***V=12.5 km***	***V=15 km***	***Light***	***Medium***	***Heavy***
SNR_P	4.90×10^4	4.95×10^4	5.02×10^4	3.14×10^4	1.83×10^4	1.45×10^4
SNR_E	3.35×10^4	3.80×10^4	4.27×10^4	2.87×10^4	2.47×10^4	2.13×10^4

Table 8-23. Comparison between LOAS prediscted and measured SNR's.

8.3 References

1. Skolnik M.I., "Introduction to Radar Systems". McGraw-Hill (New York). 1980.
2. Jelalian A.V., "Laser Radar Systems". Artech House (Boston-London). 1992.

Chapter 9

FLIGHT TEST ACTIVITIES

9.1 General

Flight test activities performed as part of the PILASTER development project, included the following:

a. **PILASTER Systems Test Campaign** (TORNADO-IDS), including:
   - Propagation Measurements in Oblique Air-to-ground Paths;
   - CLDP Pointing Accuracy Measurements;
   - CLDP FLIR Systems Flight Testing;

b. **DGPS Test Campaign**, including:
   - MB-3339C Flight Trials;
   - TORNADO-IDS Flight Trials.

c. **LOAS Test Campaign**, including:
   - Preliminary Flight Trials on the NH-300 Helicopter;
   - Final Flight Trials on the AB-212 Helicopter.

Particularly, the PILASTER STU and MSU systems were tested during their employment in real air-to-ground missions (both with and without deliveries of guided weapons). With the PILASTER systems in their operational configuration, atmospheric extinction measurements were performed with the geometries typical of air-to-ground missions (i.e., oblique and vertical laser paths), and the correction factors for the ESLM sea-level atmospheric propagation models were determined in the conditions of greatest

significance. Pointing accuracy (from geometric and energy spot centres measurements) of the CLDP were determined in flight and laser beam spread measurements were performed with various aircraft-target geometries.

The DGPS test campaign was performed with the aim of selecting a suitable Position Reference System for both experimental and training activities (i.e., real-time and post-flight mission trajectory data analysis). Furthermore, the aircraft envelope limitations associated with the use of an airborne DGPS applicable during activities carried out with laser designators and other laser systems was determined. As anticipated, also

The LOAS flight test activities were carried out in order to verify the functionality of the system in a real operational environment (preliminary trials) and to assess the system detection performance with various weather conditions/obstacles and the efficiency of the obstacle classification/prioritisation algorithms.

This chapter describes the flight test activities carried out during this research and gives indications about further activities planned to be performed in the future.

9.2 PILASTER/CLDP Test Campaign

As discussed in the previous chapters, most PILASTER systems test activities were carried out during laboratory and ground sessions. However, a number of flight sorties were performed with the CLDP on TORNADO-IDS (fully instrumented with FTI and a DGPS based PRS), in order to verify the compliance of the PILASTER systems with aircraft test/training missions requirements. This activity also served to the personnel involved (aircrews and engineering officers) to gain confidence with the PILASTER systems (STU and MSU) during their operational employment. Particularly, both dry (no LGW delivery) and hot attack profiles were flown, following flight paths and executing manoeuvres compatible with both eye-safety restrictions and DGPS data gathering requirements. During the activity, a number of measurements were performed (in real-time and in post-processing) with the PILASTER systems. Together with baseline measurements required for the PILASTER operation (pointing accuracy, beam spot diameter, energy profiles, codes characteristics, etc.), also some propagation measurements were performed with different oblique air-to-ground paths.

The CLDP-IR standard FLIR and an enhanced version of the FLIR system (CLDP-IRS version) was also tested, using the PILASTER IR target. Finally, using the data collected in flight, the PILASTER post-mission data analysis tools were also improved.

9.2.1 Atmospheric Propagation Trials

Atmospheric propagation flight test activities with the CLDP-IR on TORNADO-IDS aircraft were performed with the aim of obtaining experimental data regarding the variations of the attenuation coefficient at λ = 1064 nm as a function of altitude. In order to cope with this task, it was first of all required to correctly planning the flight sorties and selecting the test points according to the aircraft envelope limitations, to the PILASTER instrumentation mode of operation and to the CLDP-IR functional characteristics. As the target used for the trials had a size of about 10×10 metres, and the entire laser spot had to be captured by the NIR cameras for data analysis, the first concern was to determine the conditions (i.e., slant-range and incidence angle) in which the size of the laser spot would not exceed the size of the target. Imposing that the aircraft had to fly towards the target surface along the radial 130, the problem of determining the laser spot size with varying altitude was reduced to the case of a pure vertical misalignment (i.e., no azimuth misalignment). Therefore, the equation used to approximately determine the major axis of the laser spot ellipse on the target (r) was the following:

$$r = (d \cdot sin\alpha) \cdot \left[\frac{1}{cos(\alpha - \beta)} + \frac{1}{cos(\alpha + \beta)} \right] + \frac{a}{cos\,\beta} \qquad (9.1)$$

where α is the beam divergence and β is the CLDP-IR elevation angle (measured with respect to the target normal). Using this equation, two flight sorties were planned to be executed in days with visibility in excess of 15 km, including four dive manoeuvres at 45°, 35°, 25° and 15° respectively. The dive profiles envelopes are described in the Table 9-1.

Profile Envelope	20° Dive		30° Dive		40° Dive		50° Dive	
	Alt.	Dist.	Alt.	Dist.	Alt.	Dist.	Alt.	Dist.
Top	14000 ft	12.5 km	19000 ft	11.5 km	20000 ft	9.5 km	22000 ft	8.5 km
Bottom	6000 ft	5.5 km	7000 ft	4 km	8000 ft	4 km	8000 ft	3.5 km

Table 9-1. Flight profiles envelopes for atmospheric extinction trials.

When data could not be collected during the dives, straight and level passages were performed parallel to the target surface. In all cases, the CLDP-IR laser was manually activated by the WSO at the required altitudes and grazing angles.

The CLDP-IR laser eye-safety envelope is shown in Fig. 9-1, with superimposed the dive manoeuvres profiles.

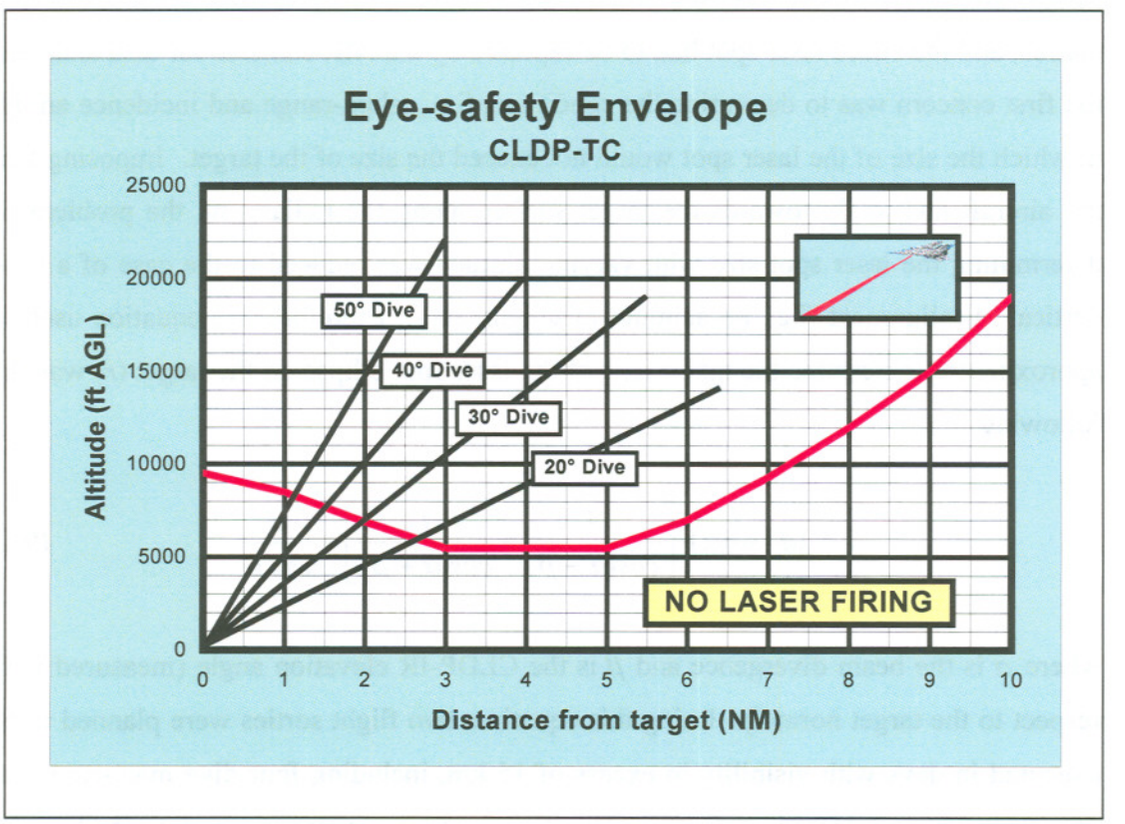

Fig. 9-1. CLDP-IR eye-safety envelope.

The flights were performed on two successive days during summer 2002. The meteorological data collected at the target location during the two sorties are reported in Table 9-2.

Sortie	Visibility (km)	Rel. Hum. (%)	Temp. (°C)	Wind (°/kts)	Cloud
1	16 km	57%	35°C	120/7	0/8
2	18 km	54%	32°C	0/0	2/8

Table 9-2. Meteorological data relative to propagation flight trials.

Following the planned flight profiles, experimental data collected during the two TORNADO-IDS sorties allowed to estimate the variations of the attenuation coefficient with altitude. Particularly, measuring transmittances for various aircraft grazing angles and altitudes (aircraft instrumented with DGPS and equipped with standard barometric/radar altimeters), the following results were found.

9.2.1.1 Tests with 50° Grazing Angle

The experimental data obtained with a grazing angle of 50° are plotted in Fig. 9-2. The following linear approximation was found for the ratio of attenuation coefficient to its sea-level value:

$$\tau_{atm}^{H}/\tau_{atm} = -1.9568 \cdot 10^{-5} H + 0.9663 \qquad (9.2)$$

where γ_{atm}^{H} is the attenuation coefficient of the slant-path, γ_{atm} is the attenuation coefficient at sea-level, and H is the aircraft Mean Sea Level (MSL) altitude in thousands of ft. The second order polynomial fit of the same experimental data is:

$$\tau_{atm}^{H}/\tau_{atm} = 5.5583 \cdot 10^{-10} H^2 - 3.6243 \cdot 10^{-5} H + 1.0810 \qquad (9.3)$$

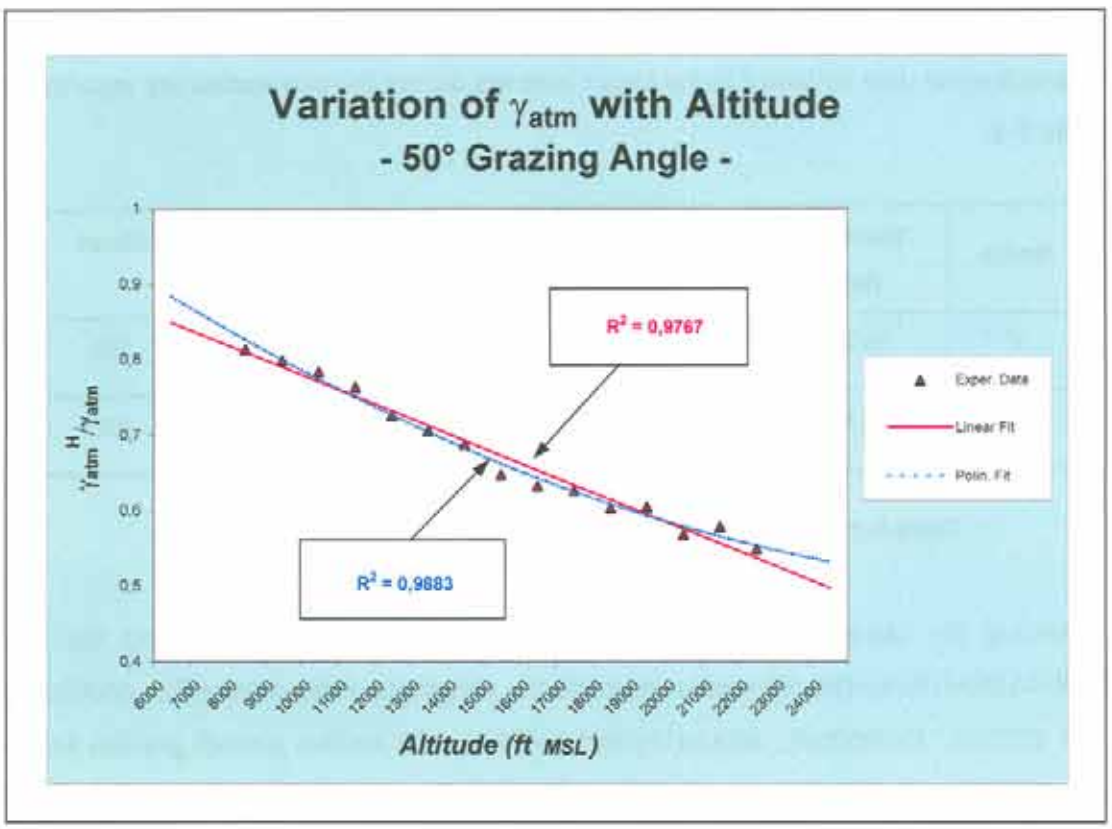

Fig. 9-2. Ratio of the attenuation coefficient to its sea-level value for slant-paths with a 50° grazing angle.

9.2.1.2 Tests with 40° Grazing Angle

The experimental data obtained with a 40° grazing angle are plotted in Fig. 9-3. The following linear approximation was found for the ratio of attenuation coefficient to its sea-level value:

$$\tau^H_{atm} / \tau_{atm} = -1.7566 \cdot 10^5 H + 0.9608 \tag{9.4}$$

The second order polynomial fit of the experimental data is:

$$\tau^H_{atm} / \tau_{atm} = 7.6424 \cdot 10^{-11} H^2 - 1.9706 \cdot 10^{-5} + 0.9747 \tag{9.5}$$

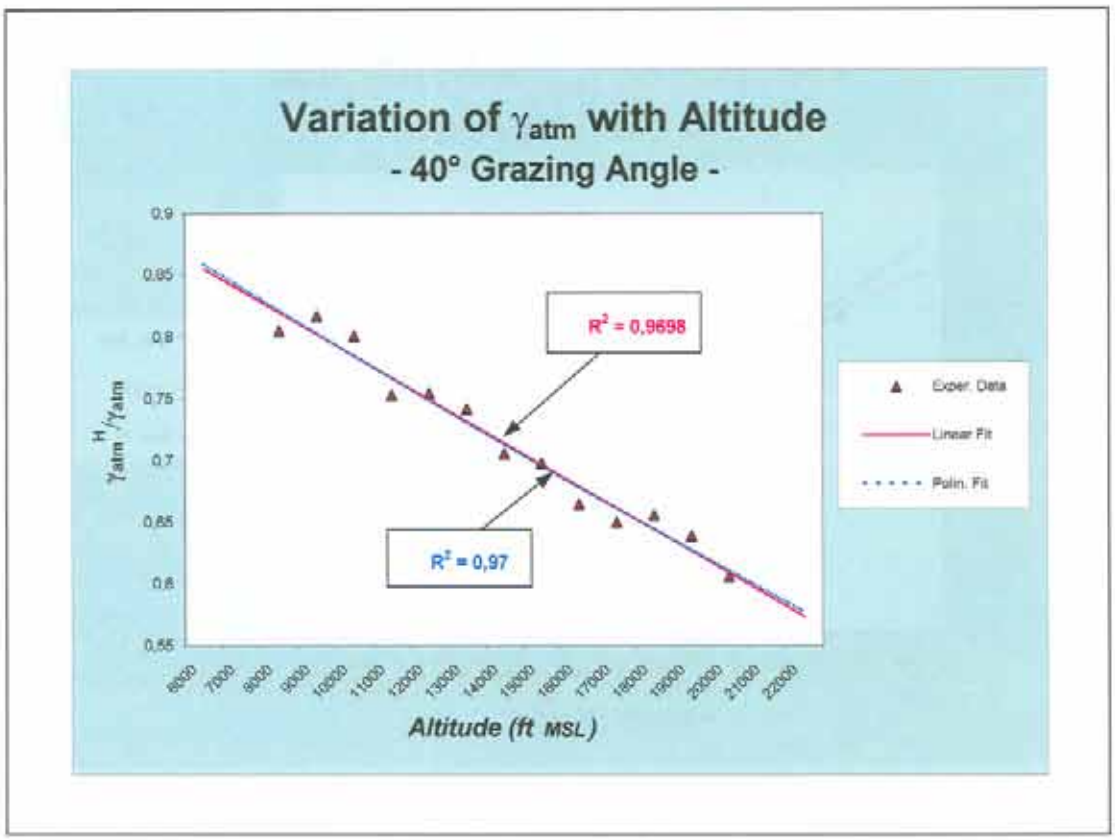

Fig. 9-3. Ratio of the attenuation coefficient to its sea-level value for slant-paths with a 40° grazing angle.

9.2.1.3 Tests with 30° Grazing Angle

The experimental data obtained with a grazing angle of 30° are plotted in Fig. 9-4. The following linear approximation was found for the ratio of attenuation coefficient to its sea-level value:

$$\tau_{atm}^{H}/\tau_{atm} = -1.5245 \cdot 10^{-5} H + 0.9626 \tag{9.6}$$

The second order polynomial fit of the same experimental data is:

$$\tau_{atm}^{H}/\tau_{atm} = 5.3447 \cdot 10^{-10} H^2 - 2.9675 \cdot 10^{-5} H + 1.0537 \tag{9.7}$$

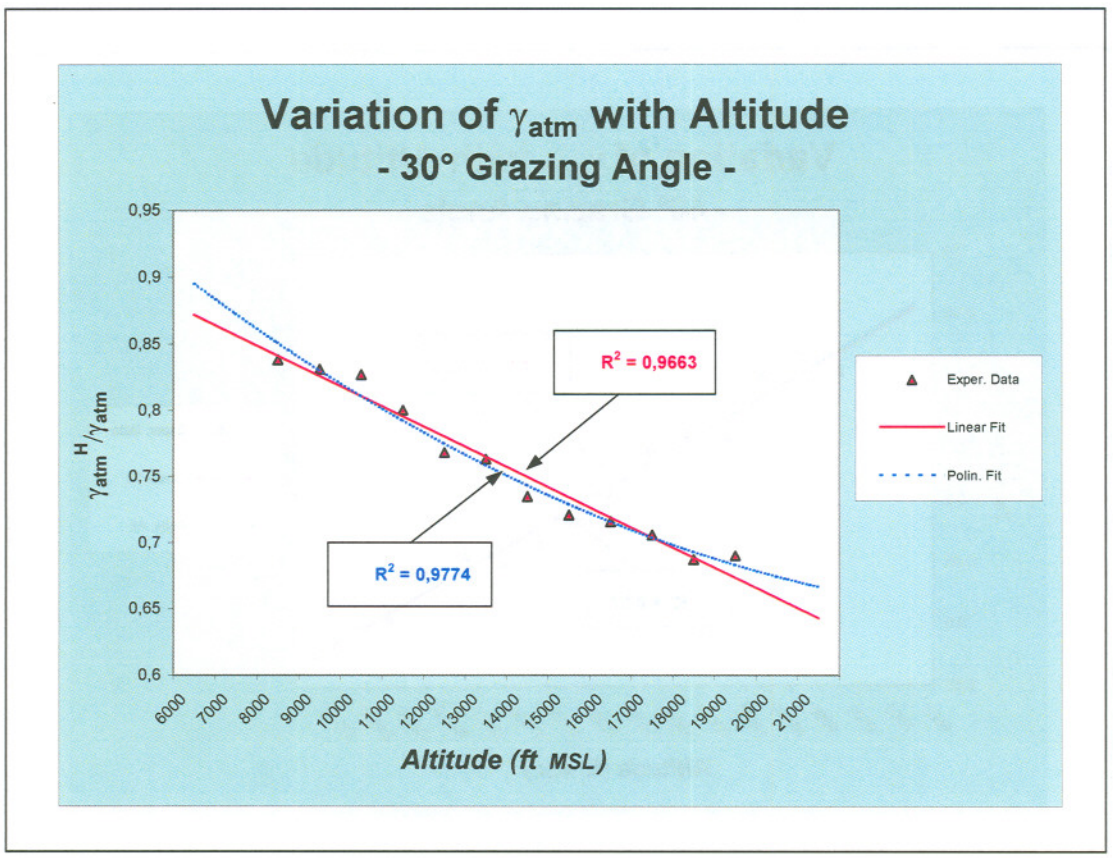

Fig. 9-4. Ratio of the attenuation coefficient to its sea-level value for slant-paths with a 30° grazing angle.

9.2.1.4 Tests with 20° Grazing Angle

The experimental data obtained with manual CLDP laser activation during the 20° dive manoeuvre are plotted in Fig. 9-5. The following linear approximation was found for the ratio of attenuation coefficient to its sea-level value:

$$\tau_{atm}^{H}/\tau_{atm} = -1.3758 \cdot 10^{-5} H + 0.9530 \qquad (9.8)$$

The second order polynomial fit of the same experimental data is:

$$\tau_{atm}^{H}/\tau_{atm} = 3.2468 \cdot 10^{-13} H^2 - 1.3765 \cdot 10^{-5} H + 0.9531 \qquad (9.9)$$

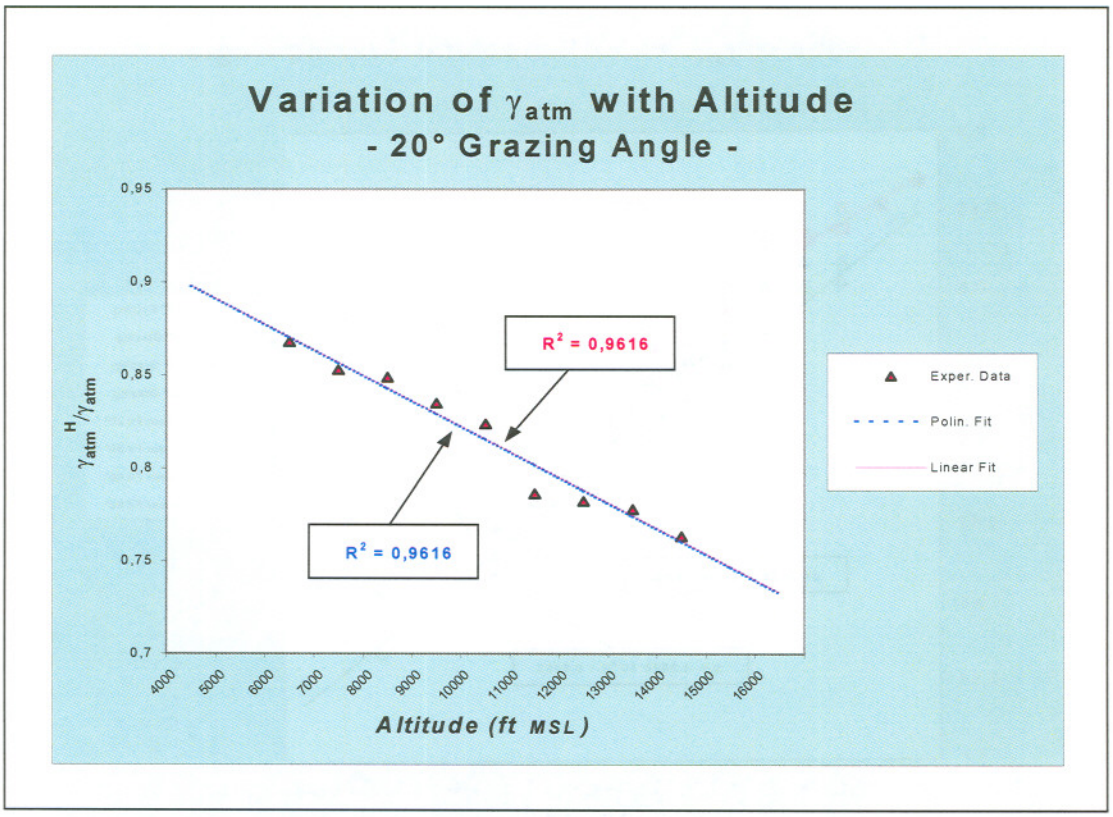

Fig. 9-5. Ratio of the attenuation coefficient to its sea-level value for slant-paths with a 20° grazing angle.

9.2.1.5 Discussion of Results

All experimental data collected during the trials are shown in Fig. 9-6. Looking at the data trends, it is evident that, as the grazing angle (ξ) becomes shallower, γ_{atm}^{H} tends to decrease at a lower rate as the altitude increases.

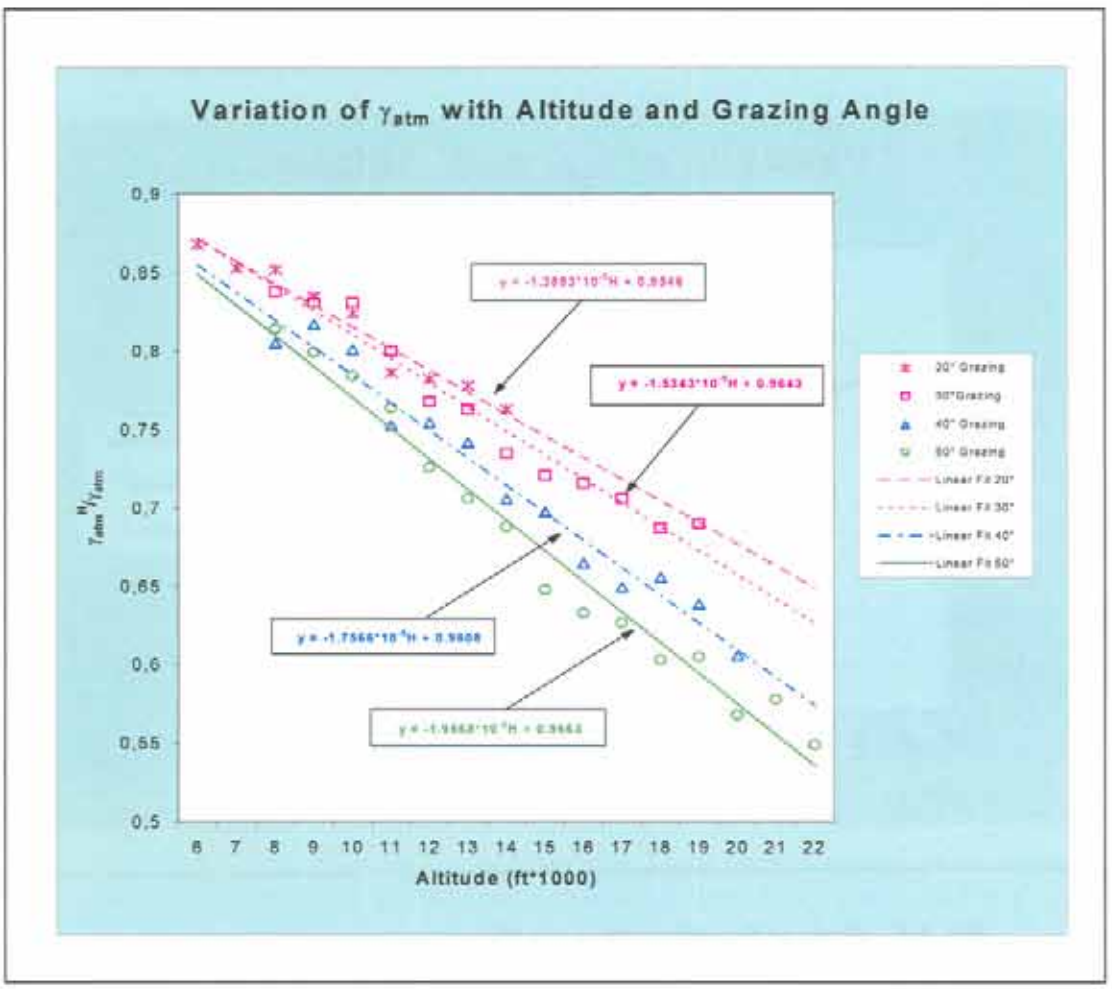

Fig. 9-6. Ratio of the attenuation coefficient to its sea-level value for slant-paths with 20°, 30°, 40° and 50° grazing angles.

It must be considered that the linear fits relative to the various grazing angles are representative of the data trends only in the altitude intervals were the experimental data were collected. Furthermore, the experimental flight sorties were carried out only in clear weather with similar values of the relevant meteorological parameters measured on the ground (i.e., visibility, relative humidity and temperature). Therefore, it is possible that using these functions beyond the respective altitude intervals and in different weather conditions may not provide reliable predictions of the attenuation coefficient.

Let us consider only the altitude interval 8000÷14000 ft in which data were collected with all grazing angles (i.e., ξ = 50°, 40°, 30° and 20°), shown in Fig. 9-7.

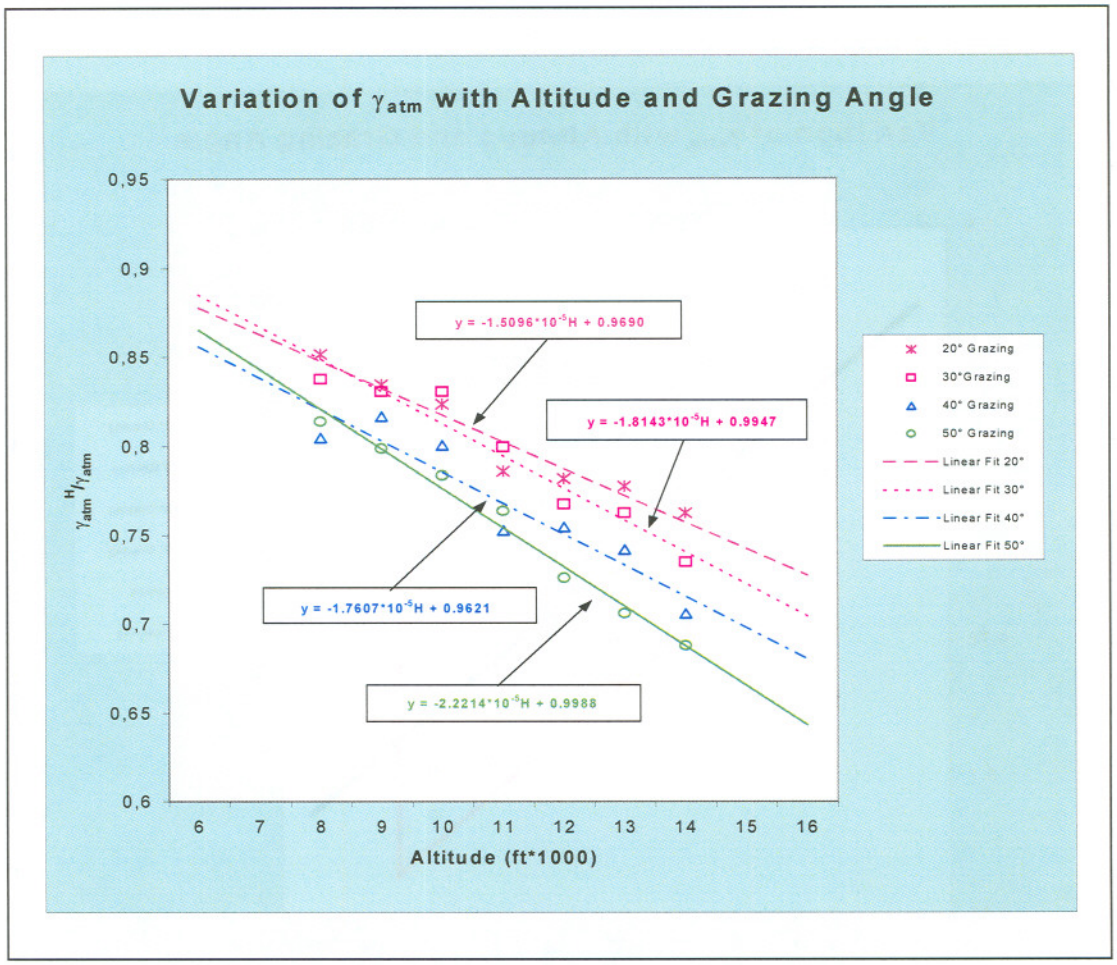

Fig. 9-7. Ratio of the attenuation coefficient to its sea-level value for various slant-paths and altitudes between 8000 and 14000 ft.

Also in this altitude interval it is confirmed that γ_{atm}^{H} tends to decrease less as the grazing angle becomes shallower. Furthermore, in this interval we may perform further analysis by determining an average fitting function for all data points collected. These elements are shown in Fig. 9-8. By doing this, we obtain a single function which allows approximate calculations of the fractional decrease in γ_{atm} for slant-paths with $20° \leq \xi \leq 50°$ from sea-level to altitudes between 8000 and 14000 ft.

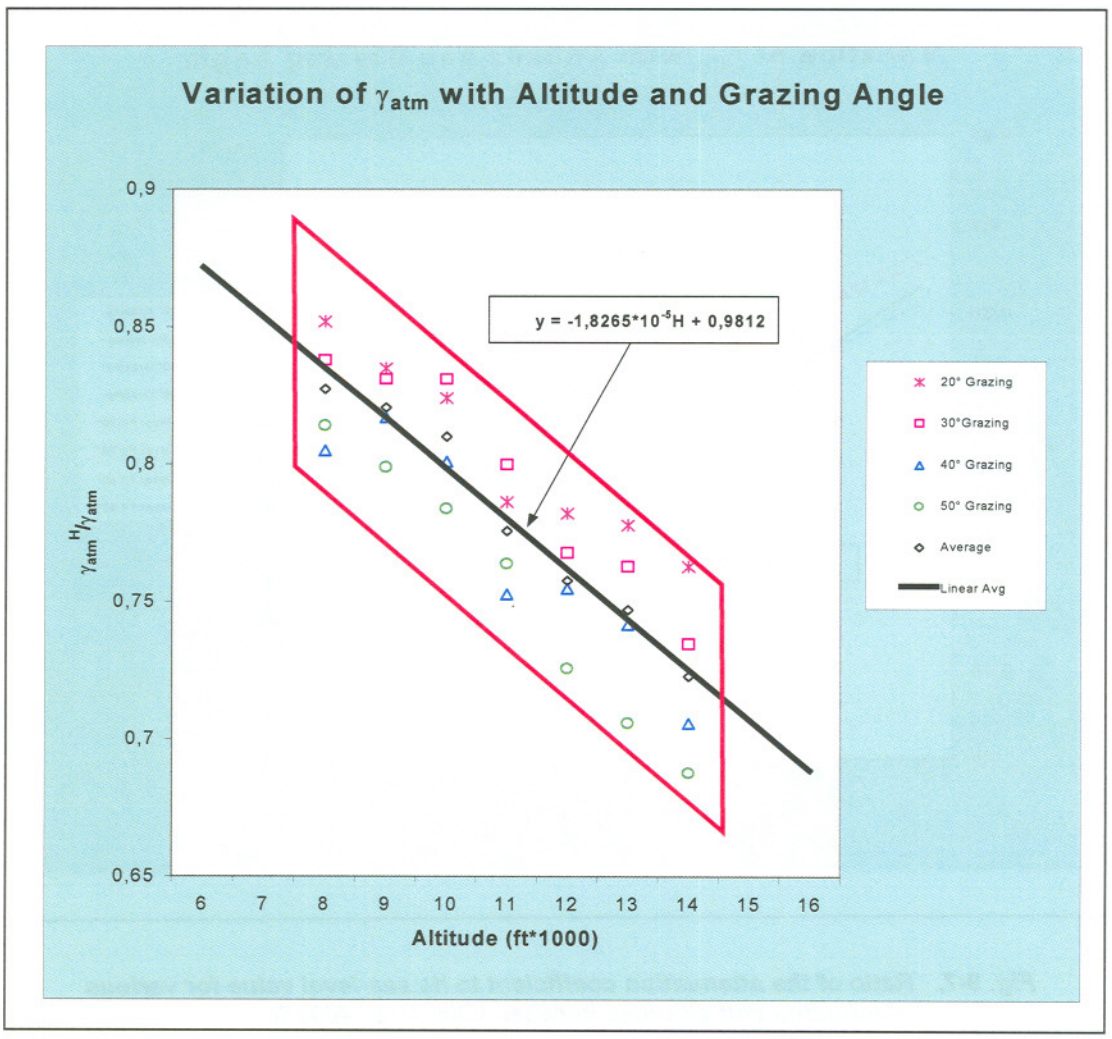

Fig. 9-8. ***Average $\gamma_{atm}^{H}/\gamma_{atm}$ for slant-paths with grazing angles between 20° and 50° and altitudes between 8000 and 14000 ft.***

A similar analysis was also performed in the altitude interval 8000÷19000 ft for the grazing angles 30°, 40° and 50°. The results are shown in the Figures 9-9 and 9-10.

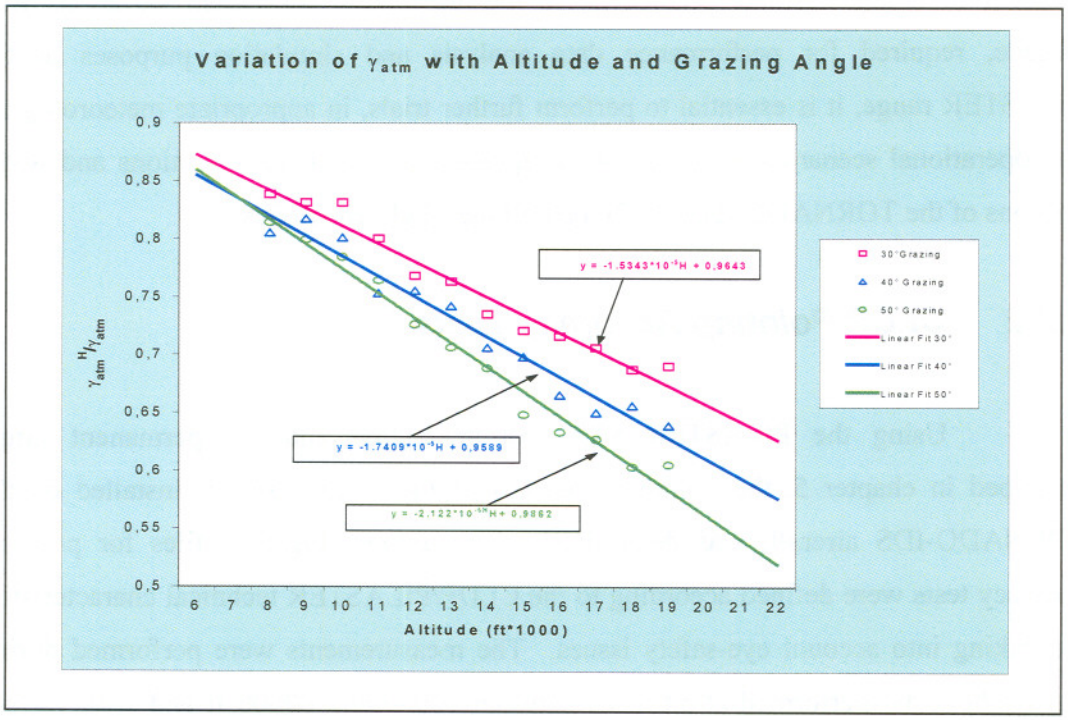

Fig. 9-9. Ratio of the attenuation coefficient to its sea-level value for various slant-paths and altitudes between 8000 and 19000 ft.

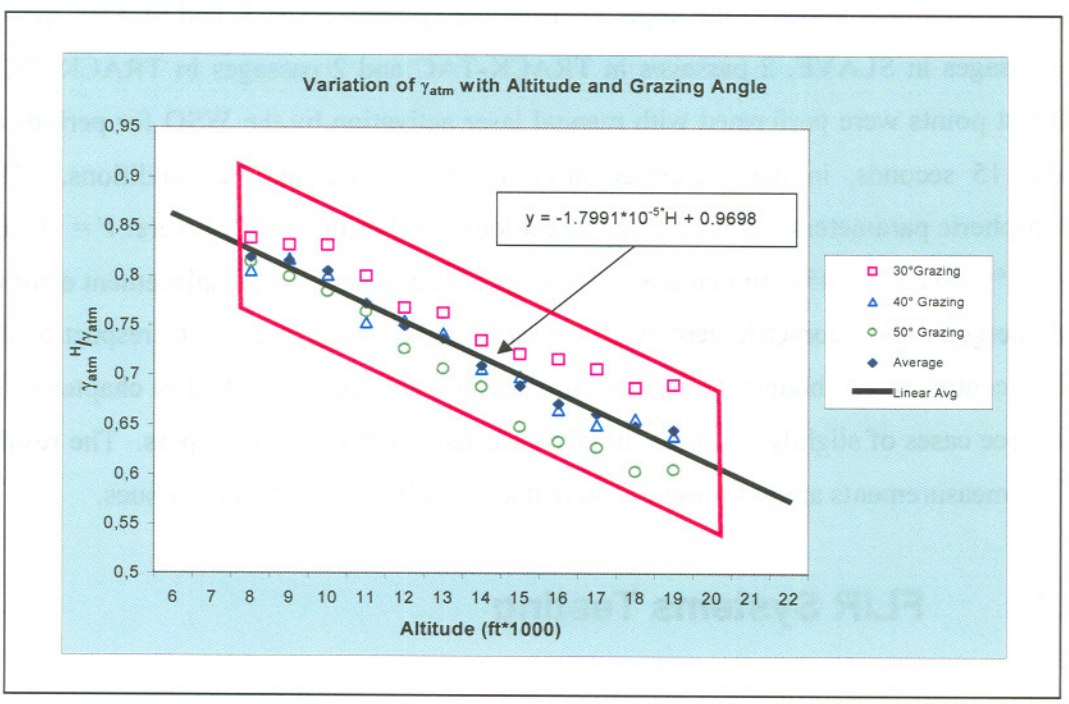

Fig. 9-10. Average $\gamma_{atm}^{H}/\gamma_{atm}$ for slant-paths with grazing angles between 30° and 50° and altitudes between 8000 and 19000 ft.

In order to obtain accurate predictions of the attenuation coefficient variations with altitude, required for performance data analysis and simulation purposes at the PILASTER range, it is essential to perform further trials, in appropriate meteorological and operational scenarios, including well representative weather conditions and wider portions of the TORNADO-IDS/CLDP operational flight envelopes.

9.2.2 CLDP Pointing Accuracy Tests

Using the PILASTER STU instrumentation and the permanent target described in chapter 5, the pointing accuracy of the CLDP system, installed on the TORNADO-IDS aircraft, was determined. The aircraft flight profiles for pointing accuracy tests were defined according to the CLDP/PILASTER technical characteristics and taking into account eye-safety issues. The measurements were performed during one flight sortie performed at altitudes between 10000 and 20000 ft and with various CLDP aspect angles and aircraft to target slant-ranges. A number of six straight-and-level passages were performed with the aircraft flying parallel to the target surface. The CLDP system was aimed at the target by using the systems TRACK and SLAVE modes (2 passages in SLAVE, 2 passages in TRACK-TAC and 2 passages in TRACK-TIC). All test points were performed with manual laser activation by the WSO for periods of about 15 seconds, in the prescribed aircraft altitude and attitude conditions. The atmospheric parameters recorded at the target location during the flight were: $V = 18$ km, $T = 31°C$ and $RH = 45\%$ (no clouds). Pointing accuracy data (i.e., displacement error of the energetic and geometric centres of the laser spots on the target with respect to the target centre) were obtained using the same methods already described in chapter 9 for the three cases of slightly distorted, highly distorted and broken laser spots. The results of the measurements are not presented here due to military classification issues.

9.3 FLIR Systems Testing

Using the PILASTER IREF target described in chapter 5, installed on the permanent FXDT target structure, the Minimum Resolvable Temperature Differences

(MRTD) with spatial frequencies (cycle/mrad) corresponding to various 2-D discrimination levels, where determined for the CLDP-IR and for the enhanced CLDP-IRS FLIR systems. Furthermore, using these experimental data it was possible to calculate the detection, recognition and identification ranges of both FLIR systems, for targets of given aspect dimensions. Although the experimental results obtained are not presented in this thesis (due to the high level of military classification), the technical approach adopted is described here, which is a reference for future FLIR test activities to be performed at the PILASTER range.

9.3.1 In-Flight Test Procedure

First of all, it is important to select appropriate aircraft to target geometries for the system under test. The (angular) spatial frequency (SF) is given by:

$$SF = \frac{R_T}{W_{1c}} \tag{9.10}$$

where:

R_T = sensor-to-target range

W_{1c} = width of one cycle of target

The 'cycle' is defined as the sum of one bar and space on the reference target. In flight test practice, the spatial frequency is adjusted by varying sensor-to-target range (i.e., flying toward the target). The PILASTER test procedure steps are the following:

a. Adjust the effective temperature differential (ΔT) of the bar target to the maximum value planned for the test.

b. Fly a prescribed flight path, at constant altitude and airspeed, on a heading designed to pass directly over the PILASTER target, and normal to the target surface.

c. Determine the sensor-aircraft position (and, hence, sensor-to-target range) with suitable range instrumentation (e.g., cinethodolites) or on-board position reference devices (e.g., DGPS).

d. Acquire the IR target on the FLIR sensor under test.

e. Continue to observe the target on the sensor until the variations in radiant intensity due to the individual bars are just discernible.

f. Measure and record the resolvable temperature differential and the range (spatial frequency) attained in step (e).

g. Repeat steps (a) through (f), substituting , in step (a), increasingly smaller target temperature differentials, until the variations due to individual bars are no longer discernible even at the minimum sensor-to-target ranges planned for the test.

During the in-flight tests, atmospheric conditions must be recorded in order to determine the transmittance (τ_{atm}). ΔT must be multiplied by τ_{atm} to get the normalised ΔT which is used for plotting test results. Additionally, thermovision should be used to record IR target differential temperature as truth data to ensure the IR board is operating properly. The relationship between sensor cut-off spatial frequency (SF_s) and sensor angular resolution (θ_R) is given by:

$$\theta_R = \frac{1}{SF_c} \tag{9.11}$$

When the resolvable temperatures determined by the in-flight test are plotted versus the spatial frequency of the target, the results should be very similar to those determined by ground tests. The only significant difference should be that the in-flight spatial cut-off frequency ($SF_{s\text{-}f}$) of the sensor should be somewhat lower than that attained in ground tests ($SF_{s\text{-}g}$). The only significant difference should be that the in-flight spatial cut-off frequency of the sensor should be somewhat lower than that attained in ground tests. An example of a plot showing both in-flight and ground test results is presented in Fig. 9-11.

For a properly integrated and properly functioning sensor, the degradation of angular resolution in flight is due primarily to sensor line-of-sight (LOS) jitter.

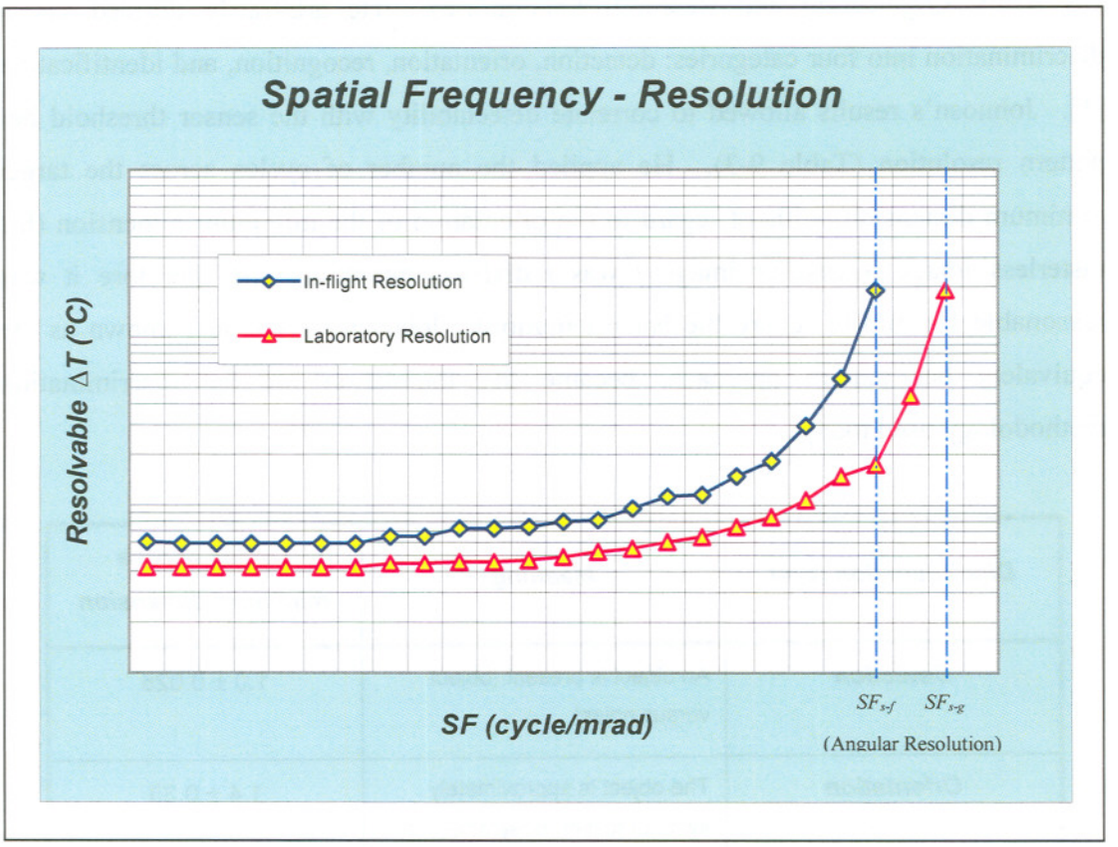

Fig. 9-11. Spatial frequency – in-flight and ground resolution.

9.3.2 Range Performance Predictions

FLIR systems range performance predictions require a mathematical model that describes the eye/brain image interpretation process. Unlike the response of an electronic circuit, the response of a human observer cannot be directly measured but only can be inferred by many visual psychological experiments. The lowest level of discrimination is a distinction between something and nothing. The final level is the precise identification and description of a particular object. Between these two extremes lay a continuum of discrimination levels.

In the late fifties, Johnson studied image intensifiers discrimination performance at the US Army Engineering and Research Laboratories. He arbitrarily divided visual discrimination into four categories: detection, orientation, recognition, and identification [1]. Johnosn's results allowed to correlate detectability with the sensor threshold bar pattern resolution (Table 9-3). He applied the number of cycles across the target minimum dimension, without regard to the orientation of the minimum dimension (his rasterless image intensifier imagery was radially symmetrical and therefore it was reasonable for him to ignore the bar orientation). Johnson's approach, known as the equivalent bar pattern approach, became the foundation for the discrimination methodology used today.

Discrimination level	***Meaning***	***Cycles across minimum dimension***
Detection	An object is present (object versus noise)	1.0 ± 0.025
Orientation	The object is approximately symmetrical or unsymmetrical and its orientation may be discerned (side view versus front view)	1.4 ± 0.35
Recognition	The class to which the object belongs (e.g., tank, truck, man)	4.0 ± 0.80
Identification	The object is discerned with sufficient clarity to specify the type (e.g., T-52 tank, friendly jeep)	6.4 ± 1.50

Table 9-3. Johnson's experimental results.

Successive studies and tests performed at the US Army Night Vision Laboratories and by industry suggested modifications to the values originally found by Johnson. Table 9-4 provides the current industry standard for one-dimensional target discrimination. Orientation is a less popular discrimination level. Because current standards are based upon Johnson's work, they are labelled as the Johnson criterion though they are not the precise values found by him.

Discrimination level	***Meaning***	***Cycles across minimum dimension (N_{50})***
Detection	An object is present	1.0
Recognition	The class to which the object belongs	4.0
Identification	The object is discerned with sufficient clarity to specify the type	8.0

Table 9-4. Current industry criterion for 1-D discrimination (50% probability level).

The Johnson criterion provide an approximate measure of the 50% probability of discrimination. Results of several tests provided the cumulative probability of discrimination or target transfer probability function (TTPF). The TTPF can be used for all discrimination tasks by simply multiplying the 50% probability of performing the task (N_{50} in Table 9-4) by the appropriate TTPF multiplier in Table 9-5 [2]. For instance, the probability of 95% recognition is $2N_{50}$ = 2(4) = 8 cycles across the target minimum dimension. Similarly, the cycles required for detection, recognition ed identification with a probability level of 80% are 1.5, 6 and 12 respectively.

Probability of discrimination	*Multipler F_m*
1.00	3.0
0.95	2.0
0.80	1.5
0.50	1.0
0.30	0.75
0.10	0.50
0.02	0.25
0	0

Table 9-5. Discrimination cumulative probability [2].

An empirical fit to the data provides [3]:

$$P(N) = \frac{\left(\frac{N}{N_{50}}\right)^E}{1+\left(\frac{N}{N_{50}}\right)^E} \tag{9.12}$$

where:

$$E = 2.7 + 0.7 \cdot \left(\frac{N}{N_{50}}\right) \tag{9.13}$$

Visual psychophysical experiments suggest that the eye response follow a log-normal distribution. The probability density function appears to follow [4]:

$$p(N) = \frac{1}{\sqrt{2\pi}\cdot log(\sigma)} \cdot e^{-\frac{1}{2}\left[\frac{log(N)-log(N_{50})}{log(\sigma)}\right]^2} \tag{9.14}$$

and the cumulative probability is:

$$P(N) = \int_{0}^{\log N} p(N)\, d\log(N) \tag{9.15}$$

where $\log(\sigma) = 0.198$. Both the empirical fit of eq. (9.12) and the log-normal approach (based upon a physically plausible foundation) of eq. (9.15) provide similar numerical results.

As clutter increases, the ability to discern a target decreases. To account for this reduced capability, N_{50} must increase. Most studies have broadly categorised clutter into high, moderate and low regions [5], and defined the signal-to-clutter ratio (SCR) as:

$$SCR = \frac{max \quad target \quad value \quad - \quad background \quad mean}{\sigma_{clutter}} \tag{9.16}$$

where:

$$\sigma_{clutter} = \sqrt{\frac{1}{N}\sum_{i=1}^{N}\sigma_i^2} \tag{9.17}$$

and σ_i is the rms value of the pixel values in a square cell that has side dimensions of approximately twice the target minimum dimension. The scene is composed of N adjoining cells. The use of adjoining cells introduces a spatial weighting factor that is similar to the spatial integration performed by the eye/brain process. Clutter sizes that are equal to the object size weigh more heavily in this calculation.

The results are presented in Table 9-6 [5]. Field experiments [6] demonstrated that the Johnson detection criterion applies to a "general medium to low clutter" environment. Therefore, the 50% probability of detection in Table 9-6 where normalised in moderate clutter to one cycle. These experimental findings roughly follow the empirical TTPF of eq. (9.12). It is convenient to use 0.5, 1.0 and 2.5 as a multiplier (F_d) to N_{50} for low, moderate, and high clutter environments respectively.

Probability of detection	Multiplier F_d		
	Low Clutter SCR>10	Moder. Clutter 1<SCR<10	High Clutter SCR<1
1.0	1.7	2.8	**
0.95	1.0	1.9	**
0.90	0.90	1.7	7.0*
0.80	0.75	1.3	5.0
0.50	0.50	1.0	2.5
0.30	0.30	0.75	2.0
0.10	0.15	0.35	1.4
0.02	0.05	0.1	1.0
0	0.0	0.0	0.0

** *No data available*
* *estimated*

Table 9-6. TTPF when clutter is present [5].

In order to obtain the two-dimensional discrimination levels required in a 2-D performance prediction model, each value in the one-dimensional criteria (Table 9-7) is multiplied by 0.75 [7]. The results are presented in Table 9-7.

Discrimination level	Meaning	Cycles across minimum dimension ($N_{50\text{-}2D}$)
Detection	An object is present	0.75
Recognition	The class to which the object belongs	3.00
Identification	The object is discerned with sufficient clarity to specify the type	6.00

Table 9-7. Discrimination levels for the 2-D model (50% probability level).

The Night Vision Laboratory Static Performance Model [Ratches J.A., et al.] uses the minimum dimension (1-D), whereas 2-D models (e.g., FLIR92 model) refer to the critical dimension of the object [7]:

$$h_c = \sqrt{W_{TGT} \times H_{TGT}} \tag{9.18}$$

where W_{TGT} and H_{TGT} are the horizontal and vertical object dimensions. In this case, the number of cycles used for range performance calculations is that associated to the object critical dimension h_c. Therefore, our 2-D FLIR range performance prediction model can be summarised by the following equations:

$$R = \frac{h_c}{(N_{50-2D} \times F_d)} \times SF \quad \text{for } \textit{detection} \tag{9.19}$$

$$R = \frac{h_c}{(N_{50-2D} \times F_m)} \times SF \quad \text{for } \textit{recognition} \text{ ed } \textit{identification} \tag{9.20}$$

where:

R = predicted slant range;
h_c = target critical dimension;
SF = measured spatial frequency;
$N_{50\text{-}2D}$ = cycles required for detection, recognition and identification (Table 9.7)
F_m, F_d = multipliers for the various discrimination levels (Table 9.5 and 9.6).

9.4 DGPS Flight Test Campaign

As described in the previous chapter, a preliminary ground trial was performed with two ASHTECH receivers in order to test the accuracy of the DGPS data and to gain a good level of confidence with differential techniques, before performing actual flight trials. The DGPS flight test activity was divided in two separate steps:

- an initial campaign, already completed on the MB339-C aircraft, aiming at assessing and comparing the performance of two DGPS receivers (TRIMBLE

TANS III and ASHTECH-12) in a dynamic environment in order to select the system with the best performance;

- a final in-flight evaluation of the selected system (ASHTECH or TRIMBLE), now ongoing on the TORNADO-IDS aircraft, required for determining the system accuracy during high-dynamics manoeuvres and to identify the critical conditions in which the DGPS is likely to lose the signal or provide inaccurate data.

9.4.1 MB-339CD DGPS Flight Trials

The general layout of the MB339-CD installation is shown in Fig. 9-12. A detail of the on-board Flight Test Instrumentation (FTI) and ASHTECH receiver installation is shown in Fig. 9-13.

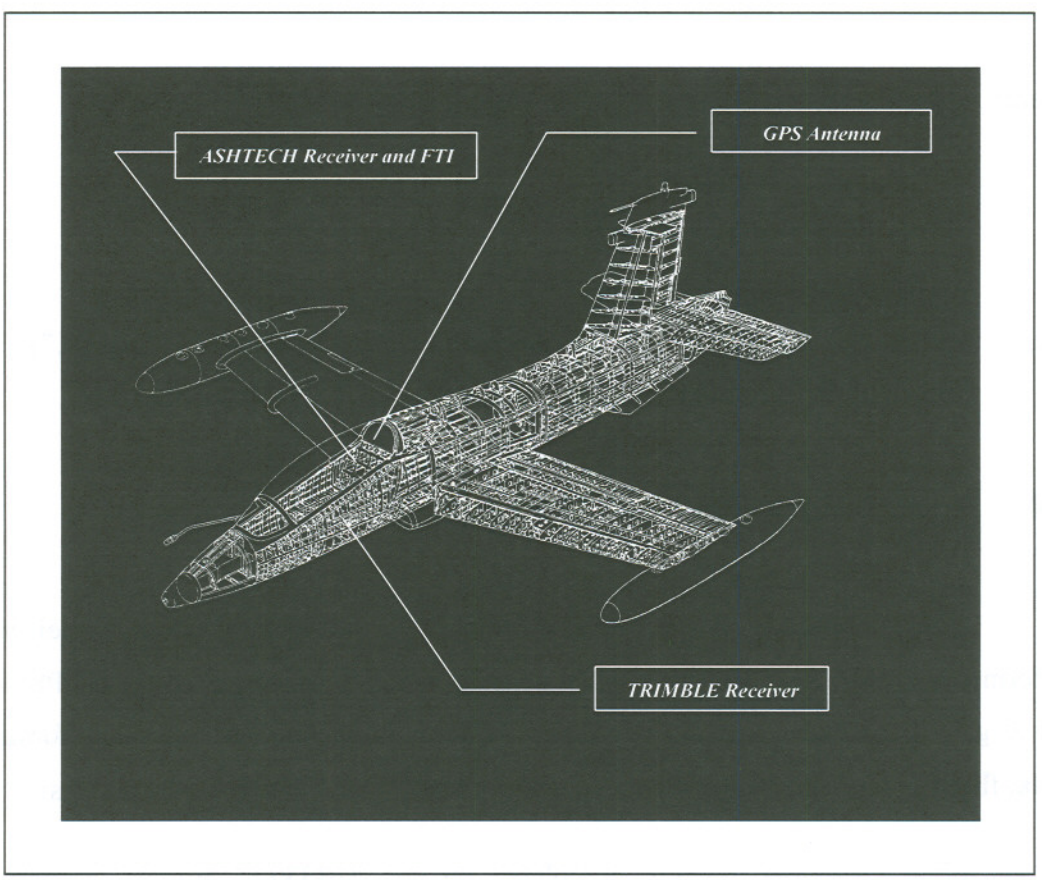

Figure 9-12. Installation on the MB339-CD aircraft.

Figure 9-13. Detail of the on-board FTI (MB 339-CD).

The TANS installation is shown in Fig. 9-14, together with a detail of the magnetic flight data recorder used for the trials.

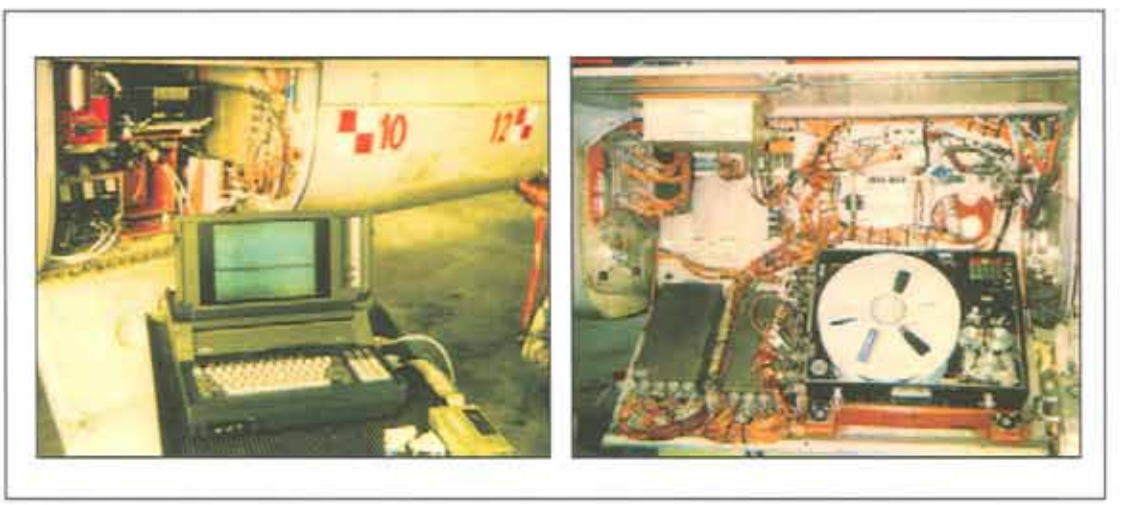

Figure 9-14. TANS installation and magnetic recorder.

During the MB339-CD test campaign, specific dynamic manoeuvres were included in the aircraft flight profiles in order to allow a comparative evaluation of the TRIMBLE and ASHTECH receivers. Particularly, the following manoeuvres, representative of the real conditions which can be encountered during operational flights, were performed:

- turns with constant bank angle (to evaluate the antenna masking effect);
- dives followed by a pull up to 4 g's long the 4 cardinal directions (typical weapon aiming manoeuvres);
- high dynamic manoeuvres as "tonneau" (rolls/barrel rolls) and stick-jerks.

It must be underlined that a determination of the accuracy provided by the systems was not considered essential in this phase. However, some over-flights of defined ground sites were performed in order to obtain a rough estimation of the systems accuracy.
As expected, during straight-and-level flight both receivers under test performed satisfactorily, with no significant data losses recorded. However, during execution of dynamic manoeuvres both systems frequently lost lock to the satellites. Analysing the data collected in flight, it was understood that this phenomenon was primarily due to shielding of the GPS antenna by the aircraft body (wings, fuselage and tails). Data analysis also confirmed that during dynamic manoeuvres both systems experienced a very significant increase of the PDOP factor. In Fig. 9-15 some curves are shown relative to the variation of the flight parameters (heading, altitude, pitch, bank, etc.) in a period of a few minutes, as given by the aircraft INS during one of the flight trials.
Identification of the parameters shown in Fig. 9-15, together with the related scales, is given below.

- B = Magnetic Heading (-180°÷180°)
- C = Roll Angle (-90÷90°)
- D = Pitch Angle (-40÷40°)
- E = Barometric Altitude (0÷40000 ft)
- F = NORTH Velocity (-800÷800 ft/s)
- G = EST Velocity (-800÷800 ft/s)
- H = Vertical Velocity (-800÷800 ft/s)
- I = Along X Acceleration (-80÷80 ft/s^2)
- J = Along Y Acceleration (-80÷80 ft/s^2)
- K = Along Z Acceleration (-80÷80 ft/s^2)
- L = Normal Acceleration (-2÷6 g)
- M = Angular Velocity X (-40÷40 °/s)
- N = Angular Velocity Y (-40÷40 °/s)
- O = Angular Velocity Z (-100÷100 °/s)

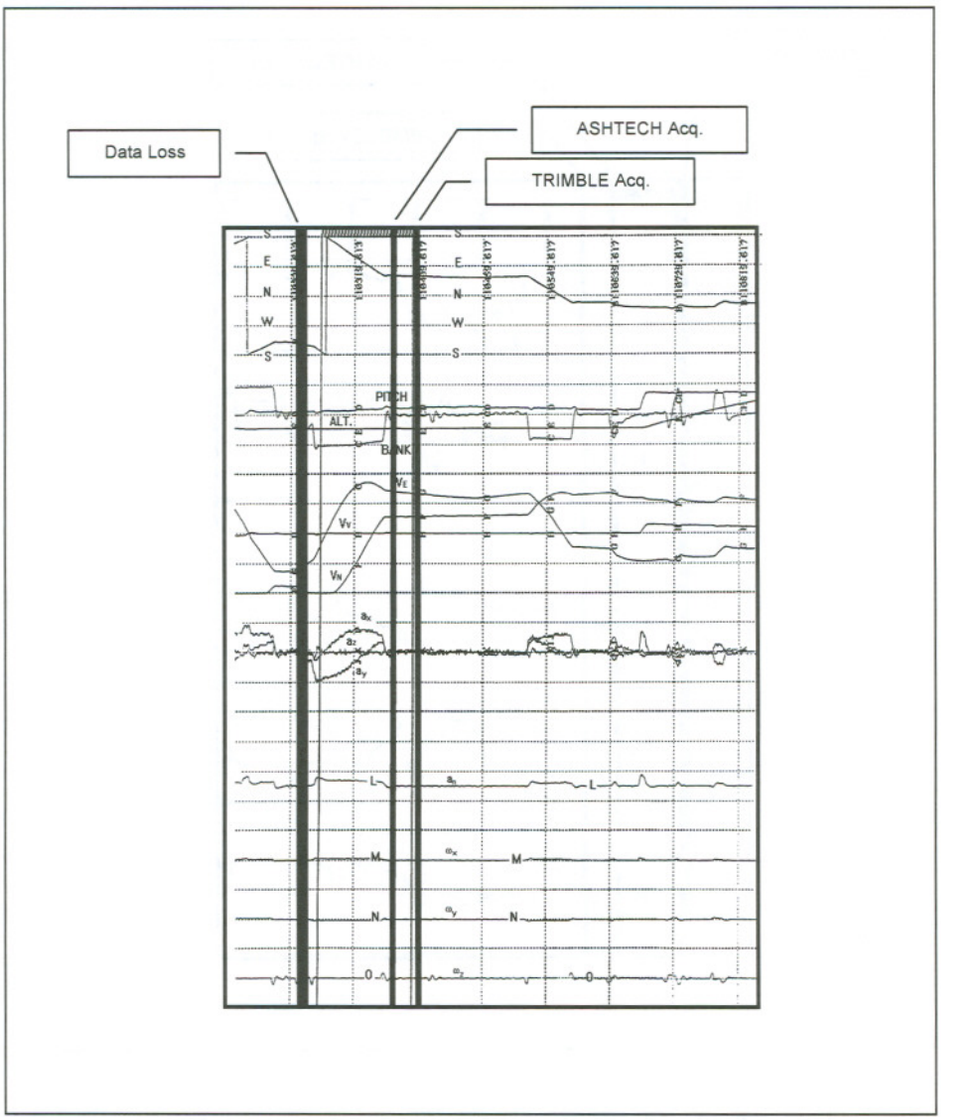

Figure 9-15. ASHTECH and TRIMBLE data loss periods (-45° turn).

Particularly, the manoeuvre shown in Fig. 9-15 is a left turn (-45° bank angle) corresponding to a GPS signal loss (for both the ASHTECH and the TRIMBLE receivers). The Signal-to-Noise Ratios (SNR) measured for each satellite are shown in Figure 9-16.

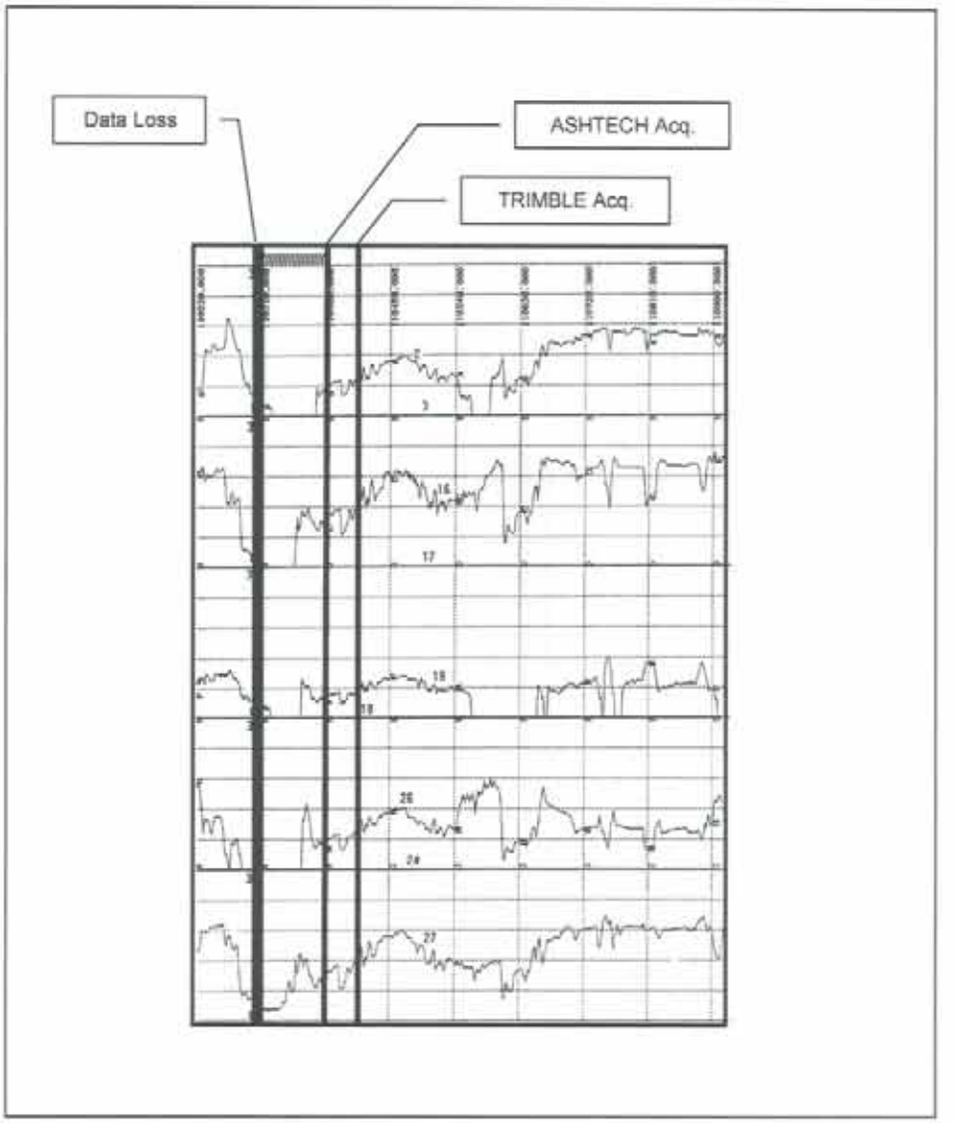

Figure 9-16. ASHTECH and TRIMBLE data losses (SNR's).

It is evident that the signal intensity did not decrease gradually. This confirms that the signal loss, in this case, was due to interposition of an obstacle between the satellites and the antenna and not to receiver tracking problems.

Fig. 9-17 gives an idea of the relative positions of the aircraft and the satellites during the manoeuvre. It can be noticed that in consequence of the left turn many satellites were masked by the aircraft body. Signal reacquisition took place when the aircraft progressively reduced the bank angle and the heading variation rate.

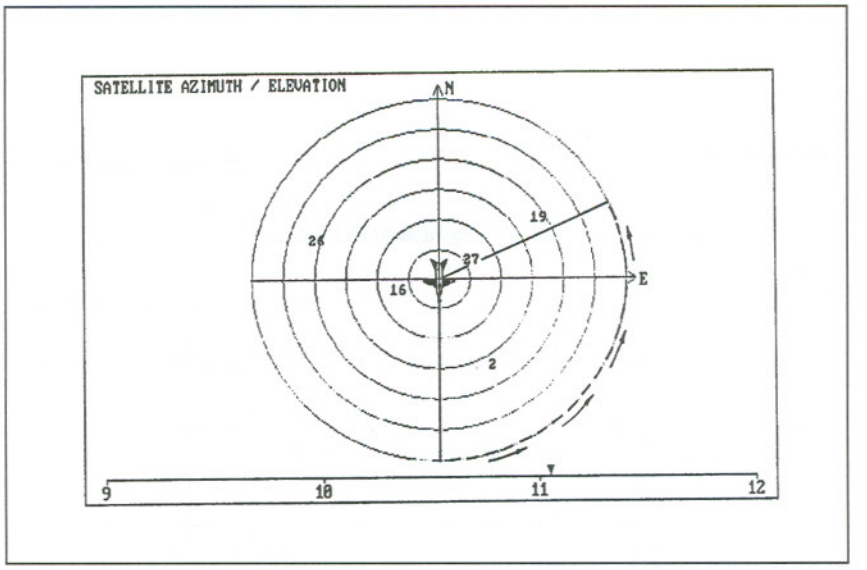

Figure 9-17. Aircraft-satellites relative positions.

Although both receivers simultaneously lost the GPS data, a difference was noticed between the two receivers in terms of reacquisition time. As the position of the aircraft longitudinal axis during the turn got closer to satellite 2 (in the horizontal plane) the TRIMBLE receiver experienced a loss of track to all satellites, while satellites 19 and 27 were still tracked by the ASHTECH receiver. This was due to the internal processing of the receiver.

Prior flight both receivers were programmed with the same PDOP threshold, but the ASHTECH receiver was able to maintain track to the satellites in view even when their SNR's were very low, while TANS lost track to all satellites. This significantly reduced the time required by the ASHTECH receiver for a new positioning fix as soon as four satellites were available again. Other trials also confirmed that the increase of PDOP and the reduction of SNR's during dynamic manoeuvres were responsible for satellite signal losses in the TRIMBLE receiver (even with small variation of the aircraft-receiver relative geometry and in absence of satellite masking), and that the ASHTECH receiver needed shorter periods to compute a new positioning solution after losses of satellite signals caused by masking.

Fig. 9-18 shows that a change of satellite configuration due to manoeuvres may determine an accuracy degradation. Particularly, the loss of one satellite (from five to four satellites tracked), determined a considerable increase of the PDOP in this case.

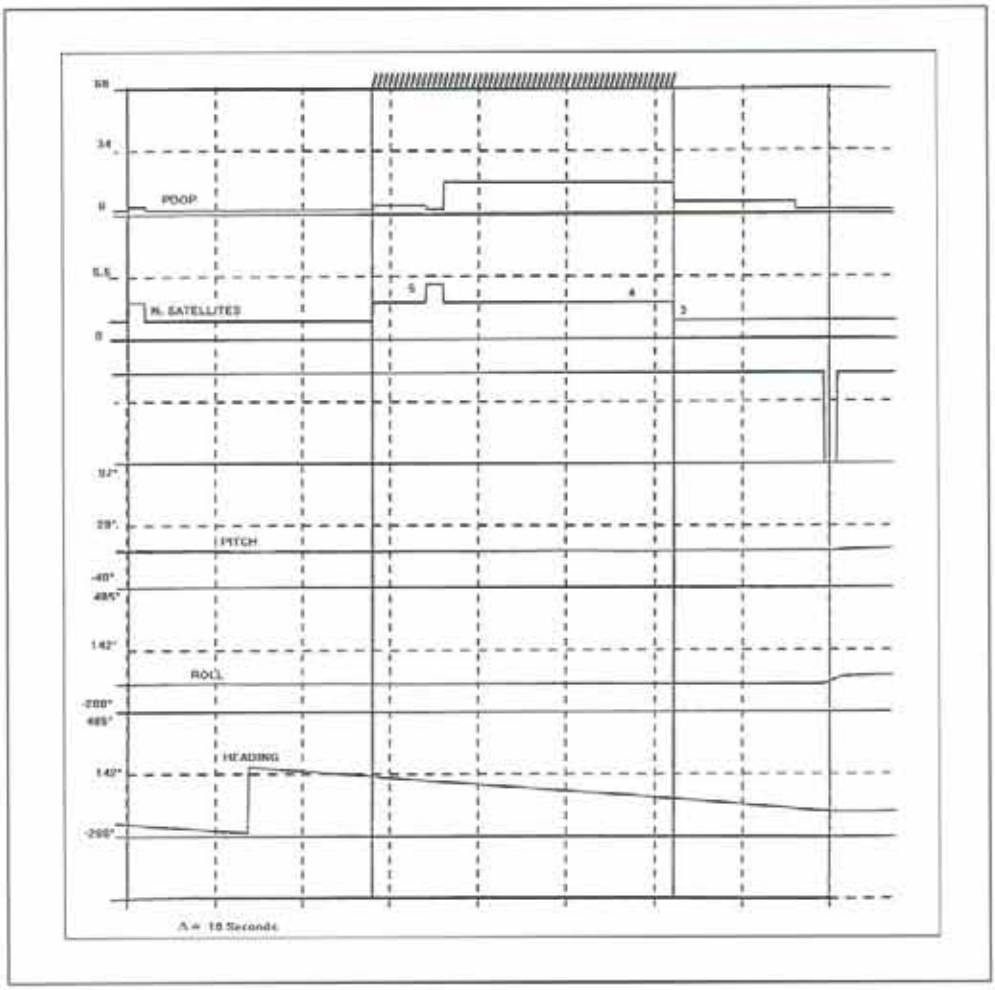

Figure 9-18. PDOP variation with loss of 1 satellite.

Data collected during a stick-jerk manoeuvre are shown in Fig. 9-19. During this manoeuvre the stick is repetitively pulled and pushed in order to obtain high jerks. This can be a very critical manoeuvre for the GPS receivers (especially for the code correlation circuits). The jerk limits were not specified for the ASHTECH receiver, while for TANS a jerk limit of 2 g/s (20 m/s^3) was quoted. During the manoeuvre a jerk of about 2.8 g/s was obtained but no data loss occurred in any of the two receivers.

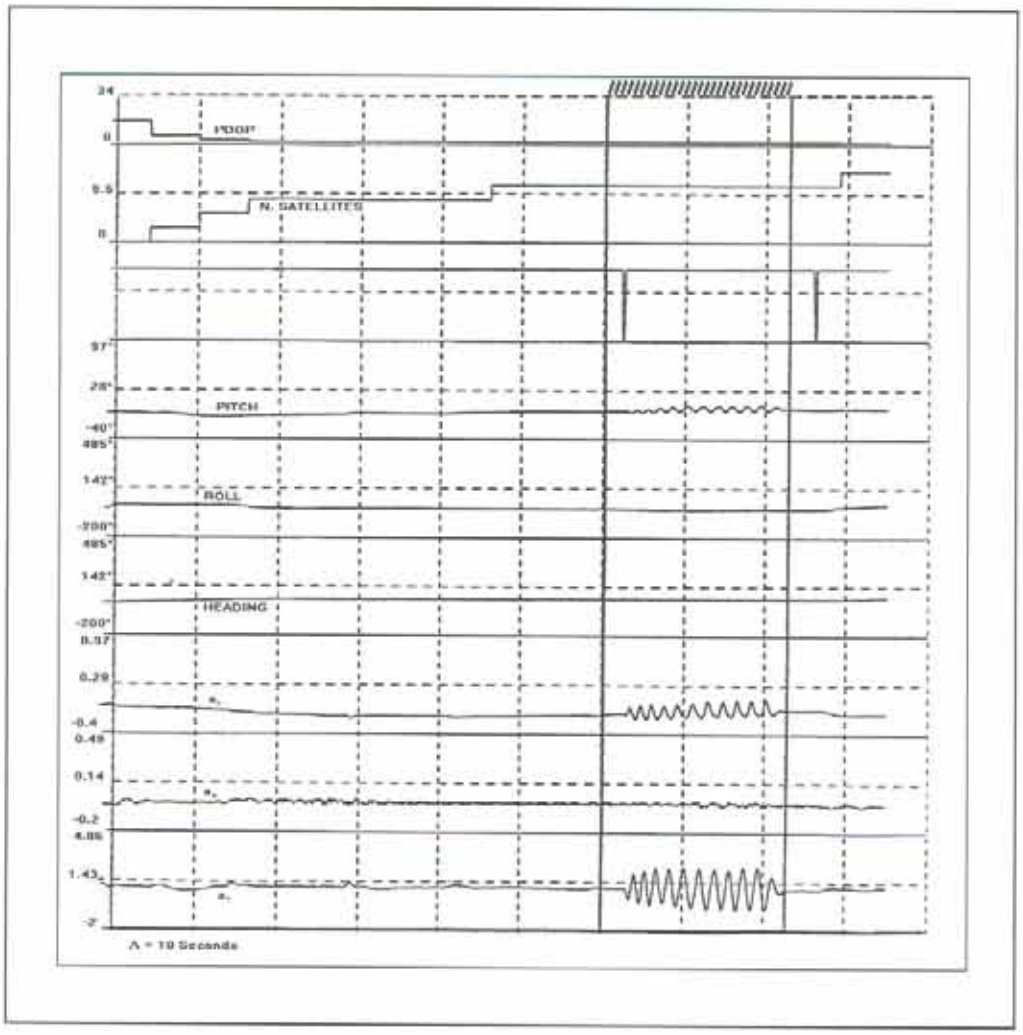

Figure 9-19. Stick-jerk manoeuvre.

The data in Fig. 9-20 were recorded during three pull up manoeuvres at 4 g's (typical in weapon delivery). While during execution of the manoeuvres lock on to the satellites was kept (between four and three satellites tracked), at the end of each manoeuvre total signal losses occurred. The three manoeuvres were always preceded by straight-and-level flight (about 30 seconds) to allow optimal satellite tracking.

The performance of the receivers during pull-up manoeuvres (typical of LGB delivery) were better than the performance during turns (typical of the escape phase of an attack).

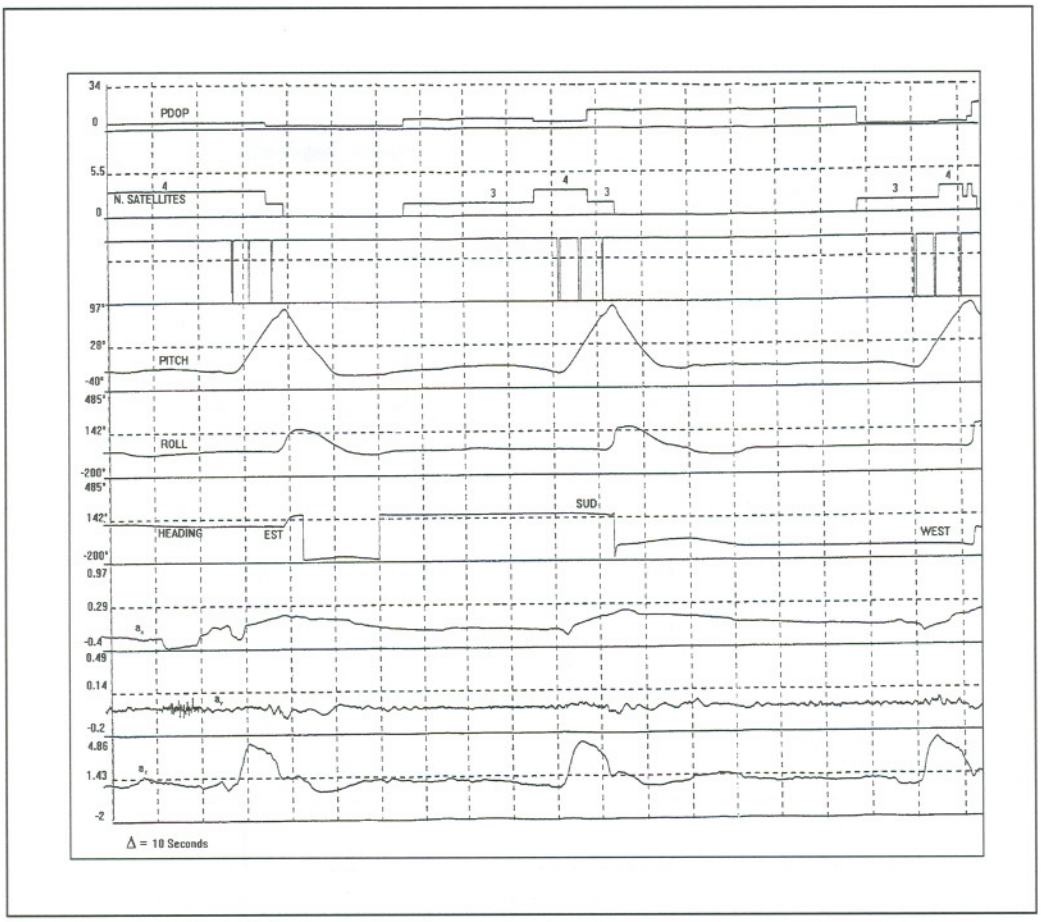

Figure 9-20. Pull-up manoeuvres (4 g's).

Analysing the data of the MB339-C test campaign, it was concluded that the ASHTECH receiver was better suited than the TRIMBLE receiver for flight testing and training with airborne laser systems (i.e., higher accuracy and data continuity). Particularly, the ASHTECH tracking and reacquisition strategy significantly reduced the time required for a new fix after data losses. The ASHTECH data continuity during dynamic manoeuvres was significantly better than that of TRIMBLE. On average, the GPS data loss occurred in 25% of the total flight time for the ASHTECH receiver and in 35% of the time for the TRIMBLE receiver. These results were obtained with an identical setting of the threshold parameters for position computation. Although the TANS receiver was able to provide a positioning solution even with only three satellites tracked (using a barometric input), in this case the accuracy degradation of the horizontal co-ordinates (especially the latitude) was very significant and not acceptable for laser systems flight test applications.

9.4.2 TORNADO-IDS DGPS flight trials

The layout of the TORNADO GPS installation (ASHTECH XII) is shown in Fig. 9-21. The antenna was located on the aircraft skin at about 1.5 m from the cockpit and a few decimetres from the telemetry antenna. The Electro-Magnetic Compatibility (EMC) of the GPS equipment with the other on-board systems has been verified before initiating the flight activity.

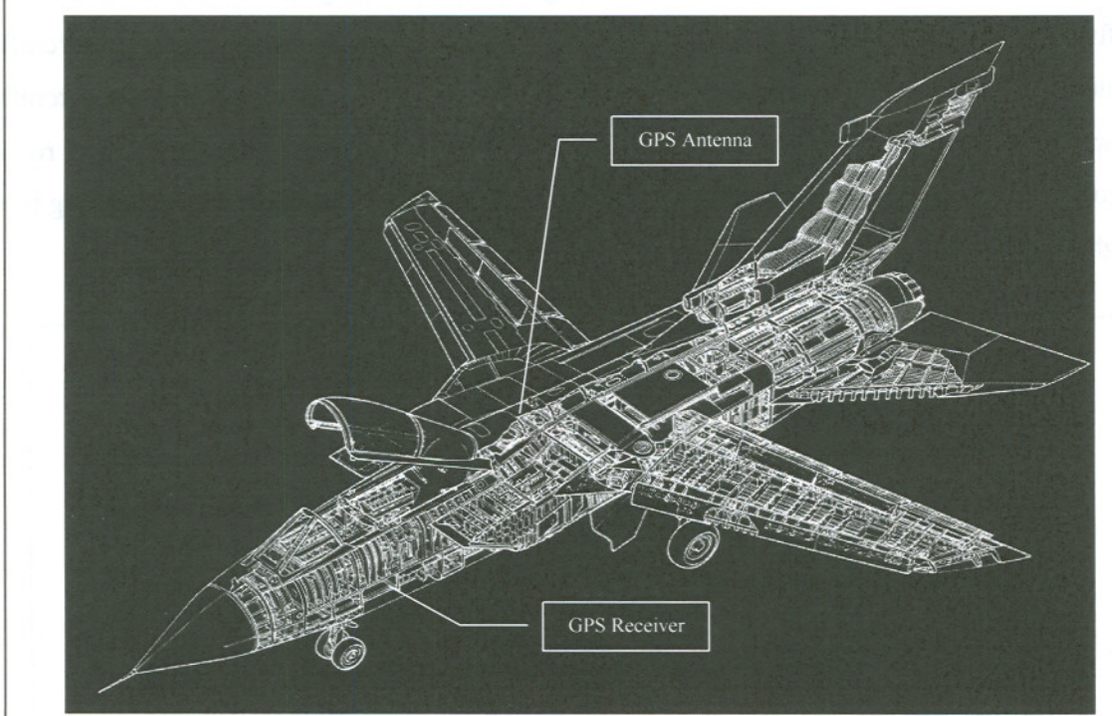

Figure 9-21. TORNADO-IDS installation.

Analysing several data from the preliminary test campaign, it was clear that the main disadvantage of the GPS is its vulnerability to signal losses caused by satellites masking. Therefore, the primary objectives of the final test campaign are to thoroughly investigate the causes of the masking problem, to test the capability of the GPS receiver to reacquire satellite signals and to provide TSPI even with degraded satellite constellations. Furthermore, a data accuracy assessment was carried out by comparing DGPS with other

known references (i.e., radar/baro altimeters, CLDP laser rangefinder and optical tracking systems), and the DGPS accuracy degradation with increasing aircraft-to-reference station slant-range (due to spatial de-correlation of the differential corrections) was determined. Finally, some optimisation criteria were defined for using DGPS in flight test and training activities at the PILASTER range.

9.4.2.1 Masking Investigation

In order to assist in the investigation of masking, a dedicated simulation software was used to calculate the global masking effect due to antenna and aircraft structural masking. The masking analysis software, called VIEWSAT, models the aircraft shape and accepts input data such as the aircraft attitude angles (yaw, pitch and roll) recorded during flight, and position (azimuth/elevation) of GPS satellites tracked during the flight (Fig. 9-22).

SV Number	20	21	22	23	24	25	26	27	28	29
Local Time	EL:AZ	EL:AZ	EL:AZ	EL:AZ	EL:AZ	EL:AZ	EL:AZ	EL:AZ	EL:AZ	EL:AZ
00:00:00	----	----------	----------	----------	-----	42:256	----	----------	-----	67:198	----	----------	-----
00:05:00	----	----------	----------	----------	-----	41:253	----	----------	-----	70:199	----	----------	-----
00:10:00	----	----------	----------	----------	-----	39:250	----	----------	-----	72:199	----	----------	-----
00:15:00	----	----------	----------	----------	-----	38:248	----	----------	-----	75:199	----	----------	-----
00:20:00	----	----------	----------	----------	-----	37:245	----	----------	-----	77:200	----	----------	-----
00:25:00	----	----------	----------	----------	-----	35:243	----	----------	-----	80:199	----	----------	-----
00:30:00	----	----------	----------	----------	-----	34:240	----	----------	-----	82:198	----	----------	-----
00:35:00	----	----------	----------	----------	-----	32:238	----	----------	-----	85:196	----	----------	-----
00:40:00	----	----------	----------	----------	-----	31:236	----	----------	-----	87:185	----	----------	-----
00:45:00	----	----------	----------	----------	-----	29:234	----	----------	-----	89: 83	----	----------	-----
00:50:00	----	----------	----------	----------	-----	27:232	----	----------	-----	86: 42	----	----------	-----
00:55:00	----	----------	----------	----------	-----	25:230	----	----------	-----	84: 37	----	----------	-----
01:00:00	----	----------	----------	----------	-----	24:229	----	----------	-----	82: 36	----	----------	-----
01:05:00	----	----------	----------	----------	-----	22:227	----	----------	-----	79: 35	----	----------	-----
01:10:00	----	----------	----------	----------	-----	20:225	----	-----	11:286	77: 35	----	----------	-----
01:15:00	----	----------	----------	----------	-----	18:224	----	-----	13:287	74: 36	----	----------	-----
01:20:00	----	----------	----------	----------	-----	17:222	----	-----	14:289	72: 36	----	----------	-----
01:25:00	----	----------	----------	----------	-----	15:221	----	-----	16:290	70: 37	----	----------	-----
01:30:00	----	----------	----------	----------	-----	13:220	----	-----	17:292	67: 38	----	----------	-----
01:35:00	----	----------	----------	----------	-----	11:218	----	-----	19:293	65: 39	----	----------	-----
01:40:00	----	----------	----------	----------	-----	10:217	----	-----	21:295	63: 40	----	----------	-----
01:45:00	----	----------	----------	----------	----------	----------	-----	22:296	60: 41	----	----------	-----
01:50:00	----	----------	----------	----------	----------	----------	-----	24:297	58: 42	----	----------	-----
01:55:00	----	----------	----------	----------	----------	----------	-----	26:299	56: 43	----	----------	-----
02:00:00	----	----------	----------	----------	----------	----------	-----	27:300	54: 44	----	----------	-----
02:05:00	----	----------	----------	----------	----------	----------	-----	29:301	52: 45	----	----------	-----

Figure 9-22. Satellite visibility from receiver almanac data.

The VIEWSAT software provided a visibility matrix (one dorsal antenna) for the defined flight conditions (Fig. 9-23).

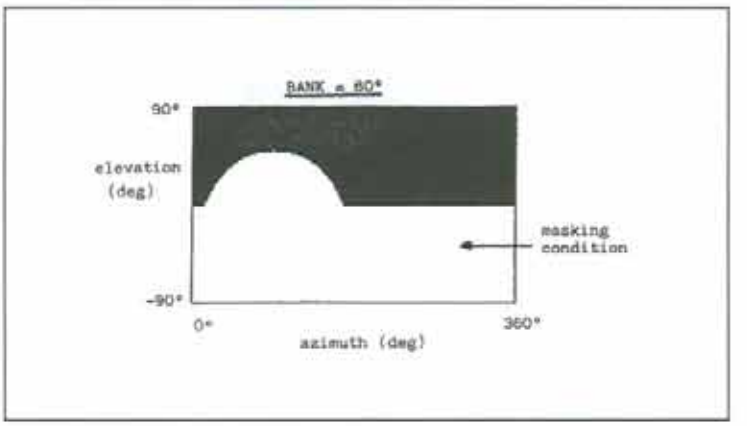

Figure 9-23. Example of VIEWSAT antenna masking matrix.

The software required definition of a simplified aircraft model of the aircraft, as shown in Fig. 9-24.

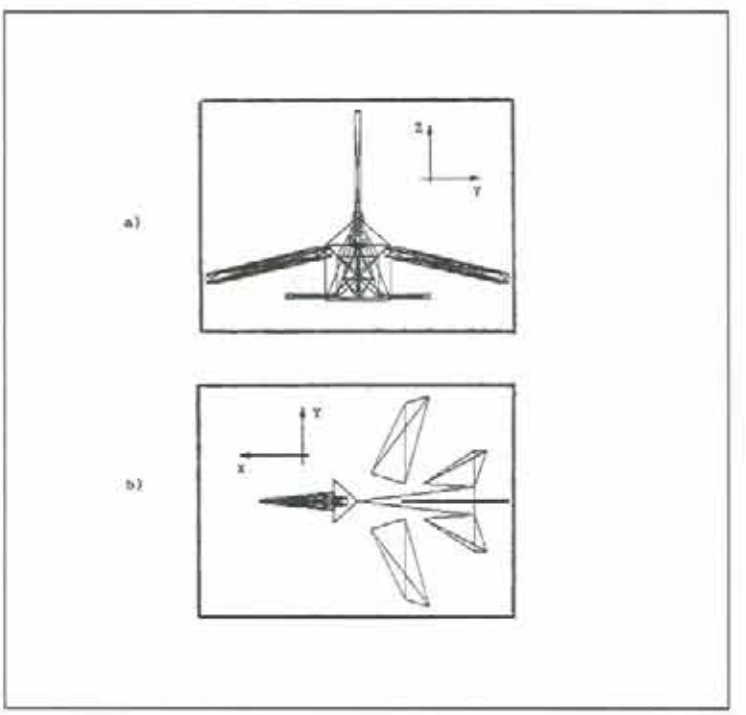

Figure 9-24. Simplified model of TORNADO.

The result was a global masking matrix, as shown in Figure 9-25.

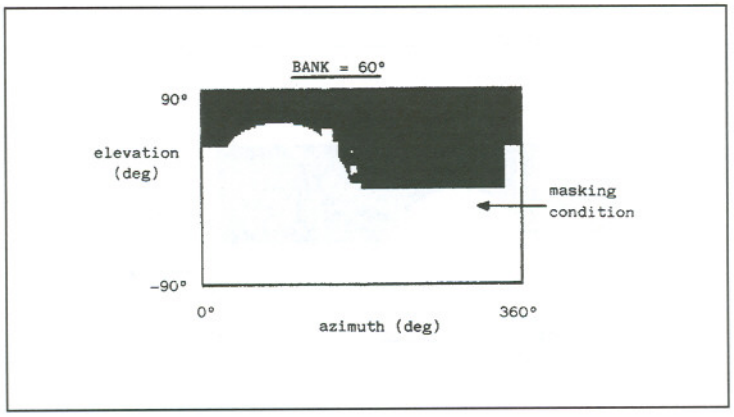

Figure 9-25. Example of VIEWSAT global masking matrix.

The program output is a binary diagram in which for every satellite masked a "0" is shown, while unmasked satellites corresponded to the status "1". An example of VIEWSAT output, together with the related flight conditions, is shown in Fig. 9-26.

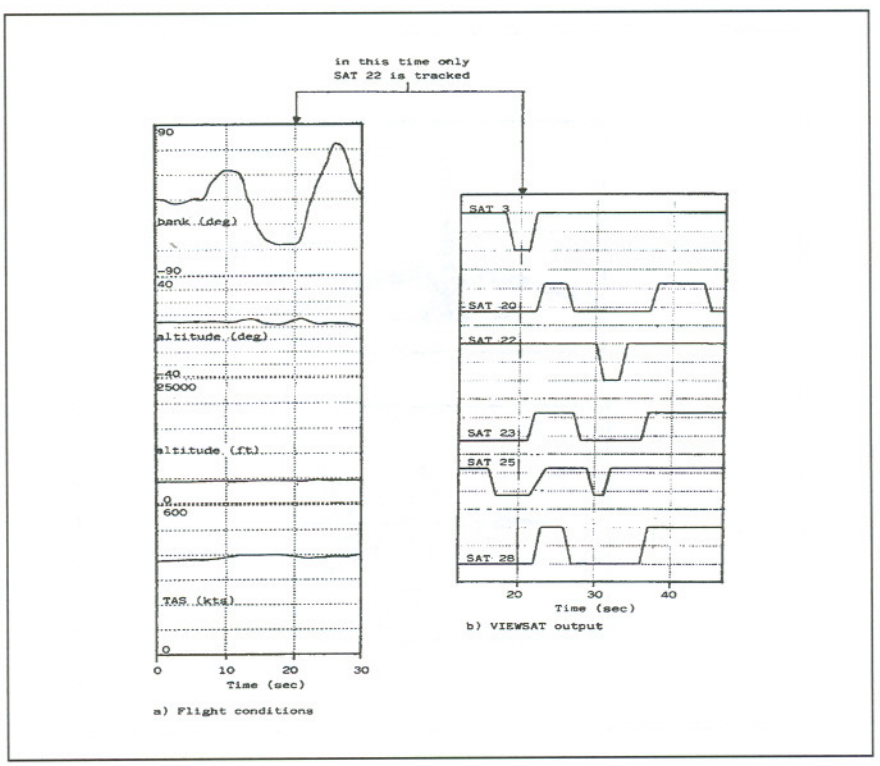

Figure 9-26. VIEWSAT output and related flight conditions.

During the flight test activity carried out, for every flight segment with loss of GPS data, satellite masking was investigated using the VIEWSAT. This was done in order to

determine the critical aircraft manoeuvres, using the time histories of the flight parameters recorded in flight (i.e., heading, bank and pitch angles, TAS, baro-height and Radalt-height).

During a flight carried out with a number of visible satellites between 6 and 7 (typical at our latitudes), aircraft attitude data analysis allowed the identification of critical manoeuvres and flight conditions. During the trial, the maximum variation of the satellite position was in the order of 30° in azimuth and 20° in elevation. Satellites out of visibility were generally characterized by a low elevation above the horizon (10° to 20°). During manoeuvres, the satellites which were more likely to be lost were the satellites with an elevation lower than 30°. The most critical manoeuvres/flight conditions were characterised by a simultaneous non-gradual variation of two asset parameters (pitch, roll or yaw). A rapid variation of height (if not associated to considerable variations in pitch/roll) was not sufficient alone to determine satellite losses (Fig. 9-27).

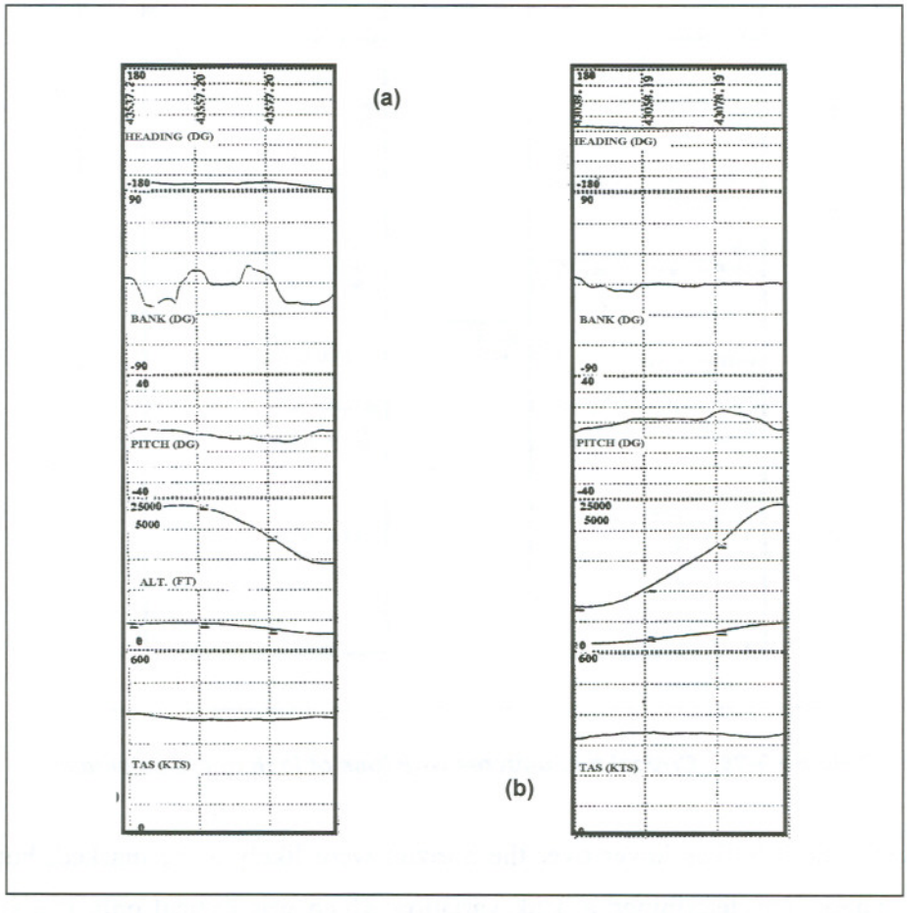

Figure 9-27. Height variations w/o satellite losses during horizontal manoeuvres (a) and in vertical flight (b).

A manoeuvre that was very critical was the turn in the following conditions:

- bank ≥ 50°;
- heading variation greater than 90°.

Two situations in which these elements can be identified are shown in Fig. 9-28.

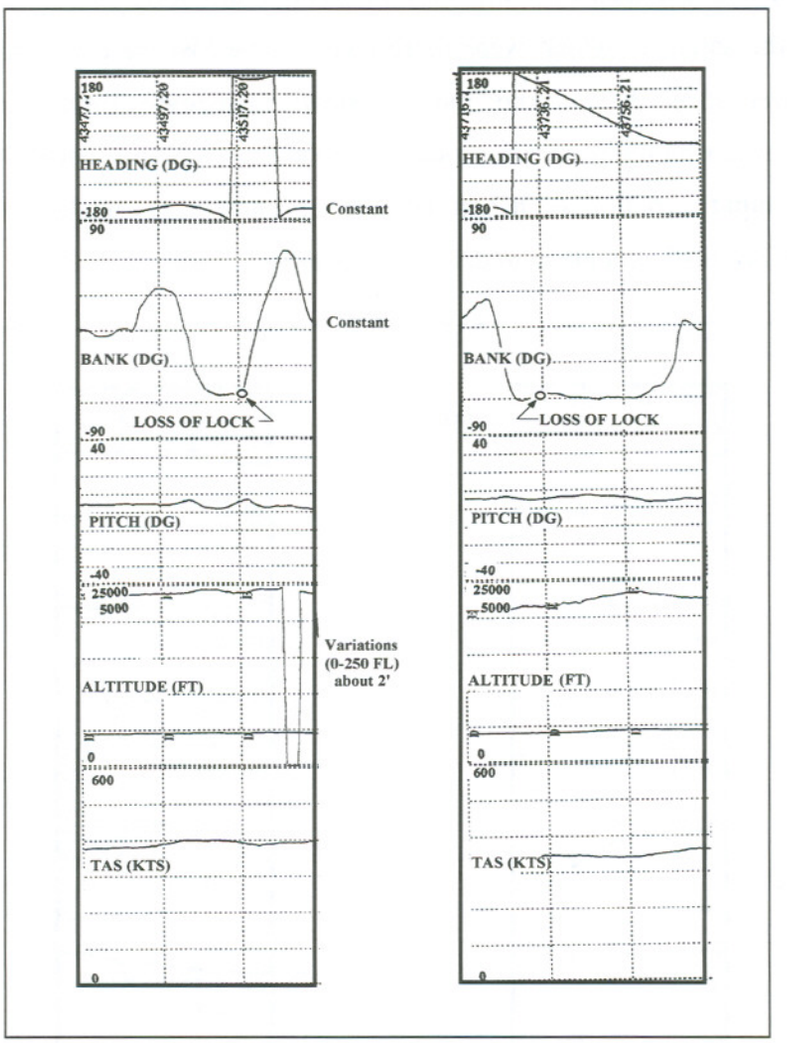

Figure 9-28. Critical manoeuvres with loss of lock to the satellites.

During turns, the satellites lower over the horizon were likely to be masked, but in most cases the manoeuvre determined a bank variation which was critical only if a significant heading change was performed along the line between two adjacent satellites (Fig. 9-29).

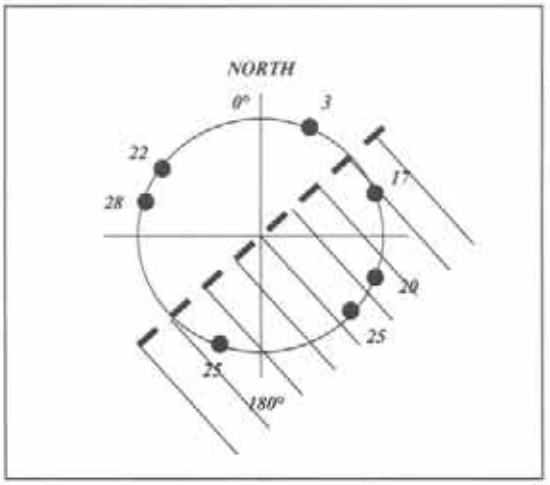

Figure 9-29. Satellite masking (SVs 17, 20, 23 and 25).

In many situations, however, similar manoeuvres did not determine the loss of lock. The difference between the two cases was represented by the fact that in the no-loss case the heading variation was gradual and followed a period of stabilized flight (without significant heading, bank and height variations) of about 40 seconds.

In Fig. 9-30(a) a manoeuvre is shown in which both the bank and the heading angles reached critical values but loss of GPS data did not occur. Similarly, Fig. 9-30(b) refers to the approach phase of a flight, in which a number of turns with high bank angles, progressively performed at lower heights, did not determine signal losses.

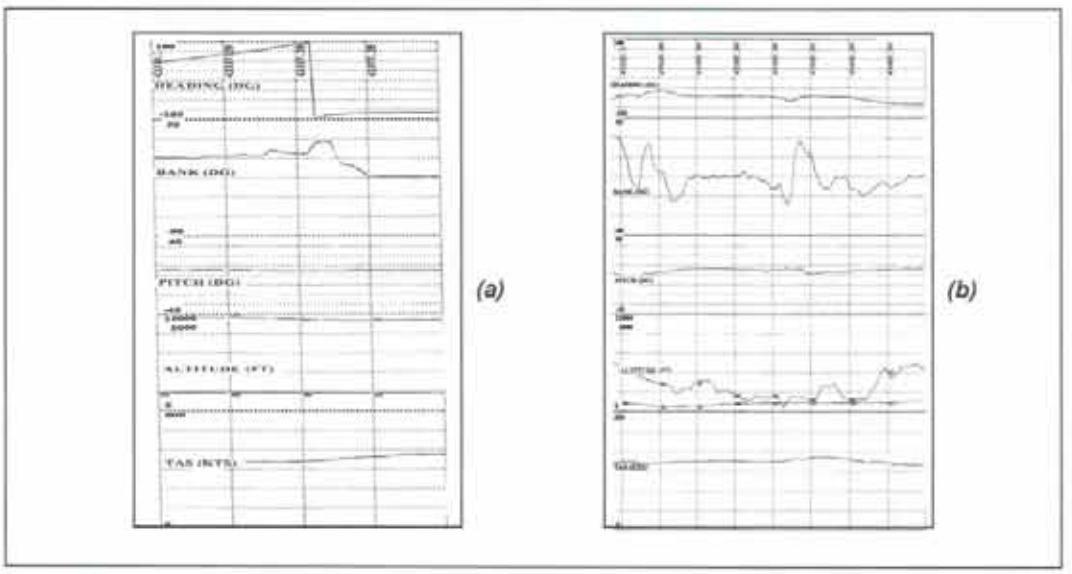

Fig. 9-30. Critical manoeuvres without loss of GPS data.

On average, the ASHTECH receiver was able to give a new positioning solution within 20 second from reacquisition of the satellite signal. Therefore, it was generally sufficient to maintain a low bank angle for about 20 seconds in order to obtain a new solution. However, if the height was kept constant the time required was reduced to about 10 seconds. Another significant aspect taken into account was the influence of the SNR on satellite reacquisition. Particularly, it was demonstrated by data analysis that the ASHTECH receiver provided a positioning solution only if the SNR of at list 4 satellites was above a certain threshold (approximately between 15 and 20 dB) which was not selectable by the user at the ground programming stage.

9.4.2.2 Doppler Effects

During the DGPS evaluation it was noted that the reacquisition time after loss of one or more satellites signals could be up to 40 seconds, depending on flight conditions and actual constellation. We wondered whether and how the Doppler effect could affect the receiver capability to track the carrier phase and rapidly reacquire the signal after a loss. The typical equation used to express the Doppler shift associated to a certain instantaneous velocity along the line of propagation of the signal, is the following:

$$\Delta f \cong \frac{v}{c} \cdot f \tag{9.21}$$

where:

Δf = frequency shift;

v = velocity of the receiver;

c = speed of light $\left(3 \cdot 10^8 m \cdot s^{-1}\right)$;

f = transmitted frequency (in our case 1575.42 MHz).

The Doppler shift directly affect the signal acquisition time of the receiver, both in terms of frequency of the code and frequency of the carrier. In general, the acquisition time increases in presence of Doppler shift as shown in Fig. 9-31[8].

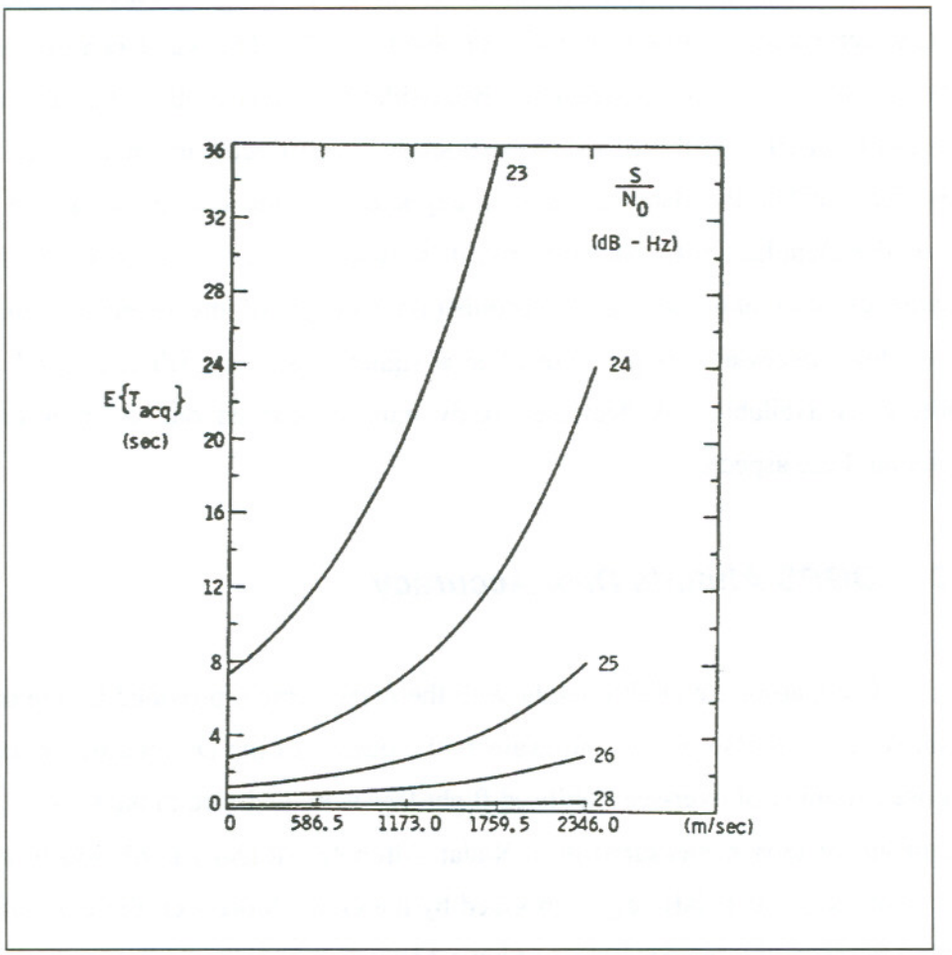

Figure 9-31. Mean GPS acquisition time as a function of relative velocity with different SNR's.

Considering the case of one satellite tracked, the Doppler shift is due to the relative velocity of the satellite and the receiver (i.e., the difference between the projections of the velocity vectors along the satellite-receiver direction). The worst case is, therefore, that of an aircraft flying along the line of sight (LOS) to the satellite, in which the full velocity vector of the aircraft must be used to determine the relative velocity (e.g., with an aircraft flying along the LOS to the satellite at a velocity of 350 kts, the Doppler shift for L1 is in the order of 10 KHz).

Analysis of GPS receiver data recorded during several flights and up to speed of 500 kts highlighted that the Doppler effect causes a frequency shift, with respect to the carrier phase L1, which reaches a maximum value of about 15 KHz. This value can be considered risible with respect to the GPS frequency bandwidth (i.e., about 30 MHz), and the high dynamic characteristics of the PLL (Phase Locked Loop) circuit internal to the receiver guarantee that neither the data accuracy is degraded nor the carrier phase can be lost because of the Doppler shift. Nevertheless, it is hypothesised that the coupling between such frequency shift and the signal reacquisition strategy of the receiver significantly affects the time necessary to get data after a signal loss, even when a good satellite configuration is available. A dedicated study must be carried out in order to deeply investigate on these aspects.

9.4.2.3 DGPS Altitude Data Accuracy

Comparing the DGPS height with the measurement provided by the on-board radar altimeter, it was also possible to evaluate the quality of the DGPS altitude data. For this purpose a number of over-sea stabilised flight legs were included in the trials.

The height above terrain measured by a Radar Altimeter (Radalt) is obviously different from the geodetic (ellipsoidal) height provided by the GPS. Moreover, there is not a fixed relationship between the height AMSL (Above Mean Sea Level) and the geodetic height. This is due to irregularities of the geoid (i.e., the equipotential surface defined in the Earth gravity field which can be approximated, for some practical applications, to MSL).

Flying over the sea, the Radalt height approximated the AMSL height. The Geoid separation was unknown, but a certain uniformity was obtained flying round tracks over a limited area (i.e., there was an unknown bias in the comparison).

Four flight tests were carried out with different satellite numbers and PDOP ranging from 2 to 5. The differences between DGPS and Radalt altitudes were measured in the range 0÷9 metres. Fig. 9-32 graphically shows the DGPS and Radalt data recorded during one of the flights. Considering the Radalt quoted error of ± 3% (of the height displayed), the results of the qualitative comparison of DGPS and Radalt data were considered satisfactory.

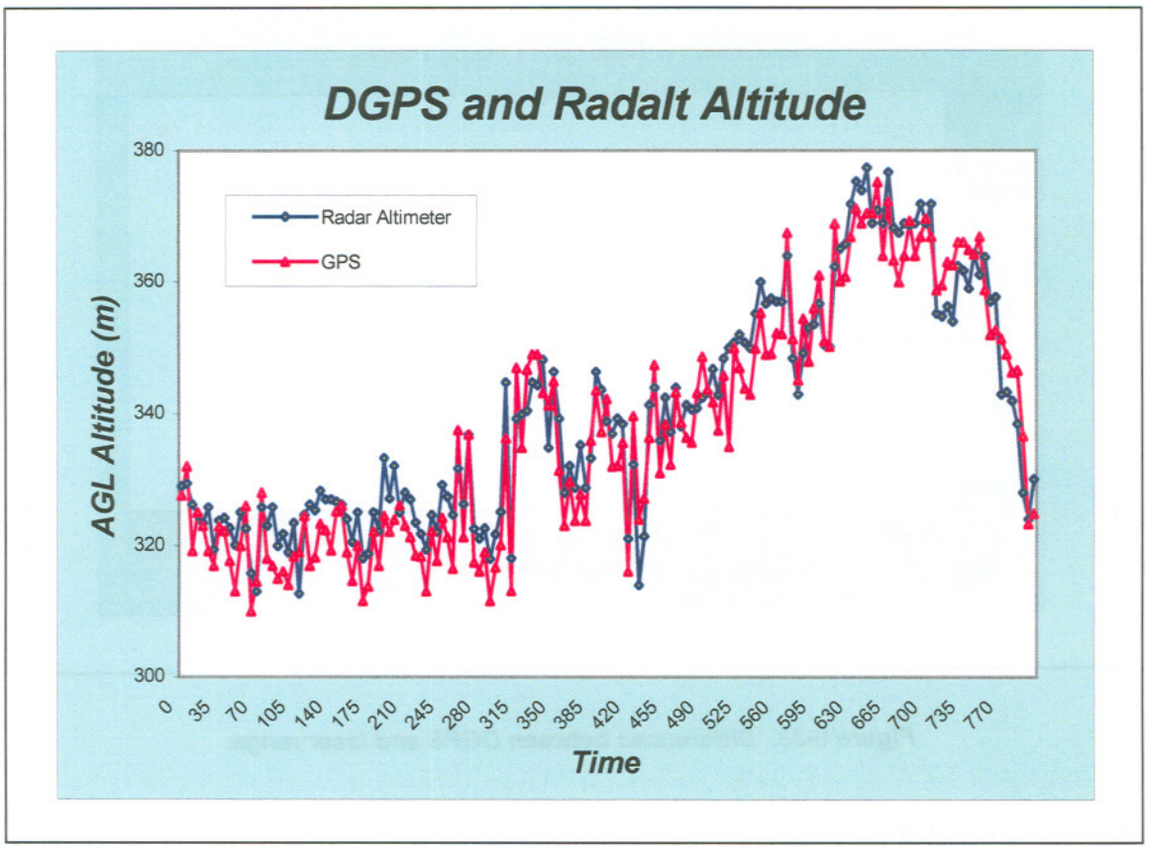

Figure 9-32. Comparison of DGPS and radar altimeter data.

9.4.2.4 DGPS Range Data Accuracy

A comparison was performed between slant-ranges computed using DGPS data and measured with the CLDP measured laser range (LRF function). Particularly, the slant ranges between the aircraft and the two PILASTER target locations obtained by using GPS latitude, longitude and altitude data, were compared with the laser range provided by the CLDP for the same two locations. The satellite constellation for both tests included 7 satellites with a PDOP value of 3.2. The calculated differences between DGPS and CLDP ranges for distances from the fix point up to about 10 km, are shown in Fig. 9-33.

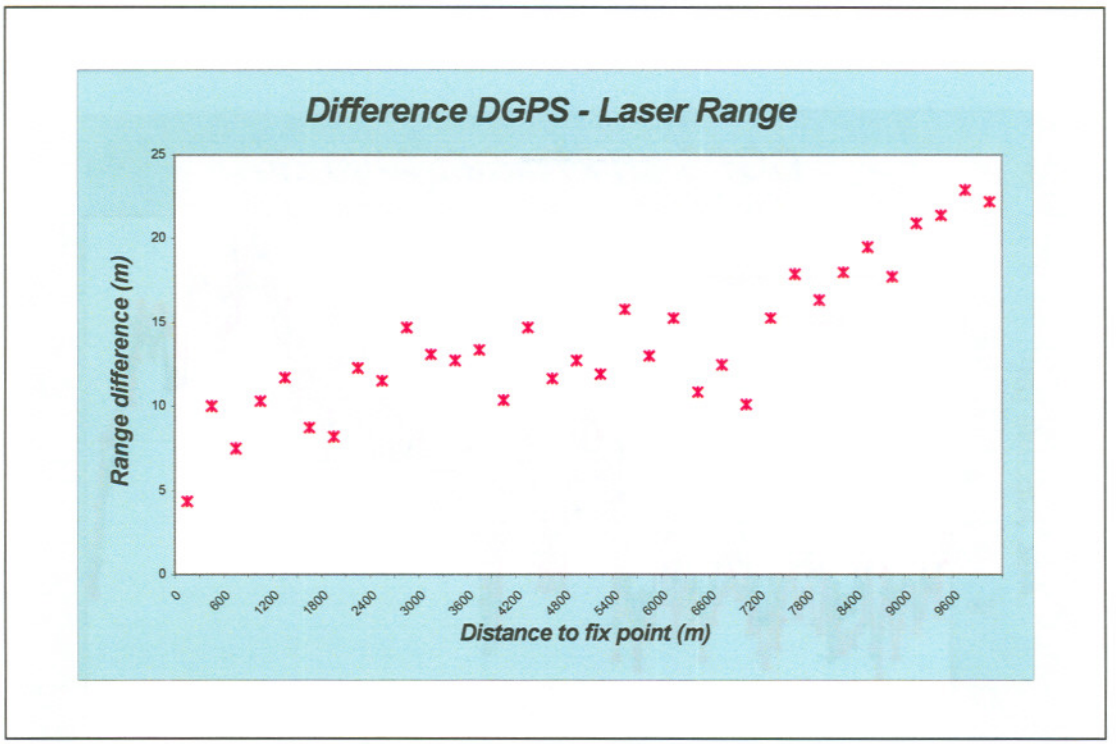

Figure 9-33. Differences between DGPS and laser range.

One can notice that the difference between calculated DGPS range and laser range is below 25 m up to a distance of about 10 km to the fix point. The "error" increases with distance mainly due to the worsening of the range measurements provided by the laser.

9.4.2.5 DGPS Positioning Data Accuracy

Some flight trials were carried out in the PILASTER range in which cinetheodolites (CITE) were available to provide the required datum accuracy (i.e., 0.5 m nominal accuracy). One of the difficulty encountered in the data analysis of these trials was the difference of the geodetic reference adopted by the two systems (Gauss-Boaga for CITE and WGS 84 for GPS), and the time decorrelation of data (CITE provided higher data rate than GPS). The first problem was solved by using a co-ordinates transformation software, while for the second problem an interpolation was required of the various measurements provided by the CITE in one second (1 Hz was the GPS data rate).

Data analysis was carried out with data samples collected in five different flights. The accuracy figures so determined were 65.3 m SEP stand-alone C/A code and 5.7 m SEP C/A code differential. The found accuracies were in fact comparable to the values quoted by ASHTECH (i.e., 100 m SEP stand-alone C/A code and 3 m SEP C/A code differential). Furthermore, a dedicated flight sortie was flown in order to verify the influence of aircraft-to-reference station (RS) slant-range on DGPS system accuracy (i.e., spatial de-correlation of differential corrections). For this purpose, a number of pre-defined ground points where over-flown (5 times each), and the exact time of over-flying was recorded in flight (by the aircrew) and on the ground. The results of the 3-D position error measurements obtained with PDOP ≤ 4 are shown in Fig. 9-34.

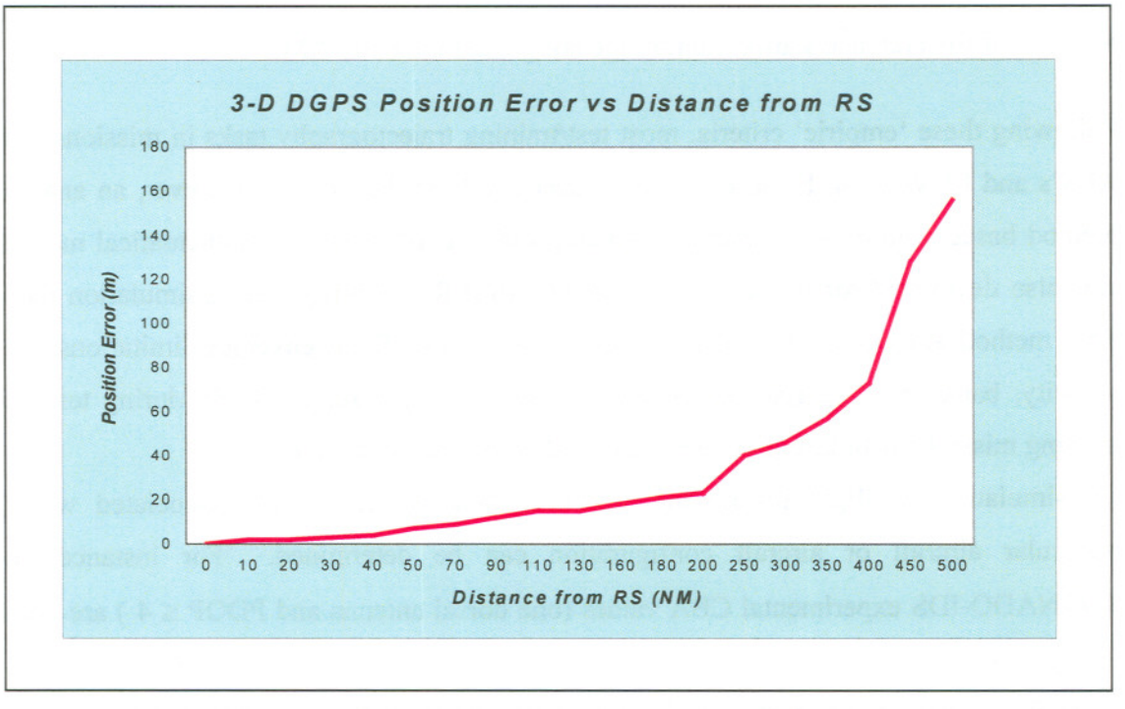

Figure 9-34. DGPS 3-D position error with increasing distance from reference station.

According to the experimental results, it was concluded that, for most PILASTER flight test and training applications, the DGPS error was acceptable (i.e., < 15 m) if the aircraft-to-RS slant-range did not exceed 100 NM.

9.4.3 Test/Training Mission Planning and Optimisation

As a result of the analysis carried out, some recommendations have been formulated in order to optimise the use of DGPS as a positioning datum during flight testing and training missions with airborne laser systems. Particularly, the following general criteria have been identified:

- 4 satellites always in view with an elevation near 50°;
- 45° maximum bank angle;
- at least 20 sec of stabilisation before and after significant flight phases;
- gradual heading variations;
- aircraft-to-reference station slant-range not greater than 100 NM.

Following these 'empiric' criteria, most test/training trajectography tasks in missions with ALS's and LGW's can be accomplished successfully at the range. However, an analytic method based both on experimental evidence and aircraft dynamics mathematical models, was also developed for implementation in PILASTER mission planning/simulation tools. This method allowed a-priori calculation of the aircraft flight envelope limitations (i.e., velocity, bank angle, engine power, etc.) related with the use of DGPS during test and training missions with laser systems. The method is described below.

By simulation or flight testing the "Critical Bank Angle" (CBA) associated with a particular aircraft or aircraft configuration can be determined. For instance, the TORNADO-IDS experimental CBA values (one dorsal antenna and PDOP ≤ 4) are given in Fig. 9-35.

The CBA is likely to be reached during the escape manoeuvres (i.e., when it is important to be able to track the aircraft position with great accuracy). Furthermore, during complex training exercises or in particular test missions it is not possible to maintain stabilised flight conditions before initiating the critical turns, and the re-acquisition times of currently available receivers (i.e., 5 to 20 sec) are not compatible with most test/training requirements.

- *CONF. 25° ⇒ 42° CBA*
- *CONF. 45° ⇒ 47° CBA*
- *CONF. 67° ⇒ 53° CBA*

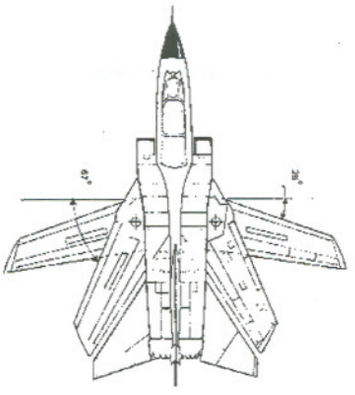

Fig. 9-35. TORNADO-IDS critical bank angles.

A dedicated study of the aircraft turning performance is therefore required in order to determine the envelope limitations associated with the use of DGPS during test and training exercises. This task can be accomplished by knowing the following data:

- aircraft structural characteristics (weight Q, wing surface S);
- polar curves for the various aircraft configurations [lift $C_L(M)$, drag $C_D(M)$];
- thrust available in the various configurations (*DRY* and with "after burner" *A-B*);
- atmosphere characteristics (air density ρ, air temperature T).

Typical input data required for performance analysis are shown in Fig. 9-36.
After analysis, the following useful results are obtained:

- determination of the envelope areas were the CBA can be reached;
- aircraft turning radius limitations at various altitudes and with various engine power settings;
- verification of compatibility between the profiles/procedures required for test and training (e.g., the altitude/velocity/direction limitations obtained from eye-safety analysis/simulation), and the CBA envelope limitations.

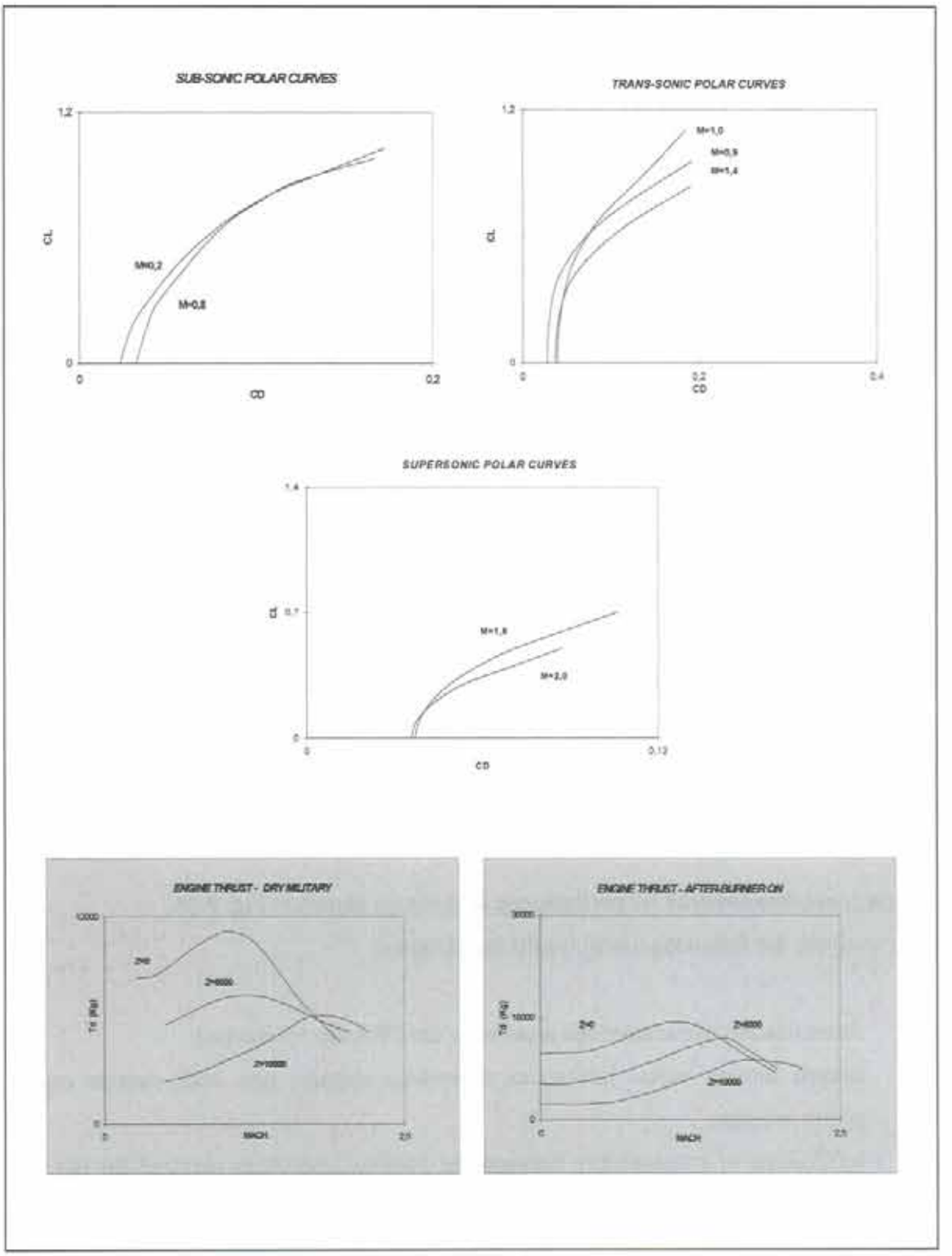

Fig. 9-36. Input parameters for performance analysis.

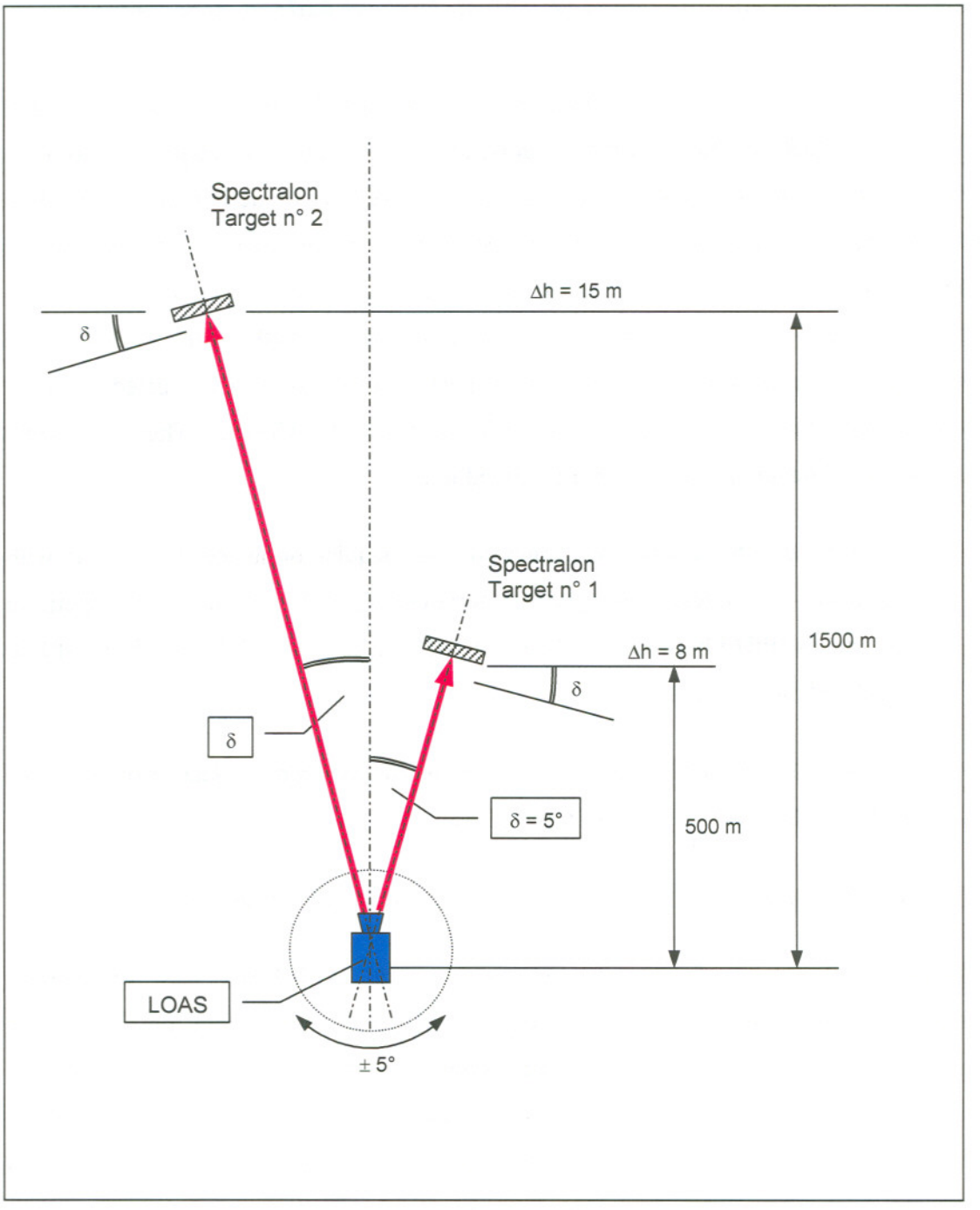

Figure 8-7. Experimental arrangement for propagation tests at λ = 1550 nm.

8.2.3 Verification and Optimisation of EMT-1 and EMT-2

During the initial phases of the experimental activity, it was understood that *Phoenix* NIR camera frame rate optimisation was crucial to data acquisition for both PILASTER techniques (EMT-1 and EMT-2), as well as to definition of the DAS (Digital Acquisition and Data Recording System) memory requirements for NIR camera data recording. Furthermore, significant differences were observed between the transmittance measurements obtained using EMT-1/EMT-2 and the transmittance values predicted by mathematical models. This aspect also had to be investigated to allow practical implementation of EMT-1 and EMT-2 at the PILASTER. Therefore, some ground experimental activities were performed in order to:

- optimise the NIR camera frame rates for data acquisition at the PILASTER with state-of-the-art systems having pulse durations P_D < 20 ns and pulse repetition frequencies (PRF) between 10 Hz and 40 kHz (e.g., 10 or 20 Hz for ELOP-PLD, and 40 kHz for LOAS);

- determine the computer memory requirements for NIR camera data recording at 10 Hz/20 Hz (ELOP-PLD) and 40 kHz (LOAS);

- evaluate/improve both EMT-1 and EMT-2 for measurements at $\lambda = 1064$ nm.

Phoenix NIR camera frame rate optimisation was carried out with preliminary calculations and two separated experimental sessions performed with the ELOP-PLD and the LOAS systems. During the same sessions, it was also verified the compatibility of the NIR camera frame rates with the commercial PC memories installed in the Phoenix DAS system. Evaluation of the PILASTER EMT-1/EMT-2 reliability was obtained by performing various test sessions with the PLD system, using EMT-CT. With this control techniques, it was also possible to determine useful correction for the EMT-1 and EMT-2 measurements at $\lambda = 1064$ nm.

8.2.3.1 NIR Camera Frame Rate Optimisation

After the initial ground tests with the NIR camera, it was decided that the NIR camera acquisition windows were not to be synchronised with the laser pulses incident on the target surface. In fact, although the NIR camera could be triggered by the laser pulses incident on the target using the PILASTER instrumentation, a good synchronisation became extremely difficult even at low PRF and almost impossible as the PRF increased (also due to the existence of dark zones in the NIR camera acquisition windows). Therefore a preliminary study was required in order to determine optimal frame rates for the NIR camera acquisition as a function of the known laser pulses parameters. After that, some experimental sessions were performed to verify the validity of the models developed.

8.2.3.2 Frame Rate Optimisation Analysis

Let us consider the train of pulses shown in Fig. 8-8. The parameters describing the train of pulses are the pulse duration (τ), the pulse period (T_P) and the PRF (f) given by:

$$f = \frac{1}{T_P} \tag{8.14}$$

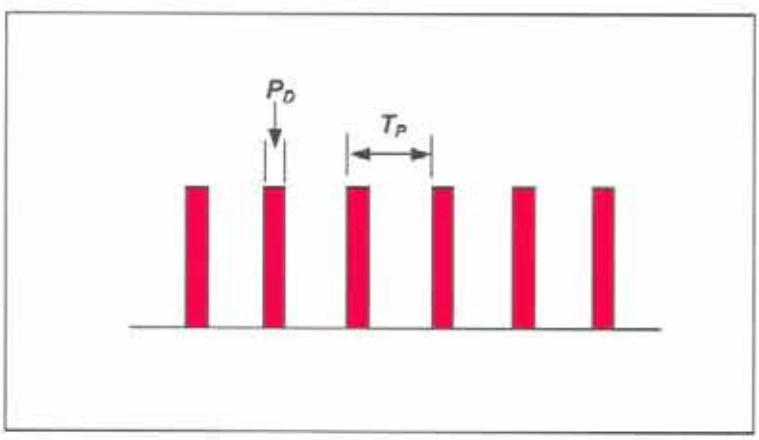

Figure 8-8. Train of pulses.

The NIR camera image acquisition process is defined by the frame period (T_F) and the corresponding frame frequency (f_F) given by:

$$f_F = \frac{1}{T_F} \tag{8.15}$$

Each frame consists of a 320×256 pixels matrix. In general, the NIR camera real acquisition time (T_A) is inferior to the corresponding framing window defined by T_F. The difference between T_F and T_A is the so called camera 'dark-time' (T_{dark}). For the Phoenix camera T_{dark} is 2% of the frame period (T_F). Therefore:

$$T_{dark} = T_{dark\%} \cdot T_f = 0.02 \cdot T_f \tag{8.16}$$

$$T_A = T_F - 0.02 \cdot T_f \tag{8.17}$$

A schematic representation of the NIR camera acquisition windows and dark zones is presented in Fig. 8-9.

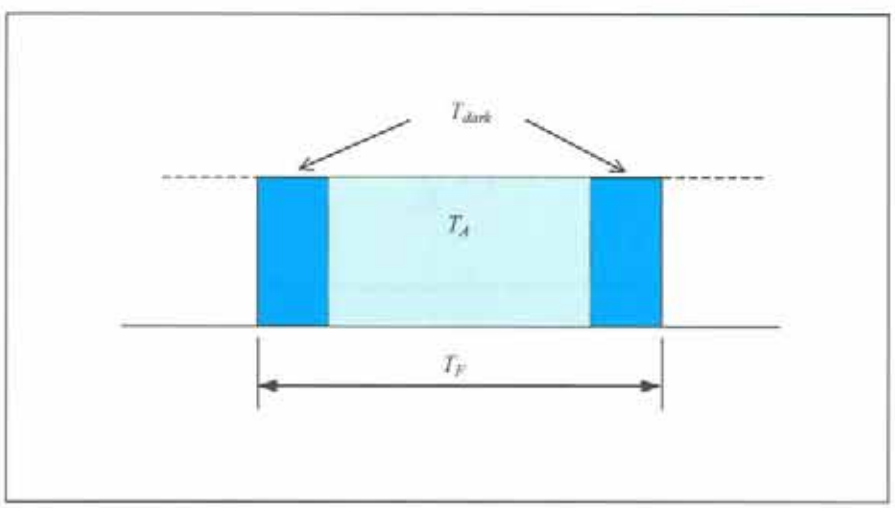

Figure 8-9. NIR camera acquisition windows and dark zones.

Since the NIR camera frames are not synchronised with the laser pulses, considering the NIR camera acquisition windows sequence as our time base (T_b), the instant of arrival of

the first laser pulse (reflected from the target) at the NIR camera (T_o) can be treated as a random variable (see Fig. 8-10).

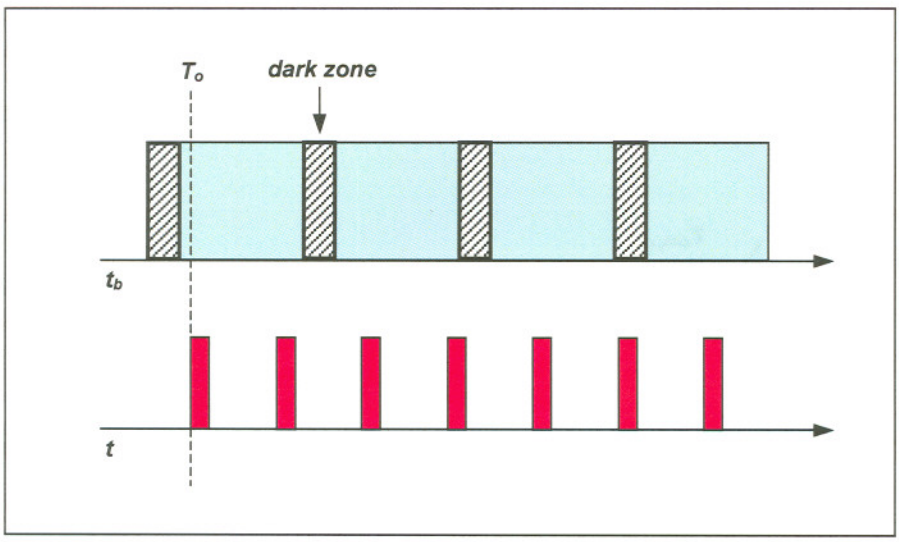

Figure 8-10. NIR camera acquisition windows sequence and laser pulses.

Therefore, our optimisation problem consists in determining the frame period (T_F) satisfying the following conditions:

Cond. 1 → Only one pulse has to be acquired in a single frame.

Cond. 2 → The probability of a laser pulse being entirely or partially in the dark zones of the NIR camera acquisition windows sequence has to be minimised.

To satisfy the first condition, we set:

$$T_F \leq T_P \tag{8.18}$$

Since we consider as 'error' the event of a laser pulse being totally or partially in the 'dark zones', we have to take into account the duration of the laser pulses (τ) in our analysis. To simplify calculations, we model the laser pulses as pure *Dirac*-pulses (i.e., pulses of zero duration), simply by adding τ to the dark periods (T_{dark}) at the beginning

and at the end of the acquisition windows (Fig. 8-11). Therefore, we define the 'effective dark time' (T_{dark_eff}) as follows:

$$T_{dark\_eff} = T_{dark\%} T_F + \tau \tag{8.19}$$

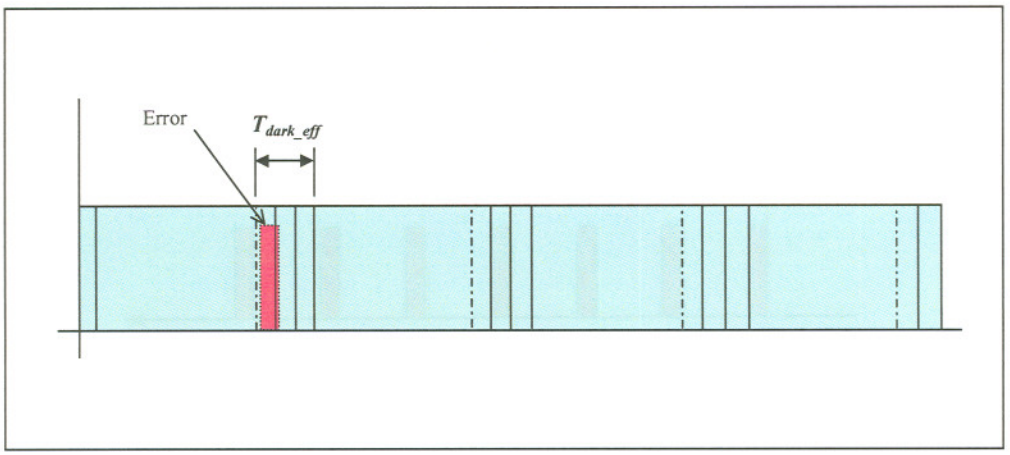

Figure 8-11. Effective dark time.

The resulting model used for analysis is shown in Fig. 8-12.

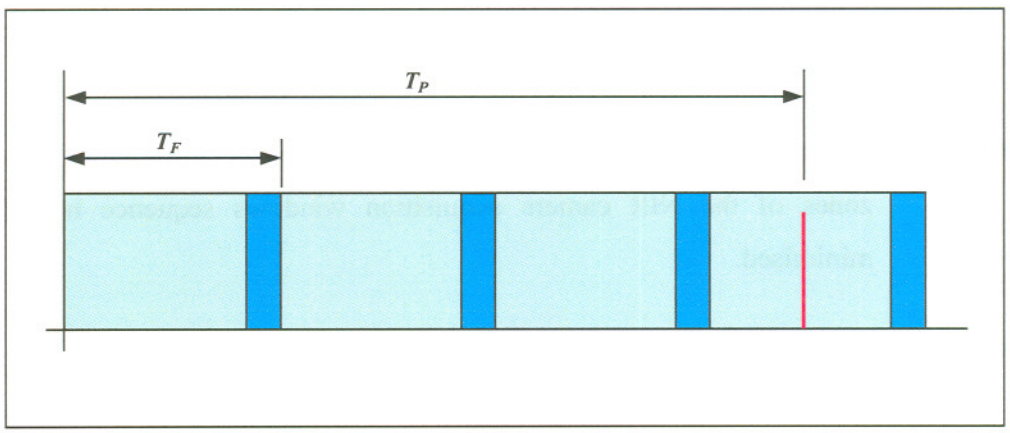

Figure 8-12. Model used for analysis.

Having defined our reference windows sequence, we have to chose the probability distribution modelling the arrival of a laser pulse into windows sequence. Since $T_F \leq T_P$, in a single pulse period there may be various acquisition windows.

Therefore, knowing that in the time interval [0; T_P] only one pulse has to be present, we model the time of arrival of the laser pulse as a uniform random variable (Fig. 8-13).

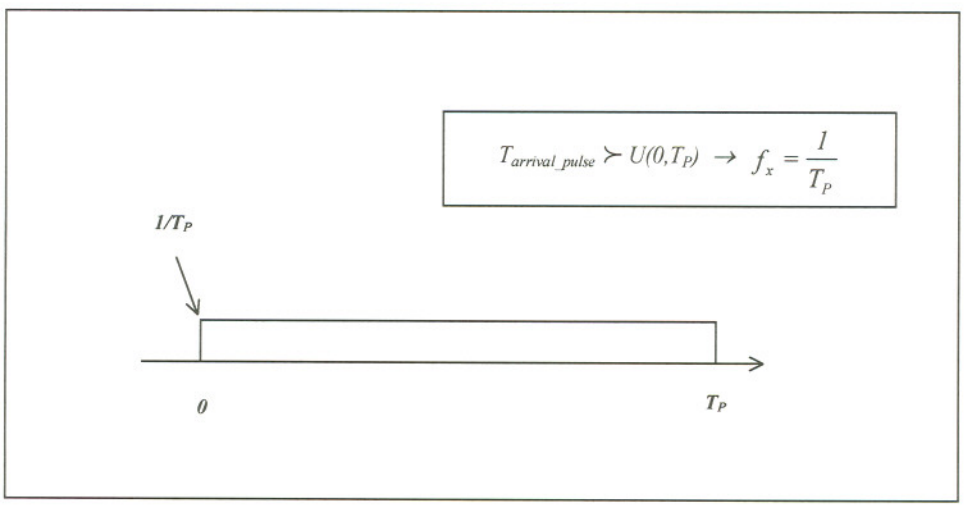

Figure 8-13. Probability distribution for pulse time of arrival.

The error probability with varying T_F is given by:

$$P_{err} = \int_{dark\ zones} \frac{1}{T_P} dx \tag{8.20}$$

We have the two cases described below.

Case-1. In the interval [0; T_P] there is an integer number of dark zones. Thus, the error probability becomes:

$$P_{err} = N_d \frac{T_{dark\_eff}}{T_P} \tag{8.21}$$

Where N_d is the number of dark zones in the interval [0; T_P].

Case-2. In the interval [0; T_P] there is a decimal number of dark zones (Fig. 8-14).

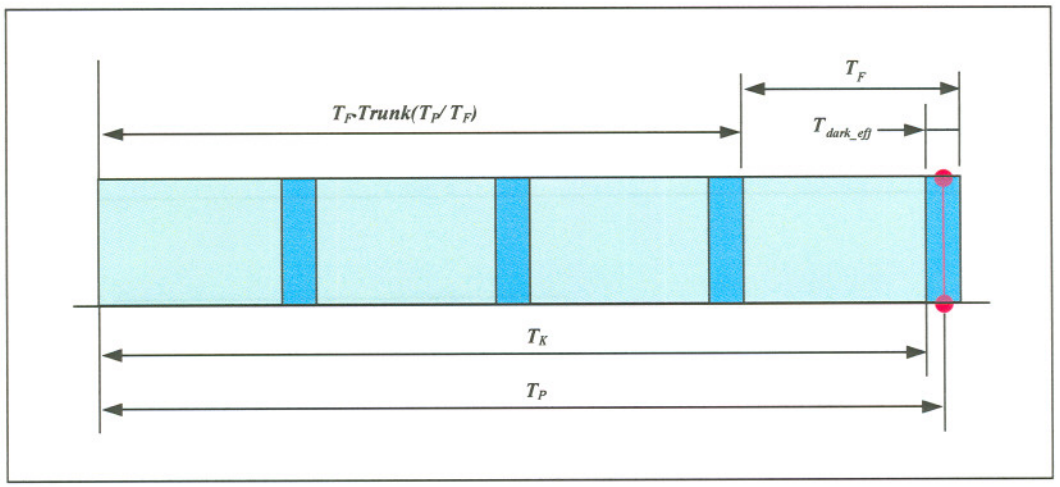

Figure 8-14. Decimal number of dark zones in the interval [0; T_P].

For our analysis, *Case-2* represents the general case (i.e., includes *Case-1*). As we notice in Fig. 8-14, we have an integer number of dark zones plus a fraction of dark zone partially included in the interval [0; T_P]. Therefore, if we let:

$$T_K = T_F\left[1 + Trunk\left(T_P / T_F\right)\right] - T_{dark\_eff} \tag{8.22}$$

the error probability in the general case is given by:

$$P_{err} = Trunk\left(\frac{T_P}{T_F}\right)\frac{T_{dark\_eff}}{T_P} + \left(\frac{1}{T_P}\int_{T_K}^{T_P} dx\right)\cdot b \tag{8.23}$$

where b is a Boolean variable of the form:

$$\begin{cases} 1 \\ 0 \end{cases} \text{ if } T_P - T_F\left[1 + Trunk\left(\frac{T_P}{T_F}\right)\right] + T_{Buio\_eff} \begin{cases} > 0 \\ < 0 \end{cases} \tag{8.24}$$

Therefore, we obtain:

$$P_{err} = \left[Trunk\left(T_P / T_F\right) + \frac{1}{T_P}\left\{T_P + T_{Buio\_eff} - T_F\left[1 + Trunk\left(T_P / T_F\right)\right]\right\}\cdot b\right]\frac{T_{dark\_eff}}{T_P} \tag{8.25}$$

where the number of dark zones in the interval [0; T_P] is:

$$N_D = Trunk(T_P/T_F) + \frac{1}{T_P}\left\{T_P + T_{dark\_eff} - T_F\left[1 + Trunk(T_P/T_F)\right]\right\} \cdot b \qquad (8.26)$$

Substituting eq. (8.19) into eq. (8.25), taking into account the eq. (8.24), we obtain the expressions of P_{err} listed in Table 8-2, where the function P_{err} has been defined with $N = 1,2,3...$

T_F	P_{err}
$\frac{T_P + \tau_{pulse}}{2(1 - T_{dark\%}/2)} < T_F < T_P$	$\frac{T_{Buio\%}}{T_P} T_F + \frac{\tau_{pulse}}{T_P}$
$\frac{T_P}{2} < T_F < \frac{T_P + \tau_{pulse}}{2(1 - T_{dark\%}/2)}$	$\left(\frac{T_{dark\%}}{T_P} T_F + \frac{\tau_{pulse}}{T_P}\right) \times \left[1 + \frac{T_P + (T_{dark\%} - 2)T_P + \tau_{pulse}}{\tau_{pulse} + T_{dark\%} T_F}\right]$
. . .	. . .
$\frac{T_P + \tau_{pulse}}{(N+1)(1 - T_{dark\%}/(N+1))} < T_F < \frac{T_P}{N}$	$N\left(\frac{T_{dark\%}}{T_P} T_F + \frac{\tau_{pulse}}{T_P}\right)$
$\frac{T_P}{(N+1)} < T_F < \frac{T_F + \tau_{pulse}}{(N+1)[1 - T_{dark\%}/(N+1)]}$	$N\left(\frac{T_{dark\%}}{T_P} T_F + \frac{\tau_{pulse}}{T_P}\right) \times \left[N + \frac{T_P + (T_{dark\%} - (N+1))T_P + \tau_{pulse}}{\tau_{pulse} + T_{dark\%} T_F}\right]$
. . .	. . .

Table 8-2. Error probability (P_{err}) equations in the definition intervals.

The function P_{err}, calculated for f = 10 Hz and τ_{pulse} = 19 nsec (ELOP-PLD system) is shown in Fig. 8-15.

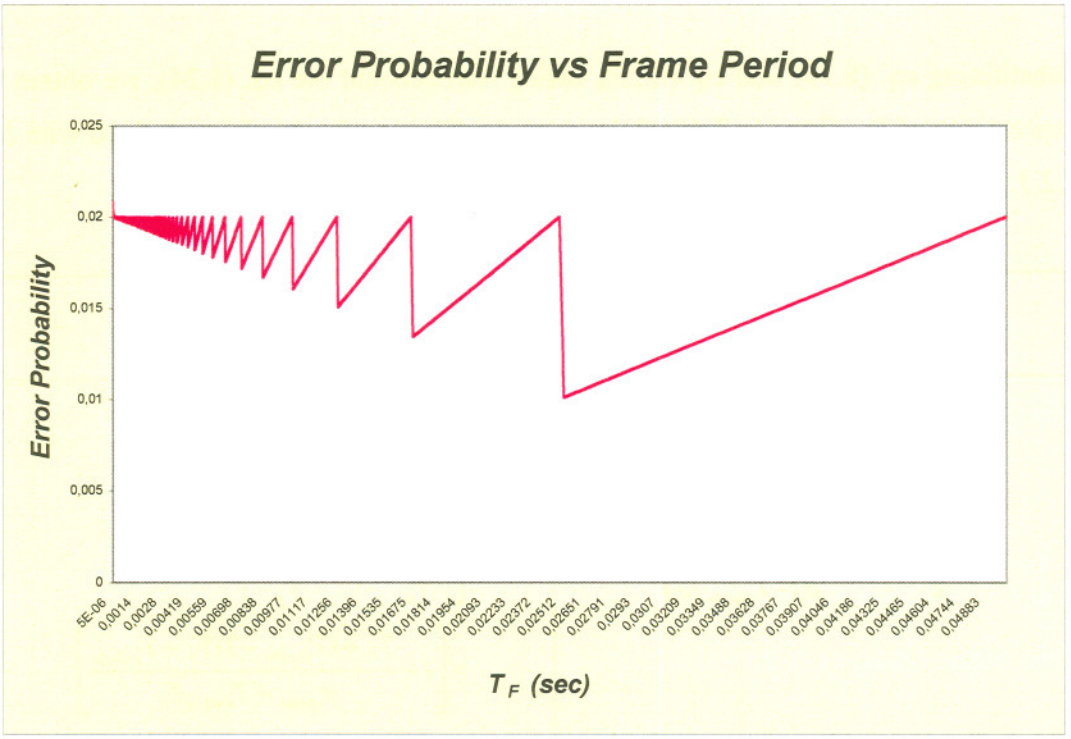

Fig. 8-15. NIR camera error probability function for f = 10 Hz.

In general, the relative minimums of the error probability function are found for:

$$T_F = \frac{T_P + \tau_{pulse}}{(N+1)\left(1 - \frac{T_{dark\%}}{N+1}\right)} \tag{8.27}$$

giving the following values of P_{err}:

$$P_{Err} = N \frac{T_P + \tau_{pulse}}{(N+1)\left(1 - \frac{T_{dark\%}}{N+1}\right)} \frac{T_{dark\%}}{T_P} + \frac{N\tau_{pulse}}{T_P} \tag{8.28}$$

The absolute minimum (optimal) value of P_{err} is found for:

$$T_{F\_opt} = \frac{T_P + \tau_{pulse}}{2\left(1 - \frac{T_{dark\%}}{2}\right)} \tag{8.29}$$

giving:

$$P_{Err\_opt} = \frac{T_P + \tau_{pulse}}{2\left(1 - \frac{T_{dark\%}}{2}\right)} \frac{T_{dark\%}}{T_P} + \frac{\tau_{pulse}}{T_P} \tag{8.30}$$

In most cases of practical interest, and particularly for both the ELOP-PLD and LOAS systems (i.e., τ_{pulse} < 20 ns and 10 Hz < f < 40 kHz), we have that $T_P >>> \tau_{pulse}$. Therefore, the equations (8.29) and (8.30) become:

$$\boxed{T_{F\_opt} = \frac{T_P + \tau_{pulse}}{2\left(1 - \frac{T_{dark\%}}{2}\right)} \cong \frac{T_P}{2\left(1 - \frac{T_{dark\%}}{2}\right)} \cong \frac{T_P}{2}} \tag{8.31}$$

$$P_{Err\_opt} = \frac{T_P + \tau_{pulse}}{2\left(1 - \frac{T_{dark\%}}{2}\right)} \cdot \frac{T_{dark\%}}{T_P} + \frac{\tau_{pulse}}{T_P} \cong \frac{T_P}{2\left(1 - \frac{T_{dark\%}}{2}\right)} \cdot \frac{T_{dark\%}}{T_P} \cong \frac{T_P}{2} \cdot \frac{T_{dark\%}}{T_P} = \frac{T_{dark\%}}{2} \tag{8.32}$$

Let us now try to interpret the behaviour of the function P_{err} taking into account the physics involved. We know that the error probability is a function of the total dark time (i.e., the sum of all dark intervals in the acquisition windows) in the pulse period. Therefore, we deduce that increasing the number of acquisition windows in the same pulse period would produce more dark intervals (i.e., the overall dark time would increase), with the consequence that P_{err} would also increase. This is confirmed by the general trend of the P_{err} function which decreases as T_F increases. However, we have to explain why the function P_{err} experiences sudden increases at the points where T_P is a multiple integer of T_F.

Using eq. (8.19), considering that $T_{dark\%} = 2\%$ for the NIR camera, and that $\tau_{pulse} < 20$ nsec, we can write:

$$T_{dark\_eff} = T_{dark\%} T_F + \tau_{pulse} \cong T_{dark\%} T_F \tag{8.33}$$

Therefore, since T_{dark_eff} is a fraction ($T_{dark\%}$) of the acquisition window, in the particular cases where T_P is a multiple integer of the acqusition window, the total dark time does not vary. In fact, if we consider n windows in the interval [0; T_P], we will have n dark intervals, with a total dark time given by:

$$T_{dark\_tot} = nT_{dark\%} T_{F1} \tag{8.34}$$

Obviously, for $n = 1$ $T_{dark\_tot} = T_{dark\%} T_F$, but $T_F = NT_{F1}$ and, therefore, as the total dark time does not vary, the error probability is the same. This is why all points of maximum have the same value for T_F far from zero. As T_F gets closer to zero, τ_{pulse} becomes significant, but this is a characteristic not useful for our analysis. Therefore, the graph in Fig. 8-15 tells us that, with a given T_P, the value of T_{dark_tot} (and T_{dark_eff}) decreases as T_F decreases, up to the point where the dark zone of the last frame enters the interval [0; T_P]. When this happens, T_{dark_tot} (and T_{dark_eff}) goes back to the previous value, but then immediately starts to decrease again. Consequently, the minimum of P_{err} does not occur exactly at $T_F = T_P/2$, but for a value of T_F a bit greater than $T_P/2$, which would guarantee the first pulse to be just outside the dark zone of the second frame (Fig. 8-16).

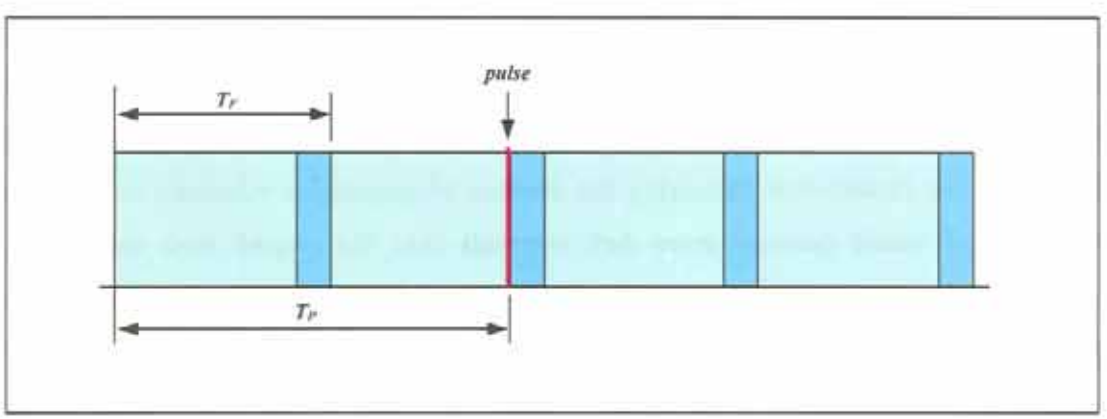

Figure 8-16. Condition of minimum error probability.

We can now select the optimal frame rate (F_{F_opt}) for f = 10 Hz (i.e., ELOP-PLD Band n° 1). As explained before, if the T_F could be set at exactly $T_P/2$ minus a small quantity (e.g., $T_F = (T_P/2)\text{-}10^{-4}$), our optimisation problem was solved. However, as T_F (and F_F) is affected by instability (i.e., a variance σ_{T_F} in the order of 10^{-4} sec about the nominal T_F), in order to avoid a possible increase of the P_{err}, it is convenient to chose our optimal T_F at about $2\sigma_{T_F}$ from the $T_P/2$ point. This is shown in Fig. 8-17, where it is evidenced that the T_F instability may cause the error to be maximised for a value of T_F not sufficiently greater that $T_P/2$ (Case 1). The improvement (reduction of P_{err}) is evident with $T_F = 2\sigma_{T_F} + T_P/2$ (Case 2). Therefore, in terms of frame rate optimisation, we can write:

$$F_{F\_opt} = 2\left(f - \sigma_{F_F}\right) \tag{8.35}$$

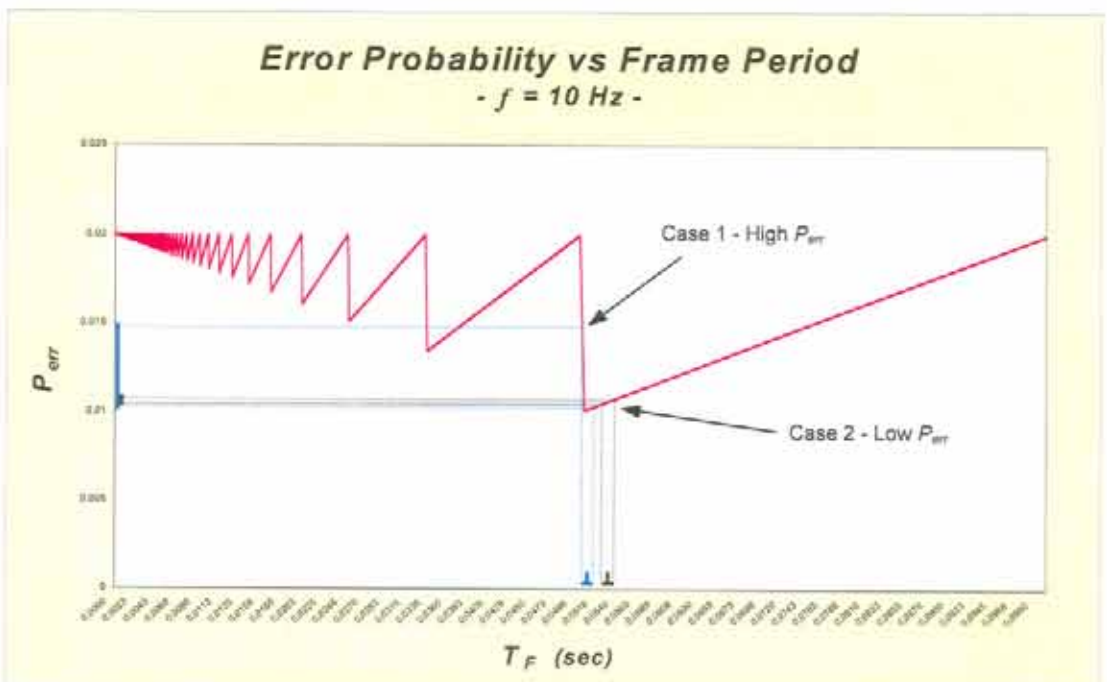

Figure 8-17. Effects of T_F uncertainty on P_{err} for f = 10 Hz.

As the P_{err} function and σ_{T_F} do not vary significantly up to f = 345 Hz for full frame NIR camera acquisition, the same optimisation criteria applies for f = 20 Hz (i.e., ELOP-PLD Band n° 2).

Let us now consider the case of f = 40 kHz (i.e., LOAS system). In this case, the function P_{err} previously defined, has the behaviour shown in Fig. 8-18. Again, the first part of the function, where T_F is still close to the pulse duration, is not interesting for our analysis. We notice that, also in this case, the minimum P_{err} is found for a T_F of about $T_P/2$. However, as in this case the variance of T_F (σ_{TF}) is in the order of about 10^{-5} sec, it is convenient to chose a T_F intermediate between $T_P/2$ and T_P (see Fig. 8-18). Therefore:

$$T_{F\_opt}' = \frac{3}{4} T_P \tag{8.36}$$

$$F_{F\_opt}' = \frac{4}{3} f \tag{8.37}$$

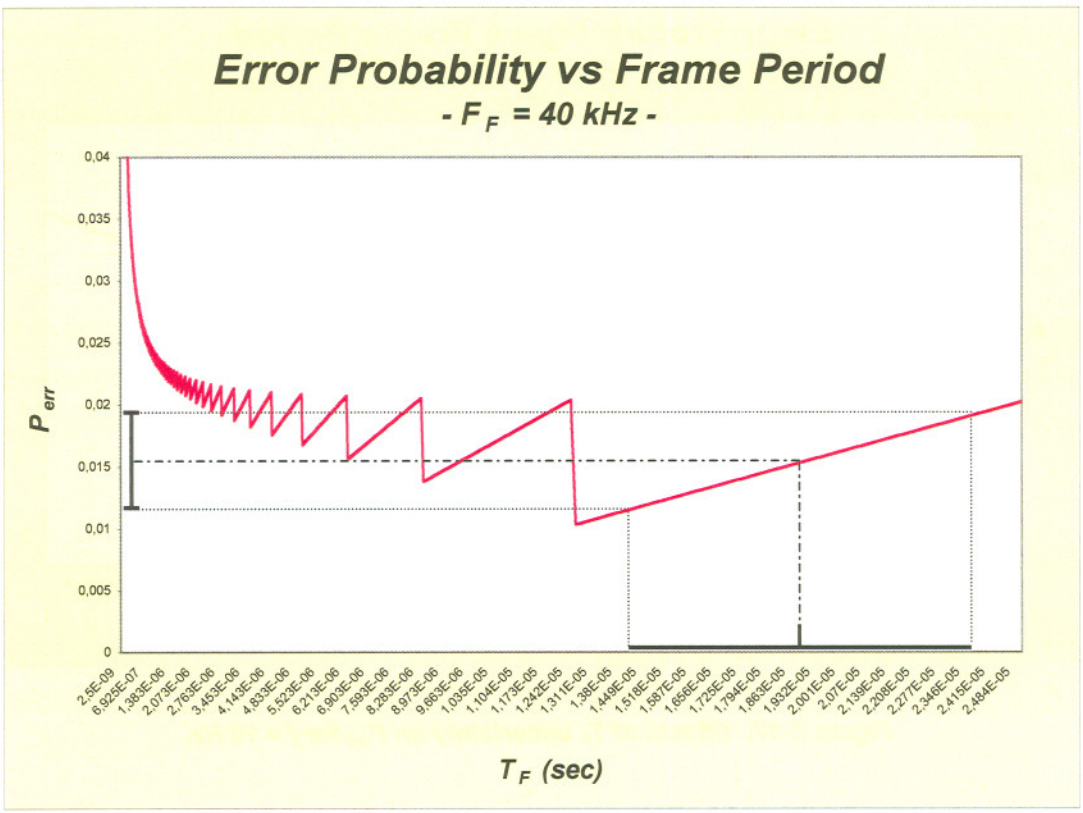

Figure 8-18. Effects of T_F uncertainty on P_{err} for f = 40 kHz.

The results of the frame rate optimisation analysis, referred to the two boundary conditions f = 10 Hz (i.e., ELOP-PLD) and f = 40 kHz (i.e., LOAS) are summarised in Fig. 8-19.

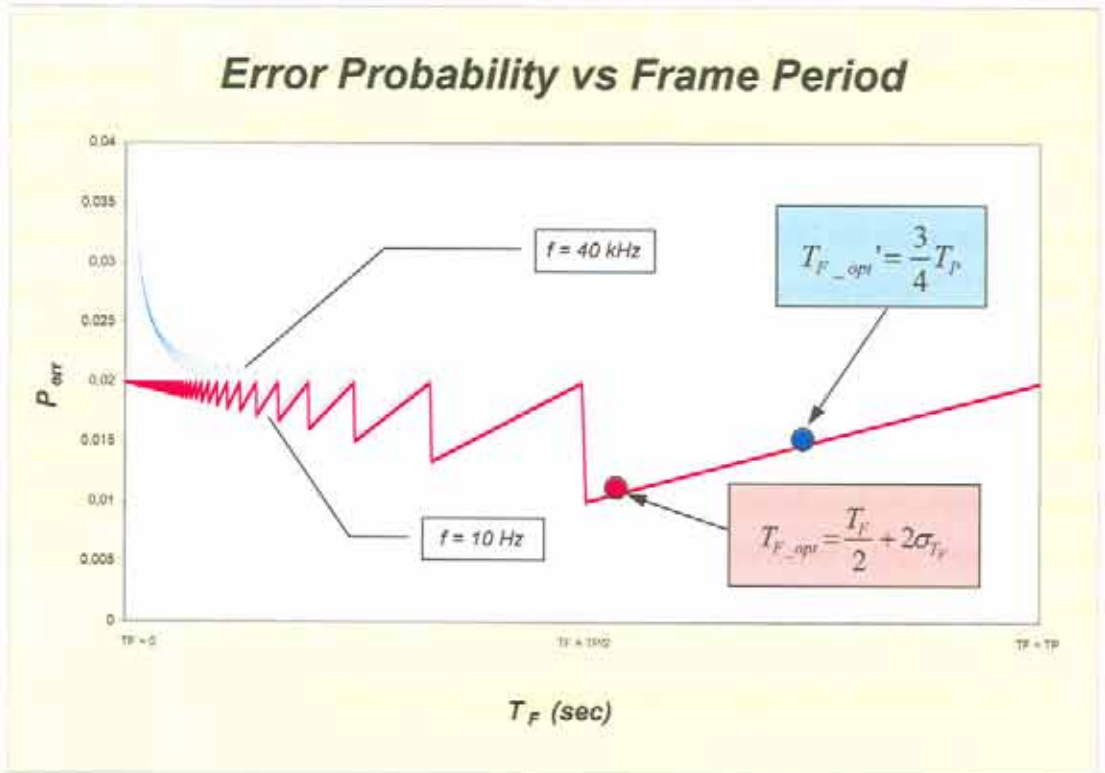

Figure 8-19. Results of NIR camera frame rate optimisation analysis.

8.2.3.3 Frame Rate Optimisation Tests

In order to verify the results of the optimisation analysis, and to find good compromises for the NIR camera F_F applicable to the real cases, two dedicated ground test sessions were performed using the PLD and LOAS systems, with laser pulse repetition frequencies (f) of 10 Hz, 20 Hz (ELOP-PLD) and 40 kHz (LOAS).

From eq. (8.35), the optimal F_F for $f = 10$ Hz was about 19.9997 Hz, and for $f = 20$ Hz was about 39.9997 Hz. However, as the NIR camera F_F settings were only possible with steps of 0.5 Hz, to avoid sudden increases of P_{err} (see discussion in paragraph 8.1.1.1), F_F was set to 19.5 Hz in the first case and to 39.5 Hz in the second case. From eq. (8.37), the optimal F_F for $f = 40$ kHz (LOAS system) was about 53 kHz. Unfortunately, the upper F_F limit of the Phoenix NIR camera with DAS was 38 kHz in smallest window (2 × 128 pixels) and 345 in full frame (320 × 256 pixels). Therefore, in this case it was not possible to use the NIR camera for full frame data recording (and therefore for EMT-1 and EMT-2 implementation), because the full frame was acquired at such a low rate (345 Hz) that a great number of laser pulses entered the same acquisition window. Furthermore, even setting F_F to the maximum value for the smallest window (e.g., for laser transmission event recording and experimental PRF determination), we had to accept a large error probability. In this case, in fact, the relatively large variance of T_F did not allow optimisation of P_{err}. Therefore, for the two test sessions F_F was initially set to the values:

- $F_{F\_10} = 19.5$ Hz in full frame with $f = 10$ Hz (ELOP-PLD);
- $F_{F\_20} = 39.5$ Hz in full frame with $f = 20$ Hz (ELOP-PLD);
- $F_{F\_40k} = 38$ kHz in smallest window with $f = 40$ kHz (LOAS).

The key parameter used for evaluating the performance of the Phoenix NIR camera was the percentage of Acquired Pulses (%AP) with respect to the total number of laser pulses transmitted in a certain Pulse Train Duration (PTD). Results relative to the NIR camera tests performed with the ELOP-PLD system are presented in Table 8-3.

ELOP-PLD Parameters			PHOENIX NIR	
PRF	PTD	τ	F_F	%AP
10 Hz	10 s	19 ns	19.5 Hz	67%
	30 s	19 ns	19.5 Hz	62%
	60 s	19 ns	19.5 Hz	71%
	120 s	19 ns	19.5 Hz	65%
20 Hz	10 s	19 ns	39.5 Hz	63%
	30 s	19 ns	39.5 Hz	68%
	60 s	19 ns	39.5 Hz	52%
	120 s	19 ns	39.5 Hz	58%

Table 8-3. Phoenix NIR Camera F_F Tests Results (f = 10 Hz and 20 Hz).

Results relative to the Phoenix NIR camera tests performed with the LOAS system are presented in Table 8-4.

ELOP-PLD Parameters			PHOENIX NIR	
PRF	PTD	τ	F_F	%AP
40 kHz	10 s	5 ns	38 kHz	17%
	30 s	5 ns	38 kHz	12%
	60 s	5 ns	38 kHz	19%
	120 s	5 ns	38 kHz	18%

Table 8-4. Phoenix NIR Camera F_F Tests Results (f = 40 kHz).

8.2.3.4 Determination of DAS Memory Requirements

The Phoenix NIR camera Digital Acquisition System (DAS), employed at the PILASTER STU, was based on commercial PC technology. Therefore, before performing ground and flight experimental activities, it was essential to define the DAS memory required for recording the digital frames acquired by the NIR camera during representative test/training missions. The duration (D) of typical test/training recording sessions was identified between 10 and 120 seconds. The maximum frame rate of the Phoenix NIR camera (with DAS) is 38 kHz. Each frame is composed by $R = 320 \times 256$ pixels, and each frame occupies memory 14 bits (grey scale images). Therefore, in the absence of any data compression and neglecting the few bits introduced by the IMAGE-PRO PLUS imaging software, the data flow from the camera to the PC, considering a typical 5% incidence of the communication flag bits, we obtain:

$$F_{data} = F_F \cdot R \cdot 14 \cdot 1.05 \quad bit/sec \tag{8.38}$$

The memory required for acquisition is given by:

$$M = \frac{D \cdot F_{data}}{8} \quad Byte \tag{8.39}$$

For instance, for D = 120 secs and F_F = 39.5 Hz (e.g., optimal F_F for ELOP-PLD in Band n° 2), considering a full frame data acquisition, we obtain:

$$M = \frac{120 \ \text{sec} \cdot 47.6 \ Mbit/\text{sec}}{8} \cong 713.50 \ MByte$$

Considering a 38 kHz data acquisition in smallest window (R = 2 × 128 pixels), assuming D = 120 secs, we obtain:

$$M = \frac{120 \ \text{sec} \cdot 143 \ Mbit/\text{sec}}{8} \cong 2.15 \ GByte$$

A graph showing the DAS memory requirements as a function of mission duration, for various representative frame rates, is shown in Fig. 8-20.

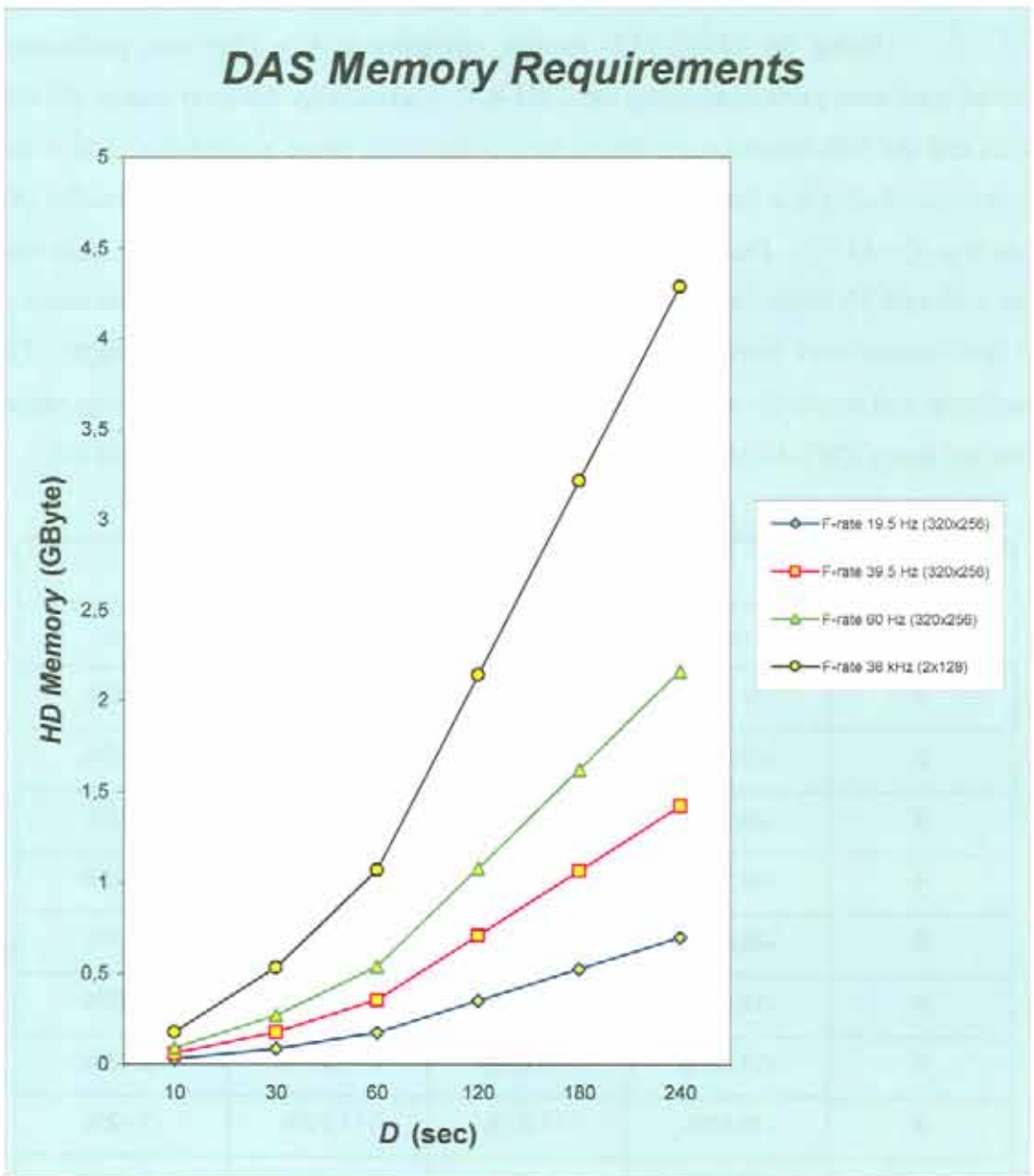

Figure 8-20. DAS computer hard-disk memory requirements.

Therefore, as the DAS memory requirements were fulfilled by commercial technology, a standard 40 GByte PC hard-disk was installed in the Phoenix DAS computer.

8.2.4 EMT-CT Sessions at λ = 1064 nm

Using the ELOP PLD system, operating at λ = 1064 nm, preliminary ground tests were performed using the EMT-CT. Particularly, the laser source (ELOP-PLD) and the NIR camera were placed very close to the target surface (i.e., 100 m and 80 m respectively) in a day with very good visibility (V = 34 km) and low humidity (RH = 41% at T = 15 °C). During the experiment with this control technique, the PLD laser was activated 10 times for periods of 30 seconds. For each test session, a minimum of 25 spot images were recorded (and at least 2 PEP readings for each spot image). The maximum and minimum differences (ε_{max} and ε_{min}) observed between the energy values obtained using EMT-1/EMT-2 and the PLD output energy are reported in Table 8-5.

Session	EMT-1		EMT-2	
	ε_{max}	ε_{min}	ε_{max}	ε_{min}
1	-27.12%	-12.51%	-11.03%	-4.86%
2	-19.34%	**-7.34%**	-10.47%	-5.12%
3	-28.06%	-18.64%	-13.95%	-6.65%
4	-33.24%	-15.04%	**-14.76%**	-10.23%
5	-28.29%	-19.12%	-12.79%	-8.49%
6	-18.02%	-10.27%	-9.87%	**-4.22%**
7	-21.13%	-18.35%	-13.57%	-9.43%
8	-15.90%	-11.67%	-11.70%	-7.42%
9	**-34.69%**	-8.78%	-9.07%	-6.43%
10	-27.42%	-10.18%	-8.48%	-5.54%

Table 8-5. Differences between PLD output and PILASTER measurements.

Both EMT-1 and EMT-2 gave under estimated values of the incident spot energy (i.e. a negative systematic error). In many cases EMT-1 could only provide rough estimations of the laser spot energy, with significant discrepancies between the various test sessions (i.e., -34.69% maximum and -7.34% minimum errors). On the other hand, using EMT-2 the error never exceeded -14.76% with an observed minimum error of -4.22%. These errors were due to sensors detection thresholds, loss of some spot fringes in the NIR images due to background noise, and other systematic or random errors affecting both techniques EMT-1/EMT-2 and the EMT-CT itself.

Cumulating the experimental data relative to the various test sessions, two samples of 300 error measurements were formed, relative to the EMT-1 and EMT-2 errors. These data were statistically analysed in order to determine corrections for the measurements performed using the two techniques. The normality of the data samples was verified using standard statistical techniques (i.e., χ^2 tests). The values of mean and standard deviation calculated for the error samples (s) and the 95% confidence intervals (CI) for the mean (μ) and standard deviations (σ) calculated for the corresponding normal populations are reported in Table 8-6. The 95% CI for μ and σ were calculated as follows:

$$\bar{x} - 1.96 \frac{s}{\sqrt{n-1}} < \mu < \bar{x} + 1.96 \frac{s}{\sqrt{n-1}} \tag{9.27}$$

$$\frac{s}{\left[1 + \left(\frac{1.96}{\sqrt{2n}}\right)\right]} < \sigma < \frac{s}{\left[1 - \left(\frac{1.96}{\sqrt{2n}}\right)\right]} \tag{9.28}$$

Fig. 8-21 shows the Probability Density Functions (PDF) obtained from the experimental data.

	EMT-1		EMT-2	
	Mean (%)	SD (%)	Mean (%)	SD (%)
Sample	$\bar{x}_1 = -17{,}57$	$s_1 = 3{,}54$	$\bar{x}_2 = -9{,}29$	$s_2 = 2{,}47$
Pop. 95% CI	$-18.06 < \mu < -17.08$	$3.28 < \sigma < 3.85$	$-9.57 < \mu < -9.01$	$2.29 < \sigma < 2.68$

Table 8-6. Results of errors statistical analysis for EMT-1 and EMT-2.

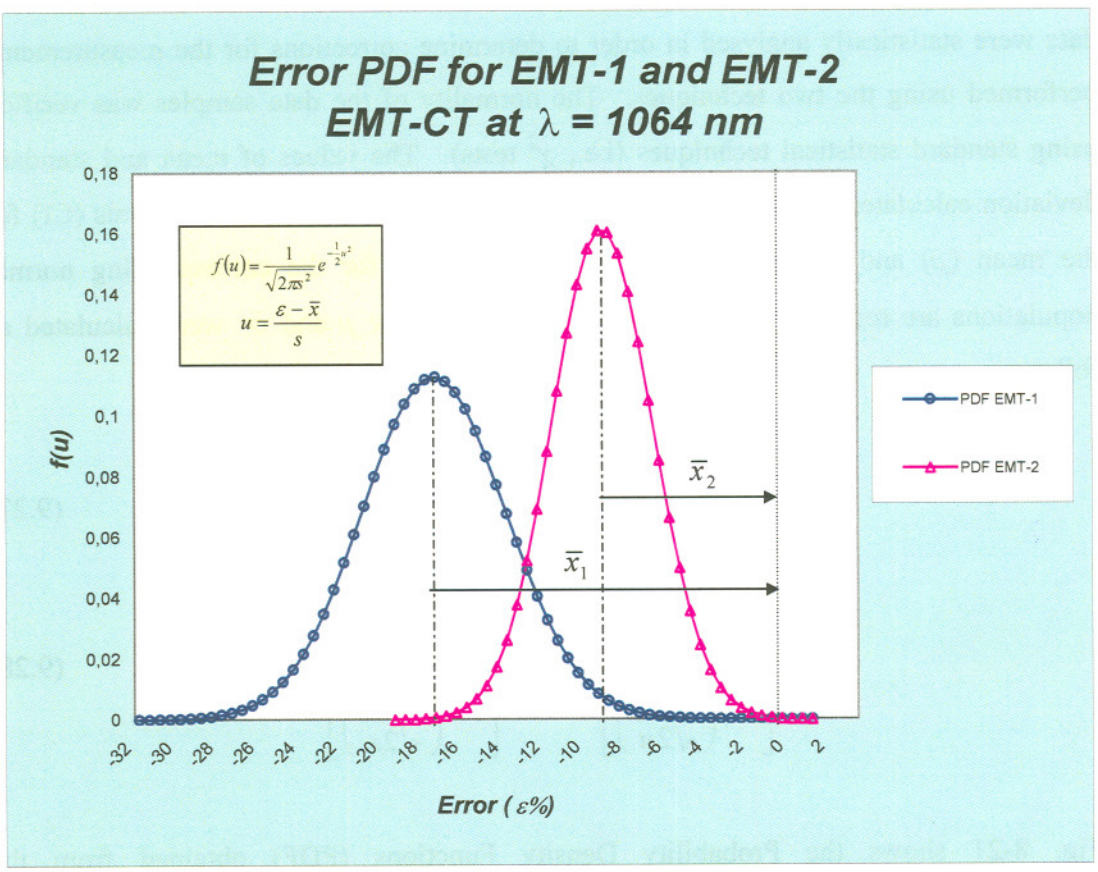

Figure 8-21. Error PDF for EMT-1 and EMT-2.

Using these results, it was possible to improve the reliability of the two techniques. This was done by applying a correction factor in the transformation from the NIR camera grey scale Pixel Intensity Matrix (PIM) to the corresponding Energy Intensity Matrix (EIM). The correction factors C_1 and C_2 (for EMT-1 and EMT-2 respectively) were:

$$C_1 = 1 + |\bar{x}_1| = 1.1757 \tag{9.29}$$

$$C_2 = 1 + |\bar{x}_2| = 1.0929 \tag{9.30}$$

The ELOP-PLD factory data gave a Probable Error (PE_{PLD}) of ±4% for the system energy output due to instability, aging, etc. (i.e., 130mJ ±4%). Considering the results of our analysis, since $PE = 0.6745 \cdot \sigma$, we obtained $PE_1 = \pm 2.39\%$ and $PE_2 = \pm 1.67\%$ for EMT-1 and EMT-2 respectively. Therefore, accumulating the errors, the PE of the measurements performed using the two techniques (PE_{M1}, PE_{M2}) were the following:

$$PE_{M1} = \sqrt{PE_{PLD}{}^2 + PE_1{}^2} = \pm 4.66\% \tag{9.31}$$

$$PE_{M2} = \sqrt{PE_{PLD}{}^2 + PE_2{}^2} = \pm 4.33\% \tag{9.32}$$

8.2.5 Propagation Trials Results

After the initial test phase devoted to PILASTER measurement techniques verification and optimisation, actual extinction measurement trials were performed at the PILASTER range using EMT-1/EMT-2 for λ = 1064 nm (ELOP-PLD) and EMT-3 for λ = 1550 nm (LOAS). Most of the test activities were carried out during fall, spring and summer in the years 2002 and 2003. Propagation tests at λ = 1064 nm were performed in dry weather conditions, while tests at λ = 1550 nm were performed in both dry and rainy weather conditions. Test conditions and results are presented below.

8.2.5.1 Propagation Trials at λ = 1064 nm

Propagation trials at λ = 1064 nm were performed using the PILASTER modular target located at the *Casa Marongiu* site and the ELOP-PLD laser system positioned along the target normal at a distance of 2.5 km, 4 km and 5.5 km. The target Mean Sea Level (MSL) altitude was about 500 m and the maximum altitude difference between the laser transmitter and the target was about 140 m at a distance of 5.5 km. The geometry of the λ = 1064 nm propagation tests performed at the PILASTER range are shown in Fig. 8-22. Table 8-7 shows the relevant data describing the meteorological conditions in which the atmospheric propagation measurements were performed (dry-air conditions). The various test cases have been grouped for classes of visibility and the corresponding International Visibility Code (IVC) classes are reported. When significant variations of T and/or RH were observed during the measurements, only the average values calculated in the relevant time intervals have been reported. The prevailing wind direction/intensity during the measurements is listed with respect to the laser to target slant-path (usual counter-clockwise convention). The values of the Turbulence Structure Constant (C_n) were determined using the *Scintec* BLS900 laser scintillometer, with a measurement baseline of 5 km between transmitter and receiver (along the target normal).

For each case listed in Table 8-7, a minimum of 25 energy measurements were performed (samples of 25 to 50 laser spot measurements were used) using at least two of the ELOP-PLD locations shown in Fig. 8-22. Dry-air extinction tests were performed in all meteorological conditions listed in Table 8-7 only with a system to target slant-range (SR) of 2.5 km. With SR = 4 km and SR = 5.5 km, extinction tests were performed in a representative sub-set of dry-air meteorological conditions. Rain extinction tests were not performed at λ = 1064 nm.

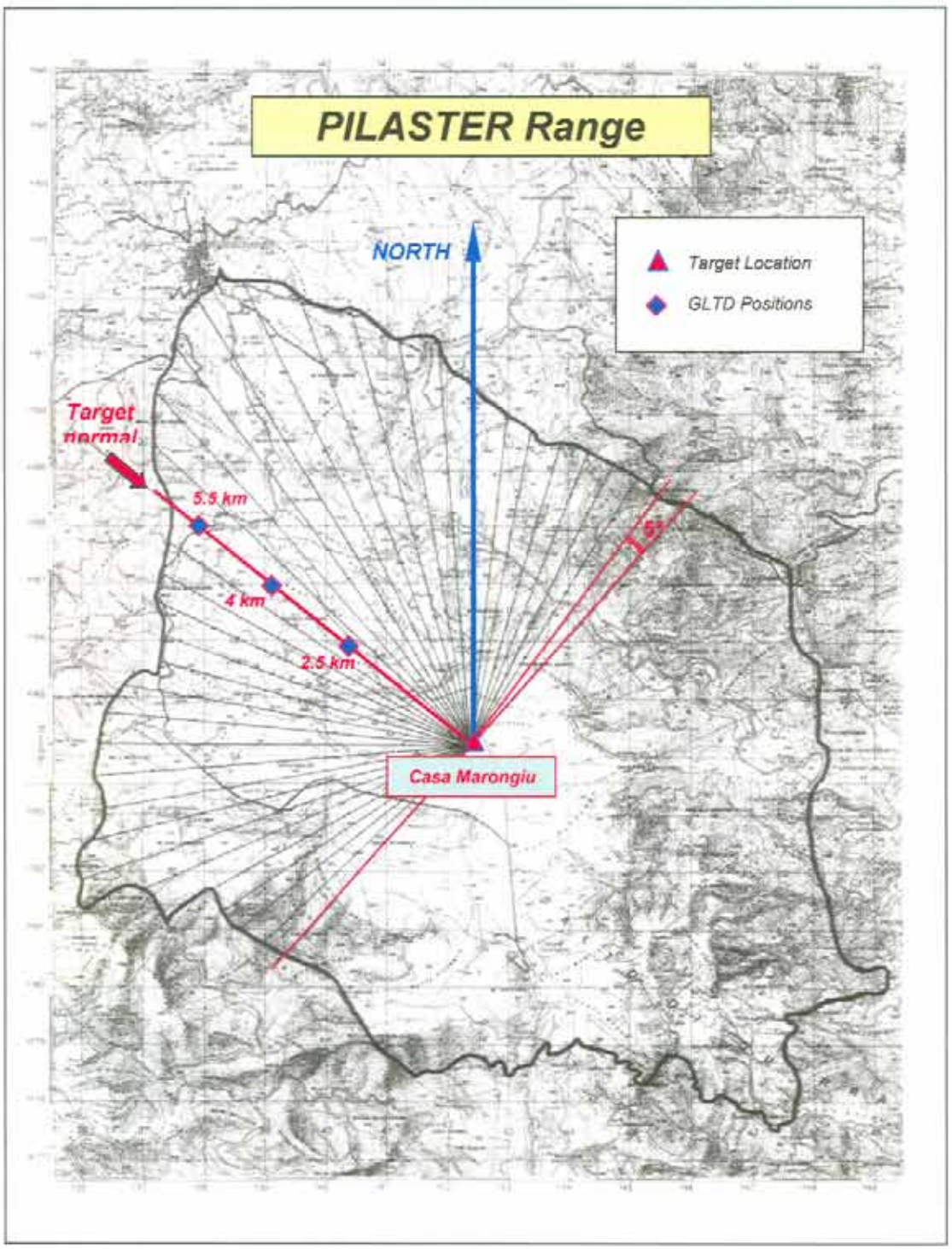

Figure 8-22. Geometry of atmospheric propagation measurements at λ = 1064 nm.

Transmittance and extinction coefficient values relative to the various test cases (i.e., meteorological conditions listed in Tables 8-7), calculated using the ESLM model with SR = 1 km, are listed in Table 8-8.

Group	Case	V (km)	RH (%)	T (°C)	C_n	Cloud	Wind (°/kts)	IVC
I	A	2.5	82	24	$6.77*10^{-8}$	6/8	0/0	Haze
	B	3.0	85	15	$1.80*10^{-8}$	5/8	0/0	
	C	3.5	76	23	$9.86*10^{-7}$	7/8	92/2	
II	A	5	73	25	$8.79*10^{-8}$	3/8	0/0	Light Haze
	B	6.0	66	27	$6.67*10^{-8}$	4/8	237/3	
	C	7.0	68	7	$1.82*10^{-7}$	7/8	0/0	
III	A	8.0	67	24	$8.96*10^{-8}$	3/8	0/0	
	B	8.5	58	28	$6.70*10^{-8}$	3/8	120/5	
	C	9.0	64	30	$2.92*10^{-7}$	4/8	0/0	
IV	A	10.0	51	20	$7.16*10^{-7}$	2/8	40/6	Clear
	B	10.5	58	28	$1.87*10^{-7}$	1/8	95/12	
	C	11	51	18	$6.39*10^{-8}$	2/8	120/8	
	D	12.5	48	32	$8.56*10^{-7}$	3/8	0/0	
V	A	14.5	52	18	$1.09*10^{-8}$	2/8	22/4	
	B	15.0	44	32	$4.87*10^{-7}$	3/8	320/7	
	C	18.5	56	24	$7.98*10^{-8}$	0/8	35/5	
VI	A	20.5	40	31	$4.49*10^{-8}$	0/8	0/0	Very Clear
	B	22.5	41	35	$5.87*10^{-7}$	2/8	25/8	
	C	25.0	47	35	$7.56*10^{-7}$	1/8	125/10	
	D	34.0	35	32	$6.84*10^{-8}$	0/8	15/7	

Table 8-7. Meteorological data for dry-air propagation measurements at λ = 1064 nm.

Group	Case	IVC Categ.	Model τ	Model γ (km^{-1})
I	A	Haze	0.077	1.025
	B		0.127	0,824
	C		0.168	0,714
II	A	Light Haze	0.287	0,500
	B		0.351	0,419
	C		0.448	0,321
III	A		0.455	0,315
	B		0.470	0,302
	C		0.476	0,297
IV	A	Clear	0.549	0,240
	B		0.532	0,252
	C		0.583	0,216
	D		0.575	0,221
V	A		0.652	0,171
	B		0.622	0,190
	C		0.675	0,157
VI	A	Very Clear	0.688	0,149
	B		0.684	0,152
	C		0.687	0,150
	D		0.755	0,112

Table 8-8. Calculated extinction coefficients for dry-air conditions (SR = 2.5 km).

The extinction coefficients in Table 8-8 were computed from ESLM model transmittances, using the simple equation:

$$\gamma = -\frac{\ln \tau}{SR} \tag{8.33}$$

However, it is important to observe that, although the ESLM model provides independent estimates of both absorptive transmittance (τ_{ai}) and scattering transmittance (τ_{si}), only the scattering contribution to the extinction coefficient (γ_{si}) is independent of range. We should remember, in fact, that the total precipitable water in mm is

$w = SR \cdot AH$ (where SR is the slant-range in km and AH is the absolute humidity in g/m^3), and AH is approximated by:

$$AH = 1322.8 \frac{RH}{T} exp\left[\frac{25.22(T - 273.16)}{T} - 5.31 ln\left(\frac{T}{273.16}\right)\right] \tag{8.34}$$

According to the ESLM model, as $w < 54$ in all cases listed in Table 8-7, the ESLM absorptive transmittance is given by:

$$\tau_{ai} = e^{-0.0363 \cdot \sqrt{w}} \tag{8.35}$$

Therefore, in this case, the absorptive extinction coefficient (γ_{ai}) is given by:

$$\gamma_{ai} = 0.0363 \cdot AH \cdot \frac{1}{\sqrt{SR}} \tag{8.36}$$

where the SR dependency of γ_{ai} is evident (obviously, for SR = 1 km the model γ_{ai} becomes a function of AH only). For instance, with SR = 10 km, the model γ_{ai} is about one third of the value calculated, with the same RH and T conditions, with SR = 1 km. In other words, the ESLM empirical model implies a range dependency of the extinction coefficient, which prevents a direct comparisons of the experimental γ values found at a certain SR with γ values predicted or measured at a different SR. Although this appears as a limitation of the ESLM model for practical applications, for all SR considered we determined τ from NIR-camera energy measurements and γ using equation (8.33), and compared the calculated values with the experimental results. Therefore, for each SR, different sets of corrections were computed simply by comparing the predicted ESLM τ and γ values with the experimental data.

Since the initial phases of the test activity, data collected in various meteorological conditions and with various laser slant-paths, demonstrated moderate discrepancies between the extinction measurements performed with EMT-1 and EMT-2 (i.e., 8% maximum difference, after EIM correction with C_1 and C_2). Furthermore, using the two techniques, no significant correlation was observed between the differences in the

measurements and the lengths of the laser slant-paths used to gather the experimental data. Table 8-9 shows the results of transmittance measurements performed using the EMT-2 technique for a laser slant-path of 2.5 km, compared with ESLM model computations.

Group	Case	IVC Categ.	Experim. τ	Model τ	Error (%)	Group Corr.	IVC Cat. Corr.
I	A	Haze	0.088	0.077	14.91	1.149	1.149
	B		0.146	0.127	15.15		
	C		0.192	0.168	14.57		
II	A	Light Haze	0.331	0.287	15.46	1.150	1.141
	B		0.406	0.351	15.69		
	C		0.510	0.448	13.80		
III	A		0.513	0.455	12.80	1.131	
	B		0.537	0.470	14.20		
	C		0.535	0.476	12.40		
IV	A	Clear	0.630	0.549	14.58	1.140	1.132
	B		0.597	0.532	12.17		
	C		0.666	0.583	14.23		
	D		0.662	0.575	15.14		
V	A		0.737	0.652	13.00	1.125	
	B		0.704	0.622	13.20		
	C		0.751	0.675	11.20		
VI	A	Very Clear	0.765	0.688	11.14	1.113	1.113
	B		0.767	0.684	12.16		
	C		0.760	0.687	10.52		
	D		0.840	0.755	11.27		

Table 8-9. Transmittance data and ESLM model corrections (λ = 1064 nm - SR = 2.5 km).

In all cases, the measured transmittance values (i.e., average of 25-50 spot measurements) were greater than the values computed using the ESLM model. The observed differences between measured and ESLM transmittances varied between 10.52% and 16.64%. The ESLM transmittance model corrections computed for each

group and for each IVC category are also listed in Table 8-9. It is evident, looking at the results in Table 8-9 and at their graphical representation in Fig. 8-23, that the difference between predicted and measured transmittance decreases significantly as atmospheric visibility increases.

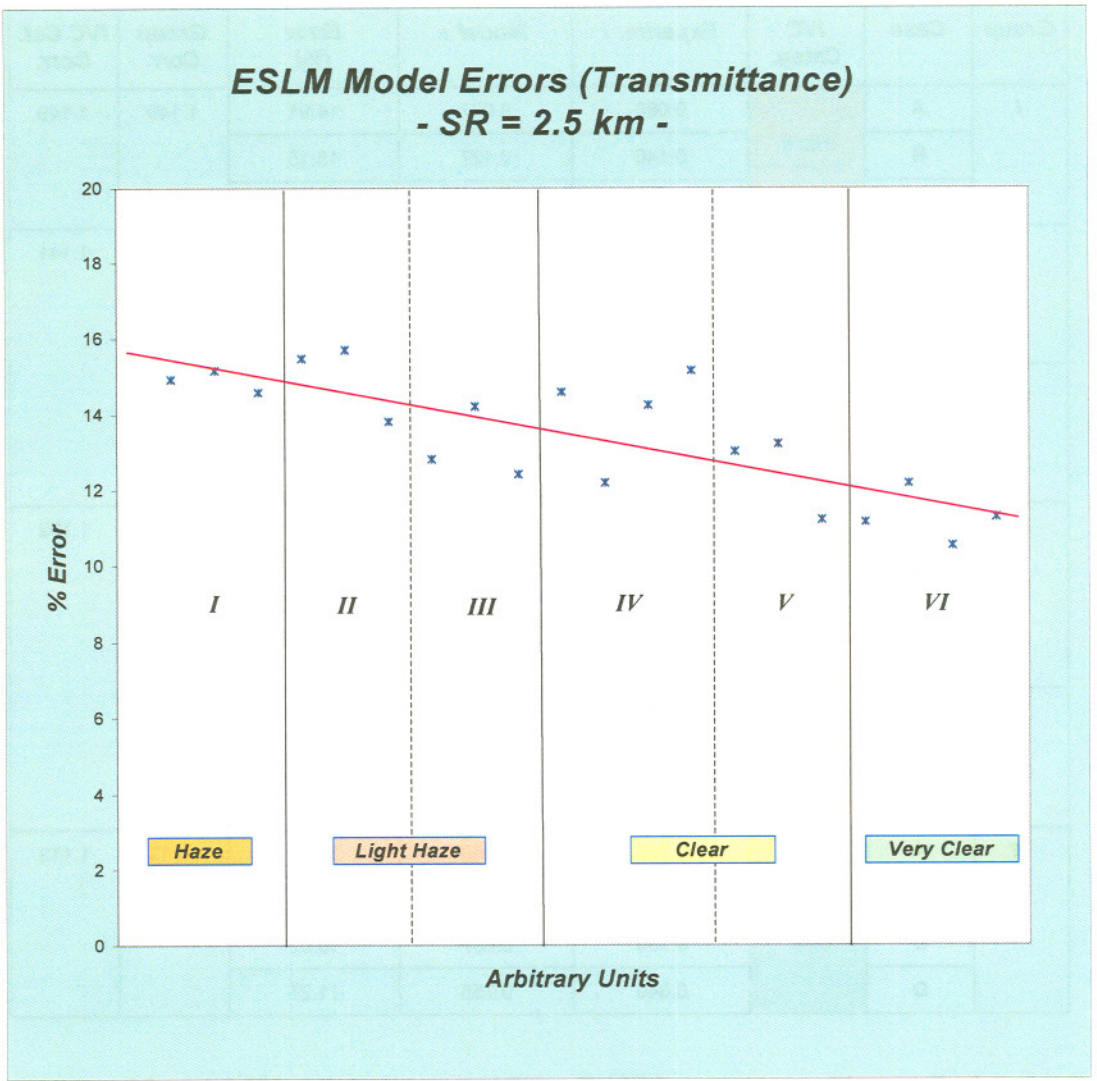

Figure 8-23. ESLM model errors (transmittance) for SR = 2.5 km.

Table 8-10 presents the same results (SR = 2.5 km) in terms of extinction coefficient.

Group	Case	IVC Categ.	Experim. γ (km^{-1})	Model γ (km^{-1})	Error (%)	Group Corr.	IVC Cat. Corr.
I	A	Haze	0.967	1,025	-5.64	0.923	0.923
	B		0.757	0,824	-8.09		
	C		0.647	0,714	-9.34		
II	A	Light Haze	0.437	0,500	-12.62	0.857	0.846
	B		0.360	0,419	-14.15		
	C		0.269	0,321	-16.10		
III	A		0.265	0,315	-15.99	0.836	
	B		0.249	0,302	-17.59		
	C		0.250	0,297	-15.75		
IV	A	Clear	0.186	0,240	-22.70	0.772	0.750
	B		0.207	0,252	-18.20		
	C		0.163	0,216	-24.66		
	D		0.165	0,221	-25.47		
V	A		0.122	0,171	-28.57	0.728	
	B		0.140	0,190	-26.11		
	C		0.115	0,157	-27.01		
VI	A	Very Clear	0.107	0,149	-28.24	0.692	0.692
	B		0.106	0,152	-30.21		
	C		0.110	0,150	-26.64		
	D		0.070	0,112	-37.99		

Table 8-10. Extinc. coeff. data and ESLM model corrections (λ = 1064 nm - SR = 2.5 km).

Experimental data and error computations relative to the measurements performed with SR = 4 km and SR = 5.5 km are presented in Tables 8-11 to 8-14. Although with these SR's measurements were not performed in all meteorological conditions listed in Table 8-7, looking at the available data it appears evident that the ESLM model errors, both for transmittance and extinction coefficient calculations, are comparable with the errors computed for SR = 2.5 km.

Group	Case	IVC Categ.	Experim. τ	Model τ	Error (%)	Group Corr.	IVC Cat. Corr.
II	A	Light Haze	0.179	0.147	17.88	1.214	1.213
	C		0.351	0.290	17.39		
III	B		0.384	0.323	15.92	1.212	
	C		0.410	0.332	18.96		
IV	A	Clear	0.489	0.406	17.03	1.192	1.168
	B		0.463	0.393	15.18		
V	C		0.652	0.570	12.52	1.143	
VI	A	Very Clear	0.681	0.590	13.34	1.154	1.154

Table 8-11. Transmittance data and ESLM model corrections (λ = 1064 nm - SR = 4 km).

Group	Case	IVC Categ.	Experim. τ	Model τ	Error (%)	Group Corr.	IVC Cat. Corr.
II	B	Light Haze	0.143	0.118	20.78	1.252	1.280
	C		0.233	0.188	19.48		
III	B		0.285	0.224	21.48	1.308	
	C		0.314	0.234	25.45		
IV	A	Clear	0.381	0.303	20.42	1.259	1.255
	B		0.371	0.294	20.69		
V	A		0.537	0.439	18.30	1.252	
	B		0.527	0.412	21.82		
VI	B	Very Clear	0.611	0.512	16.18	1.181	1.181
	D		0.726	0.621	14.41		

Table 8-12. Transmittance data and ESLM model corrections (λ = 1064 nm - SR = 5.5 km).

Group	Case	IVC Categ.	Experim. γ	Model γ	Error (%)	Group Corr.	IVC Cat. Corr.
II	A	Light Haze	0.430	0.480	-10.40	0.872	0.849
	C		0.262	0.309	-15.30		
III	B		0.239	0.283	-15.48	0.827	
	C		0.223	0.276	-19.17		
IV	A	Clear	0.179	0.225	-20.59	0.810	0.787
	B		0.192	0.233	-17.45		
V	C		0.107	0.140	-23.50	0.765	
VI	A	Very Clear	0.096	0.132	-27.19	0.728	0.728

Table 8-13. Extinc. coeff. data and ESLM model corrections (λ = 1064 nm - SR = 4 km).

Group	Case	IVC Categ.	Experim. γ	Model γ	Error (%)	Group Corr.	IVC Cat. Corr.
II	B	Light Haze	0.346	0.388	-10.80	0.881	0.850
	C		0.264	0.304	-13.00		
III	B		0.228	0.272	-16.16	0.818	
	C		0.211	0.264	-20.20		
IV	A	Clear	0.176	0.217	-19.09	0.809	0.774
	B		0.178	0.223	-19.29		
V	A		0.113	0.150	-24.71	0.738	
	B		0.116	0.161	-27.66		
VI	B	Very Clear	0.090	0.122	-26.53	0.703	0.703
	D		0.058	0.087	-32.95		

Table 8-14. Extinc. coeff. data and ESLM model corrections (λ = 1064 nm - SR = 5.5 km).

The ESLM model errors for computing γ, relative to the various test cases are shown in Fig. 8-24. The error trends were not significantly affected by the system to target SR and, in all cases, the ESLM model always over-estimated the extinction coefficient (i.e., under-estimated transmittance). Therefore, the experimental results are not in contrast

with the $1/\sqrt{SR}$ dependency of γ_{ai} implied in the ESLM empirical model. The under estimation of τ can be explained observing that the ESLM model is a two components model (i.e., scattering transmittance τ_{si} and absorptive transmittance τ_{ai}) whose empiric equations were derived from independent scattering and absorption measurements, in which either absorption or scattering were neglected due to the particular test conditions. On the other hand, the effects of turbulence and other linear and non-linear propagation phenomena not included in the ESLM model, did not seem to significantly affect the energy measurements performed using EMT-2 and the ELOP-PLD laser system in the specified test conditions.

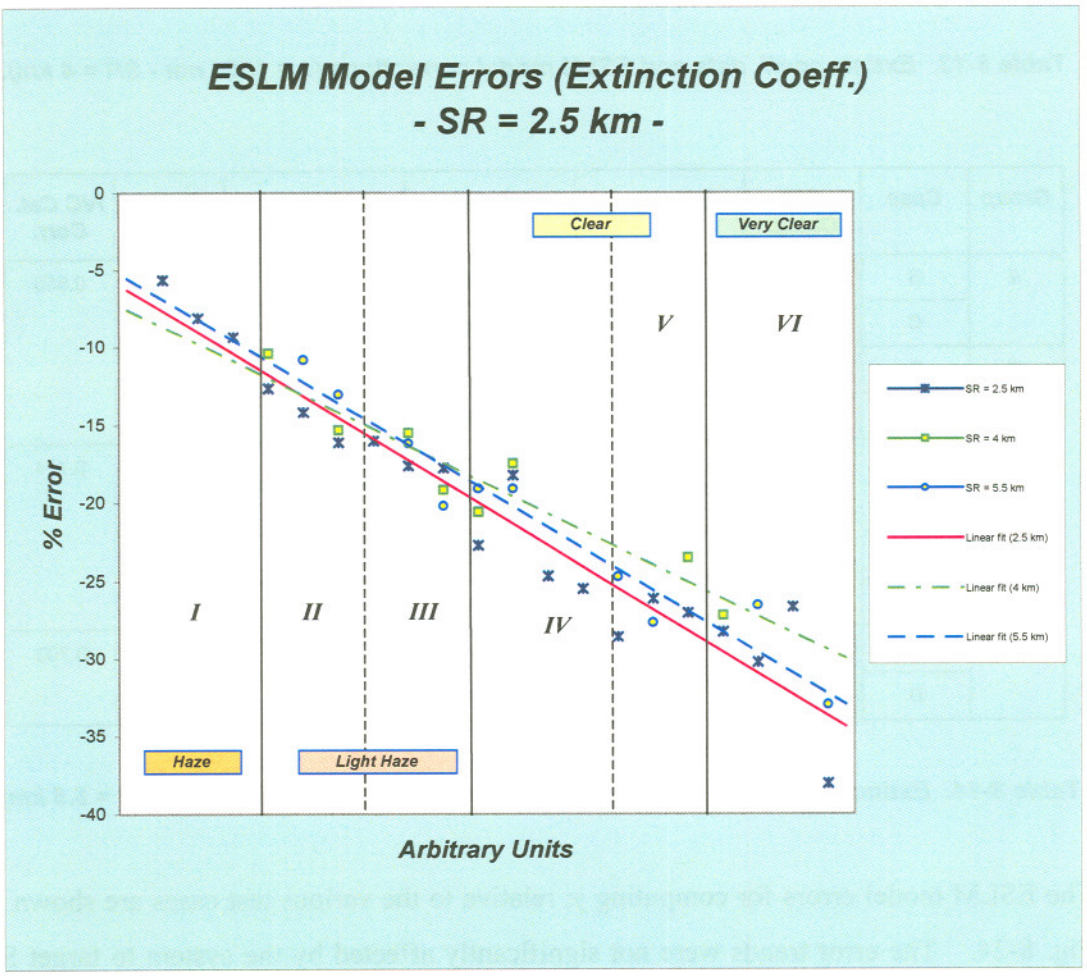

Figure 8-24. ESLM model errors for computation of γ (λ =1064 nm - SR = 2.5 km).

8.2.5.2 Propagation Tests at λ = 1550 nm

Propagation tests at λ = 1550 nm were performed using EMT-3, with the geometry illustrated in Fig. 8-7. The parameters describing the meteorological conditions during the tests are listed in the Tables 8-15 and 8-16.

Group	Case	V (km)	RH (%)	T (°C)	C_n	Cloud	Wind (°/kts)	IVC
1	a	3.0	82	25	$7.45*10^{-8}$	5/8	92/8	Haze
	b	4.0	85	21	$4.49*10^{-8}$	3/8	95/2	
2	a	7.0	78	22	$5.27*10^{-8}$	5/8	0/0	Light Haze
	b	8.0	67	25	$7.30*10^{-7}$	2/8	120/5	
	c	9.0	72	29	$2.65*10^{-8}$	4/8	45/8	
3	a	12.0	61	23	$3.15*10^{-8}$	3/8	0/0	Clear
	b	15.5	49	31	$5.90*10^{-8}$	0/8	0/0	
	c	18.0	55	28	$7.66*10^{-7}$	0/8	70/2	
	d	20.0	57	30	$5.23*10^{-7}$	2/8	54/11	
4	a	22.5	52	31	$5.80*10^{-7}$	0/8	0/0	Very Clear
	b	24.0	44	35	$4.65*10^{-7}$	0/8	130/6	
	c	28.0	57	35	$6.40*10^{-8}$	2/8	46/7	

Table 8-15. Meteorological data for dry-air propagation measurements at λ = 1550 nm.

Group	Case	V (km)	RH (%)	T (°C)	C_n	Wind (°/kts)	Rainfall (cm/hr)	Type of Rain
5	a	3.0	100	10	$3.22*10^{-7}$	23/4	2.10	Heavy rain
	b	5.0	90	12	$5.90*10^{-7}$	122/10	1.45	Med. Rain
	c	6.0	90	18	$8.12*10^{-8}$	15/5	0.30	Light rain

Table 8-16. Meteorological data for propagation measurements with rain at λ = 1550 nm.

The extinction coefficients calculated, for each case listed in the Tables 8-15 and 8-16, using the ESLM model, are listed in the Tables 8-17 and 8-18.

Group	Case	IVC	Model γ (km^{-1})
1	a	Haze	1.082
	b		0.890
2	a	Light Haze	0.689
	b		0.661
	c		0.671
3	a	Clear	0.573
	b		0.572
	c		0.556
	d		0.565
4	a	Very Clear	0.555
	b		0.556
	c		0.579

Table 8-17. Calculated extinction coefficients for dry-air.

Group	Case	Type of Rain	Model γ (km^{-1})
5	a	Heavy rain	2.944
	b	Med. rain	2.429
	c	Light rain	1.231

Table 8-18. Calculated extinction coefficients for rain.

The ESLM extinction coefficients in the Tables 8-17 and 8-18 were computed from model transmittances using the equation $\gamma = -ln\,\tau/SR$ with SR = 1 km. Experimental data and ESLM model errors relative to the measurements performed in both dry and rainy conditions are presented in the Tables 8-19 and 8-20.

Group	Case	IVC	Model γ	Exper. γ	Error %	Case Corr.	IVC Cat. Corr.
1	a	Haze	1.082	0.816	-24.56	0.754	0.745
	b		0.890	0.655	-26.43	0.736	
2	a	Light Haze	0.689	0.446	-35,20	0.648	0.647
	b		0.661	0.479	-27,58	0.724	
	c		0.671	0.381	-43,27	0.567	
3	a	Clear	0.573	0.332	-42,10	0.579	0.584
	b		0.572	0.382	-33,30	0.667	
	c		0.556	0.350	-37,10	0.629	
	d		0.565	0.261	-53,80	0.462	
4	a	Very Clear	0.555	0.324	-41,60	0.584	0.601
	b		0.556	0.354	-36,30	0.637	
	c		0.579	0.337	-41,67	0.583	

Table 8-19. Dry-air experimental data and ESLM model corrections (λ = 1550 nm).

Group	Case	Type of Rain	Model γ	Exper. γ	Error %	Case Corr.
5	a	Heavy rain	2.596	2.266	-12.70	0.873
	b	Med. rain	2.080	2.006	-3.56	0.964
	C	Light rain	0.864	0.729	-15.67	0.843

Table 8-20. Rain experimental data and ESLM model corrections (λ = 1550 nm).

It is evident that, also at λ = 1550 nm, there is a considerable difference between the experimental data and the ESLM model results. Again, the over estimation of γ can be explained observing that the ESLM model is a two components model whose empiric equations were derived from independent scattering and absorption measurements, in which either absorption or scattering were neglected due to the particular test conditions. Furthermore, as the ESLM model uses different sets of equations for modelling absorption at λ = 1064 nm and λ = 1550 nm, and slightly different parameters in the equations for modelling atmospheric scattering at the two wavelengths, remarkable

differences were observed between the results obtained at λ = 1064 nm and λ = 1550 nm. The differences in the overall (scattering plus absorption) transmittances and extinction coefficients, computed for a transmission path of 1 km and the same set of meteorological parameters listed in Table 8-15 (dry-air), are shown in Fig. 8-25. The greater contribution to the observed differences was due to absorptive extinction, which for λ = 1550 nm and $w > 1.1$, was modelled as:

$$\gamma_{ai} = -\frac{ln\left(0.802 \cdot \frac{1.1}{w}\right)^{0.111}}{SR} \tag{8.37}$$

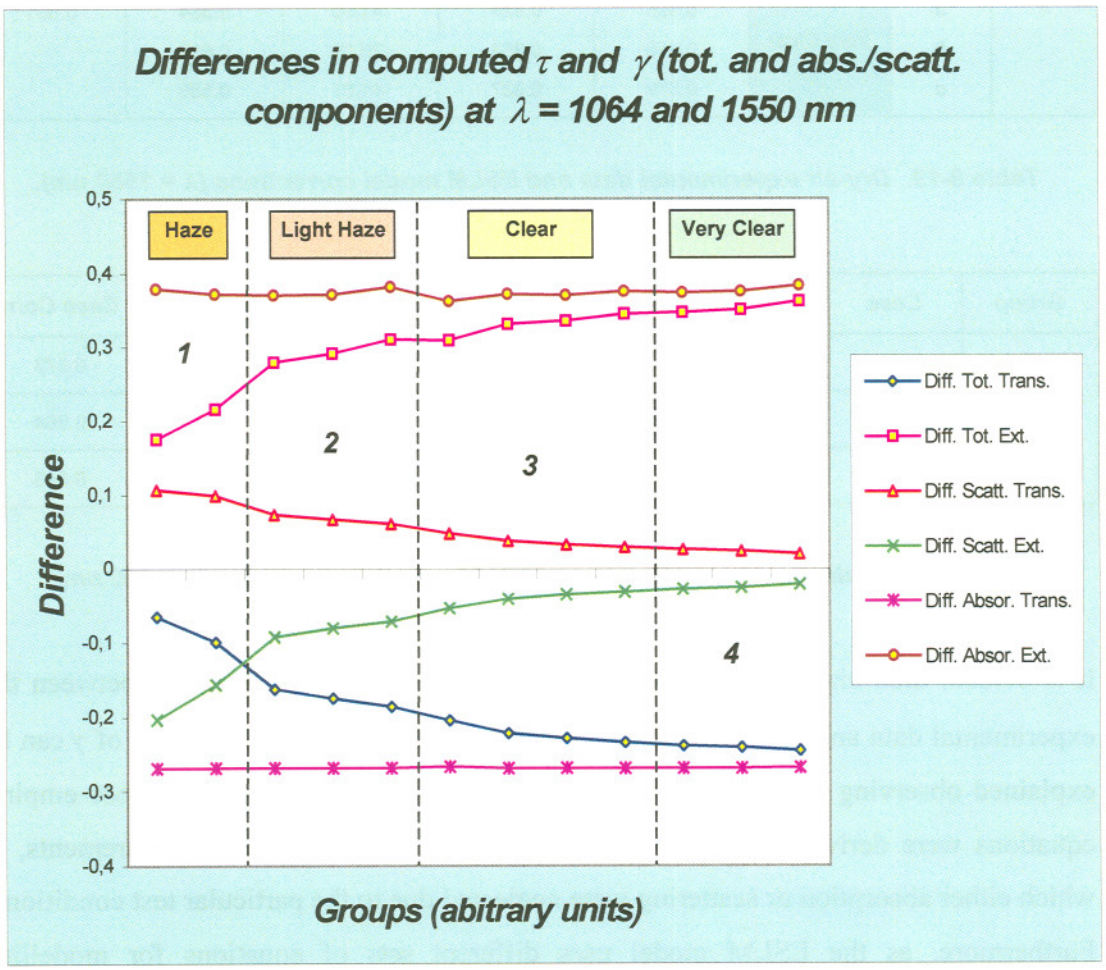

Figure 8-25. Differences in τ and γ (total and absorptive/scattering components) computed with the ESLM model for λ = 1064 nm and λ = 1550 nm.

On the other hand, the ESLM model for rainy conditions (modified using the LOWTRAN equation for estimating the scattering coefficient), fitted reasonably well the experimental data, with transmittance computation errors not exceeding 15.67% (light rain case).

8.2.5.3 Laser Propagation Data Base

Although the PILASTER Laser Propagation Data Base (LPDB) is at the initial stages of its compilation, and the quantity of experimental data collected is limited at the moment, current and future activities performed at the PILASTER range are expected to produce sufficient data to compute accurate correction factors required to increase the reliability of the propagation models used for simulation, mission planning and system performance analysis purposes.

With reference to the ESLM empirical model, the correction factors to the model presented above were computed by comparing measured and calculated transmittance/extinction values obtained from atmospheric visibility, relative humidity and temperature observations. Particularly, all experimental data (i.e., spot energy measurements) collected for each group-case were cumulated, and only results relative to the average energy measurements were presented in the various tables. Adopting this approach, it is evident that some information was lost in the process (i.e., the fluctuations experienced by the measured laser spot energies and the consequent variations of the errors/corrections computed for each spot measurement in all samples considered).

It is believed that a statistical approach, making use of the LPDB, would be well suited for a progressive refinement of the atmospheric model corrections. As an example, the *Atmospheric Model Correction Functions* (AMCF's) relative to the tests performed in dry weather at $\lambda = 1064$ nm are presented in Fig. 8-26.

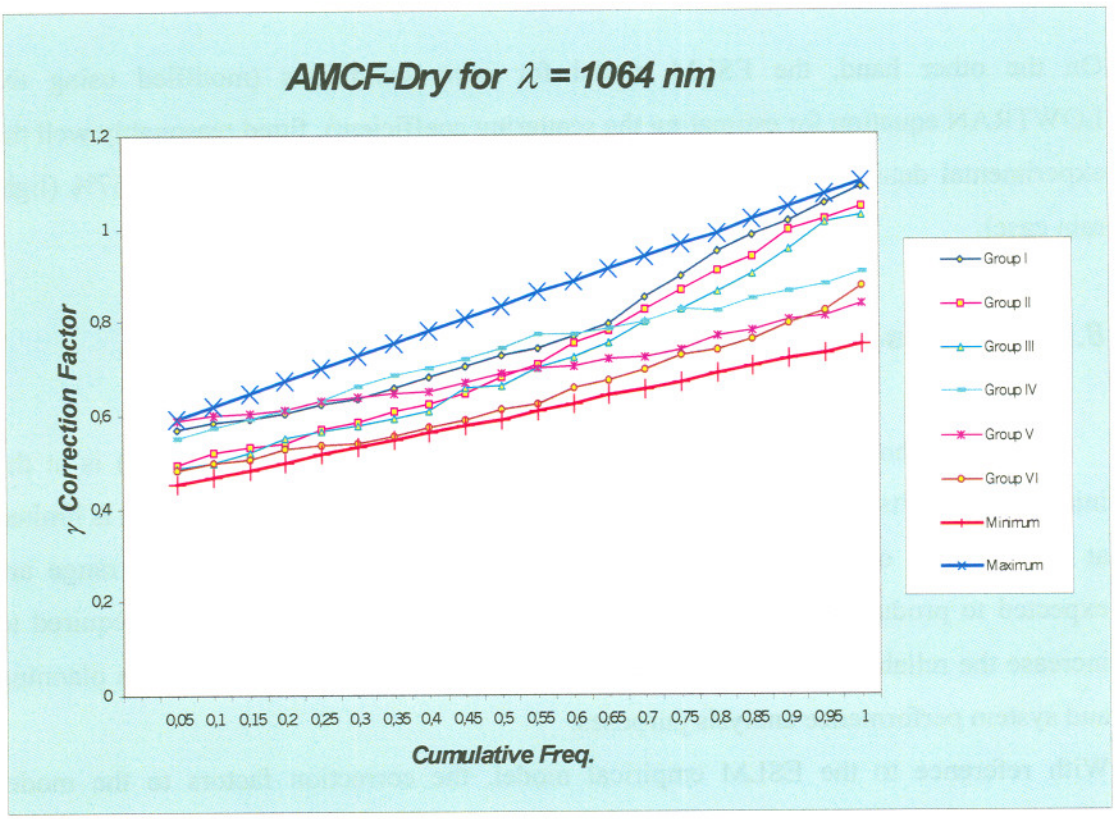

Figure 8-26. Correction functions for ESLM-Dry γ computations with λ = 1064 nm.

The lines denoted "Minimum" and "Maximum" in the graph, represent the lower and upper bounds of all AMCF's. The equations fitting these lines are the following:

$$Minimum \rightarrow y = 0.3123x + 0.4344 \tag{8.38}$$

$$Maximum \rightarrow y = 1.8812x + 1.0656 \tag{8.39}$$

Depending on the specific application, these equations can be used to determine corrections for the atmospheric propagation factors computed using the ESLM model. For instance, eq. (8.39) can be used in eye-safety studies, where a lower bound approximation for the computed atmospheric transmittance is to be considered acceptable, while eq. (8.38) is most convenient for applications like range performance

prediction and simulation studies for the operational employment of laser guided weapons, where an upper bound approximation is preferable.

It is important to note that an essential pre-requisite to this approach is the definition of a probability level which is adequate for the specific application. In most safety studies for test/training operations at the ranges a 100% probability would be adopted, while for the majority of operational mission planning tasks (e.g., range performance calculations and 'spiker' aircraft mission profile optimisation) a lower probability level may be accepted (e.g., 50-80%), depending on the operational needs and the geometric constraints of the mission (i.e., target 'lethal range', aircraft/systems limitations, time constraints, etc.).

8.2.6 LRF/LTD Systems Pointing Accuracy

Using the LTM-STU instrumentation, the pointing accuracy of various ground LRF/LTD systems (for FAC operations) was determined. The tests were performed using the PILASTER modular target and STU instrumentation. The tested Nd:YAG LRF/LTD systems were the following:

- ELOP (Electro-optics Industries Ltd) PLD;
- LITTON (Litton Systems Inc.) GLTD;
- CILAS (Compagnie Industrielle de Lasers) G3.

The measurements were performed with the 3 LRF/LTD systems (PRF = 10 Hz) located at a slant-range of 5 km from the target (laser spot perpendicular to the target). The systems were aimed at the target by qualified FAC operators and activated for periods of 30 seconds, in the same atmospheric conditions (V = 22 km, T = 32 °C and RH = 45%).

The pointing accuracy data (i.e., displacement of the energetic and geometric centres of the laser spots on the target with respect to the target centre) were obtained using the procedures described below for the three cases of slightly distorted, highly distorted and broken laser spots.

Moderately/Highly Distorted Spots. For laser spots preserving a shape almost circular and an energy profile approximately *Gaussian* (like the original laser signal at the system aperture), the geometric centre was computed as the centre of the smallest circle inscribing the laser spot. The spot energy centroid (maximum of the laser energy) was determined by using a dedicated interpolation function available with the IMAGE-PRO PLUS software (see Fig. 8-27).

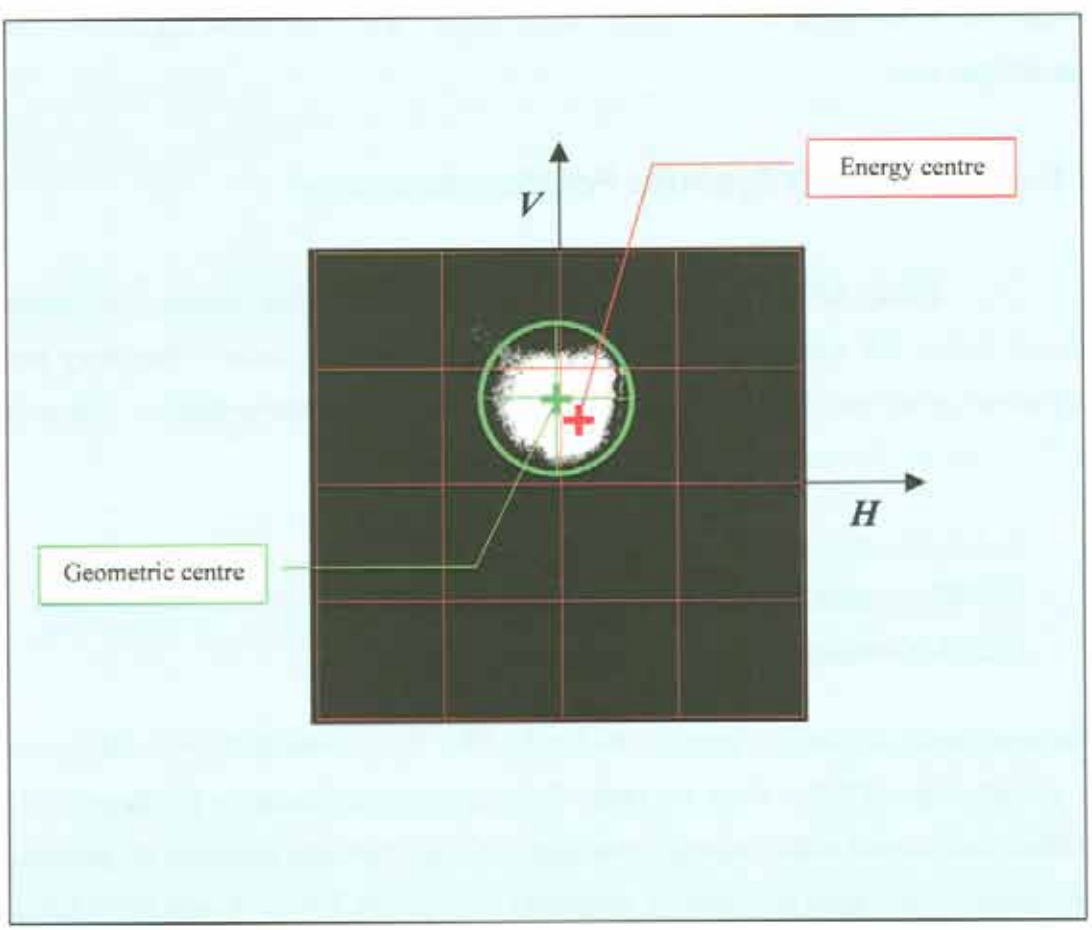

Figure 8-27. Pointing accuracy measurements on a slightly distorted laser spot.

An example of computations performed on an highly distorted laser spot is shown in Fig. 8-28.

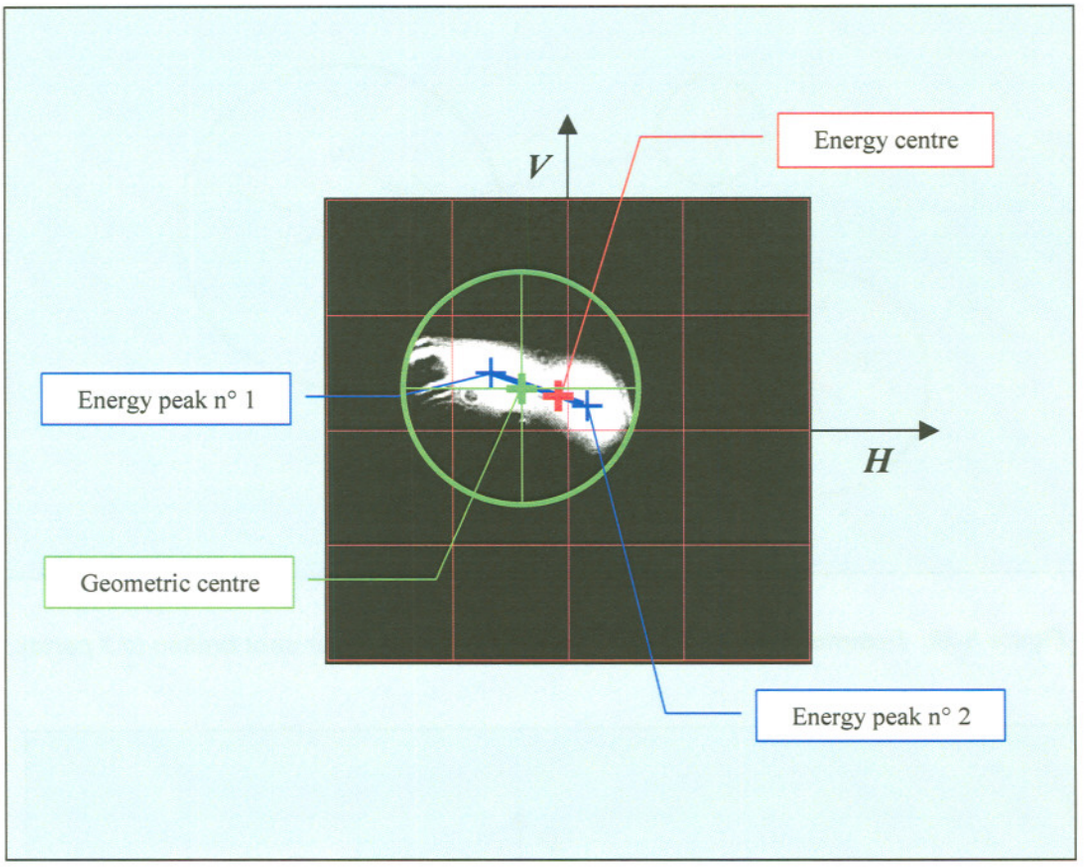

Figure 8-28. Pointing accuracy measurements on a highly distorted laser spot.

Broken spots. For broken spots (with significantly high energy densities in the broken parts), the energy centre was also computed with the same IMAGE-PRO PLUS interpolation function. In this case, however, the geometric centre of the spot was computed with a dedicated algorithm, using as many circles as the broken portions (with dimensions inscribing the portions) and performing a weighted average in which the weighting factors were the ratios of the single circle radiuses to the sum of all radiuses. Low energy spot portions (with energy content minor than 1%) were not considered in the computation algorithm. A scheme relative to the algorithm used for determining the broken spot geometric centre is illustrated in Fig. 8-29. An example of computations performed on a broken spot (3 parts) is shown in Fig. 8-30.

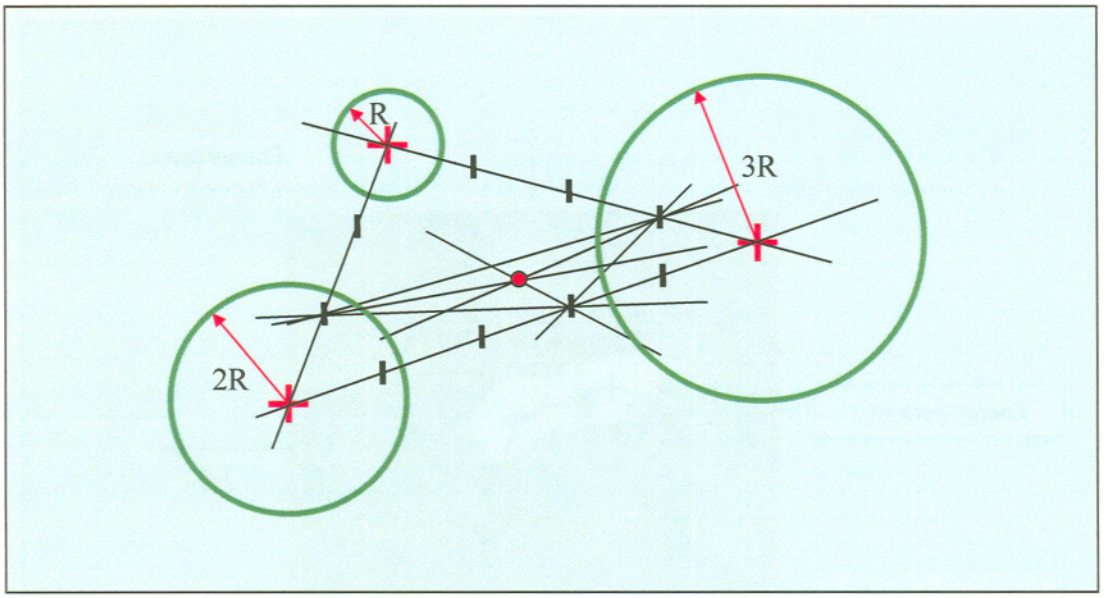

Figure 8-29. Determination of the spot geometric centre (laser spot broken in 3 parts).

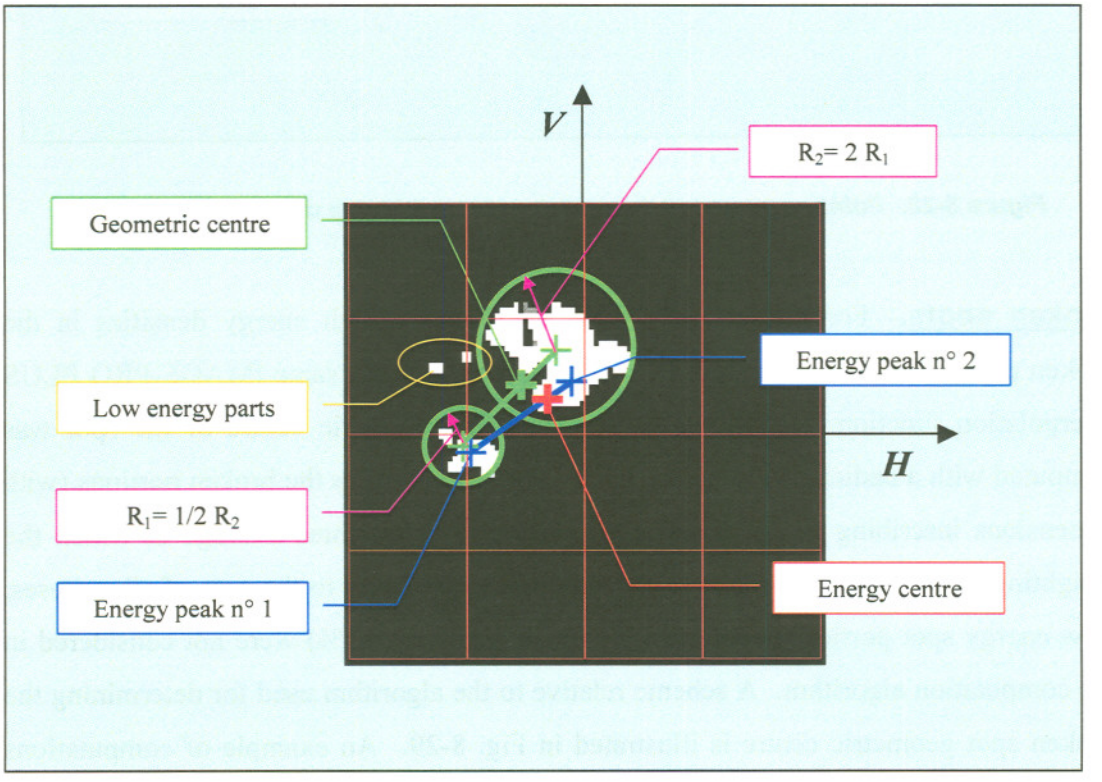

Figure 8-30. Example of pointing accuracy measurements on a broken laser spot.

In all cases, the position of the geometric and energetic centres were referenced to the target bi-dimensional Cartesian frame (i.e., horizontal/vertical scales and origin at the target centre). Since the operator aimed the LRF/LTD exactly at the centre of the target, the geometric and energetic pointing errors were determined (for each available spot frame) as the RSS of the horizontal and vertical error components. During these measurements, the relevant atmospheric parameters were recorded (i.e., visibility, temperature, relative humidity, wind intensity/direction, etc.).

Since the collected laser spot images were not simultaneous and the acquisition events were not synchronised, the positions of the geometric and energetic centres were computed at least 3 times for each second (i.e., a minimum of 90 times for each system in a 30 seconds laser illumination session), and the average displacement errors of the geometric and energetic centres (i.e., average pointing errors) were calculated for each second. The results of the measurements are shown in the Figs. 8-31, 8-32 and 8-33.

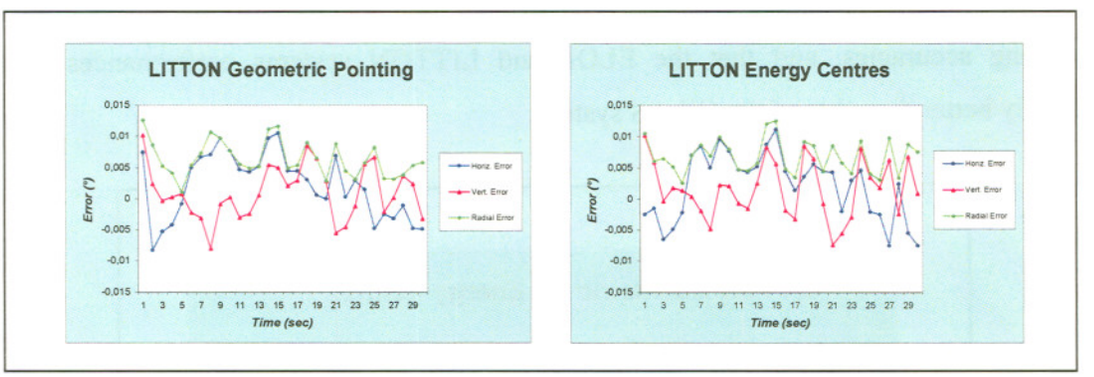

Figure 8-31. LITTON GLTD pointing accuracy measurements.

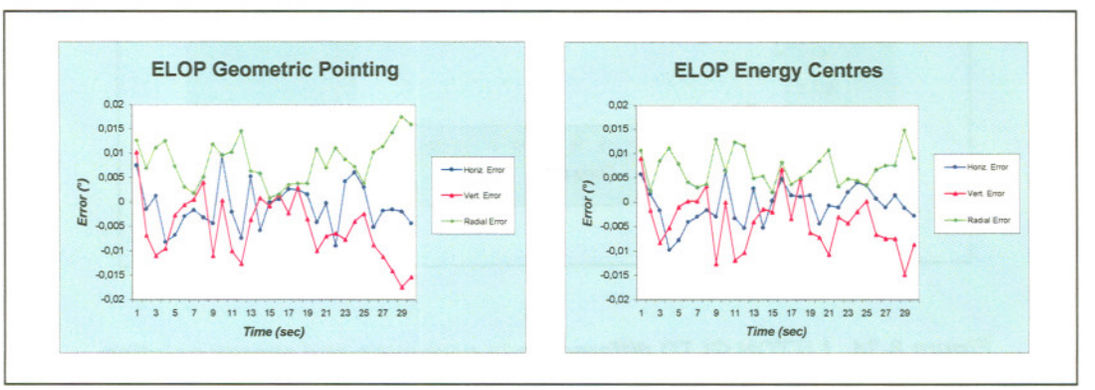

Figure 8-32. ELOP PLD pointing accuracy measurements.

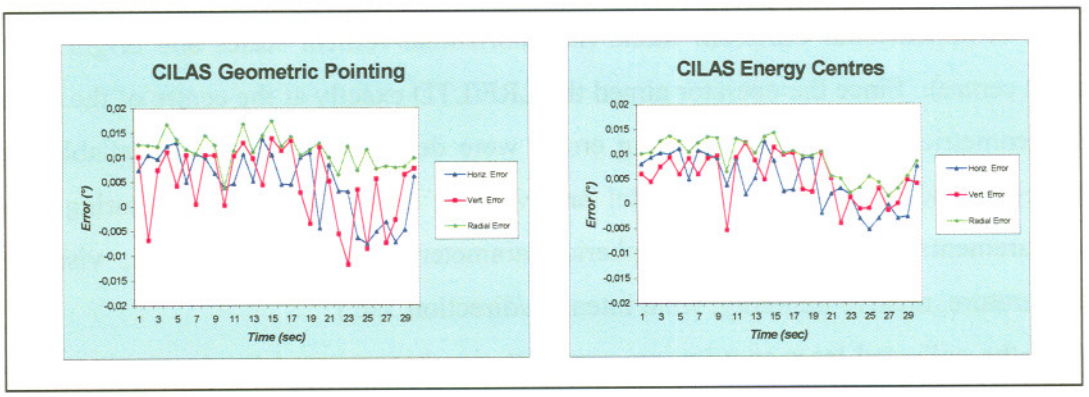

Figure 8-33. CILAS G3 pointing accuracy measurements.

Figs 8-34, 8-35 and 8-36 show the graphs relative to the differences between geometric and energetic pointing data. Table 8-21 resumes the results of the pointing errors measurements of the three systems in terms of Geometric Pointing Accuracy (GPA) and Energy Pointing Accuracy (EPA). It is evident that the three systems had similar pointing accuracies, and that the ELOP and LITTON systems performances were slightly better than that of the CILAS system.

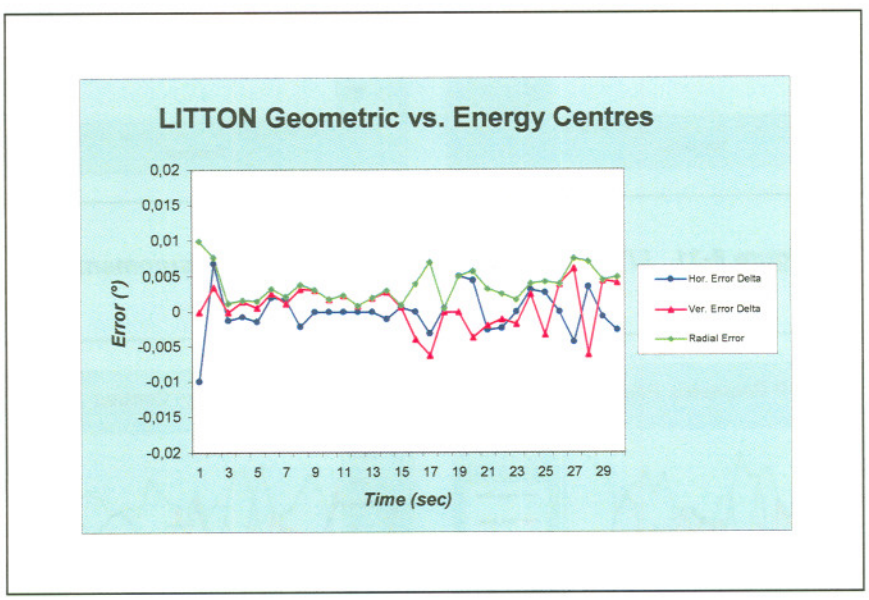

Figure 8-34. LITTON GLTD differences in geometric and energy pointing.

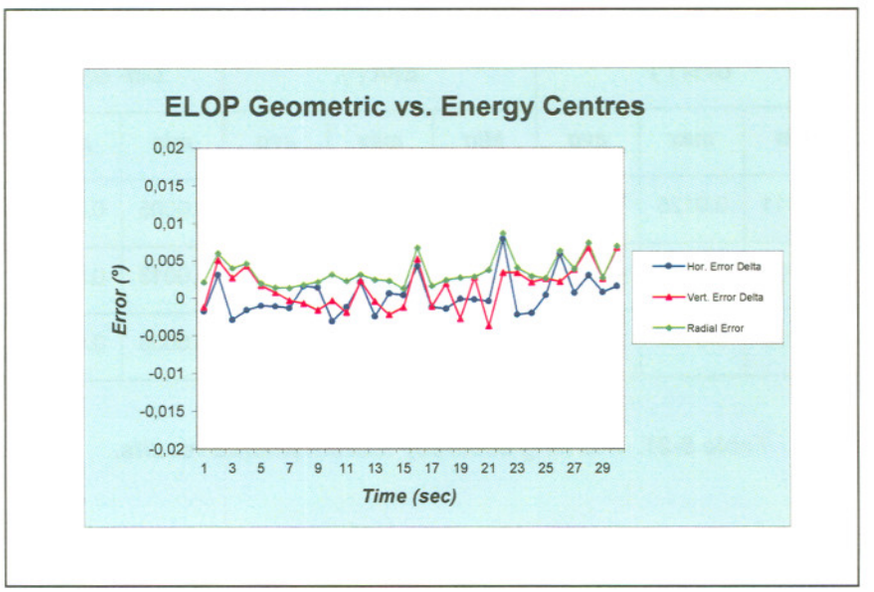

Figure 8-35. ELOP PLD differences in geometric and energy pointing.

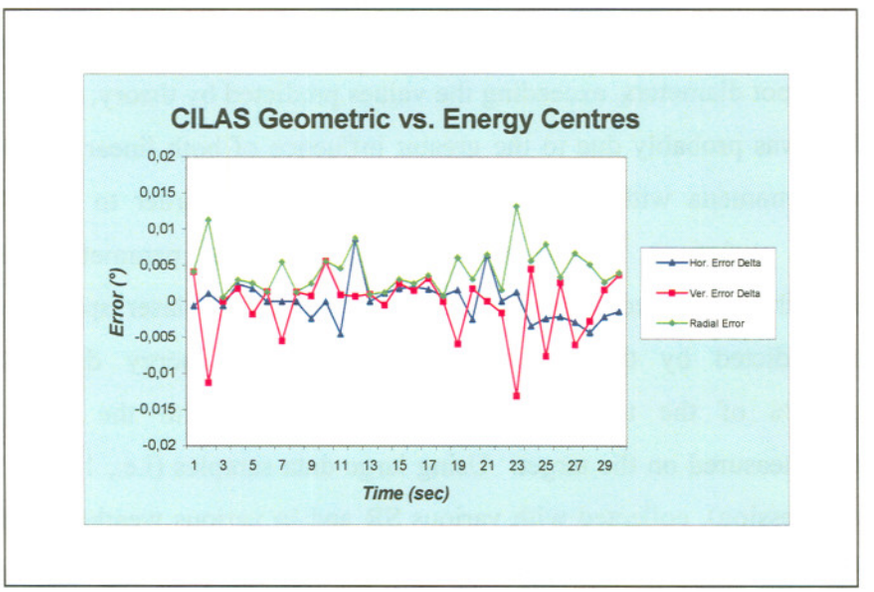

Figure 8-36. CILAS G3 differences in geometric and energy pointing.

System	GPA (°)			EPA (°)			Diff- GPA-EGA (°)		
	min	max	avg	Min	max	avg	min	max	avg
LITTON	0.0011	0.0126	0.0064	0.0026	0.0125	0.0069	0.0005	0.0099	0.0037
ELOP	0.0008	0.0175	0.0083	0.0030	0.0148	0.0070	0.0013	0.0086	0.0035
CILAS	0.0038	0.0174	0.0114	0.0014	0.0143	0.0091	0.0006	0.0132	0.0052

Table 8-21. Pointing accuracy measurements results.

8.2.7 Laser Spot Spreading and Distortion Measurements

Performing EMT tests at λ = 1064 nm (ELOP-PLD system), with system to target slant-ranges (SR) between 1500 m and 5.5 km, it was observed that the laser spot images collected by the Phoenix NIR-camera were characterised by a progressive increase of the spot diameters, exceeding the values predicted by theory, with increasing SR. This fact was probably due to the greater influence of both linear and non-linear propagation phenomena with longer propagation paths. In order to investigate, by monitoring the variations of the relevant meteorological parameters along the transmission paths, the effects induced by these phenomena, laser spots shapes and dimensions predicted by theory, assuming a *Gaussian* energy distribution and considering 95% of the total energy, were compared with the effective spot characteristics measured on the target. Using large data samples (i.e., 150 to 200 laser spots for each session), collected with various SR and in various weather conditions, it was possible to obtain useful data about laser spot spreading and distortion characteristics at λ = 1064 nm. The analytical methods used for spreading/distortion measurements with moderately and highly distorted laser spots are described below.

Using the *1/e* divergence ($\Phi_{1/e}$) of the laser beam, the laser spot divergence at 95% of total energy was computed by:

$$\Phi_{95\%} = \frac{\Phi_{1/e}}{\sqrt{\frac{ln(1-0.632)}{ln(1-0.95)}}} \tag{8.33}$$

For the ELOP-PLD, since $\Phi_{1/e}$ = 0.130 mrad, we obtained $\Phi_{95\%}$ = 0.225 mrad. The expected 95%-energy laser spot radius (R) at a given distance (d) was obtained by:

$$R = d \cdot tan\, \Phi_{95\%} + a \tag{8.34}$$

where a is the output beam diameter. For instance, for the ELOP-PLD system located at SR = 5000 m, we obtained R = 1.215 m. In order to define the laser spot distortion characteristics, the following spot measurable elements were considered (see Fig. 8-37):

- Radius of the smallest circle inscribing the entire spot (R_1);
- Radius of the smallest circle, centred in the spot geometric centre C, contained by the spot image (R_2);
- Distance between energetic and geometric centres (d_{ge}).

These spot elements were combined to conveniently describe the spot quality in terms of spreading and distortion. Particularly, the following Spot Distortion Parameters (SDP's) were defined:

$$Q_S = \frac{R}{R_1} \tag{8.35}$$

$$Q_{De} = 1 - \frac{d_{ge}}{R_1} \tag{8.36}$$

$$Q_{Dg} = \frac{R_2}{R_1} \tag{8.37}$$

The parameter Q_S describes the spot spreading, Q_{De} is relative to the energy profile distortion and Q_{Dg} is relative to the geometric distortion of the laser spot. Conveniently,

the SDP parameters were so that they equated to 1 in the ideal *Gaussian* case and tend to 0 in the worst case.

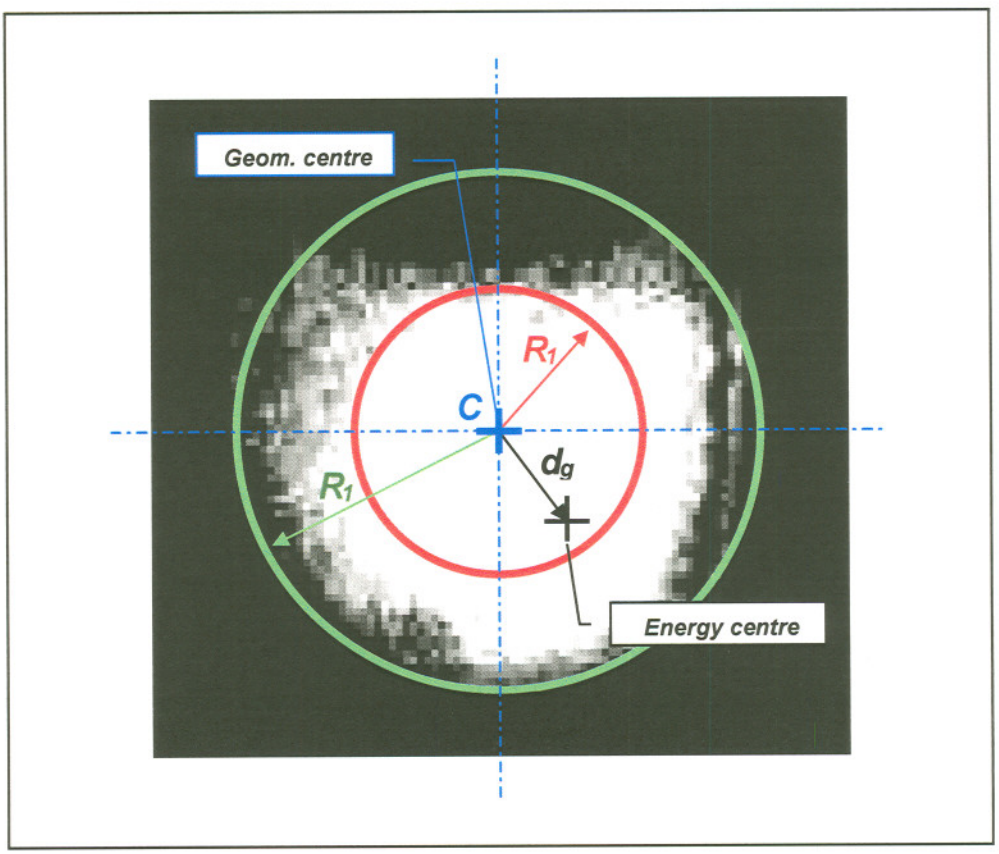

Figure 8-37. Measurable elements used for distorted spot analysis.

The results of the spot spreading measurements (average $2R_1$ values) are shown in Fig. 8-38, together with the calculated 1/e and 95%-energy spot diameters. Although in certain cases the measured spot diameter (average of 150-200 measurements) was less that the calculated 95%-energy spot diameter, the average data showed that the spot spreading was much more significant at greater slant-ranges. Furthermore, it was observed that also the SDP parameters increased significantly their values at increasing slat-ranges. The average SPD values and their variations during measurements performed with the ELOP-PLD (λ = 1064 nm) at SR = 1500 m, 3.5 km and 5.5 km are listed in Table 8-22.

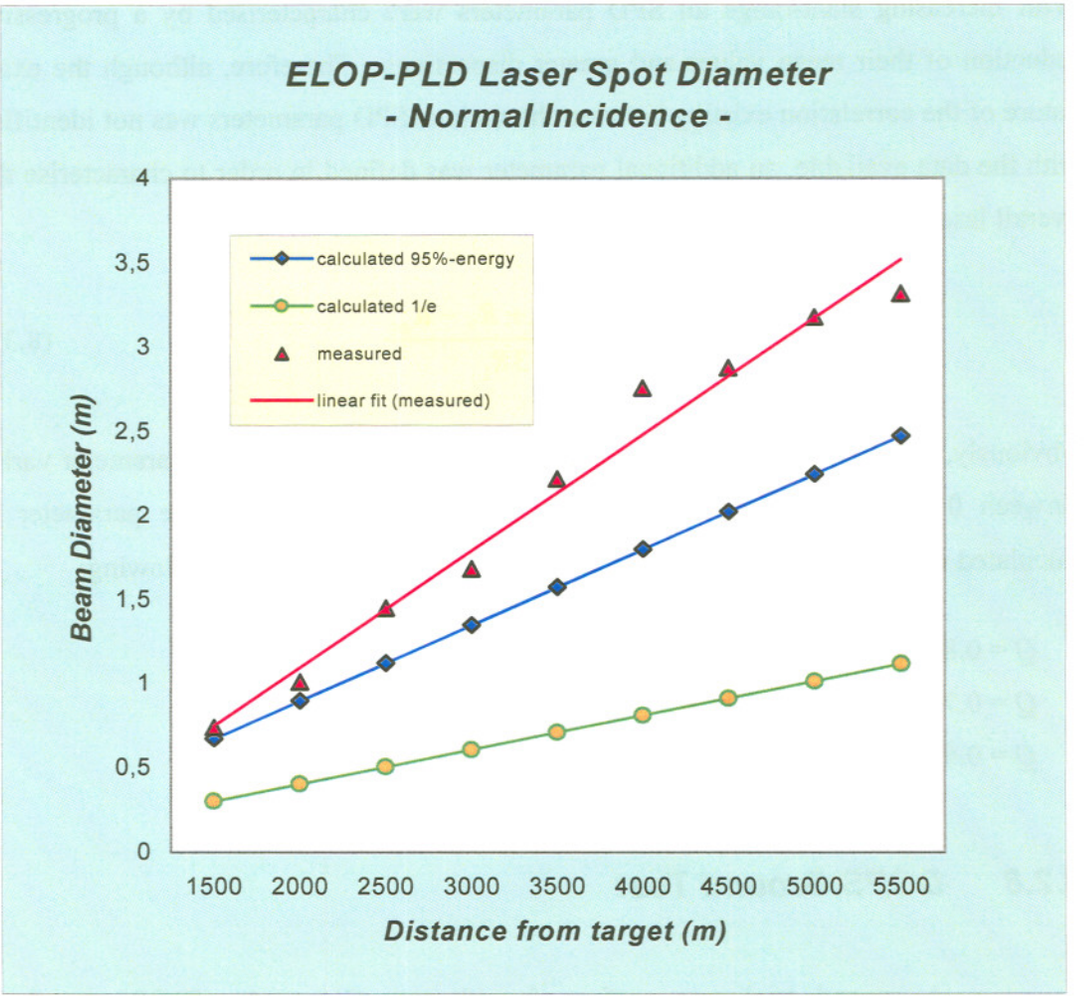

Figure 8-38. ELOP-PLD calculated/measured spot diameters for various slant-ranges.

SPD	1500 m		3.5 km		5.5 km	
	mean	σ	mean	σ	mean	σ
Q_S	0.8455	0.1350	0.8381	0.1799	0.6860	0.2830
Q_{de}	0.8329	0.0913	0.7184	0.1575	0.6119	0.1837
Q_{dg}	0.7275	0.1289	0.6930	0.1340	0.6607	0.1723

Table 8-22. SPD parameters relative to the ELOP-PLD spot distortion measurements.

With increasing slant-range all SPD parameters were characterised by a progressive reduction of their mean values and greater dispersions. Therefore, although the exact nature of the correlation existing between the various SPD parameters was not identified with the data available, an additional parameter was defined in order to characterise the overall laser spot quality:

$$Q = \frac{R + R_1 + R_2 - d_{gc}}{3R_1} \tag{8.38}$$

Obviously, as all the SPD parameters vary between 0 and 1, also the Q parameter varies between 0 and 1 (ideal *Gaussian* case). The average values of the parameter Q calculated with the available ELOP-PLD data (λ = 1064 nm) were the following:

- Q = 0.8020 for SR = 1500 m;
- Q = 0.7498 for SR = 3500 m;
- Q = 0.6529 for SR = 5500 m.

8.2.8 DGPS Ground Test

A ground trial was performed with two C/A code (D)GPS receivers (ASHTECH-12 geodetic receivers) in order to test the accuracy of the (D)GPS data (i.e., suitability for laser systems testing and post-mission analysis requirements) and to gain a good level of confidence with differential techniques, before performing flight trials.
During the preliminary ground session, one of the ASHTECH GPS receivers was installed on an electrically powered trolley and another ASHTECH receiver was located in a surveyed site to provide data for differential corrections. The trolley covered a well known route of about 3 km in the Turin International Airport (Caselle - Italy). The track was followed twice (in opposite directions) along a road about 6.2 metres wide. The trolley track is shown in Figure 8-39, where also the reference station position is evidenced. After the trial, data stored into the internal memories of the two receivers were downloaded to a personal computer for differential processing and analysis using the ASHTECH P-NAV software package.

Positioning data after differential processing and post-processing noise reduction were very precise, so that all data points were laying within the road. The stand-alone accuracy of the GPS receivers was within the specification limits (i.e., 52 m 2d-RMS against the specified 100 m 2d-RMS with SA). The final results obtained with the ASHTECH and TRIMBLE differential processing were very encouraging with a position data accuracy of about 3 m SEP.

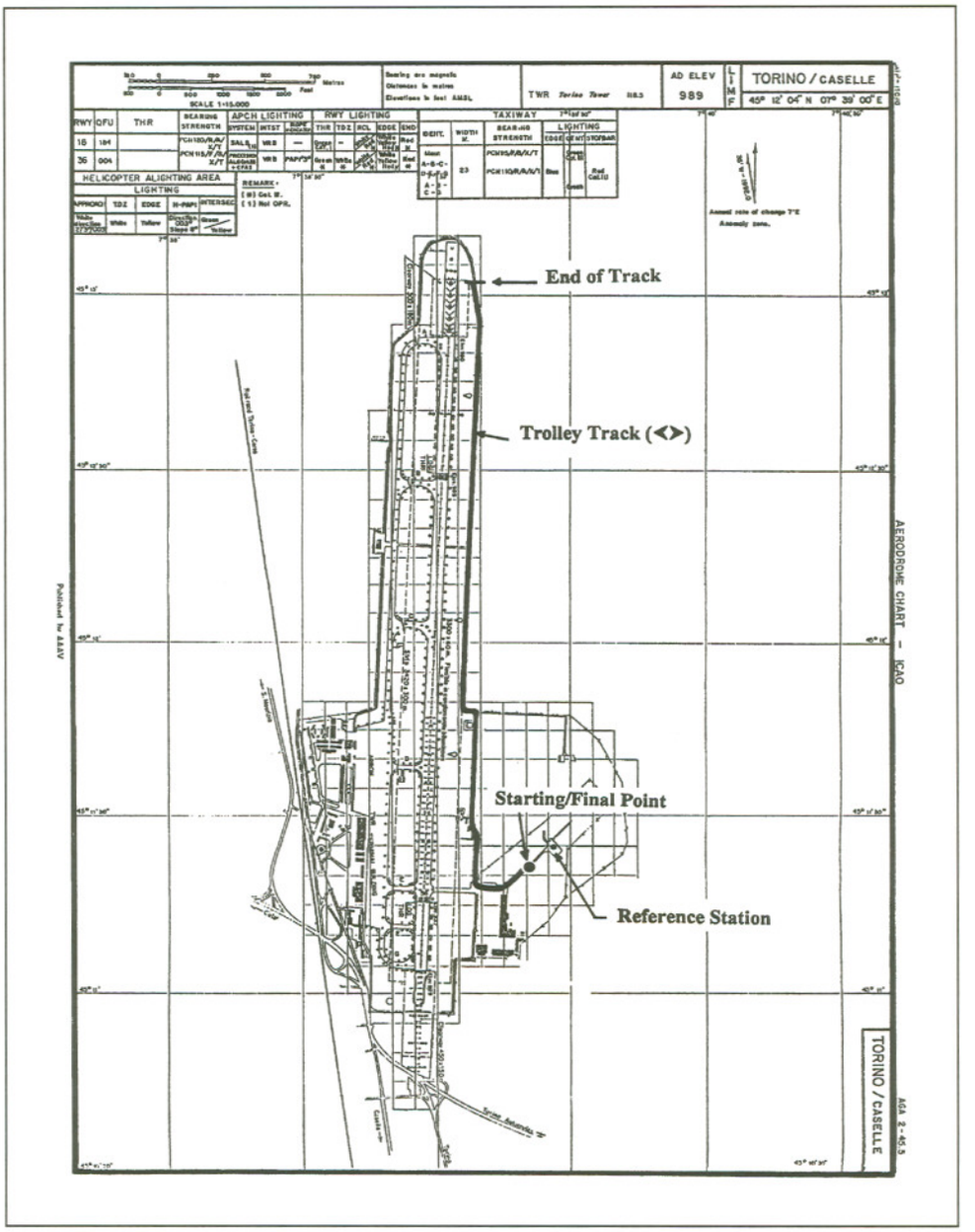

Figure 8-39. (D)GPS system ground track.

Even if the ground test results could not be considered exhaustive for demonstrating the performance of the PILASTER DGPS system, the activity permitted to gain a certain level of confidence with differential techniques, essential for planning and properly executing a dedicated flight test activity.

8.2.9 LOAS ground testing

Ground trials of the LOAS system were performed in order to preliminarily verify system detection performance in various weather conditions, and to test the validity of the mathematical models used for performance calculations. This was particularly important for preparing the LOAS flight test activity. It was in fact necessary to define a criteria for determining the system detection range performances in the worst environmental conditions, and with the worst obstacle scenarios (i.e., small wires with low reflectivity), even without performing real tests in these conditions (i.e., using experimental data collected in fear weather and with average obstacles). Mathematical modelling and ground testing of the LOAS detection performance were therefore required in order to give proper weights to the parameters playing a role in realistic operational scenarios, and to determine the target LOAS detection performances to be demonstrated in flight. Fig. 8-40 illustrates the process involved.

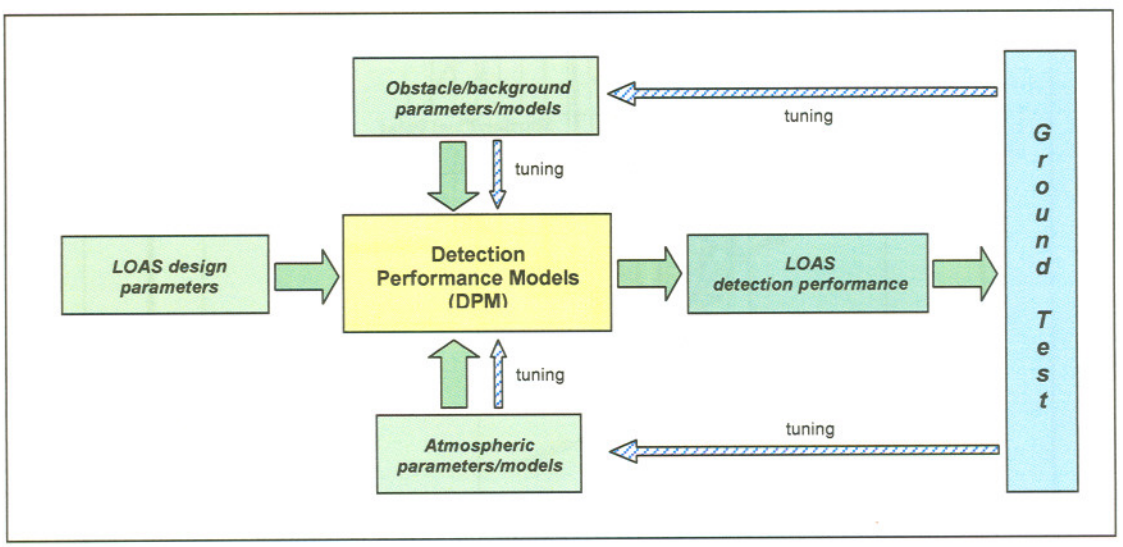

Figure 8-40. LOAS detection performance modelling and ground testing.

As the ground test activities permitted to validate the models developed, it was then possible to identify reference sets of obstacle, background and atmospheric parameters giving the absolute minimum performance of the LOAS system. This is illustrated in Fig. 8-41. Obviously, the successive flight test activities were performed only in a small portion of the LOAS/helicopter operational envelopes, but the results obtained could be extended to the entire envelopes by using the validated mathematical models.

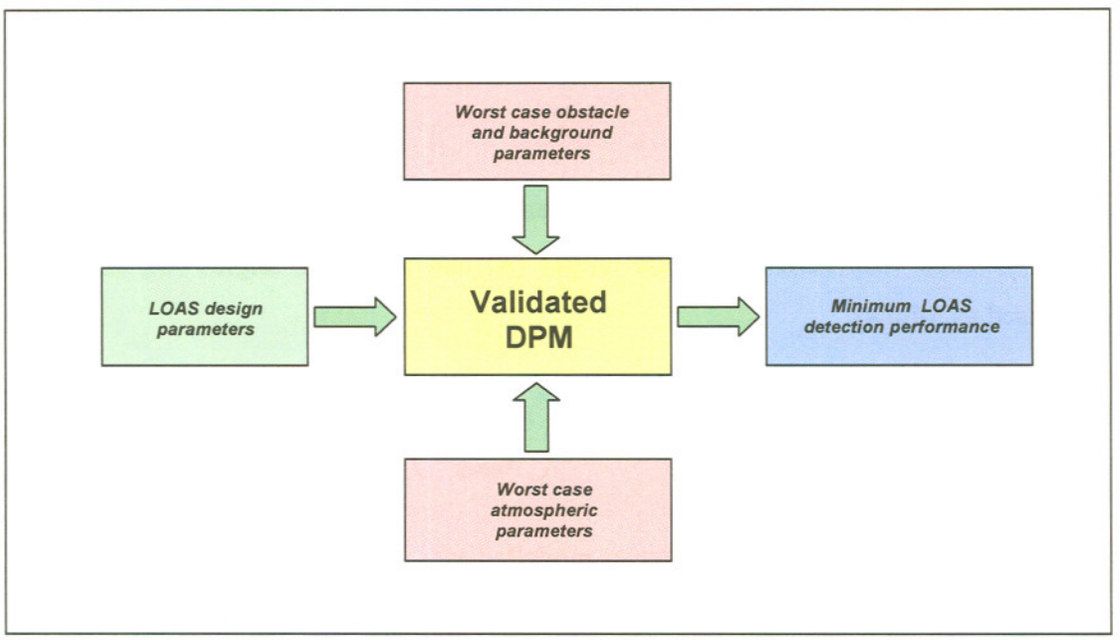

Figure 8-41. Minimum LOAS detection performance calculation.

For initial design calculations, the wire obstacle detection capability of the LOAS was modelled by the following simplified Signal to Noise Ratio (SNR) equation:

$$SNR = \frac{4E_p A_r L_T L_r e^{-2\gamma R} d_W \rho}{\pi P_D R^2 (\alpha R + D) NEP} \tag{8.39}$$

where:

E_P = output laser pulse energy

A_r = receiver aperture

L_T = transmission losses (including beam shaping)

L_r = reception losses (including optical filter)

γ = atmospheric extinction coefficient (calculated with corrected ESLM model)

d_W = wire diameter

ρ = wire reflectivity

P_D = pulse duration

R = obstacle range

α = beam divergence ($1/e^2$)

D = initial beam diameter

NEP = noise equivalent power

In order to estimate the SNR from experrimental LOAS detector current measurements (i_{SIG}), obtained with certain obstacle ranges (R) and incidence angles (θ), SNR was expressed as follows:

$$SNR = 20log\left(\frac{i_{SIG}(R,\theta)}{i_{NOISE}}\right) \tag{8.40}$$

The noise current terms in eq. (8.40) was modelled as:

$$i_{NOISE} = \sqrt{i_{TH}^{\ 2} + i_{BK}^{\ 2} + i_{DK}^{\ 2} + i_{RA}^{\ 2}} \tag{8.41}$$

where:

i_{TH} = thermal noise current

i_{BK} = background noise current

i_{DK} = dark noise current

i_{RA} = receiver amplifier noise

According to the LOAS design characteristics, we had:

$$i_{BK} = \sqrt{2qP_S P_b M_A (2 + kM_A)B} \tag{8.42}$$

performed with the procedure described above. Using filters with an optical density greater than 0.25 ND (corresponding to a 56% transmittance), the seeker under test was not activated. With 0.25 ND, the oscilloscope measured a pulse peak amplitude of 29.9 mV. Oscilloscope traces of the original and attenuated pulse trains are shown in Fig. 7-7 and 7-8.

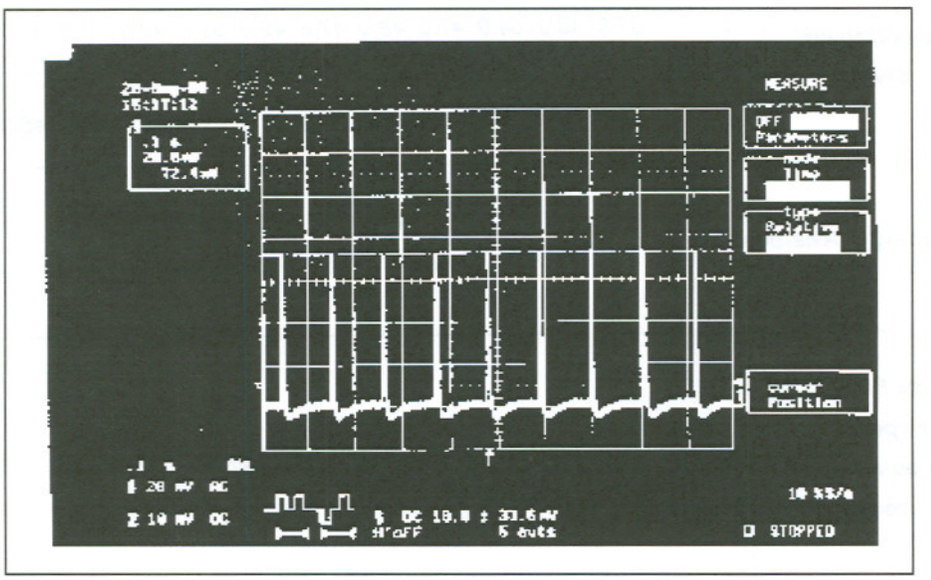

Figure 7-7. Target simulator pulses amplitude (72.4 mV).

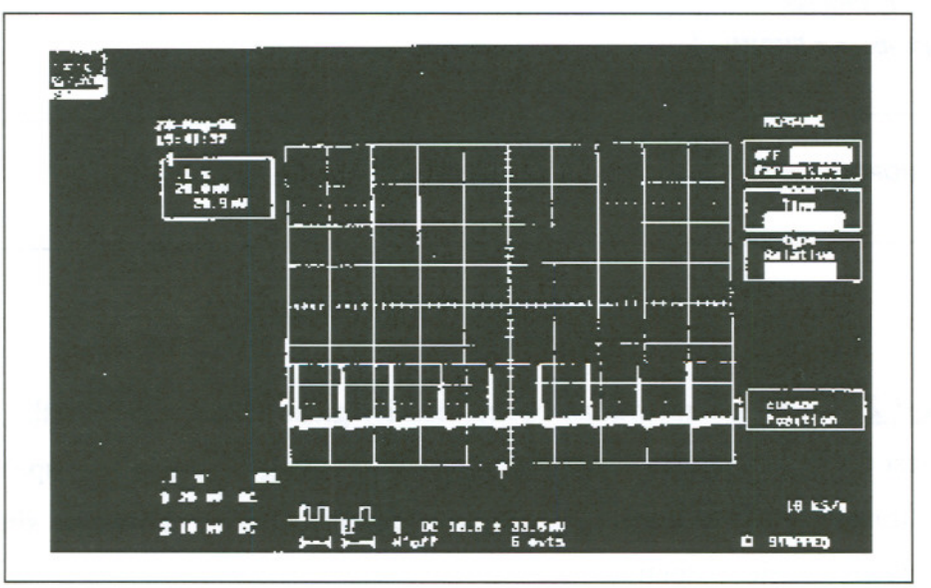

Figure 7-8. Train pulses amplitude.

Since the voltages measured by the oscilloscope were proportional to the energy measured by the power meter, the MDPD was estimated using 2 series of energy density measurements associated to the train of pulses. The results obtained with this method are given in Table 7-1.

Measurement Series	***1***	*57.8 48.0 54.0 47.0 48.0 47.5 49.0 50.0 49.0 47.0 44.0*
	2	*54.0 54.0 54.0 48.0 47.0 51.0 49.0 49.0 45.0 45.0 45.0*
Energy Densities		*Train (avg):* $E_T \cong 50\ pJ/cm^2$ *Pulse:* $E_P \cong 2.6\ pJ/cm^2$
Pulse Power Density Hypothesis (a): the pulse is assumed rectangular		$W_P \cong 2.6\ pJ/cm^2 / 9\ ms \cong 2.9 \times 10^{-10}\ W/cm^2$
Pulse Power Density Hypothesis (b): the pulse is assumed triangular (semi-base = FWHM)		$W_P \cong 2.6\ pJ/cm^2 / 4.6\ ms \cong 5.7 \times 10^{-10}\ W/cm^2$
MDPD (pulse)		$2.9\ \mu W/m^2 < MDPD < 5.7\ \mu W/m^2$

Table 7-1. MDPD estimation (Method 1).

Method 2. Using filters with an optical density greater than 0.25 ND, the seeker under test was not activated. Therefore, since this limiting condition corresponded to a 56% transmittance, the MDPD value was calculated using the target simulator known power density output:

$$MDPD = 8\,\mu W/m^2 \times 0.56 \cong 4.5\,\mu W/m^2 \qquad (7.1)$$

7.2 Laser Beam Profiling

Laser Beam Profiling (LBP) in a laboratory facility is an additional requirement for the PILASTER program, as it is necessary in order to determine the output characteristics of the laser systems under test, before performing experimental measurements at the range. Furthermore, some experiments performed during this research (i.e., laboratory tests, field trials and flight test activities) had to be carried out in well defined and repeatable conditions, in order to detect errors affecting the measurements, thus defining the validity and applicability of the results. Also in these cases LBP was used.

Therefore, various CCD cameras and suitable software packages for beam profiling were examined, in order to select a combination suitable for matching the PILASTER test requirements. The features common to all software packages included:

- Intensity distribution analysis;
- Gaussian fit analysis;
- Image, capture, store, and playback of 2-D and 3-D intensity plots;
- Printing of text and pictures.

Typical examples of a program outputs are shown in Fig. 7-9.

In order to match the various PILASTER requirements, the laser beam profiler should be able to analyse both continuous wave (CW) and pulsed lasers, and detect a wide range of different signals (power levels, PRFs, pulse durations, etc.). The main technologies available today for laser beam diagnostics are:

- Spatial cameras as the beam characterisation system.
- Moving mechanical slit or knife edges to scan across the incoming beam.

The main advantage of the mechanical scanning devices over a camera type laser beam profiler is the large dynamic range that allows accurate measurements of beams with both high and low intensities. On the other hand, camera type laser beam profilers are excellent for fast and detailed analysis of laser beam intensity profiles, but are limited in their accuracy due to a relatively low dynamic range.

However, to overcome the limited dynamic range of a camera type beam profiler and accurately measure faint laser beam structures, it is possible to sample the beam several times, each measurement being performed at a different attenuation or electronic shutter speed.

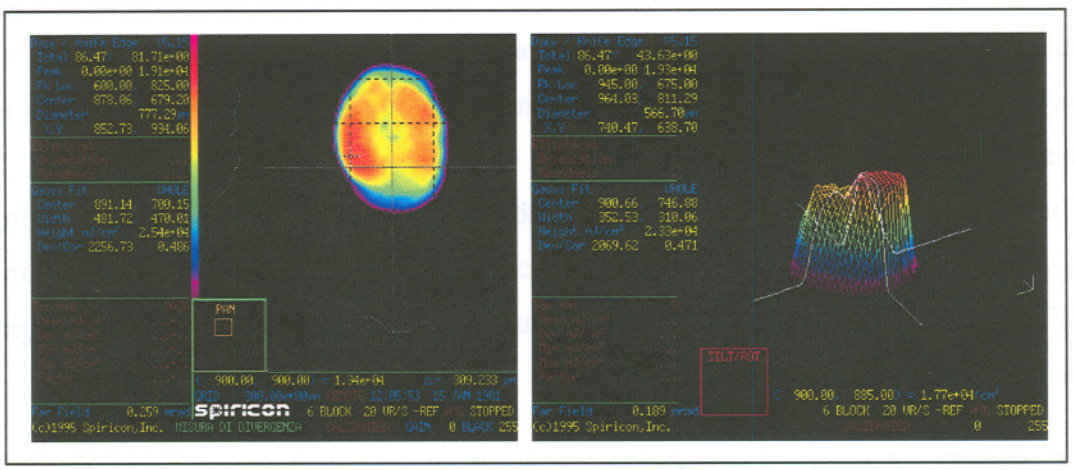

Fig. 7-9. Spiricon™ (Ophir Oprtonics Ltd.) 2-D and 3-D display format.

Although initial experiments were carried out with the Spiricon™ CCD profiler, the BeamStar™ profiler (by Duma Optronics Ltd.) was finally selected for the PILASTER program. Various types of cameras can be used with this software. The standard camera, supplied with the beam profiler software (Fig. 7-10), is a Monochrome Interline Transfer CCD ½", with an active area of 6.47×4.83 mm. The camera spectral response is 190-1100 nm and the maximum power density on filter is 50 W/cm^2. With this CCD camera, using electronic shuttering and ND filters, the system (with software) can capture and reply pictures and statistics from both continuous and pulsed lasers. In the first case, the maximum optical dynamic range is 2×10^8:1 (shutter speeds 1/50 to 1/10000 sec) and the maximum frame rate is 30 Hz. For pulsed lasers (1-100 Hz), the optical dynamic range is 256:1. For transmission of the output images (640×480 resolution) and data, an RS-232 standard interface is available (also available for a remote control).

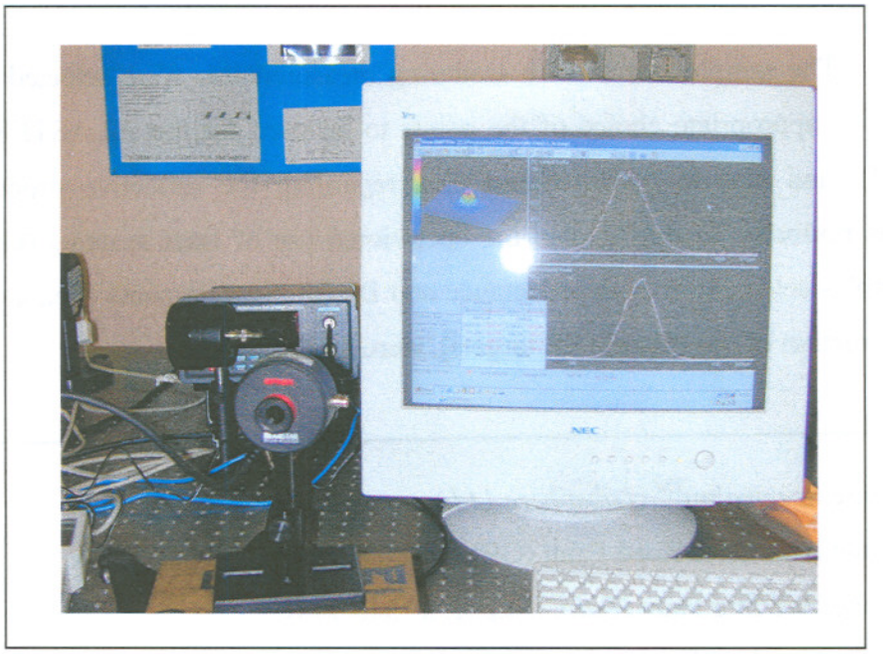

Fig. 7-10. Beamstar™ CCD camera.

7.4 Surface Reflection Measurements

Determination of target surface reflection properties at laser wavelengths is essential for predicting realistic range performance of ground and airborne laser systems, as well as for aircraft tactics (flight profile) optimisation, test range design activities, analysis of flight/ground test data and assessment of training exercises with laser systems. The concepts related with laser back-scattering measurements have been introduced in chapter 3 (and Appendix D). In the following paragraphs, we describe the test activities performed for determining both the general reflection properties of various materials/paints in the visible and infrared portions of the spectrum (i.e., in terms of total reflectance), and the specific reflection characteristics of the PILASTER target materials at Nd:YAG laser wavelength (λ = 1064 nm) subject to specific geometrical constraints (i.e., in terms of BRDF). An essential pre-requisite for both activities was the correct analysis of target materials physical properties, such as surface profile characterisation (roughness statistics, coating/painting standards, etc). LBP was also performed during BRDF measurements to ensure repeatability of the experiments.

7.4.1 Samples Identification and Surface Characterisation

The samples for surface scattering measurements were selected in order to allow an appropriate choice of the paints to be used for the PILASTER targets (Group-I), and also to gather useful data regarding the reflective properties of materials normally encountered in the operational use of laser systems (Group-II). The samples selected for both reflectance and BRDF measurements (i.e., candidates for construction of the PILASTER targets), were the following:

Group-I

a. White *Spectralon*^{TM} (*Labsphere Ltd.*)
b. White Refractive Road Paint (GEN-M-P0017);
c. White Building Paint (*Baldini S.p.A.* n° 345.998);
d. Diffusive Black Paint (*Nextel*^{TM} 97B/3W – AER-M-P039e);
e. Diffusive White Paint (*Nextel*^{TM} 3B/97W – AER-M-P039a);
f. White Non refractive Road Paint (GEN-M-P0016);
g. Dark Grey Paint (AER-M-G039f);
h. Light Green Paint (AER-M-H067d);
i. Dark Green Paint (AER-M-H074e).

The sample of Spectralon^{TM} (whose BRDF characteristics were provided by the manufacturer) also served to test the BRDF measurement instrumentation set-up.
The materials selected for reflectance measurements only (λ = 400 – 1200 nm) were the following:

Group-II

j. IR Grey Paint n° 1 (AER-M-G056);
k. IR Grey Paint n° 2 (FS 36280);
l. Concrete n° 1 – Runway;
m. Concrete n° 2 – Shelter;
n. Airport Parking Area Material;
o. Asphalt n° 1 – Runway;
p. Asphalt n° 2 – Road Material.

All paint samples were prepared using 2×2 inches polished aluminium plates. Before performing BRDF measurements, the rms surface roughness (σ) and slope (s) of the Group-I samples was measured using a surface profilometer (*Hommer Tester* T1000) which measured the surface roughness every 0.25 μm along a 15 mm scan. The rms roughness of the samples ranged from 0.42 μm to 16.87 μm. The results of the measurements are listed in Table 7-2.

Sample	rms roughness (σ)	rms slope (s)
a	0.47 μm	11.4°
b	6.88 μm	23.6°
c	19.96 μm	22.4°
d	4.80 μm	22.3°
e	4.41 μm	24.3°
f	1.76 μm	20.5°
g	1.52 μm	18.1°
h	0.60 μm	11.7°
i	0.42 μm	13.5°

Table 7-2. Surface characterisation for BRDF measurements.

7.4.2 Reflectance Measurements

As a first step into the analysis of the samples reflection properties, reflectance measurements were performed in the visible and near infra-red (λ = 400 – 1200 nm). The measurements were performed with the integrating-sphere spectrophotometer Perkin-Elmer mod. 'Lambda 19'. The results obtained for the two groups of samples are presented in Fig. 7-11 and Fig. 7-12.

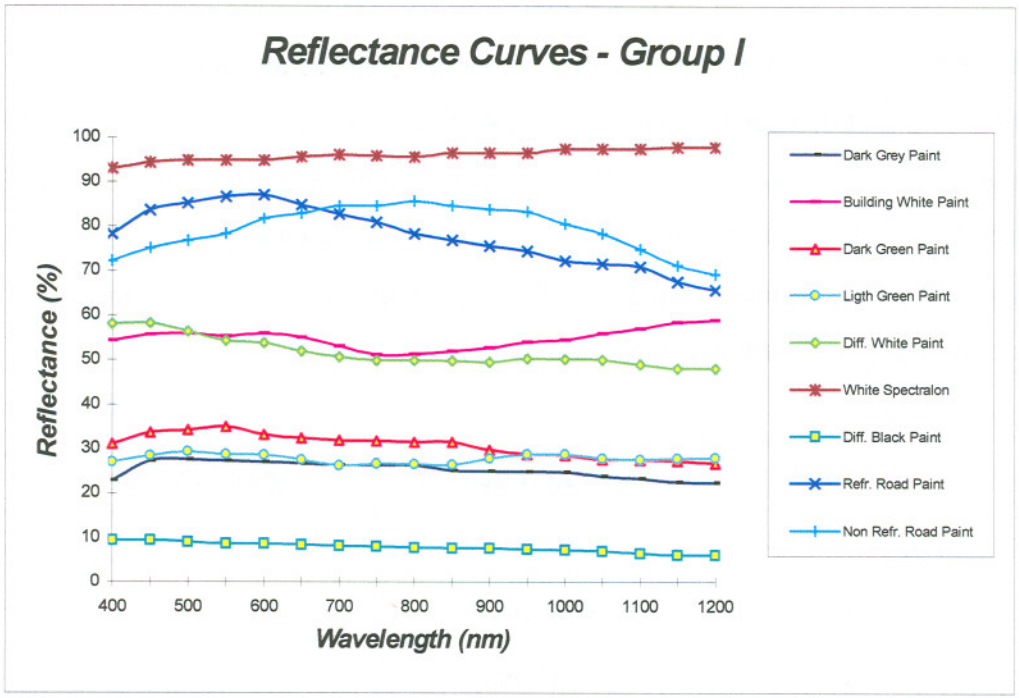

Fig. 7-11. Group-I reflectance measurements results.

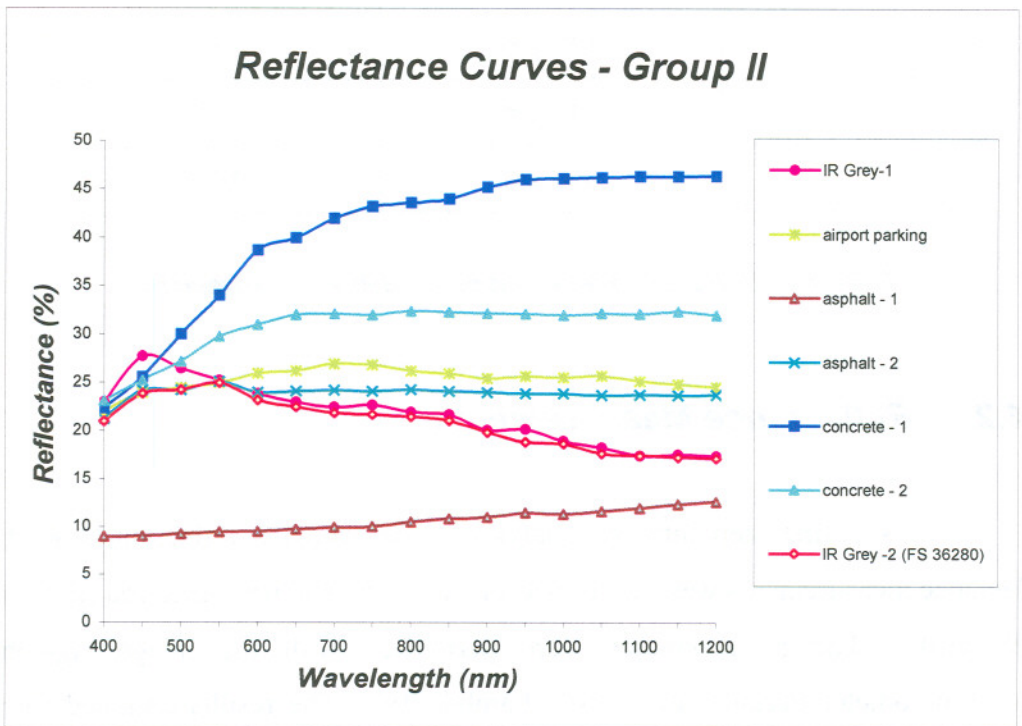

Fig. 7-12. Group-II reflectance measurements results.

7.4.3 BRDF Measurements

The Bidirectional Reflectance Distribution Function (BRDF) is defined as the ratio of the radiance of a sample to the irradiance upon that sample, for a given direction of incidence and direction of scatter. For BRDF measurements with the Group-I samples (i.e., PILASTER targets candidate paints and materials), a Laser Scatter-meter (LSM) was built. A detailed discussion about the BRDF and other scattering functions is presented in Appendix D. To briefly summarise the fundamental concepts involved, necessary to describe the LSM experimental arrangement, we refer to the LSM beam coordinate system illustrated in Fig. 7-13.

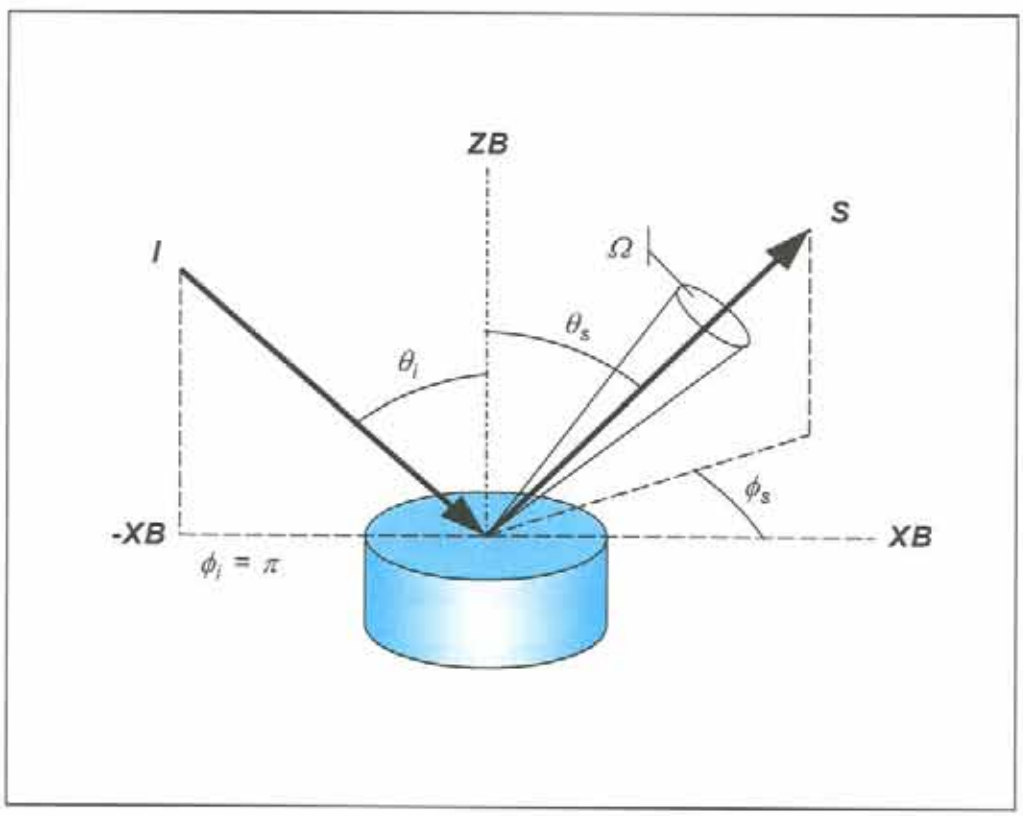

Fig. 7-13. LSM beam coordinate system.

The origin of the beam coordinate system is the point at which the central ray of the incident radiation (I) strikes the sample surface. The ZB axis is normal to the sample surface, and the XB axis lies in the plane defined by ZB and I. The incident direction is specified by two angles: the angle of incidence (θ_i), and the incident azimuth angle (ϕ_i), where $\phi_i = \pi$ by definition. Similarly, the scatter direction is specified by the

scatter angle (θ_s), and the scatter azimuth angle (ϕ_s). In order to measure BRDF, a LSM should allow the sample to be illuminated with a collimated laser beam from a range of incident directions. Furthermore, a receiver, subtending a solid angle Ω and viewing the entire illuminated area, should be positioned at a range of scatter directions. For any given LSM configuration, an average sample irradiance (E_e) is calculated from the power P_i incident on the sample and the illuminated area A. An average sample radiance L_e is calculated from the power P_s collected by the receiver, the receiver solid-angle, and the area of illumination. Therefore, the sample BRDF is calculated as the ratio of these two quantities:

$$BRDF = \frac{L_e}{E_e} = \frac{\left(P_s / \Omega A \cos\theta_s\right)}{\left(P_i / A\right)} = \frac{P_s}{P_i \Omega \cos\theta_s} \qquad \left[sr^{-1}\right] \tag{7.2}$$

Alternatively, the relative radiance of the sample may be measured versus that of a standard whose BRDF is known for the bi-directional geometry in question. The sample BRDF may then be calculated by multiplying the resulting ratio by the known BRDF of the standard.

Our LSM limits the collection of BRDF data to receiver positions in the plane of incidence, which is defined by the central ray of the incident flux and the sample normal. This is referred to as "in-plane" data (data collected with receiver positions confined to the plane perpendicular to the plane of incidence, and containing the sample normal, is referred to as "cross-plane" data).

BRDF, with its units of inverse steradians, appears as a fairly abstract quantity. The BRDF of a given sample is closely related to a more concrete quantity, however, its bi-directional reflectance factor. This is defined as the ratio of the flux scattered in a given direction by the sample, to that which would be scattered in that direction by the perfect reflecting diffuser, under identical conditions of illumination. The relation between BRDF (B) and bi-directional reflectance factor (R) is expressed by:

$$R\left(\theta_i, \phi_i, \theta_s, \phi_s\right) = \pi B\left(\theta_i, \phi_i, \theta_s, \phi_s\right) \tag{7.3}$$

It is important to observe that the BRDF of a perfectly diffuse (Lambertian) sample would be constant for all bi-directional geometries. However, the power collected by

the receiver (P_s) is strongly dependent on the scatter angle (θ_s), and becomes very small as θ_s approaches $\pi/2$. For this reason, we should expect that the effects of noise, and other sources of measurement error, become much more pronounced at large scatter angles.

Both the polarization state of the incident flux and the polarization bias of the receiver may be important variables in BRDF measurements. Many scattering materials significantly depolarise incident flux, while other materials selectively absorb flux with a certain polarization. A complete characterization of sample scattering also requires evaluation of these polarization effects.

The experimental arrangement of the LSM is shown in Fig.7-14.

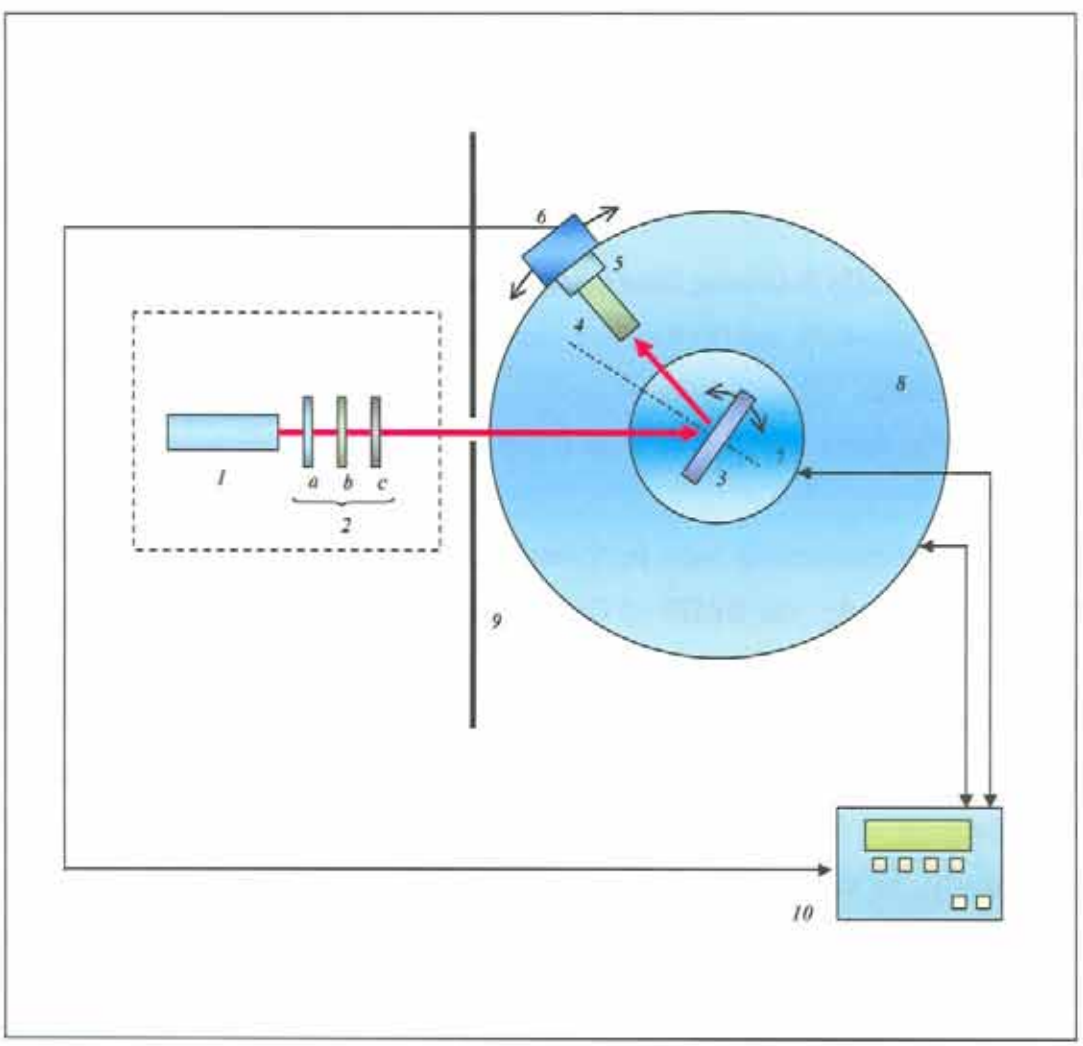

Fig. 7-14. Laser scatter-meter experimental arrangement.

The LSM was composed by three main parts: (A) the laser unit (including the laser source and the intensity/polarization control units), (B) the target turn-table unit (allowing orientation of the target sample), (C) the detection unit, mounted on a second turn-table (including the collimator, the polarizing filter and the detector), and (D) the measurements unit, including the energy/power meter and a motion control unit for automatic (continuous) data acquisition, both connected to a PC for data monitoring and recording. Particularly, with reference to Fig. 7-14, the LSM employed the following components:

1) Laser source.
2) Intensity and polarization control:
   a) ND filters;
   b) linear polarizer;
   c) retardation plates.
3) Sample.
4) Collimator, (5) Polarising filter (analyser) and (6) Detector.
7) Sample turn-table and (8) Receiver turn-table.
9) Light shield.
10) Energy/power meter, motion control unit and computer.

The BRDF measurements were performed at a wavelength of 1064 nm (Nd:YAG laser). Particularly, the BRDF of Group-I samples was determined, in order to . Before performing BRDF measurements, the characteristics of the Nd:YAG laser beam incident on the sample surface were determined using the BeamStar^{TM} CCD profiler. The parameters relative to the Gaussian fit of the horizontal and vertical cross-sections of the beam produced by a single laser pulse are shown in Fig. 7-15. Particularly, in this case, a difference is evidenced between the shapes of the horizontal and vertical cross-sections (also due to the distortions introduced by the LSM optical circuit), leading to a correlation with the Gaussian fit of about 80% in both cases. With laser sequences of up to 10 seconds in duration and PRF up to 20 Hz, it was also found that the stability of the beam shape (i.e., correlation with the Gaussian fit) was always within a limit of 73%.

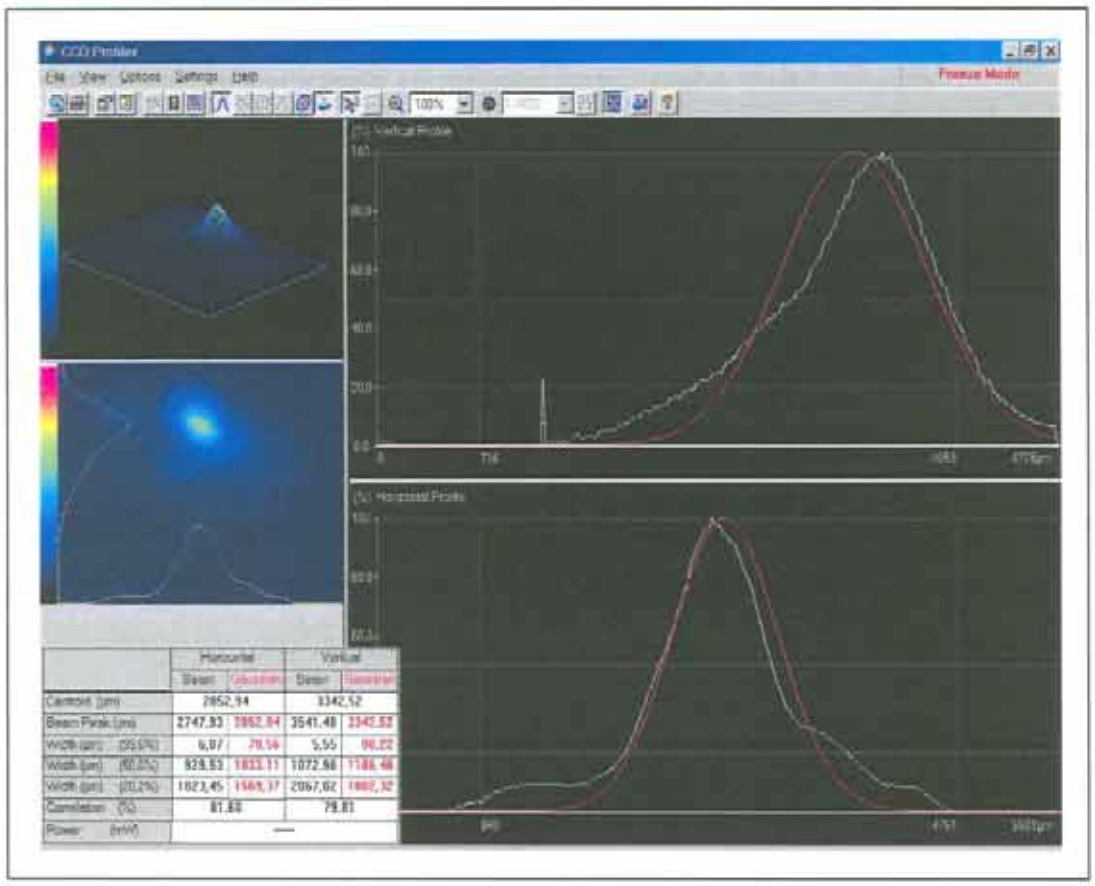

Fig. 7-15. Nd:YAG laser beam profile for BRDF measurements.

All BRDF measurements were performed with linearly polarised illumination, with the direction of polarization parallel (*P*) to the plane of incidence. In selected cases (samples d and e), the receiver was also polarised, with bias parallel (*P*) or perpendicular (*S*) to the plane of incidence. In this case, for a material which does not affect the polarization of the incident flux, the observed BRDF for the cross-polarized configuration (*PS*) would be zero. On the other hand, for a perfect depolarising sample, the BRDF values would be identical for both (*PP*) and (*PS*) measurement configurations.

The results of the BRDF measurements are reported below in the Figures 7-16 to 7-24. Particularly, the BRDF relative to all samples for three different laser incidence angles ($\psi = 0°$, 30°, 45° and 60°) are reported. Furthermore, the BRDF variations with receiver polarization parallel (P) and perpendicular (S) to the plane of incidence (with $\psi = 0°$ and 45°) are reported for the two paints that, after the initial reflectance and BRDF measurements, were identified as the best candidates for the PILASTER targets (samples d and e).

a. White Spectralon™

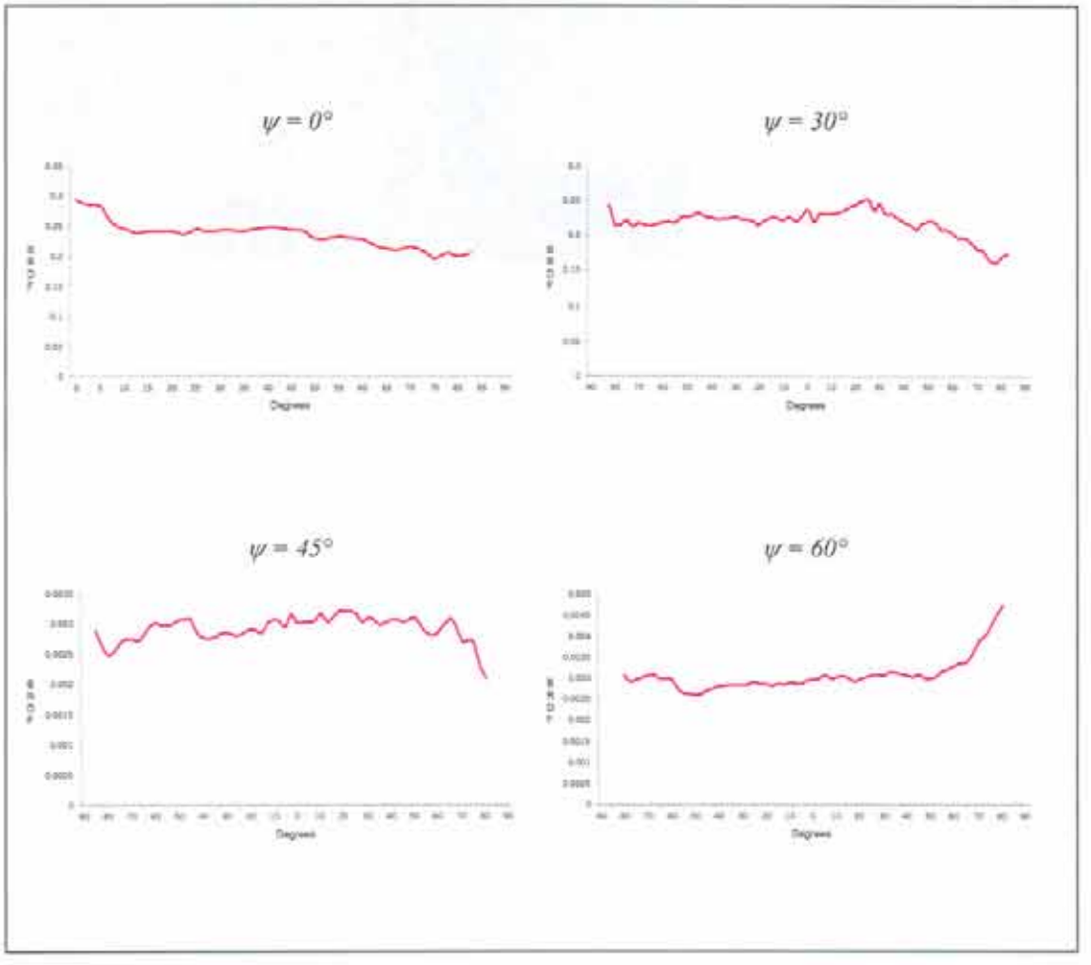

Fig. 7-16. BRDF for white Spectralon.

b. White Refractive Road Paint

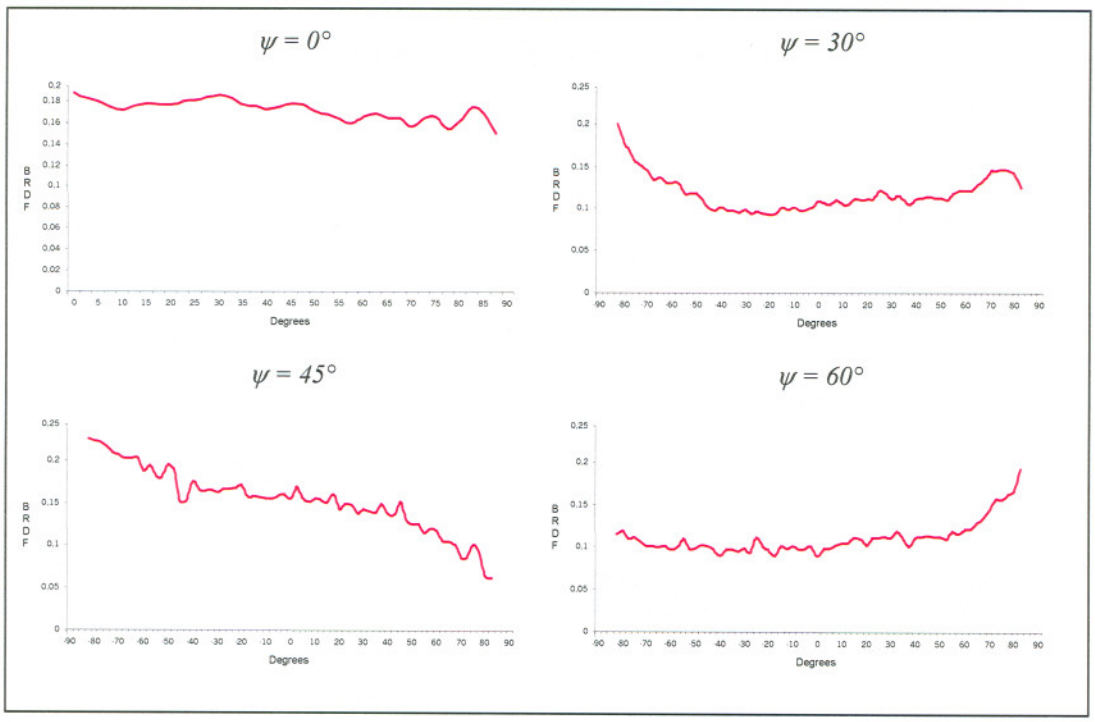

Fig. 7-17. BRDF for white refractive road paint.

c. Building White Paint

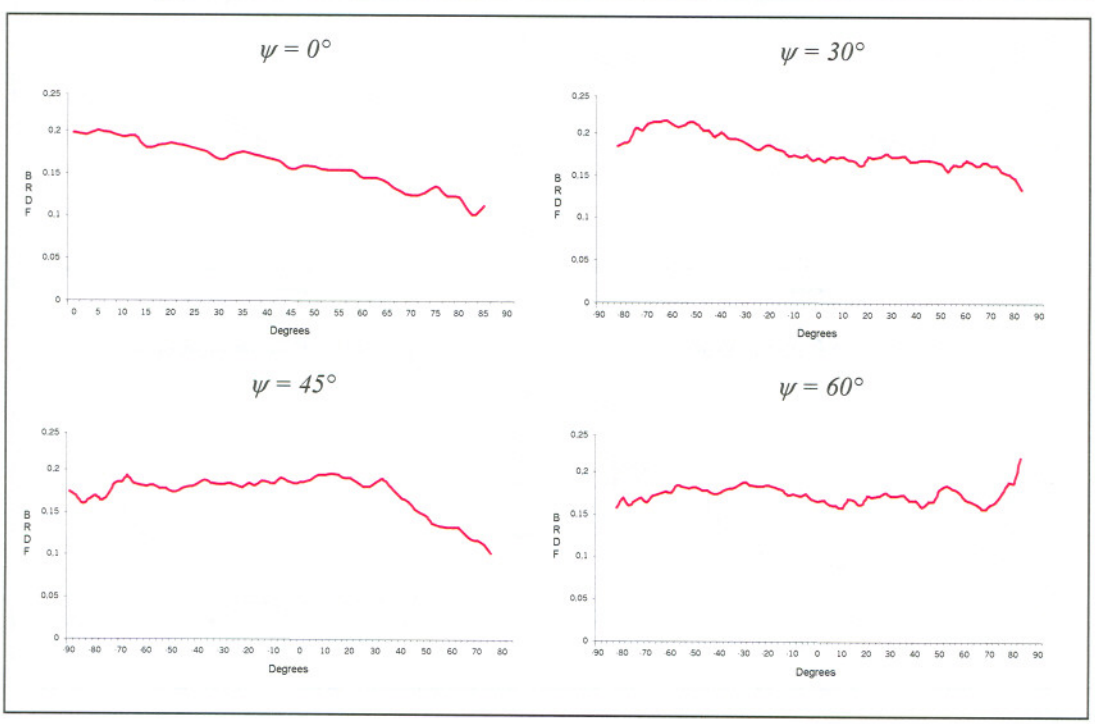

Fig. 7-18. BRDF for white building paint.

d. Diffusive Black Paint

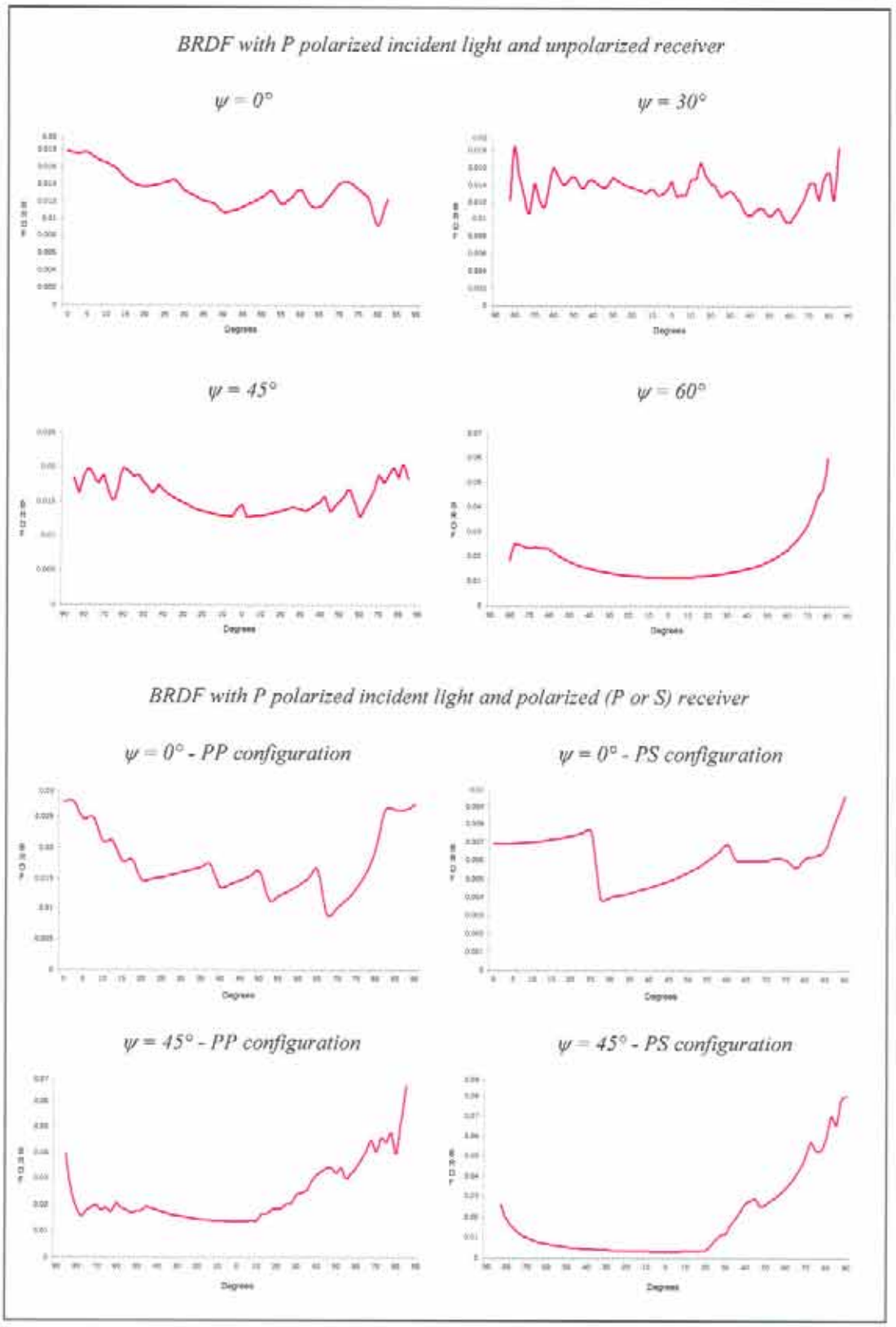

Fig. 7-19. BRDF for highly diffusive black paint.

e. Diffusive White Paint

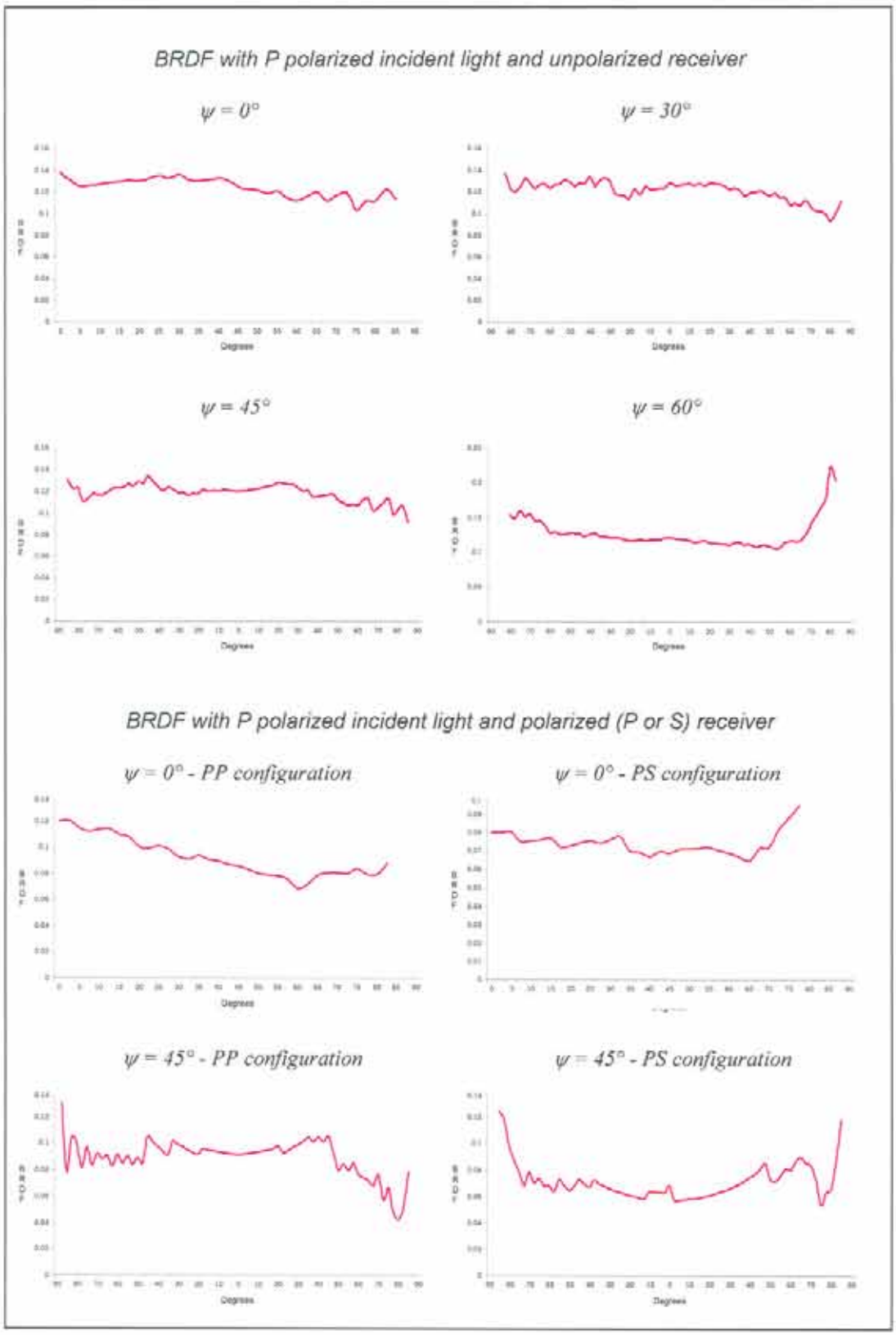

Fig. 7-20. BRDF for highly diffusive white paint.

f. White Non-Refractive Road Paint

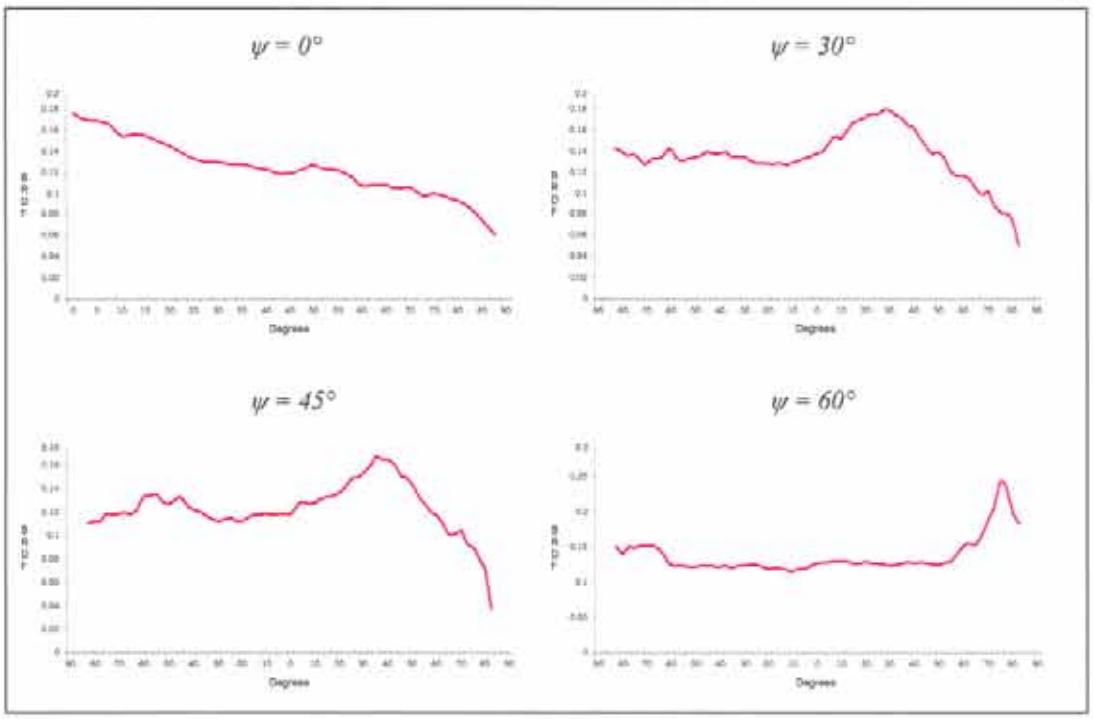

Fig. 7-21. BRDF for white non-refractive road paint.

g. Dark Grey Paint

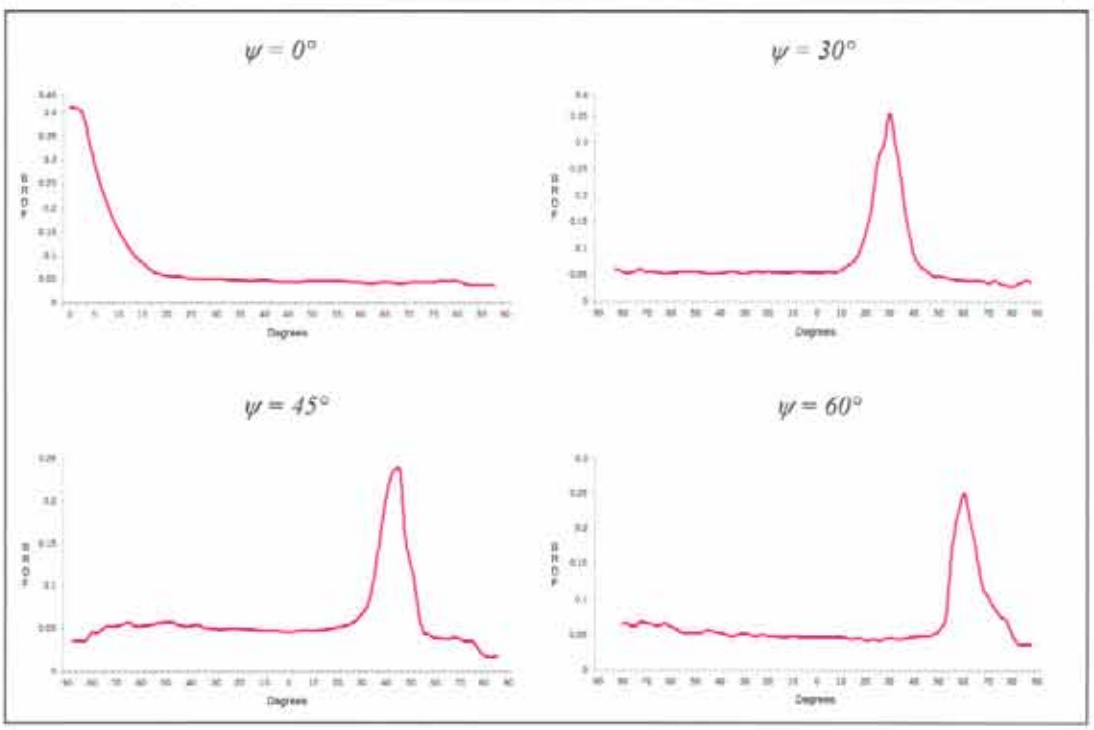

Fig. 7-22. BRDF for light grey paint.

h. Light Green Paint

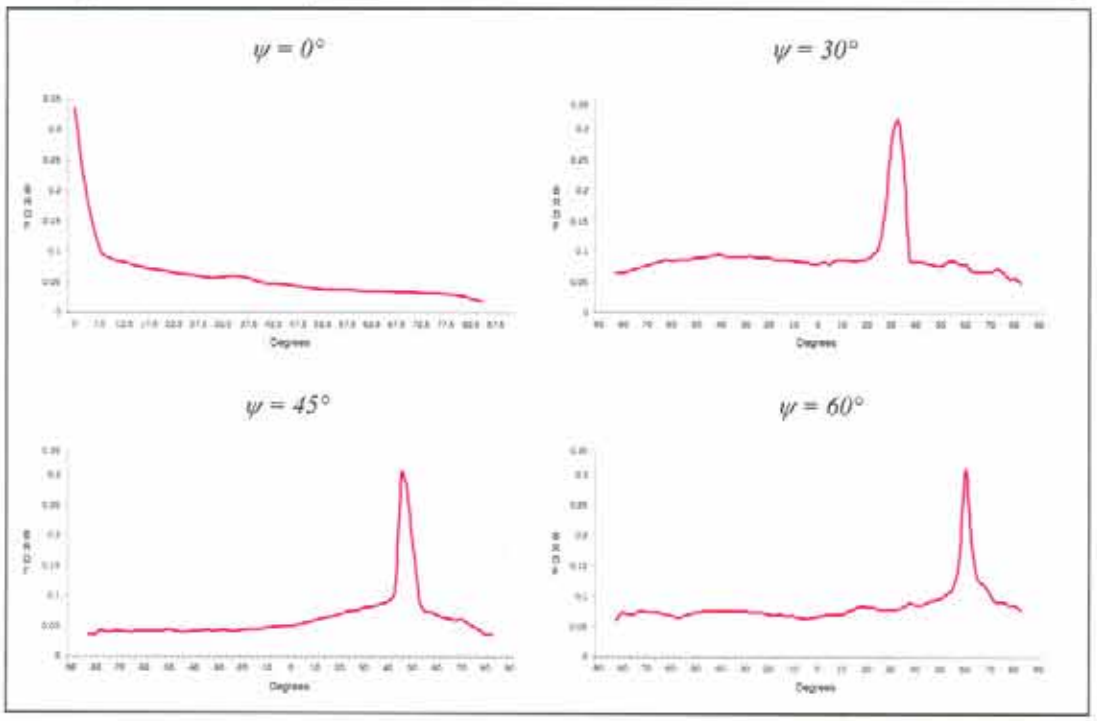

Fig. 7-23. BRDF for light green paint.

i. Dark Green Paint

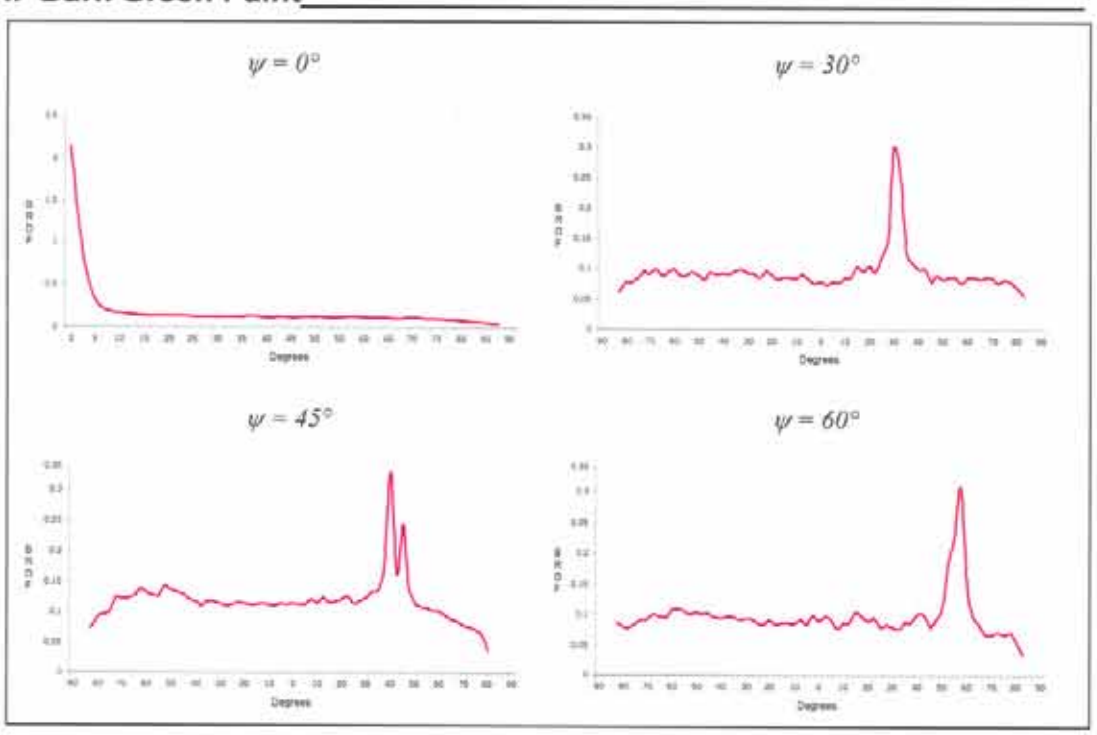

Fig. 7-24. BRDF for dark green paint.

Due to their excellent contrast in the visible and their good *Lambertian* characteristics, the Diffusive Black Paint AER-M-P039e (sample d) and the Diffusive White Paint AER-M-P039a (sample e), were selected for the PILASTER permanent target (FXDT) panels. Although these paints were technically adequate also for the PILASTER FRCT modular target (i.e., destroyable target for real weapon deliveries), they were not used for this application due to their very high cost. In this case, a combination of the Dark Grey Paint AER-M-G039f (sample g) with either the White Non refractive Road Paint GEN-M-P0016 (sample f), or the White Refractive Road Paint GEN-M-P0017 (sample b), was considered acceptable. It must be underlined that all these paints (samples b, d, e, f and g) are produced for employment by the Italian military forces, and their reflectance characteristics are claimed to remain constant in a wide range of environmental/weather conditions and due to aging.

The use of the very low cost White Building Paint *Baldini* n° 345.998 (sample c), was suggested only when laser spot measurements on the PILASTER targets were not required (being the only non military product, the characteristics of this paint may vary significantly due to aging or other factors).

7.5 PILASTER Systems Testing

Laboratory experimental activities also included initial tests for selection of the systems/sensors candidate for the PILASTER Program. These activities included:

- Near Infrared Cameras (NIR) Testing;
- Modified Laser Warning Receiver (LWR) System Testing;
- Power/Energy Meter and Detectors Testing.

Test methods and results are described in the following paragraphs.

7.5.1 NIR Cameras Testing

Two NIR cameras based on Focal Plane Array (FPA) sensors were tested for use in the PILASTER program, these are:

- the MERLIN™ NIR camera;
- the PHOENIX™ NIR camera,

both produced by the Indigo Systems Corporation (USA). Both NIR cameras had a spectral band 0.9-1.7 μm, and employed Indium Gallium Arsenide (InGaAs) detectors. In both cases, the array format was 320H×256V and the detector size was 30 microns. Furthermore, optics with different focal lengths and FOV/IFOV were available (e.g., 25 and 50 mm focal lengths with FOV/IFOV of 22°×16°/1.3 mrad and 11°×8°/0.6 mrad respectively). Both cameras were equipped with real-time imaging electronics, remote controls, and NTSC/PAL video outputs.

The PHOENIX™ camera was also equipped with a high-speed digital acquisition system, composed of a rack mount, high speed Pentium™ processor, a camera interface/sync board and Bit-Flow frame grabber. It captured the full bandwidth of digital video from the camera (40 MHz) and provided pseudo real-time VGA video for aiming and focusing the camera.

The aim of the laboratory test activity was to verify the performance of the PHOENIX and MERLIN NIR Cameras (together with the relative Data Acquisition Systems) in the presence of laser spots generated by very short laser pulses (PD < 20 nsec), with PRF, energy levels and spot characteristics compatible with the PILASTER requirements.

With reference to the test setup shown in Fig. 7-25, the following systems and instrumentation were used for the experiments:

- PHOENIX and MERLIN NIR Cameras (1);
- PC based Data Acquisition Systems (2) with IMAGE-PRO PLUS 4.1 Software;

- Laboratory Target 3.0×1.5 m (3);
- Q-Switched Nd:YAG laser (4);
- Nd:YAG Attenuation Filters (5);
- Beam Splitter (6) and Mirror (7);
- Beam Expanding Optics for Narrow (8) and Wide Laser Beams (9);
- Aberration Filter (10).

The 3.0×1.5 m target, painted in back and white with paints of considerably different reflectance at 1064 nm (i.e., 7% and 50% respectively), was located at a distance of about 5 m from the beam expanding optics (Φ_{wide} = 50 mrad and Φ_{narrow} = 2 mrad). With this geometry, the effective spot diameters were about 50 cm and 2 cm. The PHOENIX/MERLIN NIR Cameras, equipped with suitable optics (in order to see the entire target) and connected to the Data Acquisition PC, was also located at a distance of about 5 metres from the target. An Aberration Filter (AF) was also used at the expanding optics output to generate highly distorted laser spot profiles on the target (with similar characteristics to the spots expected to be encountered in the future operational use of the cameras at the PILASTER).

During the test, the different requirements associated with the intended use of the two cameras were taken into account, setting appropriate integration times for data acquisition in order to obtain:

- post-processing data analysis (i.e., geometry, energy distribution, time analysis), for the maximum number of pulses (spots) in a sequence, for the PHOENIX NIR camera;
- real-time visualization of the spot sequence, in the case of the MERLIN NIR camera.

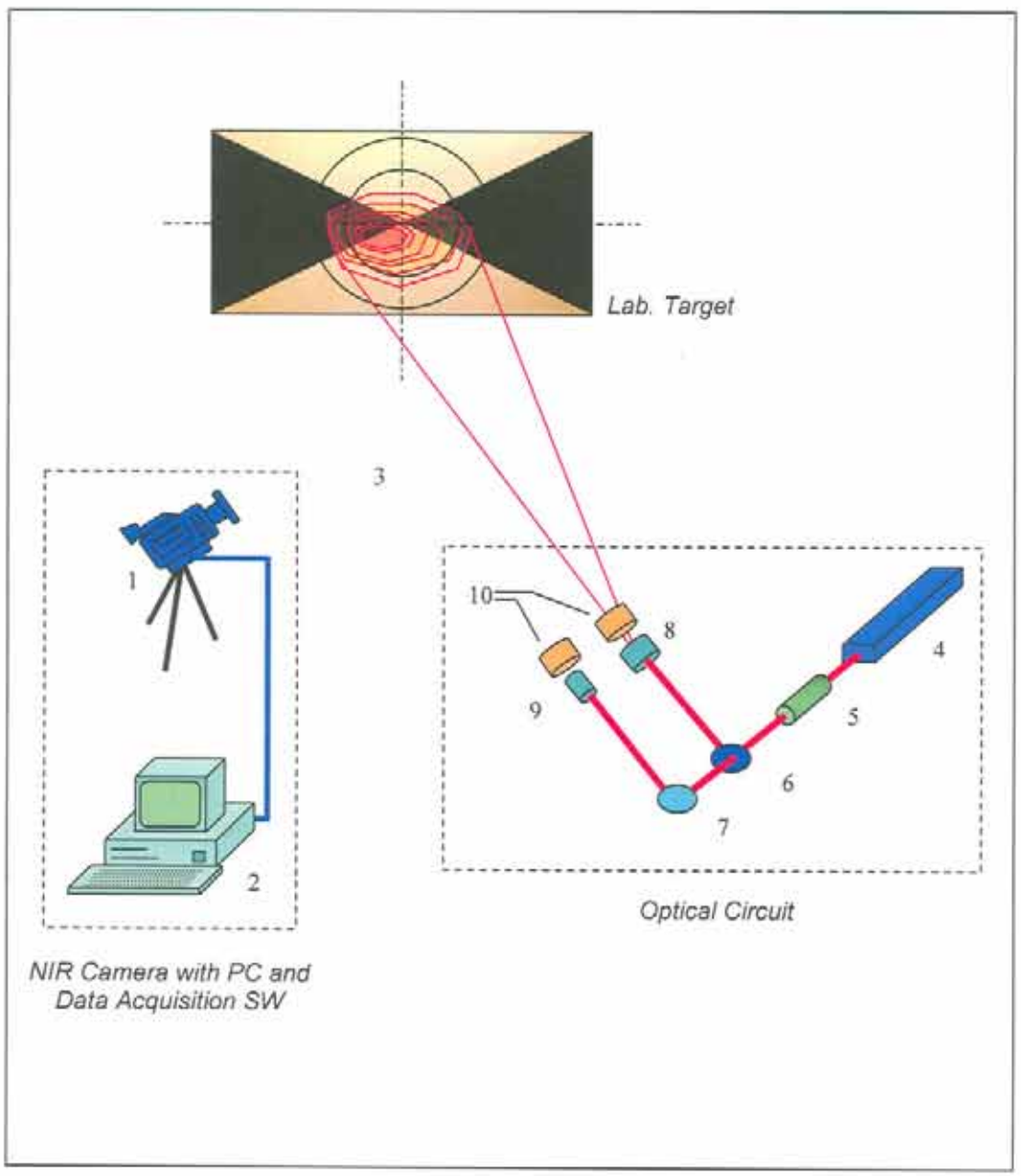

Figure 7-25. NIR cameras test instrumentation setup.

For both NIR cameras, an important requirement was to minimise the memory required for frames recording, maximising at the same time the performances of the cameras with and without synchronisation of spot data acquisition with laser signal transmission (i.e., number of useful frames for the PHOENIX NIR camera and quality of the real-time displayed image for the MERLIN NIR camera). Therefore, it was first of all necessary to find adequate Frame Frequencies (f_F) of the NIR cameras according to the specific application. This was done in order to maximise the number of recorded pulses in the first case (PHOENIX NIR camera) and to obtain high quality real-time sequences in the second case (MERLIN NIR camera). A number of tests were performed in order to experimentally determine the optimal f_F for the two NIR cameras. A more detailed analysis for f_F optimisation was performed during the ground test activities (see chapter 8). In general, setting the f_F at twice the PRF, it was empirically found to be a good compromise for the PHOENIX NIR camera, while for the MERLIN NIR camera intended application (i.e., real-time spot monitoring) a f_F of 10 Hz was adequate for PRFs of 1-4 Hz, and a f_F of 20 Hz was better suited for PRFs of 10-20 Hz. The key parameters for evaluating the performance of the two cameras were:

- Percentage of Acquired Pulses (%AP) with respect to the total number of laser pulses transmitted in a certain Pulse Train Duration (PTD) for the PHOENIX NIR camera;
- Real-time Image Quality (RIQ) for the MERLIN NIR camera.

Particularly, for the RIQ the following ranking scale was used in the assessment:

- 0/4 Spot image absent;
- 1/4 Spot image not clear (fading);
- 2/4 Spot image intermittent but clear;
- 4/4 Spot image continuous and clear;

The final results of the two performance assessments are summarized in Table 7-3.

Laser Parameters						PHOENIX		MERLIN	
PRF	PTD	Energy	BE	AF	P_D	f_F	%AP	f_F	RIQ
1 Hz	10 s	2 μJ	Wide	Yes	20 ns	2 Hz	52%	10 Hz	4/4
	10 s	2 μJ	Wide	No	20 ns	2 Hz	66%	10 Hz	3/4
	10 s	2 μJ	Narrow	Yes	20 ns	2 Hz	53%	10 Hz	4/4
	10 s	2 μJ	Narrow	No	20 ns	2 Hz	67%	10 Hz	3/4
4 Hz	10 s	2 μJ	Wide	Yes	20 ns	8 Hz	47%	10 Hz	4/4
	10 s	2 μJ	Wide	No	20 ns	8 Hz	66%	10 Hz	3/4
	10 s	2 μJ	Narrow	Yes	20 ns	8 Hz	48%	10 Hz	4/4
	10 s	2 μJ	Narrow	No	20 ns	8 Hz	62%	10 Hz	4/4
10 Hz	10 s	2 μJ	Wide	Yes	20 ns	20 Hz	66%	20 Hz	3/4
	10 s	2 μJ	Wide	No	20 ns	20 Hz	56%	20 Hz	3/4
	10 s	2 μJ	Narrow	Yes	20 ns	20 Hz	62%	20 Hz	4/4
	10 s	2 μJ	Narrow	No	20 ns	20 Hz	51%	20 Hz	3/4
20 Hz	10 s	2 μJ	Wide	Yes	20 ns	40 Hz	43%	20 Hz	3/4
	10 s	2 μJ	Wide	No	20 ns	40 Hz	65%	20 Hz	4/4
	10 s	2 μJ	Narrow	Yes	20 ns	40 Hz	52%	20 Hz	4/4
	10 s	2 μJ	Narrow	No	20 ns	40 Hz	48%	20 Hz	4/4

Table 7-3. NIR Cameras Tests Results.

7.5.2 Modified RALM-01 System Testing

This test activity was performed in order to assess the Modified RALM-01 (M-RALM-01) Laser Warning Receiver (LWR) performance in the presence of laser spots generated by very short laser pulses, with PRFs and energy/power levels compatible to the PILASTER program requirements. Particularly, the Optical Units (OUs) of the system were 'stimulated' with laser pulses of low energy levels ($E_t \leq$ 0.1 nJ) and power densities ($D_P \leq 5$ mW/m^2). The instrumentation arrangement used for the experiment is shown in Fig. 7-26.

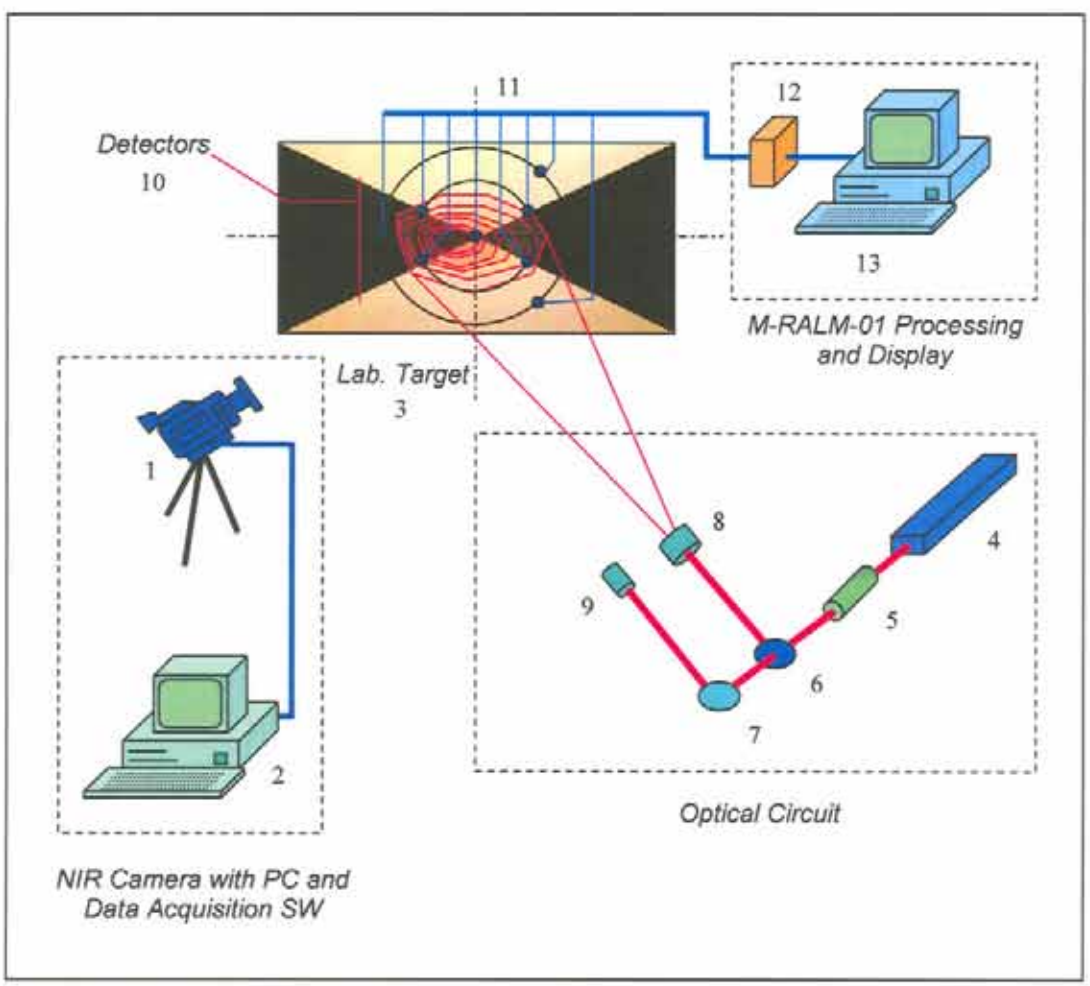

Figure 7-26. RALM-01 test instrumentation setup.

Particularly, the following equipment was used in the experiment:

- PHOENIX NIR Camera (1);
- PC based Data Acquisition Systems (2) with IMAGE-PRO PLUS 4.1 software;
- Laboratory Target 3.0×1.5 m (3);
- Q-Switched Nd:YAG laser (4);
- Nd:YAG Attenuation Filters (5);
- Beam Splitter (6) and Mirror (7);
- Beam Expanding Optics for Narrow (8) and Wide Laser Beams (9);
- M-RALM-01 Optical Units (10) and Optical Fibre (FO) Cables (11);
- M-RALM-01 Processing Units (12);
- PC based Data Recording and Display System (13).

The MARCONI LWR Optical Units (OUs) family is shown in Fig. 7-27., with evidenced the type of OU used for the M-RALM-01 test (a total number of 8 OU were used for the M-RALM-01 test).

Figure 7-27. MARCONI LWR OU family and M-RALM-01 test OU.

For comparison purposes, the M-RALM-01 system was also tested without OU, using 'shielded' OF terminations, as shown in Fig. 7-28, in order to get a maximum angle of acceptance of ± 20° in accordance with the OF specifications. The PHOENIX NIR camera was also used in the experiment, in order to measure the effective laser spot diameter on the target surface.

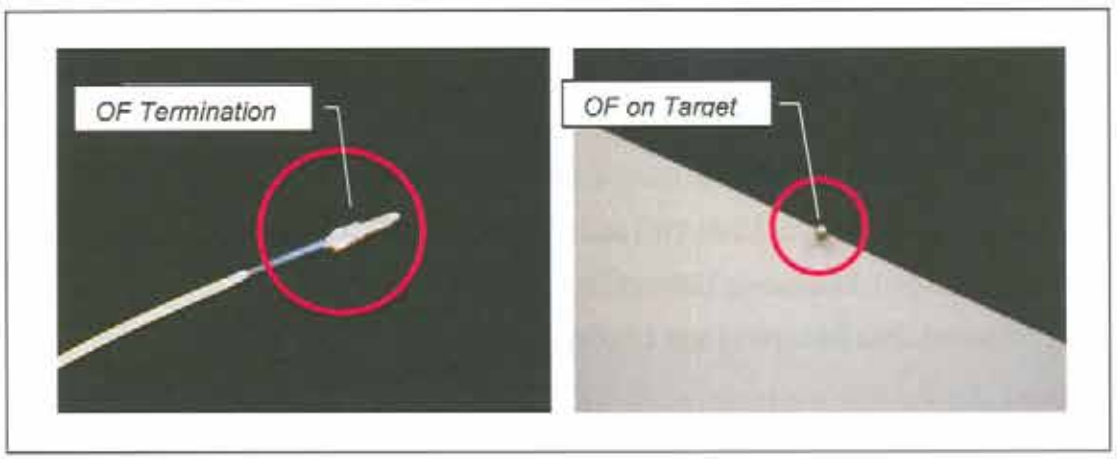

Fig. 7-28. Optical fibres shielded termination.

The M-RAM-01 Processing Unit, together with an example of the PC based display software format is shown in Fig. 7-29.

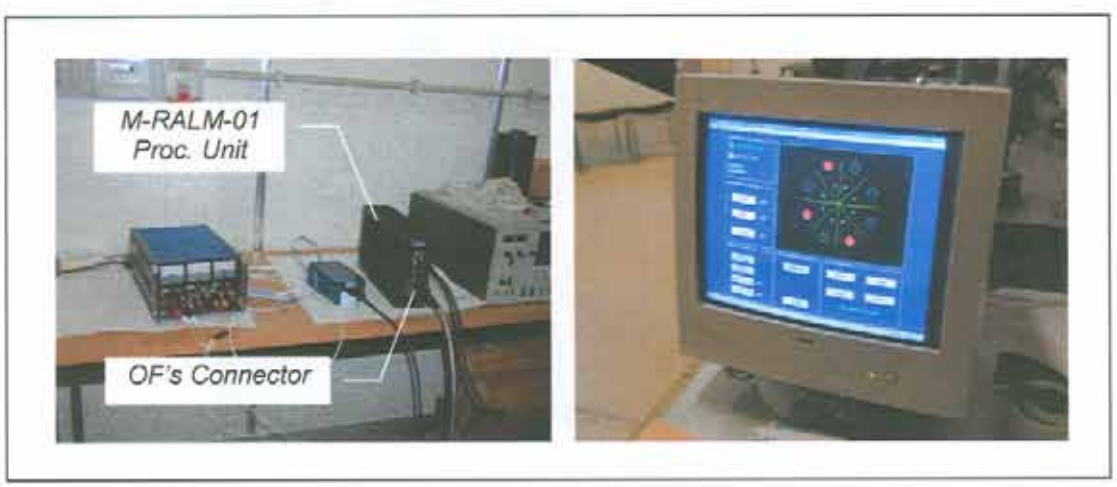

Figure 7-29. M-RALM-01 MARCONI LWR processing unit and PC display software.

In all cases, the M-RALM-01 was capable of detecting the presence of the laser spots, even when the associated pulses peak energies were of the same order of magnitude of the background noise (and the other available instrumentation was not able to detect the laser spots). Furthermore, it was verified that using the OU the directional discrimination capability was substantially increased with respect to the case of 'shielded' OF without OU. Particularly, using very narrow laser spots (i.e., few millimetres), it was observed an acceptance angle of ±5° using the OU, against an effective acceptance angle of ±26° using the 'shielded' OF. However, it was verified that, in both cases, the angular discrimination capability of the system, in the presence of larger laser spots (i.e., 10-100 cm) was seriously affected by undesired multiple reflections of the laser spots (i.e., multipath). The conclusion was that, although suitable for detecting the presence of extremely low energy laser pulses and for determining the PRF of incident laser sources, the M-RALM-01 system was not suitable for the laser spot energy measurements required for the PILASTER STU. Therefore, it was decided to use the M-RALM-01 system only as an additional sensor for confirming the presence of laser spots on the PILASTER FXDT target (or in its vicinity) for safety purposes and measuring the PRF of incident laser sources, during both test and training missions.

7.5.3 Laser Energy Meter and Detectors Testing

As described in chapter 5, the PILASTER EMT-1 technique was based on direct energy measurements performed at specific locations on the permanent target, and use of the NIR camera grey-scale PIM to reconstruct the spot energy profile. This concept presented several difficulties for its practical implementation. In fact, it was difficult to find off-the-shelf detectors with sufficiently low NEP characteristics, capable of measuring NIR laser energy from pulses of very low duration (i.e., P_D = 20 nsec) and energy levels ranging from the nJ to the mJ.

After an extensive market survey, and various preliminary laboratory experiments, the best candidate for the PILASTER EMT-1 application (i.e., direct energy measurements at the target location) was the ORIEL 70834 Laser Energy Meter (LEM), equipped with

the ORIEL 708XX Pyroelectric Probes (PEP). Some relevant information about the ORIEL 708XX Pyroelectric Probes (PEP) family are reported in Table 7-4.

The aim of this test was to verify the performance of the ORIEL 70834 Laser Energy Meter (LEM), equipped with the ORIEL 708XX Pyroelectric Probes (PEP), in terms of data accuracy obtainable using trains of laser pulses with PRF = 10 Hz, very short durations (P_D = 20 nsec) and various energy levels (ranging from the μJ to the hundreds of mJ).

PEP Size (mm)	Max. PD (μs)	Max. Pulse Energy		Max. PRF (Hz)	Max. Avg. Power (W)	Typical Voltage Resp. (VmJ^{-1})	Noise Equivalent Energy	Model No.
		@ 10 ns	@ 1 μs					
5	50	1 mJ	1 mJ	400	2	3	15 nJ	70810
9	100	4 mJ	4 mJ	200	2	0.8	35 nJ	70811
25	200	150 mJ	1250 mJ	100	5	0.008	4 μJ	70825
50	400	600 mJ	5000 mJ	50	10	0.002	50 μJ	70827

Table 7-4. PEP sensors characteristics.

The experiment was carried out using the test setup shown in Fig. 7-30, which included the following instrumentation:

- Q-Switched Nd:YAG laser (1);
- Nd:YAG Attenuation Filters (2);
- Narrow band (1064 nm) Filter (3);
- LEM (5) and PEP sensors Under Test (4);
- Oscilloscope (6);
- PC with Software for Data Display, Analysis and Recording (7).

The test was performed with different values of the Laser Output Energy (LOE), a PRF of 10 Hz and a PTD of 5 sec.

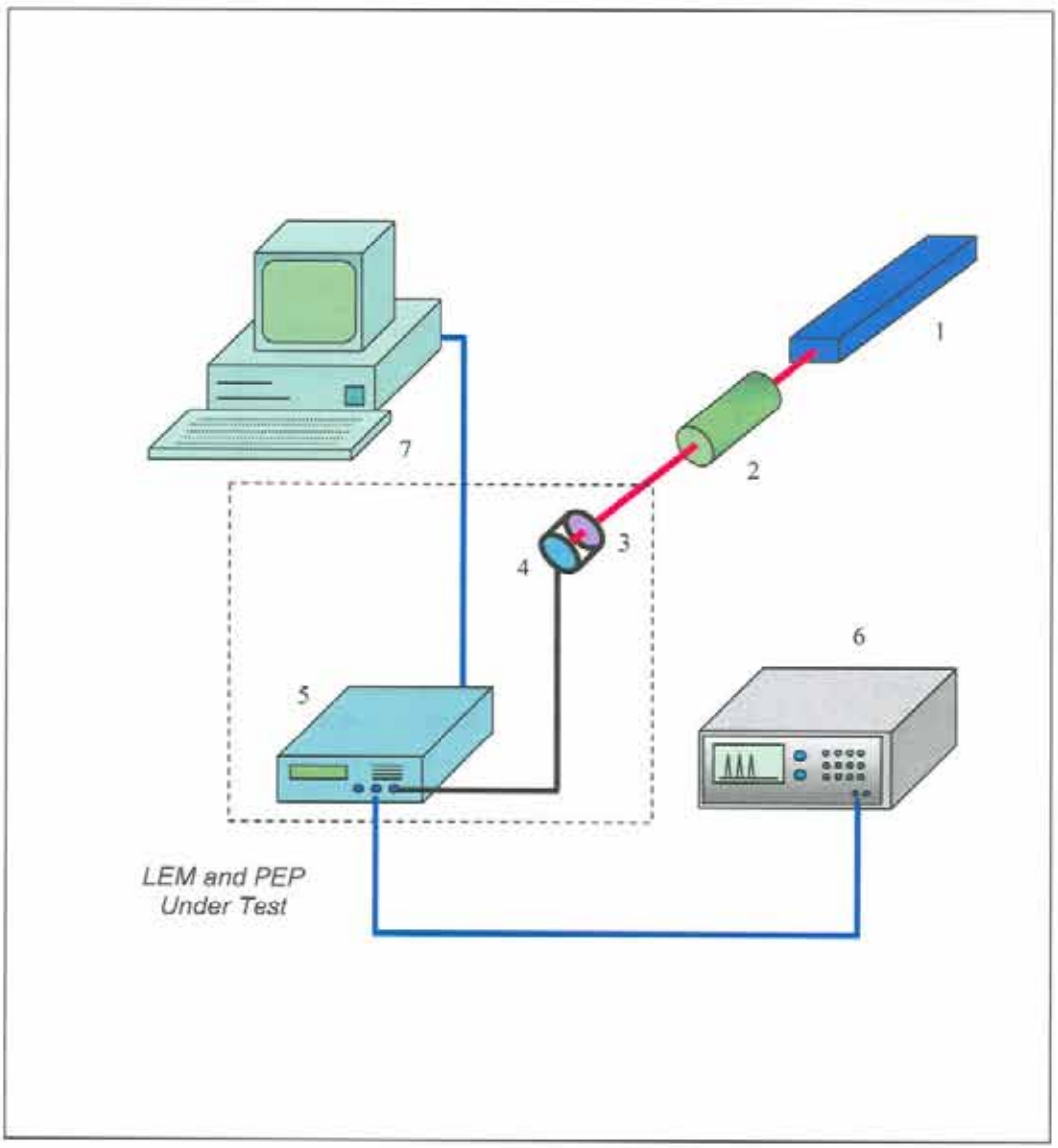

Figure 7-30. PEP/LEM initial test setup.

The results of the tests performed are reported in Table 7-5. Particularly, the differences (average of 50 measurements and relative standard deviation) between the PEP-LEM readings and the LOE values ($\Delta\%_{PEP\text{-}LOE}$), are listed in the table.

Laser Parameters					$\Delta\%_{PEP\text{-}PDD}$*	
PEP	PRF	PTD	LOE	PD	$\mu_{PEP\text{-}LOE}$	$\sigma_{PEP\text{-}LOE}$
70810	10 Hz	5 s	2 μJ	20 ns	2.876%	1.647%
		5 s	20 μJ	20 ns	1.060%	1.072%
		5 s	200 μJ	20 ns	-1.120%	2.283%
70811		5 s	200 μJ	20 ns	3.764%	1.760%
		5 s	2 mJ	20 ns	-3.022%	1.445%
70825		5 s	2 mJ	20 ns	-2.120%	1.836%
		5 s	20 mJ	20 ns	-2.334%	1.945%
70827		5 s	20 mJ	20 ns	-4.045%	2.240%
		5 s	200 mJ	20 ns	3.908%	1.808%

* From 50 PEP measurements.

Table 7-5. PEP/LEM initial test results.

7.5.4 PHOENIX NIR Camera Calibration

Definition of a reliable calibration procedure for the PHOENIX NIR camera was very important for the PILASTER program. Particularly, calibration was required in order to convert the 'grey scale' numeric information associated with the acquired laser spot images (Grey-scale Pixel Intensity Matrix – PIM), into a value of incident energy (integrated in the spectral band of the camera). For this purpose, the an Integrating Sphere was used (Fig. 7-31).

Particularly, with reference to Fig. 7-31, the following instrumentation setup was used for the NIR camera calibration:

- PHOENIX NIR Camera (1);
- PC based Data Acquisition Systems (2) with IMAGE-PRO PLUS 4.1 software;
- Q-Switched Nd:YAG laser (3);
- Nd:YAG Attenuation Filters (4);
- Beam Steering Optics (5);
- Integrating Sphere (6).

IR cameras employing photo-detectors are characterized by an output signal proportional to the incident IR energy. Particularly, in a NIR camera employing a bi-dimensional sensor matrix (i.e., Focal Plane Array - FPA) this is true for every single pixel. Therefore, from the numeric information associated to the image (i.e., Grey-scale Pixel Intensity Matrix - GPIM) it is possible to reconstruct the bi-dimensional map of the energy irradiated by a target within the scene observed by the NIR camera (integrated radiance in the camera spectral band).

In the PHOENIX NIR camera, the FPA analog signals are processed by the read-out electronic circuits, producing a digital output of the image (i.e., 12-bit Analog Digital Unit - ADU). Therefore, constructing a calibration curve for the Radiant Intensities (W/cm^2sr) associated to the ADU Grey-scale values, and using a dedicated image analysis software (i.e., IMAGE-PRO PLUS 4.1), it is possible to obtain the image Energy Pixel Intensity Matrix (EPIM) giving the energy associated to each pixel in the NIR camera image.

The linearity of the photo-detector response allows accurate measurements in the camera dynamic range, with only a limited number of calibration data points. Furthermore, NIR cameras like the PHOENIX, featuring a variable integration time (selectable by the operator), give the opportunity of performing measurements in a linear regime within a wide interval of integrated radiance values, thus obtaining reliable measurements.

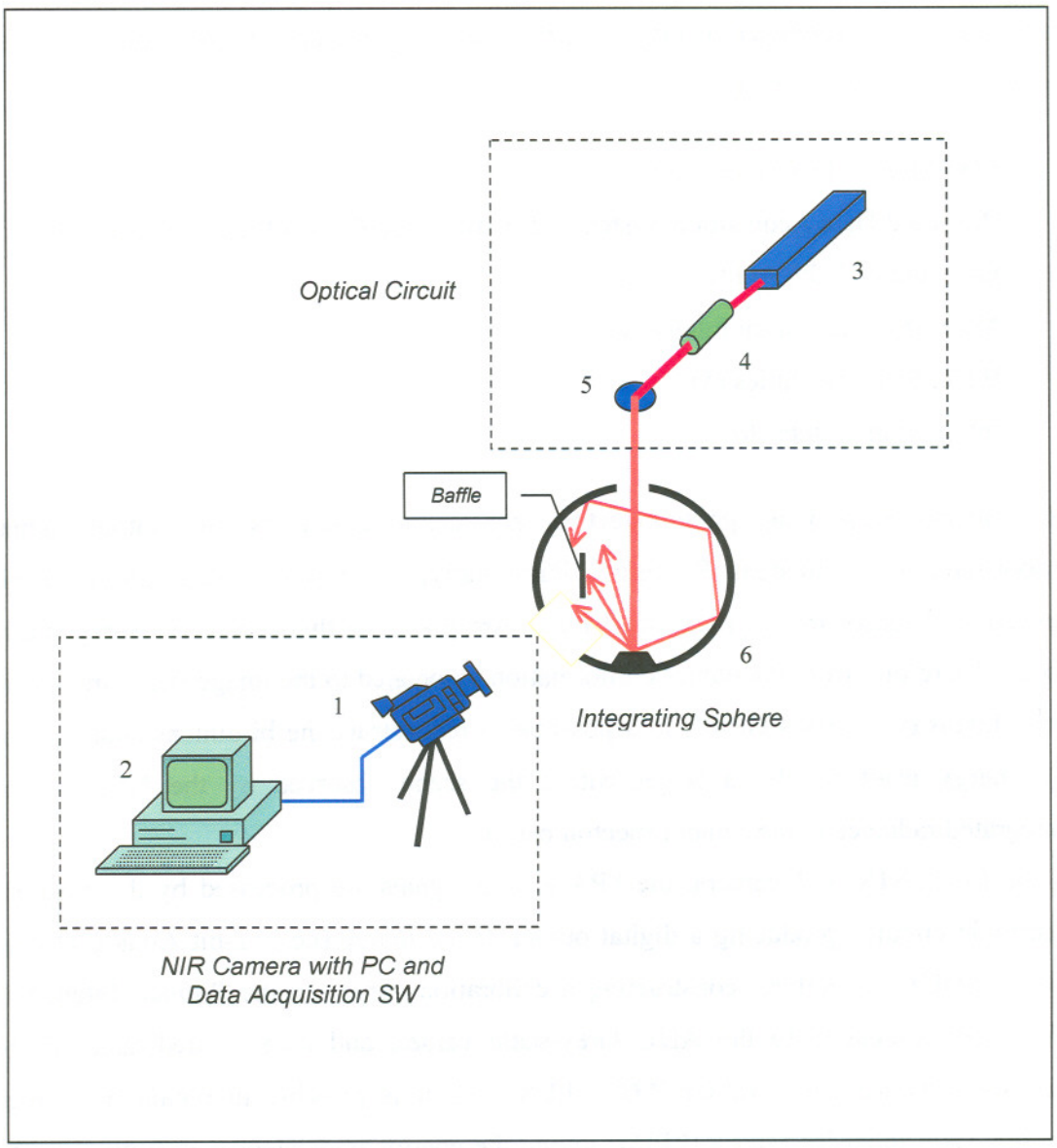

Figure 7-31. NIR camera calibration procedure.

Calibration of the PHOENIX camera can then be defined as the experimental procedure that allows determination of the ADU/Integrated Radiance Response Function (AIRF). The inverse of the AIRF is used by the image analysis software tool in order to obtain, directly as an image attribute, the values of integrated energy in the spectral band of the camera.

In the case of a photo-detector the response of a single pixel in terms of Analog Digital Unit (ADU) is:

$$ADU_{i,j} \propto \frac{A}{4 \cdot f\#^2 + 1} \cdot g \cdot i_{time} \cdot \int_{\lambda 1}^{\lambda 2} \tau_\lambda \eta \cdot E_\lambda d\lambda \qquad (7.4)$$

where λ is wavelength, λ_1 and λ_2 are the limits of the camera spectral band (with filter), η_λ is the detector quantum efficiency (whose spectral distribution is typically constant), E_λ is the spectral radiance, τ_λ is the optics transmittance, A is the pixel area (30 μm x 30 μm for the PHOENIX-NIR camera), g is the gain of the read-out electronics, $f\#$ is the f-number of the optics and i_{time} is the camera integration time.

Therefore, the experimental parameters to be controlled during the calibration procedure are the integration time, the optics *f*-number and other settings of the NIR camera (e.g., the gain of the read-out electronics which may be selected by the operator). Fixing these parameters for a certain interval of integral radiance, it is possible to determine the AIRF of the camera by using an extended reference source. The function (calibration curve) so obtained, valid for the specific setup of the camera previously defined, is then used to determine the values of integral radiance to be used for reconstructing the radiant intensity map of the target. The spectral response (determined experimentally) of the InGaAs sensor employed in the PHOENIX NIR camera is shown in Fig. 7-32.

The curve shows that the sensor output is a value of radiance integrated in the band 0.9 – 1.6 μm. This implies that, in order to perform measurements of the energy reflected by a target (with known reflectance characteristics) illuminated by a laser, it is necessary to considerably reduce the spectral response of the camera by using a narrow band filter (centred at 1064 nm), in order to drastically reduce the contributions of the background. The use of such a filter allows, using the same camera setup, accurate measurements of laser energy, independently from the ambient illumination, both in day and night conditions.

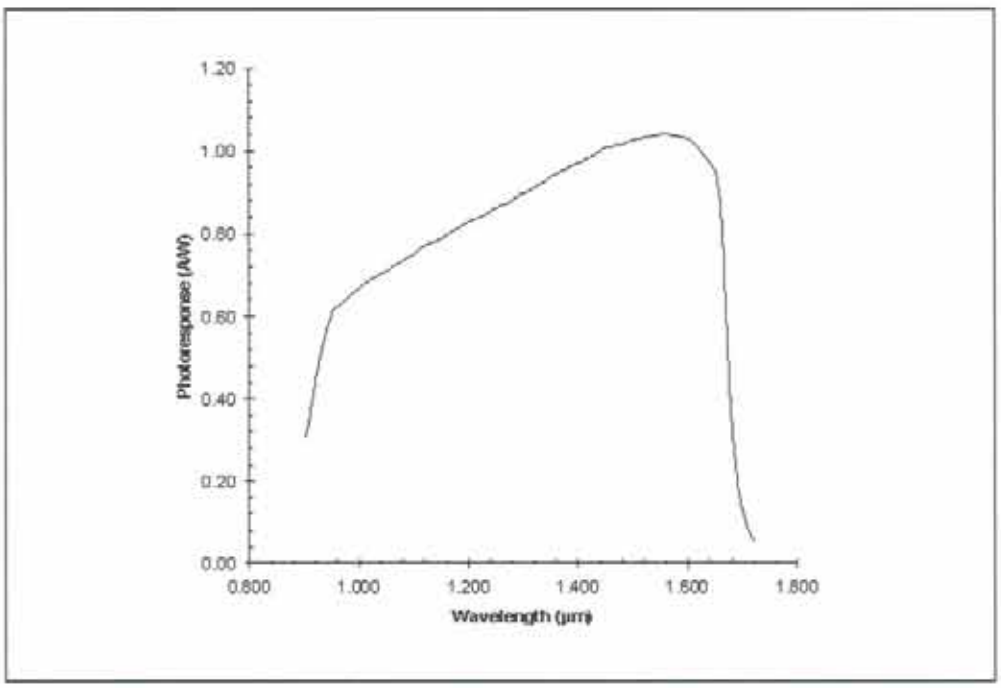

Fig. 7-32. Spectral response of the FPA employed in the PHOENIX NIR camera.

The required calibration source has to be characterised by a known (tuneable) energy intensity over an extended area. The ideal match to such requirement is to use an Integrating Sphere with an input from an external variable power reference laser. This is because the Integrating Sphere characteristics are such that it can produce an output uniform energy distribution by using a narrow beamwidth laser as an input.

The steps required to accomplish the NIR camera calibration procedure are the following:

- Define the camera setup parameters (i.e., integration time, f-number of the optics and read-out electronics gain.
- Set a value P_1 of the output power of the laser.
- Obtain the first data point (P_1, ADU_1), acquiring the camera image and determining the corresponding ADU value (ADU_1) using the image analysis and processing tool.

- Modify the laser output power (value P_2) and repeat the step 3 in order to determine the second data point (P_2, ADU_2).
- Repeat the step 4 a number of times sufficient to obtain a stable AIRF solution as the output of a linear interpolation process using all data points (P_n, ADU_n).
- Repeat the steps 1-5 as required to obtain an AIRF for each combination of camera setup parameters needed operationally.

Using these AIRF with suitable software routines in the image analysis and processing tool, allows to obtain directly on the NIR camera images the relative values of integrated radiance.

7.6 LOAS Laser Sub-system Testing

Before performing ground and flight test activities using the LOAS system, its Er^{++} doped fibre laser sub-system (IRE POLUS Group mod. ELPM-20K) was tested in the laboratory, in order to determine, against the manufacturer specification documents, the following characteristics:

- Average power transmitted;
- Pulse duration;
- Pulse Repetition Frequency (PRF);
- Laser beam misalignment with respect to the beam-expander support;
- Power consumption, Weight and Dimensions.

The ELPM-20K laser is shown in Fig. 7-33. The instrumentation used for the tests is the following:

- Tester *Hewlett Packard* 3478A;
- Surface Absorption Disk Calorimeter *Scientech* 36-0001;

- Micrometric Support;
- Multimode Optical adapter SMA-FC-PC;
- He-Ne Laser *Melles Griot* 05-LHR-991 ;
- Oscilloscope *Tektronix* 520D;
- Optical probe *Tektronix* P6703B;
- Optical probe *Tektronix* P6701B;
- Power Supply *Delta* 7020;
- ND Optical Filters.

Figure 7-33. ELPM-20K laser (LOAS).

The test setup is shown in Fig. 7-34. All the measurements were performed in a temperature interval of 18 ÷ 22 °C.

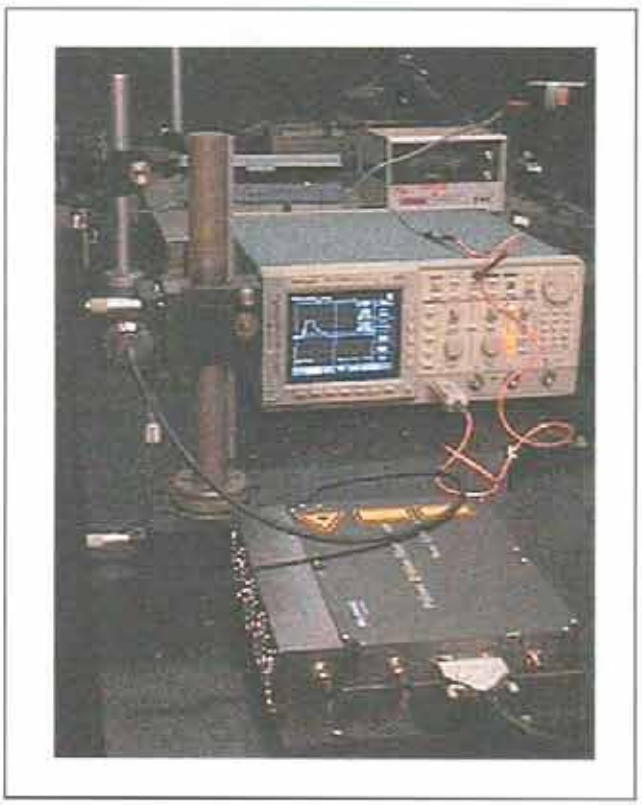

Figure 7-34. ELPM-20K test setup.

Average Power transmitted

For measuring the average optical power of the laser the disk calorimeter readout has been used, adopting the following procedure:

- Beam expander-calorimeter alignment;
- Laser activation;
- Regulation of the beam direction in order to obtain the maximum readout value on the calorimeter;
- Wait for laser stabilization (20 minutes);
- Calorimeter readout recording.

Although all prescribed calibration procedures were followed, to check the correctness of the measurement, the calorimeter internal calibration resistance was connected to the

power supply. Then the power supply was regulated in order to obtain the same readout previously recorded during the laser activation, and the voltage applied to the resistance was measured using the tester. The voltage readout was $V = 7.757$, with a resistance $R =$ 41 Ω. Using the formula:

$$P = \frac{V^2}{R \cdot C_O} \tag{7.5}$$

where C_O is the calorimeter optical absorption coefficient (whose value is 0.98), the optical power P equates to 1.49 Watt.

Pulse Duration

The laser pulse duration was measured using the oscilloscope optical probe (using the multi-mode optical adapter and ND optical filters between the optical fiber and the beam expander to avoid probe saturation). The result is shown in Fig. 7-35.

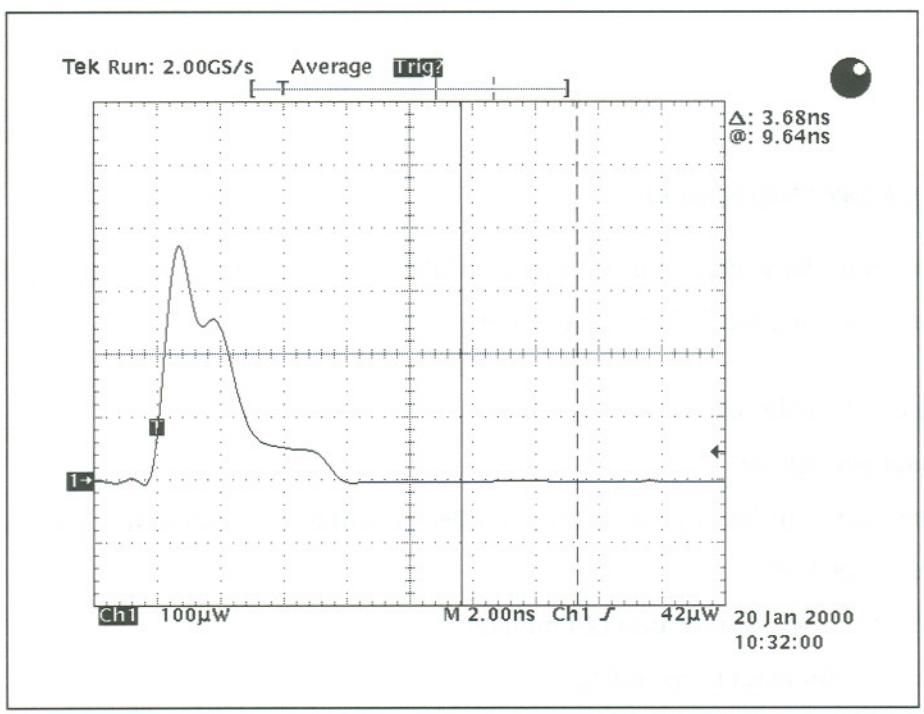

Figure 7-35. ELPM-20K pulse duration measurement.

During the measurements, it was noted a marked dependency of the pulse shape on the observation position (probably due to the different modes of propagation of the optical fiber). Therefore, further measurements were performed using the signal reflected by a surface (as in the LOAS real case, where the optical signal received by the APD is reflected from an obstacle).

The result of one of the tests performed using a green painted aluminium target are shown in Fig. 7-36. In this situation, an integration of the various optical fiber propagation modes produces a "smooth" pulse shape. This fact is beneficial in terms of the required electrical band for optical-electrical conversion (APD) and signal amplification.

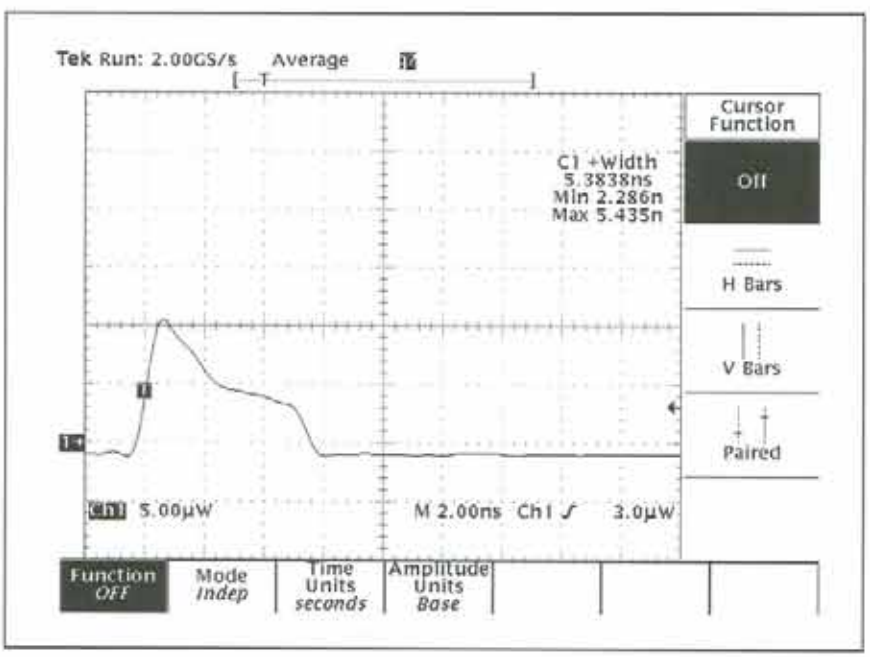

Figure 7-36. ELPM-20K pulse reflected from a green painted target.

Laser beam misalignment with respect to the beam-expander support

For measuring the beam misalignment, the beam expander was placed into the micrometric support, and regulated (azimuth and elevation), in order to obtain a maximum for the signal amplitude measured by the oscilloscope (Fig. 7-34). Then the beam expander was replaced by the He-Ne *Melles Griot* laser, whose cilindrical

packaging, with the same diameter of the beam expander, is aligned with its laser beam with an error ≤ 1 mrad (small with respect to the alignment error that had to measure: expected value ≤ 10 mrad). Using the probe 6701B (0.5 μm ÷ 0.95 μm band), the micrometric support was regulated in order to obtain a maximum for the amplitude of the signal measured by the oscilloscope. Therefore, measuring the micrometers shifts in azimuth and elevation, the laser beam misalignment was determined. Particularly, the measured misalignment was 5 mrad.

Pulse Repetition Frequency

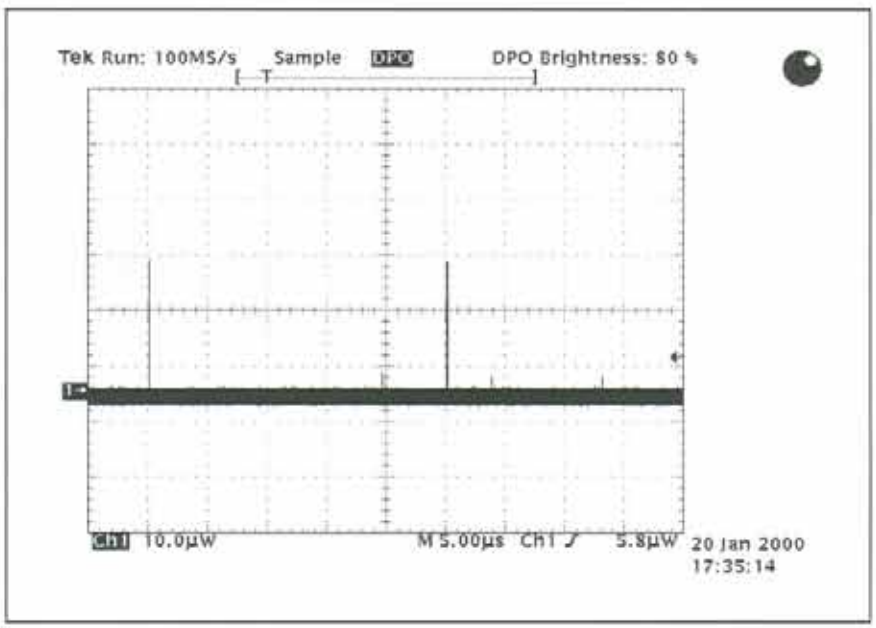

Figure 7-37. ELPM-20K Pulse Repetition Frequency (PRF).

Power Consumption, Weight and Dimensions

The power consumption measured at 25 °C was about 50 W. The need to maintain a constant temperature for the pumping diode (using *Peltier* elements), made power consumption a function of ambient temperature. Tests conducted in a thermal chamber with a temperature range of –10 °C ÷ 50 °C demonstrated a maximum consumption of 80 W. ELPM-20K laser weight and dimensions were adequate for integration in the LOAS system.

The results of all tests performed are summarized in Table 7-6.

PARAMETER	*LOAS SPEC*	*MEASURE*
Average power transmitted	1.2 W	1.49 W
Pulse duration	2 ÷ 5 nsec	2.8 nsec
Pulse Repetition Frequency (PRF)	40 KHz	40 KHz
Laser beam misalignment with respect to the beam-expander support	10 mrad	5 mrad
Power consumption	< 200 W	< 50 W @ 25 °C
Weight	< 4.8 Kg	3.1 Kg
Dimensions	270 X 50 X 190 mm (LXAXP)	270 X 35.5 X 190 mm (LXAXP)

Table 7-6. ELPM-20K laser test results.

7.7 Test of Protection Filters

During this research, a number of laboratory measurements were performed on various protection filters, in order to select the best of current (commercially available) systems (i.e., optical density, transmittance in the visible, etc.) for employment at the PILASTER. These measurements included:

- ground personnel protection goggles;
- aircrew protection visors and spectacles;
- LTR Cinetheodolites Operator Sight (COS) filters.

In the last case, the optical gain of the COS needed to be determined first. For all systems, the principal objectives of the laboratory activities were:

- determination of the filters Optical Density (OD) at $\lambda = 1064$ nm;
- determination of the transmittance in the visible.

7.7.1 Filters for Ground Personnel and Aircrew

The instrumentation arrangement required to perform the measurements on ground personnel/aircrew protection filters is illustrated in Fig. 7-38. With reference to the figure, the following equipment was used:

1) Nd:YAG laser (*Quantel* YG 780-20)
2) Neutral density filters (*Optics for Research* 0.1÷4.0 ND)
3) Beam-steering optics
4) Protection filters:
   - *Laser Vision* mod. 01.307.00 (spectacles)
   - *Laser Vision* mod. 01.606.00 (spectacles)
   - *Cilas* mod. IR3-01 (spectacles)
   - *Gentex* mod. 91A8053-3 (aircrew helmet visor)
5) Lithium tantalite energy detector (*Newport* mod. 818J-50)
6) Multi function optical meter (*Newport* mod. 2835)

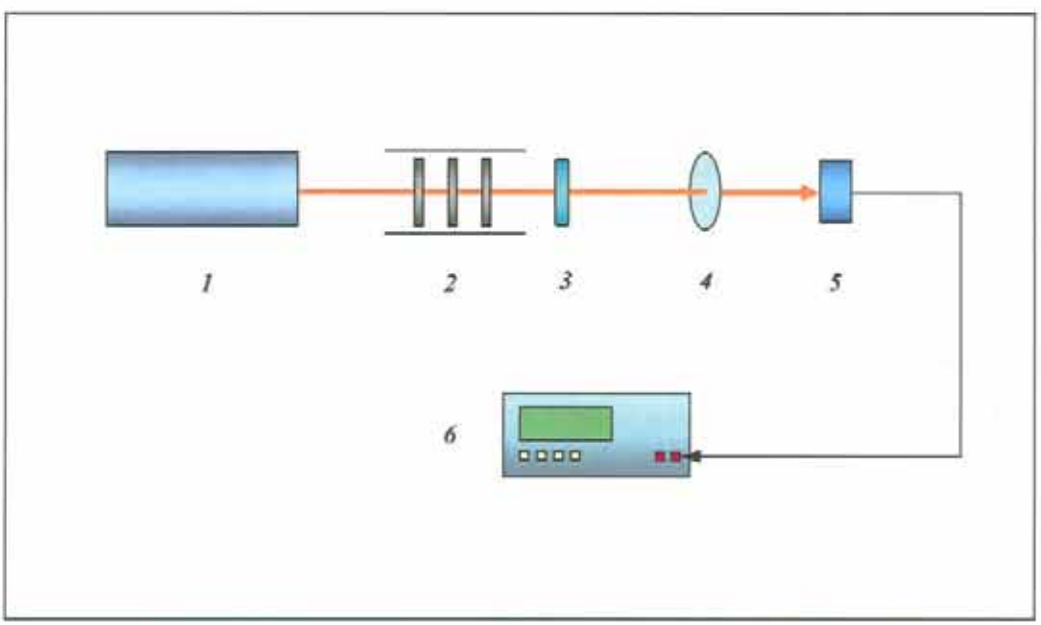

Figure 7-38. Instrumentation for filters OD determination.

The Optical Densities (OD') of each protection filter was obtained using the average of 5 energy measurements obtained with and without interposition of the protection filter in the optical circuit shown in Fig. 7-38, and using the formula:

$$OD = \log_{10} \frac{E_i(H_i)}{E_t(H_t)} \tag{7.6}$$

where $E_i(H_i)$ is the Incident Irradiance (Radiant Exposure) and $E_t(H_t)$ is the Transmitted Irradiance (Radiant Exposure). The various protection filters tested are shown in Fig. 7-39.

Figure 7-39. Tested laser protection filters.

The results of the measurements are reported in Table 7-7.

FILTERS	OD	
	Specified	Measured
Laser Vision mod. 01.307.00	5	5.4
Laser Vision mod. 01.606.00	5	5.7
Cilas mod. IR3-01	4	4.6
Gentex mod. 91A8053-3	3.5	3.5

Table 7-7. Protection filters OD measurements results.

Transmission in the visible (*T%*) was measured using the *Perkin Elmer* Lambda-19 spectrometer, equipped with an integrating sphere and capable to determine transmittance in the 350 ÷ 2500 nm spectral range. Before performing the measurements, the instrument was calibrated with a standard $BaSO_4$ reference. For each filter, it was initially performed a scan in the entire instrument spectral range in order to determine the cut-off frequencies, then a fine measurement was performed in the 350 ÷ 750 nm interval. The results of the measurements are presented in Fig. 7-40.

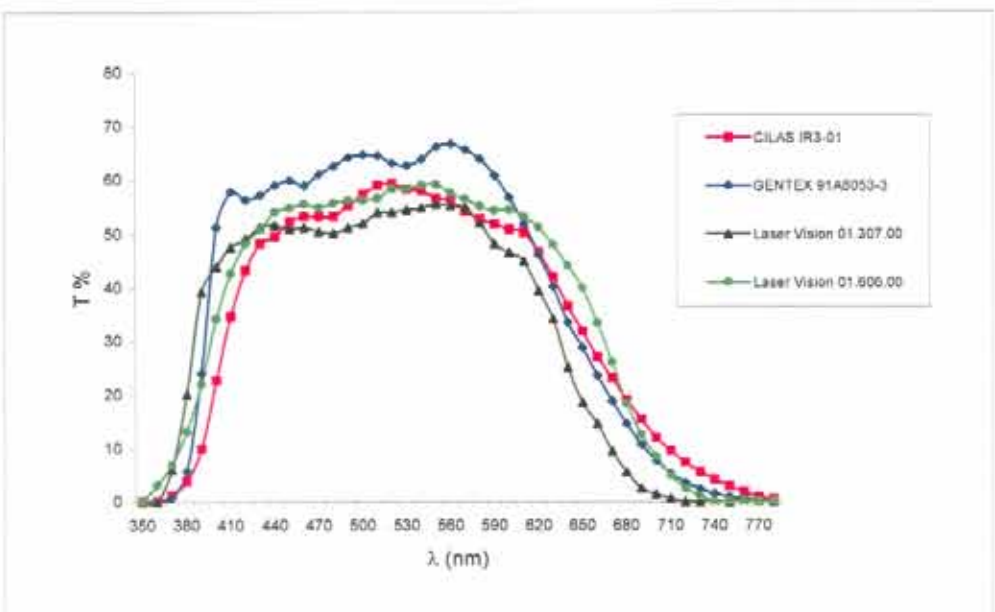

Figure 7-40. Protection filters transmission measurements results.

Although all filters matched the PILASTER program requirements, the filters finally selected were the *Laser Vision* 01.606.00 for ground personnel and the *Gentex* 91A8053-3 visor for aircrews. This last filter, in comparison with other possible laser visors and spectacles, also offered the advantage of an easy integration into the HGU-55/G standard helmet (also produced by *Gentex*) already in service with the Italian Air Force.

7.7.2 Test of PILASTER Cinetheodolite Optics

The instrumentation arrangement required to perform the measurements of COS optical gain (G) is illustrated in Fig. 7-41.

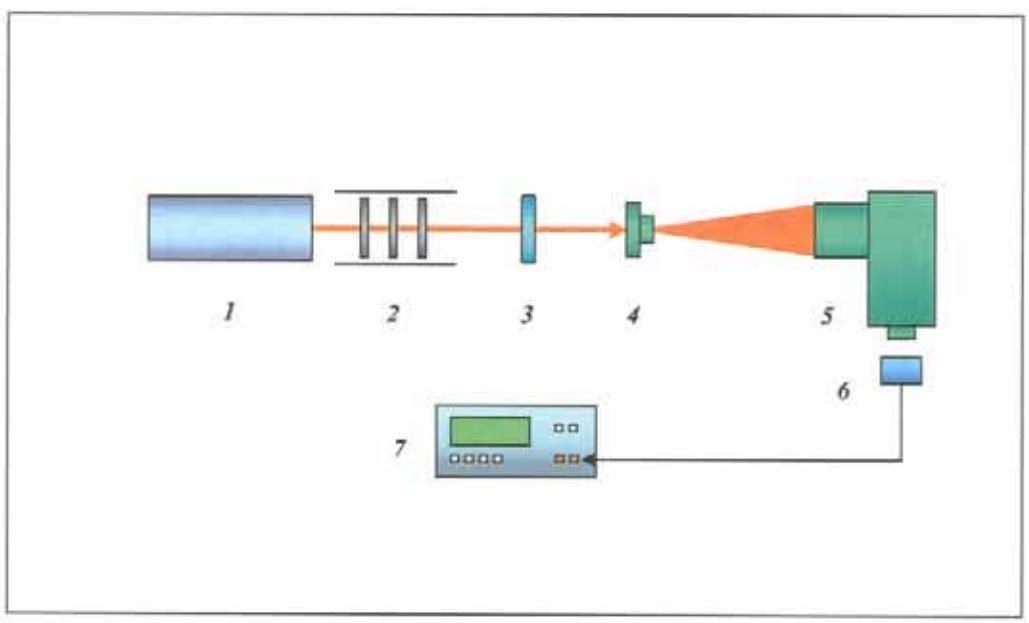

Figure 7-41. Instrumentation for COS optical gain determination.

With reference to the figure, the following equipment was used:

1) Nd:YAG laser (*Quantel* YG 780-20)
2) Neutral density filters (*Optics for Research* 0.1÷4.0 ND)
3) Beam-steering optics

4) Beam expanding optics

5) PILASTER CITE Operator Sight (*Kern "Solmar"* optics 2× and 12×)

6) Si-photodiode detector (*Newport* low-power detector mod. 818 SL)

7) Multi function optical meter (*Newport* mod. 2835)

As the COS features two different magnification options (M = 4 and M = 12), the measurements were performed with M = 12 (worst case for safety). The laser irradiance was then measured before the COS input (E_i) and successively at the exit pupil of the instrument (E_o). The measurements have been performed with different values of input irradiance. The results are reported in Table 7-8, were the values of output laser power (P_o) have been normalized (referred to the unit surface).

Measure	E_i ($\mu W\,cm^{-2}$)	P_o (μW)	E_o ($\mu W\,cm^{-2}$)	$E_o / E_i = G^2$	G
1	1.4	18.0	143.2	102.3	10.11
2	2.8	36.2	288.1	102.9	10.14
3	8.5	108.0	859.4	101.1	10.06
4	26.8	344.2	2739.1	101.5	10.07
5	49.2	635.3	5055.6	102.8	10.14

Table 7-8. COS Optical gain determination

The optical gain G is required for safety calculations and determination of the appropriate OD for COS operator protection filters. Particularly, given the NOHD of the system to be used at the PILASTER range, the Extended Nominal Ocular Hazard Distance (ENOHD) is given by:

$$ENOHD = NOHD \cdot G + \frac{a \cdot (G-1)}{\phi} \qquad (7.7)$$

The OD of the COS operator protection filter is given by:

$$OD \geq \log_{10} \frac{E_{i,KOS}}{E_{MPE}} \tag{7.8}$$

were E_{MPE} is maximum irradiance permitted for the naked human eye (either for a single pulse or for a train of pulses, depending on system mode of operation) and $E_{i,KOS}$ is the irradiance expected to reach the COS operator eye in the absence of a filter, which is given by:

$$E_{i,KOS} = E_{MPE} \cdot G^{-2} \tag{7.9}$$

From the calculation performed using the ELOP-PLD and CLDP technical data, considering the geometries involved with typical test/training missions, a filter with OD ≥ 5 could be used successfully for COS operator protection. Therefore, the *Laser Vision* 01.606.00 filter, already selected for ground personnel, was also suitable for COS operator protection during ELOP-PLD and CLDP missions at the PILASTER range.

Chapter 8

GROUND EXPERIMENTAL ACTIVITIES

8.1 General

Ground experiments performed during this research included Near Infrared (NIR) laser beam atmospheric propagation measurements, LTD/LRF pointing accuracy tests, systems harmonisation and performance evaluation trials of the STU and DGPS components of the PILASTER system. Furthermore, dedicated ground trials were performed with the LOAS system in order to assess its detection performance (in various weather conditions), and to verify the reliability of its obstacle classification algorithms. This chapter describes field trials and experiments carried out during the research. Particularly, tests objectives and procedures, instrumentation requirements and the data analysis methods are described, together with results of all ground experimental activities.

8.2 Atmospheric Extinction Measurements

In order to characterise atmospheric propagation at λ = 1064 nm and λ = 1550 nm, various tests were performed at the PISQ laser test range, using the PILASTER STU and additional instrumentation. Particularly, the following activities were performed:

- Determination of atmospheric extinction with different visibilities, temperatures, relative humidity values, wind intensities/directions, etc.;

- Determination of atmospheric extinction with different types of rain (i.e., rainfall-rate, raindrops dimensions, etc.).

For this purposes, the ELOP-PLD and a modified version of the LOAS systems were used, in conjunction with suitable weather monitoring instrumentation. The primary aim of these test activities was to start data acquisition for compilation of a Laser Propagation Data Base (LPDB), necessary to validate/improve the propagation models used for simulation and analysis at the PILASTER range.

Propagation measurements at λ = 1064 nm were performed using the same basic equipment employed for the PILASTER STU, including detectors at the targets locations and NIR cameras for beam characterization (i.e., energy measurement systems). Furthermore, some additional instrumentation was used for performing extinction measurements at λ = 1550 nm, in conjunction with the modified LOAS system. During the measurements, a number of atmospheric parameters were monitored and recorded: meteorological visibility (V), temperature (T), relative humidity (RH), atmospheric pressure (P), wind direction and velocity (W_d and W_v), solar radiation (E_s), and cloud amount. The local atmospheric parameters were continuously measured/recorded, during the test sessions, using the PILASTER meteorological instrumentation. These parameters were also monitored by the local Air Force Meteorological Offices (the relevant vertical profiles were determined with the aid of instrumented meteorological-balloons).

Meteorological data were collected at the PILASTER test range in different seasons and at different times of the day (4 times a day with 6 hours sampling intervals), in order to define a set of representative weather conditions for performing laser propagation measurements. The WMO scales used to classify cloud amount and horizontal visibility are defined in Table 8-1. The Cumulative Frequency Distribution Functions (CDF) relative to the data collected in the years 1888-2003 (divided in four groups of three months: Dec/Jan/Feb, Mar/Apr/May, Jun/Jul/Aug and Sept/Oct/Nov) are shown in the Figures 8-1 to 8-3.

WMO code	Cloud amount
0	No clouds
1	1/8
2	2/8
3	3/8
4	4/8
5	5/8
6	6/8
7	7/8
8	8/8
8	Upper air not visible

WMO code	Horiz. visib.
80	< 50 m
81	50-200 m
82	200-500 m
83	500-1000 m
84	1-2 km
85	2-4 km
86	4-10 km
87	10-20 km
88	20-50 km
88	>50 km

Table 8-1. WMO scales used to classify cloud amount and horizontal visibility.

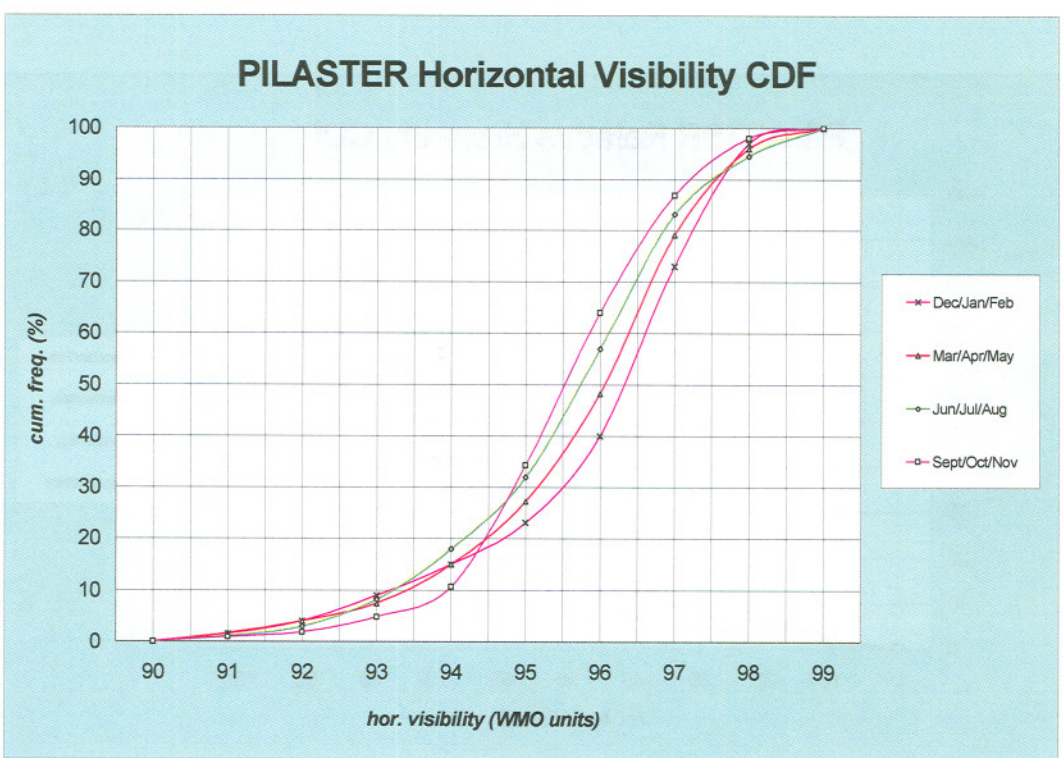

Figure 8-1. PILASTER horizontal visibility CDF (1998-2003).

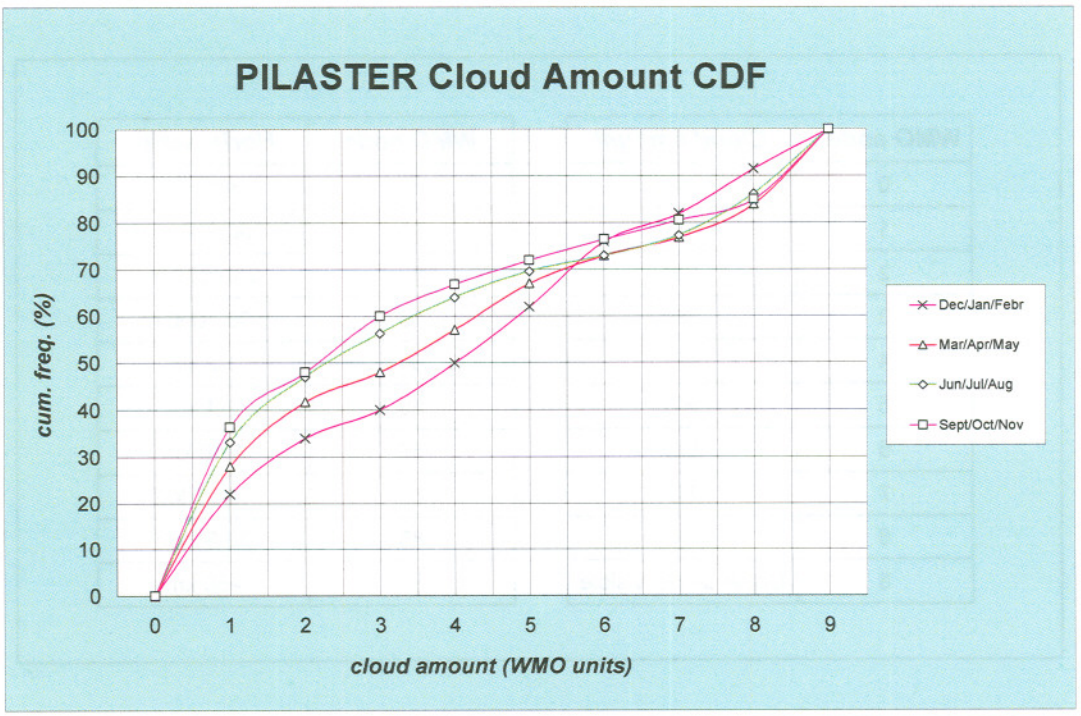

Figure 8-2. PILASTER cloud amount CDF (1998-2003).

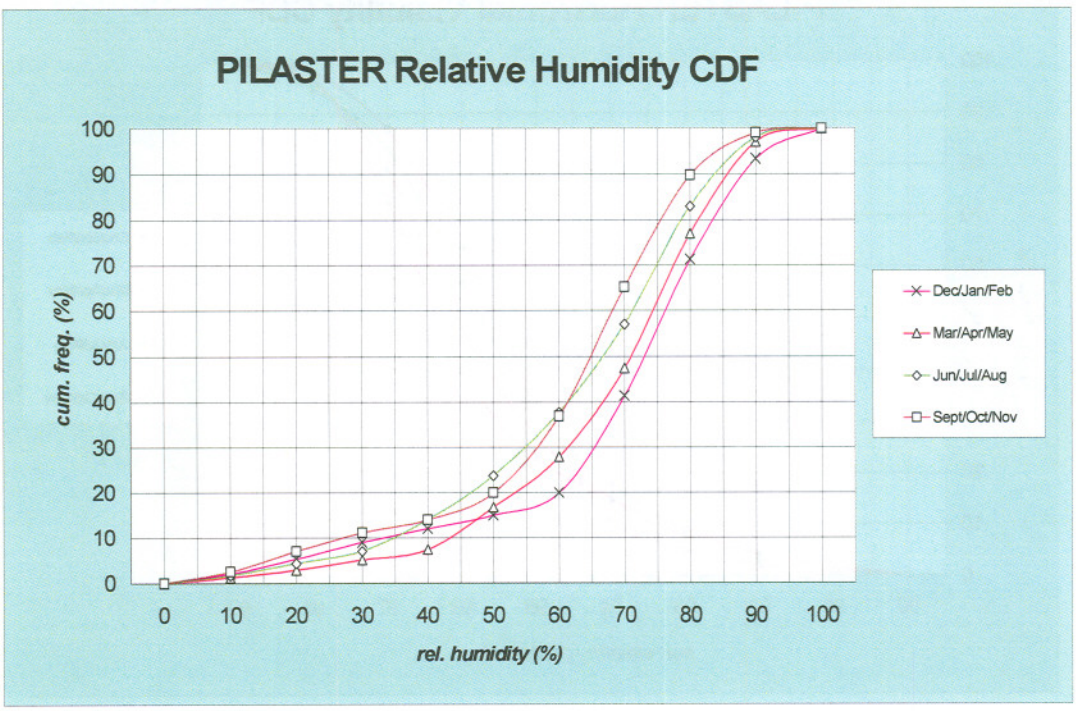

Figure 8-3. PILASTER relative humidity CDF (1998-2003).

The ELOP-PLD (λ = 1064 nm) and the LOAS (λ = 1550 nm) systems were used as the laser sources for propagation measurements. Particularly, in order to perform measurements at λ = 1550 nm the LOAS transmitter and receiver sub-systems were mounted on a tripod, as shown in Fig. 8-4.

ELOP-PLD *LOAS transmitter/receiver*

Fig. 8-4. ELOP-PLD and modified LOAS systems.

The PILASTER test range areas used for laser beam propagation measurements and the locations of systems and targets used for tests at λ = 1064 nm and λ = 1550 nm are shown in Fig. 8-5. More details about propagation tests geometries are presented later in this chapter.

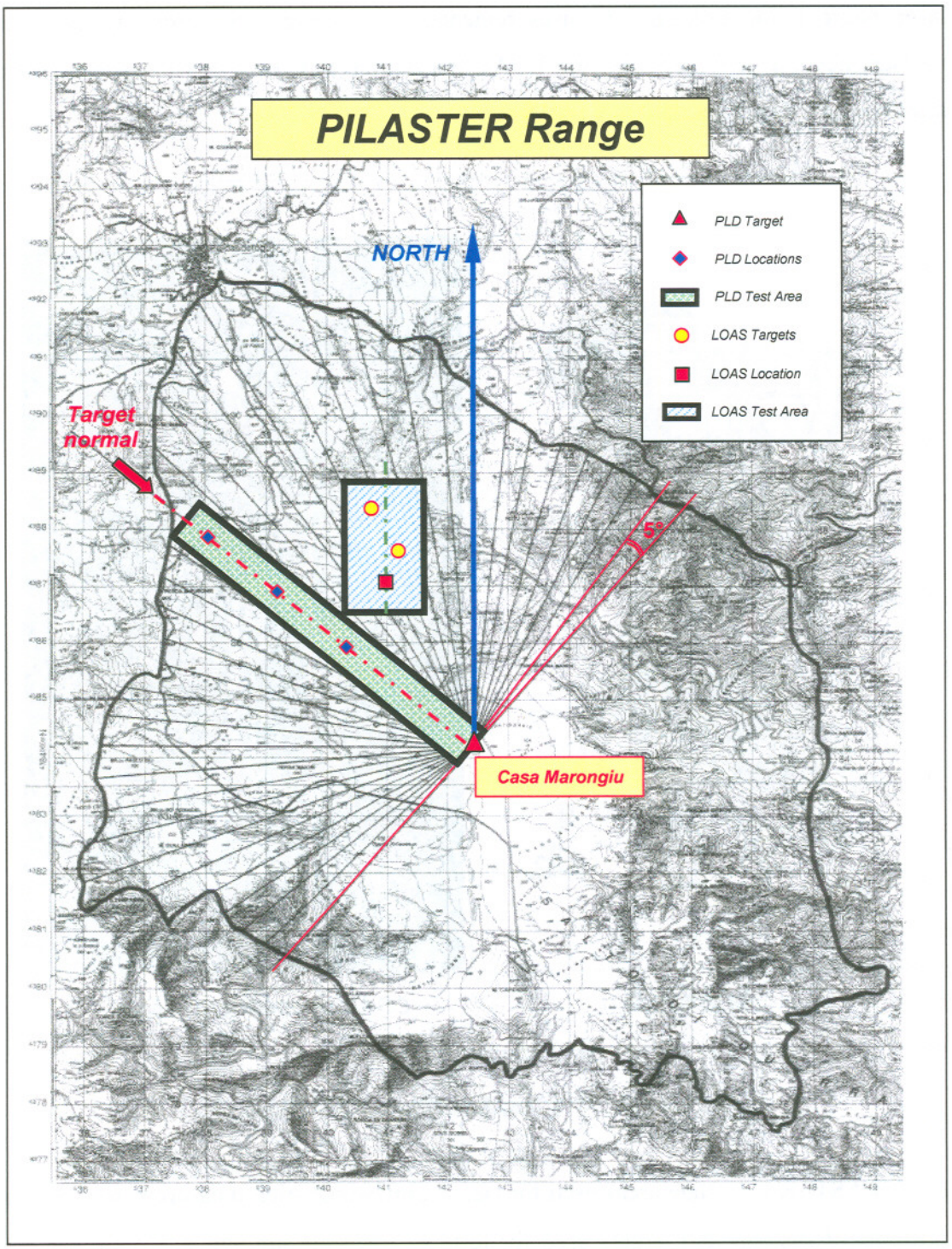

Figure 8-5. PILASTER areas used for atmospheric propagation measurements.

The three techniques used for atmospheric propagation tests were the following:

- Extinction Measurement Technique n° 1 (EMT-1), employing PILASTER STU instrumentation (i.e., non-calibrated Phoenix NIR camera and PEP sensors), for measurements at $\lambda = 1064$ nm.

- Extinction Measurement Technique n° 2 (EMT-2), employing the PILASTER calibrated Phoenix NIR camera, for measurements at $\lambda = 1064$ nm.

- Extinction Measurement Technique n° 3 (EMT-3), specifically developed for measurements at $\lambda = 1550$ nm, using the modified LOAS system.

EMT-3 had to be adopted instead of EMT-1 and EMT-2 (PILASTER standard techniques), because the LOAS laser transmitter presented a PRF of 40 kHz, not compatible with the standard PILASTER STU sensors response. Therefore, the Phoenix NIR camera was filtered and calibrated only for measurements at $\lambda = 1064$ nm. Furthermore, a Control Technique (EMT-CT) was adopted for field calibration of the PILASTER EMT-1 and EMT-2. The EMT-1 and EMT-2 techniques were described in chapter 5. The rationales of EMT-CT and EMT-3 are presented below.

8.2.1 EMT Control Technique (EMT-CT)

A control techniques was adopted to preliminarily verify the reliability and accuracy of the PILASTER EMT-1 and EMT-2. This control technique was based on a very simple concept (see Fig. 8-6). Placing the PLD/LOAS systems and the PILASTER NIR camera (with appropriate optics) very close to the target surface (100 m and 80 m respectively) in conditions of very good visibility ($V > 20$ km) and low humidity ($RH < 65\%$ at $T < 25°$), it was reasonable to assume that the entire output laser energy reached the target surface (i.e., $\tau_{atm} \cong 100\%$), and that the NIR camera detected the whole laser spot energy.

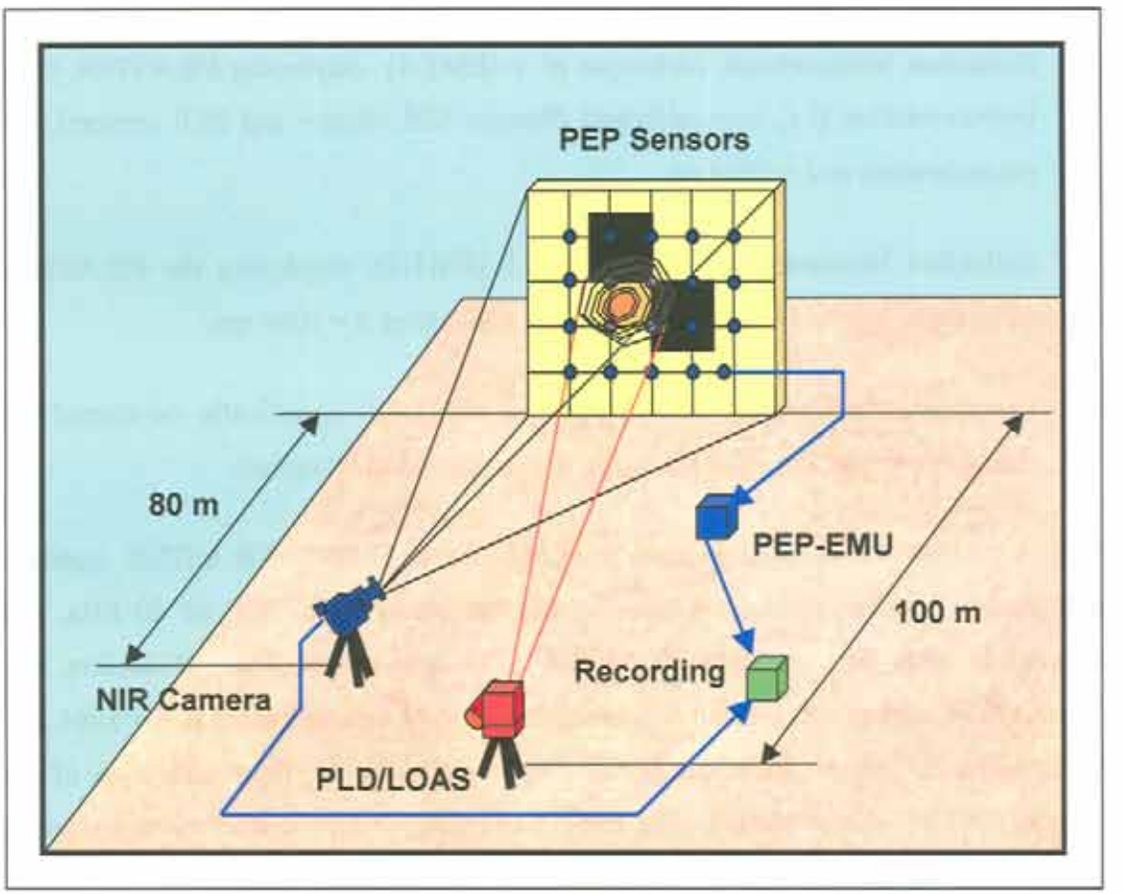

Figure 8-6. Experimental arrangement for EMT-CT tests.

Beam expansion and calibrated attenuation optics were used to conveniently modify the output laser beam for performing simultaneous NIR camera and PEP sensors measurements. Therefore, using the test instrumentation set up shown in Fig. 8-6 and performing a large number of measurements, the errors of the PILASTER instrumentation in measuring atmospheric transmittance (EMT-1 and EMT-2) could be estimated by standard mathematical and statistical techniques.

8.2.2 Description of EMT-3

Since the LOAS laser transmitter presented a PRF of 40 kHz, not compatible with the standard PILASTER STU sensors response (*Phoenix* NIR camera full-frame), an additional technique was developed for performing atmospheric propagation measurements at λ = 1550 nm. This technique allowed indirect determination of atmospheric extinction measuring the LOAS transmitted laser power and the anodic voltage at the receiver. The rationale of this new technique is the following.

In general, the function describing the anodic voltage at the receiver can be expressed in the form:

$$V = R_L \cdot R_S \cdot P \tag{8.1}$$

where V is the anodic voltage, R_L is the anodic load (Ω), R_S is the detector responsivity (A/W), and P is the power reaching the receiver detector (W).

From the discussion about laser systems performance calculation (chapter 3), assuming an extended target, the power at the detector can be expressed as follows:

$$P = K_{SYS} \cdot \rho \cdot \frac{1}{d_O^{\,2}} \cdot e^{-2\gamma d_O} \tag{8.2}$$

where ρ is the target reflectivity, d_O is the distance of the target from the transmitter/receiver, and γ is the extinction coefficient. K_{SYS} is a constant which accounts for all relevant transmitter/receiver systems parameters (e.g., transmitted laser power (P_O), efficiency of the transmitting and receiving optics (η_{TX}, η_{RX}), output beam diameter and divergence (D_L, α_T), transmitter/receiver LOS geometry, etc.).

Therefore, using two identical *Lambertian* targets placed at slant-ranges d_1 and d_2 respectively from the laser transmitter/receiver with a similar LOS geometry, and assuming that the extinction coefficient is constant in the slant-ranges considered, the

following expressions can be written for the two anodic voltages measured at the receiver using target n° 1 (V_1) and target n° 2 (V_2):

$$V_1 = R_L \cdot R_S \cdot \left(K_{STS} \cdot \rho \cdot \frac{1}{d_1^{\,2}} \cdot e^{-2\gamma d_1} \right) \tag{8.3}$$

$$V_2 = R_L \cdot R_S \cdot \left(K_{STS} \cdot \rho \cdot \frac{1}{d_2^{\,2}} \cdot e^{-2\gamma d_2} \right) \tag{8.4}$$

It is reasonable to assume that, measuring the anodic voltages V_1 and V_2, all system parameters remain constant, except the transmitted laser power (P_O) which may vary significantly in the time intervals where the two measurement sessions are performed. With these assumptions, we can write the following expressions:

$$V_1 = K \cdot P_{O1} \cdot \frac{e^{-2\gamma d_1}}{d_1^{\,2}} \tag{8.5}$$

$$V_2 = K \cdot P_{O2} \cdot \frac{e^{-2\gamma d_2}}{d_2^{\,2}} \tag{8.6}$$

where P_{O1} and P_{O2} are the transmitted laser powers, and the factor K contains all constant terms. Therefore:

$$\frac{V_1}{V_2} = \frac{P_{O1}}{P_{O2}} \cdot \frac{d_2^{\,2}}{d_1^{\,2}} \cdot e^{2\gamma(d_2 - d_1)} \tag{8.7}$$

and finally we obtain:

$$\gamma = \frac{1}{2\Delta d} \cdot \ln \left[\frac{\left(\frac{V_1}{P_{O1}} \right) \cdot d_1^{\,2}}{\left(\frac{V_2}{P_{O2}} \right) \cdot d_2^{\,2}} \right] \tag{8.8}$$

where the difference of the system to target slant-ranges (d_1 - d_2) has been replaced by the symbol Δd. It should be noted that all parameters contributing to the constant K do not affect the measurements (i.e., knowledge of these parameters is not required if their value remains constant during the measurements performed on target n° 1 and n° 2). TObviously, the accuracy in the measurement of γ is affected by:

- the error in measuring the distances d_1 and d_2;
- the error in measuring the voltages V_1 and V_2;
- the error in measuring the powers P_{O1} and P_{O2}.

Therefore, considering the errors relative to the measured parameters (σ_{d1}, σ_{d2}, σ_{V1}, σ_{V2}, σ_{PO1}, σ_{PO2}), we can write:

$$\sigma_\gamma^{\,2} = \frac{1}{(2\Delta d)^2}\cdot\left(\frac{\sigma_{V_1}^{\,2}}{V_1^{\,2}}+\frac{\sigma_{V_2}^{\,2}}{V_2^{\,2}}\right)+\frac{1}{(2\Delta d)^2}\cdot\left(\frac{\sigma_{P_{O1}}^{\,2}}{P_{O1}^{\,2}}+\frac{\sigma_{P_{O2}}^{\,2}}{P_{O2}^{\,2}}\right)+ \\ +\frac{\gamma^2}{\Delta d^2}\cdot\left(d_2+\frac{1}{\gamma}\right)^2\cdot\frac{\sigma_{d_2}^{\,2}}{d_2^{\,2}}+\frac{\gamma^2}{\Delta d^2}\cdot\left(d_1+\frac{1}{\gamma}\right)^2\cdot\frac{\sigma_{d_1}^{\,2}}{d_1^{\,2}} \tag{8.9}$$

Assuming that the error σ_d and the relative errors σ_V/V and σ_{PO}/P_O are the same for the measurements performed with target n° 1 and target n° 2, we have:

$$\sigma_\gamma^{\,2} = \frac{1}{2\Delta d^2}\cdot\left(\frac{\sigma_V^{\,2}}{V^2}+\frac{\sigma_{P_O}^{\,2}}{P_O^{\,2}}\right)+\frac{\gamma^2}{\Delta d^2}\cdot\left[\left(d_1+\frac{1}{\gamma}\right)^2\cdot\frac{\sigma_d^{\,2}}{d_1^{\,2}}+\left(d_2+\frac{1}{\gamma}\right)^2\cdot\frac{\sigma_d^{\,2}}{d_2^{\,2}}\right] \tag{8.10}$$

Rearranging the terms in eq. (8.10), we obtain:

$$\sigma_\gamma = \frac{1}{\Delta d}\cdot\sqrt{\left\{\frac{1}{2}\cdot\left(\frac{\sigma_V^{\,2}}{V^2}+\frac{\sigma_{P_O}^{\,2}}{P_O^{\,2}}\right)+\gamma^2\cdot\left[\left(d_1+\frac{1}{\gamma}\right)^2\cdot\frac{\sigma_d^{\,2}}{d_1^{\,2}}+\left(d_2+\frac{1}{\gamma}\right)^2\cdot\frac{\sigma_d^{\,2}}{d_2^{\,2}}\right]\right\}} \tag{8.11}$$

Thus, it is evident that the error in the measurement of γ is strongly affected by the distance between the two targets. For instance, in the case of the LOAS transmitter/receiver parameters, $\sigma_V/V = 5\%$ and $\sigma_{P_O}/P_O = 2\%$. Assuming $\sigma_d = 1$ m, $d_1 = 800$ m, $\Delta d = 100$ m, $d_2 = 800$ m, $\gamma = 7\times10^{-4}$ m^{-1}, from eq. (8.11) we obtain a relative measurement error σ_γ/γ of about 54%. Obviously, doubling the distance between the two targets (e.g, assuming $\Delta d = 200$ m and $d_2 = 1000$ m), the estimated relative error would be 27% (half of the previous case).

The experimental arrangement used for the extinction measurements at $\lambda = 1550$ nm is shown in Fig. 8-7. Since the LOAS and the targets coordinates were determined by means of Differential GPS (DGPS) static surveys, we had $\sigma_d \leq 0.01$. Therefore:

$$\frac{1}{2}\cdot\left(\frac{\sigma_V^{\,2}}{V^2}+\frac{\sigma_{P_O}^{\,2}}{P_O^{\,2}}\right) >>> \gamma^2\cdot\left[\left(d_1+\frac{1}{\gamma}\right)^2\cdot\frac{\sigma_d^{\,2}}{d_1^{\,2}}+\left(d_2+\frac{1}{\gamma}\right)^2\cdot\frac{\sigma_d^{\,2}}{d_2^{\,2}}\right] \qquad (8.12)$$

and:

$$\sigma_\gamma \cong \frac{1}{\Delta d}\cdot\sqrt{\frac{1}{2}\cdot\left(\frac{\sigma_V^{\,2}}{V^2}+\frac{\sigma_{P_O}^{\,2}}{P_O^{\,2}}\right)} \qquad (8.13)$$

As in our case $\Delta d = 1000$ m, the estimated measurement error was:

$$\sigma_\gamma \cong \frac{1}{\Delta d}\cdot\sqrt{\frac{1}{2}\cdot\left(\frac{\sigma_V^{\,2}}{V^2}+\frac{\sigma_{P_O}^{\,2}}{P_O^{\,2}}\right)} = 3.81\cdot10^{-5}\ \text{m}^{-1} \qquad (8.13)$$

Therefore, since in general $\gamma > 10^{-4}$ m^{-1}, we calculated a maximum relative error σ_γ/γ of about 4%.

Chapter 6

SYSTEMS EYE-SAFETY ANALYSIS

6.1 General

The methods developed for evaluating the hazards associated with the use of ground and airborne laser systems operating in the visible and near infra-red non-eyesafe portions of the spectrum is presented in this chapter. Particularly, safety issues of state-of-the-art Nd :YAG target designators (LTD) are thoroughly investigated, in order to identify operational procedures and limitations for employment of such equipment at the PILASTER range during execution of both test and training missions.

Various mathematical algorithms are presented, developed for employment in the PILASTER mission planning tools, that allow a complete verification of laser-safety for ground and airborne laser systems. A description of the laser-safety simulation programs developed, together with sample simulation results are given in the chapter 10 of this thesis.

Although the results presented were originally developed for airborne/ground pulsed laser target designators, they also apply to other non-eyesafe laser systems including pulsed range finders and beam riders operating in the visible and near-infrared portions of the electromagnetic spectrum.

6.2 Laser Safety Standards

The methodology to be used in laser safety assessments is prescribed by various NATO and national laser safety standards [1-8], including the STANAG 3606, the SMD-W-001 Italian military standard, the JSP 390 British military

standard, etc.. However, none of these standards focuses on Airborne Laser Systems (ALS's), and only generic suggestions are given on how to apply the various proposed safety areas calculation routines to the case of highly dynamic platforms, such as airborne designation systems. Furthermore, also in the cases of Ground Laser Systems (GLS's), the deterministic approaches described in the NATO/national standards often lead to safety areas calculations exceeding the dimensions of most existing test ranges. The alternative statistic approaches proposed in the standards, on the other hand, are based on several assumptions/system models and imply a clear definition of risk levels (e.g., maximum probability of eye injury), which in various NATO countries (and in Italy as well) are not jet available. Therefore, new algorithms and procedures were developed which, respecting all necessary safety criteria, lead to practical laser safety areas for both ALS and GLS systems. These newly developed algorithms and procedures, which represented an important integration of the existing NATO/Italian standards, are being used at the PILASTER range in Sardinia, during execution of both test and training missions. Furthermore, following the results of this research, some actions are now being taken by the Italian Ministery of Defence in order to propose modifications/integrations to the existing STANAG 3606 and related national documents.

6.3 Ocular Hazard Distance

According to NATO STANAG 3606 and the Italian SMD-W-001 military laser safety standard (developed in accordance with the STANAG 3606 and quite similar to the JSP 390 British military standard), the Ocular Hazard Distance (OHD) is required for calculating all laser hazard areas. The factors affecting the OHD are:

a. design characteristics of the laser system;
b. atmospheric attenuation;
c. atmospheric scintillation;
d. use of laser protective eyewear;
e. viewing through magnifying optics;
f. near-field effects;
g. use of beam attenuating filters.

In this paragrph, only the most important equations necessary to calculate the OHD for pulsed ALS/GLS due to the factors *a*-*g* are presented. More detailed information about the various models presented here, together with additional equations accounting for different systems/scenarios may be found in the literature (see, for gudance, the *Laser Safety Standards* listed in the references).

The key system-related parameters to be taken into account for calculation of the OHD are the Maximum Permissible Exposure (MPE) and the Nominal Ocular Hazard Distance (NOHD). The MPE, generally expressed in J/cm^2 is a function of the Exposure Time *(T_E)*. Knowing the MPE for a single pulse, the MPE for a train of pulses can be calculated using the following equation:

$$MPE_T = MPE_P \times \frac{1}{\sqrt[4]{f \times T_E}} \tag{6.1}$$

where:

MPE_P = maximum permissible exposure (single pulse)
MPE_T = maximum permissible exposure (train)
f = pulse repetition frequency
T_E = time of exposure

There are various expressions used to calculate the value of the NOHD, depending on the characteristics of the laser (i.e., pulsed/CW, single-pulse/train of pulses, *Gaussian* or non-*Gaussian* beam, etc.), and the location of the observer (direct illumination or diffuse reflection). A form of the NOHD equation valid for direct vision of pulsed lasers with *Gaussian* beam distributions, is the following:

$$NOHD = \frac{\sqrt{\frac{1.27 \cdot Q \cdot \sqrt[4]{f \cdot T_E}}{MPE_P}} - a}{\Phi} \tag{6.2}$$

where:

Q = output laser pulse peack energy
a = output beam diameter

According to the Italian Safety Standard SMD-W-001, for non-Gaussian beams Q in equation (6.2) should be multiplied by a factor of 2.5. The cumulative OHD arises from the full or partial application of correction factors to the NOHD allowing for near-filed effects, magnifying optics, atmospheric extinction, atmospheric scintillation, beam attenuating filters and protective laser eyewear.

If the laser radiation is viewed through magnifying optical instruments, the NOHD will increase to a distance called the Extended Ocular Hazard Distance (EOHD), which can be calculated using the following equation:

$$EOHD = NOHD \cdot \sqrt{K} \tag{6.2}$$

where K is a factor depending on the laser wavelength and the viewing conditions (refer to SMD-W-001 or JSP 390 for details about calculation of K).

Both SMD-W-001 and JSP 390 include the following equation for calculating the reduction of the hazard distance due to atmospheric attenuation:

$$OHD_{\gamma} = \frac{NOHD}{2 - e^{-0.5\gamma \cdot NOHD}} \tag{6.3}$$

where γ is the atmospheric attenuation coefficient. Both standards also refer to the following model for calculating the atmospheric extinction coefficient for laser wavelengths between 400 and 2000 nm:

$$\gamma = 10^{-3} \cdot \left(\frac{3.91}{V}\right) \cdot \left(\frac{550}{\lambda}\right)^{A} \tag{6.4}$$

where:

V = meteorological range (km)

λ = laser wavelength (nm)

A = exponent varying with V and given by $0.585 \cdot V^{0.33}$

It is evident that eq. (6.4) is one of the equations already used in the ESLM empiric model (see chapter 3) to determine the scattering coefficient without rain. It is obvious that, using only eq. (6.4) for calculating the atmospheric extinction

coefficient would lead to underestimated γ values for most weather conditions and at most wavelengths of practical interest, which is acceptable for eye-safety calculations but implies a simplifying conservative assumption (i.e., absorption is neglected).

Because the meteorological conditions can change rapidly, any allowance for atmospheric attenuation should be applied with caution. For practical reasons, it is suggested that γ is taken to be zero if a reliable estimate of V cannot be made.

Together with attenuation, when a laser beam propagates in the atmosphere (especially with slant paths close to the ground) its radiance may be modified by focusing (scintillation) or defocusing effects caused by turbulence (see chapter 3). In the first case (scintillation), the values of the beam irradiance may be significantly greater than the MPE, and therefore it is prudent to make some allowance for this effect. According to the SMD-W-001 safety standard, when scintillation is likely to occur at the range (e.g., due to high measured or predicted C_n values), *NOHD* should be modified as follows:

$$OHD_S = 2.662 \cdot NOHD \tag{6.5}$$

A better approach to this problem is presented in the JSP 390 British (Military) safety standard (1998 Edition). In this document, the following analiysis is presented to correct the NOHD for atmospheric scintillation.

If N_l is less than the parameter N_{max}, where:

$$N_{max} = 2.2 \times 10^{-7} \frac{\lambda^{0.64}}{C_n^{\,1.09}} \tag{6.6}$$

Then, to take account of scintillation, N_l is modified to obtain OHD_S using the following equation:

$$OHD_S = \left(2.66^{N_1 / N_{max}}\right) N_l \tag{6.7}$$

where N_l is either the NOHD or the cumulative OHD arising from the full or partial application of factors allowing for near-field effects, magnifying optics, beam attenuating filters, atmospheric extinction and laser protective eyewear.

If $N_I \geq N_{max}$, or if it is not possible to determine C_n, then OHD_S is given by:

$$OHD_S = 2.66 N_I \tag{6.8}$$

Both the JSP 390 British safety standard and the Italian SMD-W-001 safety standard present the following equations for correcting the N_I parameter (i.e., the NOHD or the cumulative OHD calculated taking into account a part or all other correction factors) due to laser protective eyewear (OHD_{PE}), near-filed effects (OHD_{NF}), and beam attenuating filters (OHD_{AF}):

$$OHD_{PE} = N_I \cdot 10^{-OD/2} \tag{6.9}$$

$$OHD_{NF} = N_I \sqrt{1 - \left(\frac{R_N}{N_I}\right)^2} \tag{6.10}$$

$$OHD_{AF} = N_I \sqrt{\tau} \tag{6.11}$$

where:

OD = eyewear optical density

R_N = 'near-field' range of the laser

τ = transmittance of the beam attenuating filter at the laser wavelength

6.4 ALS Study Analysis

During test range and training operations with non-eyesafe airborne laser systems, it is essential to determine the hazards associated with the use of the systems, taking into account the factors directly or indirectly affecting eye-safety. These factors include the geometry of the attack (i.e., aircraft maneouvres), the horography of the area around the target, the probabilities of inadvertent laser activation, the presence of reflecting materials in the area illuminated (or potentially illuminated) by the laser, and so on. It is therefore meaningful to take into account the mission profiles of typical self-designation attacks illustrated in Fig. 6-1 (the co-

operative attack geometry can be considered a sub-case of this, where laser designation is performed by a companion of the attacking aircraft).

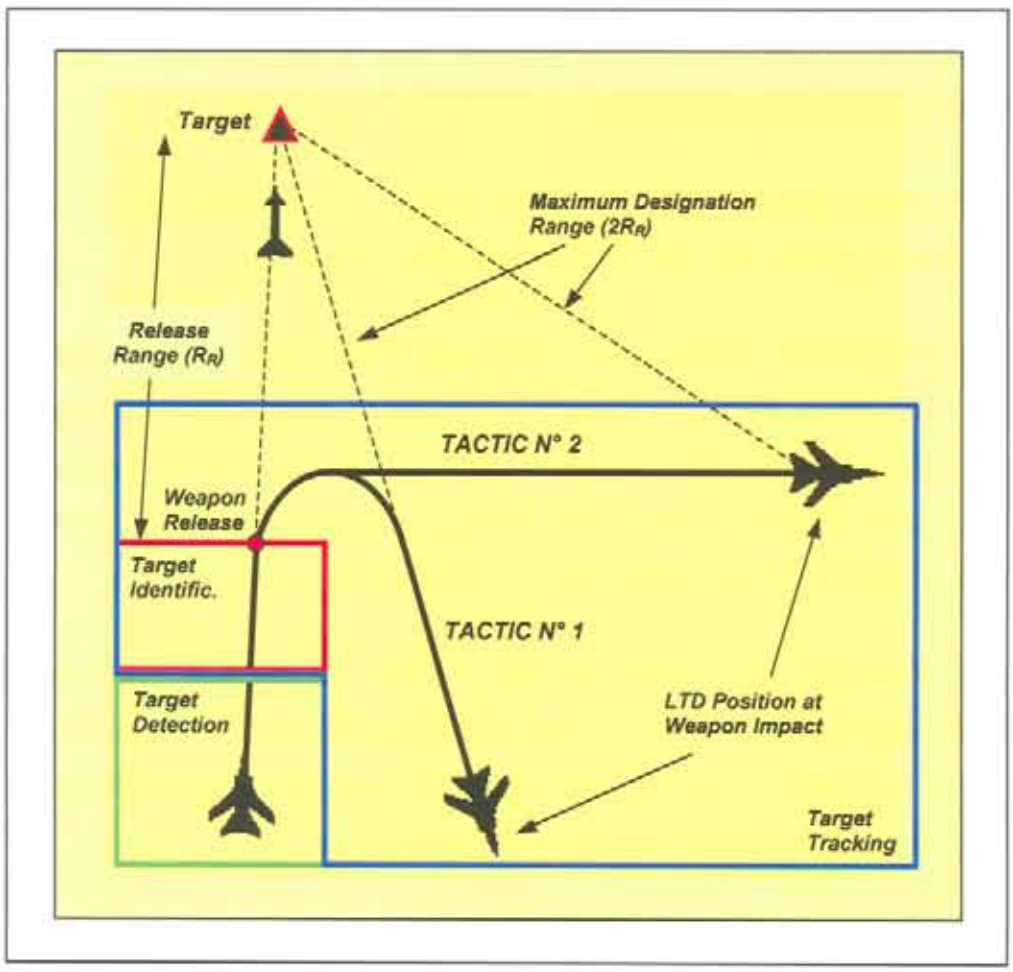

Figure 6-1. LTD/LGW mission profile (self-designation).

Designation in initiated in the final portion of the bomb trajectory, and it is generally performed at a considerable range from the target (comparable to the visual range). This means that, normally, the grazing angle to the target can be very small, and the ground area effectively illuminated by the laser during the attack can be quite large. Moreover, once designation has initiated, there is a further hazard related either with the inherent pointing accuracy of the laser designation system and the probability of inadvertent rotation of the designator line-of-sight during laser firing. Finally, we must consider that also the simple carriage of the system by the a/c may be dangerous to people on the ground if the probability of inadvertent activation is too high and the a/c is flying lower than the OHD.

6.4.1 ALS Hazard Areas

A dedicated analysis was required in order to define the models for defining and modelling the laser hazard areas associated with airborne systems. Particularly, the following areas where identified:

- ***ALS Beam Hazard Area*** (A-BHA), defined as the area which may be illuminated by the laser beam in the event of inadvertent firing;

- ***ALS Buffer Zone*** (A-BZ), given by the sum of the area directly illuminated by the laser beam during the firing (a function of beam output diameter and divergence) and the area around the laser beam that may be inadvertently illuminated considering the overall pointing accuracy of the LTD, the reaction time of the aircrew and the probability of failure of the system;

- ***ALS Extended Buffer Zone*** (A-EBZ), defined as the area which may be illuminated due to specular reflection within the A-BZ. The existence of an EBZ can be prevented by removing all possible reflectors laying within the BZ (e.g., residues of previous bomb drops, metal objects, etc.).

For air-to-groung LTD operations, the A-BHA is given by the intersection with the ground of a sphere with centre at the aircraft location in space and a radius equivalent to the OHD (Fig. 6-2). Therefore, the radius of the A-BHA (R_{BHA}) is given by the following equation:

$$R_{BHA} = \sqrt{OHD^2 - z^2} \tag{6.12}$$

where z is the AGL aircraft altitude.

From the definition given above, it appears evident that, in the practical case of an airborne LTD (A-LTD), the actual existence of an A-BHA is related with the following factors:

- inadvertent activation of the laser in the various modes of the LTD;
- inadvertent rotation of the LOS during commanded laser activation.

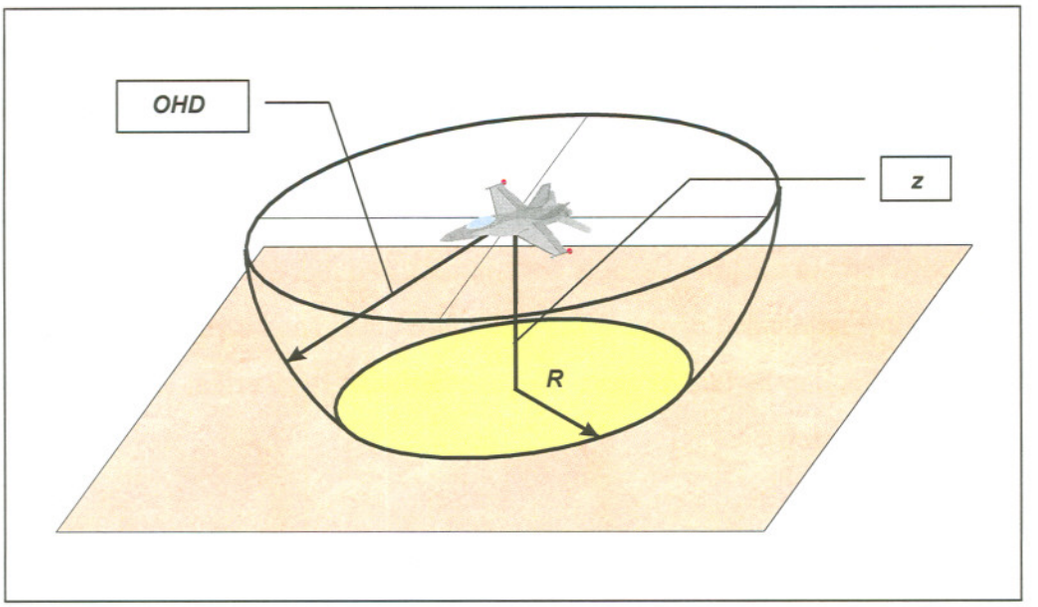

Figure 6-2. ALS Beam Hazard Area (A-BHA) geometry.

Therefore, it is acceptable to calculate the A-BHA using the OHD for exposition to a single pulse (since the airborne LTD is in continuous motion, it is extremely improbable that an observer is illuminated by a train of pulses during accidental laser activation or LOS rotation). As an example, we consider the probabilities given in Table 6-1 for the a typical airborne A-LTD system (entire system operational life).

A-LTD Mode	*Hazardous Event*	*Probability*
OFF	Inadvertent Activation	**0**
ON	Inadvertent Activation	**5E-16**
SLAVE/TRACK	Inadvertent Activation	**8E-9**
Laser Arm	Inadvertent Activation	**3E-4**
Laser Fire (SLAVE/TRACK)	Inadverted LOS Rotation	**2E-6**

Table 6-1. Hazard probabilities in the various A-LDT modes.

The data in Table 6-1 must be linked to the reliability data of the aircraft avionics systems connected with the LTD. In our example, we assume that the A-LTD system is commanded by the Weapon Systems Operator (WSO) trough a cockpit control panel with a SAFE and an ARM position (i.e., a stand-by mode in which the laser cavity is powered but the laser beam is not emitted), and that the laser emission (laser FIRE mode) is commanded by the WSO with a dedicated hand control (also used for manual target tracking). In this case, the probability of inadvertent laser activation ($P_{SAFE \rightarrow FIRE}$) is given by:

$$P_{SAFE \rightarrow FIRE} = P_{SAFE \rightarrow ARM} \times P_{ARM \rightarrow FIRE} \tag{6.13}$$

Assuming that the probability of inadvertent activation of the ARM mode from the SAFE condition ($P_{SAFE \rightarrow ARM}$) referred to the entire A-LTD operational life is 7E-4, and that the probability of inadvertent activation of the FIRE mode from the ARM condition ($P_{ARM \rightarrow FIRE}$) is 1 for missions in which the WSO acts on the cockpit commands (i.e., simulated or real attack missions) and 1E-2 in missions were the WSO does not act on the cockpit commands (e.g., ferry flights), then the overall probabilities of inadvertent laser activation (with the A-LTD in SAFE mode) are given in Table 6-2.

A-LTD Mode	***Mission***	$P_{SAFE \rightarrow FIRE}$
ON/SAFE	Ferry flight	**7E-6**
ON/SAFE	Test/Training	**7E-4**

Table 6-2. A-LTD risk levels with laser SAFE.

The A-BZ is given by the sum of the area directly illuminated by the laser beam during the firing (a function of beam output diameter and divergence) and the area around the laser beam that may be inadvertently illuminated considering the overall pointing accuracy of the LTD system, the reaction time of the aircrew and the

probability of failure of the system. In other terms, at any instant, the A-BZ shape can be approximated by an ellipse where the target occupies one of the foci.

With reference to Fig. 6-3, the dimensions of the A-BZ can be calculated for any given location of the aircraft in space by using the following equations:

$$R_1 = \left[\frac{1}{\tan\varphi} - \frac{1}{\tan(\varphi+\delta)}\right] \cdot z \tag{6.14}$$

$$R_2 = \frac{z \cdot \sin\delta}{\sin\varphi \cos\delta} \tag{6.15}$$

$$R_1 = \left[\frac{1}{\tan(\varphi-\delta)} - \frac{1}{\tan\varphi}\right] \cdot z \tag{6.16}$$

where:

φ = angle between LOS and horizontal in the plane containing the LOS
δ = pointing error plus safety margin

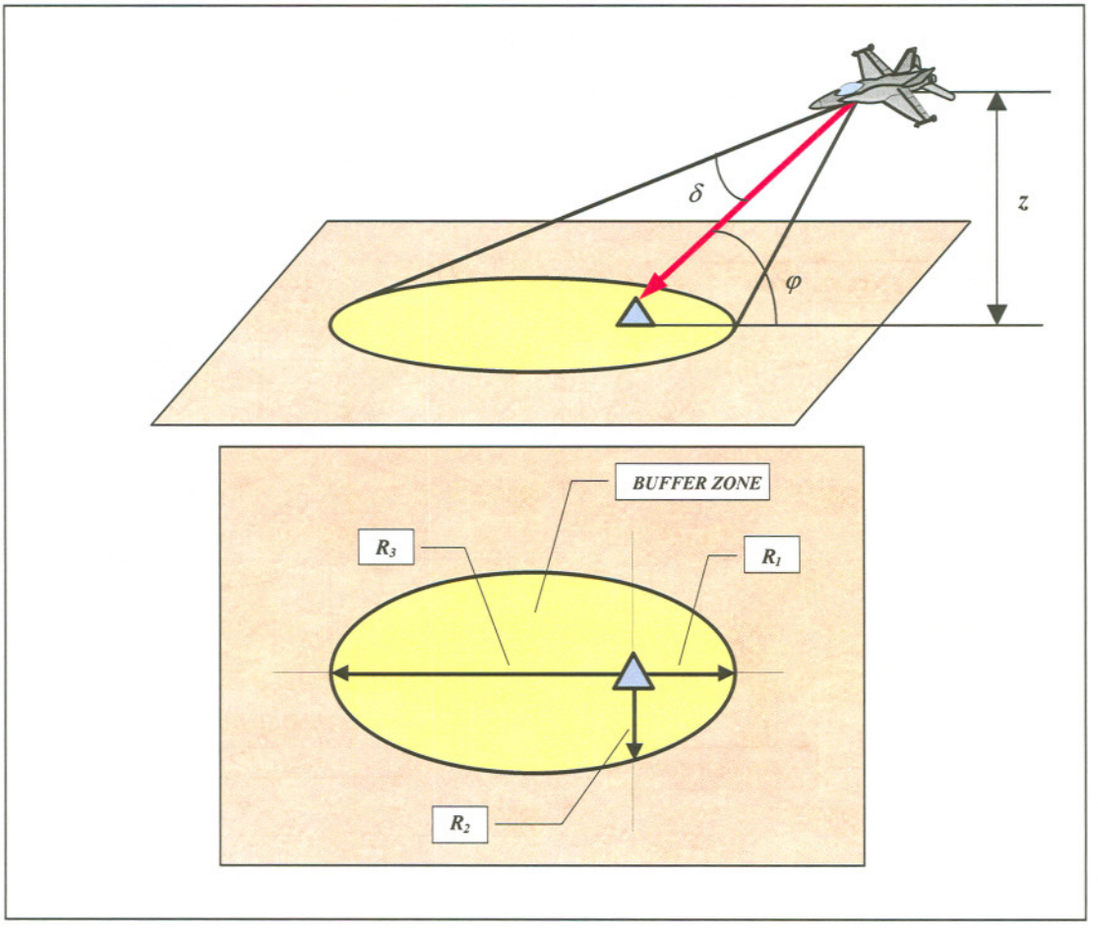

Figure 6-3. ALS Buffer Zone (A-BZ) geometry.

The last area to be determined is the ALS Extended Buffer Zone (A-EBZ), defined as the area which may be illuminated due to specular reflection within the A-BZ. The existence of an A-EBZ can be prevented by removing all possible reflectors laying within the A-BZ (e.g., residues of previous bomb drops, metal objects, etc.). However, while evacuation of people can be performed quite easily, removal of all reflecting materials from the A-BZ can be a very demanding task for a test range and often it is impracticable. Therefore, in general, we must consider the A-EBZ as the laser hazard area to be evacuated. Determination of the A-EBZ area is not an easy task, since its dimension and shape are dependant upon the aircraft position in space and its angular velocity with respect to the reflection points located in the A-BZ (varying continuously during a mission). This is true because the hazard to the naked human eye is a function of the exposure time (T_E) and T_E to a specularly reflected laser beam varies with aircraft relative velocity. It is therefore necessary to implement a simulation tool in order to calculate the aircraft envelope limitations due to a certain pre-defined maximum evacuation area or, conversely, the dimension of the evacuation area required with a certain pre-defined mission profile. Fig. 6-4 gives an idea of the various geometric and physical parameters involved.

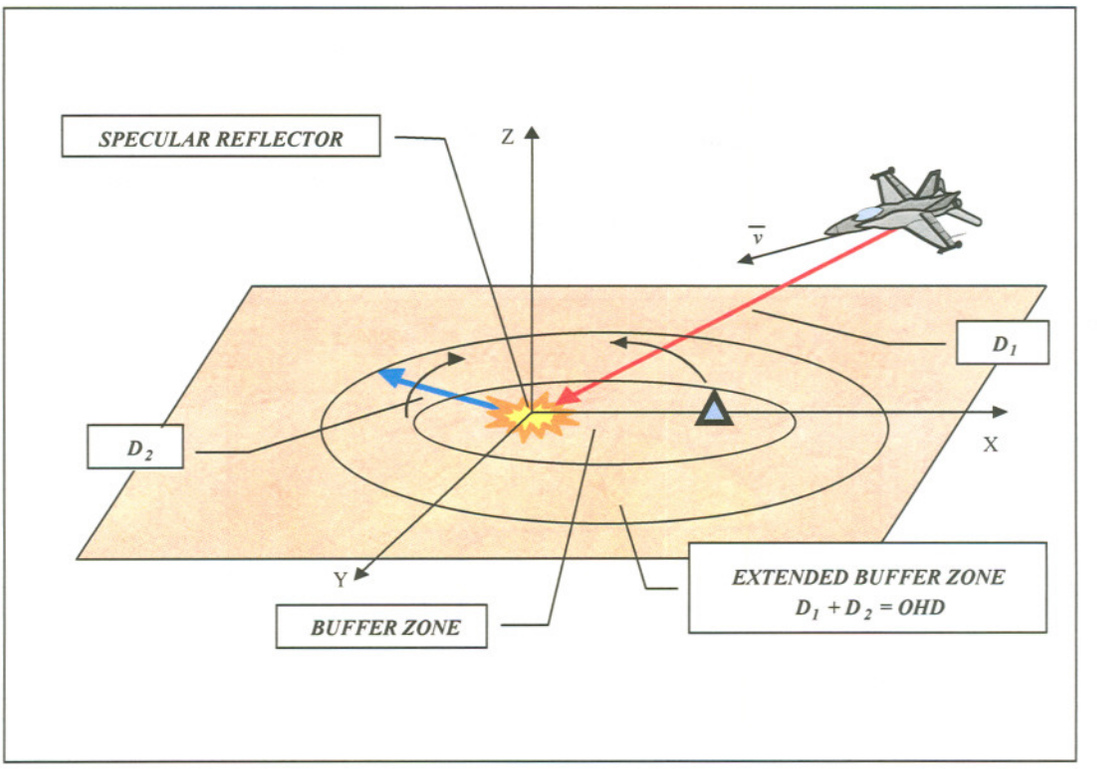

Figure 6-4. ALS Extended Buffer Zone (A-EBZ) geometric elements.

The algorithms needed to calculate the A-EBZ given a certain aircraft flight envelope (or the envelope restrictions to be applied for a certain pre-defined ground evacuation area), is given in the following paragraph.

6.4.2 Safety Verification Algorithm

In a Cartesian reference frame centred at the point of intersection of the LOS with the ground (point A in Fig. 6-5), the velocity vector of the aircraft ($\bar{v}$) can be expressed as:

$$\bar{v} = \overline{\Omega} \times \bar{r} \tag{6.17}$$

where:

$\overline{\Omega}$ = the aircraft angular velocity vector
$\bar{r}$ = aircraft position vector

Therefore, the module of the angular velocity of the laser beam with respect to the reflection point on the ground, is given by:

$$\left|\overline{\Omega}\right| = \frac{\left|\bar{v}\right|}{\left|\bar{r}\right|} \cdot \sin\alpha \tag{6.18}$$

where α is the angle between the aircraft position and the velocity vector. This is given by:

$$\alpha = \arccos \frac{\bar{v} \cdot \bar{r}}{\left|\bar{v}\right| \cdot \left|\bar{r}\right|} \tag{6.19}$$

Therefore, knowing the vectors $\bar{v}$ and $\bar{r}$ at any point in space it is possible to calculate the corresponding value of $\left|\overline{\Omega}\right|$. This value can then be compared with the minimum sweep velocity admitted for the reflected laser beam, which is a function, at any point on the ground, of beam dimension (i.e., output area and divergence) and maximum permissible exposure time $T_{E\,(MAX)}$.

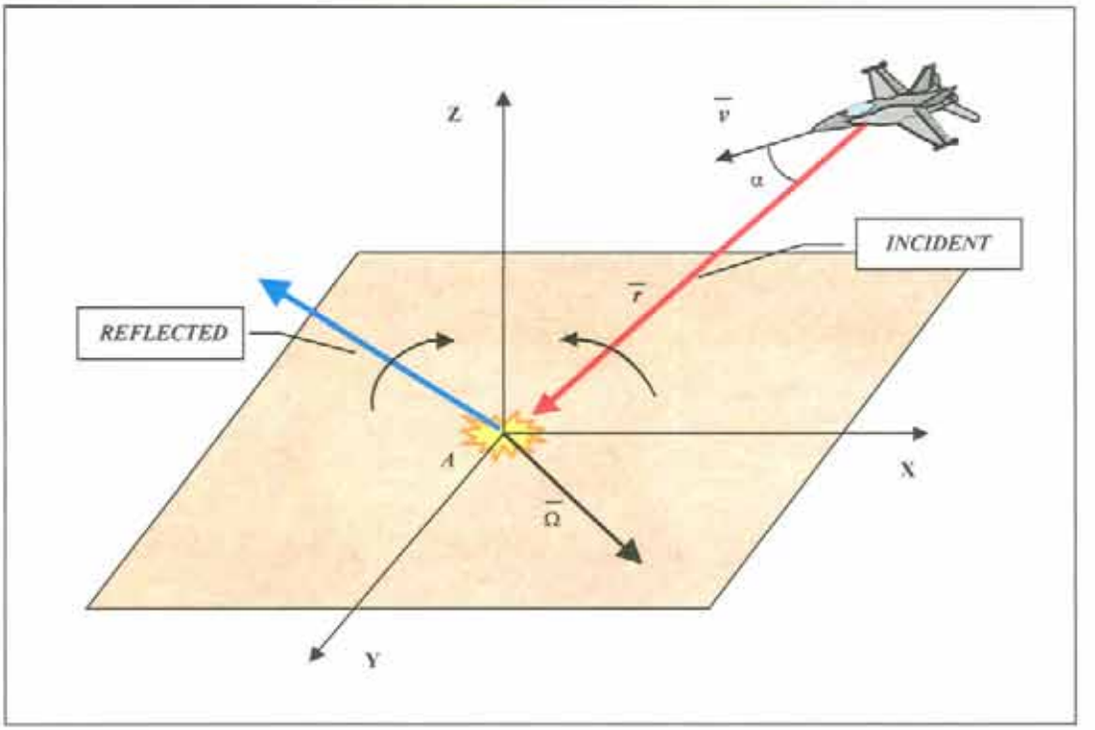

Figure 6-5. ALS Extended Buffer Zone (A-EBZ) geometry.

In other terms, since the actual exposure time of an observer to the reflected laser radiation is a function of the angular velocity $\overline{\Omega}$, of the beam divergence and of the distance between the observer and the point A, knowing the effective time of exposure (and therefore the effective OHD), it is possible to verify the safety of a scenario, taking into account the elements listed below.

- aircraft position and velocity
- observer position
- reflection point
- laser characteristics

and comparing the effective NOHD with the sum of the distances observer-point A and point A-aircraft. The procedure described is illustrated in Fig. 6-6.

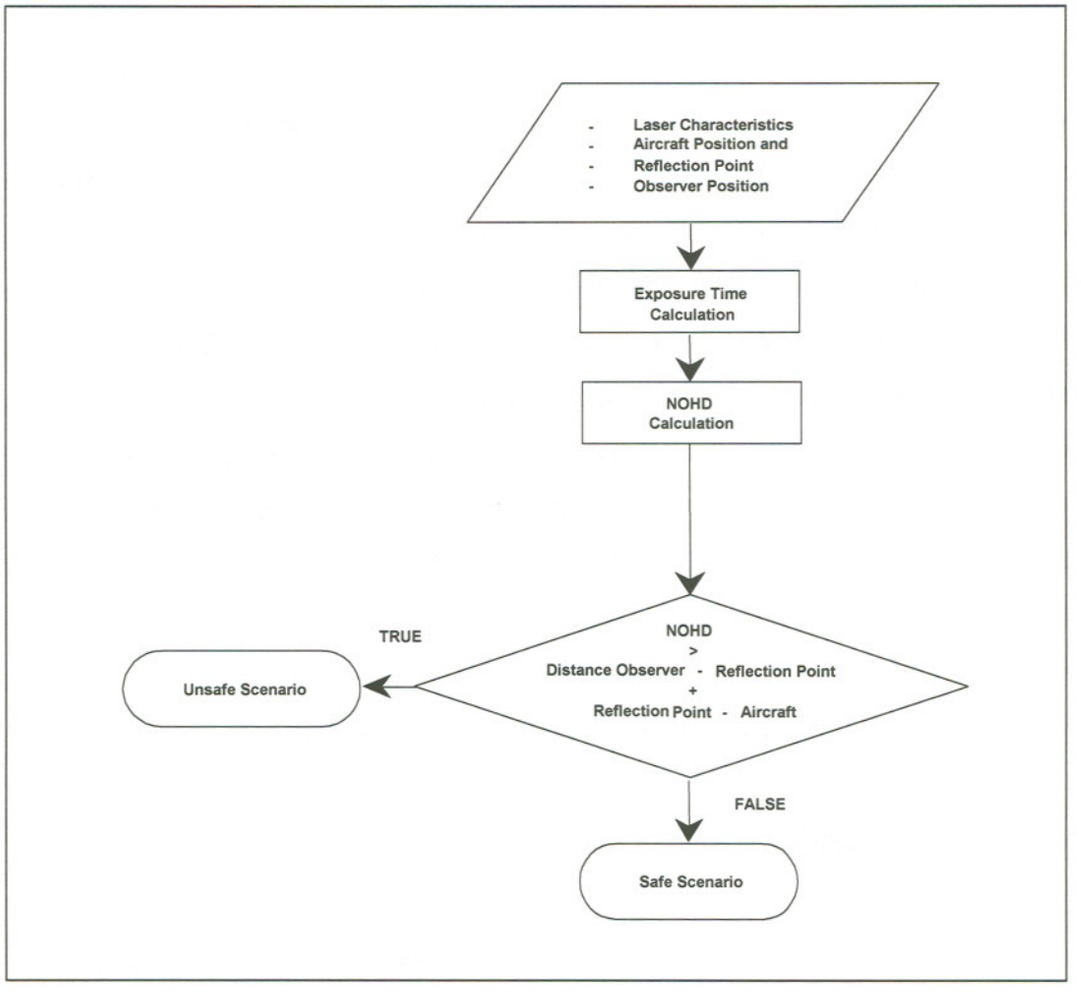

Figure 6-6. ALS safety verification algorithm.

Knowing the dimensions of the BZ, it is possible to verify the observer's safety, using the procedure described in Fig. 7-5 in an iterative manner for the entire BZ area. Therefore, simulation is required in order to determine the flight envelope rescrictions due to eye-safety (or, conversely, the ground evacuation requirements for a given aircraft flight profile). Details about the simulation program are given in chapter 14 of this report.

6.5 GLS Safety Analysis

In order to allow a safe use of Ground Laser Systems (GLS) at the range, it is essential to perform dedicated safety studies with the aim of defining the

operational conditions best matching both the test/training requirements and the constrains imposed by laser safety standards. One problem often encountered is due to the fact that state-of-the-art GLS are characterised by very high output energy and very low beam divergence. These parameters, associated to the operational need of executing test/training missions with both representative geometries and co-operative scenarios, determine laser hazard areas that in most cases are not compatible with the range size. In the following paragraphs, the general criteria for GLS laser safety are identified and various alternative methods for satisfying the SMD-W-001 Italian national safety standard are described. Furthermore, an innovative approach is proposed (not currently contemplated by the SMD-W-001 standard) allowing to perform in fully safe conditions (also with GLS systems with high output energy and low divergence), test/training operations at the PILASTER range, with scenarios representative of real operational tasks. These include Forward Air Controllers (FAC) training missions and combined employment of Ground Laser Target Designators (GLS) and Laser Guided Weapons (LGW) from tactical aircraft.

6.5.1 GLS Laser Hazard Area

As in the case of ALS, the overall Laser Hazard Area (LHA) associated to GLS such as a LRF or a LTD, is given by the sum of three different areas:

- ***GLS Beam Hazard Area*** (G-BHA), which exists even in the absence of commanded laser firing, and takes into account the maximum distance where the laser can be dangerous to the naked human eye (OHD), of the beam divergence and of possible events of accidental laser activation;

- ***GLS Buffer Zone*** (G-BZ), existing only in the event of laser firing, which accounts for the system pointing errors and for possible uncontrolled movements of the system Line of Sight (LOS) during laser firing;

- ***GLS Extended Buffer Zone*** (G-EBZ), which is due to possible reflections of the laser beam within the buffer zone.

6.5.2 GLS Beam Hazard Area

In general, the G-BHA is a spherical sector with the system pointing direction as the geometrical axis, the laser beam divergence as the sector semi-aperture and a radius given by the sum of the OHD and a distance *b* calculated taking into account the laser beam output diameter *a* (see Fig. 6-7).

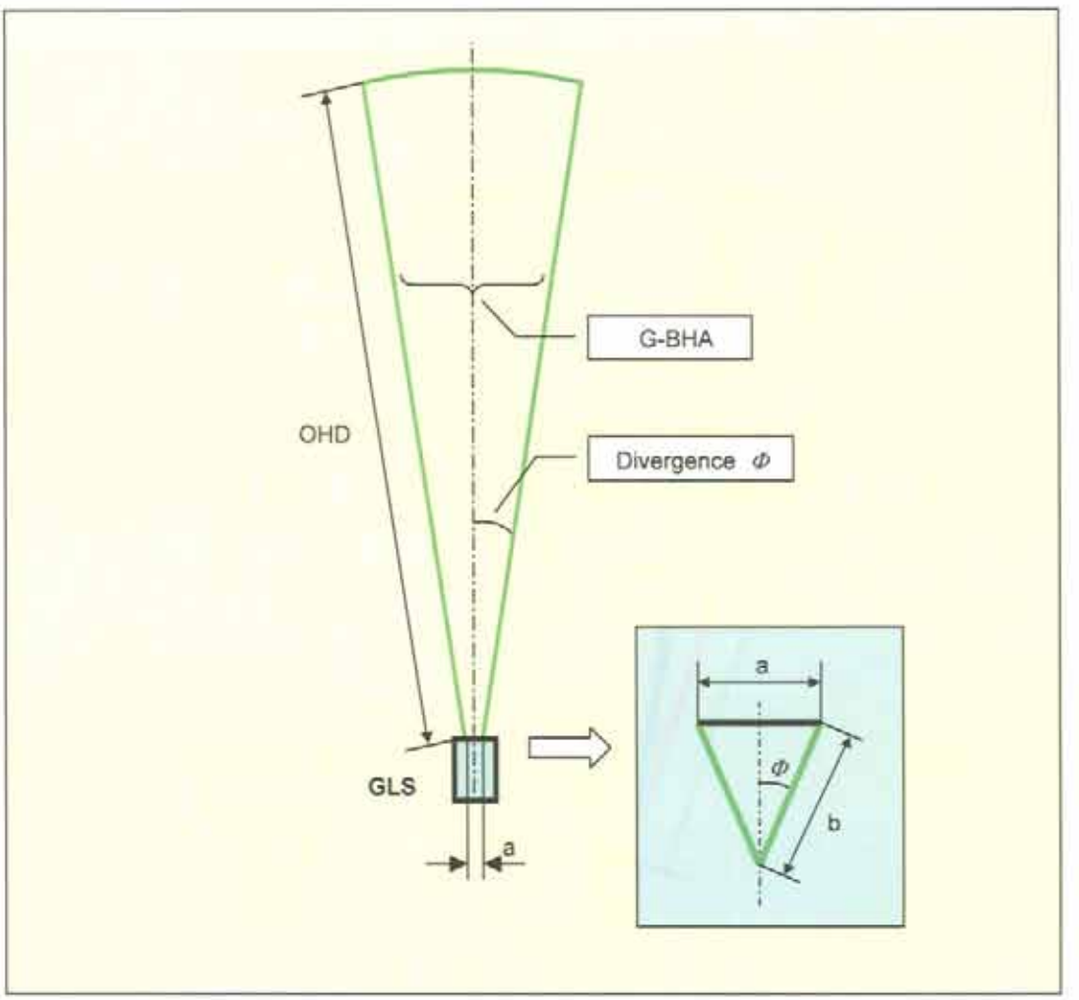

Figure 6-7. GLS Beam Hazard Area (G-BHA) geometry.

6.5.3 GLS Buffer Zone

The G-BZ is the area which may be directly illuminated by the laser beam when the system is aimed at the target, taking into account the total GLS pointing error budget and possible events of uncontrolled LOS movements during a

commanded laser activation. Therefore, also the G-BZ can be represented by a spherical sector with the system pointing direction as the geometrical axis, and with an aperture (α) given by the sum of the beam divergence (Φ), the GLS Pointing Error (PE) and the Safety Margin (SM) defined by the applicable laser safety standard (e.g., SMD-W-001); and whose radius is given by the sum of the GLS OHD and the distance c calculated taking into account the output diameter of the laser beam (a), as shown in Fig. 2.

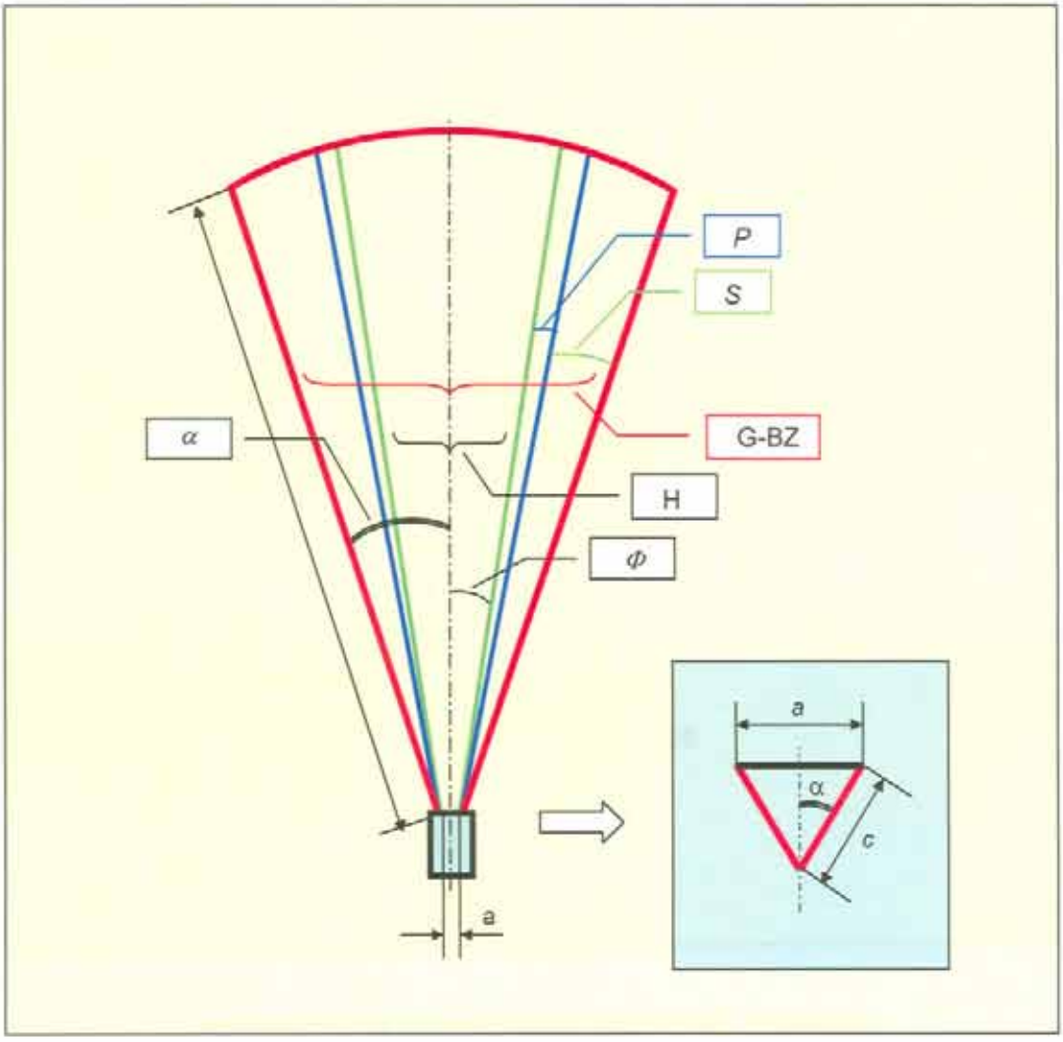

Figure 6-8. GLS Buffer Zone (G-BZ).

Obviously, the shape and dimension of the effective G-BZ (BZE) vary depending on the GLS position relative to the target, and also depending on the relative dimensions of the target with respect to thre incident laser beam (also affected by the GLS-target relative geometry). These aspects are illustrated in Fig. 6-9.

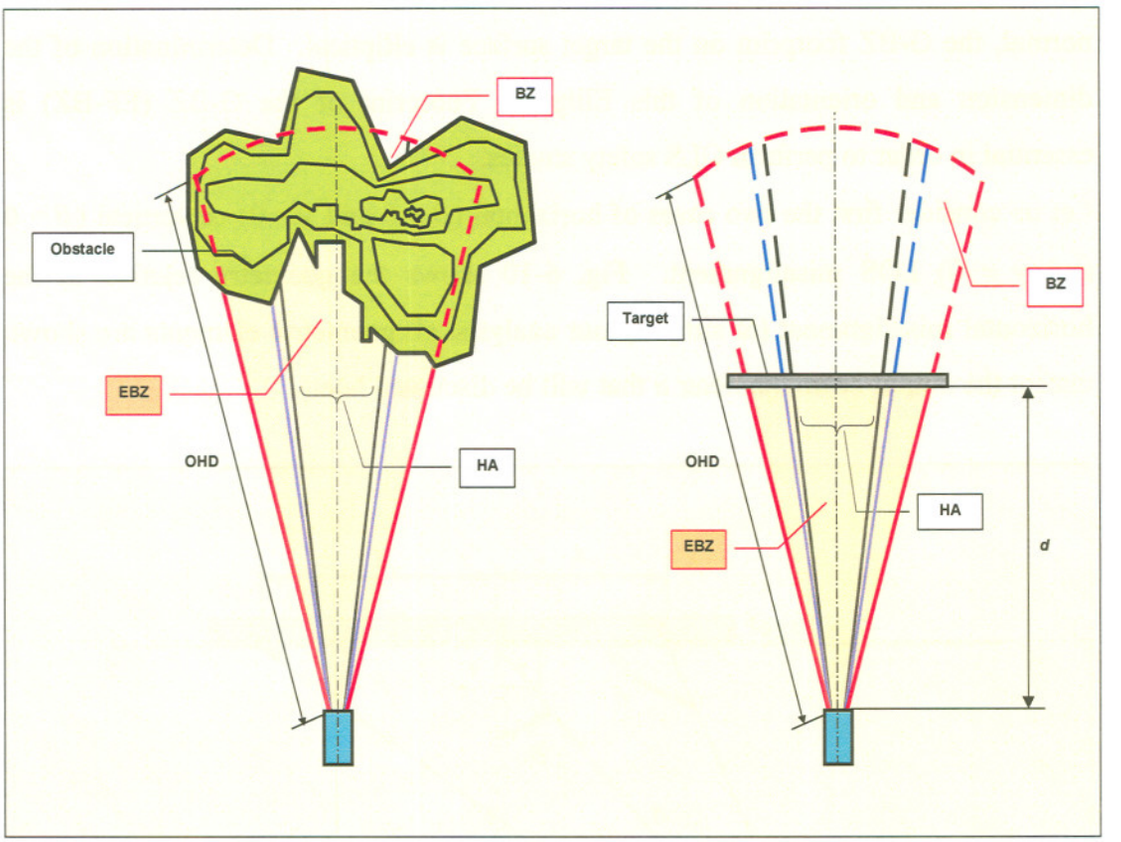

Figure 6-9. GLS effective G-BZ (BZE) geometry.

6.5.3.1 BZE for Single Axis LOS Misalignment

For a generic distance $d \leq$ OHD of the GLS from the target, the BZE is a spherical sector if the target dimensions are inferior to the G-BZ orthogonal section at the target location (at the specified distance and laser beam incidence angle), and is a conical section if the dimensions of the target are greater than the corresponding G-BZ orthogonal section. In the case of a laser beam normal to the target surface, the G-BZ orthogonal section is a circle with radius (r) given by:

$$r = \left[d \cdot tan\left(\Phi + PE + SM\right)\right] + a/2 \tag{6.20}$$

Therefore, since $\alpha = \Phi + PE + SM$, we can write:

$$r = \left(d \cdot tan\,\alpha\right) + a/2 \tag{6.21}$$

When the GLS LOS is not aligned in elevation (γ) and/or in azimuth (β) to the target normal, the G-BZ footprint on the target surface is elliptical. Determination of the dimension and orientation of this Elliptical Footprint of the G-BZ (EF-BZ) is essential in order to perform GLS safety studies.

Let us consider first the two cases of horizontal ($\beta \neq 0$ and $\gamma = 0$) or vertical ($\beta = 0$ and $\gamma \neq 0$) LOS misalignment. Fig. 6-10 shows the geometry relative to the horizontal misalignment (to simplify our analysis, all geometric elements are shown except the output beam diameter a that will be discussed later).

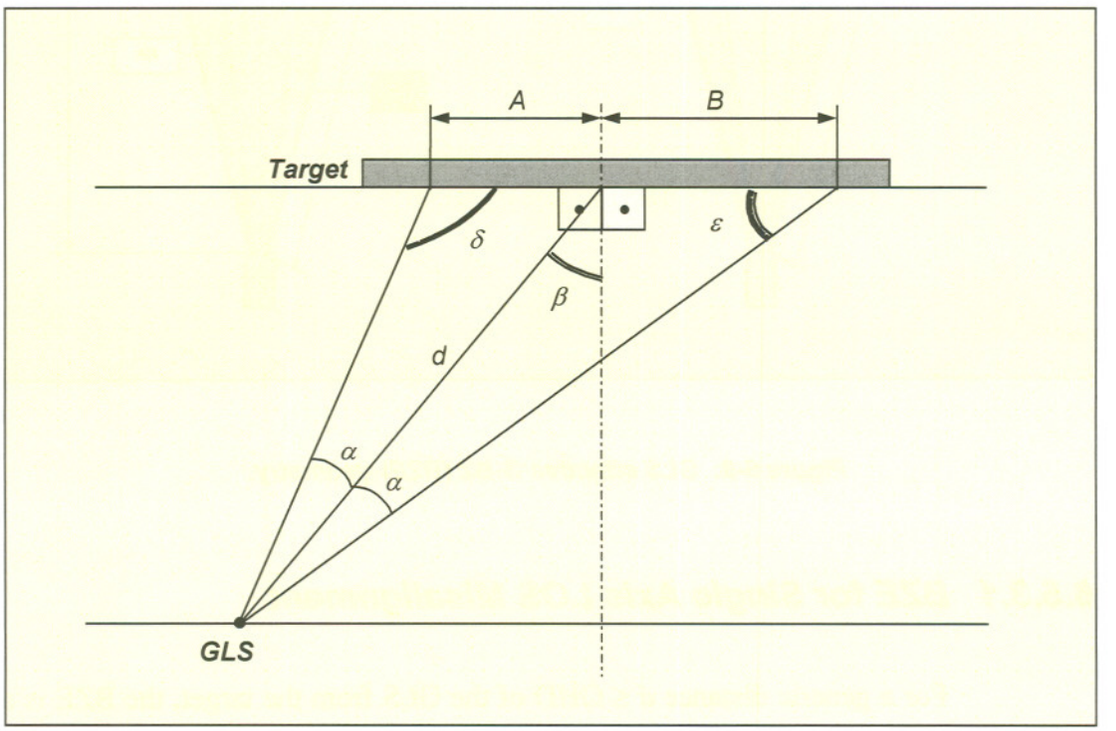

Figure 6-10. Geometry for EF-BZ calculation.

From Fig. 6-10, we notice that:

$$\varepsilon = 90 - \alpha - \beta \tag{6.22}$$

$$\delta = 90 - \alpha + \beta \tag{6.23}$$

Therefore, we can write:

$$A = \frac{d}{\cos(\alpha - \beta)} \cdot sen\alpha \tag{6.24}$$

$$B = \frac{d}{cos(\alpha + \beta)} \cdot sen\alpha \tag{6.25}$$

With reference to Fig. 6-11, the dimensions of the EF-BZ (not considering the output beam diameter), for the case of horizontal LOS misalignment only, are given by::

$$r_1 = A + B = d \cdot sen\alpha \cdot \left[\frac{1}{\cos(\alpha - \beta)} + \frac{1}{\cos(\alpha + \beta)} \right] \tag{6.26}$$

$$r_2 = 2 \cdot d \cdot tan\alpha \tag{6.27}$$

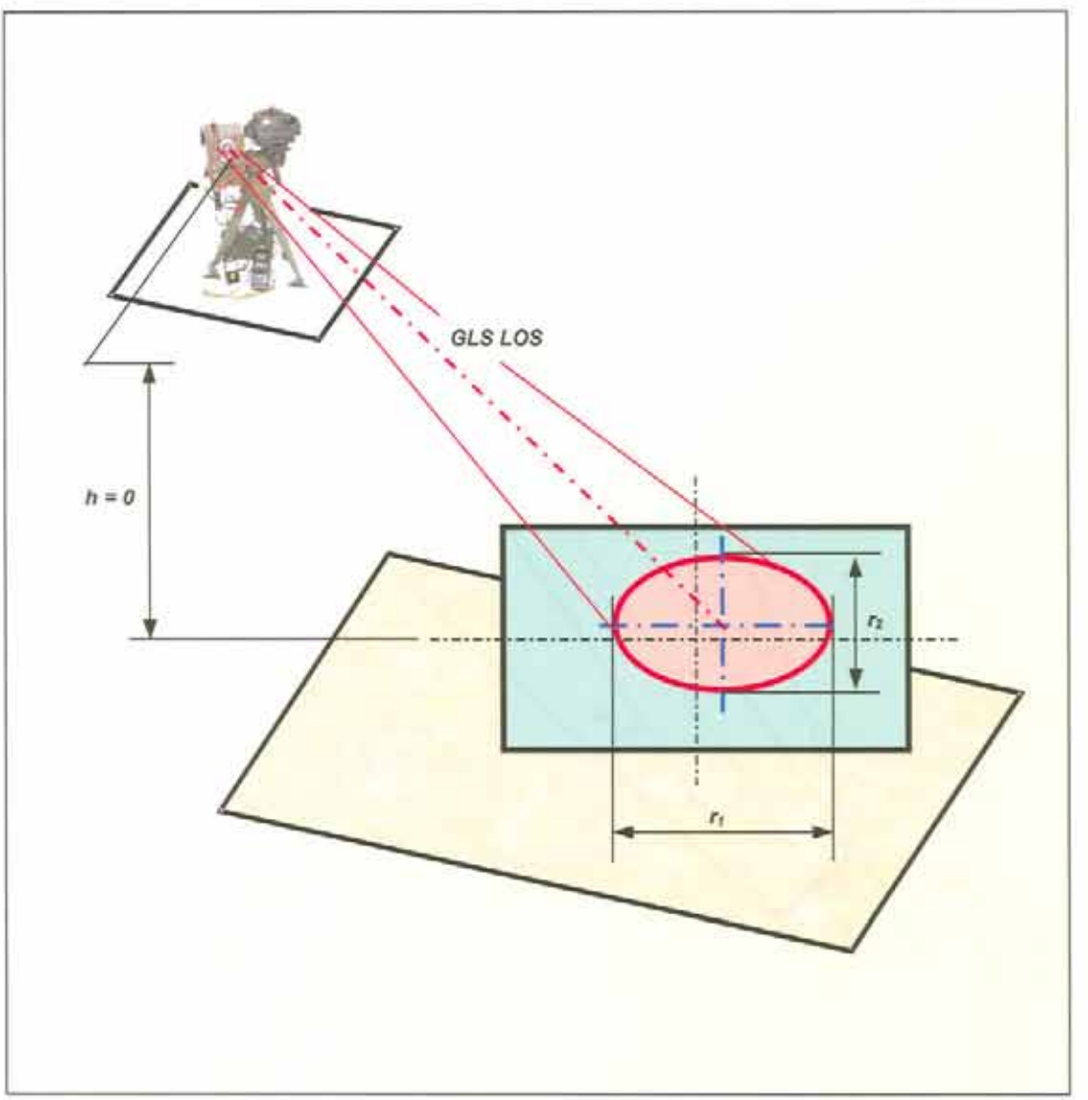

Figure 6-11. Geometry of the EF-BZ with horizontal LOS misalignment only.

Obviously, in the case of vertical LOS misalignment only ($\beta = 0$ and $\gamma \neq 0$), we have:

$$r_1 = 2 \cdot d \cdot tan\alpha \tag{6.28}$$

$$r_2 = d \cdot sen\alpha \cdot \left[\frac{1}{\cos(\alpha - \gamma)} + \frac{1}{\cos(\alpha + \gamma)} \right] \tag{6.29}$$

Let us now consider the GLS laser beam output diameter (a). Adopting the geometry in Fig. 6-12, we can write:

$$C = \frac{a}{cos\,\beta} \tag{6.30}$$

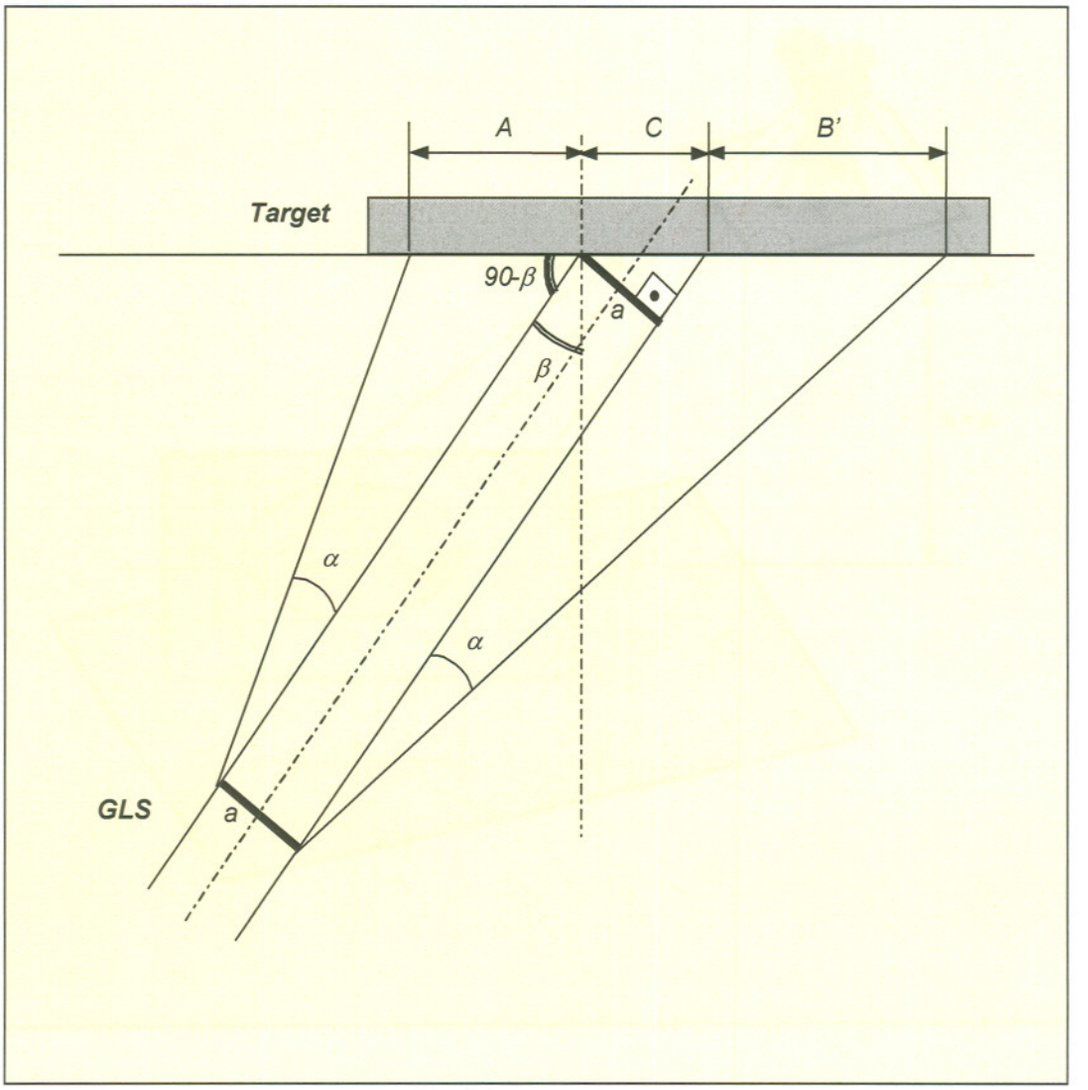

Figure 6-12. Projection of the GLS output beam diameter on the target.

Neglecting the difference between the segments B and B' (in Fig. 6-10 and Fig. 6-12 respectively), since the projection C is an additive element to the lengths r_1 and r_2 in Fig. 6-12 (as well as to the lengths A and B in Fig. 6-10), the equations for the EF-BZ with horizontal or vertical LOS misalignment can be written in the form:

Horizontal LOS Misalignment ($\beta \neq 0$ and $\gamma = 0$)

$$r_1 = d \cdot \sin\alpha \cdot \left[\frac{1}{\cos(\alpha - \beta)} + \frac{1}{\cos(\alpha + \beta)} \right] + \frac{a}{\cos\beta} \tag{6.31}$$

$$r_2 = 2 \cdot d \cdot tan\alpha + a \tag{6.32}$$

Vertical LOS Misalignment ($\beta = 0$ and $\gamma \neq 0$)

$$r_1 = 2 \cdot d \cdot tan\alpha + a \tag{6.33}$$

$$r_2 = d \cdot \sin\alpha \cdot \left[\frac{1}{\cos(\alpha - \gamma)} + \frac{1}{\cos(\alpha + \gamma)} \right] + \frac{a}{\cos\gamma} \tag{6.34}$$

6.5.3.2 BZE for Double Axis LOS Misalignment

In order to extend our results to the case of simultaneous aziumuth and elevation LOS misalignment we must define the conditions for the validity of equations (6.31) and (6.34), also when $\beta \neq 0$ and $\gamma \neq 0$. To facilitate the operational use of the models developed, we shall express these conditions as mathematical functions of parameters readily measurable with the instrumentation already available at the test/training range (i.e., GPS systems, theodolites and LRF). These parameters include the distance d of the GLS from the target (which, for instance, can be measured directly by the GLS) the azimuth angle β (which can be determined using GPS or theodolite measurements) and the relative height of the GLS system with respect to the target.

Let us consider, first of all, that the dimensions of the EF-BZ on the target surface do not vary if the GLS laser aperture is positioned along the perimeter of a circle laying

on a plane parallel to the target syrface. With reference to Fig. 6-13, the EF-BZ dimensions are the same for any position of the GLS corresponding to the points of the circle with radius $\overline{BE}$ (only varies the EF-BZE orientation). Similarly, the dimensions of the EF-BZ would be inaltered if the GLS was positioned along the perimeter of the crcle with radius $\overline{BC}$. The angle δ_{MAX} in Fig. 6-13 represents the maximum misalignment in aziumuth or in elevation admitted at a given distance (d) of the GLS from the target. This angle can be calculated using equation (12) or (15), taking into account the dimensions of the target surface. Particularly, writing this equation:

$$r_{MIN} = d \cdot \sin\alpha \cdot \left[\frac{1}{\cos(\alpha - \delta_{MAX})} + \frac{1}{\cos(\alpha + \delta_{MAX})} \right] + \frac{a}{\cos\delta_{MAX}} \qquad (6.35)$$

the value of δ_{MAX} can be calculated by knowing the minimum dimension of the illuminated target surface (r_{MIN}).

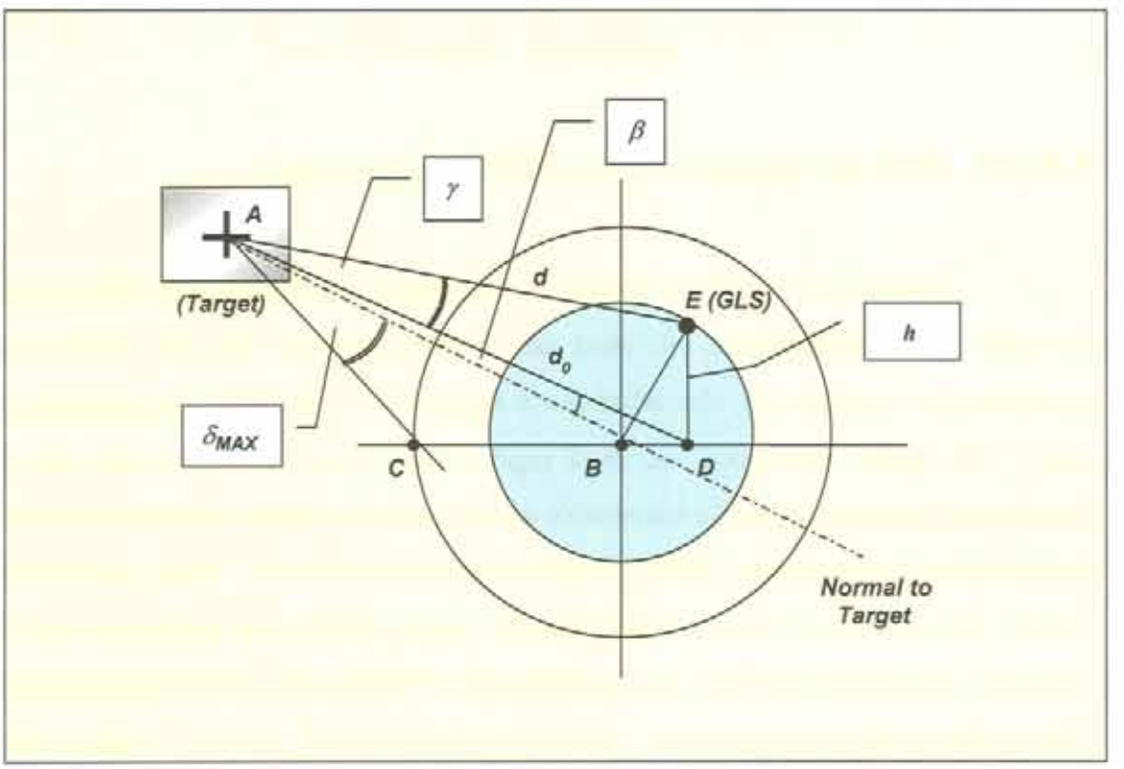

Figure 6-13. GLS-target geometry with horizontal and vertical LOS misalignment.

From Fig. 6-13 we observe that a condition sufficient to avoid that the EF-BZ exceeds the target dimensions is the following:

$$\overline{BE} \leq \overline{BC} \tag{6.36}$$

therefore:

$$\overline{BE} \leq \overline{AB} \cdot tan\delta_{MAX} \tag{6.37}$$

$$\overline{BE}^2 \leq \left(d^2 - \overline{BE}^2 \right) \cdot tan^2 \delta_{MAX} \tag{6.38}$$

$$\overline{BE}^2 \leq \frac{d^2 \cdot tan^2 \delta_{MAX}}{1 + tan^2 \delta_{MAX}} \tag{6.39}$$

In order to express $\overline{BE}$ as a function of the known parameters, we can write:

$$d_0{}^2 \cdot sen^2 \beta + h^2 \leq \frac{d^2 \cdot tan^2 \delta_{MAX}}{1 + tan^2 \delta_{MAX}} \tag{6.40}$$

and then:

$$\left(d^2 - h^2 \right) \cdot sen^2 \beta + h^2 \leq \frac{d^2 \cdot tan^2 \delta_{MAX}}{1 + tan^2 \delta_{MAX}} \tag{6.41}$$

From the (6.41), setting:

$$K_1 = \frac{d^2 tan^2 \delta_{MAX}}{1 + tan^2 \delta_{MAX}} \tag{6.42}$$

$$K_2 = d^2 sen^2 \beta \tag{6.43}$$

$$K_3 = 1 - sen^2 \beta \tag{6.44}$$

we obtain:

$$h_{MAX} = \sqrt{\frac{K_1 - K_2}{K_3}} \tag{6.45}$$

$$\beta_{MAX} = arcsen \sqrt{\frac{h^2 - K_1}{h^2 - d^2}} \tag{6.46}$$

where h_{MAX} is the maximum altitude difference admitted between the GLS and the target, with the GLS positioned at a known slant-range (d) from the target and with a known LOS azimuth (β); while β_{MAX} is the maximum admitted horizontal LOS misalignment of the GLS with respect to the target normal, with the GLS positioned at a known slant-range (d) from the target and with an altitude difference GLS-target (h) also known. As already mentioned, the G-BZ can be represented by a tri-dimensional geometric figure (i.e., spherical sector or conical sectuion). Therefore, depending on the GLS position and algular displacement with respect to the target, and the characteristics of the natural and man-made obstacles existing in the range area, there will be different requirements for both the Ground Evacuation Areas (GEA) and the Hazard Air Space (HAS). Particularly, while the GEA is clearly defined by the G-BZ intersection with the ground surface, the HAS exists only if the G-BZ is not entirely limited by natural/man-made obstacles (including the target), or if the GLS/target are located in a position higher than the possible air traffics. The concepts illustrated are summarised in Fig. 6-14.

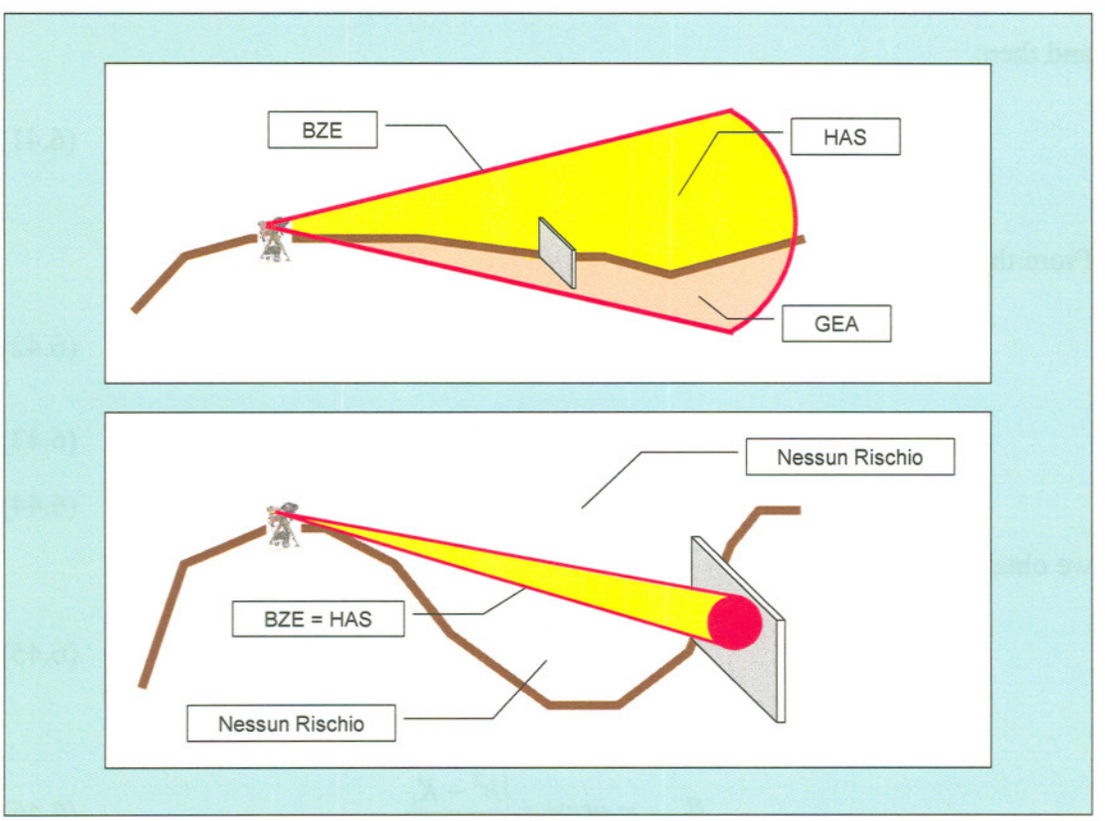

Figura 6-14. Ground Evacuation Area (GEA) and Hazard Air Space (HAS).

6.5.4 Extended Buffer Zone

As already seen in the case of ALS systems, when reflecting objects are present in the G-BZ, it is necessary to consider another hazard area, called Extended Bufer Zone (G-EBZ). According to the SMD-W-001 laser safety standard, the dimensions of the G-EBZ are calculated in diferent ways, depending on the type of reflector (i.e., specular or diffuse) present in the G-BZ. In general, however, in the case of diffuse reflection (e.g., reflection from a target suitably built and painted to maximise the Lambertian reflection component), the G-EBZ usually is so small that they can neclected. On the other hand, in the worst case of a specular reflection in the G-BZ, the G-EBZ will in general determine the existance of an Extended GEA (EGEA) and/or Extended HAS (EHAS), with dimensions and geometries affected by the ground altitude profile, by the obstacles and by the GLS position relative to the target (similarly to ALS, the EGEA/EHAS for GLS are bounded by a surface generated by a vector centred at the reflection point, whose intensity is such that the sum of the distance GLS-reflector with the vector length itself is equal to the OHD). Obviously, removal of reflecting objects in the GEA prevents the existance of an EGEA.

6.5.5 Range Safety Procedures

According to laser hazard areas calculatios results, appropriate procedures can be defined for implementation at the laser range, in order to guarantee a safe and practical employment of GLS. These procedures, have to follow, in general, the national safety regulations and standards (e.g., SMD-W-001 or JSP 390). However, in many real cases the calculated laser hazard areas for the required mission geometries, are not be compatible with the range size. This is mainly due to the very high energy output and low divergence of state-of-the-art GLS. Therefore, there are cases where additional criteria have to be adopted in order to allow a safe execution of test/training tasks with representative mission geometries and co-operative scenarios.

6.5.5.1 Procedures in Accordance with SMD-W-001

The Safety Margin (SM) to be adopted for G-BZ calculations is defined by the applicable laser safety standards (e.g., STANAG 3606 and SMD-W-001). Referring to the STANAG 3606 and to the Italian SMD-W-001 national standard, the SM to be adopted for ground systems is 10, 5 or 2 mrad depending on the stability of the system LOS. Furthermore, the following procedures have been developed in accordance with the GLS safety analysis concepts previously illustrated and with the safety standards recommendations.

Procedure n° 1

- A target should be used with shape and dimensions adequate to contain the entire EF-BZ at the defined GLS-target slant-ranges and GLS LOS incidence angles. The G-BZ has to be calculated taking into account the ouput diameter of the laser beam (a), the beam divergence (Φ), the pointing error (PE) of the GLS, and the additional safety margin (SM) contemplated by the applicable safety standards (e.g., STANAG-3606 and SMD-W-001). The target has to be free from fenditures or apertures and to be charcterised by a difuse reflectivity.

- Access in the G-BZ should be prohibited to unprotected personnel.

- Intersection of the G-BZ with the ground and natural/man-made obstacles should be avoided.

- The GLS operator should verify, before activating the laser, that the LOS of the GLS is aimed at the centre of the selected target (GLS operator).

- The use of magnifying optical intruments not suitably filtered should be prohibited in the entire laser range.

Procedure n° 2

If it is not possibile to use a target with the characteristics previously mentioned, the following actions should be implemented:

- Remove all reflecting objects present in the GEA.
- Prohibit access of unprotected personnel in the GEA.
- Prohibit flying into the HAS without suitable aircrew protection.
- Prohibit the use of magnifying optical intruments not suitably filtered in the laser range.

Procedure n° 3

If it is not possibile to remove reflecting objects in the GEA, it is required to:

- Prohibit access of unprotected personnel in the EGEA.
- Prohibit flying into the EHAS without suitable aircrew protection.
- Prohibit the use of magnifying optical intruments not suitably filtered in the laser range.

6.5.5.2 PILASTER GLS Safety Procedure

An additional option was conceived in order to allow a safe execution of test/training tasks at the PILASTER laser range, with representative mission geometries (i.e., GLS-target slant-ranges, height differences and LOS incidence angles). An essential pre-requisite for implementation of this procedure is a dedicated test activity aimed at determining the GLS LOS pointing accuracy (PE_{eff}) and the effective beam divergence (Φ_{eff}), by measuring the GLS laser spot position/diameter on the target surface. Both parameters may in fact be significantly different from those predicted by calculations or quoted in the technical

documentation provided by the manufacturer. Using the experimental data the EF-BZ can be calculated with $\alpha = \Phi_{eff} + PE_{eff}$ (i.e., without considering any additional SM), and the following procedure can be implemented.

Procedure n° 4

- A target is used with shape and dimensions adequate to contain the entire EF-BZ at the defined GLS-target slant-ranges and GLS LOS incidence angles. The G-BZ has to be calculated taking into account the ouput diameter of the laser beam (a), the effective beam divergence (Φ_{eff}) and the effective pointing error (PE_{eff}) of the GLS. The target has to be free from fenditures or apertures and to be charcterised by a difuse reflectivity.

- Access in the G-BZ is prohibited to unprotected personnel.

- Intersection of the G-BZ with the ground and natural/man-made obstacles has to be avoided.

- The GLS operator verifies, before activating the laser, that the LOS of the GLS is aimed at the centre of the selected target (GLS operator).

- The laser spot is monitored in real-time by using the PILASTER NIR cameras, in order to continuously verify that during laser firing the entire spot is on the illuminated target surface. The GLS laser is immediately deactivated if the laser spot deviates from the target centre (significantly exceeding the PE_{eff}) or if the spot is not entirely on the target surface.

- The use of magnifying optical intruments not suitably filtered is prohibited in the entire laser range.

6.5.5.3 Operational Considerations

There are important operational considerations to be done about the procedures previously described. Although in theory all of them are possible options for GLS safe operation at the range, for reasons of practicality the procedures n° 2

and n° 3 are not commonly implemented. The removal of reflecting objects in the GEA, imposed by procedure n° 2, is in fact extremely difficult (if not impossible) to be done at a test/training range. Procedure n° 3, on the other hand, may determine an EGEA with dimensions exceeding the size of the laser range ground area. Furthermore, implementation of both procedures n° 2 and n° 3 determine the existance of no-flying areas (HAS and EHAS respectively) which, in some cases, may exceed the dimensions of the range controlled air-space. Therefore, only the procedures n° 1 and n° 4 are to be considered viable options in most cases of practical interest. However, the procedure n° 1 has the disadvantage of requiring the adoption of a SM in the EF-BZ calculations (following the safety standards recommendations), which determines considrerable limitations in the GLS-target slant-range, relative height and angular displacement envelopes. Therefore, the procedure n° 4, developed during this research for employment at the PILASTER range, is the option best matching both the eye-safety requirements and the need of executing test/training missions in a variety of conditions (i.e., GLS-target geometry, terrain profiles, co-operative tasks, guided weapons deliveries, etc.) representative of the real operational scenarios.

6.6 References

1. STANAG 3606 – Edition V. "Evaluation and Control of Laser Hazards". Nov 1991.
2. Italian Standard CEI –76/2 – Edition II. "Apparecchi Laser – Sicurezza delle Radiazioni, Classificazione dei Materiali, prescrizioni e Guida per l'Utilizzatore". Mar 1993.
3. International Electrotechnical Commission IEC 825 – (Amendment 2). "Radiation Safety of Laser Products, Equipment Classification, Requirements and User's guide". 1993.
4. American National Standard Institute ANSI Z136.1. "Safe Use of Laser". 1976.
5. American National Standard Institute ANSI Z136.4. "Laser Safety Measurements and Instrumentation". 1990.

6. Italian Regulation DL 04.12.1992 - n. 475. "Attuazione della direttiva 89/686/CEE relativa ai dispositivi di protezione individuale";
7. Italian Military Safety Standard SMD-W-001. "Regolamento Interforze di Sicurezza per l'impiego degli apparti laser". Second Edition. 1995.
8. JSP390 – Military Laser Safety. UK Ministry of Defence – Ordnance Board D/OB/2407/2. Ed. 1998.

Chapter 7

LABORATORY EXPERIMENTAL ACTIVITY

7.1 General

A number of experiments were performed in order to selecting suitable sensors/systems for the PILASTER range, optimising operational and test/training activities with the systems in service (e.g., LTD's and LGW's), and developing new systems (e.g., LOAS). Some of these experiments, such as LGW seeker detection threshold determination, PILASTER sensors selection/characterisation tests and measurements of target materials reflection properties, were conveniently performed in a laboratory facility. On the other hand, further important measurements and tests were performed during appropriate field and flight test sessions.

Laboratory experimental activities performed during this research included the following:

- Determination of LGW Seekers Detection Thresholds;
- Measurements of Surface/Pants Reflection Properties (PILASTER targets);
- PILASTER Sensors Testing and Calibration;
- LOAS Laser System Testing;
- Test of protection filters and eye-wears (cinetheodolites, ground crew and aircrew).

This chapter describes the laboratory experimental activities carried out during this research. Particularly, the test aims, specific test methods (i.e., instrumentation requirements, details of measures performed, etc.) and test results, are discussed in the following sections.

7.2 LGW Seeker Detection Threshold

The primary aim of this experiment was to determine the Minimum Detectable Power Density (MDPD) of a real LGW seeker. The secondary aim was to develop a test method valid for any LGW seeker system. For classification reasons, the name of the tested LGW seeker is omitted. With the available instrumentation, seeker detection threshold determination was performed in two steps:

- Seeker activation codes generation (i.e., pulse duration, PRF and train);
- Measurement of the MDPD (pulse), based on train energy measurements.

The two steps are discussed below.

7.2.1 Seeker Activation Codes Generation

The STANAG 3733 titled: "Laser Pulse Repetition Frequencies (PRF) Used for Target Designation and Weapon Guidance", defines the LGW activation codes characteristics and the related tolerances.

This activity was performed in order to check the LGW seeker functionality and properly preparing the successive power density measurements. The activity consisted in determining adequate pulse and pulse train durations, matching the instrumentation response and compatible with activation of the LGW seekers (i.e., PRF codes defined by the STANAG 3733).

In order to perform these measurements, the following instrumentation was used:

- Q-Switched Nd:YAG laser (Quantel STU-452/N);
- Nd:YAG Attenuation Filters (Quantel);
- Beam collimating optics (FIAR STU-452/N);
- Silicon Photodiode Detector (Newport *Low Power Detector* mod. 818-SL);
- Laser Power-meter (Newport *Dual Channel Optical Meter* mod. 2835);
- Digital Oscilloscope (HP mod. 54502A and LeCroy mod. 154-B54).

Additionally, a control panel was required, including the laser remote control and the LGW seeker electrical and mechanical interfaces (necessary for guidance circuits activation). The instrumentation set-up is shown in Fig. 7-1. A detail of the target simulator is shown in Fig. 7-2.

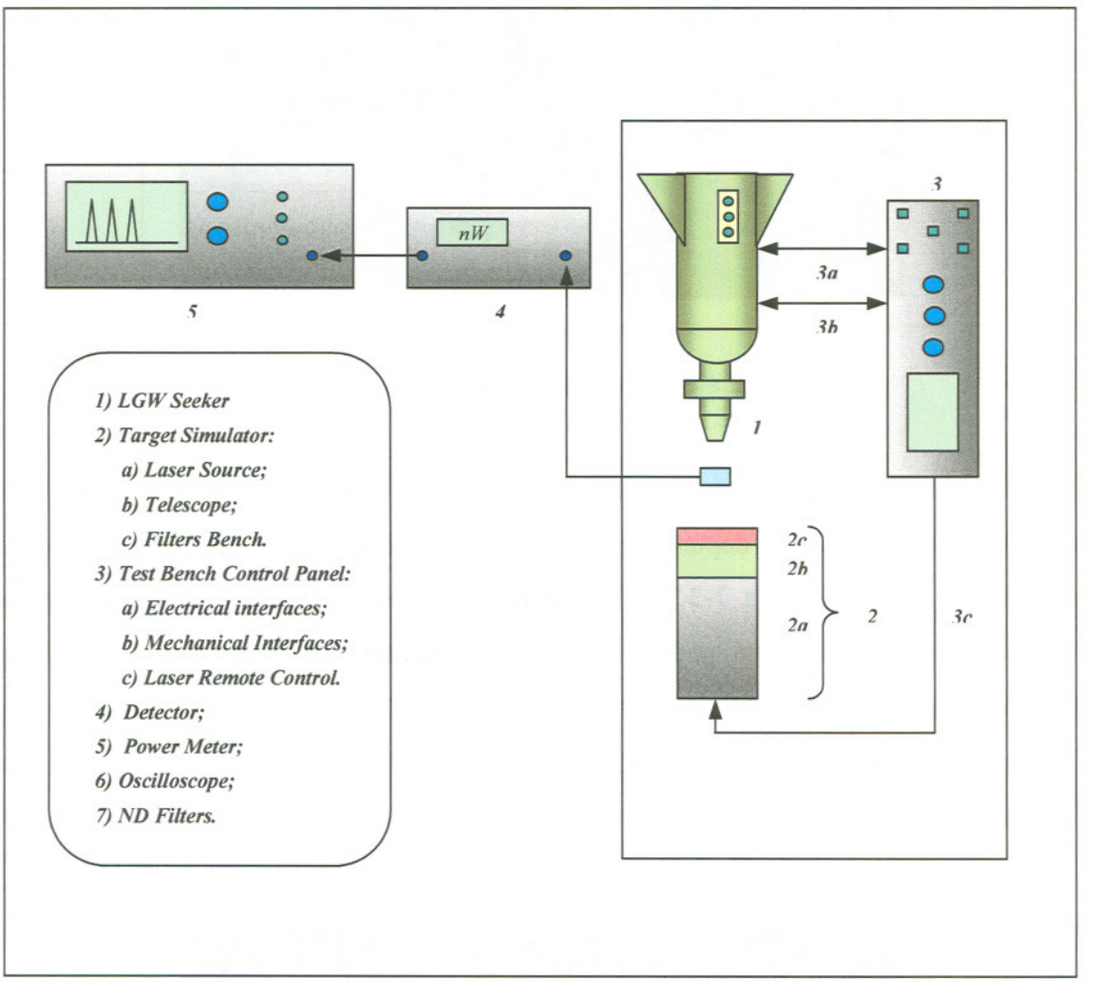

Figure 7-1. Seeker test Instrumentation set-up.

An initial experiment, performed with a real LGW seeker and the described instrumentation, permitted to fully characterise and reproduce some LGW activation codes (PRF according to STANAG 3733). A number of 24 activation codes were reproduced during the test (in the 10 *Hz* nominal band). After various attempts, it was verified that, for the seeker under test, the minimum pulse train duration for guidance circuits activation was about 0.5 *sec* (0.5 ± 0.1 *sec*).

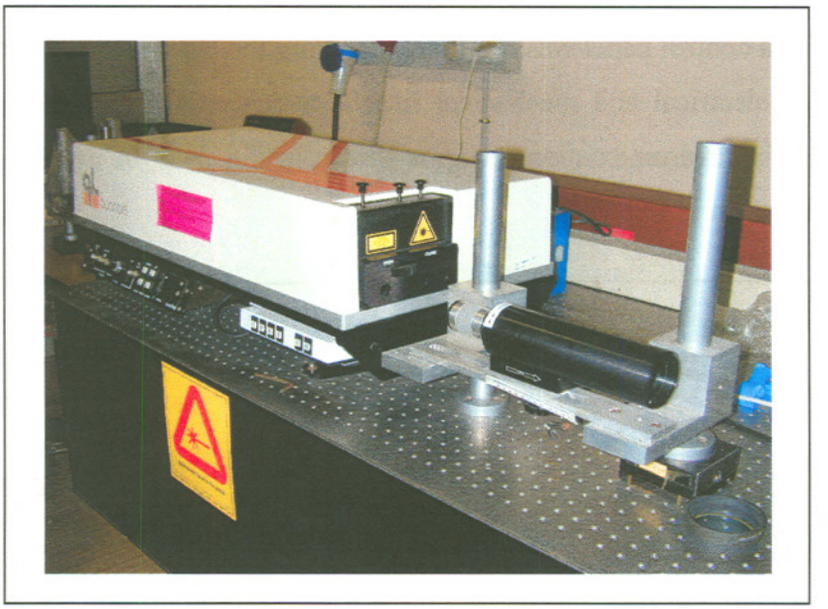

Figure 7-2. Target simulator.

The minimum number of pulses contained in each guidance activation train was variable between 5 and 6 depending on the selected code. Some oscilloscope traces are shown in the Figures 7-3 to 7-5 relative to measurements performed with a specific code. Using that code, with a pulse duration of 9 *ms* and an average amplitude of 72.4 *mV* displayed on the oscilloscope (72.4 ± 2.0 *mV*), corresponding to a laser energy density of about 120 pJ/cm^2 (train of 19 pulses), the Full Width at Half Maximum (FWHM) was about 4.6 *ms* (4.6 ± 0.5 *ms*).

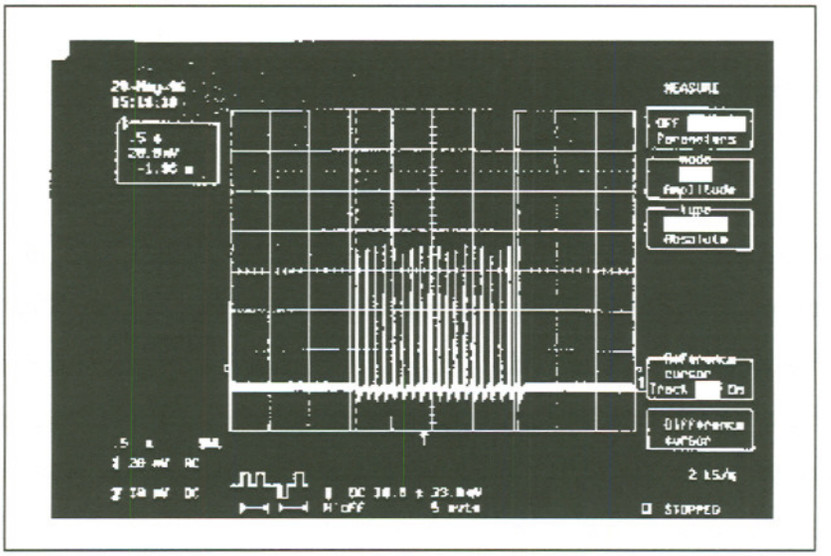

Figure 7-3. Typical train profile.

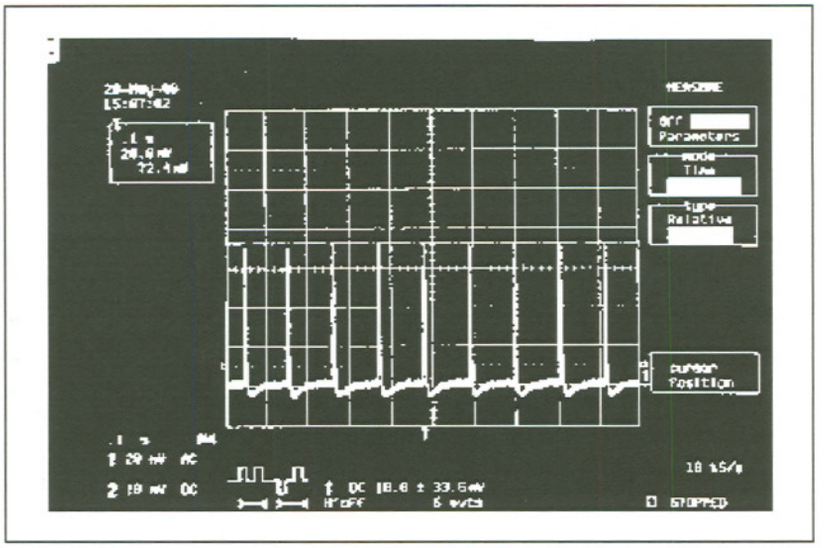

Figure 7-4. Train pulses amplitude.

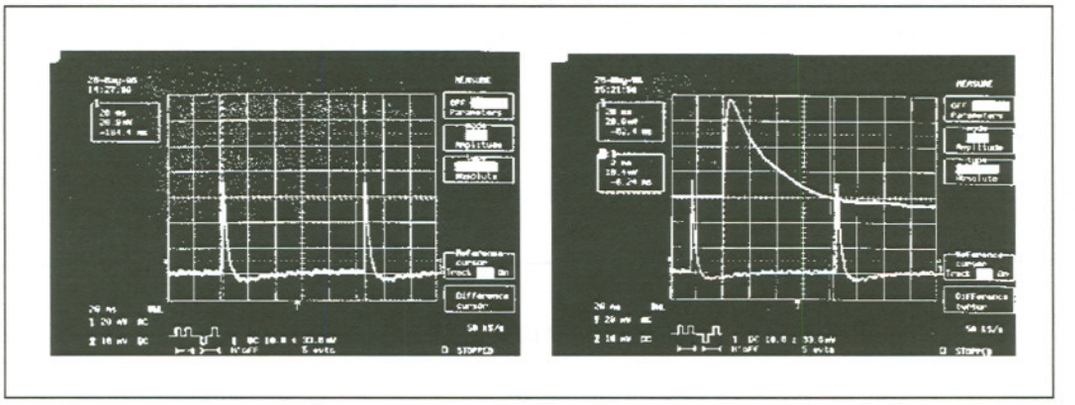

Figure 7-5. Pulse-to-pulse period and pulse duration.

7.2.2 MDPD Determination

The approach adopted for determining the Minimum Detectable Power Density (MDPD) of the seeker is described in this paragraph. The laser output energy was progressively reduced using filters of increasing neutral optical densities. Adding various suitable filters, the laser power reached a threshold value (i.e., a further small increase of attenuation prevents the seeker activation). The experimental set-up is shown in Fig. 7-6.

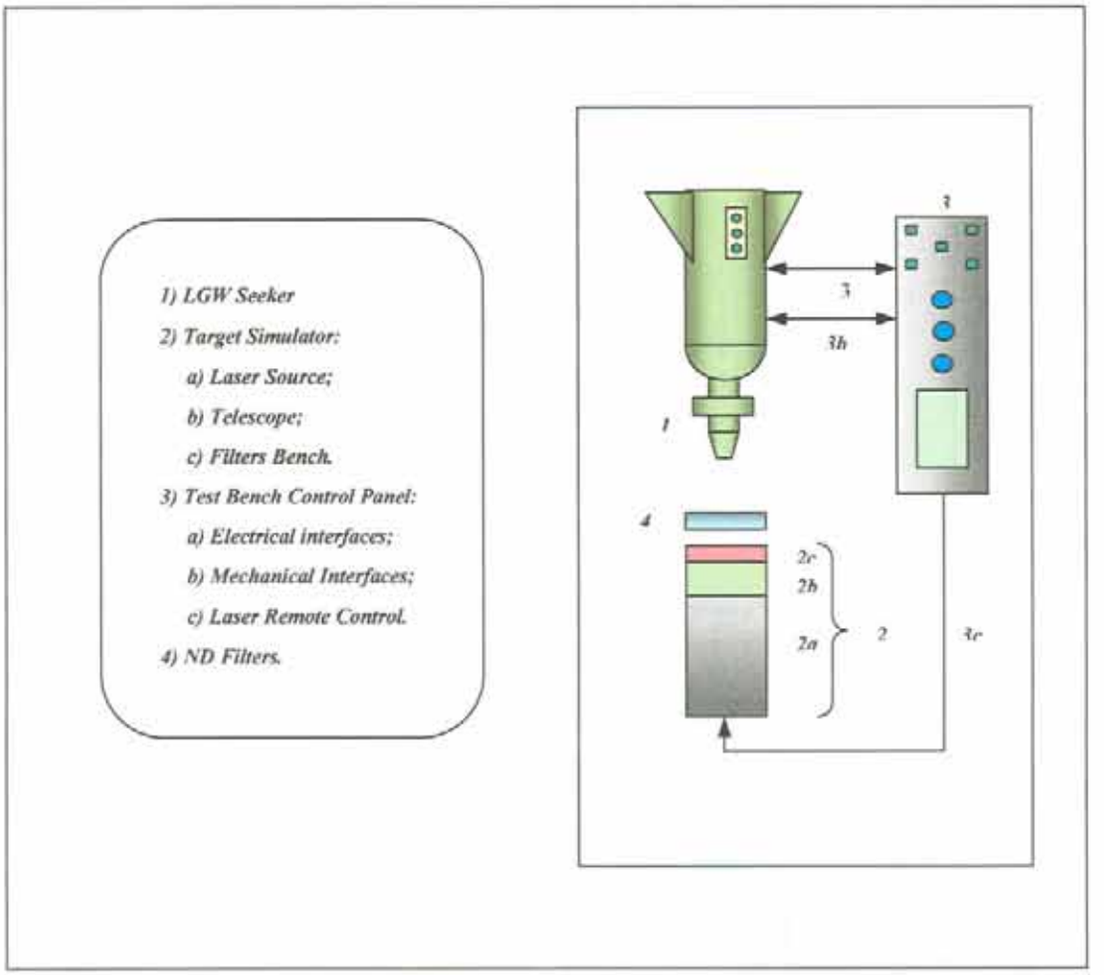

Figure 7-6. Seeker MDPD test instrumentation set-up.

After determining the limiting condition (i.e., maximum attenuation compatible with seeker activation), the MDPD value was determined with 2 different methods:

1) by measurement, adopting the instrumentation set-up described in Fig. 7-1 (with interposition of the ND filters between the detector and the target simulator), using the power meter and oscilloscope readouts;
2) by calculation, knowing the peak power output of the target simulator and the transmittance of the ND filters.

Method 1. Using the same seeker mentioned in the previous paragraph and the same activation code (i.e., pulse peak amplitude 72.4 ± 2.0 mV, train energy density 120 pJ/cm^2 , FWHM 4.6 ± 0.5 ms and max pulse duration 9 ms), an experiment was

Chapter 4

PILASTER GENERAL REQUIREMENTS

4.1 Introduction

This chapter describes the requirements for upgrading the PISQ (*Poligono Interforze del Salto di Quirra* – Sardinia, Italy), adding new facilities for carrying out safe training and experimental activities using the ground and airborne laser systems already in service or under test with the Italian Air Force (ItAF), and installed on its tactical aircraft (TORNADO-IDS, AM-X, Eurofighter TYPHOON, etc.) and helicopters (AB-212, AB-412, NH-90, etc.). Other national or international customers will be allowed to use the new facilities on case-by-case basis and according to agreements, memorandums of understanding or international co-operation agreements in force at the time concerned. The ItAF research and development program aiming to the PISQ facilities upgrade for laser test and training activities, is herein identified as **PI**SQ **LAS**er **T**est and Tactical **E**valuation **R**ange program (**PILASTER** program). According to the program requirements, the PILASTER facilities have grown modularly in two different phases. The aim of the first phase of the program (1999-2002) was to provide an initial operational capability for carrying out, in fully safe conditions, ground tests and flight experimental activities (with related measurements and data analysis), required for performance evaluation of military laser systems. The successive phase of the program (still ongoing) is aimed to implementing the PILASTER full operational capability, required for performing all required laser test and training activities (2002-2004).

In this chapter, the laser range concept of operation is described and the general requirements set in 1998 for the PILASTER program are presented. More information about the PILASTER range design and technical characteristics, progressively refined during the various implementation stages of the program, are given in chapter 5.

4.2 PILASTER Concept of Operation

The PILASTER concept of operation is depicted in Fig. 4-1. The on-board operator of a training/experimental aircraft aims the Airborne Laser Target Designator (ALTD) system at the centre of a cooperating target. A Laser Safety Officer (LSO), located in the PISQ Control Centre (PCC) building, verifies that the laser Armament is aimed at the proper target and (for laser designators) the target lock-on status has been achieved. For this purpose, a real-time video link (video telemetry ground unit) is available between the aircraft and the PCC for safe operations. The LSO then authorises activation of the laser system. Should the video link be unavailable, as in the case of a Ground Laser Target Designator (GLTD) system operated from a ground Forward Air Controller (FAC) or a training aircraft not equipped with the video telemetry unit, the LSO may authorise the laser activation upon receiving confirmation (via voice link) that the planned target has been unambiguously recognised and aimed to by the aircraft Pilot/Weapon Systems Operator (WSO) or by the ground FAC.

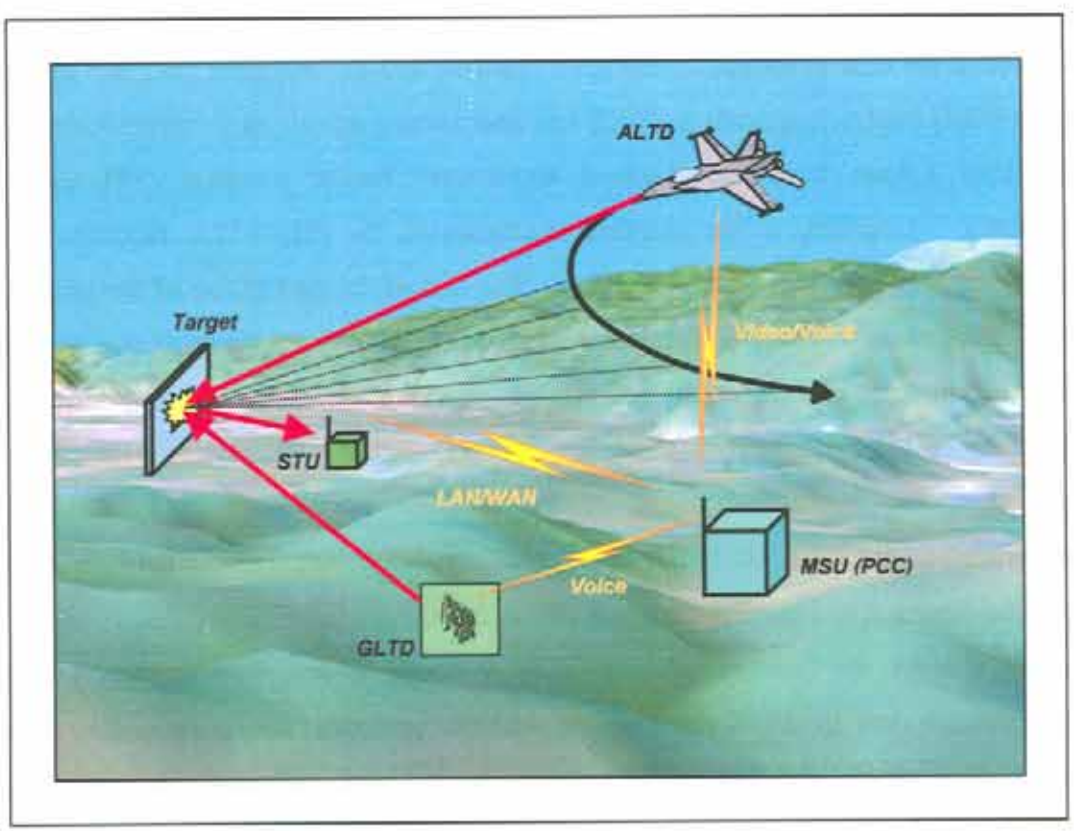

Figure 4-1. PILASTER concept of operation.

The Sensor Tracking and Measurement Unit (STU) detects the laser spot spatial energy distribution, calculating the spot centroid as well as its position with respect to the target centre (global pointing error). The captured laser spots, as well as the others applicable measurements, are recorded on a magnetic support.

During laser activation, the STU sends to the PILASTER Monitoring and Control Station Unit (MSU), located at the PCC, the laser spot parameters (dimension and position with respect to the target centre). These parameters are represented on the MSU display to allow the Safety Officer to supervise the operations. When the laser spot approaches the target peripheral zones and the LSO believes there is a possibility for the laser spot to fall outside the target itself, he might order the WSO/FAC to deactivate the laser (through the voice link).

4.2.1 PILASTER Training Activities

Training with both self-designation and co-operative attacks shall be possible, both by laser guided inert bomb releasing and by simulated attack. These types of missions are described in the following sub-paragraphs.

4.2.1.1 Training by Real LGB Releasing

In self-designation attacks, the aircraft follows the flight plans up to the optimal estimated release point, and then releases the inert Laser Guided Bomb (LGB). Then, it performs the escape manoeuvre, activating the airborne laser designator at a proper time. In co-operative attacks (two aircraft with a "spiker" and a "bomber"), the bomber releases the weapon and the spiker aircraft performs illumination as required for an effective guidance on the designated target. During this type of attack, both aircraft manoeuvre as required by the planned training tactics. In both self-designation and co-operative attacks with inert bomb delivery, the STU starts measuring and recording the laser spot applicable parameters (e.g. spot centroid, time of laser activation, time of laser deactivation, etc.).

Measurement of the attack radial error is done by detecting the target/ground impact point of the laser-guided bomb. Consequently, one (or more) high-speed digital TV

camera(s) shall be used at the STU to collect images of a relevant volume around the target. TV camera(s) frames shall be recorded as well for analysis purposes.

4.2.1.2 Training by Simulated Attack

In simulated self-designation attacks, the aircrew follows the flight plans up to the optimal estimated release point, and then simulates the release itself, manoeuvring as if it had occurred. At the required time, the pilot/WSO performs target illumination. In co-operative simulated attacks ("spiker" and "bomber" aircraft), the spiker aircraft performs illumination as required and both bomber and spiker aircraft manoeuvre following the planned training tactics. For both self-designation and co-operative attacks, the following information shall be supplied to the MSU (in the PCC).

a. During the entire attack, the aircraft (self-designation) or the bomber/spiker (co-operative) flight parameters up to the instant of release, from an available Data-link, the PISQ Radars/Cinetheodolites (filtered or automated) or other TSPI systems (e.g., GPS/INS or DGPS/INS).

b. At the instant of simulated release, with a synchronous signal (SRTOA), from an available Data-link or manually from a PCC operator (using the Voice-link with the aircrew).

c. After the simulated release, with the laser activation time signal (LATOA), marking the beginning of the laser designation, and the detected laser spot parameters until designation is completed (planned designation time). The LATOA signal will be supplied either by the available Data-link or by means of the Voice-link with the aircrew/FAC. Should the laser spot on the target be undetected by the STU sensors (when expected to be on the target), a warning signal shall be sent to the PCC, allowing the LSO to order the immediate laser deactivation (emergency procedure). In both normal and emergency procedures, the time of laser deactivation (LDTOA) shall be supplied, with similar modalities (Data-link/Voice-Link), and confirmed as well by the STU sensors.

d. Before mission is initiated, with the relevant atmospheric parameters in the area of operations (i.e., visibility, relative humidity, air temperature, wind speed/direction, etc.) and target parameters (i.e., reflectivity, geometry, etc.).

The MSU then calculates the optimal "Bomb Release Corridor" (BRC) taking into account the bomber flight parameters and gives an output of the computed errors in quasi-real-time (i.e. before the beginning of a new releasing exercise, within 1 minute) if Data-link is available, or in deferred time (i.e. post-mission analysis performed using the data of all releasing exercises done) if Data-link is unavailable. The training crew(s) will be supplied, in quasi-real or deferred time (according to the previous statement), with the information listed below.

- ***Self designation attacks***

  a. The calculated optimal time of release (and the difference with the real one), keeping fixed all flight parameters, taking into account the designation time and STU detected laser spot characteristics (on target).

  b. The calculated optimal aircraft speed (ground speed) at the simulated time of release (and the difference with the real one), keeping fixed all the other flight and designation parameters.

  c. The calculated optimal aircraft designation time and range envelope (distances from the target outside the simulated target lethal-range but within the maximum range for an effective designation) and the differences with the real designation time and profile.

- ***Co-operative attacks (Bomber-Spiker Aircraft)***

  a. The calculated optimal time of release (and the difference with the real one), taking into account the spiker designation time and STU detected laser spot characteristics (on target), keeping fixed all flight parameters of both spiker and bomber aircraft.

b. The calculated optimal bomber aircraft speed (ground speed) at the simulated time of release (and the difference with the real one), keeping fixed all the other (spiker/bomber) flight parameters and designation parameters.

c. The calculated optimal spiker aircraft designation time and range envelope (distances from the target outside the simulated target lethal-range but within the maximum range for an effective designation) and the differences with the real designation time and profile.

- ***Co-operative attacks (Bomber-FAC)***

a. The calculated optimal time of release (and the difference with the real one), taking into account the GLTD designation time and STU detected laser spot characteristics (on target), keeping fixed all bomber flight parameters.

b. The calculated optimal bomber aircraft speed (ground speed) at the simulated time of release (and the difference with the real one), keeping fixed all the other flight parameters and GLTD designation parameters;

c. The calculated optimal designation time and the difference with the real designation time, using the aircraft flight parameters during the simulated release.

4.2.2 Experimental activities

The PILASTER shall allow measurement of the applicable laser spot parameters, such as the laser spot diamensions, energy distribution and centroid position, laser spot quality, atmospheric extinction measurements, and code-signal measurements (on target).

4.3 PILASTER Composition

Unless otherwise specified, all the components of PILASTER will comply with the all applicable systems and laser safety standards approved by the ItAF [1-26]. The PILASTER shall be fully operational with the present generation laser systems and armaments. Furthermore, its design shall be modular and expandable in order to allow future upgrades which may become necessary for test/training operations with next generation laser systems and armaments.
According to the general description and concept of operation previously illustrated, the PILASTER will be composed by the following main systems:

- Modular Target(s) for Real Attacks (Weapon Deliveries);
- Permanent Target(s) for Simulated Attacks (No Weapon Deliveries);
- Standing/Mobile Laser Sensor and Tracking Unit(s) (STU);
- Monitoring Control and Display Station Unit (MSU);
- LAN/WAN (between MSU and STU);
- Video Link (Aircraft to MSU);
- Voice Link (V/UHF radio communications).

Furthermore, the use of a Bi-directional Data-link (MSU-Aircraft), and Encryption/Decription of the Video Link, are considered as growth options for future PILASTER upgrade programs.

4.3.1 Targets

In order to fulfil the various test/training mission requirements, the following different kinds of targets are envisaged:

- ***Fast-recoverable Target(s).*** This type of target (FRCT) shall be used for the effective laser-guided inert bomb releasing, and shall have a goal Mean Time To Repair (MTTR) of 1 hour;

- ***Fixed Target(s).*** This type of target (FXDT) shall be used for simulated laser-guided bomb releasing.

- ***Destroyable Target(s).*** This target (DEST) shall simulate a tactical target, and shall be used for releasing laser-guided weapons with their normal (or reduced) warhead explosive charges;

- ***IR Reference Target(s).*** Using this target (IREF), the Minimum Resolvable Temperature Differences (MRTD) and Spatial Frequencies (corresponding to various 2-D discrimination levels), can be determined for the FLIR systems integrated with airborne laser systems.

- ***Acquisition Training Target(s).*** This kind of target (ATGT) shall simulate a tactical target for acquisition training (i.e. shelter, tank, bridge, etc.).

The FRCT and FXDT targets are considered essential, and will be implemented since the first phases of the PILASTER program. The DEST, IREF and ATGT targets are considered as growth options. Both the FRCT and FXDT will have a dimension of approximately 10×10 m^2 in order to be extended for the majority of laser systems (ground and airborne) currently in service, at most ranges and grazing angles of practical interest. Furthermore, they will be painted with a highly diffusive paint of known reflection properties (i.e., reflectance and BRDF), in order to allow STU spot energy measurements. The DEST and ATGT targets shall have dimensions and shapes appropriate to simulate real targets and to perform real-time (in flight) and post-mission damage-assessment (DEST). The IREF target shall be a standard IR multiple bars target, whose bars shall be heated at precisely tuneable temperature differences (ΔT) with respect to the background.

4.3.2 Sensor Tracking and Measurement Unit

The STU shall be positioned nearby the targets. An hardened location (e.g., a little bunker) will be constructed nearby the FRCT and DEST targets. The STU shall be composed by the following elements:

- IR and TV Cameras;
- Detector Arrays and Processing Units (to be placed on the FXDT target only);
- Recording Systems;

- Computer System(s) with Windows NT or other operating system;
- Data Acquisition and Processing Application Software.

The STU shall calculate the position of the laser spot energy centroid with respect to the target centre. A representation of this position within the target shall be supplied in real-time to the MSU. The STU will also determine and record the laser spot geometric dimensions on the target.

Using the FXDT detectors array, the STU shall also provide laser energy measurements (on the target) and therefore allow, in post-processing, atmospheric extinction determination (by comparison with the known aircraft/system coordinates). Furthermore, the FXDT detectors will allow PRF measurements for pulsed laser systems. All these measurements will allow to verify the impact of atmospheric and operational mission parameters on systems effectiveness.

The STU shall be capable of analysing, in the first development phases, 1.064 μm wavelength lasers (NIR) and shall be extensible, in successive phases, to analyse additional laser systems, such as the Near Infrared (NIR) 1.54-1.55 μm eye-safe lasers, Mid-Infrared (MIR) and Far-Infrared (FIR) lasers.

4.3.3 Monitoring and Control Station Unit

The MSU shall be installed in the PCC building. The MSU receives the data from the STU and shows, on dedicated displays, the laser spot on the target and the video signal received from the aircraft (Video-link). Particularly, the MSU shall be capable of:

- showing, simultaneously on the same display, the data output coming from at least two different STU positions;
- providing aural/visual warnings to the LSO when the expected laser signal is not detected by the STU;
- showing in real-time the video signal received from the aircraft (Video-link), on a dedicated display.

The MSU shall be designed to add, in successive development phases, the possibility of automatically deactivating the on board laser armament, when critical safety conditions are detected. The MSU shall be basically composed of :

- a computer based workstation with a powerful CPU, high-speed graphic and recording capabilities (adequate RAM and internal/external mass memory devices), analogue and digital I/O and LAN/WAN interfaces;
- a Video-link ground unit;
- a Voice-link (V/UHF radio);
- a Data-link ground unit (growth option).

4.3.4 LAN/WAN Networks

The PISQ shall be provided with local or wireless area networks (LAN/WAN) for interconnecting the STU and the MSU. The choice and combination of LAN/WAN networks, shall be as suitable for a correct operability of the PILASTER systems from the available STU/MSU locations.

4.3.5 Meteorological Sensors

In order to perform measurements of the relevant meteorological parameters, the PILASTER range must employ two meteorological stations, both equipped with the sensors necessary for accurate measurements, during test/training missions, of temperature (T), pressure (QHN), wind speed (W_s), relative humidity (RH), rainfall rate ($\Delta x/\Delta t$), and turbulence structure constant (C_n). Each of the two groups of sensors will be mounted on a tower with height adjustable between 0 and 8 metres. For trials/training activities with ground laser systems, the sensors towers will be placed at the target and laser system locations, and all data relative to the two locations will be gathered and recorded at the meteorological stations. During trials/training missions with airborne laser systems, only the data relative to the relevant target(s) location(s) will be recorded. All collected meteorological data will

be used for post-mission analysis of laser beam atmospheric propagation performance.

4.3.6 Video Link

The PILASTER will be provided with a Real-time Video Link from the aircraft to the MSU, to allow Safety and Trial Officers (in the PCC) to monitor and control the whole laser test/training operations. Particularly, the laser system video signal (also available to the on-board operator) must be sent to the ground MSU.
Two functional blocks shall be considered: an On-board Unit, to be installed on the training/experimental aircraft, and a Ground Unit, to be installed in the PCC and interfacing with the MSU. Provision for additional encryption/decryption modules for the video signals should be also incorporated in the system.

4.3.7 Voice Link

The Voice Link between the aircraft and the MSU will be provided by installing a V/UHF radio communication system (including the relative antenna and control panel) at the PCC. The system shall be fully compatible with radio-communication systems currently installed or expected to be installed on-board aircraft.

4.3.8 Data Link

The Data Link is only considered as an option (growth potential) for the PILASTER. If implemented, it can be used to perform the following functions:

a. To maximise laser safety, the MSU may have the capability of controlling the laser armament's key-data signals, such as the ***Laser ON***, ***Track Mode***, ***Lock-On*** or ***Track Lost*** signals. For this purpose, the MSU shall be capable of integrating additional HW/SW modules for analysing in real time the 1553/1760 or other Data Bus messages exchanged between the laser system and the on-board mission computer via Data Link (LINK-16 or other).

b. To perform a real-time attack simulation (self-designation or co-operative), the MSU shall have the capability of acquiring in real-time the significant flight parameters, by reading the applicable bus messages (MIL-STD-1553 or other avionic bus). In order to provide the crew(s) with quasi real-time feedback during simulated attacks, the relevant MSU outputs can be also sent to the aircraft.

4.4 Other Requirements

A feasibility study has to be carried out in order to investigate the possibility of using the cinetheodolite (CITE) systems presently available at PISQ (non-automatic systems), by filtering the operator-telescopes from the laser radiation that might reach the eyes of the systems operators, or by using automatic systems and/or visible cameras applied at the current CITE systems oculars (to avoid any operator injury risk). Analysis will be carried out to specify the optimal solution (e.g. determination of the optical density for the protective filters, or modification of the CITE systems optics design using visible cameras).

As an alternative to the current CITE, automatic CITE systems, Differential GPS (DGPS), Analog/Digital Translators, or Integrated (D)GPS/INS systems may be used (for both aircraft and weapon tracking). The final solution shall be selected balancing cost-effectiveness and minimising the related requirements in terms of aircraft/weapon and ground installations.

4.5 Growth Potentials

As already mentioned in the previous paragraphs, the PILASTER systems shall be designed to respond, at successive stages, to the following additional needs:

- ***Video Link Encryption*** (On-board Module) and ***Video Link Decryption*** (Ground Module);

- ***Use of a DATA LINK***, to allow the real-time availability of the status words of the laser systems. This will allow ***Real-time Simulation*** of bomb releasing and

Improved Laser Safety by monitoring at the MSU the Laser Armed, Target Lock-on (active or lost) and other significant signal status, in connection with the laser spot parameters measured by the STU (and transmitted to the MSU). Particularly, using a Data-link, Automatic deactivation of the laser firing is foreseen an a feasible growth option. The MSU may in fact be capable of automatically deactivating the laser firing, according to the tracking status (active or lost) when the STU detects a possibility for the laser beam to fall outside the target. For this purpose, a Laser De-Activation (LDAC) signal may be generated. This signal, sent to the aircraft by means of the bi-directional link, will set off the Laser Arm signal by means of an encoded-remote-controlled relay circuitry;

- ***Upgrades for new laser systems.*** The STU shall have the possibility of extending the measurement capability to wavelengths other than 1.064 μm, such as the 1.54-1.55 μm lasers, and MIR/FIR lasers;

- ***Construction of additional targets,*** such as Destroyable Targets (DEST), IR Reference Targets (IREF) and Acquisition Training Targets (ATGT).

4.6 References

1. STANAG 3606 – Edition V. "Evaluation and Control of Laser Hazards". 1991.
2. Italian Military Safety Standard SMD-W-001. "Regolamento Interforze di Sicurezza per l'impiego degli apparti laser". Second Edition. 1995.
3. Italian Standard CEI –76/2 – Edition II. "Apparecchi Laser – Sicurezza delle Radiazioni, Classificazione dei Materiali, prescrizioni e Guida per l'Utilizzatore". 1993.
4. International Electrotechnical Commission IEC 825 – (Amendment 2). "Radiation Safety of Laser Products, Equipment Classification, Requirements and User's guide". 1993.
5. Italian Regulation DL 04.12.1992 - n. 475. "Attuazione della direttiva 89/686/CEE relativa ai dispositivi di protezione individuale". 1991.

6. STANAG 3350 – Edition 3. "Analogue Video Standards for Aircraft System Applications". 1989.

7. MIL-C-49142. "Connectors, Plugs and Receptacles Electrical Tri-axial Radio Frequency General Specification". 1989.

8. MIL-C-38999. "Connectors, Electrical, Miniature, High Density, Quick Disconnect, Environment, Resistant, Removable Crimp Contacts, General Specification". 1990.

9. MIL-810-E. "Environmental Requirements and Test Methods". 1992.

10. MIL-M-7793. "Meter, Time Totalising". 1991.

11. MIL-P-116J. "Methods of Preservation". 1990.

12. MIL-S-5002. "Surface Treatment and Inorganic Coating for Metal Surfaces of Weapon Systems". 1990.

13. MIL-STD-100A. "Engineering Drawing Practices". 1994.

14. MIL-STD-129K. "Marking for Shipment and Storage". 1997.

15. MIL-STD-1472A. "Human Engineering". 1998.

16. MIL-STD-1553B. "Digital Division Command/Response Multiplex Data Bus". 1999.

17. MIL-HDBK-217F. "Reliability Prediction of Electronic Equipment". 1990.

18. MIL-HDBK-454K. "Standard General Requirements for Electronic Equipment". 1990.

19. MIL-STD-20731. "Procedure for Packaging and Packing Parts and Equipment". 1991.

20. MIL-T-28800. "General Specification for Test Equipment for Use with Electronic and Electrical Equipment". 1991.

21. NPRD-95. "Non Electronic Parts Reliability". 1990.

22. DOD-STD-2167A. "Defence System Software Development". 1992.

23. EIA RS 170. "Electrical Performance Standards Monochrome Television Studio Facilities". 1990.

24. EIA RS 232C. "Interface Between Data Terminal Equipment and Data Communication Equipment". 1992.

25. EIA RS 422A. "Electrical Characteristics of Balanced Voltage Digital Interface Circuits". 1993.

26. STANAG 3750. "Characteristics of Analogue Video Signals for Aircraft System Applications". 1992.

Chapter 5

PILASTER SYSTEMS DESIGN

5.1 General

An important achievement of this research was the design, and initial construction/testing of the PILASTER Sensor Tracking and Measurement Unit (STU) and Monitoring and Control Station Unit (MSU). In the following, the STU/MSU combination will be denoted PILASTER Laser Tracking and Monitoring System (LTM). The PILASTER LTM system allows accurate measurement on the ground (i.e., target location) of various important laser parameters (beam pointing accuracy, energy received at the target location, spot geometry on the target, etc.), display at a remote location (i.e., control room) of the information required for real-time eye-safety and test/training missions management, and recording (both at the STU and MSU locations) of the relevant information.

During this research, the architecture of the LTM system was progressively refined, based on sensors/systems test results and additional monitoring station (control room) requirements. Furthermore, the PILASTER permanent and modular targets were constructed, after various design calculations and performing field tests with prototype targets and target modules (useful guidelines for the target maintenance/reconstruction during real test/training missions were also identified). This chapter presents the current status of the PILASTER development, with results of the main design activities performed.

5.2 PILASTER LTM Design

As illustrated in chapter 4, the PILASTER LTM system is composed by the Sensor Tracking and Measurement Unit (STU) located in the vicinity of the target, and the Monitoring and Control Station Unit (MSU) located in the remote control room (PCC). This architecture approach was dictated by eye-safety and operational considerations. In fact, the sensor unit must be placed in the vicinity of the illuminated target to perform its functions (i.e., within the "Buffer Zone" for non-eye safe systems), where all unprotected personnel has to be evacuated. Furthermore, in general, it should be possible to perform "laser attacks" with both "dummy" or reduced-warhead weapons (hard targets), and the real-time availability of the "spot-on-target" information at the control room enhances the Laser Safety Officer (LSO) situation awareness and, in the case of test missions, gives to the Trial Officer (TO) an immediate perception of the laser LOS stability and a way of promptly verifying the success of the various test runs being performed, therefore increasing the probability of overall test mission success.

5.2.1 PILASTER LTM Architecture and Functions

According to the operational requirements described in chapter 4, the PILASTER LTM main functions (already implemented) are the following:

- measuring the pointing accuracy of LTD/LRF systems, using reference ground targets;
- measuring the temporal power distribution of the laser footprint on the target;
- measuring the laser spot geometry on the target;
- processing the above measurements, transmitting the results via LAN/WAN, and displaying the data in real-time at the control room;
- recording all measurements, together with the relative time tags, in order to allow post-mission visualisation and plotting of the data.

Essential to the LTM design was definition of the size and location of the targets. The STU is a fixed or mobile unit, to be placed at a distance of 100 m from the FRCT and FXDT targets (these targets have a dimension of approximately 10×10 m^2 in order to be extended for the majority of laser systems currently in service, at ranges and grazing angles of practical interest). The STU employ a data-link for sending in real-time all information required to the MSU. The distance and relative displacement of the STU and MSU is optimised in order to guarantee a minimum number of RF repeaters.

Once the Weapon System Operator (WSO) on board the aircraft initialises the LTD firing procedure, a portion of the designated target is illuminated (i.e., a function of the beam output diameter/divergence and aircraft-target distance). The STU tracks the laser spot on the target (NIR cameras) and records the relevant spot frames. At the same time, for each spot, the data relative to the incident laser radiance are collected, and the energy centroids of the laser spots are determined and recorded. Similarly, the spots geometric centres are determined and recorded.

The STU will also determine and record the laser spot effective dimensions on the target (allowing an estimation of the effective laser beam divergence, using the aircraft/system trajectory data), and compute various parameters for charactering the degree of distortion of the laser spot.

Using Arrays of Detectors (DEA's) installed on the FXDT target, the STU also provides laser energy measurements on the target and therefore allows, in post-processing, atmospheric extinction determination for both airborne and ground laser systems (by using the known aircraft/system positioning data). Furthermore, the FXDT detectors allow time laser signal measurements for CW and pulsed systems (pulse duration $P_D \geq 2$ ns and PRF = $1 \div 100$ Hz). These features allow to verify the impact of atmospheric and geometric mission parameters on system effectiveness.

The STU is currently capable of analysing laser signals at 1.064 μm and 1.54/1.55 μm wavelengths and will be capable, in future upgraded versions, to analyse signals from other sources, such as the 10.6 μm CO_2 lasers.

Real-time aircraft trajectory data are currently obtained using the tracking radars operating at the PILASTER range, and presented the PCC. More Accurate positioning data, relative to both the aircraft and the LGW, are obtained in post-processing using

cinetheodolites (existing CITE with filtered optical sights and/or automatic CITE systems) and/or Differential GPS (DGPS).

5.2.1.1 PILASTER Sensor and Tracking Unit

The general architecture of the PILASTER STU is shown in Fig. 5-1. The STU electro-optical sensors include an Array of Detectors (DEA) for direct energy/signal measurements on the target, two IR cameras (one for real-time spot monitoring and one for post-processing laser spot analysis) and a TV camera (for LGW impact data collection). The computer units perform the following functions:

- STU configuration control;
- acquisition, processing and recording of the IR/TV cameras raw data (i.e., digital images);
- data exchange, via LAN/WAN, with the MSU.

The BITE pulse generator, commanded by the local control panel or by a remote MSU operator (via LAN/WAN) is activated in the system BITE MODE. The audio channel is available for communications with the MSU during the STU location and calibration phase.

After calibration has been performed, the STU can work as an automatic unit, executing the commands received from the MSU. For certain specific locations of the STU in the test range (6 possible and 2 existing FXDT/FRCT locations), a permanent hard-wired link (fibre-optics cables connected to the PISQ existing network) has been adopted for data exchange and communications with the MSU. The power supply unit generates all stabilised low voltages required by the other units.

In the operational mode (OPR MODE) of the LTM (see para 5.2.2), the FXDT DEA's detect the laser spot on the target and their Processing Units (DPU's) measure the temporal and energetic characteristics of the laser signals incident to each detector. The Synchronisation Module (SYM) generates the "time label" used to synchronise the TV/IR cameras images and the DEA measurements.

The TV and IR cameras acquire the target and laser spot images, and send the video signals to their respective Frame Grabbers (FRG's). The FRG's convert the video signals into a digital format, associate to the converted signals the relative "time labels", and send the labelled digital signals to the computer processors. The computer units process the frame grabbers and DPU outputs and associates synchronised DEA measurements to each IR frame (post-processing IR camera), and a TV frame to each IR frame (real-time IR camera). The real-time IR camera and TV camera images can be viewed by an operator at the STU (e.g., during the initial installation/calibration of the STU) through a computer monitor.

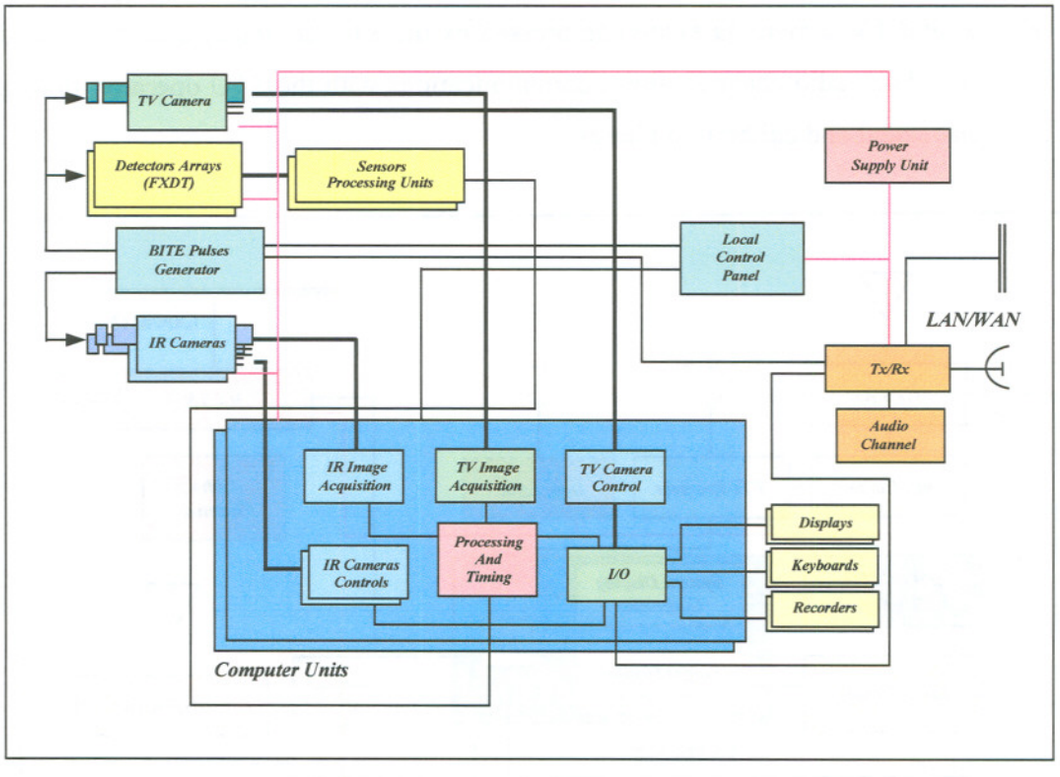

Figure 5-1. PILASTER STU architecture.

During the mission, the raw data (i.e., the valid images acquired with relative time labels, the frequency data, etc.) are processed at the STU to obtain the required outputs. Both the raw and the final data are then recorded in the computers mass memories and also downloaded to external memory devices.

5.2.1.2 PILASTER Monitoring and Control Station Unit

The general architecture of the PILASTER MSU is shown in Fig. 5-2. The computer, with its peripherals, allows the operator to select the LTM operational mode and the data exchange with the STU. The MSU receives, via LAN/WAN, the data processed by the STU computer. The computer displays show the laser beam pointing data (real-time IR camera raw frames and computed pointing data) and the visible target images (TV camera data) to the MSU operator. If requested by the MSU operator, the raw data acquired in a certain number of test runs by the STU (real-time/post-processing IR cameras and TV camera data) are compressed by the STU computer and transmitted to the MSU. The audio channel allows communications with the STU operator, during the STU placement and calibration phases.

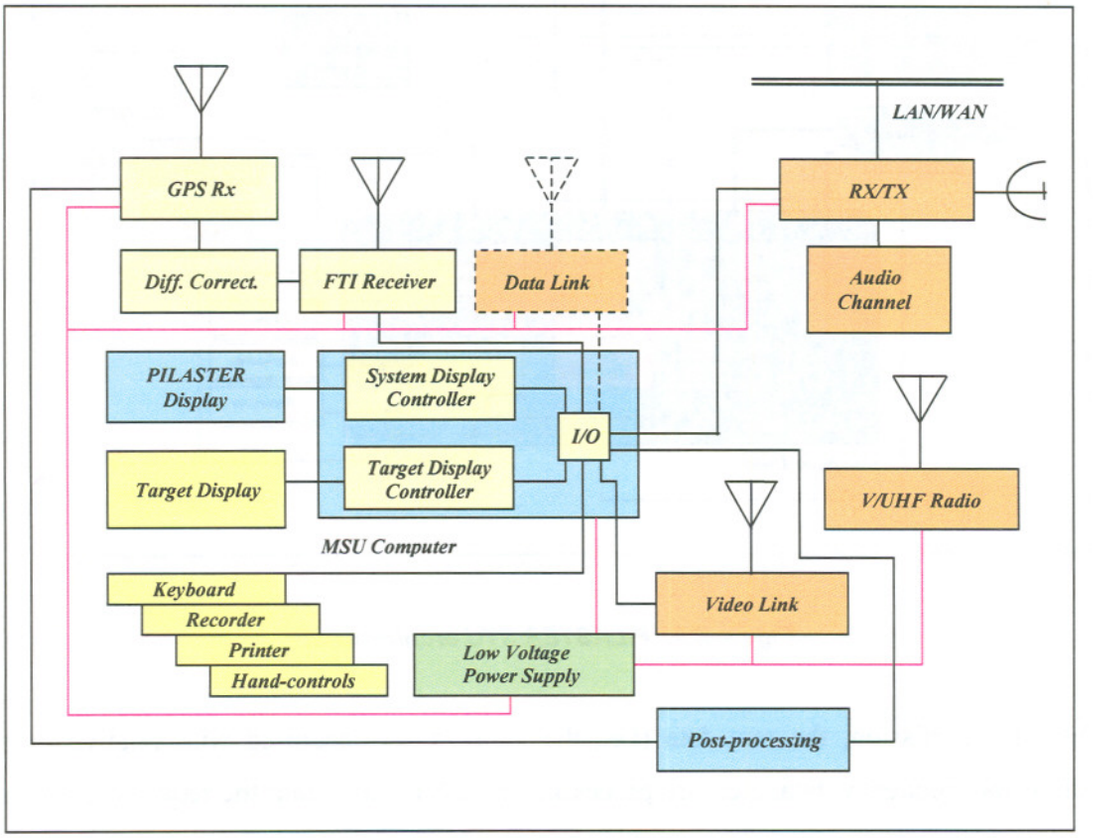

Figure 5-2. PILASTER MSU architecture.

Currently, a dedicated software tool is also being developed for automatic post-mission correlation between the aircraft cinematic data, stored by the aircraft on-board recorders or by dedicated (D)GPS data recorders, and the laser footprint data. This tool will also serve as a mission debriefing aid for training activities performed with airborne laser systems.

5.2.2 PILASTER LTM Functional Modes

Currently, the following PILASTER LTM functional modes have been implemented:

- **INST MODE**, required for the installation (i.e., alignment, calibration, etc.) of the STU TV and IR cameras in the vicinity of the selected target. In this mode, the TV and IR target images can be viewed on the STU computer displays, allowing an initial alignment of the sensors. After this operation has been completed and the relevant data have been inputted to the STU computer, the LTM system fully defines the target-sensors relative geometries.

- **BITE MODE**, required to check the correct functioning of the complete LTM system, including DEA and camera sensors. To obtain this, an array of LED's generates a signal with characteristics similar (i.e., energy, time and frequency) to a laser beam on the target. Using this signal, all units are activated in turn, allowing a complete system check. The BITE cycle execution time is about 60 seconds.

- After the BITE sequence has been completed successfully, the system automatically enters the **OPR MODE** (Operational Mode). In this mode, the system determines the laser footprint dimensions, the laser footprint geometric centre, the location of the beam energy centroid, the energy measured by each DEA detector, the laser PRF and P_D, the total number of pulses received, and the time labels associated with the acquired laser pulses. The instantaneous laser spot images and the geometric centre data are presented in real-time at the MSU. All

other information are available in about 1 minute after each test/training mission run, and presented at the MSU operator through a dedicated software menu (the design time interval between one test/training mission run and the following is 2 minutes).

- The **TRF MODE** (Transfer Mode), is a reversionary mode for transferring the STU recorded data (relative to the last 10 test/training runs) to the MSU computer (via LAN/WAN). The compressed data relative to the 10 mission runs are transferred from the STU to the MSU in a time not exceeding 5 minutes.

5.3 PILASTER Sensors Characteristics

According to PILASTER general requirements presented in chapter 4, various types of sensors were selected for the laser range. Particularly, the PILASTER STU and the FXDT target were equipped with sensors for laser spot monitoring and geometric/energy measurements. Furthermore, appropriate meteorological sensors were selected for laser beam atmospheric propagation data analysis.

Selection of the PILASTER sensors was the result of many engineering design calculations, compromise of various technical and operational requirements (use with airborne and ground laser systems, constraints imposed by the other STU hardware and software component, FXDT target design, etc.), actual laboratory and field tests, and last (but not least), cost-effectiveness considerations. In the following sections, the design characteristics of the main sensors selected for the PILASTER program are presented. More information about the STU sensors selection process is given in chapters 7 and 8 (Laboratory and Ground Experimental Activities).

5.3.1 IR Cameras and Digital Image Acquisition Systems

The IR cameras integrated in the STU (real-time spot monitoring and post-processing spot data analysis), had to be equipped with suitable optics (barrels and filters) and digital image acquisition systems in order to match the PILASTER

requirements. Particularly, according to the calculations performed, they had to be able to acquire, both in day and night conditions, laser spots with minimum dimensions of 0.1×0.1 metres and with a minimum energy density of a 10 μJoule/m^2, produced by lasers beams at λ = 1064 nm and λ = 1550 nm incident on targets with 5% minimum reflectivity. Furthermore, both raw and processed data (i.e., acquired NIR camera frames and measurements/analysis results) had to be transferred to the PILASTER LAN/WAN networks for real-time and off-line reading at the MSU. Finally, a remote control system (through LAN/WAN) was required for the NIR cameras. In order to match these requirements, the following NIR cameras/optics, digital image acquisition systems and interface electronics were integrated in the PILASTER STU:

- *Phoenix*™ *NIR* camera produced by *Indigo Systems Inc.*, for post-mission laser spot data analysis (i.e., determination of laser spot geometric and energetic characteristics).

- *Merlin*™ *NIR* camera produced by *Indigo Systems Inc.*, for real-time laser spot monitoring (i.e., laser spot position determination for real-time monitoring at the STU and/or MSU locations).

- The barrels for the *Phoenix*™ *NIR* and *Merlin*™ *NIR* cameras required to frame (entirely) a target with dimensions 10×10 metres (located on the ground), and also to frame a central portion of the same target with dimensions 4×4 metres (about 3 metres above the ground), from a distance varying between 50 metres and 250 metres.

- Narrow band filters for the *Phoenix*™ *NIR* and *Merlin*™ *NIR* cameras suitable for laser radiation at λ = 1064 nm and λ = 1550 nm.

- A Digital Acquisition System (DAS) for the *Phoenix*™ *NIR* camera composed by a rack with a portable PC, the hardware peripherals and the software (based on *Media Cybernetics* IMAGE-PRO PLUS™ version 4.1) necessary for digital image acquisition, determination of the geometric/energetic characteristics of the

laser spots, and memorization of raw data (acquired frames) and measurements data (off-line analysis results).

- A Digital Image Acquisition Computer (DAC) for the *Merlin*™ *NIR* camera composed by a portable PC, the hardware peripherals and the software (based on *Media Cybernetics* IMAGE-PRO PLUS™ version 4.1) necessary for real-time digital image acquisition and memorization of data.

- A real-time remote control system (hardware and software) for the *Phoenix*™ *NIR* and *Merlin*™ *NIR* cameras, integrated with the PILASTER LAN/WAN networks.

- The interface electronics for the *Phoenix*™ *NIR* camera, required for processed (off-line) data transmission through the PILASTER LAN/WAN networks (and visualisation at the PCC), and for real-time remote control of the camera.

- The interface electronics for the *Merlin*™ *NIR* camera, required for real-time data transmission through the PILASTER LAN and WAN networks (and real-time visualisation at the PCC), and for real-time remote control of the camera.

5.3.2 STU-FXDT Sensors and Processing Units

A Laser Energy Measurement System (LEMS), constituted by various Laser Energy Meter (LEM) electronic units, equipped with 4÷16 Pyroelectric Probe (PEP) sensors (FXDT-mounted), were also integrated in the PILASTER STU. The LEMS is suitable for measuring pulsed laser signals with very short pulse duration (P_D) and low peak energy (E_P), at λ = 1064 nm and λ = 1550 nm (10 mJ/m^2 ≤ P_D ≤ 10 μJ/m^2, P_D ≥ 2 nsec, PRF = 1 ÷ 400 Hz).

Together with the PEP sensors, eight sensors-heads connected via fiber optics cables to a modified version of the *Marconi Selenia Communications S.p.A.* RALM-01 Laser Warning Receiver (M-RALM-01) were installed on the FXDT target. A remote control and display unit of the M-RALM-01 system was also installed in the STU, and the system data were sent to the MSU through the LAN/WAN networks. The M-RALM-01

system was used to accurately measure the PRF of the incident laser signals, and as an additional back-up sensor for confirming the presence of laser signals on the PILASTER FXDT target, for safety purposes during both test and training missions (see chapter 7 for more details about the LEMS/PEP and M-RALM-01 systems characteristics).

5.3.3 Meteorological Sensors

Two wireless commercial meteorological stations, equipped with all sensors required for measuring relative humidity (RH), pressure (P_a), temperature (T), differential temperatures (T_d), rainfall-rate ($\Delta x/\Delta t$), wind speed (W_s) and wind direction (W_d), were used to collect the relevant data at the FXDT target location and at the transmitter locations (for ground systems testing), necessary for propagation and performance analysis. Furthermore, two additional sensors were employed for measuring the turbulence structure constant (C_n) and turbulent heat flux (H_f) at the FXDT target and ground laser systems locations. Particularly, the following systems/sensors were employed:

- Two Wireless Meteorological Stations (WMS) constituted by a 0÷10 metres tower for sensors installation (i.e., hygrometers, barometers, thermometers, thermocouples, rainfall-rate meters and anemometers) and a local display unit (maximum distance from the sensor tower: 100 metre) with standard PC interfaces.

- A portable Display and Recording Station (DRS), connected to the WMS (RS232 serial port), for real-time data display (touch-screen display with retro-illumination) and recording (data from all meteorological sensors acquired during a period of 24 hours at a sampling frequency of 1 Hz).

- Two calibrated thermometers with 0.1 °C precision (T range: –20°C ÷ +60°C).

- Two calibrated hygrometer with a precision of 1% (RH range: 15% ÷ 100%).

- Two barometers with 1 hPa precision, for atmospheric pressure measurement.

- Two rainfall-rate meters for measurement of relative and total $\Delta x/\Delta t$, with a precision of 0.1 mm/hr.

- Two anemometers for wind speed (precision 1 Km/h), and wind direction determination (precision 2°).

- A scintillometer (composed by a laser transmitter and a remote measurement unit) for determination of the turbulence structure constant (C_n), and turbulent heat flux (H_f), with measurement baselines between 500 m and 5 km.

5.4 PILASTER TSPI Systems

During test and training activities with Airborne Laser Systems (ALS) and Laser Guided Weapons (LGW) at the PILASTER range, accurate Time and Space Position Information (TSPI) can be provided by using existing cinetheodolite systems (with filtered operator optical sights), tracking radars (or laser tracking systems), and various ground-based radio positioning systems. These systems, however, have a variety of limitations. First of all, they provide a TSPI solution based on measurements relative to large and costly fixed ground stations. Weather has an adverse effect on many of these systems, and all of them are limited to minimum altitudes or to limited portions of the PILASTER range area. The number of participants each system can support is very limited, and correlation with other systems is extremely difficult, if not impossible. These limitations greatly increase instrumentation costs and impose severe constraints on test/training scenarios. Clearly, a more cost-effective TSPI source is needed for the final PILASTER implementation.

5.4.1 DGPS Range Applications

The Global Positioning System (GPS) provides a cost-effective capability that overcomes nearly all the limitations of existing TSPI sources. GPS is a passive

system using satellites which provide universal and accurate source of real-time position and timing data to correlate mission events. The coverage area is unbounded and the number of users is unlimited. The use of land-based Differential GPS (DGPS) reference stations improves accuracy to about one metre for relatively stationary platforms, and to a few metres for high performance tactical aircraft. Further accuracy enhancement can be obtained by using GPS carrier phase measurements, either in post-processing or in real-time. Accuracy does not degrade at low altitudes above the earth's surface, and loss of navigation solution does not occur as long as the antenna has an open view of the sky. However, DGPS performance in terms of data continuity and accuracy during high dynamics manoeuvres, even if sufficient for many tasks, can not cover the entire flight envelope of modern high performance fighter aircraft (see chapter 9). Moreover, the update-rate of GPS receivers is too low for many tasks. Currently, the integration of GPS with an inertial navigation system (INS) is considered to be the optimal solution to the above mentioned shortcomings. This integration, performed either in real-time or in post-processing, can provide in fact the required update rate and have a higher data continuity and integrity. The other advantages of an INS: low short term drift and low noise, are combined with the advantages of GPS: high position accuracy and no long term drift. Moreover, the combination of an INS with (D)GPS is a natural evolution of existing airborne navigation systems, the majority of which is currently based on an INS, updated by other positioning systems to compensate for the shortcomings of the inertial system. In the following paragraph, some information is given about the initial selection process of DGPS systems for the PILASTER program. Ground and flight test activities performed with the DGPS systems selected after the initial technical evaluation, are described in the chapters 8 and 9 of this thesis.

5.4.2 PILASTER DGPS Equipment Selection

As discussed in the previous paragraph, accurate determination of aircraft TSPI is a strong requirement for both flight test and training applications with ALS/LGW. The foreseen capabilities of GPS, in terms of data accuracy, quickness of data availability and reduction of cost, moved to undertake a study aimed at defining the

requirements of a DGPS based system for integration in the PILASTER range. The study was mainly addressed to GPS using C/A code, with post-flight differentiation. This was preferred to GPS using P-code due to both simplicity of use and high accuracy attainable notwithstanding its lower cost. After contacting many potential suppliers, an initial assessment of different systems was conducted in order to select the DGPS systems best matching the technical requirements. The technical specifications were submitted to a number of companies producing GPS systems. Of the 12 companies contacted, four were able to provide systems with good technical characteristics. Therefore, a comparison was necessary in order to select the system with the best performance. The results of the technical analysis are shown Table 5-1. The system proposed by ELMER (ELMER R202 P-code airborne receiver) did not satisfy the essential accuracy requirements. The system proposed by this company could only operate in P-code and therefore its quoted accuracy (16 m SEP) was better than any other stand-alone GPS system operating with the C/A code (100 m 2d-RMS), but less than the accuracy normally provided by a GPS in differential mode (1-5 m SEP). Moreover, the number of channels available was less than required and the overall cost of the system was very high. Also the system proposed by TECHNITRON (GPS120 airborne receiver and ASHTECH-XII ground receiver) was unsatisfactory. Particularly, the airborne system was a 5 channels receiver and the quoted accuracies were inferior to the other systems. Moreover, the RTCM-SC-104 standard protocol was not available. The system proposed by ASHTECH ITALY (ASHTECH XII for both the AR and the ground RS) satisfied the essential requirements stated in the specification document. Even if the interface available on the ASHTECH XII receiver (RS-232) was different from the one desired (RS-422), the technical problem could be easily solved. Also the system proposed by TRIMBLE ITALY (TANS airborne receiver and 4000SE ground receiver) fulfilled the essential requirements stated in the PILASTER specification documents.

As a final result of the technical analysis, the systems proposed by ASHTECH and TRIMBLE were selected. Therefore, various ground and flight test activities were performed with these two systems, in order to select the DGPS combination with the best technical and operational characteristics (see chapters 8 and 9).

REQUIREMENTS		WEIGHT	MARCONI-ELMER			ASHTECH ITALY			TECHNITRON			TRIMBLE ITALY		
			PERFORM.	MARK	MARK × WEIGHT	PERFORM.	MARK	MARK × WEIGHT	PERFORM.	MARK	MARK × WEIGHT	PERFORM	MARK	MARK × WEIGHT
Airborne equipment	N. of channels (6 min.)	3	5 parallel	3	9	12 parallel	5	15	5 parallel	5	9	6 parallel	5	15
	C/A code (L1)	5	C/A + P	1	5	C/A	5	25	C/A	5	25	C/A	5	25
	Aided Mode (vel. a/o alt.)	1	YES	5	5	(Alt. only)	5	5	YES (option)	5	5	YES (option)	5	5
	Acc. Pos. w/o SA (25m SEP)	1	16 m SEP	5	5	25 m SEP	5	5	25 m SEP	5	5	25 m SEP	5	5
	Acc. Pos. with SA (100m 2dRMS)	3	16 m SEP	5	15	100 m 2dRMS	5	15	100m 2dRMS	5	15	100m 2dRMS	5	15
	Acc. Vel. w/o SA (0.02 m/s RMS)	1	0.1 m/s RMS	3	3	0.1 m/s RMS	5	5	0.1 m/s RMS	5	3	0.02 m/s RMS	5	5
	Acc. Vel. with SA (0.1 m/s RMS)	3	0.1 m/s RMS	5	15	0.1 m/s RMS	5	15	0.1 m/s RMS	5	15	0.1 m/s RMS	5	15
	Standard I/O	5	OK	5	25	RS232	3	15	RS232	5	15	OK	5	25
	SUBTOTAL				**89**			**100**			**92**			**110**
Ground Station	N. of channels (9 min.)	5	5 parallel	3	15	12 parallel	5	25	12 parallel	5	25	9 parallel	5	25
	Code	5	C/A + P	1	5	C/A	5	25	C/A	5	25	C/A	5	25
	(L + L option)	5	YES	5	15	YES	5	15	YES	5	25	YES	5	15
	Recording memory	3	UN	1	3	20 h	5	15	20 h	5	15	6 h	5	15
	RCTM format	5	NO	1	5	OK	5	25	NO	1	5	OK	5	25
	SUBTOTAL				**43**			**105**			**95**			**105**
Software Accuracy	Real-time differential mode:													
	- Position (10 m SEP)	3	-	"	N/A	3 m SEP	5	15	25 m SEP	1	3	10 m SEP	5	15
	- Velocity (0.02 m/s)	3	-	"	"	0.01 m/s RMS	5	15	0.1 m/s	3	9	0.02 m/s	5	15
	Post FLT differential mode:													
	- Position (5 m SEP)	5	-	"	"	3 m SEP	5	25	10 m SEP	1	5	5 m SEP	5	25
	- Velocity (0.02 m/s)	5	-	"	"	0.01 m/s RMS	5	25	0.05 m/s RMS	3	15	0.02 m/s RMS	5	25
	SUBTOTAL				**N/A**			**80**			**32**			**80**
Tech. ass.		5	-	5	25		5	25		5	25		5	25
TOTAL		**64**			**150**			**310**			**244**			**320**

ACC. = Accuracy, POS. = Position, VEL. = Velocity, SA = Selective Availability, W/O = Without, I/O = Input/Output, A/O = And/Or, N/A = Not Applicable, UN = Unknown.

Table 5-1. Technical comparison of four DGPS systems for the PILASTER range.

5.5 PILASTER Extinction Measurement Techniques

The standard techniques used for PILASTER laser extinction measurements (atmospheric propagation tests) are the following:

- Extinction Measurement Technique n° 1 (EMT-1), using the PILASTER non-calibrated *Phoenix*^{TM} NIR camera and the FXDT-mounted PEP sensors measurements.

- Extinction Measurement Technique n° 2 (EMT-2), using the PILASTER calibrated *Phoenix*^{TM} NIR camera measurements.

The rationales of the EMT-1 and EMT-2 techniques are described below. An additional technique (EMT-3), developed to perform extinction measurements when PILASTER standard techniques (EMT-1 and EMT-2) could not be implemented (e.g., laser transmitter characteristics not compatible with the standard PILASTER STU sensors response), and a Control Technique (EMT-CT) for systems field calibration and preliminary verification of the EMT-1 and EMT-2 techniques, are described in chapter 8 (Ground Experimental Activities).

5.5.1 Description of PILASTER EMT-1

This technique is based on direct measurements of laser energy at pre-defined locations on the target (DEA detectors) and use of the *Phoenix*^{TM} NIR camera spot frames (NIR camera non-calibrated) to reconstruct, by means of the IMAGE-PRO PLUS^{TM} pixel intensity matrixes (associated to each frame), the overall energy intensity profile (from which atmospheric extinction is computed). The logical steps involved in this technique are shown in Fig. 5-3.

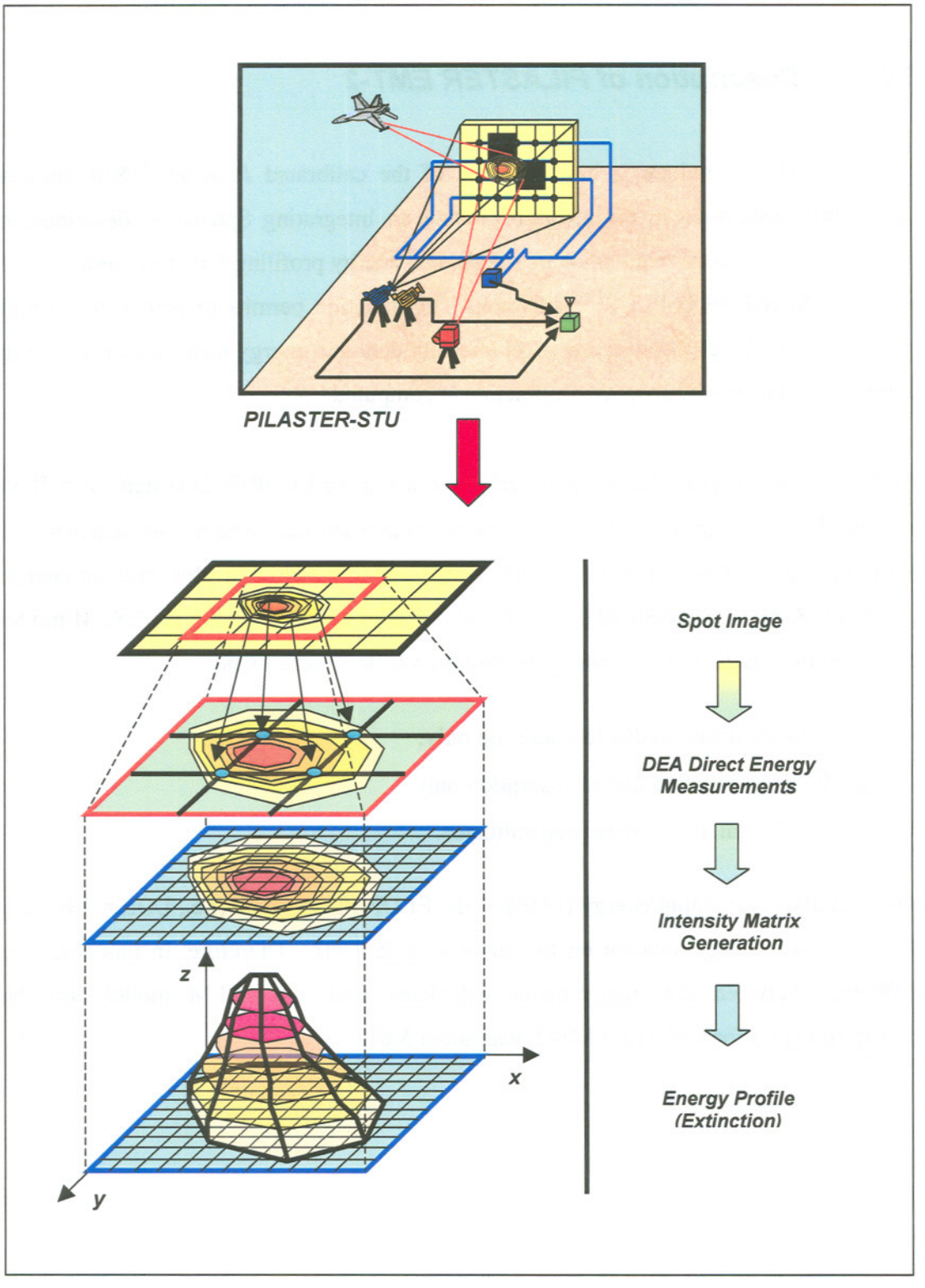

Figure 5-3. EMT-1 laser spot energy profile reconstruction.

5.5.2 Description of PILASTER EMT-2

This technique is based on use of the calibrated *Phoenix*^{TM} NIR camera (calibration performed in the laboratory using an Integrating Sphere, as described in chapter 7) and successive adoption of a dedicated energy profiling function implemented with the IMAGE-PRO PLUS^{TM} software. This function permits to obtain the overall spot energy by directly converting pixel intensity data into energy measurements. Using these measurements, atmospheric extinction is computed.

As an example, a spot measurement performed using the ELOP-PLD system (λ = 1064 nm) and EMT-2 is shown in Fig. 5-4. The test was performed with a laser slant-path of 4 km, during a day with V = 11 km, RH = 65% and T = 18°C. In this case, an energy (E) of 52.76 mJ was measured by the *Phoenix*^{TM} NIR camera. Using the ESLM model presented in chapter 3, the following propagation factors were found:

- τ_{si} = 0.54 contribution due to scattering only;
- τ_{ai} = 0.79 contribution due to absorption only;
- τ_{atm} = 0.43 total atmospheric transmittance.

Knowing the laser output energy (LOE) of the ELOP-PLD system (i.e., LOE = 130 mJ), the calculated energy incident on the target was 55.9 mJ. Therefore, in this case, the difference between the transmittance calculated with the ESLM model and the measurement performed with EMT-2, was about 5.6%.

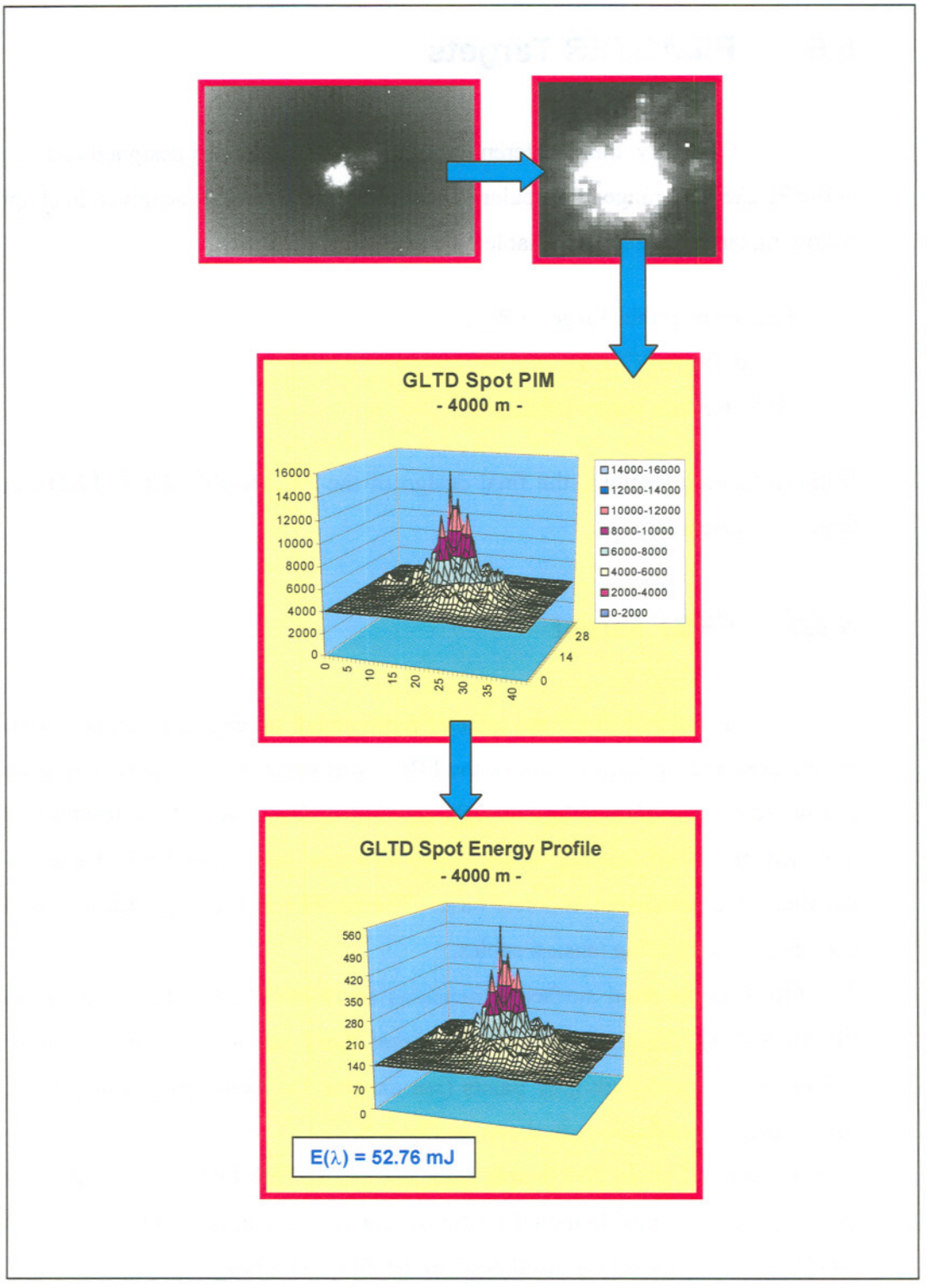

Figure 5-4. EMT-2 laser spot energy measurement.

5.6 PILASTER Targets

Currently, three different types of targets have been designed and constructed at the PILASTER range. Particularly, according to the definitions given in chapter 4, the following targets are now available:

- Fast-recoverable Target (FRCT);
- Fixed Target (FXDT);
- IR Reference Target (IREF).

In the following sections, the final design of the PILASTER FRCT, FXDT and IREF targets is presented.

5.6.1 FRCT Target

In order to fulfil the general requirement described in chapter 4 (i.e., large frontal area and MTTR of 1 hour), the FRCT was designed as a vertical modular target, composed by a number of light-weight wood modules (covering the frontal target area), mounted on a load bearing wood planks structure (also modular and easy to repair), installed on a permanent concrete base. The rigidity of the load bearing structure was also increased by using tension cables.

The FRCT target front surface dimensions are 9.76×7.925 metres. According to the PILASTER requirements, the FRCT target front surface was painted with highly diffusive white and dark grey paints (see chapter 8). Some phases of the PILASTER FRCT target construction are shown in Fig. 5-5.

At a distance of about 250 metres from the PILASTER FRCT target, along the target normal (i.e., well outside the CEP of most current laser armaments), a hardened shelter (HSH) was constructed for installation of the STU sensors/systems.

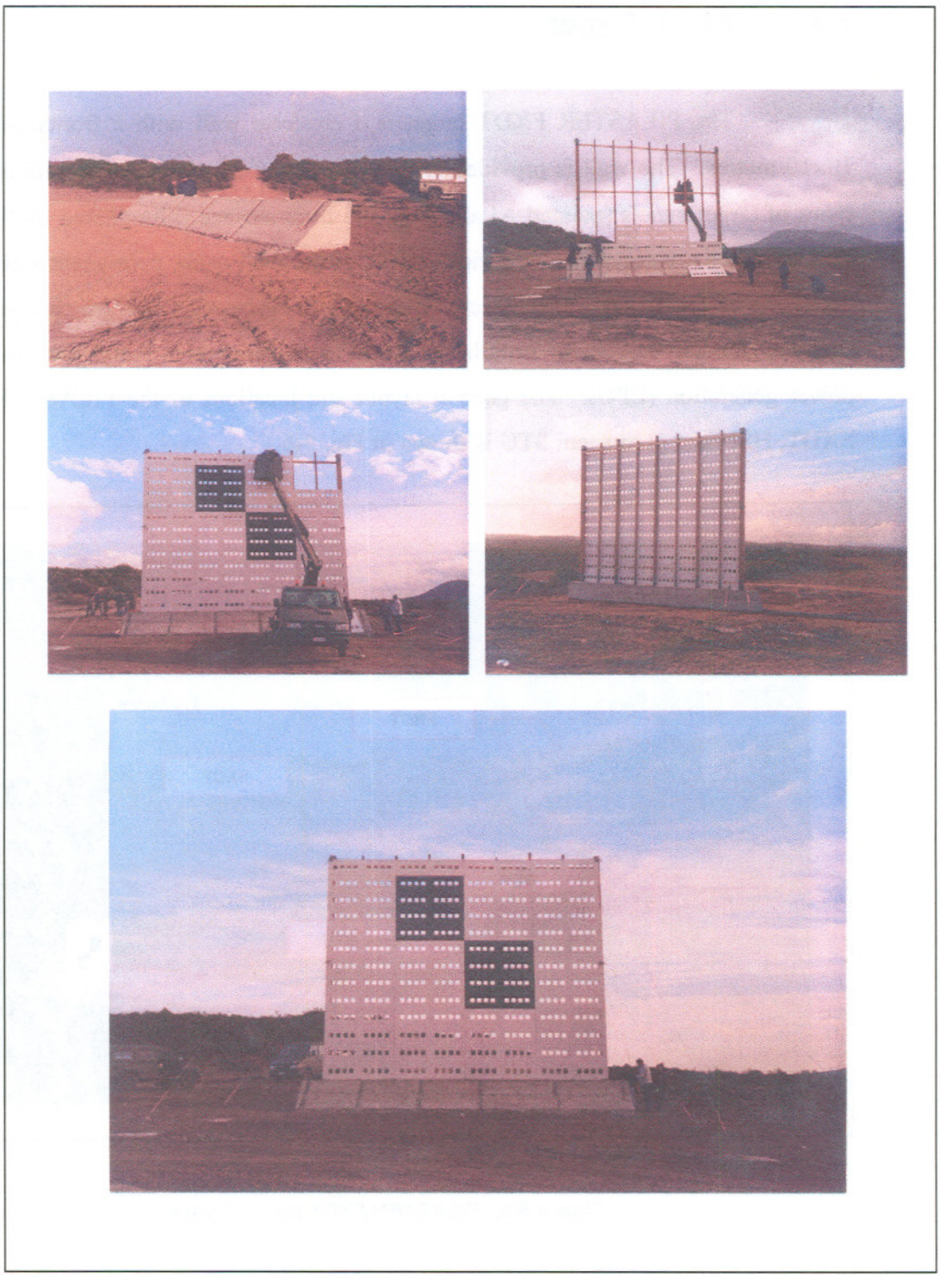

Figure 5-5. PILASTER FRCT target construction.

5.6.2 FXDT Target

The PILASTER FXDT target is a concrete wall with a frontal surface of 10×10 metres. The wall is provided with a number of apertures for installing various types of target panels (painted Al alloy) on the front surface (illuminated by the laser). The apertures are accessible at various levels of the wall using permanent stairs on the back side of the target. In the vicinity of the FXDT target, there are two permanent shelters, one for permanent installation of STU sensors/systems and one for electric power generation (EPG). The general layout and locations of the PILASTER FRCT, FXDT, HSH and permanent STU is shown in Fig. 5-6.

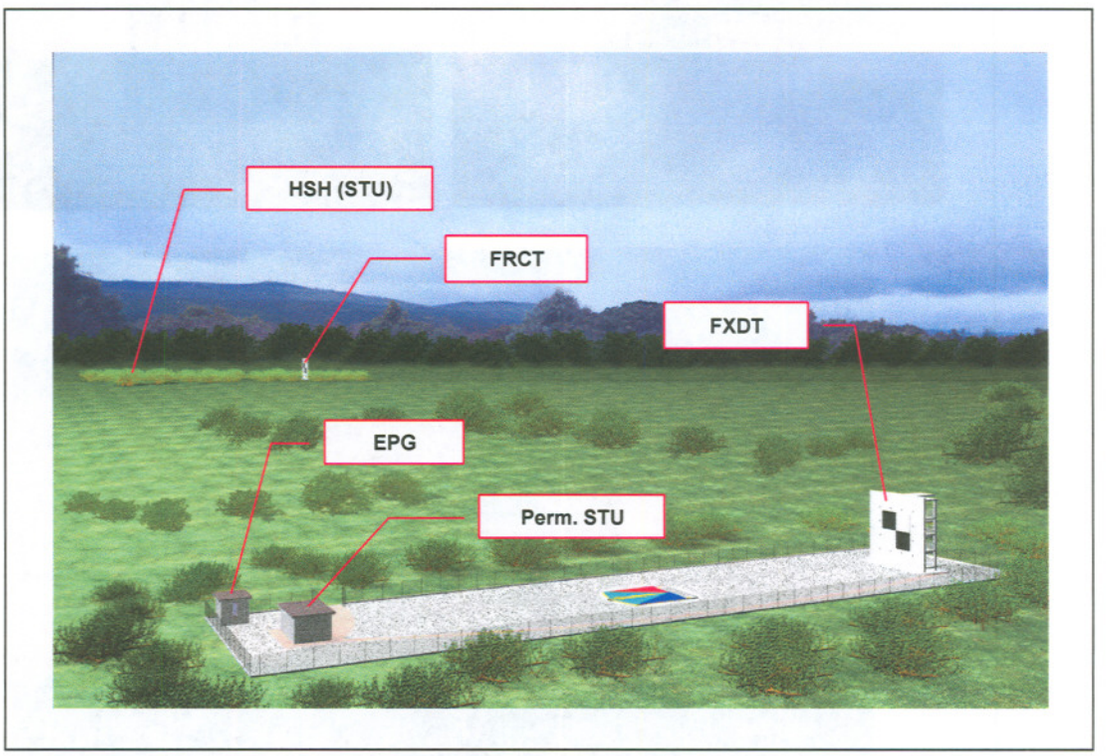

Figure 5-6. PILASTER FXDT target layout.

The Figures 5-7 and 5-8 show the layout of the three FXDT target panels. Various apertures are present on the panels for installation of the STU target detector units

(lenses and optical fibers). These apertures are occluded if not occupied by sensors during the PILASTER activities.

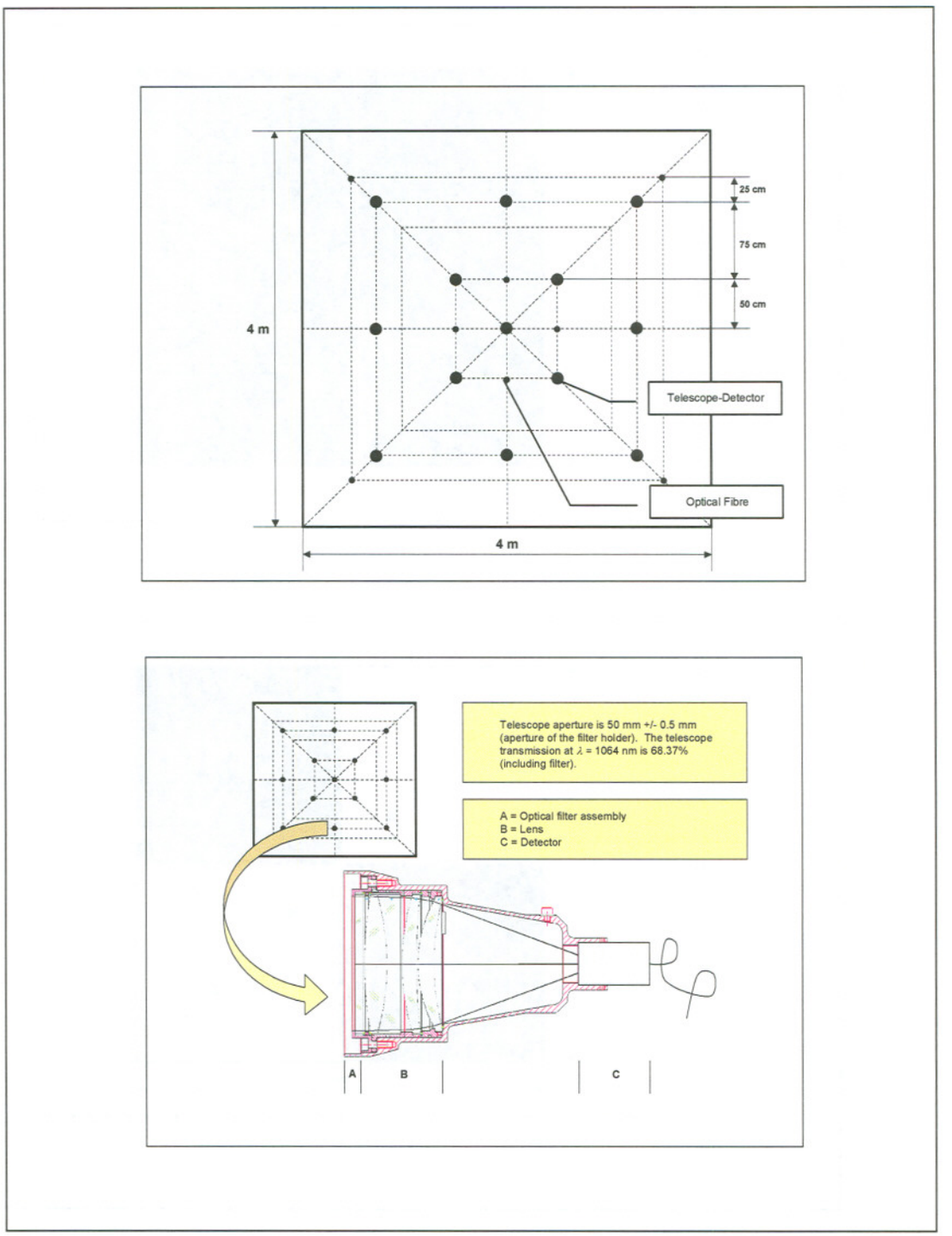

Figure 5-7. PILASTER FXDT target standard panel n° 1.

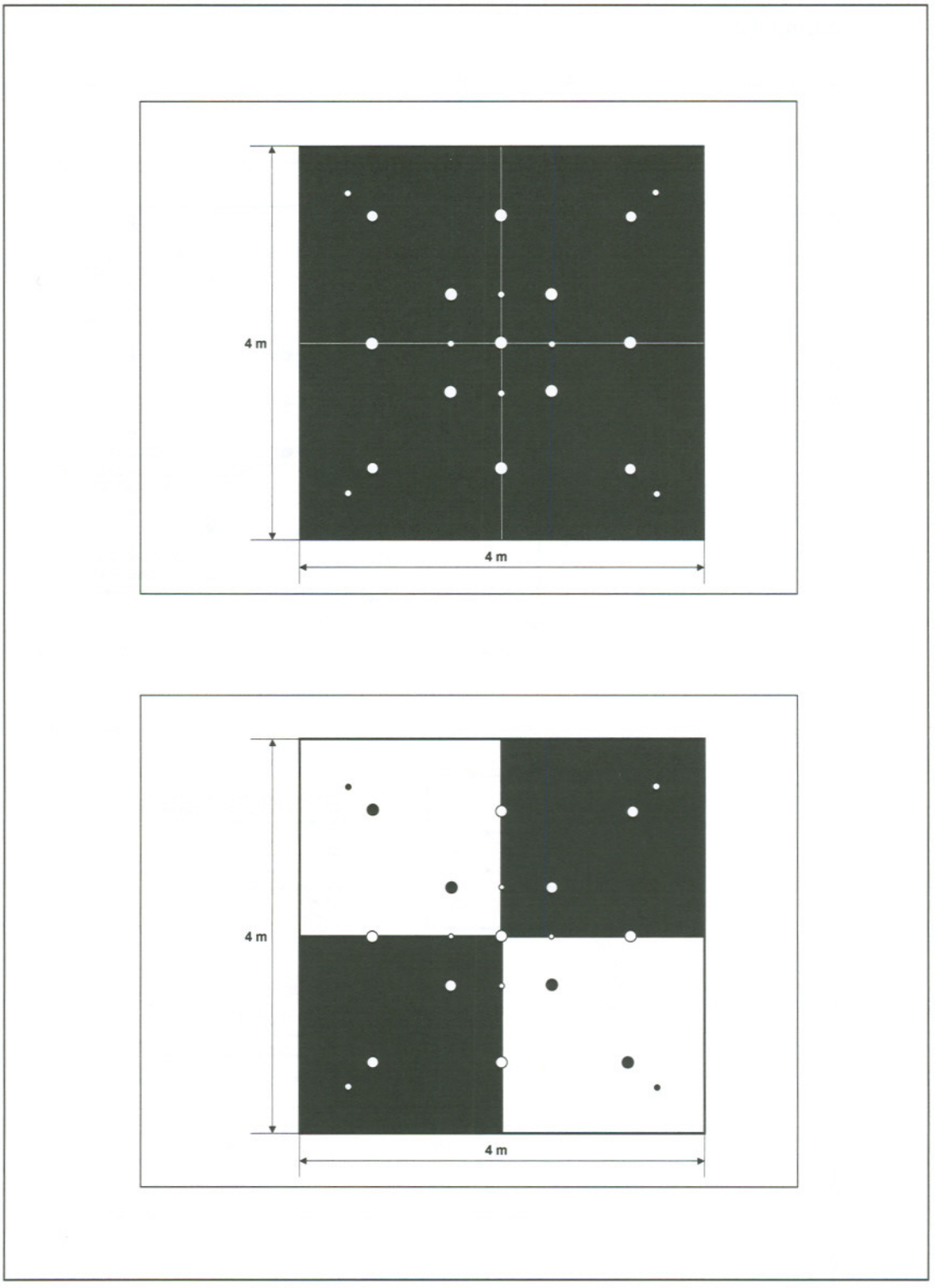

Figure 5-8. PILASTER FXDT target standard panels n° 2 and n° 3.

According to the PILASTER requirements, the FXDT target panels were painted with highly diffusive paints (of known BRDF at λ = 1064 nm and known NIR reflectance characteristics), in order to perform STU spot energy measurements. After various laboratory experiments (see chapter 7), the *Nextel*™ paints and coatings produced by *Mankiewicz Gebr. & Co.* (Georg Wilhelm Straβe, 189 D-21107 Hambug – Germany), were selected for the FXDT target panels. The *Nextel*™ paints used for the PILASTER FXDT target panels are listed in Table 5-2. Further details about the reflection properties of the *Nextel*™ paints are given in chapter 7.

PAINT DESCRIPTION
♦ **Nextel Primer 5523 including Hardener 5524** • White 9125 • Anthracite 7525
♦ **Nextel Suede Coating 428-22** • White 919X • Black 9218 • Hardener 405-12
♦ **Nextel Thinner 8061**

Table 5-2. Nextel™ paints used for the PILASTER FXDT target.

5.6.3 IREF Target

The PILASTER IREF is a thermal target panel with eight vertical bars of equal width, four of which are heated at specified temperature differences (ΔT) with respect to the unheated bars and background. Particularly, the IREF target bars ΔT is tuneable with steps of 0.5 °C (temperature controlled by thermocouples and thermography). Using the IREF target, the Minimum Resolvable Temperature

Differences (MRTD) with spatial frequencies (cycle/mrad) corresponding to various 2-D discrimination levels, can be determined for the FLIR systems integrated with modern laser designation devices. Furthermore, using experimental data collected in flight, it is possible to calculate the detection, recognition and identification ranges of the FLIR systems, for targets of given aspect dimensions. The technical approach adopted at the PILASTER range for collecting and analysing flight test data using the IREF target, is described in chapter 9.

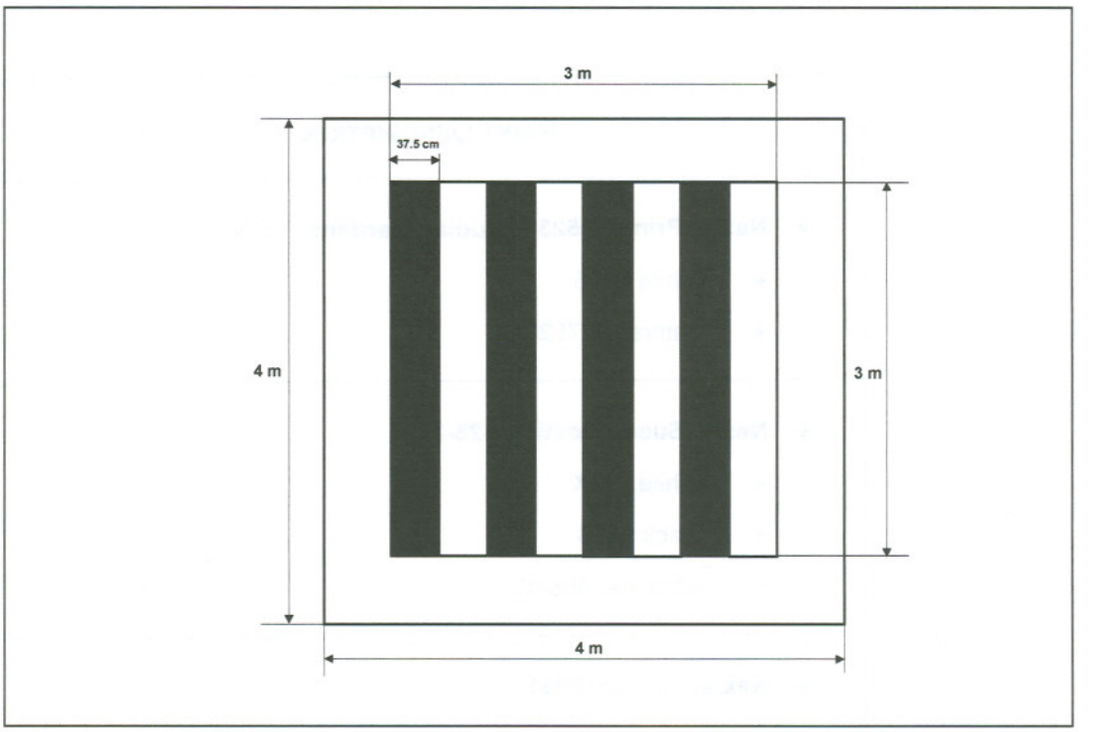

Figure 5-9. PILASTER IREF target for FLIR systems testing.

The IREF thermal target panel front dimensions are shown in Fig. 5-9. The target reflectance is about 0.1 in the NIR waveband. This is obtained by painting the panel surface with dead matt black *Trimite*^{TM} J133 paint, coated with *Bubbleflex*^{TM} B792 (*Playlite Ltd.)*. The IREF target elevation is adjustable with mechanical devices from horizontal to vertical through 90°. The IREF target panel can be used independently, or can be installed on the PILASTER FXDT permanent structure (like the standard panels used for laser spot measurements, with an additional mechanical device for elevation control).

The atmospheric spectral transmittance $\tau(\%)$ measured over a 1820-m horizontal path at sea level is shown in Fig. 3-2.

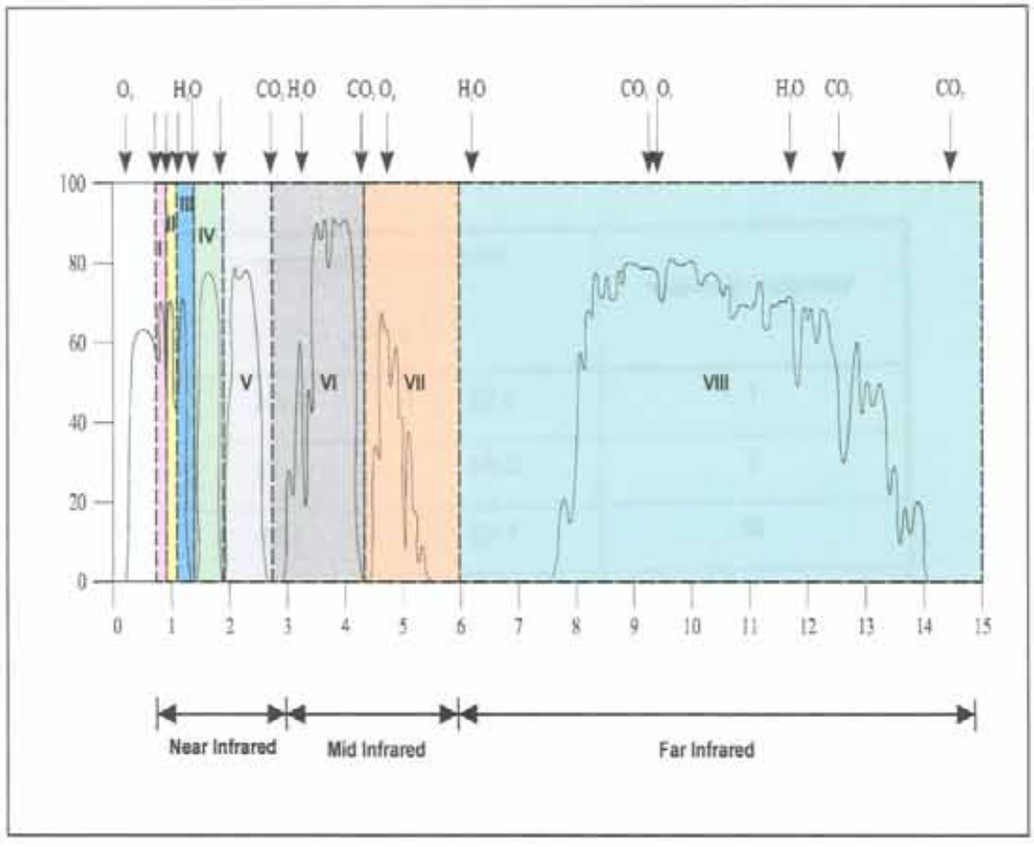

Figure 3-2. Sea-level transmittance over a 1820 m horizontal path [adapted from Ref. 3].

The molecule responsible for each absorption band is shown in the upper part of the figure. It is evident that H_2O and CO_2 are by far the most important absorbing molecules. This is also the case for the range of altitudes extending from sea level to about 12 km. Depending on weather conditions, altitude, and geographical location, the concentration of H_2O varies between 10^{-3} and 1 percent (by volume). The concentration of CO_2 varies between 0.03 and 0.04 percent. Other absorbing molecules found in the atmosphere are methane (CH_4), with a concentration of around 1.5×10^{-4} percent; nitrous oxide (N_2O), with a concentration of around 3.5×10^{-5} percent; carbon monoxide (CO) with a typical concentration of 2×10^{-5} percent; and ozone (O_3), with a concentration as large as 10^{-3} percent at an altitude

of around 30 km. The concentration of ozone near sea level is negligible. In Fig. 3-2 the wavelength intervals where the transmittance is relatively high are called "atmospheric windows". Obviously, for efficient energy transmission the laser wavelength should fall well within one of these windows. There are a total of eight such windows within the wavelength range extending from 0.72 to 15.0 μm. The window boundaries are listed in Table 3-1.

Window Number	*Window Boundaries (μm)*	
I	0.72	0.94
II	0.94	1.13
III	1.13	1.38
IV	1.38	1.90
V	1.90	2.70
VI	2.70	4.30
VII	4.30	6.00
VIII	6.00	15.0

Table 3-1. Wavelength regions of atmospheric windows.

The scattering coefficient β in eqs. (3.20) and (3.22) also depends on the frequency of the incident radiation as well as the index of refraction and radius of the scattering particle. The incident electromagnetic wave, which is assumed to be a plane wave in a given polarization state, produces forced oscillations of the bound and free charges within the sphere. These oscillating charges in turn produce secondary fields internal and external to the sphere. The resulting field at any point is the vector sum of the primary (plane wave) and secondary fields. Once the resultant field has been determined, the scattering cross section is obtained from the following relationship:

$$\sigma_s = \frac{total\ power\ scattered\ by\ scatterer}{magnitude\ of\ the\ time-averaged\ incident\ poynting\ vector} \qquad (3.25)$$

In the scattering process there is no loss of energy but only a directional redistribution which may lead to a significant reduction in beam intensity for large path lengths. As is indicated in Table 3-2, the physical size of the scatterer determines the type of scattering. Thus, air molecules that are typically several angstrom units in diameter lead to *Rayleigh* scattering, whereas the aerosols scatter light in accordance with the *Mie* theory. Furthermore, when the scatterers are relatively large, such as the water droplets found in fog, clouds, rain, or snow, the scattering process is more properly described by diffraction theory.

Type of Scattering	***Size of Scatterer***
Rayleigh Scattering	Larger than electron but smaller than λ
Mie Scattering	Comparable in size to λ
Non-selective Scattering	Much larger than λ

Table 3-2. Types of atmospheric scattering.

3.3.2 Computer Codes

In principle, one could determine the exact composition of the atmosphere over the path of interest and, employing the physics of molecular and aerosol extinction, compute the atmospheric extinction coefficient. Because of the wide variations in weather conditions and sparsity of data on some atmospheric constituents, it is desirable to adopt an engineering approach to atmospheric modelling. The required model should include several weather conditions and should be validated with laboratory and field data.

To deal with these complex phenomena, the Phillips Laboartory of the Geophysics Directorate at Hanscom Air Force Base (Massachusetts) has developed codes to predict transmittance/radiance effects for varying conditions. Particularly, they have created LOWTRAN (LOW spectral resolution TRANsmission code), FASCODE

(FASt atmospheric signature CODE), MODTRAN (MODerate spectral resolution TRANsmission code), and HITRAN (HIgh resolution TRANsmission code). Furthermore, in recent years, powerful tools for the assessment and exploitation of propagation conditions together with range performance models for military systems have become available.

It is impossible to present in a fully comprehensive way all available tools. Instead, some relevant information are given in Appendix C. In the following paragraphs, only the empirical models selected for the initial versions of the PILASTER Mission Planning and Analysis (MPA) software tools are described.

3.3.3 Elder-Strong-Langer (ESL) Model for τ_{ai}

A simple approach, yielding approximate values of the absorption coefficient, has been suggested by Elder and Strong [4] and modified by Langer [5]. Their approach is particularly useful because it provides a means of relating the atmospheric transmission of the i^{th} window to the relative humidity (i.e., a readily measurable parameter). The assumption is that variations in the transmission are caused by changes in the water content of the air. Specifically, changes in the concentration of H_2O cause changes in the absorption, and changes in the size and number of water droplets with humidity cause changes in the scattered component. This is a valid assumption since the other atmospheric constituents have a reasonably constant effect on the transmittance of a given atmospheric window.

It is customary to express the number of H_2O molecules encountered by the beam of light in terms of the number of precipitable millimetres of water in the path. Specifically, the depth of the layer of water that would be formed if all the water molecules along the propagation path were condensed in a container having the same cross-sectional area as the beam is the amount of precipitable water. A cubic meter of air having an absolute humidity of ρ grams per m^3 would yield condensed water that cover a 1 m^2 area and have a depth of:

$$w' = 10^{-3}\rho \tag{3.26}$$

w' is the precipitable water having units of mm per meter of path length.

For a path length of z meters eq. (3.26) becomes:

$$w = 10^{-3} \rho \cdot z \tag{3.27}$$

where w is now the total precipitable water in millimetres. The value of ρ, the density of water vapour, can be found by multiplying the appropriate number in Table 3-3 by the relative humidity (RH).

	Temperature									
(°C)	0	1	2	3	4	5	6	7	8	9
-20	0.89	0.81	0.74	0.67	0.61	0.65				
-10	2.15	1.98	1.81	1.66	1.52	1.40	1.28	1.18	1.08	0.98
-0	4.84	4.47	4.13	3.81	3.52	3.24	2.99	2.75	2.54	2.34
0	4.84	5.18	5.54	5.92	6.33	6.76	7.22	7.70	8.22	8.76
10	9.33	9.94	10.57	11.25	11.96	12.71	13.50	14.34	15.22	16.17
20	17.22	18.14	19.22	20.36	21.55	22.80	24.11	25.49	27.00	28.45
30	30.04	31.70	33.45	35.28	37.19	39.19				

Table 3-3. Mass of water vapour in saturated air (g/m^3).

Similar numerical results can be obtained using the following equation [6], which is convenient for computer code implementation:

$$\rho = 1322.8 \cdot \frac{RH}{T} exp\left[\frac{25.22 \cdot (T - 273.16)}{T} - 5.31 \cdot ln\left(\frac{T}{273.16}\right)\right] \tag{3.28}$$

where RH is the relative humidity (as a fraction), and T is the absolute temperature (°K).

Based on the work done by Elder and Strong [4], two empirical expressions, developed by Langer [5], can be used to calculate the absorptive transmittance τ_{ai} for the i^{th} window for any given value of the precipitable water content. These expressions are:

$$\tau_{ai} = e^{-A_i\sqrt{w}}, \text{ for } w < w_i \tag{3.29}$$

$$\tau_{ai} = k_i\left(\frac{w_i}{w}\right)^{\beta_i}, \text{ for } w > w_i \tag{3.30}$$

where A_i, k_i, β_i and w_i are constants whose values for each atmospheric window are listed in Table 3-4.

Constants / Window	A_i	k_i	β_i	w_i
I	0.0305	0.800	0.112	54
II	0.0363	0.765	0.134	54
III	0.1303	0.830	0.093	2.0
IV	0.211	0.802	0.111	1.1
V	0.350	0.814	0.1035	0.35
VI	0.373	0.827	0.095	0.26
VII	0.598	0.784	0.122	0.165

Table 3-4. Constants to be used in eqs. (3.34) and (3.35).

In summary, eqs. (3.29) and (3.30), together with eq. (3.27) and Table 3-3 (or eq. 3.28), provide information that can be used to obtain an estimate of the absorptive transmittance (τ_{ai}) of laser beams having wavelengths that fall within the various atmospheric windows. The results apply to horizontal paths in the atmosphere near sea level and for varying relative humidity. To obtain the total atmospheric

transmittance we must multiply τ_{al} by τ_{sl} (i.e., the transmittance due to scattering only).

3.3.4 Empirical Expressions for τ_{sl}

Based on rigorous mathematical approaches, the scattering properties of the atmosphere due to the aerosol particles are difficult to quantify, and it is difficult to obtain an analytic expression for the scattering coefficient that will yield accurate values over a wide variety of conditions (see Appendix C). However, an empirical relationship that is often used to model the scattering coefficient [7] has the form:

$$\beta(\lambda) = C_1\lambda^{-\delta} + C_2\lambda^{-4} \tag{3.31}$$

where C_1, C_2, and δ are constants determined by the aerosol concentration and size distribution, and λ is the wavelength of the radiation. The second term accounts for *Rayleigh* scattering. Since for all wavelengths longer than about 0.3 μm the second term is considerably less than the first, it may be neglected. It has been found that $\delta \approx 1.3 \pm 0.3$ produces reasonable results when applied to aerosols with a range of particle sizes.

An attempt has also been made to relate δ and C_1 to the meteorological range. The apparent contrast C_z, of a source when viewed at λ = 0.55 μm from a distance z is by definition:

$$C_z = \frac{R_{sz} - R_{bz}}{R_{bz}} \tag{3.32}$$

Where R_{sz} and R_{bz} are the apparent radiances of the source and its background as seen from a distance z.

For $\lambda = 0.55\,\mu\text{m}$, the distance at which the ratio:

$$V = \frac{C_z}{C_0} = \frac{\dfrac{R_{sz} - R_{bz}}{R_{bz}}}{\dfrac{R_{s0} - R_{b0}}{R_{b0}}} = 0.02 \tag{3.33}$$

is defined as the meteorological range V (or visual range). It must be observed that this quantity is different from the standard observer visibility (V_{obs}). Observer visibility is the greatest distance at which it is just possible to see and identify a target with the unaided eye. In daytime, the object used for V_{obs} measurements is dark against the horizon sky (e.g., high contrast target), while during night time the target is a moderately intense light source. The International Visibility Code (IVC) is given in Table 3-5. It is evident that, while the range of values for each category is appropriate for general purposes, it is too broad for scientific applications.

DESIGNATION	*VISIBILITY*
Dense Fog	0 – 50 m
Thick Fog	50 – 200 m
Moderate Fog	200 – 500 m
Light Fog	500 – 1 km
Thin Fog	1 – 2 km
Haze	2 – 4 km
Light Haze	4 – 10 km
Clear	10 – 20 km
Very Clear	20 – 50 km
Exceptionally Clear	> 50 km

Table 3-5. International Visibility Code (IVC).

Visibility is a subjective measurement estimated by a trained observer and as such can have large variability associated with the reported value. Variations are created by observers having different threshold contrasts looking at nonideal targets. Obviously, visibility depends on the aerosol distribution and it is very sensitive to the local meteorological conditions. It is also dependent upon the view angle with respect to the sun. As the sun angle approaches the view angle, forward scattering

into the line-of-sight increases and the visibility decreases. Therefore, reports from local weather stations may or may not represent the actual conditions at which the experiment is taking place. Since meteorogical range is defined quantitatively using the apparent contrast of a source (or the apparent radiances of the source and its background) as seen from a certain distance, it eliminates the subjective nature of the observer and the distinction between day and night. Unfortunately, carelessness has often resulted in using the term "visibility" when meteorological range is meant. To insure that there is no confusion, "observer-visibility" (V_{obs}) will be used in this thesis to indicate that it is an estimate.

If only V_{obs} is available, the meteorological range (V) can be estimated [6] from:

$$V \approx (1.3 \pm 0.3) \cdot V_{obs} \tag{3.34}$$

From eq. (3.33), if we assume that the source radiance is much greater than the background radiance (i.e., $R_s >> R_b$) and that the background radiance is constant (i.e., $R_{bo} = R_{bz}$), then the transmittance at λ = 0.55 μm (where absorption is negligible) is given by:

$$\frac{R_{sv}}{R_{s0}} = e^{-\beta V} = 0.02 \tag{3.35}$$

Hence, we have:

$$\ln\left(\frac{R_{sv}}{R_{s0}}\right) = -\beta V = -3.91 \tag{3.36}$$

and also:

$$\beta = \frac{3.91}{V} = C_1 \lambda^{-\delta} \tag{3.37}$$

It follows from eq. (3.36) that the constant C_1 is given by:

$$C_1 = \frac{3.91}{V} \cdot 0.55^{\delta} \tag{3.38}$$

With this result the transmittance at the centre of the i^{th} window is:

$$\tau_{si} = e^{-\frac{3.91}{V}\cdot\left(\frac{\lambda_i}{0.55}\right)^{-\delta}\cdot z} \tag{3.39}$$

where λ_i must be expressed in microns. If, because of haze, the meteorological range is less than 6 km, the exponent δ is related to the meteorological range by the following empirical formula:

$$\delta = 0.585\sqrt[3]{V} \tag{3.40}$$

Where V is in kilometres. When $V \geq 6$ km, the exponent δ can be calculated by:

$$\delta = 0.0057 \cdot V + 1.025 \tag{3.41}$$

For exceptionally good visibility δ = 1.6, and for average visibility $\delta \approx 1.3$. In summary, eq. (3.39), together with the appropriate value for δ, permits us to compute the scattering transmittance at the centre of the *ith* window for any propagation path, if the meteorological range V is known. It is important to note here that in general the transmittance will, of course, also be affected by atmospheric absorption, which depending on the relative humidity and temperature may be larger than τ_{si}.

3.3.5 Propagation Through Haze and Precipitation

Haze refers to the small particles suspended in the air. These particles consist of microscopic salt crystals, very fine dust, and combustion products. Their radii are less than 0.5 μm. During periods of high humidity, water molecules condense onto these particles, which then increase in size. It is essential that these condensation nuclei be available before condensation can take place. Since salt is quite hygroscopic, it is by far the most important condensation nucleus. Fog occurs when the condensation nuclei grow into water droplets or ice crystals with radii exceeding 0.5 μm. Clouds are formed in the same way; the only distinction between

fog and clouds is that one touches the ground while the other does not. By convention fog limits the visibility to less than 1 km, whereas in a mist the visibility is greater than 1 km.

We know that in the early stages of droplet growth the Mie attenuation factor K depends strongly on the wavelength. When the drop has reached a radius a $\approx 10\ \lambda$ the value of K approaches 2, and the scattering is now independent of wavelength, i.e., it is non-selective. Since most of the fog droplets have radii ranging from 5 to 15 μm they are comparable in size to the wavelength of infrared radiation. Consequently the value of the scattering cross section is near its maximum. It follows that the transmission of fogs in either the visible or *IR* spectral region is poor for any reasonable path length. This of course also applies to clouds.

Since haze particles are usually less than 0.5 μm, we note that for laser beams in the *IR* spectral region $a/\lambda << 1$ and the scattering is not an important attenuation mechanism. This explains why photographs of distant objects are sometimes made with infrared-sensitive film that responds to wavelengths out to about 0.85 μm. At this wavelength the transmittance of a light haze is about twice that at 0.5 μm. Raindrops are of course many times larger than the wavelengths of laser beams. As a result there is no wavelength-dependent scattering. The scattering coefficient does, however, depend strongly on the size of the drop. Middleton [7, 8] has shown that the scattering coefficient with rain is given by:

$$\beta_{rain} = 1.25 \cdot 10^{-6} \frac{\Delta x/\Delta t}{a^3} \tag{3.42}$$

where $\Delta x/\Delta t$ is the rainfall rate in centimetres of depth per second and a is the radius of the drops in centimetres. Rainfall rates for four different rain conditions and the corresponding transmittance (due to scattering only) of a 1.8-km path are shown in Table 3-6 [9]. These data are useful for order of magnitude estimates. In order to obtain accurate estimates, the concentrations of the different types of rain drops (radius) and the associated rainfall rates should be known. In this case, the scattering coefficient can be calculated as the sum of the partial coefficients associated to the various rain drops.

Rainfall (cm/h)	*Transmittance (1.8 km path)*
0.25	0.88
1.25	0.74
2.5	0.65
10.0	0.38

Table 3-6. Transmittance of a 1.8-km path through rain.

A simpler approach, used in LOWTRAN, gives good approximations of the results obtained with eq. (3.42) for most concentrations of different rain particles. Particularly, in LOWTRAN, the scattering coefficient with rain has been empirically related only to the rainfall rate $\Delta x/\Delta t$ (expressed in mm/hour), as follows [6]:

$$\beta_{rain} \approx 0.365 \cdot \left(\frac{\Delta x}{\Delta t}\right)^{0.63} \tag{3.43}$$

Table 3-7 provides representative rainfall rates which can be used in eqs. (3.42) and (3.43), when no direct measurements are available, to obtain order of magnitude estimations of β_{rain} [10].

Rain Intensity	*Rainfall (mm/hour)*
Mist	0.025
Drizzle	0.25
Light	1.0
Moderate	4.0
Heavy	16
Thundershower	40
Cloud-burst	100

Table 3-7. Representative rainfall rates.

In the presence of rain, in addition to the scattering losses calculated with eq. (3.42) or (3.43), there are, of course, losses by absorption along the path, and these must be included in the calculation of the total atmospheric transmittance with rain.

3.3.6 PILASTER Combined Model

Combining the equations presented in the paragraphs 3.2.2, 3.2.3 and 3.2.4, the set of equations presented in Table 3-8 were obtained, for calculating the atmospheric transmittance (τ_{atm}) in the various conditions, with transmitter and receiver collocated.

Case	Cond.	Equations	n°
A	$V \geq 6$ km $w>w_i$	$\tau_{atm} = k_i \cdot \left(\frac{w_i}{w}\right)^{\beta_i} \cdot e^{-z \cdot \frac{3.91}{V}\left(\frac{\lambda_i}{0.55}\right)^{-(0.0057 \cdot V + 1.025)}}$	(3.44)
B	$V \geq 6$ km $w<w_i$	$\tau_{atm} = e^{-z \cdot \left[A_i \sqrt{w} + \frac{3.91}{V}\left(\frac{\lambda_i}{0.55}\right)^{-(0.0057 \cdot V + 1.025)} \right]}$	(3.45)
C	$V < 6$ km $w<w_i$	$\tau_{atm} = e^{-z \cdot \left[A_i \sqrt{w} + \frac{3.91}{V}\left(\frac{\lambda_i}{0.55}\right)^{-0.585 \sqrt[3]{V}} \right]}$	(3.46)
D	$V < 6$ km $w>w_i$	$\tau_{atm} = k_i \cdot \left(\frac{w_i}{w}\right)^{\beta_i} \cdot e^{-z \cdot \frac{3.91}{V}\left(\frac{\lambda_i}{0.55}\right)^{-0.585 \sqrt[3]{V}}}$	(3.47)
R_1	Rain $w<w_i$	$\tau_{atm} = e^{-A_i \sqrt{w}} \cdot e^{-z \left[0.365 \left(\frac{\Delta r}{\Delta t}\right)^{0.63} \right]}$	(3.48)
R_2	Rain $w>w_i$	$\tau_{atm} = k_i \left(\frac{w_i}{w}\right)^{\beta_i} \cdot e^{-z \left[0.365 \left(\frac{\Delta r}{\Delta t}\right)^{0.63} \right]}$	(3.49)

Table 3-8. Transmittance equations for transmitter and receiver collocated.

The cases R_1 and R_2 in Table 3-8 are independent of meteorological range (V). Straightforward numerical analysis shows that the τ_{atm} estimates obtained with rain using eqs. (3.48) and (3.49), are always less than the corresponding transmittance estimates obtained with eqs. (3.46) and (3.47) with dry-air conditions and $V < 6$ km, for rainfall rates $\Delta x/\Delta t \geq 1$ (i.e., from light rain to cloud-burst).

In the case of transmitter and receiver not collocated (e.g., LTD/LGW combination), the equations in Table 3-8 have to be modified, taking into account that the total laser path (z) is given by the sum of the range transmitter-target and target-receiver (see Fig. 3-1). Therefore, we have:

$$z = R_t + R_r \tag{3.50}$$

Denoting with the subscripts t and r the terms relative to the transmitting and receiving paths respectively, we have that the total atmospheric transmittance (τ_{tot}) is given by:

$$\tau_{tot} = \tau_t \cdot \tau_r \tag{3.51}$$

Therefore, in order to account for all possible cases, we have to consider the 2^3 possible combinations referring to dry-air ($V \geq 6\,\text{km} \leftrightarrow V < 6\,\text{km}$, $w_t \geq w_i \leftrightarrow w_t < w_i$ and $w_r \geq w_i \leftrightarrow w_r < w_i$), and the 2^2 combinations relative to rainy conditions ($w_t \geq w_i \leftrightarrow w_t < w_i$ and $w_r \geq w_i \leftrightarrow w_r < w_i$). It should be considered, however, that the condition $w_t < w_i$ is not likely to occur in many cases of practical interest with LTD/LGW systems. From eq. (3.27), we obtain the maximum transmitter distance (R_{max}) from which the condition $w_t < w_i$ is verified:

$$R_{max} < \frac{w_i}{\rho} \cdot 10^3 \tag{3.52}$$

In normal dry-air conditions (e.g., $T = 24$ °C and $RH = 75\%$) R_{max} equates to about 3 km. This is a distance very short in many real operational scenarios. Obviously, whit rainy conditions, the range R_{max} would be even shorter. Tables 3-9 and 3-10 show the equations developed for all dry-air and rain cases considered.

Case	Cond.	Equations		n°
E	V ≥ 6 km $w_t \geq w_l$ $w_r \geq w_l$	$k_l\left(\frac{w_l}{w_t}\right)^{\beta_l} e^{-\frac{3.91}{V}\left(\frac{\lambda_l}{0.55}\right)^{-(0.00574V+1.025)} R_t} \cdot k_l\left(\frac{w_l}{w_r}\right)^{\beta_l} e^{-\frac{3.91}{V}\left(\frac{\lambda_l}{0.55}\right)^{-(0.00574V+1.025)} R_r}$	$k_l^2\left(\frac{w_l^2}{w_t w_r}\right)^{\beta_l} e^{-\frac{3.91}{V}\left(\frac{\lambda_l}{0.55}\right)^{-(0.00574V+1.025)} (R_t+R_r)}$	(3.53)
F	V ≥ 6 km $w_t \geq w_l$ $w_r < w_l$	$k_l\left(\frac{w_l}{w_t}\right)^{\beta_l} e^{-\frac{3.91}{V}\left(\frac{\lambda_l}{0.55}\right)^{-(0.00574V+1.025)} R_t} \cdot e^{-A_l\sqrt{w_r}-\frac{3.91}{V}\left(\frac{\lambda_l}{0.55}\right)^{-(0.00574V+1.025)} R_r}$	$k_l\left(\frac{w_l}{w_t}\right)^{\beta_l} e^{-A_l\sqrt{w_r}-\frac{3.91}{V}\left(\frac{\lambda_l}{0.55}\right)^{-(0.00574V+1.025)} (R_t+R_r)}$	(3.54)
G	V < 6 km $w_t \geq w_l$ $w_r < w_l$	$k_l\left(\frac{w_l}{w_t}\right)^{\beta_l} e^{-\frac{3.91}{V}\left(\frac{\lambda_l}{0.55}\right)^{-0.585\sqrt[3]{V}} R_t} \cdot e^{-A_l\sqrt{w_r}-\frac{3.91}{V}\left(\frac{\lambda_l}{0.55}\right)^{-0.585\sqrt[3]{V}} R_r}$	$k_l\left(\frac{w_l}{w_t}\right)^{\beta_l} e^{-A_l\sqrt{w_r}-\frac{3.91}{V}\left(\frac{\lambda_l}{0.55}\right)^{-0.585\sqrt[3]{V}} (R_t+R_r)}$	(3.55)
H	V < 6 km $w_t \geq w_l$ $w_r \geq w_l$	$k_l\left(\frac{w_l}{w_l}\right)^{\beta_l} e^{-\frac{3.91}{V}\left(\frac{\lambda_l}{0.55}\right)^{-0.585\sqrt[3]{V}} R_t} \cdot k_l\left(\frac{w_l}{w_r}\right)^{\beta_l} e^{-\frac{3.91}{V}\left(\frac{\lambda_l}{0.55}\right)^{-0.585\sqrt[3]{V}} R_r}$	$k_l^2\left(\frac{w_l^2}{w_t w_r}\right)^{\beta_l} e^{-\frac{3.91}{V}\left(\frac{\lambda_l}{0.55}\right)^{-0.585\sqrt[3]{V}} (R_t+R_r)}$	(3.56)
I	V ≥ 6 km $w_t < w_l$ $w_r \geq w_l$	$e^{-A_l\sqrt{w_t}-\frac{3.91}{V}\left(\frac{\lambda_l}{0.55}\right)^{-(0.00574V+1.025)} R_t} \cdot k_l\left(\frac{w_l}{w_r}\right)^{\beta_l} e^{-\frac{3.91}{V}\left(\frac{\lambda_l}{0.55}\right)^{-(0.00574V+1.025)} R_r}$	$k_l\left(\frac{w_l}{w_r}\right)^{\beta_l} e^{-A_l\sqrt{w_t}-\frac{3.91}{V}\left(\frac{\lambda_l}{0.55}\right)^{-(0.00574V+1.025)} (R_t+R_r)}$	(3.57)
J	V ≥ 6 km $w_t < w_l$ $w_r < w_l$	$e^{-A_l\sqrt{w_t}-\frac{3.91}{V}\left(\frac{\lambda_l}{0.55}\right)^{-(0.00574V+1.025)} R_t} \cdot e^{-A_l\sqrt{w_r}-\frac{3.91}{V}\left(\frac{\lambda_l}{0.55}\right)^{-(0.00574V+1.025)} R_r}$	$e^{-A_l\sqrt{w_t}-A_l\sqrt{w_r}-\frac{3.91}{V}\left(\frac{\lambda_l}{0.55}\right)^{-(0.00574V+1.025)} (R_t+R_r)}$	(3.58)
K	V < 6 km $w_t < w_l$ $w_r < w_l$	$e^{-A_l\sqrt{w_t}-\frac{3.91}{V}\left(\frac{\lambda_l}{0.55}\right)^{-0.585\sqrt[3]{V}} R_t} \cdot e^{-A_l\sqrt{w_r}-\frac{3.91}{V}\left(\frac{\lambda_l}{0.55}\right)^{-0.585\sqrt[3]{V}} R_r}$	$e^{-A_l\sqrt{w_t}-A_l\sqrt{w_r}-\frac{3.91}{V}\left(\frac{\lambda_l}{0.55}\right)^{-0.585\sqrt[3]{V}} (R_t+R_r)}$	(3.59)
L	V < 6 km $w_t < w_l$ $w_r \geq w_l$	$e^{-A_l\sqrt{w_t}-\frac{3.91}{V}\left(\frac{\lambda_l}{0.55}\right)^{-0.585\sqrt[3]{V}} R_t} \cdot k_l\left(\frac{w_l}{w_r}\right)^{\beta_l} e^{-\frac{3.91}{V}\left(\frac{\lambda_l}{0.55}\right)^{-0.585\sqrt[3]{V}} R_r}$	$k_l\left(\frac{w_l}{w_r}\right)^{\beta_l} e^{-A_l\sqrt{w_t}-\frac{3.91}{V}\left(\frac{\lambda_l}{0.55}\right)^{-0.585\sqrt[3]{V}} (R_t+R_r)}$	(3.60)

Table 3-9. ESLM-dry equations for transmitter and receiver not collocated.

Case	Cond.	Equations		N°
R_3	**Rain** $w_t \geq w_i$ $w_r \geq w_i$	$k_i\left(\frac{w_i}{w_t}\right)^{\beta_i} e^{-0.365\left(\frac{\Delta x}{\Delta t}\right)^{0.63} R_t} \cdot k_i\left(\frac{w_i}{w_r}\right)^{\beta_i} e^{-0.365\left(\frac{\Delta x}{\Delta t}\right)^{0.63} R_r}$	$k_i^2\left(\frac{w_i^2}{w_t w_r}\right)^{\beta_i} e^{-0.365\left(\frac{\Delta x}{\Delta t}\right)^{0.63}(R_t+R_r)}$	(3.61)
R_4	**Rain** $w_t \geq w_i$ $w_r < w_i$	$k_i\left(\frac{w_i}{w_t}\right)^{\beta_i} e^{-0.365\left(\frac{\Delta x}{\Delta t}\right)^{0.63} R_t} \cdot e^{-A_i\sqrt{w_r}-0.365\left(\frac{\Delta x}{\Delta t}\right)^{0.63} R_r}$	$k_i\left(\frac{w_i}{w_t}\right)^{\beta_i} e^{-A_i\sqrt{w_r}-0.365\left(\frac{\Delta x}{\Delta t}\right)^{0.63}(R_t+R_r)}$	(3.62)
R_5	**Rain** $w_t < w_i$ $w_r \geq w_i$	$e^{-A_i\sqrt{w_t}-0.365\left(\frac{\Delta x}{\Delta t}\right)^{0.63} R_t} \cdot k_i\left(\frac{w_i}{w_r}\right)^{\beta_i} e^{-0.365\left(\frac{\Delta x}{\Delta t}\right)^{0.63} R_r}$	$k_i\left(\frac{w_i}{w_r}\right)^{\beta_i} e^{-A_i\sqrt{w_t}-0.365\left(\frac{\Delta x}{\Delta t}\right)^{0.63}(R_t+R_r)}$	(3.63)
R_6	**Rain** $w_t < w_i$ $w_r < w_i$	$e^{-A_i\sqrt{w_t}-0.365\left(\frac{\Delta x}{\Delta t}\right)^{0.63} R_t} \cdot e^{-A_i\sqrt{w_r}-0.365\left(\frac{\Delta x}{\Delta t}\right)^{0.63} R_r}$	$e^{-A_i\left(\sqrt{w_t}-\sqrt{w_r}\right)-0.365\left(\frac{\Delta x}{\Delta t}\right)^{0.63}(R_t+R_r)}$	(3.64)

Table 3-10. ESLM-rain equations for transmitter and receiver not collocated.

The equations presented in the Tables 3-8, 3-9 and 3-10 represent the combined Elder-Strong-Langer-Middleton (ESLM) model, relative to laser beam horizontal-path propagation at sea-level both in dry-air and rain conditions. The validation process of the ESLM model, before incorporation in the PILASTER MPA tools, was undertaken during this research using experimental data collected during ground trials. Furthermore, corrections to be applied with increasing altitudes and with various laser slant-path grazing angles were determined using data collected in flight tests. The results of these activities are described in the chapters 8 and 9 of this thesis.

3.3.7 Refractive Index Variations

When a laser beam passes through air, the randomly fluctuating air temperature produces small density and refractive index inhomogeneities that affect

the beam in at least three different ways. Considering for example an initially well-defined phase front propagating through a region of atmospheric turbulence. Because of random fluctuations in phase velocity the initially well defined phase front will become distorted. This alters and redirects the flow of energy in the beam. As the distorted phase front progresses, random changes in beam direction ("Beam Wander") and intensity fluctuations ("Scintillation") occur. The beam is also found to spread in size beyond the dimensions predicted by diffraction theory.

The cause of all this, as we have stated, is atmospheric turbulence that arises when air parcels of different temperatures are mixed by wind and convection. The individual air parcels, or turbulence cells, break up into smaller cells and eventually lose their identity. In the meantime, however, the mixing produces fluctuations in the density and therefore in the refractive index of air. To describe these random processes, one must have a way of defining the fluctuations that are characteristic of turbulence. The most common approaches adopted may be found in Strohbehn [12] and Weichel [3]. The most relevant concepts of turbulence related studies are presented in Appendix C.

3.3.8 Other Propagation Effects

The propagation of a laser beam through atmospheric turbulence is a linear phenomenon in that the air is not affected by the beam. Strictly speaking, this is only true for beams of relatively low irradiance. As the beam irradiance is increased, molecular absorption will lead to temperature gradients in the medium that in turn induce density and index-of-refraction changes. The final result is a medium whose optical properties have been altered. This phenomenon is non-linear, in that the beam irradiance distribution leads to index-of-refraction changes, which in turn alter the beam's irradiance distribution, which alters the refractive index, etc.

Non-linear propagation effects typically include: "Thermal Blooming" (whose consequence is that the divergence angle is considerably more than that due to diffraction alone), "Kinetic Cooling" (resulting in a temporary focusing effect and less than diffraction limited beam spreading), and "Bleaching" (1-5 μsec duration pulses may under certain conditions saturate the absorption mechanism and thereby reduce the atmospheric transmittance). Also aerodynamic effects influence the

performance of the airborne systems [13]. These effects can be grouped in two categories:

- Aeromechanical effects, arising from interactions of the external flow field with the airborne platform. This base motion, in concert with intrinsic platform sources of vibration (e.g., engines, pumps, fluid flow, etc.), defines the overall mechanical jitter environment in which the laser system must operate. Jitter can result in spurious laser beam motion on target, as well as general misalignment of optical elements.

- Aero-Optical (AO) effects. These are caused by refraction index variations induced by the platform moving through the flow field. This results in reduced far-field peak intensity as well as beam spread and wander for outgoing wave fronts (for imaging systems, these several effects manifest themselves as loss of contrast and resolution).

A brief outline of these additional propagation effects is given in Appendix C.

3.4 Laser Scattering and Target Cross Section

The scattering and propagation of laser light obey the same set of laws as radio frequency waves, that is, those set forth by Maxwell's equations and the boundary conditions. However, the wavelength of laser light is so small that minute particles and even molecules represent significant scatterers. Target surfaces are generally very rough at laser wavelengths and, consequently, the random or diffuse reflection component frequently dominates. In fact, there may not be any significant specular component to the laser cross section, in many cases. Sometimes, however, significant specular reflections and retro-reflections (opposition effects) are observed from certain target surfaces. Furthermore, in general, the overall scattering pattern produced by a certain (complex) target illuminated by a laser beam shows a marked dependency on the illumination incidence angle.

When examining the diffuse reflection component, the maximum amount of reflected energy is reflected 90° (normal) to the surface - independent of the incoming beam angle of arrival, and the energy falls off as a function of the cosine of the angle off of surface normal.

A surface that is a perfect diffuser scatters incident light equally in all directions. For such an "ideal" surface, the intensity (W/m^2) of diffusely reflected light is given by:

$$I_d = I_i k_d \cos\theta \quad \text{with } \theta \in \left[0, \frac{\pi}{2}\right] \tag{3.65}$$

where I_i is the intensity of the light source at the target, θ is the angle between the surface normal and a line from the surface illuminated point to the light source (considered as a point source). The constant k_d is the diffuse reflectivity, which depends on the nature of the material and the wavelength of the incident light.
Eq. (3.70) may be also expressed in the vector form:

$$I_d = I_i k_d \left(\hat{L} \cdot \hat{N}\right) \tag{3.66}$$

where $\hat{L}$ and $\hat{N}$ are the vectors illustrated in Fig. 3-3.

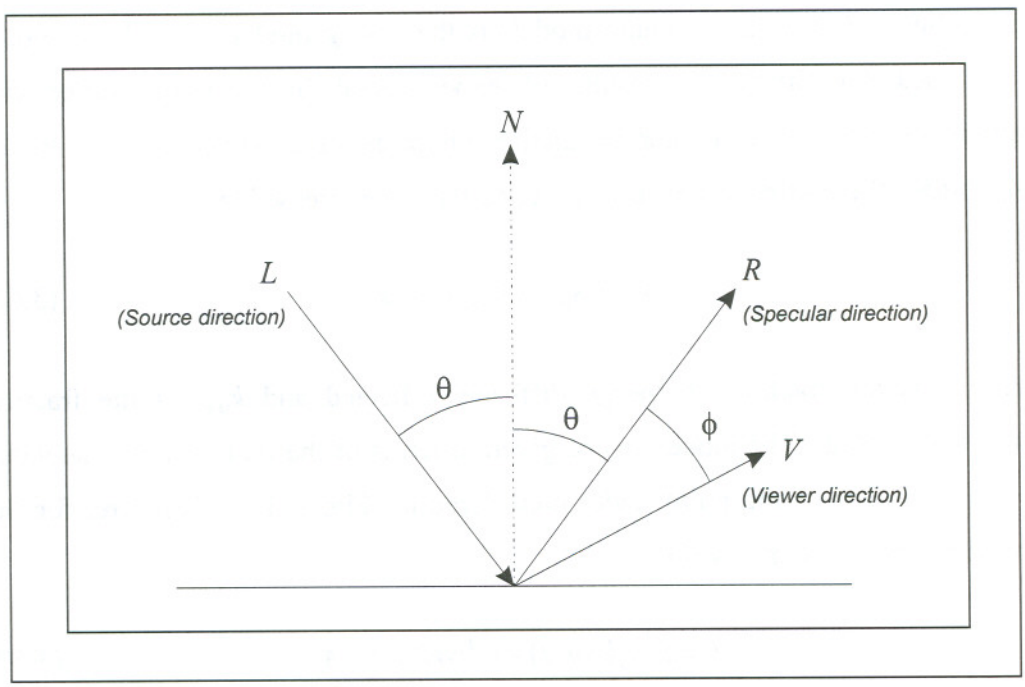

Figure 3-3. Reflection geometry.

As described before, any reflection from a practical surface should be considered as (at least) the sum of a specular component and a diffuse component. The existence

of these two component has been shown experimentally and is not a consequence of choice of a particular model. A surface attribute that is important to model is the surface roughness. A perfectly smooth surface reflects incident radiation in a single direction. A rough surface tends to scatter incident radiation in every direction, although certain directions may contain more reflected energy than others. This behaviour is obviously also dependent on the wavelength of radiation; a surface that is smooth for certain wavelengths may be rough for others. For example, oxidised or unpolished metal is smooth for radio waves ($\lambda=10^{-2}$ m) and rough for radiation in the near-infrared (NIR) part of the spectrum. In general, metals can be prevalently diffuse or specular reflectors in the NIR depending on whether they are polished or not. So reflection is not only dependent on the material but also on its surface properties. Another factor in reflection in the grazing angle of the incident laser source. This can in fact determine the entity of the overall reflected signal and of the two reflection components.

Therefore, a "realistic" reflection model should at least represent the target surface as some combination of a perfect diffuse reflector and a perfect specular surface. One of the earlier and still quite popular models is the *Phong* model [14]. This model can be used for fitting the results of experimental bi-directional reflectivity measurements and for computer simulation programs (see Appendix E). In the *Phong* model, the bi-directional spectral reflectivity is expressed by:

$$\rho_{\lambda}^{'} = k_{diff} + k_{spec}\cos^{n}\phi \tag{3.67}$$

where k_{diff} is the fraction of energy diffusely reflected and k_{spec} is the fraction specularly reflected. The model can be given in terms of the unit vectors associated with the geometry of the point under consideration (Fig. 3-3). Therefore, for the reflected intensity, we may write:

$$I = I_i\left[k_d(\cos\theta) + k_s\left(\cos^{n}\phi\right)\right] + A \tag{3.68}$$

$$I = I_i\left[k_d(L\cdot N) + k_s(R\cdot V)^{n}\right] + A \tag{3.69}$$

where k_s is the specular reflection coefficient (a function of the material characteristics and incidence angle), n is the index that controls the dimensions of the

specular highlight, and A is an additional term accounting for reflection of sunlight at the wavelength considered (day-time operations). This can be also modelled as:

$$A = E_\lambda \left[k_d \left(\cos\theta' \right) + k_s \left(\cos^n \phi' \right) \right] \tag{3.70}$$

where E_λ is the solar spectral irradiance at the wavelength of the laser λ, and θ' is the angle between the solar illumination and the normal to the target reflecting surface.

Fig. 3-4 shows the variation in light intensity at a point P on a surface calculated using eq. (3.69). The intensity variation is shown as a profile (i.e., a function of the orientation of V). The intensity at P is given by the length of V from P to its intersection with the profile. The semicircular part of the profile is the contribution from the diffuse term. The specular part of the profile is shown for different values of the index n.

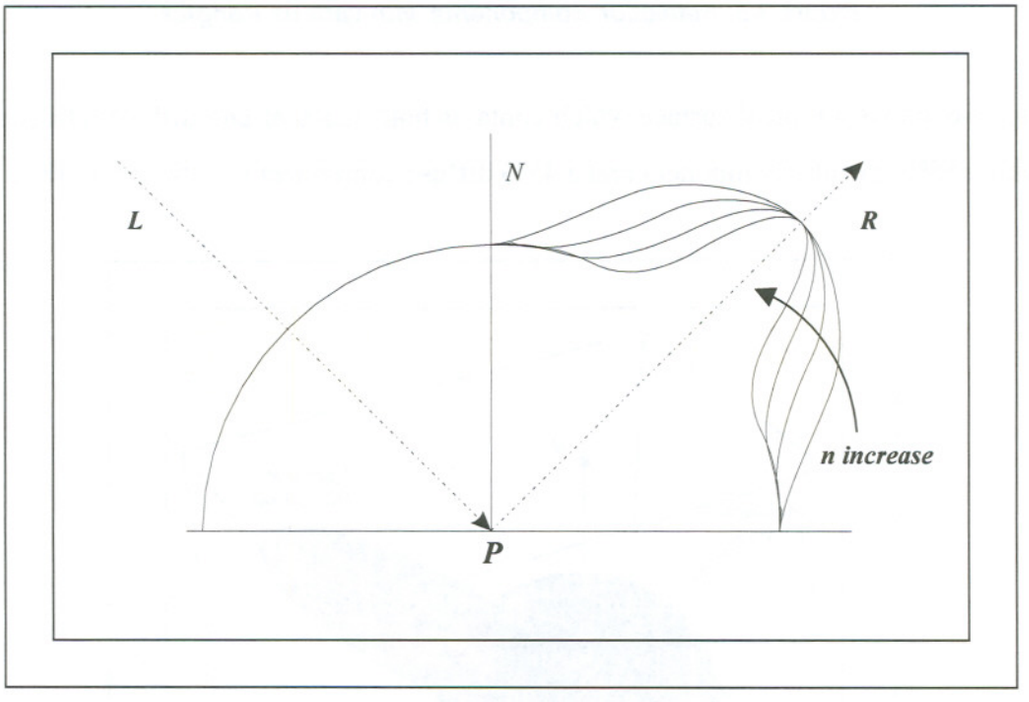

Figure 3-4. Intensity as a function of V orientation (with different values of n).

Note that, in general, the higher is the value of n, the tighter is the specular higlight. Fig. 3-5 shows the resulting combinations of the two reflection components, obtained by keeping fixed the value of n (e.g., $n = 100$) and varying the angle θ,

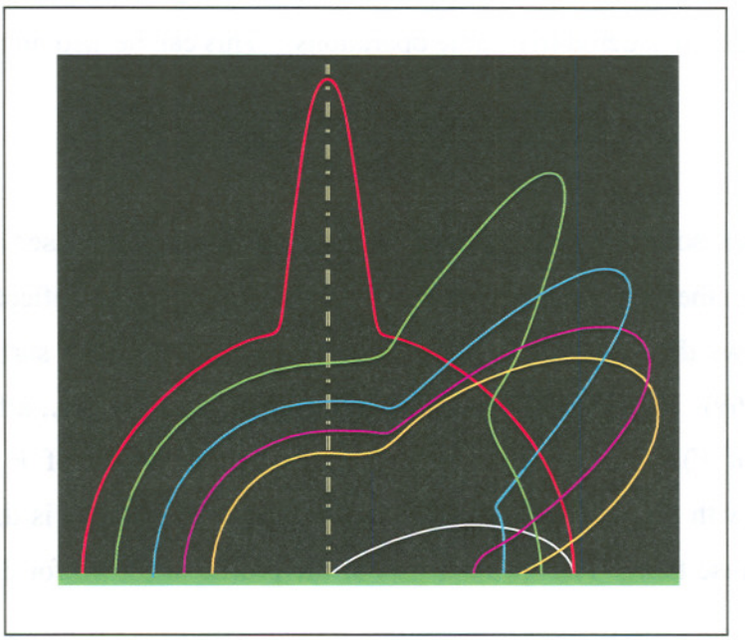

Figure 3-5. Reflection components with various θ angles.

Fig. 3-6 shows a typical surface which contains both specular and diffuse reflections with a 55% specular component and a 45% diffuse component ($\theta = 50°$, $n = 100$).

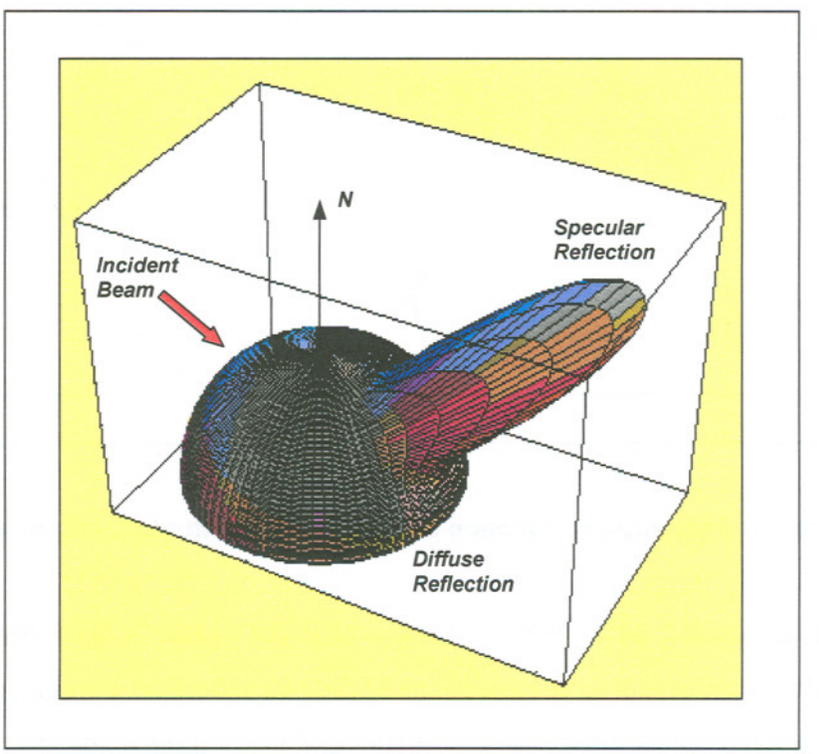

Figure 3-6. Specular and diffuse reflection components.

In most practical cases with LTD/LGW systems, the diffuse component alone is assumed when describing target reflectivity, since the diffuse reflection component is what the weapon will have the highest probability of tracking during flight. Typical diffuse reflectivity values at λ = 1.064 μm are listed in Table 3-10. It is worth to notice that glass, water and highly polished surfaces are poor surfaces to designate since they reflect most of the laser energy back along one direction only (i.e. they are specular reflectors).

Material	Diffuse Reflectivity
Matt Black Paint	4 – 15%
Dirty Olive Drab Paint	5 – 15%
Soil	15 – 25%
Brick	15 – 65%
Vegetation (glossy foliage)	30 – 70%
Asphalt	10 – 25%
Concrete	10 – 40%
IR Reflecting Paint	30 – 55%

Table 3-10. Approximate reflectivity at λ = 1.064 μm.

Some fundamental concepts relevant to this research, related with laser scattering and target cross section measurements and modelling are presented in Appendix D.

3.5 LTD/LGW Operational Considerations

Global requirements for mission planning with a particular laser designation system may be initially established by examining the LTD and LGW operating slant ranges required to successfully perform the mission (e.g., optimal delivery of a particular laser weapon). These ranges may vary from a few hundred feet for a ground designator to over 100,000 feet for operational delivery of a

Paveway III LGB. Thus, mission planning with a particular LTD system must have an operational input that factors in the slant-ranges expected for various types of delivery tactics. Mission planning to determine the optimal weapon release point involves a number of factors, including the post-release designation manoeuvre to be employed, the maximum slant range at weapon impact, the target size, laser system error budget, laser power, etc. What follows is a discussion of the primary factors necessary for determining the optimal release range.

3.5.1 Target Size

Target dimensions are a critical factor in LTD/LGW mission planning. These dimensions, along with the slant-range requirements must then be factored together with the characteristics of the designator. In addition, it must be remembered that designation tactics will generally reduce the apparent target size by varying degrees due to the oblique perspective most manoeuvres will generate.
As an example, if a weapon can achieve a 10 feet Circular Error Probability (CEP), then it is appropriate that the designator aiming capability must equal or exceed that requirement in order to meet a suitable weapon impact criteria for the weapon. As an example problem, a hardened shelter access cover, roughly 20 feet in diameter, will be used as a target. This target dimension equates to a 10 feet CEP where 50 percent of our hypothetical weapon releases should fall on the target face. Thus, one must see and identify this target from the desired vantage point and also be able to maintain the laser energy on the target from release to impact. Weapon system error sources challenge this ability to keep the spot on the target as described below.

3.5.2 LTD Systems Error Sources and Effects

Error sources such as laser spot spillover, boresight errors, jitter, and tracking errors, cause large reductions in LGW delivery effectiveness. The following is a discussion of the most common error sources in laser designator systems and the effects of these errors on designation performance.

3.5.2.1 Laser Spot Spillover

Several characteristics of the laser beam must be tightly controlled if the beam is to be maintained on the desired target surface. First, the laser beam spot should be smaller than the target face. As the LTD produces a beam that diverges as it propagates along the path between the laser and the target, beam spillover effects often degrade weapon accuracy both when designation is performed by a ground LTD or an airborne LTD (see Fig. 3-7).

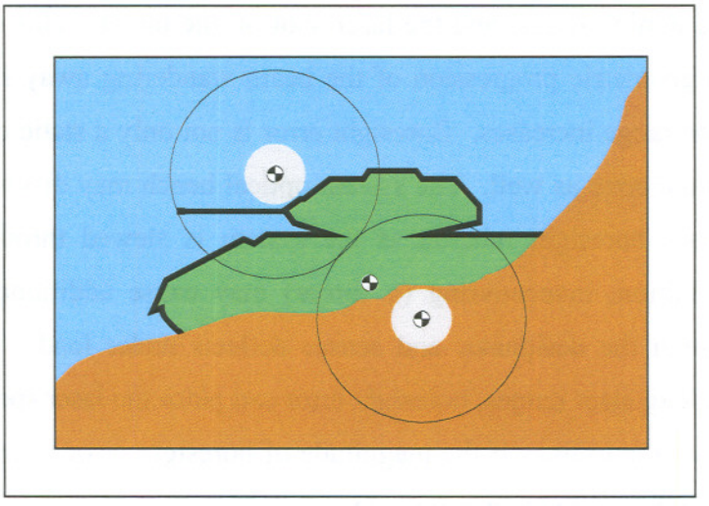

Figure 3-7. Laser spot spillover

Laser beam divergence should therefore be accounted, and appropriate terminal slant-ranges and grazing angles should be chosen such that the spot elongation will not cause spillover around the target.

3.5.2.2 Laser Spot Jitter

Laser spot jitter is defined as the high frequency motion of the laser spot on a pulse-to-pulse basis, usually of low amplitude, and ostensibly due to minute flexures of the optical bench caused by aircraft vibration. These rapid angular movements of the beam degrade weapon accuracy only slightly when the laser beam is normal to the target face. However, at shallow grazing angles and large slant-ranges, jitter may cause each spot to move hundreds of feet in relation to the

aimpoint and in relation to the previous spot location. In many cases (e.g., most self-designation LGB deliveries), this movement is near perpendicular to the weapon flight path and create false left-right commands. Therefore, as the weapon manoeuvres to intercept the moving spot, this factor may cause rapid depletion of the LGB available energy and may cause large miss distances to be generated.

3.5.2.3 Laser Boresight Error

Laser boresight error is defined as the misalignment between the location of the aiming reticle and the laser spot on the target. This error is easy to visualize as a geometric progression of the beam wandering away from the sensor sight line as the range increases. Boresight error is not only a static error source but can be a dynamic error as well. The system optical bench may distort, changing the designator/sensor boresight relation as the system is slewed through its field of regard. In addition, manoeuvring (g forces) may cause additional shifts as the structure between the designator and sensor deflects under load. In some cases, particularly at long slant ranges, boresight error can place the laser spot off the target, resulting in a weapon miss. If the magnitude of boresight error is known, however, the aimpoint can be shifted to compensate.

3.5.2.4 Laser Pointing Error

Laser pointing error is defined as the inability to place the laser spot at the exact desired location on the target. This is usually observed when trying to designate a small target from long ranges, where the reticle size can obscure the target. If the sensor magnification of the target is insufficient, it is difficult to know exactly where the aiming reticle is located on the target and, sometimes, it may be also difficult to know if it is on the target at all.

3.5.2.5 Tracking Error

Tracking error is a generic term that encompasses other forms of spot movement from the desired aim point. Where jitter is a random movement of the

beam around a central axis, tracking error may be described as undesired movement of this central axis around or away from the aim point. This movement of the central beam axis may or may not be visible to the operator depending on the magnitude of the error and the quality of the sensor presentation to the operator. At long slant-ranges, automatic tracking systems can exhibit beam wander that overwhelms other sources of error. This wander is caused by movement of the video tracking gates on-or-about the aimpoint as the viewing aspect changes. The changing aspect or look angle produces changes in the aim point contrast with respect to its background. This, in turn, varies the location of the contrast driven tracking gate position with a consequent shift in beam position. Other causes for tracking error may include *g* forces (mentioned earlier), transient angle rate errors due to rapid bank angle changes, or momentary errors due to LOS masking. Motion of the laser spot during the last three seconds prior to impact may induce unnecessary corrections to the weapon flight and result in a miss.

3.5.3 Podium Effect

For an LGB to guide, the seeker must be in a position to receive the reflected laser energy. During a self-designation attack against a vertical target, there is a risk that the laser spot will move around the target face relative to the weapon LOS, as the designator aircraft flies the recovery manoeuvre, and that the weapon will not receive the reflected laser energy during the final critical moments before impact. This phenomena, known as the "podium effect", is particularly apparent when the designator to target line is significantly different to that of the weapon's flight path. To avoid the podium effect, the designating aircraft should maneuver such that the target face is always in front of the aircraft and that the appropriate terminal slant range/angle occurs at weapon impact. This problem can often be eliminated by lasing on top of a horizontal target.

3.5.4 Beam Divergence and Reflected Power

Another effect of beam divergence is to reduce the maximum reflected power available to the weapon as the beam strikes the target off-axis. Fig. 3-8

illustrates the laser spot shape and intensity versus various designation angles of incidence. The calculations assume a 100% diffuse surface, no atmospheric attenuation, and an illuminating beam with a *Gaussian* distribution.

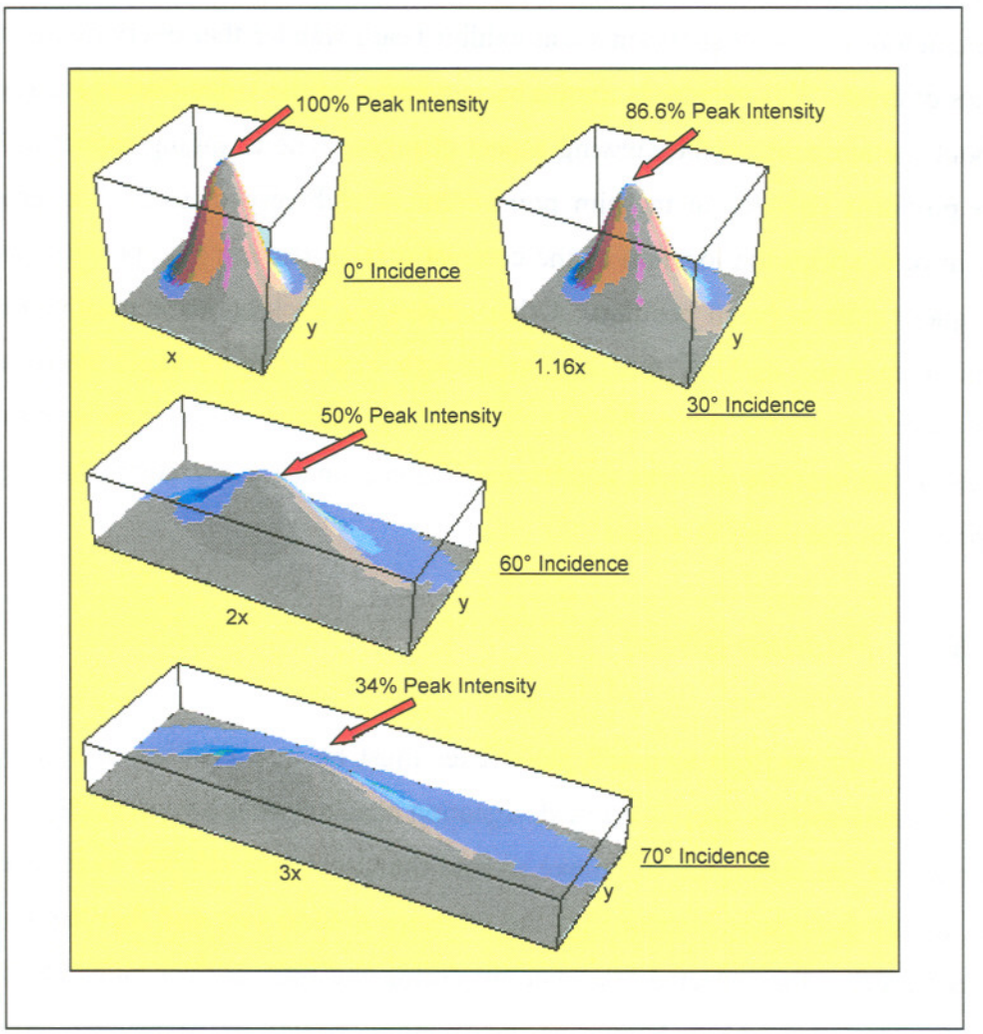

Figure 3-8. Laser spot intensity vs. angle of incidence.

3.5.5 Sensor Resolution

The size of the target must also be factored against the resolution abilities of the sensor element (FLIR and/or TV) to determine the maximum usable delivery slant range. This will ensure that the operator will be able to resolve the target at a range that is in excess of the maximum range capability of the weapon. This excess or redundant range requirement is necessary to properly detect and then identify the target prior to weapon release. This target detection and identification requirement prior to release has become of almost paramount importance in punitive

or other high visibility actions where the blind launches required by other weapon systems prevent their use.

As mentioned earlier, the maximum slant-range from which a designator is intended to be operated must be determined as part of the mission planning process as a function of target size, laser system error budget, and laser power. In addition, an attempt should be made to determine what additional range should be selected in order for the target to be properly identified prior to weapon release. This requires an estimate of the time required to first detect the target on the sensor set and then add the time required to fully resolve the target for a positive identification. With current TV/FLIR technologies and good initial cueing, it is usually estimated that at least ten seconds are required to detect the target. Further five to ten seconds are then required to properly identify the target itself.

3.5.6 Airborne LTD/LGB Mission Geometry

Let us consider again the LTD/LGW attack geometry already described in Fig. 3-1. With reference to this geometry, the maximum range performance of an LTD/LGB combination can be estimated using the eq. (3.21), which we write again:

$$MDED = \frac{4\rho_T U A \cos\theta_t \cos\theta_r \cos\gamma_R \tau_{atm}}{\pi^2 (D_L + \alpha_T R_T)^2 R_R^2} \tag{3.71}$$

Conveniently, in eq. (3.71), we have replaced the term $e^{-[\sigma_\alpha(\alpha_{HR}R_T + \beta_{HR}R_R)]}$ (i.e., two-ways atmospheric transmittance) with the symbol τ_{atm}, and the returned energy density (I) with the Minimum Detectable Energy Density (MDED) of the LGB seeker-head unit.

There are three cosine factors in eq. (3.71). They are related to the assumption of a *Lambertian* reflection (i.e., diffuse reflection of the laser signal incident on the target surface). It is important, in order to determine the performance of an LTD/LGW combination during an attack, to take into account the variations of the angles θ_t, θ_r and γ_r. On the other hand, in order to calculate the maximum range for an effective illumination in the worst geometric case, it is important to determine the maximum values assumed by these angles during the attack. Moreover, for mission planning purposes, it is useful to express the angles θ_t, θ_r and γ_r as functions of other physical

or geometrical parameters that are known prior the mission (e.g., seeker FOV, target inclination, etc.). Using eq. (3.76), the maximum theoretical value of the angle γ_r can be determined as a function of the seeker Minimum Detectable Energy Density (MDED). However, we must consider that the seeker of the LGW must always intercept a portion of the reflected signal sufficient to produce a response of the detector in order to guide the weapon against the target. In other words, the angle $\gamma_r(MDED)$ should always be greater than the FOV of the seeker (Fig. 3-9).

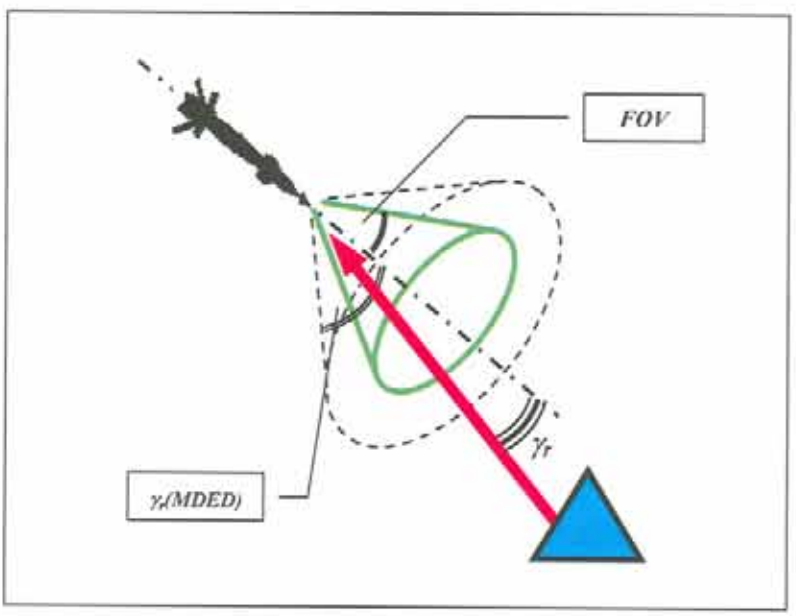

Figure 3-9. LGB-target geometry.

Considering the geometry of typical ground attack missions with LGB, the angles θ_t (angle between the LOS transmitter-target and the normal to the target surface) and θ_r (angle between the LOS receiver-target and the normal to the target surface), can be expressed as function of other geometric parameters and their maximum theoretical values (corresponding to the minimum relative range performance) can be determined. With reference to Fig. 3-2, the angles θ_t and θ_r can be expressed as:

$$\theta_t = i + \varphi_t - \frac{\pi}{2} \tag{3.72}$$

$$\theta_r = \frac{\pi}{2} - i - \varphi_r \tag{3.73}$$

where i is the target inclination, φ_t is the angle between the transmitted beam axis and the horizon and φ_r is the angle between the LGW-target LOS and the horizon ($\varphi_r = \varphi_t - \theta_t - \theta_r$). Knowing θ_d, α and γ, it is possible to determine the value of the angle θ_t during the attack, solving the equation:

$$\theta_t = i + \theta_d - \gamma + \alpha - \frac{\pi}{2} \tag{3.74}$$

More difficult is the determination of θ_r, since the angle φ_r can not be determined without knowing continuously the position assumed by the line of sight LGW-target (i.e., the guidance algorithms and corrected ballistics of the LGW). However, knowing the angle ε at the beginning of the designation (from the ballistics of the unguided weapon) and taking γ_r equivalent to the seeker FOV, we have that:

$$\varphi_r = \varepsilon \pm \gamma_{r(MAX)} = \varepsilon \pm FOV \tag{3.75}$$

Since it is reasonable to assume that, after the designation is initiated, the angle γ_r will be kept as low as possible by a PG-LGW, we can assume that $\varphi_r \approx \varepsilon$ in this case. Therefore, the approximate value of the angle θ_r during an attack with PG-LGB and BTB-LGB, can be determined solving the equations:

$$\theta_r = 90° - i - \varepsilon \qquad \text{for PG-LGW} \tag{3.76}$$

$$\theta_r = 90° - i - \varepsilon + FOV \qquad \text{for BTB-LGW} \tag{3.77}$$

For the purpose of determining the maximum values that the angles θ_t and θ_r can reach during an attack, which determine the absolute minimum performance of a particular LTD/LGB combination (worst case), it is meaningful to take into account the tactics of typical self-designation attacks illustrated in Fig. 3-10. Since the designation is initiated in the final portion of the bomb trajectory (i.e., with an LTD-target range typically between 1.2 and 2.0 times the release range), it is generally performed at a considerable range from the target. This means that, normally, the angles θ_t and θ_r never reach values close to 90° during an attack, even in the worst case when i = 90°. On the other hand, in the case of horizontal target (i = 0°), the cases where θ_t and θ_r are close to 90° are of little practical interest.

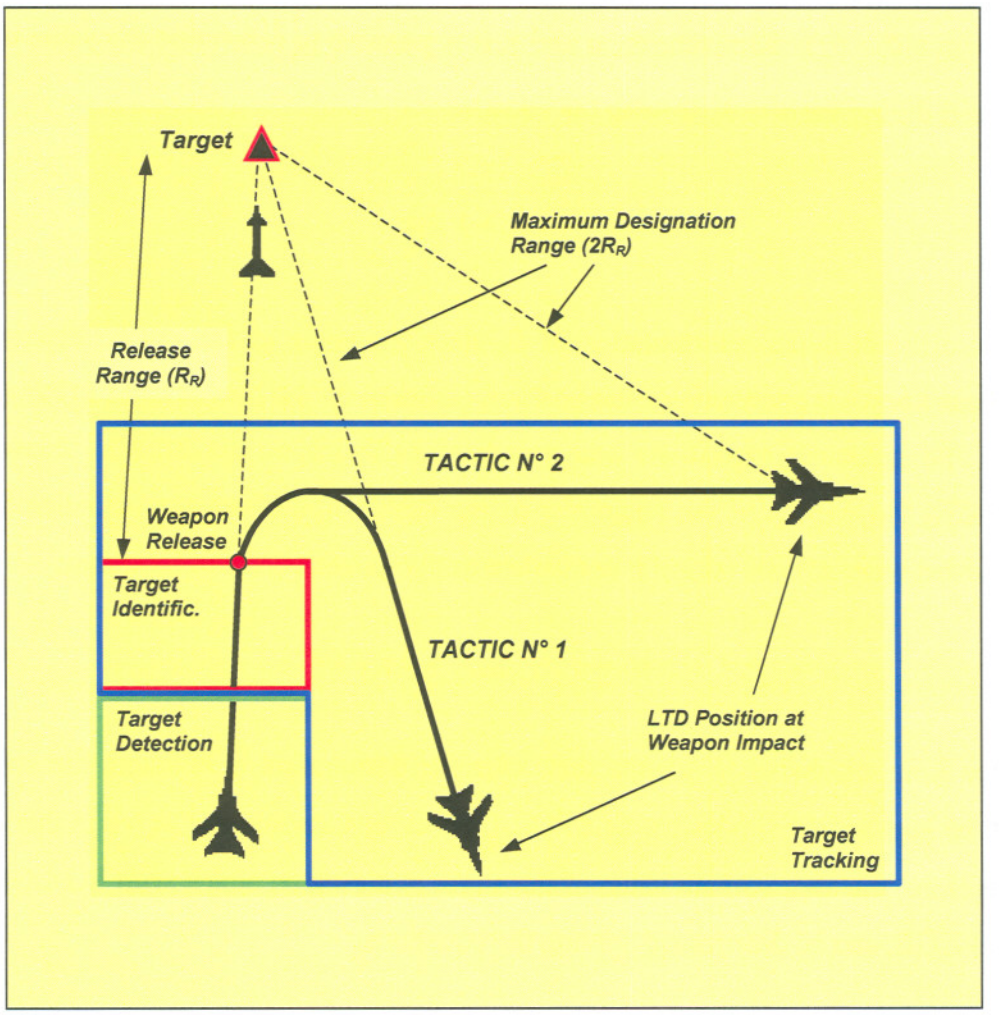

Figure 3-10. LTD/LGB mission horizontal profiles (self-designation).

Looking at Fig. 3-12, it appears evident that the angle θ_t is smaller than i when $i > 45°$, while it is generally smaller than the complementary of i when $i < 45°$. Similar considerations apply to θ_r. Therefore, with these assumptions, the worst case conditions for θ_t and θ_r are the following:

$$\begin{cases} \theta_{t(MAX)} = \dfrac{\pi}{2} - i \\ \theta_{r(MAX)} = \dfrac{\pi}{2} - i \end{cases} \quad \text{for } i < 45° \; ; \qquad \begin{cases} \theta_{t(MAX)} = i \\ \theta_{r(MAX)} = i \end{cases} \quad \text{for } i \geq 45° \qquad (3.78)$$

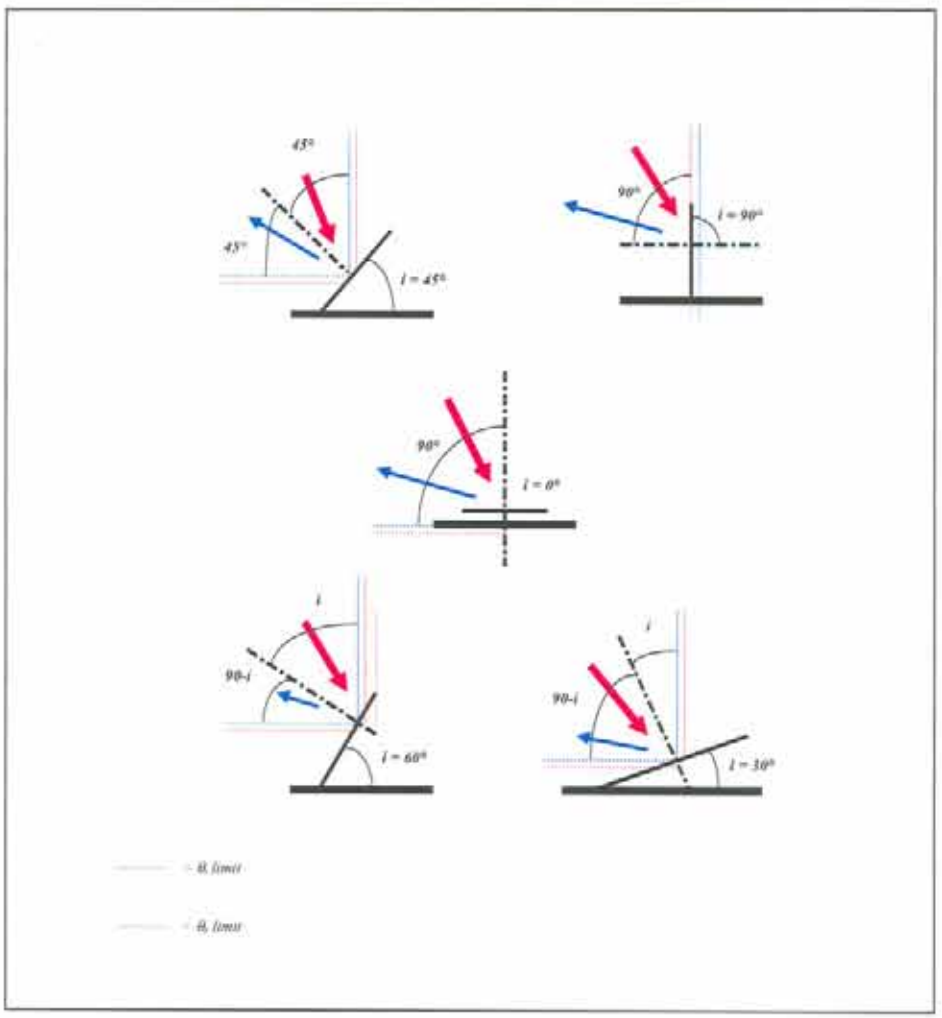

Figure 3-11. Limits of the angles θ_t and θ_r.

3.5.7 LTD System Error Budget

As an example, we consider a LGB which can achieve a 10 feet Circular Error Probability (CEP). In this case, it is appropriate that the designator aiming capability must equal or exceed that requirement in order to meet a suitable weapon impact criteria. If a hardened shelter access cover, roughly 20 feet in diameter, is considered as a target in our example, this target dimension equates to a 10 feet CEP where 50 % of our hypothetical weapon releases should fall on the target face. Using Tactic 2 shown in Fig. 3-10 against a vertical target, and choosing a desired release range (R_R) of 35,000 feet, it is necessary that our designator must be capable of keeping its beam on a 20 feet diameter target at a Terminal Slant Range (TSR) of

70,000 feet. This equates to a total allowable Maximum Error Budget (EB_{max}) of 285 μrad (20ft/70Kft). We also assume that the target is designated at the corresponding terminal designation angle (Ψ) of 60° off of the line normal to the target face. This 60° offset reduces the gross error budget to approximately 143 μrad ($EB_{max} \times cos60°$). This means that all pointing and beam divergence error sources, when added in a worst case fashion, must fall within a cone that subtends 143 μrad if 50% of our hypothetical weapons are to hit the 20 feet target mentioned above.

In the light of the above considerations, the maximum allowable error budget can be expressed as:

$$EB_{max} = \frac{T_S \cdot cos\Psi}{TSR} \tag{3.79}$$

where T_S is the target size and TSR is the Terminal Slant Range. Using Tactic 2 in Fig. 3-10, the terminal slant range can be expressed as:

$$TSR = \frac{R_R}{cos\Psi} \tag{3.80}$$

3.5.8 Release Range

Given a fixed error budget and known designation tactic (e.g., Tactic 2), we can solve for the optimal release range:

$$R_R = \frac{Tgt\ Size \cdot (cos\alpha)^2}{EB_{max}} \tag{3.81}$$

Using for example a "worst case" error budget of 208 μrad (given by the sum of all pointing error contributions), the optimal release range against a 20 feet target with a 60° terminal designation angle is approximately 24Kft (i.e., not 35Kft as originally desired). This example demonstrates that, in most cases with LGW, the engagement scenario is usually limited by designator and/or sensor capability, and not by the standoff capability of the weapon itself, particularly at extreme slant ranges and/or low graze angles.

3.5.9 Maximum Egress Range

Due to the tracking error of the LTD system described above, a 600 kts ingress would require approximately 15 to 20 thousand feet of additional range over that of the desired release range. In other words, a 600 KTAS ingress to a 35,000 foot release point would require a detection range of over 50,000 to 55,000 feet. However, both designation and sensor capabilities should be geared toward the egress side of the picture.

During egress, the designator aircraft would desirably turn to a heading that provides maximum standoff and yet provide a flight path that will stay within designator constraints up until weapon impact. With reference to Fig. 3-10 (showing two possible tactics that might be used), Tactic 1 is probably the most desirable in terms of standoff, however, it requires a designator with full hemispheric coverage below the aircraft for high altitude delivery or full coverage above the aircraft for low altitude deliveries. Tactic 2 shows a probable tactic that could be used when a rear gimbal limit has been placed on the LTD aiming system. While standoff is probably acceptable, a major constraint then becomes the look angle at a vertical target face from the LTD perspective ("Podium Effect"). As the designator proceeds outbound after weapon release, the perceived horizontal dimension of the target decreases by up to 50 percent (for an optimum attack heading). Where the attack heading is constrained and an optimum attack solution is not available, the off axis perspective may reduce one target dimension by another 20%.

Ordinarily, as in both of the above cases, the range attained during egress is normally greater than the ingress range required for detection. For present LGB weapons, the range during egress at weapon impact time typically varies from approximately 1.2 to 2.0 times the release range. This ratio shifts towards 2.0 as standoff is increased towards maximum range. For the example given earlier, the designator aircraft would be at a slant range of between 42,000 and 70,000 feet at weapon impact.

3.5.10 Masking

Another important problem with airborne laser systems is "masking" of the equipment field of regard caused by the aircraft structure and loads (e.g.,

weapons, external tanks, etc.). Although masking can be reduced/eliminated by a careful aircraft/system design in the case of embedded systems, this is generally a very important constraint for operations with podded systems (e.g., the CLDP integrated on the Italian TORNADO-IDS). A useful way of characterising systems masking characteristics is the so called "Masking Matrix". This is a Cartesian coordinate system in which (most conveniently) azimuth and elevation are plotted for the equivalent FOV of the system. This is given by intersection of the system "visibility matrix" and the "aircraft matrix" (e.g., an aircraft/loads CAD model).

For the airborne LTD system in service with the Italian Air Force (CLDP), the system masking is essentially given by a backward cone with an aperture of 30° and 20°, for the IR and the TV front sections respectively (Fig. 3-12).

During the CLDP integration on TORNADO-IDS, analysis was required in order to fully characterise the masking phenomenon and obtain the related mathematical model to be used by the aircraft MC for CLDP inhibition during impingement.

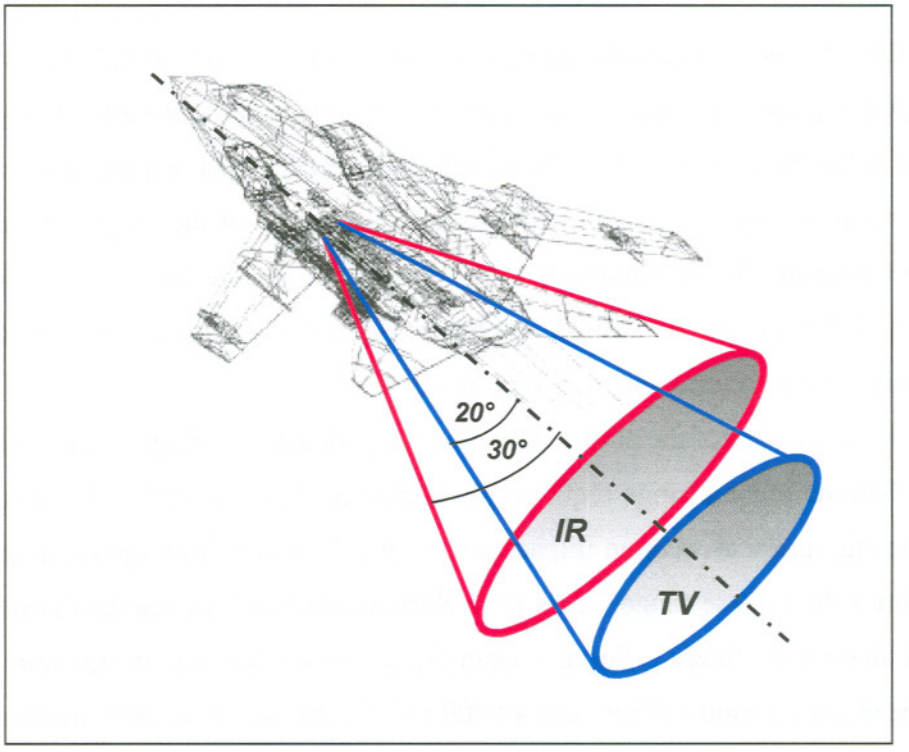

Figure 3-12. CLDP FOV limitations (TV and IR).

The initial TORNADO-IDS masking model (developed by ALENIA) was obtained through a computer CAD simulation, that consisted in defining the aircraft shape

with different external stores configurations. As a result of the analysis/simulation, the proposed masking function logic was defined (Fig. 3-13).

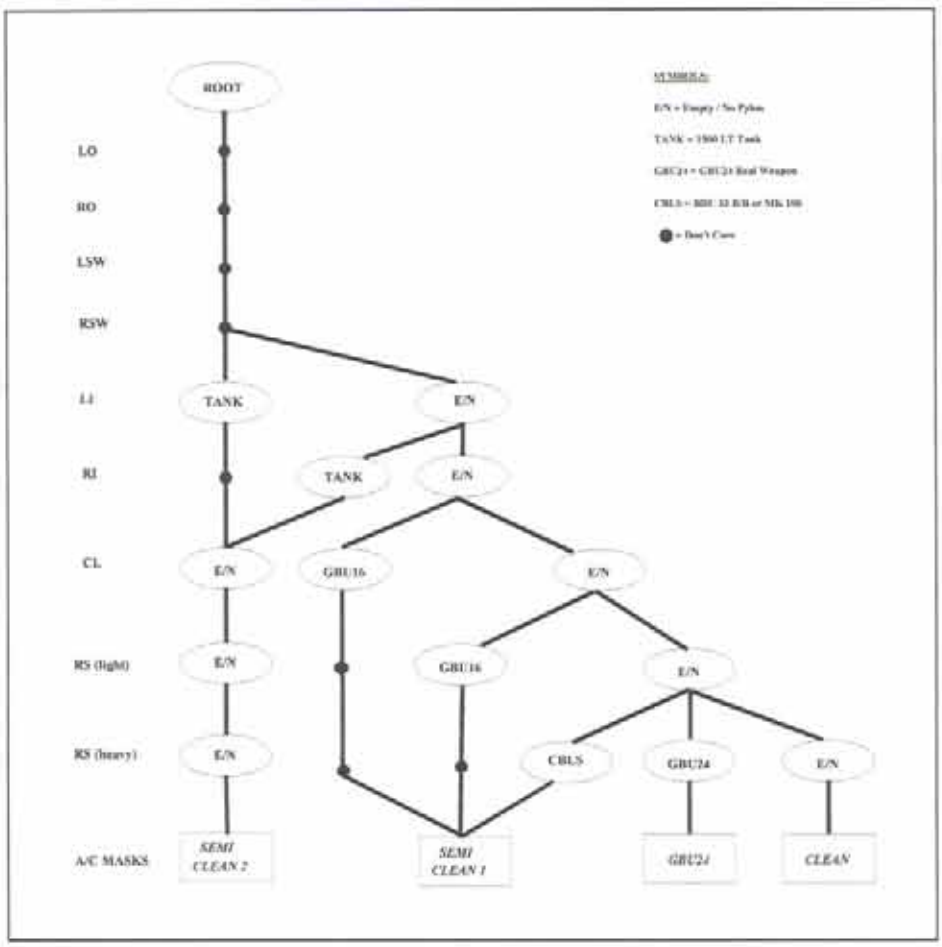

Figure 3-13. CLDP masking selection logic.

Particularly, the aircraft "masking function" was conceived in order to manage the basic real GBU-16 and GBU-24 Stores Configurations ("worst case" masking profile) and their derived sub-configurations (i.e., semi-clean and clean), providing appropriate aural/visual warning to the pilot/WSO and inhibition commands to the CLDP laser in case of LOS impingement with aircraft and stores. Furthermore, a "pre-masking" function was implemented in order to provide aural/visual advise to the pilot/WSO in case of approximation to the masking conditions.

The validity of the solutions developed for masking/attack profiles and Laser illumination phase, was verified through simulation and flight tests (jointly by ALENIA and the Italian Air Force). The developed simulation tool, fitted with the suitable problem oriented routines, allowed the exploration of the system behaviour

under the influence of a large number of parameters. Particularly, simulation was used to monitoring the LOS components (Azimuth and Elevation) in an Hammer/Aitoff diagram where mask and pre-mask conditions were plotted.

The trajectory of the LOS, marked in time between the bomb release and impact, gave an immediate understanding about the effect of the aircraft manoeuvre on the LOS pointing direction. By varying the aircraft manoeuvre parameters (i.e., turning direction, turning load factor, roll rate, and egress heading), the LOS trajectory gave an indication on the critical conditions that could arise with the chosen parameters.

The basic software tool was composed by an aircraft mathematical dynamics model, based on the classical equations set, used in conjunction with a simplified aircraft data bank containing the main TORNADO-IDS characteristics. The aircraft model was provided with a simplified autopilot able to maintain flight path parameters (i.e., height, velocity and heading) aimed at performing automatic attack manoeuvres (e.g., turns, climbs, dives), used during the evaluation phase.

Furthermore, a simplified program that simulated the LGB ballistic trajectory was used. This code run as a stand alone task and was used to compute in advance range and time of flight of the bomb for the chosen release conditions. These data were then loaded into the simulator memory to command the post weapon delivery manoeuvre.

Flight test activities performed by ALENIA and the Italian Air Force Official Flight Test Centre (RSV), permitted to finally tune and validate the masking and pre-masking algorithms [15]. Particularly, tests were conducted in selected portions of the operational flight envelopes, representative of real LTD/LGB attack missions and of the boundary conditions for activation of the masking and pre-masking functions.

3.6 References

1. Jelalian A.V., "Laser Radar Systems". Artech House Boston-London. 1992.
2. Sabatini R., ""Tactical Laser Systems Performance Prediction in Various Weather Conditions". 1st Symposium of the NATO-RTO SET Panel (former AGARD-SPP Panel). Italian Air Force Academy. Naples (Italy). 16-19 March 1998.

3. Weichel H., "Laser Beam Propagation in the Atmosphere". SPIE Optical Engineering Press. Second Printing. 1990.
4. Elder T. and Strong J., "The Infrared Transmission of Atmospheric Windows". J. Franklin Institute 255 - 189. 1953.
5. Langer R.M., Signal Corps Report n° DA-36-039-SC-72351. May 1957.
6. Kneizys F.X., Shuttle E.P., Abreau L.W., Chetwynd J.H., Anderson G.P., Gallery W.O., Selby J.E.A., and Clough S.A., "Users Guide to LOWTRAN 7". Air Force Geophysical Laboratory Report AFGL-TR-88-0177. Hansom AFB (MA). 1988.
7. Middleton W.E.K., "Vision Through the Atmosphere". University of Toronto Press. 1952.
8. Middleton W.E.K., "Vision Through the Atmosphere". Handbuch der Physik 48. Geophysics 2. Springer (Berlin). 1957.
9. Hudson R.D., "Infrared Systems Engineering". Wiley & Sons. 1969.
10. Holst G.C., "Electro-Optical Imaging System Performance". SPIE Optical Engineering Press. Bellingham, Washington USA. 1995.
11. Chu T.S. and Hogg D.C., "Effects of Precipitation on Propagation at 0.63, 3.5 and 10.6 Microns". Bell Systems Technical Journal 47 - No. 5. 1968.
12. Strohbehn J.W. et al., "Laser Beam Propagation in the Atmosphere". Topics in Applied Physics Series – Vol. 25. Sprienger-Verlag. 1978.
13. Keith G.G., Otten L. J., and Rose W.C., "Aerodynamic Effects". ERIM-SPIE IR&EO Systems Handbook (Vol. 2 – Chapter 3). Second Printing. 1996.
14. Phong B.T., "Illumination for computer generated pictures". Communications of the ACM. Vol. 18-6 (pag. 311-317). 1975.
15. Sabatini R., Guercio F., Marciante A., Campo G., "Laser Guided Bombs and Convertible Designation Pod Integration on Italian TORNADO-IDS". 31st Annual Symposium of the Society of Flight Test Engineers. Turin (Italy). 18-22 September 2000.

modification is necessary and these weapons may be carried (upon certification) by any aircraft capable of carrying the parent unguided warheads.

Differently from PAVEWAY II, the GBU-24 is a "Proportional Guidance" LGB, which continuously track the maximum of the target reflected laser energy and directs toward it by actuating its aerodynamic surfaces, giving commands proportional to the measured offset. The bomb has four different operational modes, selectable on the ground prior mission, depending on the target characteristics (i.e., hard or soft) and the desired bomb impact angle. For each mode of operation, the GBU-24 computer unit automatically selects a suitable flight profile (from a number of pre-set profile types) depending on the release conditions.

2.3.5 LIZARD LGB Description

The LIZARD Laser Guided Bomb, developed by *ELBIT Systems Ltd* (Israel), consists of a standard MK-82 (500 lbs) warhead attached to a Proportional Guidance System (PGS) at the front end and a Folding Tail Assembly (FTA) at the rear. The LIZARD general view and its assemblies/subassemblies are shown in Fig. 2-10 [6].

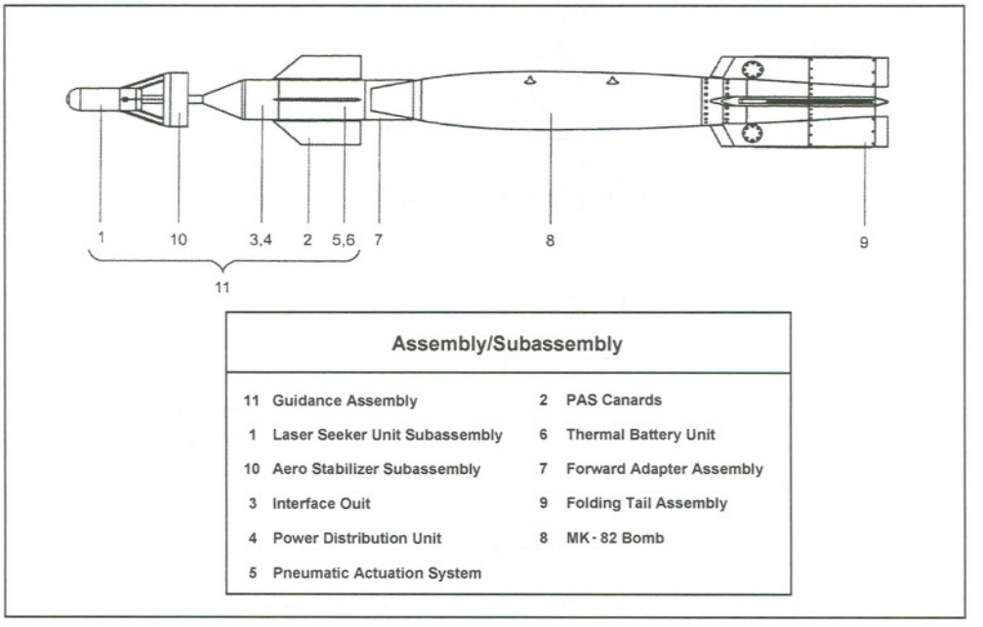

Fig. 2-10. LIZARD LGB configuration.

The PGS comprises a Laser Seeker Unit (LSU) which detects reflected laser energy (coded sequences of laser pulses) from the designated target and produces guidance commands to the Pneumatic Actuation System (PAS), according to the target position. The PAS guides the LIZARD by controlling the guidance fins to home on the target. The FTA is used to stabilize the LIZARD after launching and to provide the lift required for manoeuvrability. The system also includes provisions for a GPS add-on kit (to enhance guidance accuracy).

The LIZARD sequence of operation is shown in Fig. 2-11.

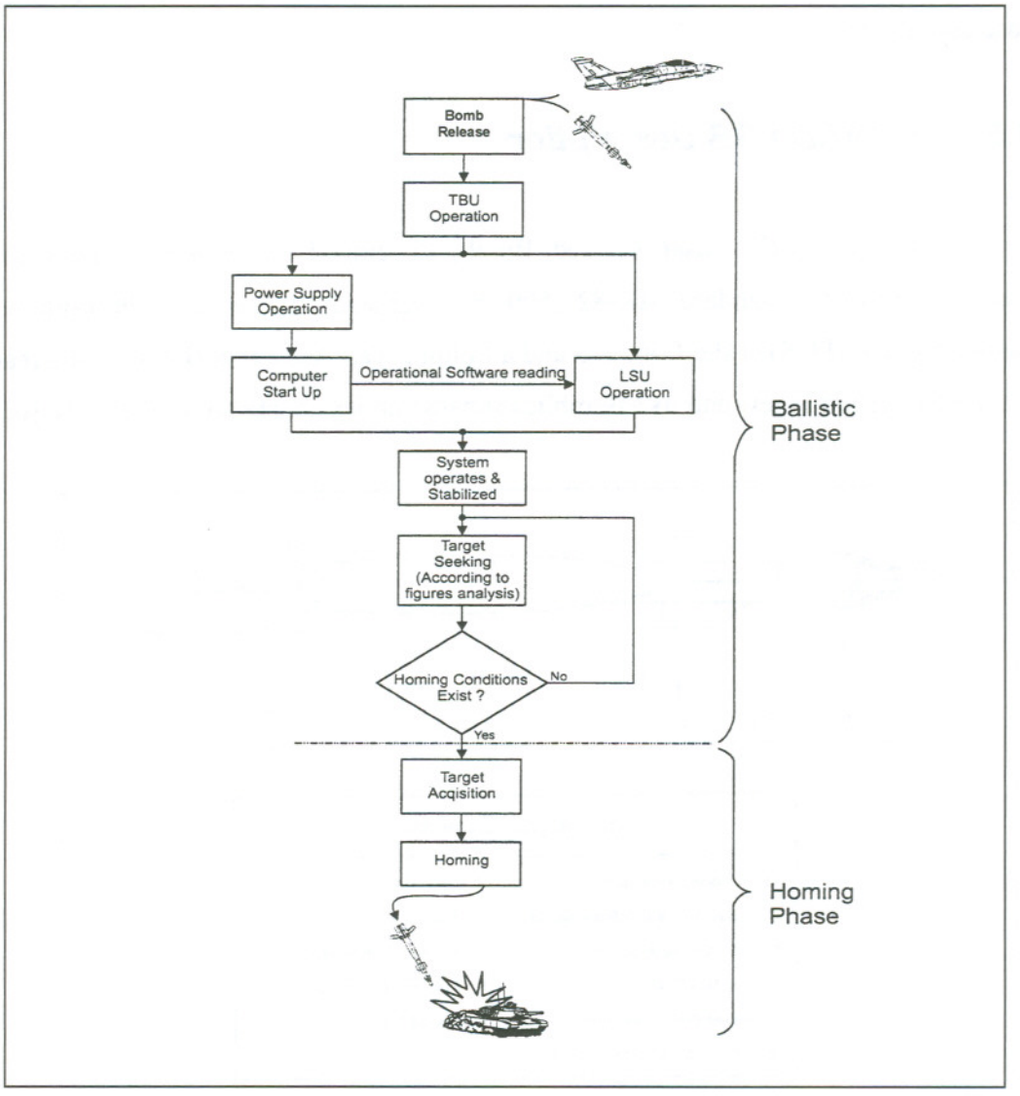

Fig. 2-11. LIZARD sequence of operation.

After launching, the LIZARD operates in two sequential trajectory phases until it hits the target: a Ballistic Phase and a Homing Phase (Terminal Guidance Phase). During the Ballistic Phase, the bomb follows in a ballistic trajectory towards the target. The start range to target at acquisition is dependent on laser light reflected from the target and transmitted through the atmosphere. At a range generally varying between 2000 and 5000 metres the LSU detects the laser spot generated by the laser designator. The first few seconds of this phase are used to stabilize all the electronics and zero aeromechanical transients in the system. Once the weapon is fully operational, it searches for the target until it is detected and the acquisition criteria is accomplished. The Ballistic Phase ends with the actual target acquisition. After target acquisition, the bomb guides itself towards the target using tracking algorithms for flight control. The bomb steers its way towards the target using the movable guidance fins deflected by the Pneumatic Actuation System (PAS), commanded by the LSU (i.e., the LSU generates steering commands proportional to the location of the target in the FOV of the seeker). During the year 2003 the LIZARD LGB was successfully tested and integrated on the AM-X ground attack aircraft in service with the Italian Air Force and further test activities will be conducted in the 2004-2005 timeframe for integrating the LIZARD LGB on the Italian TORNADO aircraft.

2.4 Laser Radar Systems

The term radar originated during World War II as an acronym for radio detection and ranging. At that time, it referred to the technique of monitoring reflected, radio frequency, electromagnetic radiation to locate remote objects. Since that time, the basic radar technique has been applied to progressively shorter (and in some cases, longer) wavelengths so that the term radar no longer applies only to systems that operate at radio frequencies. Laser radar is simply radar that operates at optical frequencies and uses a laser as its source of electromagnetic radiation.

Laser radars are commonly referred to as LADAR for laser radar or as LIDAR for light detection and ranging. Ranging is accomplished by measuring the time delay to and from the target. Angular information is obtained from the beam-pointing direction. Laser radars are capable of extremely accurate angular measurement because of the small beam diameters of lasers (on transmit) and narrow fields of view (on receive). On the negative side, the detection and tracking ranges are much shorter than microwave radar because of lower transmitter power and higher atmospheric attenuation.

LADAR's usually operate at a wavelength of 10.6-μm in the far infrared and at a wavelength of 1.064-μm in the near infrared. The former use CO_2 lasers and the latter Nd:YAG crystal lasers, with typical efficiencies of 10% and 3%, respectively. Other available technologies include 1.5 μm "Eye-safe" Erbium doped fibre (Er:fibre) laser and Raman-shifted Nd:YAG lasers. Possible airborne LADAR applications include the following:

- Aircraft guidance (obstacle avoidance and terrain following);
- Tactical imaging systems (surveillance and reconnaissance);
- Wind velocity measurement (clear air turbulence and severe storm sensors).

The various types of Laser radars and some typical airborne applications are described in Appendix A. In the following paragraphs, after a brief introduction to Laser Obstacle Warning Systems (OWS's), a technical description of the Laser Obstacle Avoidance System (LOAS), developed by *Marconi-Selenia Communications S.p.A.* for the Italian Military Forces and tested by the Air Force Flight Test Centre (RSV), is presented.

2.5 Laser Obstacle Warning Systems

The first laser experiment directed towards a laser obstacle detection and avoidance system started in 1965 with a Nd:YAG laser [7]. This system demonstrated the feasibility of using lasers to detect obstacles such as wires.

Semiconductor lasers, such as GaAs and GaAlAs have been experimented since 1966. These lasers radiate in the wavelength region of 0.84 to 0.9 μm. The experience gained

with these experimental systems pointed out many features that were then incorporated into successive research. In the 70's and 80's, due to eye-safety and adverse weather (fog) propagation concerns, further development with Nd:YAG and the various semiconductor lasers was substantially reduced, in favour of CO_2 lasers. One of the first heterodyne detection CO_2 systems was the LOWTAS, developed by UTRC. More recent developments include CLARA, the Anglo-French compact laser radar demonstrator program [8]; HIWA, a German system built and tested by Eltro and Dornier [9]; and OASYS, developed in the U.S. by Northrop [10].

Currently, research is concentrating on 1.54-1.55 μm (Raman-shifted Nd:YAG and Er:fibre) solid state lasers. One 1.55 μm system is currently being developed in Italy by *Marconi-Selenia Communications S.p.A.* and tested by RSV. The equipment, here named LOAS (Laser Obstacle Avoidance System), is a "navigation aid system" for rotary wing platforms specifically designed to detect potentially dangerous obstacles placed in or nearby the flight trajectory and to warn the crew in a time suitable to implement effective avoiding manoeuvres. The first airborne prototype of the LOAS system was assembled by *Marconi* during this research. Extensive laboratory and field tests were then performed by RSV on the various LOAS system sub-units, and the overall system was also tested at the PILASTER range both on the ground and in flight (between 2001 and 2003). In the following paragraphs, a brief technical description of the LOAS system is given.

2.5.1 LOAS Development in Italy

The LOAS system is capable of detecting obstacles placed in or nearby the helicopter trajectory, classifying/prioritising the detected obstacles, and providing obstacle warnings (both aural and visual) and information to the crew [11].

The system laser beam scans periodically the area around the flight trajectory inside a FOV of 40° in azimuth and 30° (now being extended to 40°) in elevation, and centred on the optical axis of the system (see Fig. 2-12).

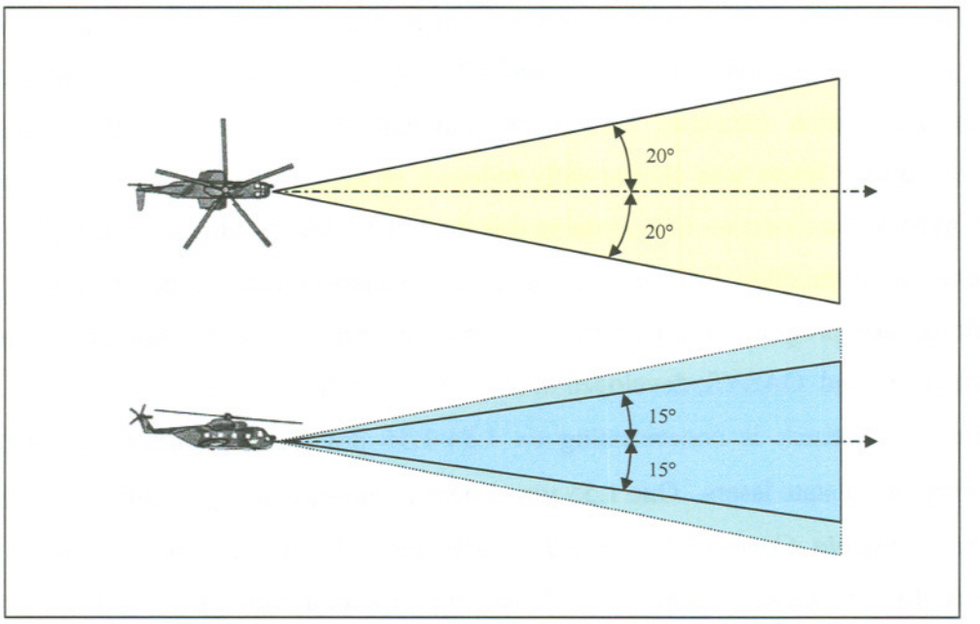

Figure 2-12. LOAS horizontal and vertical FOV.

Furthermore, the LOAS allows the operator to select the azimuth orientation of the FOV among three possible directions (see Fig. 2-13), so that the relevant optical axis will be oriented either in the same direction of the platform "heading" (normal flight envelope), or 20° left/right with respect to the platform "heading" (to optimise coverage during turning manoeuvres at high angular speed).

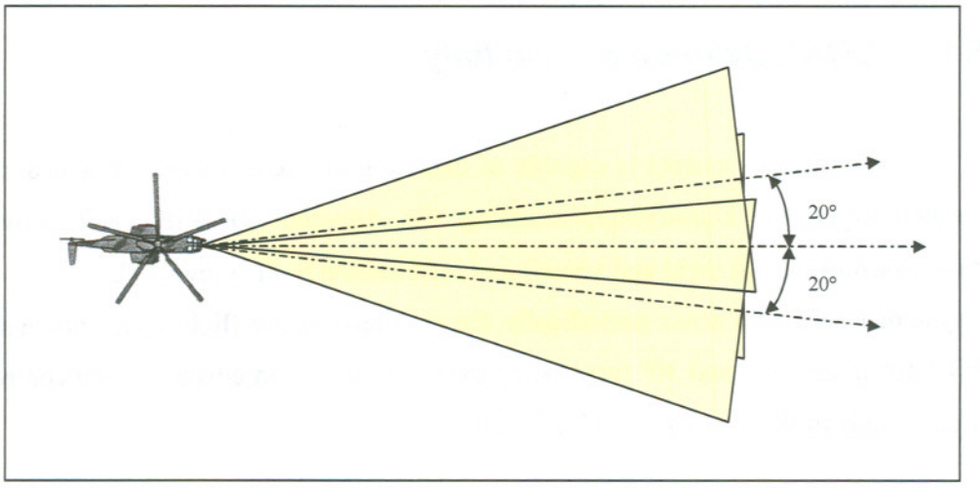

Figure 2-13. LOAS FOV orientation.

During every scan period, the laser beam changes its orientation producing a scanned elliptical pattern across the FOV with the characteristics shown in Fig. 2-14.

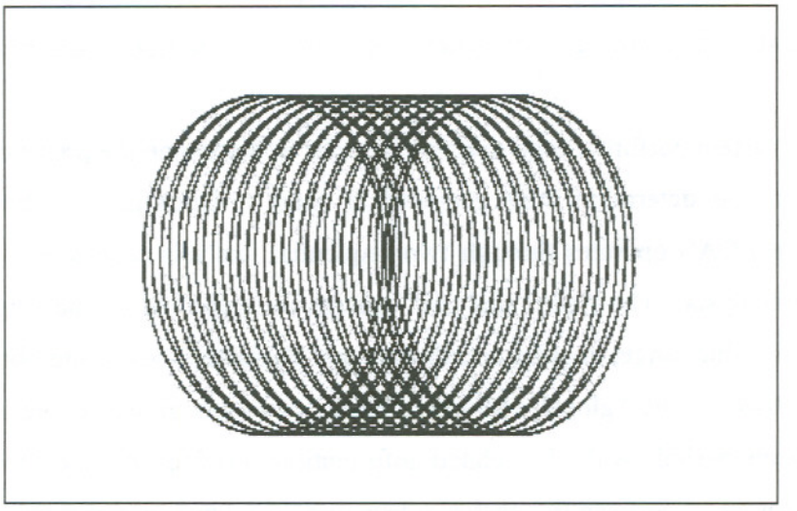

Figure 2-14. LOAS scan pattern.

After various experiments performed with different patterns, the scanned elliptical pattern was selected. The main advantages of the scanned elliptical pattern are:

- it is well suited to detection of the most dangerous obstacles, like wires, due to the several and equally spaced vertical lines;

- it holds an intrinsically high capability to maintain the detected obstacle shape unaffected by the helicopter motion during the frame acquisition, providing the possibility of reconstructing the obstacle shape without using navigation data;

- it can be obtained with very reliable scanning mechanisms with reduced weight.

The LOAS system performs echo detection through an analogue process comprising an optical-electrical conversion, a signal pre-amplification and a threshold comparison. Signal pre-amplification is achieved by an automatic controlled gain amplifier to increase the system sensitivity as the elapsed time from the laser emission increases in order to adjust the sensitivity on the basis of the expected return signal power in

connection with the obstacle range. Furthermore, an adjustable threshold level is also provided to take into account the background conditions. These features reduce the probability of false echo detection due to the atmospheric back-scatter near the laser beam output and optimise the system sensitivity in various operational weather conditions.

The LOAS system performs echo analysis in order to determine the presence of possible obstacles and to determine their geometrical characteristics and position. For this purpose, the LOAS operates through two sequential analysis processes: local analysis and global analysis. The "local analysis" process is performed on the single echoes in order to determine range, angular coordinates and characteristics of the obstacle portion generating them. The "global analysis" process manages groups of echoes, detected during a scan period, with the related information provided by the "local analysis" process, in order to perform the obstacle detection as a whole and determine the related obstacle shape and type.

The LOAS is capable of automatically classifying obstacles according to the following classes:

- ***Wire.*** This class groups all thin obstacles like wires and cables (e.g., telephone cables, electrical cables and cableways).

- ***Tree/Pole.*** This class groups vertical obstacles of large vertical and small horizontal dimensions such as, for example, trees, poles and pylons.

- ***Structure.*** This class groups extended obstacles such as, for example, bridges, buildings and hills.

Furthermore, the LOAS system performs automatic prioritisation of the detected obstacles according to the relevant range data and associated risk levels (taking into account the obstacle type/shape and helicopter flight dynamics), and provides the crew with timely warnings and information on the detected obstacles in order to allow the implementation of effective avoidance manoeuvres. For this purpose, the LOAS system can deliver both visual and audio warnings.

The LOAS information relative to the detected obstacles are provided on a dedicated display (NVG compatible), whose screen represents the FOV of the system. The detected obstacles can be displayed in a synthetic form through three different symbols which represent the three different classes of targets (i.e., wire, tree/pole, structure) of the detected objects. Both 3-D and a 2-D representations are possible, together with an altimetric profile format. An example of a 3-D LOAS display format is shown in Fig. 2-15. The LOAS 2-D and altimetric display formats are shown in Fig. 2-16. The "Safe Line" in Fig. 2-16 represents the line above which flying is considered safe (i.e., obstacles cleared). Furthermore, the following information can be displayed nearby the obstacle symbols:

- obstacle range;

- highest priority mark, which indicates the most dangerous obstacles.

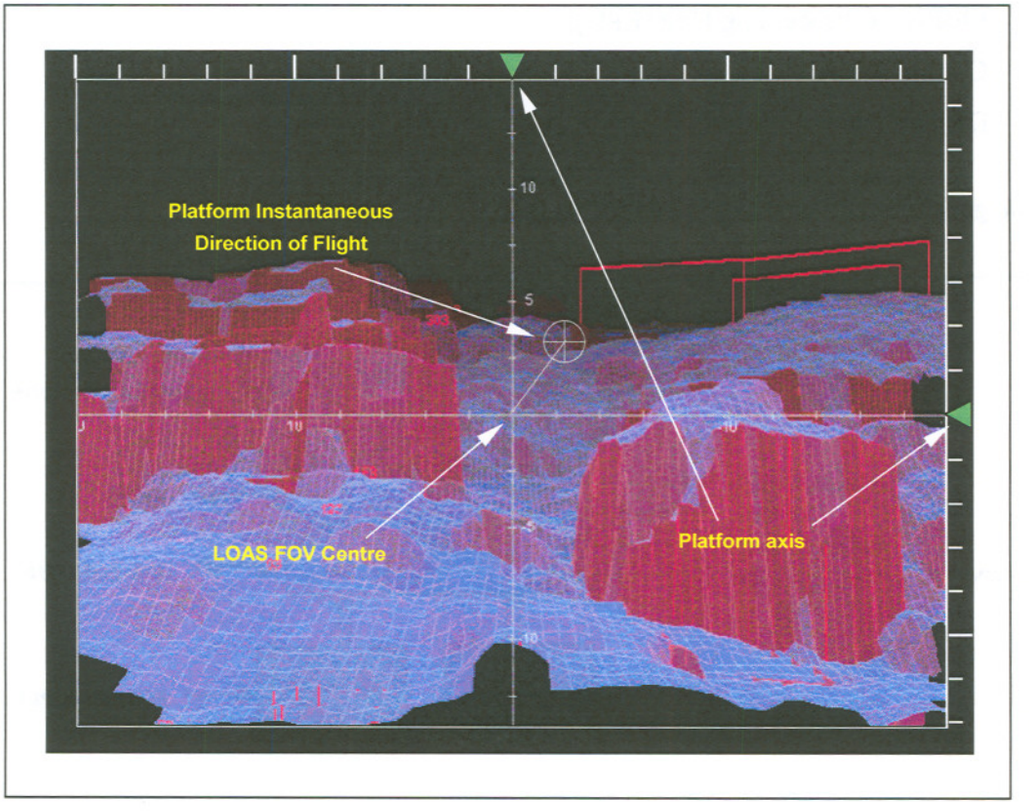

Figure 2-15. LOAS 3-D Display Format.

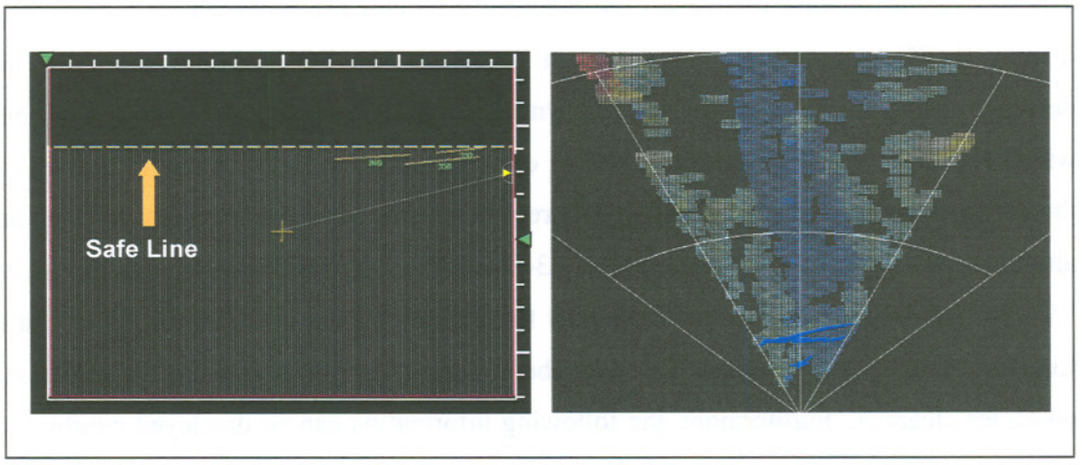

Figure 2-16. LOAS 2-D and altimetric display format.

The main electronics components of the LOAS system are the following:

- Sensor Head Unit (SHU);
- Electronic-Processing Unit (EPU);
- Control Panel;
- Display Unit.

The general architecture of the LOAS system is shown in Fig. 2-17.

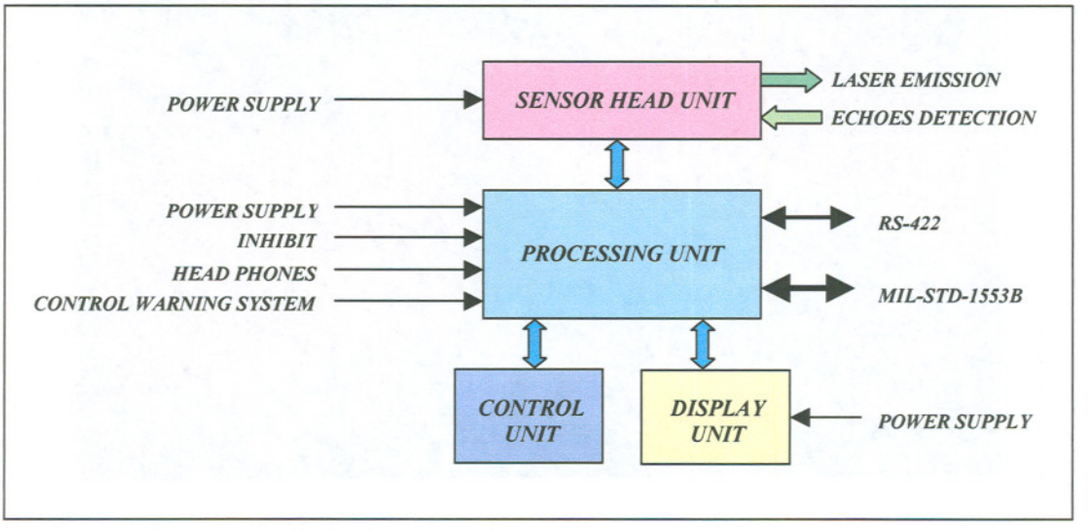

Figure 2-17. LOAS architecture.

In the following sub-paragraphs a brief description of the LOAS SHU is given, together with an outline of the main EPU functions.

2.5.1.1 LOAS Sensor Head Unit

The LOAS SHU performs the following main functions:

- it generates a laser beam and scan the area around the flight trajectory;
- it detects return echoes;
- it analyses detected echoes in order to compute ranges, coordinates and local geometrical characteristics (attributes) of the obstacles they come from;
- it provides echoes data to the LOAS EPU, or to other on board systems.

As illustrated above, the SHU scans a laser beam in the area around the flight trajectory, performs echo detection through an analogue process comprising an optical-electrical conversion (by means of an avalanche photodiode - APD), a signal pre-amplification and a threshold comparison (adjustable threshold).
The SHU performs echo analysis in order to compute range, coordinates (azimuth, elevation with respect to the LOAS reference frame) and local geometrical characteristics (attributes) of the obstacles they come from. For this purpose:

- the echo angular coordinates are determined on the grounds of the scanner orientation;
- the echo range is calculated computing the "two-way" travelling time of the scan laser pulse;
- the geometrical characteristics of the echo are determined with a local "geometrical" analysis of nearby echoes along the scanner pattern and on the ground of the "absolute" power returned.

The LOAS SHU provides the echoes ranges, coordinates and attributes to the LOAS EPU, or to other on board systems, via a RS-422 high speed serial data link. Furthermore the SHU has the following interfaces:

- one RS-232 serial link to the PU for controls and BIT activation;
- one RS-232 serial link for off-line test purpose;
- one discrete input signal to inhibit laser emission;
- one discrete input signal to switch on/switch off the unit.

According the architecture scheme reported in Fig. 2-18, the SHU comprises the following sub-units:

- Window Assembly;
- Scanner Assembly;
- TX/RX Optics Assembly;
- Laser Assembly;
- Detector Assembly;
- Electronic Assembly;
- Power Supply Assembly;
- Gyro Assembly;
- Chassis.

The Window Assembly allows the transmission and the reception of the laser beam across the SHU chassis. The Window Assembly is made with a slice of synthetic fused silica of dimensions 240 × 144 mm and thickness of 10 mm.

The Scanner Assembly integrates the H/W resources necessary to scan the laser beam, and the virtual input pupil of the detector, throughout the overall FOV. It also allows Line of Sight (LOS) orientation. For this purpose, the Scanner Assembly comprises:

- a swash mirror mounted on an azimuth turret;
- an electrical motor to allow the swash mirror motion;
- an electrical motor to allow the azimuth turret motion.

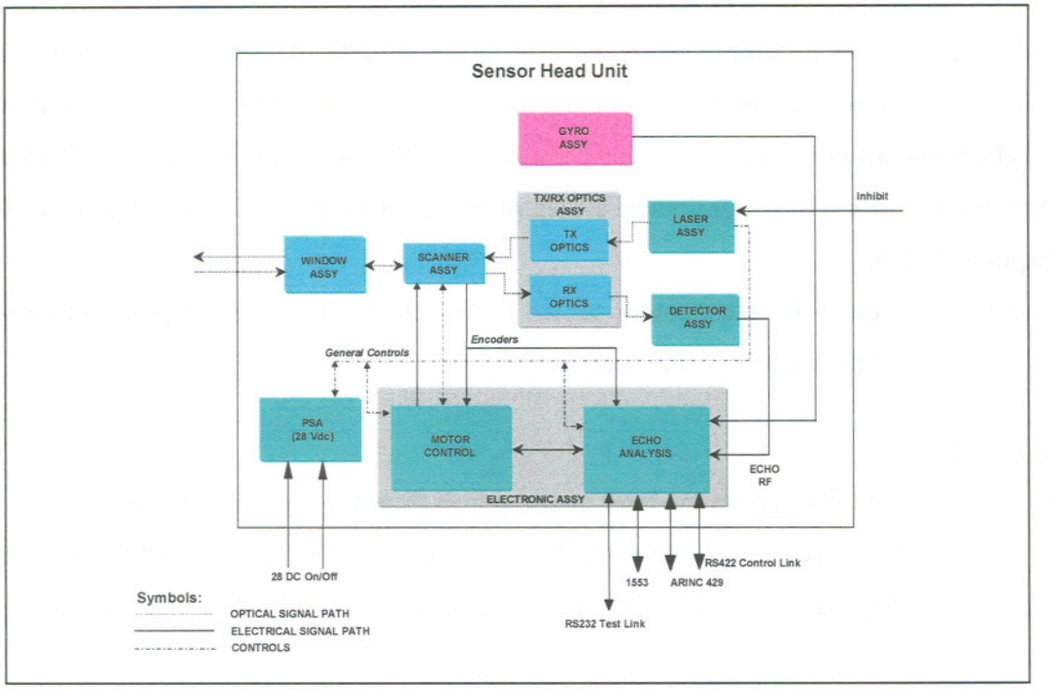

Figure 2-18. LOAS SHU architecture.

The LOAS swashing mirror is shown in Fig. 2-19.

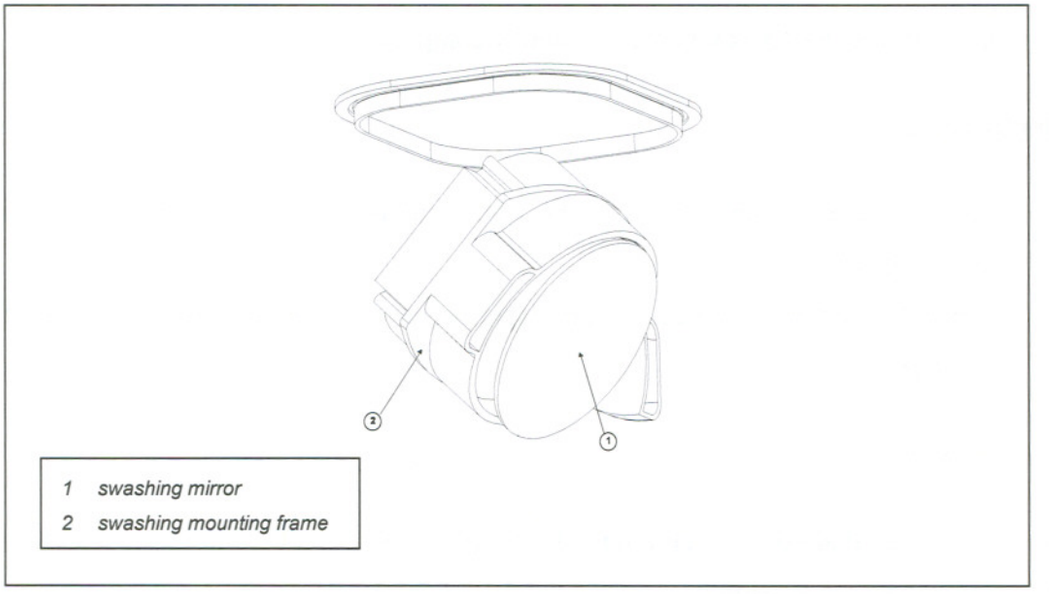

Figure 2-19. LOAS swashing mirror.

The swash mirror rotates at a constant speed around its axis reflecting the laser beam such that it draws an ellipse in space. The turret periodically sweeps in azimuth the FOV. The composition of these two movements allows to produce the required scanned elliptical pattern previously described. Change in LOS orientation is achieved offsetting the central position of the periodical sweep of the turret by an angular value equal to the required change.

According to the SHU architecture shown in Fig. 2-18, the TX/RX Optics Assembly integrates the optical components necessary:

in transmission:

- to collect via fiber optics the laser output power from the Laser Assembly;
- to generate the scan laser beam with the required optical divergence and dimensions;
- to projecting the scan laser beam on the swashing mirror of the Scanner Assembly;

in reception:

- to collect the echo return power reflected by the swashing mirror of the Scanner Assembly;
- to focalise the collected power on the photodiode of the Detector Assembly.

For this purpose, the TX/RX Optics Assembly comprises:

for transmission:

- a beam expander that collects the laser output power via optics fibre and expands/parallelises it;
- a prism that allows to reflect the generated beam onto the swashing mirror with the due alignment;

for reception:

- a telescope that collects the returned echo power and focalises it on the photodiode of the Detector Assembly.

The LOAS TX/RX Optics Assembly and Detector Assembly are shown in Fig. 2-20.

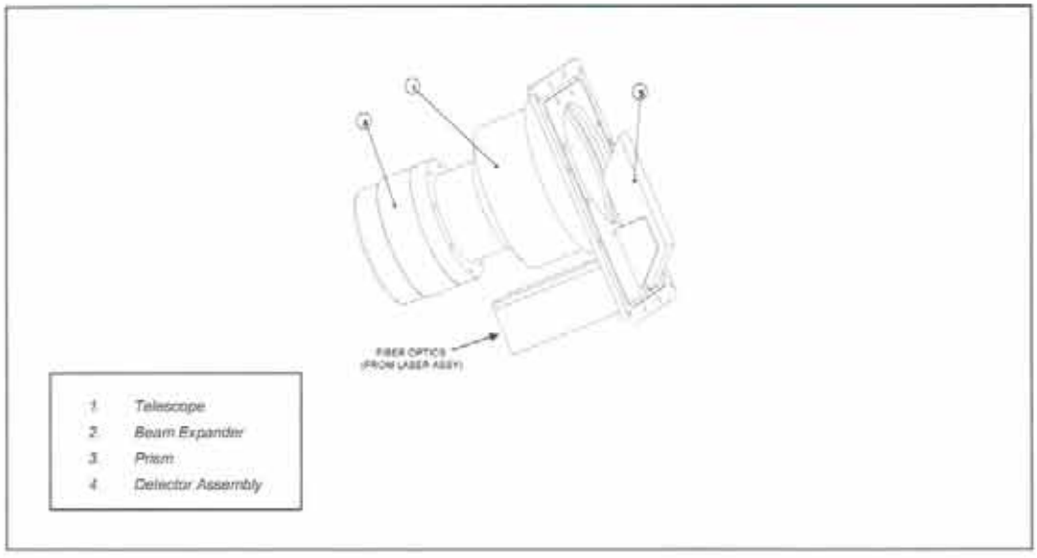

Figure 2-20. LOAS TX/RX optics assembly and detector assembly.

The Detector Assembly detects laser echoes on the grounds of the laser power received through the TX/RX Assembly. For this purpose, the Detector Assembly comprises an Avalanche Photodiode (APD) with related bias circuitry, a controlled gain amplifier and the threshold circuitry necessary for the echoes detection, all integrated in a single mechanical module directly connected to the telescope of the TX/RX Assembly.
The LOAS Electronic Assembly performs the following functions:

- analyses detected echoes, received as a RF signal from the Detector Assembly, and sends the relevant information through the RS-422 interface;
- controls the scanner assembly motors;
- handles SHU general controls and BIT operations.

All the relevant electronics to accomplish the above mentioned functions is integrated in a single analogue/digital printed circuit board.
The Laser Assembly provides the required laser power. It comprises an Er:fibre laser, the related control circuitry and power supply, all integrated in a single box. The laser

power delivery to the TX/RX Optics Assembly is provided via an optical fibre connected to the beam expander.

The Power Supply Assembly fulfils the power requirements of all the SHU sub-units, except for the Laser Assembly which is straight connected to the platform mains. For this purpose, the Power Supply Assembly comprises in a single box all the circuitry necessary to interface with the platform mains and to generate output voltages as required by the SHU sub-units.

The Gyro Assembly provides, as an option, reference signals to the Electronic Assembly to uncouple echoes coordinates with respect to the helicopter motion if required to compensate rotation for image presentation. The Gyro Assembly is composed by 3 gyros integrated in a single mechanical module.

The Chassis is realised by a casting aluminium mechanical envelope that encloses and protect all the SHU sub-units. The Chassis is designed in such a way that all the optical sub-units are allocated in a sealed environment filled with nitrogen gas to avoid condense effect. The CAD representation of the SHU Chassis and the location of the Laser Assembly, the Detector Assembly, the TX/RX Optics Assembly, the Scanner Assembly and the Window Assembly inside the Chassis are shown in Fig. 2-21.

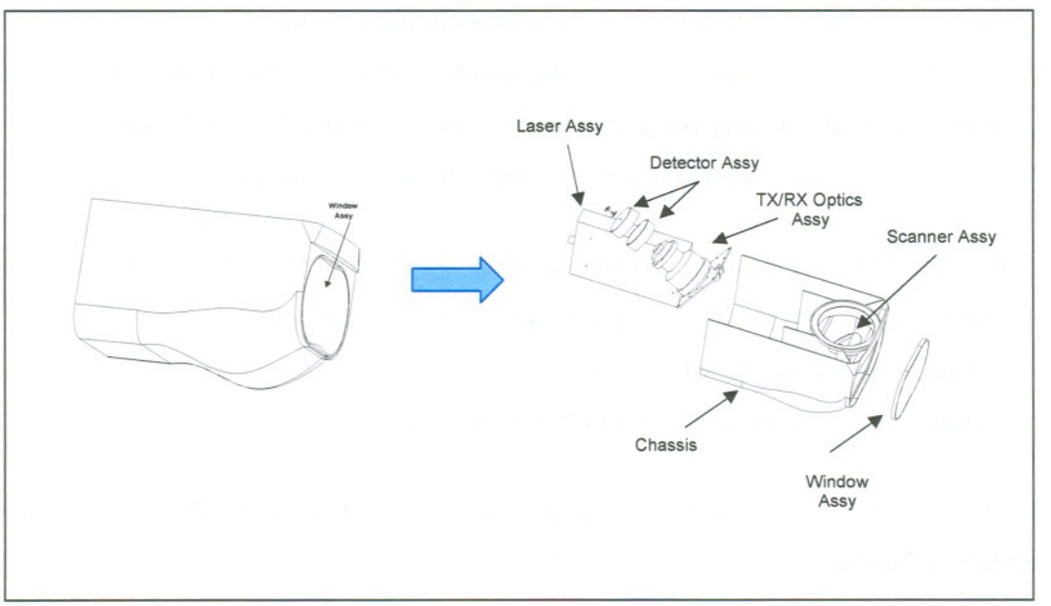

Figure 2-21. LOAS system sub-units location.

Some relevant electro-optical parameters relative to the various LOAS sub-units are listed in the Tables 2-2 through 2-4.

Parameter	Description	Value
Wavelength	Laser emission wavelength	1.55μm
Peak Power	Laser pulse power at the "Laser Assembly" output	6 kW
Pulse Duration	Laser pulse duration	2 ns
Frequency	Laser pulse repetition frequency	40 kHz

Table 2-2. LOAS laser parameters.

Parameter	Description	Value
Divergence	Laser beam divergence at the "Window Assembly" output	1 mrad
Optical diameter	Diameter of the virtual input pupil of the detector (i.e. the area in which the collected power from the echo is transferred to the detector)	85 mm
Window Transmission	Transmission coefficient (P_{in}/P_{out}) of the "Window Assembly"	0.99
Scanner Transmission	Transmission coefficient (P_{in}/P_{out}) of the "Scanner Assembly"	0.99
TX optics Transmission	Transmission coefficient (P_{in}/P_{out}) of the TX optical path of the "TX/RX Optics Assembly"	0.98
RX optics Transmission	Transmission coefficient (P_{in}/P_{out}) of the RX optical path of the "TX/RX Optics Assembly"	0.63

Table 2-3. LOAS optical parameters.

Parameter	Description	Value
Detector Noise	Equivalent optical noise power including the optical background noise and the photodiode and preamplifier electrical noise	1.2 nW
Detector Bandwidth	Electrical bandwidth of photodiode and relevant preamplifier of the "Detector Assembly".	160 MHz
Detector Field of View	Instantaneous field of view in which the laser power of a given echo is collected and transferred to the photodiode of the "Detector Assembly".	1.5 mrad
Detector Filter Bandwidth	Bandwidth of the optical filter of the detector centred at the laser emission wavelength.	20 nm

Table 2-4. LOAS detector parameters.

The noise value stated in Table 2-4 was calculated assuming a background power of 10 Watt/m^2/sr/μm. As described before, signal pre-amplification in the Detector Assembly is performed by an automatic controlled gain amplifier that increases the system sensitivity as the elapsed time from the laser emission increases, in order to adjust the sensitivity on the basis of the expected return signal power in connection with the obstacle range. Therefore, the electrical noise of the pre-amplifier is not a constant value, but it varies in time with the gain. The value sated in Table 2-4 is applicable to 40% of the scanning time (i.e. 400 ms). For the remaining 60% of the scanning time the noise is so low with respect to the expected return power that it can be considered negligible for the computation of the false alarm rate. It also has to be considered that any calculation, arising from the stated values concerning false alarm rate and detection probability, only refers to single echoes and not to the overall performance of the system in terms of obstacle detection and false alarm delivery to the crew, which are strictly dependent on the processing algorithms of the Processing Unit.

2.5.1.2 LOAS Electronic-Processing Unit Functions

The LOAS EPU performs the following main functions:

- interfaces with the SHU via serial link in order to acquire the information related to echoes coordinates and attributes;
- processes the acquired information in order to detect, isolate and calculate position and characteristics of potential obstacles;
- computes display information and symbols data;
- provides the warning information to the Display Unit;
- interfaces with the Control Unit in order to receive commands and controls provided by the operator;
- manages communication data with other on-board equipment
- manages BIT procedures of the system

The EPU is realised integrating in a standard 3/8 ATIR (short) mechanical frame all the electronic sub-assemblies necessary to implement the functions described above. Particularly, the EPU comprises the following sub-assemblies:

- Processing Assembly. This assembly comprises the logic circuitry necessary to control the system, to analyse the information received by the SHU and to communicate the warning information to the Display Unit
- Interface Assembly. This assembly comprises the circuitry necessary for the electrical interface of the system and for data communication to external equipment.
- Power Supply Assembly. This assembly comprises the circuitry necessary to fulfil all the DC requirements of the EPU.

2.5.1.3 LOAS Processing Algorithms

In an obstacles detection and warning system, there is the need to provide the pilot only with the essential information. The scanner system, in fact, detects the position of every potential obstacle in the environment where the helicopter is moving. In a generic scenario, with many obstacles in the field of view of the warning system, it may be difficult to control them for the pilot. For this reason, a system able to discriminate the most dangerous obstacles and to supply the relative information to the pilot, is required. To solve this problem, three algorithms have been developed for incorporation in the LOAS EPU:

- calculation of future trajectory;
- calculation of intersections with the obstacles;
- determination of alternative (optimal) trajectory.

To validate the algorithms, a simulation environment and actual flight tests were performed. The experimental results obtained allowed both verification and refinement of the processing performance. More details the ground and flight test activities performed with the LOAS system are given in the chapters 8 and 9.

2.5.1.4 Obstacle Detection and Classification Algorithms

As described before, the LOAS anti-collision system performs obstacle detection based on the laser radar technique. Once the echoes energy has been optically collected, obstacle detection/classification is performed through an analog detection of the echoes and two successive analysis processes. The first process, named "Pre-processing", is performed at a very high rate during the echo acquisition in order to obtain single-echo specific data and to characterize it on the basis of local range contrast analysis with respect to nearby echoes. The second process, named "Processing", is

performed at a lower rate and manages groups of pre-processed echoes in order to achieve, by a two step analysis, the final obstacle recognition and classification [12].

The LOAS incorporates two different types of processing algorithms: the first is optimised to process echoes generated by thin objects, like wires and poles, the second is optimised to process all echoes generated by extended obstacles, like houses, trees, woods and other solid objects. These algorithms identify the boundaries of the obstacles; additional geometrical criteria allow to distinguish "wire-class", "tree/pole class" and "extended class" obstacles. In order to perform their tasks, the LOAS processing algorithms make use of image and data segmentation and data validation [11]. Fig. 2-22 shows the three levels of processing algorithms, conceived and optimised for the scanned elliptical scanning pattern described before.

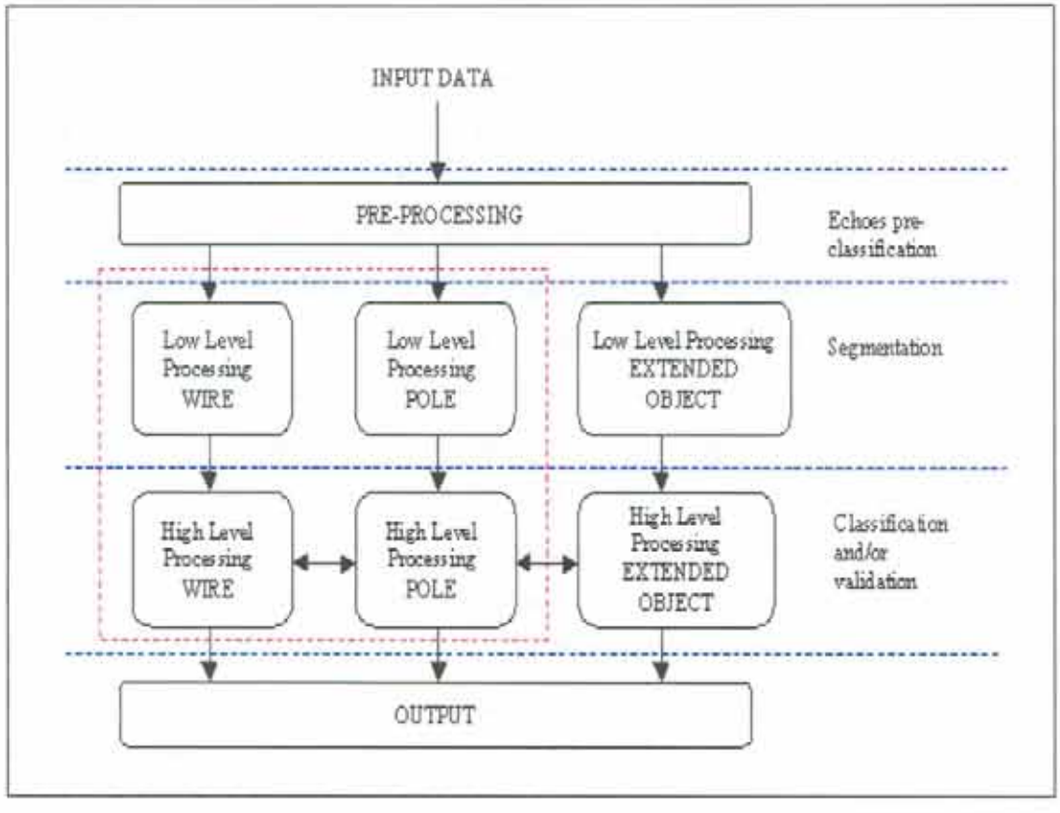

Figure 2-22. LOAS three levels processing algorithms.

The thin-object classification algorithm (for wire and tree/pole classes of objects) works on a subset of echoes of the current frame. It processes only the echoes whose attributes, defined by the pre-processing algorithms, are "weak echo" and "thin object". An initial geometric analysis is performed on pre-processed data to initially separate wire class obstacles and tree/pole obstacles. Image segmentation is the process of dividing the image into areas where the echoes are characterised by relatively "aligned" range data and possible thin obstacles are extracted from this subset of data. After image segmentation, the different clusters must be validated. This means that the detected echoes are processed by a statistical algorithm to determine if the obstacles are generated by real "aligned" echoes or by noising data.

Also the algorithm dedicated to classification of extended objects is divided in two different steps: echoes classification and segmentation. The echoes with pre-processing "extended object" attributes need to be processed by a dedicated selection algorithm because many of these are not generated by real extended obstacles. A well-defined number of echoes, acquired in a short time interval, have some common geometric characteristics which can be extracted. With these additional information, the data are passed to the segmentation algorithm, where the different clusters are rearranged and validated with suitable statistical algorithms [11].

The results of the developed processing algorithms were tested with experimental data, acquired with a sensor prototype, and then displayed/analysed with the LOAS Debugging Interface (LDI). With commands available in the LDI, the user could change the key parameters defining the processing algorithms, so that their optimal values could be determined observing the experimental results. An example of the debugging interface is shown in Fig. 2-23.

Processing experimental data collected on the ground, it was initially verified that the algorithms were capable of detecting and classifying the different obstacles. Furthermore, thanks to the flight test activities performed on helicopters, the key parameters were definitively set and optimised.

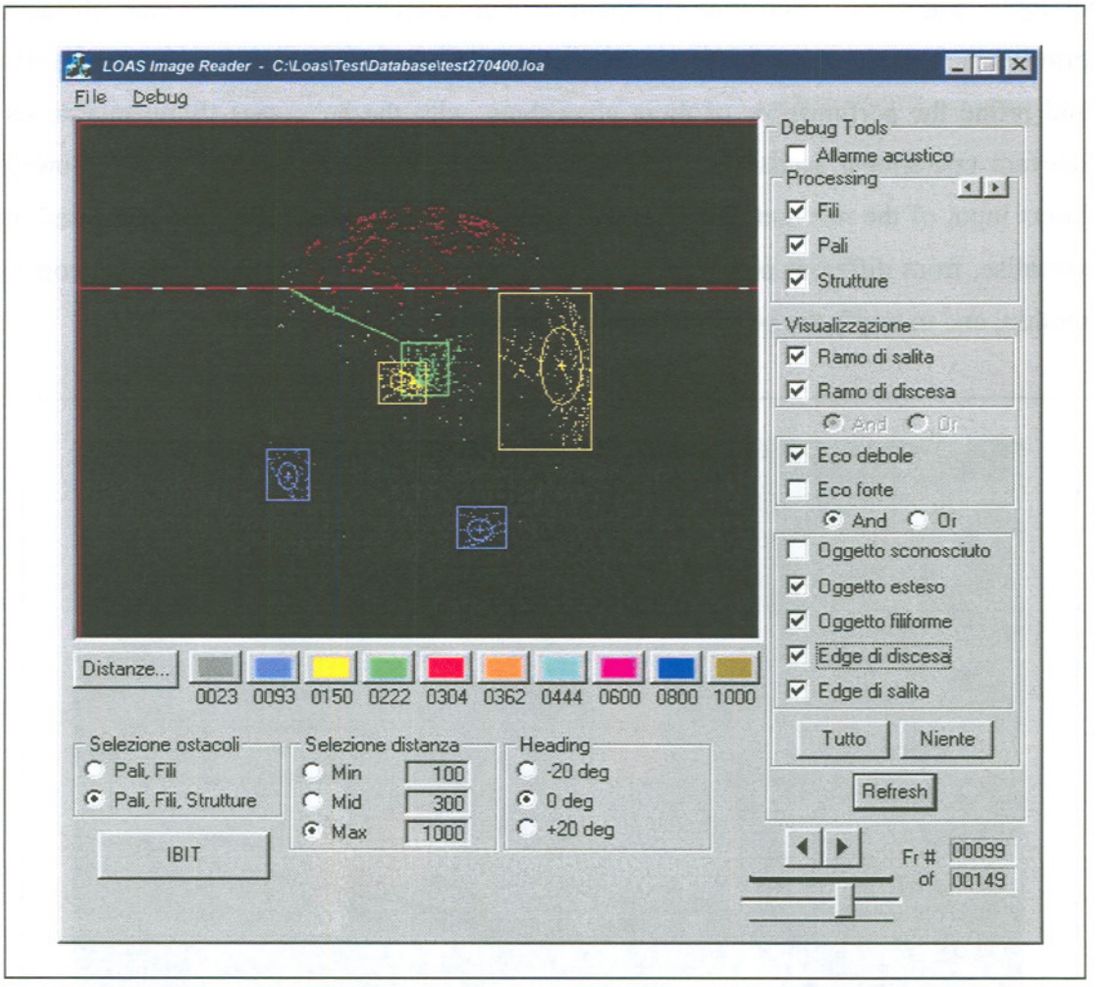

Figure 2-23. LOAS experimental data analysis debugging Interface.

2.5.1.5 Obstacle Prioritisation Algorithms

In a laser obstacle detection and warning system, there is also the problem of providing only essential information to the pilot. The LOAS system, in fact, detects the position of every potential obstacle in the environment where the helicopter is moving. In a generic scenario, with many obstacles in the field of view of the warning system, it may be difficult for the pilot to monitor all of them. For this reason, a system able to discriminate the most dangerous obstacles and to supply the relative information

is required. To solve this problem, three algorithms have been implemented: calculation of future trajectory, calculation of possible intersections with obstacles, and obstacle prioritisation [11]. A three-dimensional simulation environment was required to test and refine the performance of these algorithms, with the helicopter flying in various relevant operational scenarios. This simulation environment (see Fig. 2-24) allowed direct input of the relevant obstacles and helicopter flight parameters, and permitted to visualise, from different points of view, the scene scanned by the laser, the helicopter motion, and to verify the possible intersections with the obstacles [12].

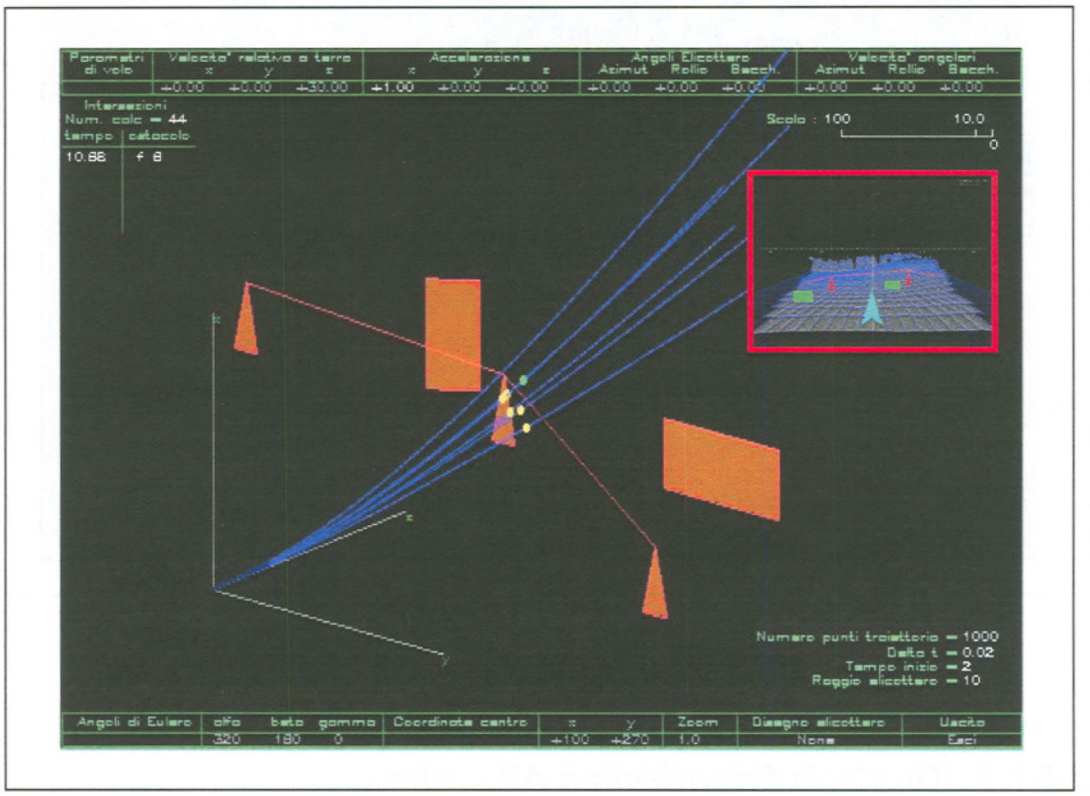

Figure 2-24. LOAS simulation environment.

2.5.1.6 LOAS History Function

Due to the restricted system field of view, during helicopter motion some information acquired in the previous frames may be lost successively. To keep

obstacles information when they are outside the present frame, it is necessary to store the position of every object detected and then update the coordinates with respect to the helicopter body-fixed reference system. The LOAS History Function stores data relative to the detected obstacles for a time interval which is dependent on helicopter velocity, and deletes them when they are outside the helicopter possible trajectories (outside its flight envelope). Since the motion data supplied from the navigation system are, like every measure, affected by errors, it is necessary to evaluate how these errors affect the positions calculated for every obstacle. To do so, appropriate *Gaussian* errors are added to every data and the statistics of the resulting position errors are calculated for obstacles near and far from the aircraft. When the impact warning processing establishes that the trajectory currently flown by the aircraft has a collision risk, the algorithm searches the corrections necessary to avoid the obstacles, and provides the pilot with an indication about the alternative (optimal) direction to fly [11, 12]. The optimal trajectory is the one having the minimum correction (necessary to avoid the obstacles) and which is compatible with a safe flight path.

2.6 References

1. THOMSON-CSF Optronique, "Convertible Laser Designation Pod Technical Description". Doc. LSA 95/086. Ed. 1995.
2. Sabatini R., Richardson M., "System Integration and Flight Testing of a Laser Designation Pod and Laser-guided Bombs on the Italian Interdiction Strike Aircraft". Journal of Battlefield Technology (Vol. 4 – n° 2). July 2001.
3. ELOP Electro-optics Industries. PLD SYSTEM "Operation and Operator Level Maintenance Technical Manual for the Italian Armed Forces". Doc. TM-8335-0060-90. Ed. 2001.
4. Raytheon Industries. "Paveway II System Description". Public release version. Ed. 1994.
5. Raytheon Industries. "Paveway III System Description". Public release version. Ed. 1999.
6. ELBIT Industries. "LIZARD Technical Manual". Ed. 2001.

7. Kellington C.M., "An Optical Radar System for Obstacle Avoidance and Terrain Following". AGARD CP-148. 1986.
8. Hogg G.M., Harrison K. and Minisclou S., "The Anglo-French Compact Laser Radar Demonstrator Programme". AGARD-CP-563. 1995.
9. Büchtemann W. and Eibert M., "Laser Based Obstacle Warning Sensors for Helicopters". AGARD-CP-563. 1995.
10. Holder S.L. and Branigan R.G., "Development and flight testing of an Obstacle Avoidance System for the U.S. Army Helicopters". AGARD-CP-563. 1995.
11. Marconi Communications Systems. "LOAS Technical Specification". 1999.
12. Sabatini R., Roviaro E., "Development of a Laser Collision Avoidance System for Helicopters: Obstacle Detection/Classification and Calculation of Alternative Flight Paths". NATO RTO-SET Symposium "Complementarity of Ladar and Radar". Prague (Czech Republic). 22-23 April 2002.

Chapter 3

LASER SYSTEMS PERFORMANCE

3.1 General

A fundamental problem in laser systems performance analysis is determination of the total optical power that is present at the receiver aperture (case of LADAR and LRF) or LGW seeker (case of LTD) and, consequently, the total optical power incident on the photosensitive element of the receiver: the detector. The laser range equation is used to determine the power received under specific conditions and against a particular target. For laser systems performance analysis specific models are also needed for atmospheric propagation, target reflection, detection performance, etc..

In general, a laser beam is attenuated as it propagates through the atmosphere. In addition, the beam is often broadened, defocused, and may even be deflected from its initial propagation direction. The attenuation and amount of beam alteration depend on the wavelength of operation, output power and characteristics of the atmosphere. When the output power is low, the effects are linear in behaviour (absorption, scattering, and atmospheric turbulence are examples of linear effects). On the other hand, when the power is sufficiently high, new effects are observed that are characterised by non-linear relationships (e.g., thermal blooming, kinetic cooling, bleaching, and atmospheric breakdown). In both cases, the atmospheric effects can be significant and severely limit the usefulness of the beam.

Another key element of laser systems performance analysis, is the knowledge of target reflection properties. In general, the reflectivity of a surface can be expressed by two components: the specular component and the diffuse component. The specular component is the energy that reflects away from the surface at the opposite

of the angle of incidence with the exit beam remaining narrow. The diffuse (*Lambertian*) component, on the other hand, is the energy reflected in all directions with a maximum along the normal to the target surface and falling off as a function of the cosine of the angle off of surface normal.

In most practical cases, target surfaces are very rough at laser wavelengths and, consequently, the diffuse scattering component frequently dominates (in some cases, however, significant specular components are observed). Furthermore, most targets exhibit a marked dependency of the overall scattering characteristics on the illumination incidence angle.

In this chapter, some theoretical background is given of laser systems performance analysis, including discussions about mission performance requirements, atmospheric propagation and target reflection properties.

3.2 Laser Range Equation

The classical forms of the laser range equation, applicable to extended, point and linear ("wire" type) targets are presented in Appendix B. Furthermore, various considerations are presented relative to laser radar systems detection performances. Particularly, the signal-to-noise ratio (SNR) equations applicable to both coherent and incoherent detection laser radar system are presented, and the influence of both background and system/detector noise terms on the overall systems performance are investigated.

The range equations presented in Appendix B assume that the transmitter and receiver are collocated and have the same optics diameter. In some cases (e.g., for LTD/LGW combinations), these assumptions are not valid and other forms of the range equation need to be developed.

3.2.1 Range Equation for Airborne LTD/LRF Systems

With reference to the geometry of a typical ground attack mission with laser guided weapons shown in Fig. 3-1, the range performance of an LTD system can be estimated using the procedure described below [2].

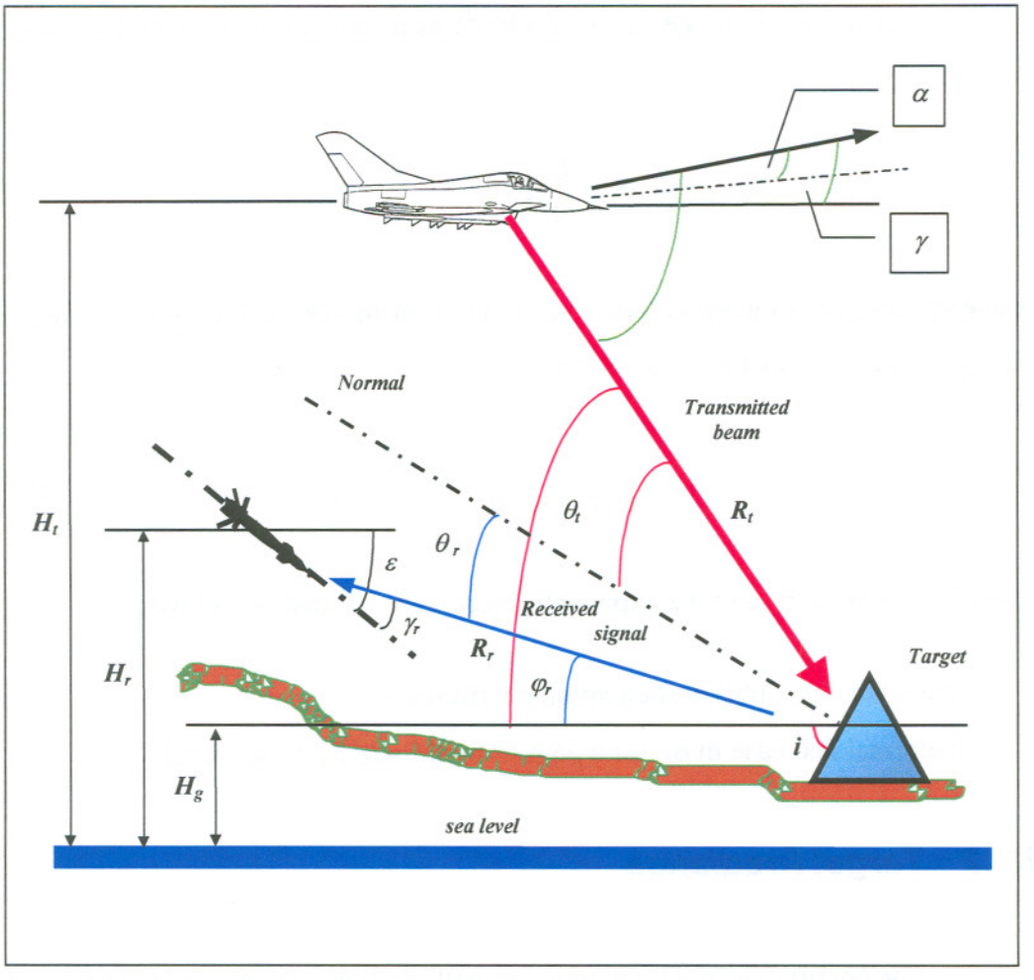

Figure 3-1. LTD/LGW mission geometry (vertical profile).

3.2.1.1 Energy Density on the Target

The laser beam area at a distance R_T is given by:

$$A_b = \frac{\pi\left(D_L + \alpha_T R_T\right)^2}{4} \tag{3.1}$$

where:

D_L = Transmitted beam diameter (m);

α_T = Output laser beamwidth (rad).

The energy density at the target location (J/m^2) as a function of transmitted energy (U) is given by:

$$F = \frac{U}{A_b} e^{-(\sigma_w \alpha_{Ht} R_T)} \tag{3.2}$$

This energy density is measured normally to the transmitter line of sight. Using eq. (3.1), eq. (3.2) can be written in the form:

$$F = \frac{4U}{\pi (D_L + \alpha_T R_T)^2} e^{-(\sigma_w \alpha_{Ht} R_T)} \tag{3.3}$$

The parameters appearing in the exponential factor are defined as follows:

σ_w = sea level atmospheric attenuation coefficient;

α_{Ht} = fractional decrease in σ_w for a path from altitude H_t to sea level.

3.2.1.2 Target Irradiance

The energy (G) of a laser spot that will irradiate a given target surface (A) is that portion passing through the projected area (A_N) in the plane orthogonal to the sight line. Therefore, the irradiance of the target surface can be calculated using the equation:

$$G = F \frac{A_N}{A} \tag{3.4}$$

and, using the eq. (3.2):

$$G = \frac{U A_N}{A_b A} e^{-(\sigma_w \alpha_{Ht} R_T)} \tag{3.5}$$

or:

$$G = \frac{4 U A_N}{A \pi (D_L + \alpha_T R_T)^2} e^{-(\sigma_w \alpha_{Ht} R_T)} \tag{3.6}$$

As $A_N = A\cos\theta_t$, we also have:

$$G = \cos\theta_t \frac{4U}{\pi\left(D_L + \alpha_T R_T\right)^2} e^{-(\sigma_w \alpha_{HT} R_T)} \tag{3.7}$$

where θ_t is the incidence angle to the target surface as measured from the sight line to the target normal.

3.2.1.3 Target Brightness

The brightness of the irradiated target is determined by the irradiance level and by the reflectance characteristics of the target surface.

The laser energy reaching the target is partially absorbed and partially reflected, either specularly and diffusely. The probabilities of each of these occurrences are called the coefficients of absorption, specular reflection, and diffuse reflection, and must satisfy: $C_a + C_s + C_d = 1$. More details about target reflection properties are given in successive sections of this chapter. Assuming now that a the target is a perfectly diffuse reflector, with a *Lambertian* radiation pattern, the brightness (B) is given by:

$$B = \frac{\rho_T G}{\pi} \tag{3.8}$$

where ρ_T is the target reflectivity.

3.2.1.4 Energy at the Receiver

The energy (E_R) collected by a receiving aperture observing this target is obtained from the expression:

$$E_R = \frac{B A_R A_M}{R_R^{\,2}} e^{-(\sigma_w \beta_{HR} R_R)} \tag{3.9}$$

where:

A_R = receiver aperture area;

A_R/R_R^2 = solid angle subtended by the receiving aperture;

A_M = projected spot area in the plane normal to the receiver sight line;

β_{HR} = fractional decrease in σ_w for a path from sea level to H_R.

A_M is related to the target laser spot area by:

$$A_M = A\cos\theta_r \tag{3.10}$$

Therefore, the final expression for energy density (I) at the receiver aperture for the *Lambertian* target is, by substitution:

$$I = \frac{E_R}{A_R} \qquad (\mathrm{J/m^2}) \tag{3.11}$$

$$I = \frac{BA_R A_M e^{-(\sigma_w \beta_{HR} R_T)}}{R_R{}^2} \cdot \frac{1}{A_R} \tag{3.12}$$

$$I = \frac{G\rho_T A_M e^{-(\sigma_w \beta_{HR} R_T)}}{\pi R_R{}^2} \tag{3.13}$$

$$I = \frac{4U\cos\theta_t e^{-(\sigma_w \alpha_{HR} R_T)}}{\pi(D_L + \alpha_T R_T)^2} \cdot \frac{\rho_T}{\pi} \cdot \frac{A\cos\theta_r}{R_R{}^2} \cdot e^{-(\sigma_w \beta_{HR} R_R)} \tag{3.14}$$

$$I = \frac{4\rho_T UA\cos\theta_t \cos\theta_r e^{-[\sigma_w(\alpha_{HR} R_T + \beta_{HR} R_R)]}}{\pi^2 (D_L + \alpha_T R_T)^2 R_R{}^2} \tag{3.15}$$

If the seeker of the LGW is not turned towards the target, an additional cosine factor would be introduced reducing the effective receiving aperture as a function of the angle between the line of sight and the normal to the aperture (γ_R). Therefore, in general:

$$I = \frac{4\rho_T UA\cos\theta_t \cos\theta_r \cos\gamma_R e^{-[\sigma_w(\alpha_{HR} R_T + \beta_{HR} R_R)]}}{\pi^2 (D_L + \alpha_T R_T)^2 R_R{}^2} \tag{3.16}$$

If the transmitter and receiver a collocated (case of LRF), the equation can be simplified by setting:

$$H_r = H_t \qquad \beta_{HR} = \beta_{HT} \qquad \gamma_r = 0$$
$$R_r = R_t = R_o \qquad \theta_r = \theta_t$$

Therefore:

$$I = \frac{4\rho_T UA\cos^2\theta_t e^{-(2\sigma_w R_o \alpha_{HT})}}{\pi^2 (D_L + \alpha_T R_o) R_o^{\,2}} \tag{3.17}$$

The term $e^{-[\sigma_w(\alpha_{HR}R_T + \beta_{HR}R_R)]}$ in eq. (3.16) represents the two-ways atmospheric transmittance for the general case (i.e., transmitter and receiver not collocated), denoted as τ_{atm} in the rest of this thesis. The term $e^{-(2\sigma_w R_o \alpha_{HT})}$ in eq. (3.17) represents the two-ways transmittance for the case of transmitter-receiver collocation (also denoted with τ_{atm} in this thesis).

The expressions derived can be used to evaluate the maximum range performance of a LRF or LTD system, by substituting the various transmitter and receiver parameters, and solving for R_t and R_r. For this purpose, the Minimum Detecatable Energy Density (MDED) at the receiver aperture is substituted for energy density in the Eq. (3.16) or (3.17). From a practical point of view, the difficulties of this approach for operational-level performance analysis are represented by the calculation of τ_{atm} (a function of R_T , R_R, visibility, humidity, altitude, grazing angle, etc.), the knowledge of the target characteristics (i.e., shape, reflectivity, etc.) and, very often, the unavailability of technical data on the seeker-head detectors and active laser systems.

Since the physical characteristics of the target are often known before performing an attack and the target is generally extended at ranges of practical interest, it is generally sufficient to use the diffuse reflectivity of the surface that will be illuminated, at the wavelength considered (e.g., 1.064 μm). Moreover, since the characteristics of target designators laser signals are standardised within NATO countries by the STANAG 3733, there is no much the system designer can do in order to enhance the performance of a designating system, except than increasing the output power of the system and reducing the beam divergence. On the other hand,

some laboratory experiments (see chapter 8 of this thesis) have shown that direct measurement of the seeker minimum detectable energy is possible, directly using the seeker and a relatively simple instrumentation.

In most cases, it is therefore possible to estimate the performance of a LRF/LTD system as long as the atmospheric propagation of the laser beam can be adequately modelled. This is not an easy task, especially taking into account the considerable variation that the atmospheric parameters may experience during real missions and for propagation paths that may exceed 10-15 km.

Additional parameters to be considered are the transmitting and receiving optics losses and the limited integration time of the detection circuits. When the target is an extended horizontal surface, for example, the laser can illuminate target areas whose slant range varies significantly. This is especially true when the laser is operating from low altitudes (i.e., low grazing angles). The result is to cause target reflections from a given pulse transmission to be received during a relatively long time interval compared to the transmitted pulsewidth. Receiver sensitivity, in terms of the capability of detecting a given reflected energy, is degraded when the received pulse duration is longer than the receiver integration time. In fact, when the detector is a peak reading threshold detector, only the energy received during an integration period contributes effectively in achieving detection. Although the integration output does continue to rise as long as energy is being received, the rate of rise is so slight that precise timing of the threshold crossing becomes impossible in the presence of receiver and background noise. Accordingly, the energy received after expiration of the integration time is useless in determining target range or performing other timing functions. The end effect is reduced receiver sensitivity.

3.3 Laser Beam Atmospheric Propagation

Many studies have been undertaken for characterising and modelling linear and non-linear atmospheric propagation effects on laser beams. In the following paragraphs, only a brief introduction to the fundamentals of laser beam propagation is presented, with emphasis on those phenomena affecting the peak irradiance at the target. Furthermore, an outline is presented of the empiric models currently used by the Italian Air Force for PILASTER test/training operations (i.e.,

mission planning, safety studies and performance analysis) with ground/airborne laser systems. A more complete discussion of laser beam propagation physics is presented in Appendix C.

3.3.1 Atmospheric Transmittance

Attenuation of laser radiation in the atmosphere is described by the Beer's law:

$$\tau = \frac{I(z)}{I_0} = e^{-\gamma z} \tag{3.18}$$

where τ is the transmittance, γ is the attenuation coefficient, and z is the length of the transmission path. If the attenuation coefficient is a function of the path, then eq. (3.18) becomes:

$$\tau = e^{-\int_0^z \gamma(z)dz} \tag{3.19}$$

The attenuation coefficient is determined by four individual processes: molecular absorption, molecular scattering, aerosol absorption, and aerosol scattering. The atmospheric attenuation coefficient is:

$$\gamma = \alpha_m + \beta_m + \alpha_a + \beta_a \tag{3.20}$$

where α is the absorption coefficient, β is the scattering coefficient, and the subscripts m and a designate the molecular and aerosol processes, respectively. Each coefficient in eq. (3.20) depends on the wavelength of the laser radiation.

We find it convenient at times to discuss absorption and scattering in terms of the absorption and scattering cross sections (σ_a and σ_s, respectively) of the individual particles that are involved. Thus, we can write:

$$\alpha = \sigma_a N_a \tag{3.21}$$

and

$$\beta = \sigma_s N_s \tag{3.22}$$

where N_a and N_s are the concentrations of the absorbers and scatterers, respectively. In the absence of precipitation, the atmosphere contains finely dispersed solid and liquid particles (of ice, dust, aromatic and organic material) that vary in size from a cluster of a few molecules to particles of about 20 μm in radius. Particles larger than this remain airborne for a short time and are only found close to their sources. Such a colloidal system, in which a gas (in this case, air) is the continuous medium and particles of solid or liquid are dispersed, is known as an aerosol. Aerosol attenuation coefficients depend considerably on the dimensions, chemical composition, and concentration of aerosol particles. These particles are generally assumed to be homogeneous spheres that are characterized by two parameters: the radius and the index of refraction.

In general, the index of refraction is complex. Therefore, we can write:

$$\tilde{n} = n - ik = n\left(1 - i\frac{k}{n}\right) = n(1 - i\kappa) \tag{3.23}$$

where n and k are the real and imaginary parts and $\kappa = k/n$ is known as the extinction coefficient. In general, both n and k are functions of the frequency of the incident radiation. The imaginary part (which arises from a finite conductivity of the particle) is a measure of the absorption. In fact, k is referred to as the absorption constant. It is related to the absorption coefficient α of eqs. (3.20) and (3.21) by:

$$\alpha = \frac{4\pi f k}{c} \tag{3.24}$$

where c is the speed of light in a vacuum and f is the frequency of the incident radiation. For the wavelength range of greater interest in laser beam propagation (the visible region to about 15 μm) the principal atmospheric absorbers are the molecules of water, carbon dioxide, and ozone. Attenuation occurs because these molecules selectively absorb radiation by changing vibrational and rotational energy states. The two gases present in greatest abundance in the earth's atmosphere, nitrogen (N_2) and oxygen (O_2), are homonuclear, which means that they possess no electric dipole moment and therefore do not exhibit molecular absorption bands.

is the distortion parameter for a collimated *Gaussian* beam of 1/e radius a_0 and uniform wind velocity v_0 in the weak attenuation limit ($\gamma z << 1$). The quantities n_T, d_0 , and c_p are, respectively, the coefficients of index change with respect to temperature, density, and specific heat at constant pressure, and P and z are the laser output power and range, respectively.

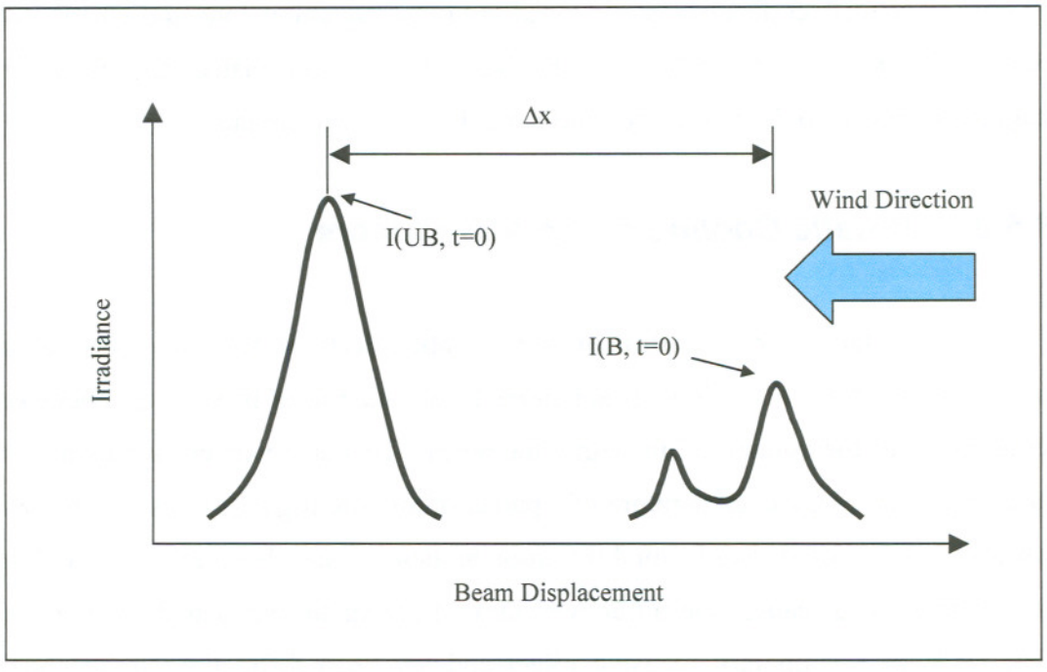

Figure C-16. Irradiance distribution before (t=0) and after blooming (t>0), with wind causing the beam to be deflected from its initial position by the amount Δx into the wind direction.

The expression in brackets in eq. (C.48) accounts for the finite attenuation of P with increasing z, the focusing or divergence of the beam, and the non-uniform velocity in the case of slewing. The focused beam profile is given by:

$$a(z') = a_0 - (a_0 - a)\frac{z'}{z} \tag{C.50}$$

where a is the undistorted beam radius at the focal plane, and the wind velocity due to slewing is given by:

$$v(z') = v_0 + \omega z' \tag{C.51}$$

where ω is the slew rate (assumed to be in the direction opposite the wind).

A problem associated with beam slewing arises when the beam is slewed in the direction of the wind. In this case, at some position along the beam a condition is reached where the beam is moving at the same speed as the wind. At this position, called the stagnation zone, the beam undergoes strong thermal blooming. The severity of this effect depends on the location of the stagnation zone and whether the beam is focused or collimated. If the beam is well collimated, the closer the stagnation zone is to the transmitter, the more the beam will spread.

3.5.2 Kinetic Cooling of the Atmosphere

So far in our description of thermo-optic effects we have assumed that the energy removed from the laser beam immediately manifests itself as an increased temperature of the column of air within the beam. This is, however, not always the case. For example, the temperature of a parcel of air entering a CO_2 laser beam may initially drop before it rises beyond the ambient temperature. Such transient cooling, or kinetic cooling, causes the refractive index of the air to rise near the beam axis. This leads to a temporary focusing effect and less than diffraction limited beam spreading. Of course, the cooling cannot last for very long, since energy absorbed by atmospheric gases (momentarily stored in molecular vibrations) ultimately is converted to kinetic motion that manifests itself as an increase in the gas temperature (atmospheric nitrogen plays an important role in this process).

With a water vapour concentration relatively low (such as it is at higher altitudes), the kinetic cooling has been estimated to last for more than 0.2 sec by Wood et al. [21]. On the other hand, at sea level on a moist day the heating rate of the air may be only slightly affected by kinetic cooling. The same authors have also calculated the difference between temperature within the beam and the ambient temperature (see Fig. C-17). It is important to note that the amount and duration of the cooling are actually quite small. Typical cooling times vary from a few milliseconds to a fraction of a second, and temperature differences are of the order of 10^{-2} °K. Since the cooling times are much longer than typical laser pulse durations, the effects of kinetic cooling on beam spreading may be significant in pulsed operation.

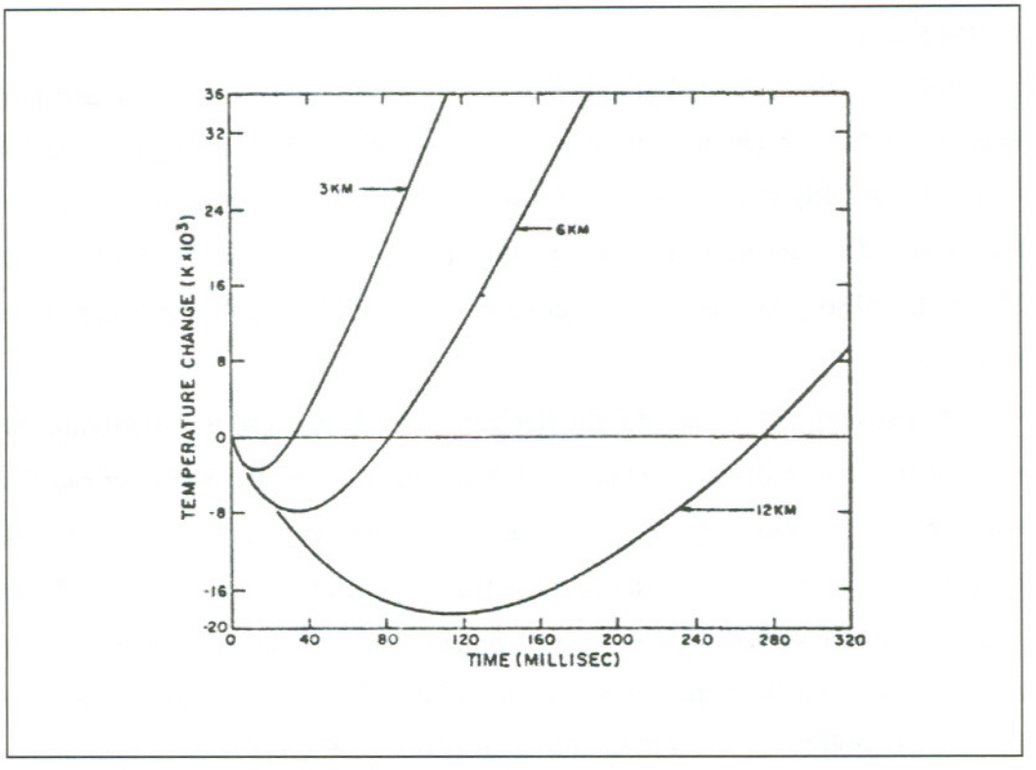

Figure C-17. Temperature change due to kinetic cooling for various altitudes.

In general, if a wind is blowing (or the beam is slewed), air at ambient temperature is constantly entering the beam. The extent to which it is cooled or heated will depend on the relaxation rate of nitrogen and on the amount of time that the unit volume of air is in the beam. Therefore, if the parcel of air is cooled and has passed through the beam before it can heat up, better than diffraction limited beam propagation is possible.

3.5.3 Bleaching

In the preceding section we considered thermo-optic phenomena for laser beams with pulse durations t that were longer than the hydrodynamic time w/v_s , where w is the beam spot size and v, is the speed of sound. By using pulses of time duration $t << w/v_s$, the deleterious effects of the thermo-optic phenomena may be removed entirely. However, pulses of such short duration (about 1 to 5 μsec) may under certain conditions saturate the absorption mechanism and thereby reduce the

atmospheric transmittance. The saturation of the absorption mechanism is referred to as "bleaching".

In general, low irradiance pulses are strongly altered in both pulse shape and pulse energy, while high irradiance pulses are deformed only on the leading edge and the pulse is only weakly attenuated. Fig. C-18 shows the relative absorption coefficient for a 4 μsec CO_2 laser pulse for various irradiances [3]. The figure shows that at 1 MW/cm^2 the absorption coefficient can drop to 10% of its low-power value in less than 1 μsec.

Evidently, bleaching of the absorption mechanism holds promise for improving laser beam transmission in the atmosphere. For example, for the 10.6 μm laser radiation in the atmosphere, bleaching of the CO_2 absorption mechanism can occur for pulse durations less than $t \sim 3.5\times10^{-4}$ sec and irradiance values larger than $I \sim 10^5$ W/cm^2, as long as the atmospheric water vapour content is negligible. For other radiation sources, the specific absorption processes must be individually looked at in order to judge the feasibility of saturating the absorption coefficient with short, intense pulses.

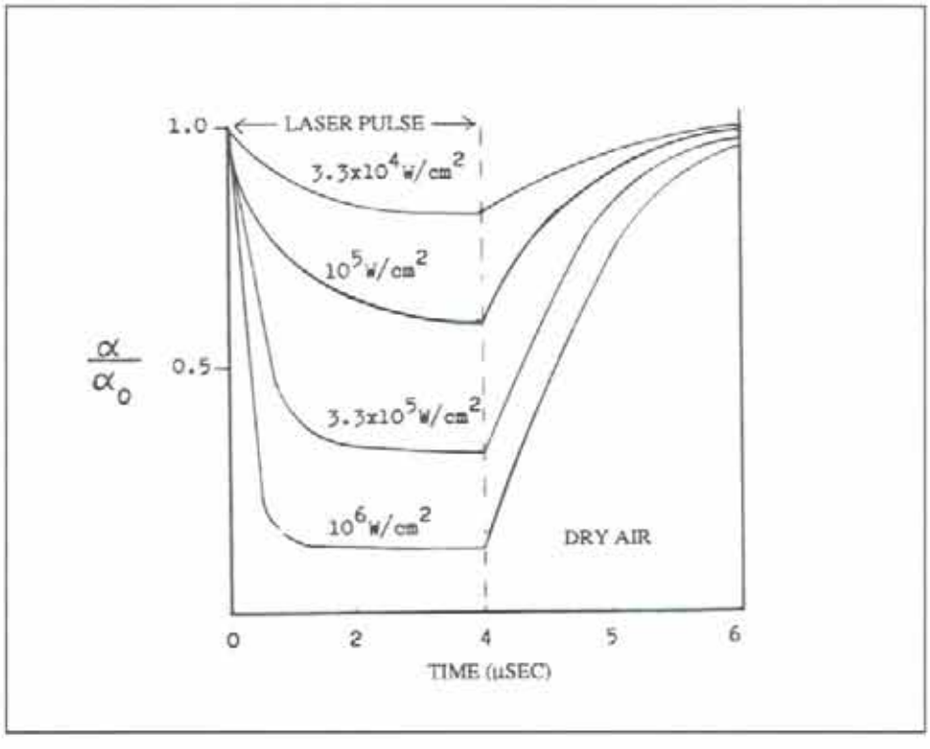

Figure C-18. Fractional absorption coefficient as a function of time for a 4 μsec square pulse.

3.6 Aerodynamic Effects

It is beyond the scope of this appendix to described in depth the influences of aerodynamics on optical systems. However, some of the basic principles more relevant to airborne laser systems are described in this paragraph. Optical aberrations resulting from aerodynamic flow fields can be placed in two categories :

- viscous flow phenomena including laminar and turbulent boundary layers, shear layers, and wake turbulence;

- inviscid or potential flow, arising from the acceleration of (compressible) fluid, generally along the fuselage contours or around protuberances.

For wavelengths ranging from the visible to the mid-IR, flush-mounted material windows generally can be employed to shield the optical components from the external aerodynamic flow field. An exception may occur if a high-power laser is to be transmitted through the window; in this case, thermal-induced distortions or potential damage may preclude its use. If such installations are feasible, then the aeromechanical issue is only associated with the aircraft motion. The resulting aero-optical performance is driven by the aerodynamic flow field that exists over the external portion of the aircraft and window itself. These aerodynamic flow fields, if laminar, tend to be relatively benign and are influenced by the mean flow field that exist over the aerodynamic contours. However, if the surface boundary layer over the window is turbulent, as is more likely in operational settings, the resulting unsteady air density variations (resulting in unsteady index of refraction fields) can yield significant optical aberrations [22].

For long-wavelength IR transmission and reception ($\lambda \geq 10\mu m$), a material window becomes much less attractive owing to optical transmission losses and window radiative effects. For such applications, cavities that are open to the surrounding aerodynamic flow field may be used. Also in this case, however, the AO flow field can cause a whole range of optical aberrations (e.g., considerable intensity reductions due to scattering, absorption, refraction and reflection by the AO interface, etc.). It is evident that an effective control of these aberrations is a prerequisite to any airborne

laser application. Once the basic requirements of an airborne laser system have been defined, some scaling relations may be used to prioritise the undesired AO effects, and various options need to be taken into account for ameliorating these effects (e.g., changing optics beam diameter or wavelength, tailoring the flow field, introducing advanced beam control techniques, etc.). Sometimes several approaches must be combined.

Random flow fields include turbulent boundary layers and shear layers, the latter being developed at a flow discontinuity (e.g., fuselage protuberance or recession). As reported in *Keith et al.* [22], the optical aberrations impressed on a beam transiting these random flows are determined by three aerodynamic parameters: the field fluctuating density ρ', the correlation length along the optical axis l_z, and the total path length through the disturbance L. The predicted wave-front variance, assuming isotropic turbulence, is given by [23]:

$$\sigma^2 = 2G^2 \int_0^L \left\langle \rho'^2 \right\rangle l_z dz \quad \text{for } l_z << L \tag{C.52}$$

with G being the Gladstone-Dale parameter [24], relating medium index of refraction to density fluctuations. If the condition $l_z << L$ is not fulfilled (e.g., in the case of shear layers), then the eq. (C.52) overestimates the actual aberrations.

In general, the complexity of the AO field for an airborne system increases with both the *Mach* number ($M = V/a$ where V is the fluid velocity and a the velocity of sound) and *Reynolds* number ($Re = VW/v$ where W is the size of flow pattern and v is the kinematic viscosity). For velocities below $M = 0.3$ compressibility effects are negligible and there are little optical aberrations. As M increases beyond 0.3, compressibility effects become important. The flow velocity, which is zero at the wall (airborne platform surface), and increase away from the wall to the free-stream velocity. The ensuing acceleration yields rotational flow near the surface, leading to either steady or unsteady density variations.

The flow is heated as it is compressed and accelerated from the free-stream velocity to stagnation at the wall. Assuming an adiabatic process, we can approximate this heating by [22]:

$$T_w = bT_0 \left[1 + r \frac{(\gamma - 1)}{2} M_0^2 \right] \tag{C.53}$$

where:

T_w = adiabatic wall temperature;

T_0 = free-stream temperature;

M_0 = free-stream *Mach* number;

r = recovery parameter (r = 0.85 laminar, 0.89 turbulent);

γ = adiabatic index (ratio of specific heat at constant pressure to that at constant volume). For most AO conditions of interest $\gamma \approx 1.4$ (air);

b = constant reflecting real gas effects. For $M_0<6$, $b \approx 1.0$; for $M_0 > 8$, $b \approx 0.5$.

As M_0 continues to increase, the fluid temperature and velocity changes induce increasing density changes. From eq. (C.52) we note that this yields greater optical aberrations. In the transonic regime ($0.8 \leq M \leq 1$), local supersonic flows (in which shocks appear) cause additional reflection and refraction effects. In the supersonic regime ($1 \leq M \leq 8$) the high stagnation temperatures can cause thermo-optical window distortions (in some cases a coolant is needed). In the transonic regime ($M >$ 8) dissociation and ionisation result from the gas heating. These plasmas introduce another level of optical distortion, with particularly strong vibrational absorption bands. In this regime, strong coupling between acoustical and turbulence fields occurs [22].

As already mentioned, boundary layers can be either laminar or turbulent, the first being characterised by smooth density variations (except for the case of external heating or cooling of the flow), and the second being characterised by a chaotic flow (although the chaos is known to be statistically definite). Extensive research has demonstrated that the magnitude of the density fluctuations in a turbulent boundary layer is driven by the difference between the density at the wall ρ_w and the free-stream density ρ_0 [25]. The density at the wall in the regime of no shock waves and assuming zero pressure gradient across the boundary layer is given by [22]:

$$\rho_w = \rho_0 \left[1 + r \frac{(\gamma - 1)}{2} M_0^2 \right] \tag{C.54}$$

Other relationships have also been developed for evaluating the optical effects for both subsonic flow and transonic/supersonic regimes.

For an inviscid flow, the density ratio from one streamline to another (no shock waves) is given by:

$$\frac{\rho_b}{\rho_a} = \left\{ \frac{1 + r\dfrac{(\gamma - 1)}{2} M_a^2}{1 + r\dfrac{(\gamma - 1)}{2} M_b^2} \right\}^{\frac{1}{\gamma - 1}} \tag{C.55}$$

Using this equation and the *Gladestone-Dale* relationship $N'=G\rho'$ (where n' is the index of refraction variation and ρ' is the density fluctuation), the corresponding optical phase $\Delta\phi$ can be determined, by integrating $\rho' \equiv |\rho_a - \rho_b|$ |through the disturbance in the z (optical axis) direction:

$$\Delta\phi = KG \int_0^L \rho' \, dz \tag{C.56}$$

where K is the wavenumber and L is the path length through the disturbance.

In the case of shock waves, the relationship between the densities ahead (ρ_0) and behind (ρ) the shock is:

$$\frac{\rho}{\rho_0} = \frac{(\gamma + 1) M_0^2 \sin^2 \theta}{(\gamma - 1) M_0^2 \sin^2 \theta + 2} \tag{C.57}$$

where θ is the shock angle at the optical axis. In general, it is a complex function of body shape, angle of attack and *Mach* number. No analytical scaling relationships are available for estimating this shock angle; however, Computational Fluid Dynamics (CFD) can yield useful approximations. The main disturbances introduced by shock waves in optical systems are: tracking errors, focal length variations and optical reflections at the shock interface [22].

More detailed discussions about inviscid and viscous/random flows, as well as shock waves effects on airborne systems performance may be found in the literature [22, 25, 26, 27].

3.7 Propagation Equation

For many applications, it is necessary to determine system performance in terms of the peak irradiance in the focal plane. In this section we describe a method for calculating the mean peak focal irradiance due to diffraction, random jitter, atmospheric turbulence, and thermal blooming.

We assume for convenience a *Gaussian* beam at the source and an average focused irradiance, which because of beam jitter and turbulence-induced spreading also has a *Gaussian* distribution. The peak irradiance for such a beam is [28]:

$$I_p = \frac{Pe^{-\gamma z}}{\pi\left(a_d^2 + a_j^2 + a_t^2\right)} \tag{C.58}$$

where P is the output power, γ is the attenuation coefficient, a is the *1/e* beam radius, and the subscripts *d, j,* and *t* refer to diffraction, jitter, and turbulence.

The contributions to the focal spot area due to diffraction, jitter, and turbulence are, respectively, given by:

$$a_d^2 = \left(\beta z\lambda / 2\pi a_0\right)^2 \tag{C.59}$$

$$a_j^2 = 2 < \theta_x^2 > z^2 \tag{C.60}$$

$$a_t^2 = \frac{4C_N^{12/5} z^{16/5}}{\lambda^{2/5}} \tag{C.61}$$

whereβ is the beam quality factor (i.e., the observed beam radius divided by the diffraction- limited radius), and $< \theta_x^2 >$ is the variance of the single axis jitter angle that is assumed to be equal to $< \theta_y^2 >$. In order to account for the thermal blooming effect, eq. (C.58) is multiplied by the factor R from eq. (C.47). Therefore, we have:

$$I_p = \frac{Pe^{-\gamma z}}{\pi\left(a_d^2 + a_j^2 + a_t^2\right)} \times \frac{1}{1 + 0.0625N^2} \tag{C.62}$$

Eq. (C.62) is the propagation equation for *Gaussian* beams. It has been used by *Gebhardt* [28] to compare the propagation of seven laser wavelengths for CW operation. The seven laser wavelengths chosen by *Gebhardt* are listed below:

- CO2 P(20) → $\lambda = 10.591$
- CO P4(15) → $\lambda = 4.989$
- DF P2(8) → $\lambda = 3.8007$
- HF P1(12) → $\lambda = 2.9573$
- Nd → $\lambda = 1.06$
- Ar → $\lambda = 0.5145$
- N2 → $\lambda = 0.3371$

The specific wavelengths chosen to represent HF, DF, and CO lasers are those with the best transmission characteristics. Only the mid-latitude winter and mid-latitude summer models were considered. The aerosol absorption and scattering data used were for clear (23-km visibility) and hazy (5-km visibility) conditions.

The results for the mid-latitude summer condition and an output power of 25 kW, with the laser beams focused at the range z = 3km and a uniform wind velocity of 10 mph (no beam slewing), are shown in Fig. C-19. The triangles and circles denote intermediate and strong turbulence levels, respectively, and the clear and hazy visibility conditions are indicated by open and solid symbols, respectively. The line connecting the pairs of like symbols for each wavelength indicates the variation in peak irradiance due to the variation in turbulence level. The line labelled vacuum is the ideal diffraction-limited peak irradiance that varies as λ^{-2}. For the CO_2, CO, and DF lasers, Fig. C-19 shows that the peak irradiance increases with decreasing wavelength for clear, moderate turbulence conditions. For the N_2, Ar, and Nd lasers, the peak irradiance is reduced significantly from the vacuum limit by the atmospheric effects of aerosol scattering and turbulence. It is interesting to note that for the CO_2 wavelength, which is dominated by thermal blooming due to stronger molecular absorption, the peak irradiance is relatively insensitive to both turbulence and aerosol effects. At the shorter wavelengths the effects of turbulence and aerosol attenuation produce wide variations in the peak irradiance.

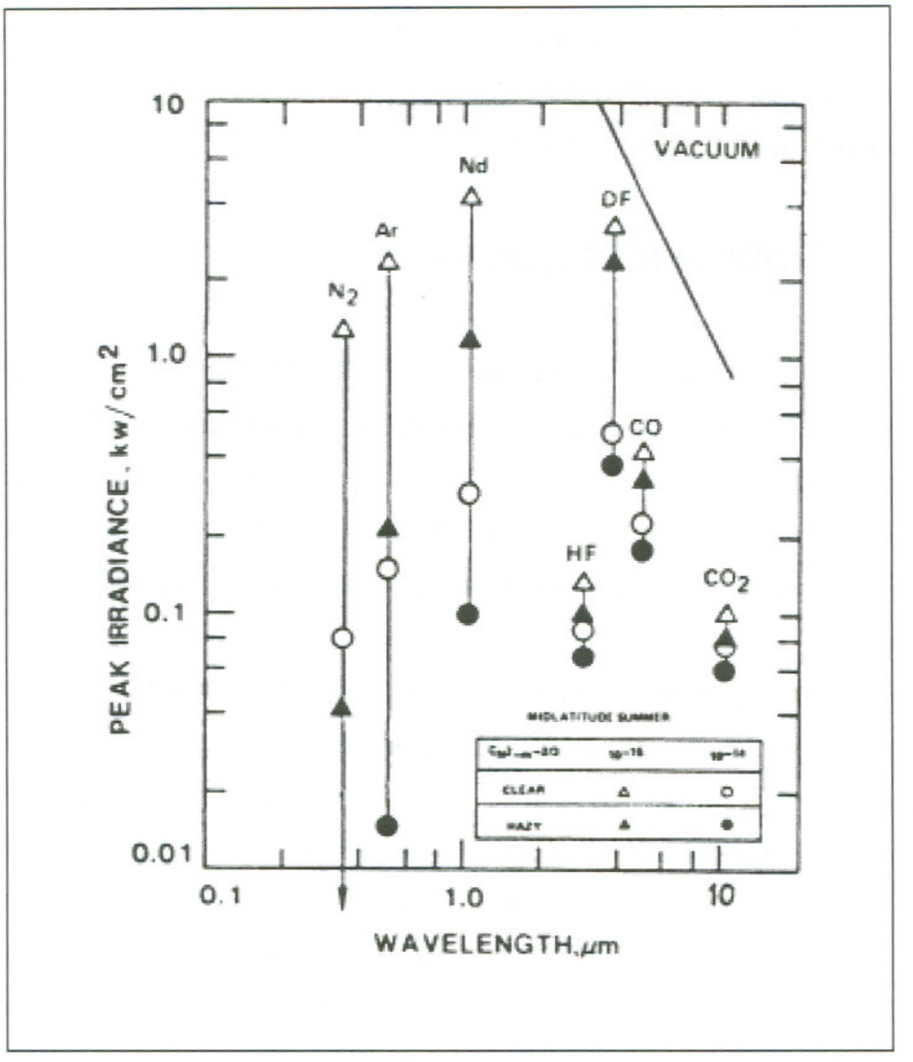

Figure C-19. ***Peak irradiance values of seven laser wavelengths for mid-latitude summer conditions. Identical laser and range characteristics are assumed for each wavelength.***

The importance of both aerosol scattering and turbulence effects clearly increases at the shorter wavelengths. The analysis conducted by *Gebhardt* shows that the near to mid-IR regions offer the best overall transmission characteristics; in particular, the 3.8-μm DF wavelength is optimum for varying aerosol and turbulence conditions.

In summary, the propagation of high-power laser beams through the atmosphere is affected by a host of optical phenomena. For CW beams the most significant phenomena are absorption and scattering by molecules (H_2O, CO_2, O_3, etc.) and aerosols, as well as atmospheric turbulence and thermal blooming. In general, thermal blooming tends to dominate the longer wavelengths (5-10 μm), while aerosol

and turbulence effects are more important at the shorter wavelengths and result in larger variations in peak irradiance in the focal plane as atmospheric conditions change. Some of these effects can be overcome by using laser pulses rather than CW beams and/or adaptive optical techniques.

3.8 Computer Programs

Over the last 25 years powerful tools for the assessment and exploitation of propagation conditions together with range performance models for military systems have become available. It is impossible to explain in depth and in a fully comprehensive way all available tools in this report. However, a selection of models is made, based on experience with sensor evaluation and adaptation to atmospheric conditions.

Due to the large number of parameters involved in optical transmission through the atmosphere, numerical calculations of atmospheric transmission is an unavoidable process. The aim of the numerical calculation is to predict with a high degree of accuracy the transmittance through the atmosphere, given a path, atmospheric conditions, wavelength, and a set of measured or predicted meteorological parameters. The computer codes applied here are transmission models or computational techniques implemented in computer programs that generate the transmittance or a transmittance spectrum, given the necessary input by the user.

Three numerical methods for atmospheric transmission calculations widely in use are LOWTRAN, MODTRAN and FASCODE, developed at the Air Force Geophysics Laboratory (AFGL), Hanscom AFB, Ma., USA, which is now the Phillips Laboratory, Geophysics Directorate.

FASCODE contains the molecular database HITRAN and is a high-resolution transmission code, whereas LOWTRAN is a low-resolution transmission code, whereas MODTRAN offers medium resolution. As new measurements became available and better understanding of the extinction process were reached, FASCODE and LOWTRAN were modified and updated in the last 20 years.

Once LOWTRAN became available other computer models, more specifically designed to simulate tactical battlefield situations, could be built around it. Such is the case for EOSAEL (Electro-Optical Systems Atmospheric Effects Library)

designed by the U.S. Army Atmospheric Sciences Laboratory which is now the U.S. Army Research Laboratory. EOSAEL offers many different modules for calculating the effects of battlefield-induced contaminants like smoke, high explosive dust, and vehicular dust. Various other modules are concerned with the effects of turbulence and with absorption and backscattering of laser radiation, effects of clouds and so on. Prediction of laser systems range performance is essential especially for mission planning purposes. It is not possible to describe all models in details here. Instead, some typical examples are given in the next paragraphs.

3.8.1 LOWTRAN

The latest versions of LOWTRAN covers the wavelength range from 0.2 μm in the ultraviolet to the millimetre wave region (0-50,000 cm^{-1}). The spectral resolution is 25 cm^{-1}. The computer program was designed as a simple and flexible band model that allows fast, reasonably accurate, low-resolution atmospheric transmittance and radiance calculations to be made over broad regions of the spectrum for any required atmospheric path geometry.

LOWTRAN also offers the possibility of radiance calculations including atmospheric self-emission, solar and/or lunar radiance single scattered into the path, direct solar irradiance through a slant path to space, and multiple scattered solar and/or self-emission radiance into the path.

3.8.2 MODTRAN

MODTRAN (MODerate resolution LOWTRAN), is a radiative transfer model with a spectral resolution of 2 cm^{-1} (FWHM) which has been developed based on the LOWTRAN 7 model. MODTRAN is identical to LOWTRAN except it contains another band model. Fig. C-20 shows a comparison of MODTRAN 2 and LOWTRAN 7 calculations for a slant path from 5 to 10 km height [29]. Validation studies, based on comparisons to FASCODE 2, have also indicated no significant discrepancies at 2 cm^{-1} resolution (FWHM).

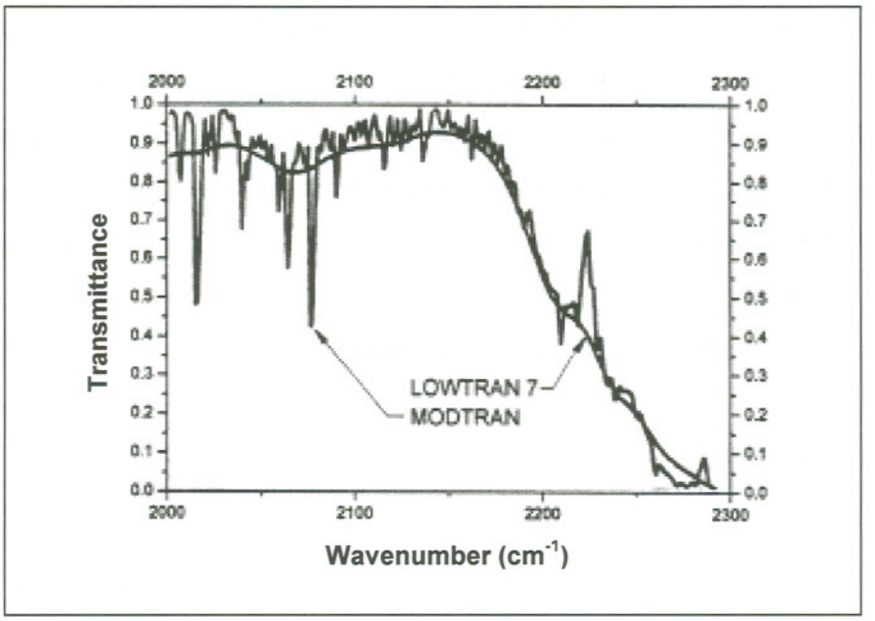

Figure C-20. Atmospheric transmittance for a slant path from 5 to 10 km at 15° from zenith and through U.S. standard atmosphere with no haze.

3.8.3 FASCODE

For studies involving the propagation of very narrow optical bandwidth radiation, such as lasers, the high resolution atmospheric transmission code FASCODE, also developed and maintained by the Phillips Laboratory, Geophysical Directorate, Hanscom AFB, Ma., can be applied. Characterisation of the aerosol and molecular continuum in FASCODE is much the same as that for LOWTRAN, The spectral molecular transmission is calculated by a line-by-line monochromatic calculation method. These resolution calculations require a detailed database (e.g., HITRAN) of spectral-line parameters. The Geophysics Directorate is the centre for establishing and maintaining the HITRAN database. FASCODE 3P is available also from ONTAR Corp. Brookline, Ma., USA, as PC-version. This is a menu-driven package that allows line file generation, creation of the input file for FASCODE, execution of the transmission calculations, and subsequent plotting of results. Fig. C-21 [30] shows the spectral transmission for an entire range of 850 to 1100 cm^{-1} of a sample calculation for a 100 km long slant path from an altitude of 6.096 km down to ground.

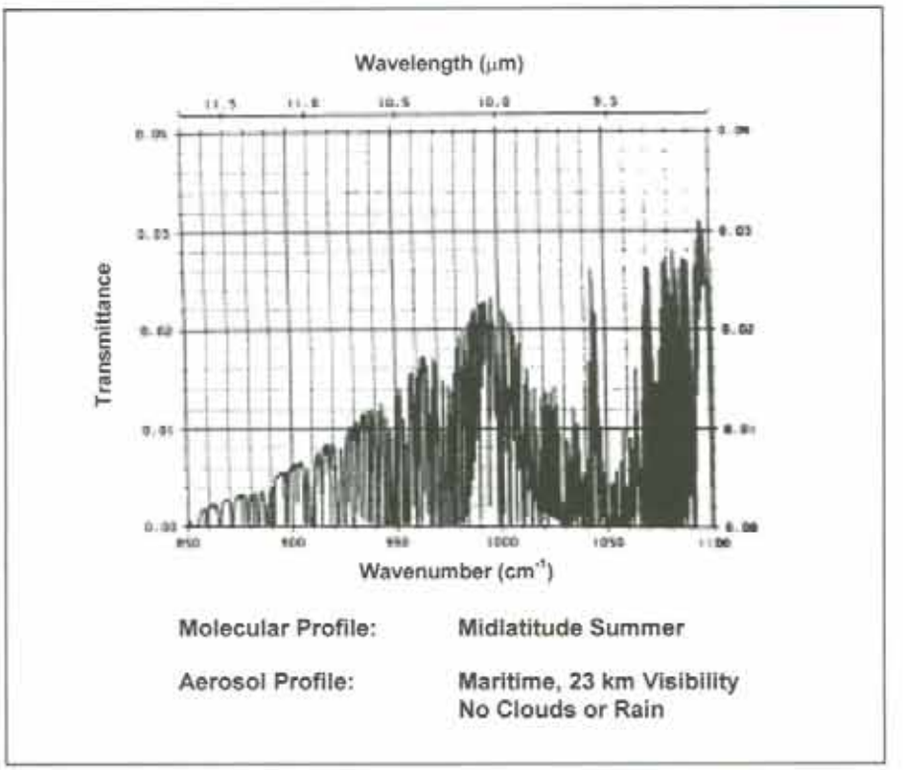

Figure C-21. FASCODE transmission estimates in the 850 to 1100 cm^{-1} range for a 100 km slant path from an altitude of 6.096 km down to ground.

3.8.4 EOSAEL

The Electro-Optical Systems Atmospheric Effects Library (EOSAEL) is a comprehensive library of computer codes specifically designed to simulate tactical battlefield situations. EOSAEL has been designed and steadily updated by the U.S. Army Atmospheric Sciences Laboratory, White sands, NM, which is now the U.S. Army Research Laboratory. EOSAEL is a state-of-the-art computer library comprised of fast-running theoretical, semi-empirical, and empirical computer programs (called modules) that mathematically describe various aspects of electromagnetic propagation in battlefield environments. The modules are connected through an executive routine but often are exercised individually. The modules are more engineering oriented than first-principles. The philosophy is to include modules that give reasonably accurate results with the minimum in computer time for conditions that may be expected on the battlefield. EOSAEL models comprise

clear air transmission, transmission through natural and man-made obscurants, turbulence, multiple scattering, contrast and contrast transmission, and others.

3.9 References

1. La Rocca A.J. and Turner R.E., "Atmospheric Transmittance and Radiance: Methods of Calculations". Environmental Research Institute of Michigan Ann Arbor. 1975.
2. Thomas M.E. and Donald D.D., "Atmospheric Transmission". ERIM-SPIE IR&EO Systems Handbook (Vol. 2 – Chapter 1). Second Printing. 1996.
3. Weichel H., "Laser Beam Propagation in the Atmosphere". Second Printing. SPIE Optical Engineering Press. 1990.
4. Electro-Optical Handbook. RCA Commercial Engineering. Harrison (N.J.). May 1968.
5. Barnhard E.A. and Streete J.L., "Atmospheric Aerosol Scattering Coefficient Measurements". Applied Optics - Vol. 6 (p. 1337). 1970.
6. Chu T.S. and Hogg D.C., "Effects of Precipitation on Propagation at 0.63, 3.5 and 10.6 Microns". Bell Systems Technical Journal Vol. 47 - No. 5. 1968.
7. Bisyarin V.P., Bisyarina I.P., Rubash V.K., and Sokolov A.V., "Attenuation of 10.6 and 0.63 Micron Laser Radiation". Radio Engineering and Electronic Physics - Vol. 16 (pp. 1594-1597). 1971.
8. Fried D.L., "Statistics of a Geometric Representation of Wavefront Distortion". Journal of the Optical. Society of America - Vol. 55 (pp. 1427-1435). 1965.
9. Brookner E., "Improved Model for the Structure Constant Variations with Altitude". Appl. Opt. 10 (pp. 1960-1962). 1971.
10. Tatarski V.I., "Wave Propagation in a Turbulent Medium". McGraw-Hill. New York (USA). 1961.
11. Hufnagel R.E., "Variations of Atmospheric Turbulence". Digest of Technical Papers - Topical Meeting on Optical Propagation Through Turbulence. Optical Society of America. Washington DC (USA). 1974.

12. Lei F. and Tiziani H.J., "Atmospheric Influence on Image Quality of airborne Photographs". Optical Engineering - Vol. 32, No 9 (pp. 2271-2280). 1993.
13. Ochs G.R., Wang T, Lawrence R.S., and Clifford S.F., "Refractive-Turbulence Profiles Measured by One-dimensional Spatial Filtering of Scintillation". Applied optics 15 (pp. 2504-2510). 1976.
14. Chiba T., "Spot Dancing of the Laser Beam Propagated Through the Turbulent Atmosphere". Applied Optics – Vol. 10 (p. 2456). 1971.
15. Strohbehn J.W. et al., "Laser Beam Propagation in the Atmosphere". Topics in Applied Physics Series – Vol. 25. Sprienger-Verlag. 1978.
16. Buck A.L., "Effects of the Atmosphere on Laser Beam Propagation". Applied Optics – Vol. 6 (p. 703). 1967.
17. Yura H.T., "Atmospheric Turbulence Induced Laser Beam Spread". Applied Optics - Vol. 10 (p. 2771). 1971.
18. Ochs G.R. and Lawrence R.S., "Measurements of Laser Beam Spread and Curvature". Laser Journal. 1971.
19. Gebhardt F.G. and Smith D.C., "Effects of Wind on Thermal Defocusing of CO_2 Laser Radiation". Applied Physics Lett. - Vol. 14 (p. 52). 1969.
20. Gebhardt F.G., "High Power Laser Propagation". Applied Optics – Vol. 15 (p. 1479). 1976.
21. Wood D., Comac M., and Gerry E.T., "Effects of 10.6-μ Laser Induced Air Chemistry on the Atmospheric Refractive Index". Applied Optics – Vol. 10 (p. 1877). 1971.
22. Keith G.G., Otten L. J., and Rose W.C., "Aerodynamic Effects". ERIM-SPIE IR&EO Systems Handbook (Vol. 2 – Chapter 3). Second Printing. 1996.
23. Sutton G.W., "Effect of Turbulent Fluctuations in an Optically Active Fluid Medium". AIAA Journal - Vol. 7 (pp. 1737-1743). 1969.
24. Gladstone J.H. and Dale J., "On the Influence of Temperature on the Refraction of Light". Phil. Trans. – Vol. 148 (p. 887). 1858.
25. Gilbert K.G. and Otten L.J., "Aero-Optical Phenomena". Progress in Astronautics and Aeronautics (Vol. 80). American Institute of Aeronautics and Astronautics. New York. 1982.

26. Graig J.E. and Rose W.C., "The Optics of Aircraft Shear Flows". AAIA Paper 85-0557. 1985

27. Lorah L.D. and Rubin E., "Aerodynamic Influences on Infrared System Design". The Infrared Hadbook by Wolfe W.L. and Zissis G.J., Eds. The Environmental Research Institute of Michigan. Ann Arbor (MI). 1985.

28. Gebhardt F.G., "High Power Laser Propagation". Applied Optics – Vol. 15 (p. 1479). 1976.

29. Kohnle A. and Höhn D.H., "Atmospheric Propagation and background Effects as relevant to Counter Measures Against Electro-Optical and Laser systems". AGARD-CP-573(S). 1996.

30. Thomas M.E. and Donald D.D., "Atmospheric Transmission". ERIM-SPIE IR&EO Systems Handbook (Vol. 2 – Chapter 1). Second Printing. 1996.

Appendix D

LASER SCATTERING AND TARGET CROSS SECTION

D.1 General

Our present understanding of radiation theory does not permit an analytical description, in closed form, of the exact relationship between the radiation emitted by a source (whether natural or artificial) and the radiation received by a remote sensor after having been reflected by object under surveillance. There are well known laws to describe the simple case of an electromagnetic wave incident upon a perfectly planar interface between two media. In this case, the reflected wave depends upon the radiation wavelength , the angle of incidence, and the physical properties (permittivity, permeability and conductivity) of the two adjoining media. The laws governing such a case are sufficiently understood so that the refractive index and extinction coefficient of materials involved may be found by determining the reflection coefficients of the materials. For the more complicated case involving a surface with periodic or random surface irregularities, an analytic determination of the properties of the reflected electromagnetic field may only be approximated.

In the past ten years, many papers have been published on scattering, or reflection from rough surfaces. Many theories have been developed, but none is both general and rigorous at the same time. To perform reasonably simple numerical calculations on the basis of these theories, certain simplifying assumptions are introduced, usually including one or more of the following:

- The dimensions of scattering elements of the rough surface are either much smaller or much greater than the wavelength of the incident radiation.
- The radii of curvature of the scattering elements are much greater than the wavelength of the incident radiation.
- Shadowing or obscuration effects occurring at the surface may be neglected.

- Only the far field is to be considered.
- Multiple reflections may be neglected.
- Consideration is restricted to a particular model of surface roughness (e.g., saw-tooth, sinusoidal protrusions of definite shape and in random position, with random variations in height given by their statistical distribution and correlation function).

Electromagnetic scattering theory has bee used in the past to compute radiation backscattering from targets in the microwave region of the spectrum, where the radiation wavelength is much greater than the minute irregularities of the target surface, and where the conductivity of the target material is infinite. In the optical region, where materials have finite conductivity and the surface irregularities have a wide range in size relative to the radiation wavelength, present electromagnetic scattering theory is applicable to only a few special cases, so the only way to determine reflectance in this region for target and background objects is by experimentation.

D.2 Definitions and Terminology

Light scattering has traditionally been a separate discipline from radar scattering. This has led to separate notation and terminology in the two communities that research these topics. Optical scattering has some terminology in common with *radiometry* (the passive sensing and identification of targets based on their natural microwave emissions). Engineering symbols and physics symbols generally used are compared in Table D-1. Fig. D-1 defines the basic quantities used in the definitions that follow [1]. Note that these quantities vary from point to point on the surface although the dependence on position vector ($\vec{r}$ or $\vec{r}'$) is not explicitly indicated.

1) *Radiant flux*: The rate of emission of power from a source. The symbols are Φ or P and the unit is watts.

2) *Radiant emittance*: Also called the *excitance*, this is used to characterize extended sources. Most sources of light are large in terms of wavelength and do not

emit uniformly in intensity. The radiant emittance is an indicator of the intensity variation across the surface. It is the power radiated per unit source surface area. Therefore:

$$M = \frac{d\Phi}{ds} \tag{D.1}$$

The physics symbol is W and the units are watts per square meter.

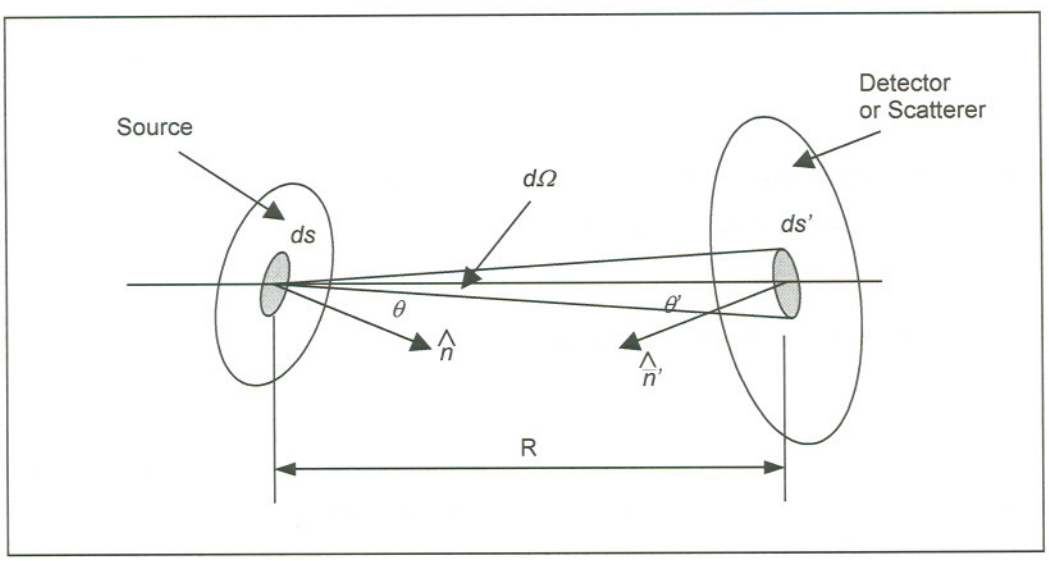

Fig. D-1. Source and scatterer geometry for LCS definitions.

3) *Radiant intensity*: The radiation from sources is not only non-uniform in intensity but also in direction. Radiant intensity is the radiant source power per unit solid angle:

$$I = \frac{d\Phi}{d\Omega} \tag{D.2}$$

The physics symbol is J and the unit is watts per steradian. This is the *candlepower* of the source.

4) *Irradiance*: This is the power per unit surface area being received by a differential surface *ds'*:

$$E = \frac{d\Phi}{ds'} \tag{D.3}$$

The physics symbol is H and the unit is watts per square meter. This is the *illumination* of the surface.

5) *Radiance*: The intensity per unit area per steradian of a source. This essentially combines the directional and intensity characteristics of an extended source into a single parameter:

$$L = \frac{I}{ds_n} = \frac{d\Phi}{\cos\theta ds d\Omega} \tag{D.4}$$

The unit is watts per square meter steradian, and the physics symbol is N. This is also referred to as the *brightness* of the source.

6) *Radiant flux density*: The Pointing vector W.

Quantity	*Units*	*Engineering symbol (LCS)*	*Physics symbol (Optics)*
Radiant flux	W	Φ	P
Radiant emittance (excitance)	W/m^2	M	W
Radiant intensity	W/sr	I	J
Radiant flux density	W/m^2	W	-
Irradiance	W/m^2	E	H
Radiance	W/m^2sr	L	N

Table D-1. Symbols and terminology.

When a target is illuminated, the primed quantities in Fig. D-1 apply; that is, the target is a receiving surface. Subsequently, the target becomes a source as it scatters the incident light, and the unprimed quantities in Fig. D-1 are appropriate. Subscripts i and r can be used to indicate *incident* (from a laser) or *reflected* (to a detector).

D.3 Reflectance Functions

It is possible to arrive at the most general definition of reflectance ρ' (called bidirectional reflectance) by considering an infinitesimal element of surface, dA , upon which radiation of infinitesimal solid angle $d\omega_i$ and radiance N_i are incident. Tanking a coordinate system fixed with respect to dA, with polar angle θ' measured from the normal and azimuth angle ϕ' , measured from a fixed line (see Fig. D.2), the contribution to the reflected radiance, $dN_r(\theta_r', \phi_r')$, in the reflected pencil for the direction (θ_r', ϕ_r') is:

$$dN_r(\theta_r', \phi_r') = \rho' N_i(\theta_i', \phi_i') \cos\theta_i' d\omega_i \tag{D.5}$$

Generally, ρ' is a function of the incident and reflected directions (θ_i', ϕ_i' and θ_r', ϕ_r', respectively), the polarization (P), the wavelength (λ), and the optical parameters of the surface. Total radiance in a given reflected direction is obtained by integrating Equation (A.1) over all incident directions, which yields:

$$N_r(\theta_r', \phi_r') = \int \rho' N_i(\theta_i', \phi_i') \cos\theta_i' d\omega_i' \tag{D.6}$$

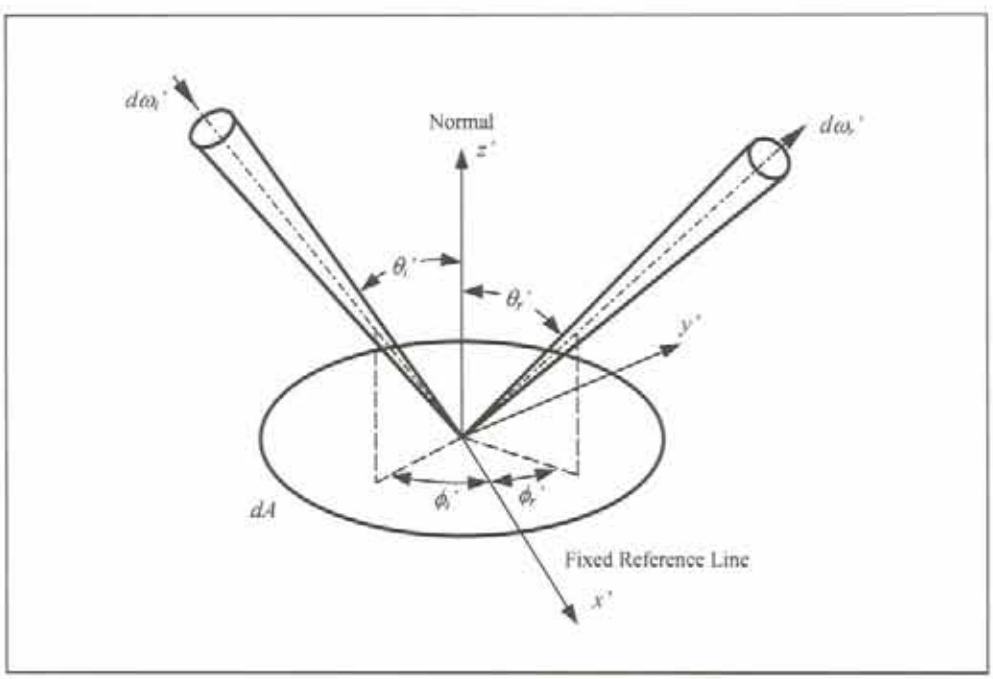

Figure D-2. Local coordinate system for defining bi-directional reflectance.

Also, by Helmhotz's reciprocity theorem, if the directions of the incident and reflected pencils are interchanged, the bidirectional reflectance is unchanged:

$$\rho'(\theta_1', \phi_1'; \theta_2', \phi_2'; P; \lambda) = \rho'(\theta_2', \phi_2'; \theta_1', \phi_1'; P; \lambda) \tag{D.7}$$

Since the optical constants of materials may change from point to point, bidirectional reflectance becomes a function of the location of dA. If it is then assumed that the surface can be described by the $z' = f(x', y')$, the correct functional dependence for reflectance is:

$$p'(\theta_i', \phi_i'; \theta_r', \phi_r'; P; \lambda; x', y', z')_{z'=f(x',y')} \tag{D.8}$$

Generally, the direction of the normal to dA is also a function of the location of dA on the surface of the object. Hence, even if the incident and reflected radiation have a constant direction with respect to the (x', y', z') coordinates, the angles (θ_i', ϕ_i') and (θ_r', ϕ_r'), taken with respect to the local normal, would be a function of location of the surface element dA. For convenience, a second, absolute coordinate system is usually introduced, namely, (x, y, z). The x-z plane of this system is coincident with the average value of $z' = (x', y')$ along the surface A, and is, therefore, the average plane of the reflector. The normal to this average plane is parallel to the z axis. Instead of referring the incident and reflected radiation to the local coordinates, they are then referred to the absolute system, with θ as the polar angle and ϕ as the azimuthal angle. The bidirectional reflectance with respect to this system is:

$$p'(\theta_i, \phi_i; \theta_r, \phi_r; P; \lambda; x, y) \tag{D.9}$$

Another type of reflectance commonly considered is the directional reflectance ρ_d, which is a function of only one direction, either the incident or reflected direction. In the case where reflected power is integrated over a hemisphere and incident power is from a specific direction, directional reflectance is denoted by ρ_{di}. The incident power dp_i is:

$$dp_i = dN_i(\theta_i, \phi_i; P_i) \cos\theta_i d\omega_i dA \tag{D.10}$$

Using eq. (D.6), we have:

$$dN_r = \rho' \frac{dp_i}{dA} \tag{D.11}$$

Since the reflected power dp_r is given by:

$$dp_r = dA \int_{2\pi} dN_r \cos\theta_r d\omega_r = dp_i \int_{2\pi} p' \cos\theta_r d\omega_r \tag{D.12}$$

Therefore:

$$\rho_{di}(\theta_i, \phi_i; P; \lambda; x, y) = \int_{2\pi} p' \cos\theta_r d\omega_r \tag{D.13}$$

When dA is uniformly illuminated from all directions (N_i= constant), the corresponding directional reflectance, ρ_{dr} , is defined as the ratio of the radiance reflected in a given direction to the incident radiance. Proceeding as previously, we have:

$$N_r = \int_{2\pi} \rho' N_i \cos\theta_i d\omega_i = N_i \int_{2\pi} p' \cos\theta_i d\omega_i \tag{D.14}$$

And, thus:

$$p_{dr}(\theta_r, \phi_r; P; \lambda; x, y) = \int_{2\pi} p' \cos\theta_i d\omega_i \tag{D.15}$$

From comparison of Equations (D.12) and (D.13), we obtain:

$$\rho_{di}(\theta, \phi; P; \lambda; x, y) = \rho_{dr}(\theta, \phi; P; \lambda; x, y) = \rho_d \tag{D.16}$$

ρ_d is called total directional reflectance.

D.4 Bidirection Reflectance Distribution Function

In general, the distribution of light scattered from a sample is a function of incident angle, wavelength, and power, as well as sample parameters (orientation, transmittance, reflectance, absorptance, surface finish, index of refraction, bulk

homogeneity, contamination, etc.). The *Bidirectional Reflectance Distribution Function* (BRDF) is commonly used to describe scattered light patterns.

Using the notation presented by Stover [2], the BRDF can be described as follows. Let us consider the geometry shown in Fig. D-3 where the subscripts *i* and *s* are used to denote incident and scattered quantities, respectively. Thus the direction of the specular beam is $\theta_s = \theta_i$ and $\phi_s = 0$. The retroreflection (for light scattered back into the incident specular beam) is given by $\theta_s = \theta_i$ and $\phi_s = 180°$.

The BRDF is defined in radiometric terms as the surface radiance divided by the incident surface irradiance. As described before, the surface irradiance is the light flux (watts) incident on the surface per unit illuminated surface area. The scattered surface radiance is the light flux scattered through solid angle Ω_s per unit illuminated surface area per unit projected solid angle. The projected solid angle is the solid angle times $\cos\theta_s$. Thus the BRDF becomes:

$$BRDF \equiv \frac{diff.\ radiance}{diff.\ irradiance} \cong \frac{dP_s/d\Omega_s}{P_i \cos\theta_s} = \frac{P_s/\Omega_s}{P_i \cos\theta_s} \tag{D.17}$$

and has units of steradian^{-1}.

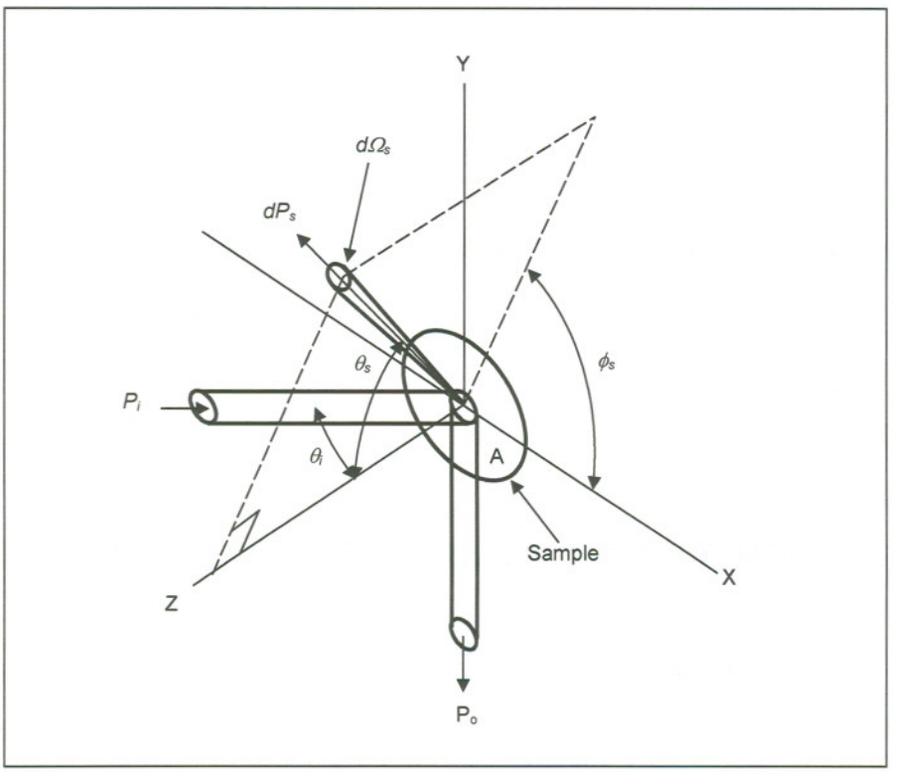

Figure D-3. Geometry for the definition of BRDF.

The differential form of the BRDF equation is more correct, but because of the convolution effects [Stover, 1990], it is only approximated when measurements are taken with a finite-diameter aperture. The approximation is very good when the flux density is reasonably constant over the measuring aperture, but can be very poor when using a large aperture to measure focused specular beams. The numerical value is bi-directional in that it depends on both the incident direction (θ_i , 0) and the scatter direction (θ_s , ϕ_s), and may be viewed as directional reflectance per unit solid angle (in steradians) of collected scatter.

Using the notation presented in paragraph D.1, the BRDF can be represented by:

$$\rho_{pq}\left(\vec{r}',\theta_i,\phi_i,\theta_r,\phi_r\right)=\frac{L_{rp}(\theta_r,\phi_r)}{E_{iq}(\theta_i,\phi_i)} \tag{D.18}$$

Therefore, the BRDF gives the radiance in the direction (θ_r, ϕ_r) as a function of:

- incidence direction (θ_i, ϕ_i);
- location of reflection point in the target surface $\vec{r}'$;
- polarization of the incident wave q;
- polarization of the observer p.

Typical BRDF values, measured at 0.633 μm, are shown in the Figs. D-4 and D-5 for light and dark materials [2].

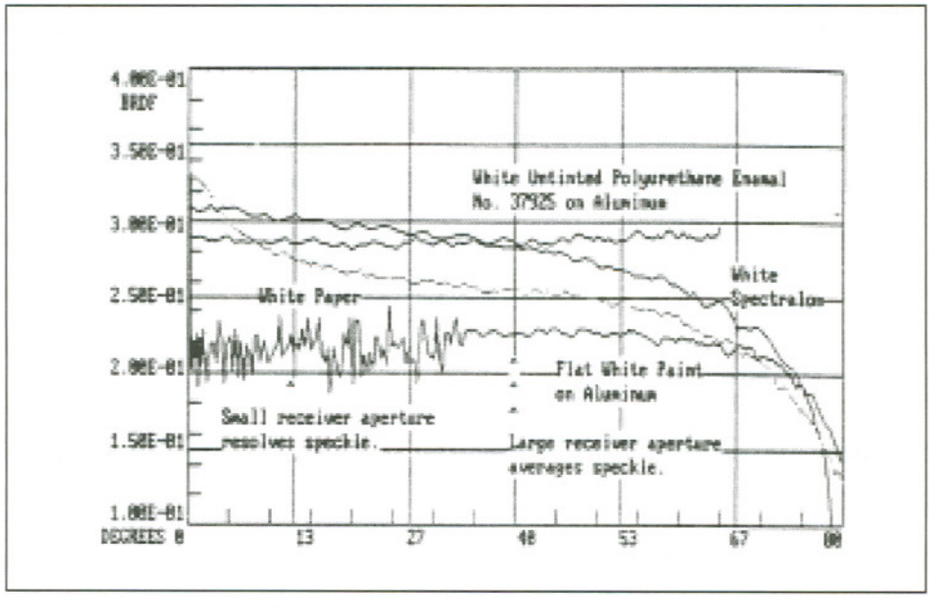

Figure D-4. BRDF of some white surfaces.

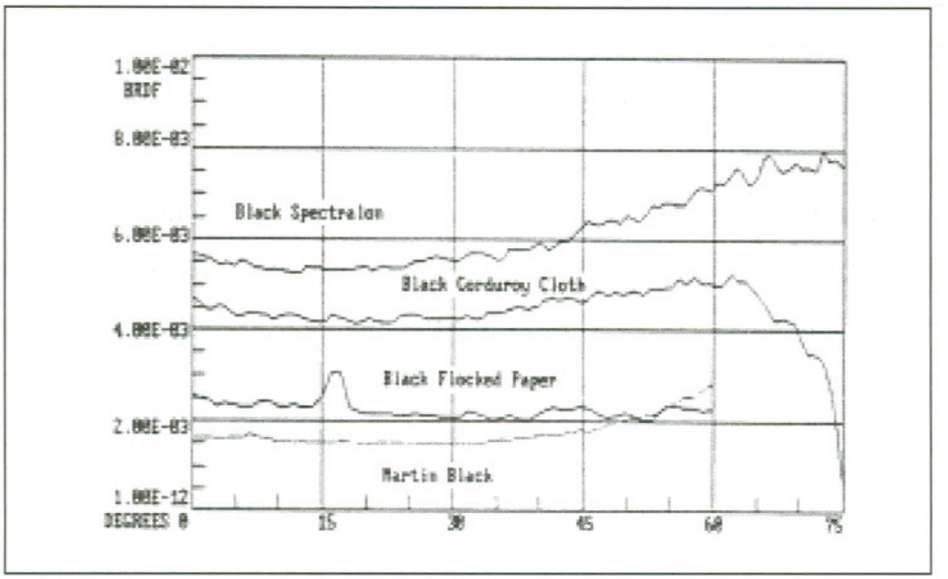

Figure D-5. BRDF of some black surfaces.

The difference is several orders of magnitude, and this points to one obvious method of LCS reduction: flat dark paints as opposed to glossy light paints.

D.5 Other Scattering Functions

The assumptions implied in the definition of BRDF (differential radiance L divided by the differential irradiance E) are that the illuminating beam is uniform, that scattering occurs from the surface of the target, and that the differential scattering area is isotropic. When these conditions do not exist, which is typically the situation for a measurement, then the measured quantities are not the radiance and irradiance. Functions similar to the BRDF have been defined to compensate for these shortcomings. They are the *Bidirectional Scatter Distribution Function* (BSDF), the *Cosine-corrected BSDF* (or simply *Scatter Function*), and a related quantity, the *Total Integrated Scatter* (TIS). As reported in Stover [2], surface roughness characteristics can be extrapolated using scattering functions measurements and, conversely, reliable scatter predictions can be made using surface statistics.

The BSDF was introduced after BRDF in order to include other types of scatter, such as that from transmissive optics. From a practical point of view, the BSDF can be

defined as exactly the last term in eq. (D.5), and not as the ratio of radiance and irradiance. Therefore:

$$BSDF \equiv \frac{P_s/\Omega_s}{P_i \cos\theta_s} \tag{D.19}$$

For this reason, the $\cos\theta_s$ term (present in the definition of surface radiance) is often disregarded, since no longer adds any mathematical (or physical) value to the expression. When it is dropped, the result is often called the *Cosine-corrected BSDF* or, sometimes, the *Scatter Function (SF):*

$$SF \equiv \frac{P_s/\Omega_s}{P_i} \tag{D.20}$$

With the cosine dropped, the light scattered from a particular optic into any given solid angle, from any hypotetical source, may be found by multiplying the appropriate value of the SF by the incident power and solid angle.

The earliest scatterometers were not designed to measure light scattered as a function of angle. Instead, these instruments gather (or integrate) a large fraction of the light scattered into the hemisphere in front of a reflective sample and focus it into a single detector. The measured scattered power is then normalized by the reflected specular power and the ratio defined as the Total Integrated Scatter (TIS). The result is an instrument that provides repeatable results, fast throughput, and (without looking too closely) a single number to characterize sample scatter. In a paper published in 1954, Davies [3] reported the following relationship for fractional scattered power from a smooth, clean, conducting surface:

$$TIS \equiv \frac{P_s}{RP_i} = \frac{P_s}{P_o} \cong \left(\frac{4\pi\sigma\cos\theta_i}{\lambda}\right)^2 \tag{D.21}$$

In addition to the smooth-surface requirement ($\lambda << 4\pi\sigma\cos\theta_i$, where σ is the root mean square (rms) roughness), Davies assumed that the height-distribution function was *Gaussian* and that most of the light was restricted to scatter angles close to specular ($\theta_s \cong \theta_i$). Davies extended his results to very rough surfaces and compared them to experimental data obtained at radar frequencies, with encouraging results.

Further developments, based on the Rayleigh-Rice approach (which relate scatter to the surface power spectrum independent of the form of the height distribution), showed that the *Gaussian* assumption adopted by Davies was not necessary, therefore removing this restriction [2].

D.6 Laser Cross Section

Laser cross section (LCS) can be defined in the same way as Radar Cross Section (RCS). Therefore we can write the following expression [1]:

$$\sigma_{pq}(\theta_i,\phi_i,\theta_r,\phi_r) = \lim_{R\to\infty} 4\pi R^2 \frac{W_{rp}(\theta_r,\phi_r)}{W_{iq}(\theta_{iq},\phi_i)} \tag{D.22}$$

where the subscripts i and r refer to incident and reflected and p and q denote the polarizations of the reflected and incident waves, respectively. Given that:

$$W_{rp} = \frac{I_{rp}}{R^2} \tag{D.23}$$

the LCS can be written in terms of the radiant-intensity:

$$\sigma_{pq}(\theta_i,\phi_i,\theta_r,\phi_r) = 4\pi \frac{I_{rp}(\theta_r,\phi_r)}{W_{iq}(\theta_i,\phi_i)} \tag{D.24}$$

For the monostatic case (i.e., transmitter and receiver co-located), this simplifies to:

$$\sigma_{pq}(\theta,\phi) = 4\pi \frac{I_{rp}(\theta,\phi)}{W_{iq}(\theta,\phi)} \tag{D.25}$$

In practice, LCS is a function of many parameters in addition to the target characteristics. These include: beam profile, beamwidth, laser temporal and spatial coherence, target surface characteristics, receiver aperture, and detector averaging. Furthermore, satisfying the far-field criterion (nD^2/λ where n is generally 2) is difficult at laser frequencies because λ is so small. Thus, unlike RCS, the far-field limiting process cannot be strictly applied to LCS. It may be tempting to discard the

concept of LCS, but LCS does provide useful and repeatable data at distances that can be accommodated by indoor and outdoor facilities.

D.6.1 BRDF and Laser Cross Section

Considering a differential surface area *ds* illuminated with a radiant flux density $W_{iq}(\theta_i, \phi_i)$, as shown in Fig. D-6, the power collected by the differential patch is given by [1]:

$$W_{iq}(\theta_i, \phi_i)\cos\theta_i ds \tag{D.26}$$

The BRDF of this patch is ρ_{pq} and, therefore, we have:

$$L_{rp}(\theta_r, \phi_r) = \rho_{pq} w_{iq}(\theta_i, \phi_i)\cos\theta_i ds \tag{D.27}$$

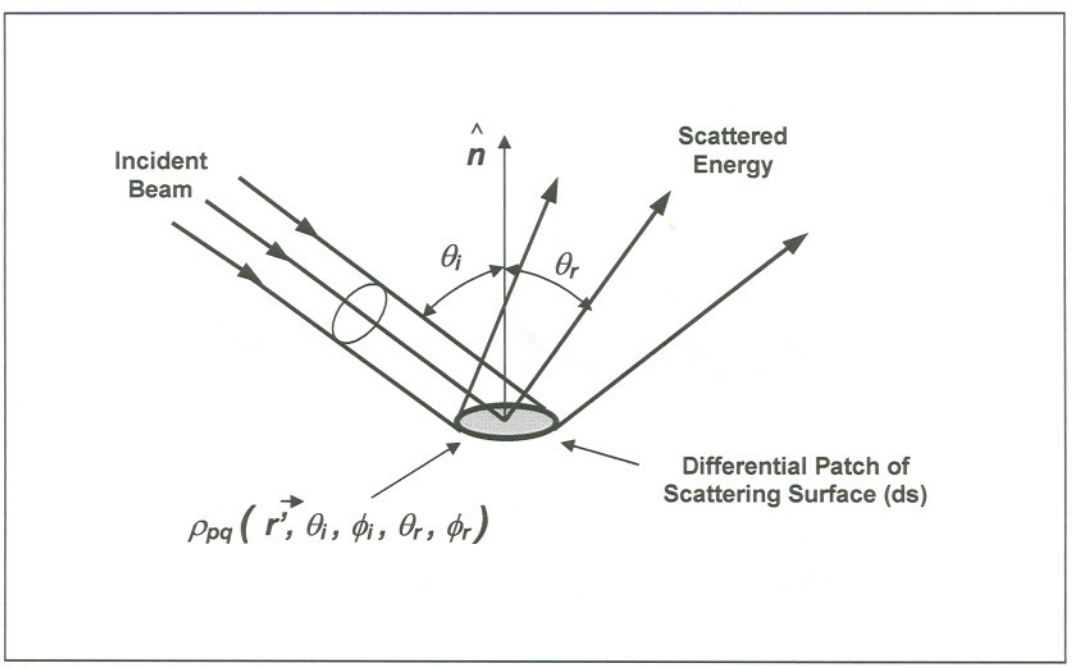

Figure D-6. Beam illuminating a differential surface patch.

From the definition of LCS, we can write:

$$d\sigma_{pq} = 4\pi \frac{dI_{rp}}{W_{iq}} = 4\pi \frac{L_{rp}\cos\theta_r ds}{W_{iq}} = 4\pi\rho_{pq}\cos\theta_i \cos\theta_r ds \tag{D.28}$$

The explicit angle dependencies have been dropped for notational convenience. This is the fundamental equation for the LCS of a surface.

D.6.2 Diffuse Surfaces - Rayleigh Condition

At optical wavelengths, almost all surfaces can be considered rough. The irregularities are comparable to or greater than a wavelength. The standard criterion for a rough surface is the Rayleigh condition:

$$h \leq \frac{\lambda}{8 \sin \psi} \tag{D.29}$$

where h is the average height of the irregularities and ψ is the grazing angle, as shown in Fig. D-7.

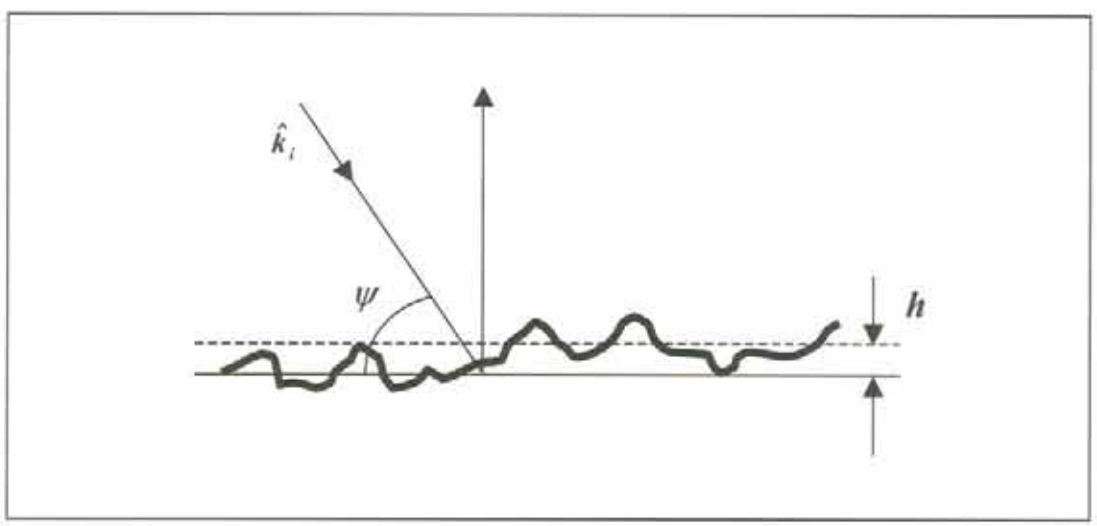

Figure D-7. Rayleigh condition for a rough surface.

Increasing the surface roughness is equivalent to introducing path differences relative to a smooth surface. If the surface irregularities are random, the phase error due to path differences will also be random, and the final result is a LCS noise floor. This random component is called diffuse scattering, as opposed to specular scattering. For laser scattering, the diffuse component can dominate. In fact, there may be no specular component present in many instances, as illustrated in Fig. D-8 [1].

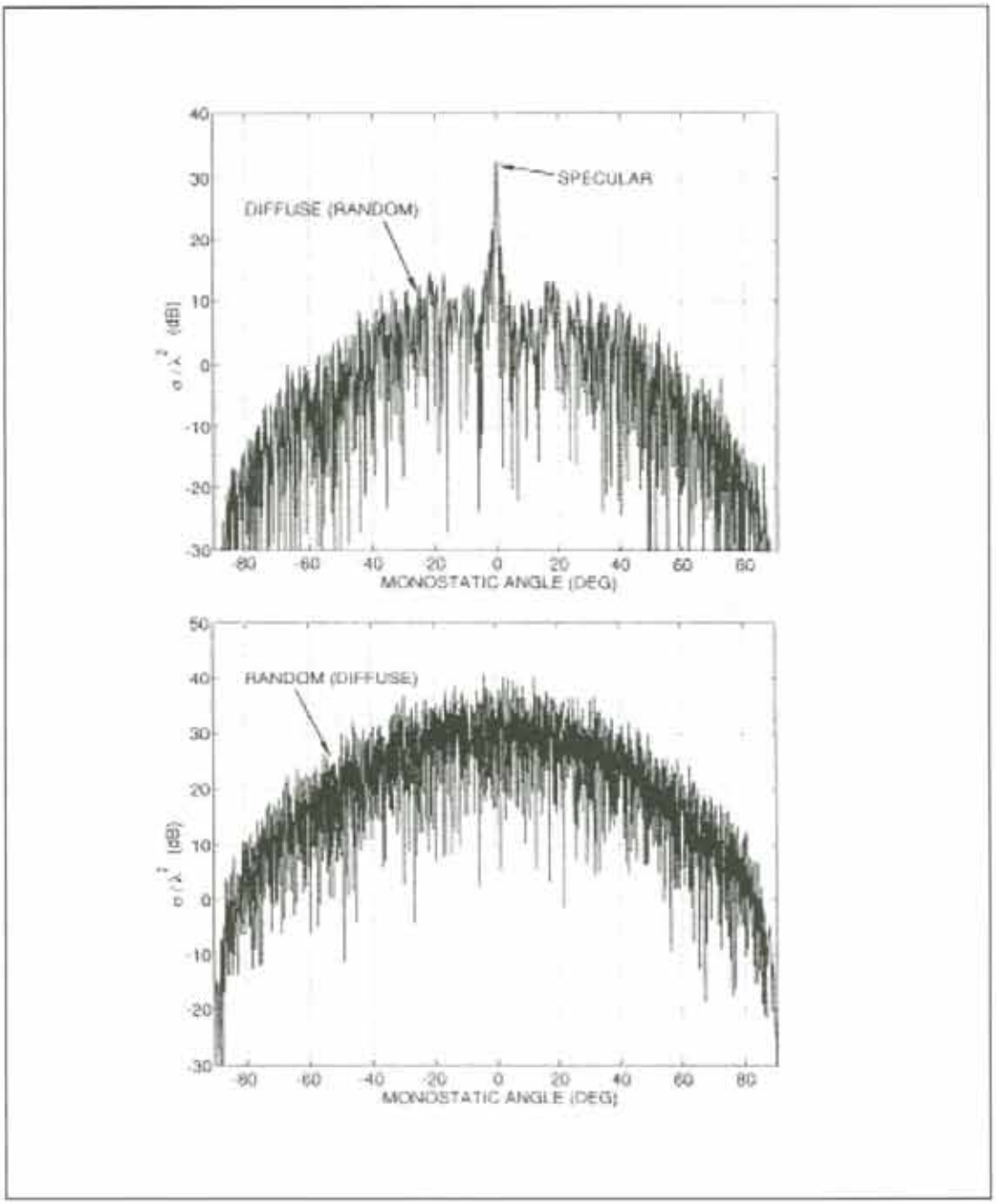

Figure D-8. Scattering from very rough and extremely rough surfaces.

In general, the scattering from a surface has the three distinct features shown in Fig. D-9. The first is the uniform scattering at most angles that is characteristic of a diffuse surface. This is true for all angles of incidence θ_i. One exception to this is the specular direction, which satisfies Snell's law, $\theta_s = -\theta_i$. If the surface is smooth enough, a specular lobe occurs, and the height of the lobe increases with surface smoothness. The second angle of enhanced scattering is in the back direction. This

is referred to as the *opposition effect* and is due to secondary scattering mechanisms. They include local shadowing and interactions between adjacent surface areas [4].

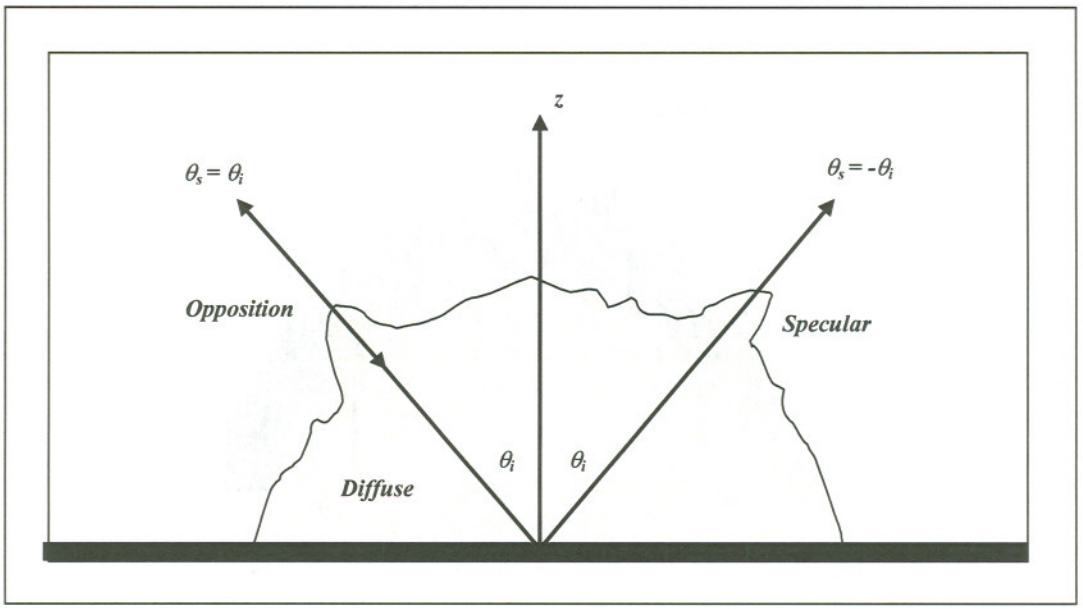

Figure D-9. Typical bistatic scattering pattern for a rough flat surface.

D.6.3 Perfectly Diffuse Surfaces

Diffuse surfaces have a constant BRDF, as they scatter equally in all directions independently of the illuminating direction, and all points on the surface scatter identically. Thus, we have:

$$\rho_{pq}(\vec{r}', \theta_i, \phi_i, \theta_r, \phi_r) = \rho_o \tag{D.30}$$

where ρ_o is a constant. In this case, it makes sense to define a total *hemispherical reflectance*:

$$R_d = \int_0^{2\pi} \int_0^{\pi/2} \rho_o \cos\theta_r \sin\theta_r d\theta_r d\phi_r \tag{D.31}$$

where the subscript d indicates "diffuse". For a perfectly diffuse surface eq. (D.19) integrates to:

$$R_d = \pi\rho_o \tag{D.32}$$

D.6.4 LCS Components

Empirically, LCS has been found to be composed of three components: 1) specular, σ_s; 2) diffuse, σ_d; and 3) projected area, σ_p. The total LCS is:

$$\sigma = \sigma_s + \sigma_d + \sigma_p \tag{D.33}$$

The specular component has the potential for extremely large values because of the small wavelength. However, the majority of the incident light is scattered diffusely for most surfaces. Frequently, the specular "flash" cannot even be identified. In theory, the diffuse component varies as $\cos^2\theta$. However, measured data for diffuse surfaces generally fall off more slowly than $\cos^2\theta$, approaching $\cos\theta$, which is more characteristic of the projected component.

Reflectance R, defined in eq. (D.19) for perfectly diffuse surfaces, is a measure of reflectivity of a target. Essentially, it is a ratio of all the power scattered by the target to the power incident on the target. A fraction of the reflected light can be associated with each of the LCS components listed earlier. By conservation of energy, the sum of the reflectances must be less than or equal to 1:

$$R = R_d + R_s + R_p \leq 1 \tag{D.34}$$

The portion of scattered energy allocated to each LCS component is frequently determined after the fact. The values of R_d, R_s, and R_p are chosen to provide good agreement between measured and predicted LCS values.

D.6.5 Specular Laser Cross Section

Physical optics (PO) or geometrical optics (GO) can be used to compute the specular component. The expressions for a perfectly reflecting surface must be reduced by R_s:

$$\begin{aligned} &\text{GO:} \quad \sigma_s = R_s \pi R_1^s R_2^2 \\ &\text{PO:} \quad \sigma_s = R_s 4\pi A^2/\lambda^2 \end{aligned} \tag{D.35}$$

Statistical analysis can be used to estimate the value of R_s. For example, if only specular and diffuse scattering occurs for a particular target ($R_p = 0$), R_d and R_s can be approximated by the following expressions [1]:

$$R_s = e^{-\overline{\Delta^2}} \qquad R_d = 1 - e^{-\overline{\Delta^2}} \tag{D.36}$$

where $\Delta = 2k(\delta_{ab} - \delta_{cd})$ is a random variable generated as difference of two samples from a normal distribution (δ_{ab} and δ_{cd} are the errors at elements (a, b) and (c, d); and $k = 2\pi/\lambda$). From statistics:

$$\overline{e^{j\Delta}} = \overline{\cos\Delta} + j\sin\Delta = \begin{cases} e^{-\overline{\Delta^2}} & a \neq c \quad and \quad b \neq d \\ 1 & a = c \quad and \quad b = d \end{cases} \tag{D.37}$$

where $\overline{\Delta^2} = 4k^2\overline{\delta^2}$. The specular beamwidths predicted by physical optics are usually much smaller than those encountered in measurements, especially when the specular lobe intensity is of the same order of magnitude as the diffuse component. Frequently, cosine fits of measured data are used to model the specular component. With the specular peak represented by a cosine shape of power n, we have:

$$d\sigma_s = 2nR_n \cos^n\theta ds \tag{D.38}$$

Considering a circular, flat surface of radius a with no azimuthal (ϕ) scattering dependence, we have:

$$\sigma = 2nR_n 2\pi a^2 \int_0^{\pi/2} \cos^n\theta \sin\theta d\theta \tag{D.39}$$

or

$$\sigma_s = 4\pi a^2 R_n \frac{n}{n+1} \tag{D.40}$$

Comparing to the PO result gives:

$$R_s = 4R_n \frac{n}{n+1} \tag{D.41}$$

When $n = 1$, $\sigma_s \sim \cos\theta$, and eq. (D.28) reduces to the projected area LCS. When $n = 2$, $\sigma_s \sim \cos^2\theta$, and eq. (D.28) reduces to the diffuse LCS.

D.6.6 Projected Area Cross Section

As mentioned earlier, many scatterers do not have the monostatic $\cos^2\theta$ dependence expected of a perfectly diffuse surface. This is usually due to beam profile effects. Adding a projected area component can improve the agreement between predicted and measured data. This term has the form:

$$d\sigma_p = 2R_p \cos\theta dA \tag{D.42}$$

where θ is the angle from the surface normal and R_p the projected area hemispherical reflectance (e.g., the projected area of a sphere is simply a disk).

D.6.7 Multiple Reflections

Multiple reflections can contribute significantly to the LCS at an observation point. With reference to the geometry illustrated in Fig. D-10, relative to multiple diffuse scattering in a laser "corner reflector", the expression for double bounce reflection is the following [1]:

$$\sigma_{12} = \frac{4R_d}{\pi}\cos\theta_{i1}\cos\theta_{r2}\int_{A_1}\int_{A_2}\frac{\cos\theta_{i2}\cos\theta_{r1}}{R_{12}^2}ds_1 ds_2 \tag{D.43}$$

This expression must be evaluated numerically.

Results of computations relative to a corner reflector composed by two 6 in. plates are presented in Fig. D-11. Note that the singly reflected term is a constant when both plates are considered. The cosine factor for one plate is compensated for by the cosine factor of the second plate for 90° corner angle. The addition of the doubly reflected field has no effect at the grazing angles but does increase the LCS at other angles. The method presented by Jenn [1995] can be extended to higher-order reflections as well.

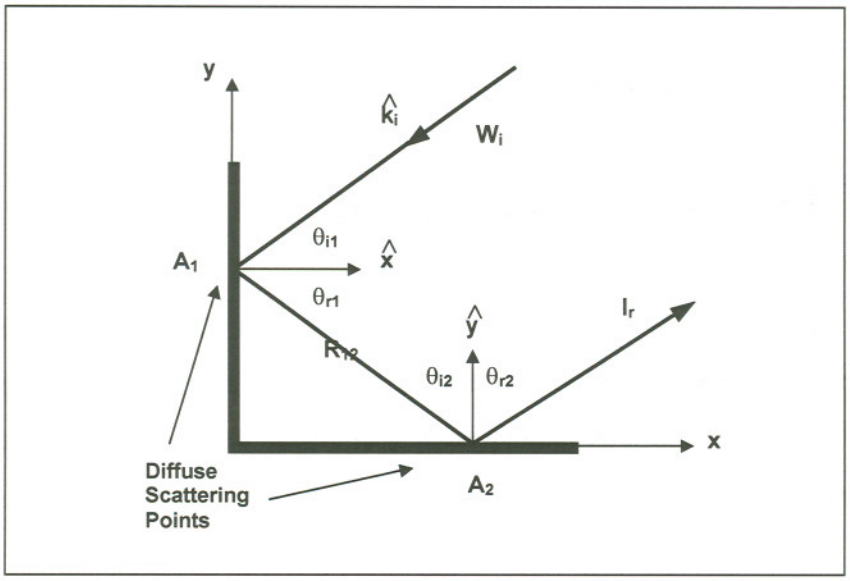

Figure D-10. Diffuse scattering by a corner reflector.

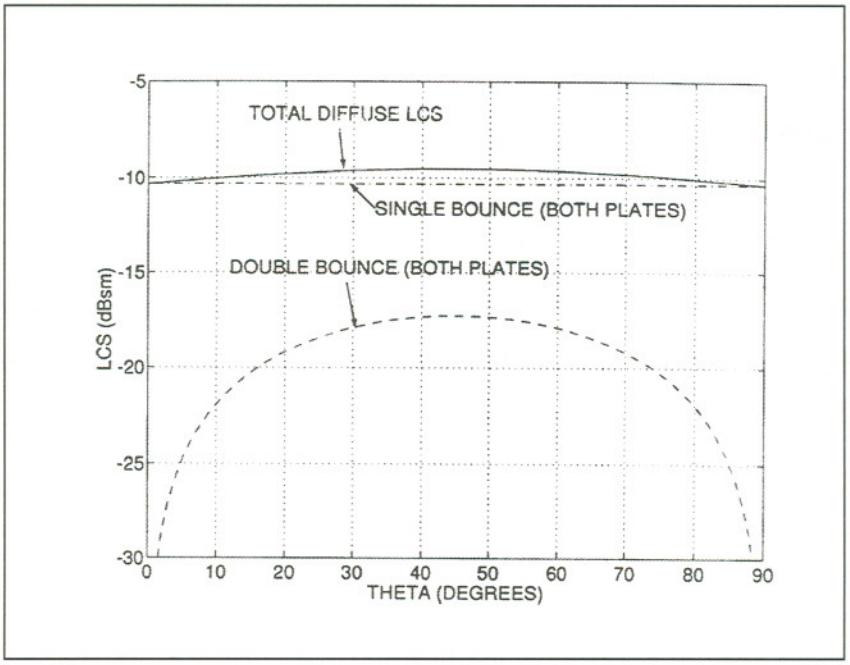

Figure D-11. Laser cross section of a diffuse corner reflector.

D.6.8 Laser Cross Section Prediction for Complex Targets

Diffuse scattering is the primary mechanism of light scattering by targets with "average" surface characteristics. Average refers to maintenance of the target's surface; that is, no special surface preparation or polishing is performed. Relatively

accurate LCS predictions for complex targets can be made using the geometrical components method. In many cases, multiple reflections can be neglected and the LCS estimates are still within a couple of decibels of measured data.

The overall LCS level at any particular observation point is determined primarily by the amount of projected target area presented to the LADAR system. Therefore, it is important to include shadowing. For diffuse scattering, the relative phases of the target components are not important. The total LCS is simply a noncoherent sum of all "subsurface" LCS contributions.

The restrictions and limitations imposed by the definition of LCS are seldom satisfied. Issues such as coherence, beam profile, volume scattering by the target, and so forth, have a significant effect on LCS and are usually included in simulation codes. As in the case of radar, it is the signal-to-noise ratio that ultimately determines system performance, and LCS is just one of many parameters that affect SNR. Signal-to-noise ratios can be significantly enhanced by signal-processing techniques. Most LCS computer codes simulate the processing and image formation components of the system, as well as LCS computation and atmospheric effects. This provides a more accurate estimate of system performance than is possible from a simple LCS number [1].

D.6.9 Laser Cross Section Reduction Methods

In principle, the same methods used in RCS reduction can be applied to LCS. They are: shaping, materials selection and coatings, passive cancellation, and active cancellation.

Shaping primarily affects the specular component, which is generally negligible unless the surface is optically polished. Shaping has only a small effect on the diffuse component (which varies as $cos^2\theta$) and the projected area component (which varies as $cos\theta$). Active and passive cancellation are effective only when applied to coherent scattering sources and, therefore, are not practical at laser frequencies.

The most effective means of LCS reduction is materials selection and the application of coatings. In fact, properly designed films cause multiple reflections at the two interfaces air/film and film/target to cancel. One common method for reducing reflection from a dielectric body is the application of quarter-wave films, also known

as antireflection coatings. For a normally incident wave, a quarter-wave film thickness causes equal reflections at both interfaces to cancel, yielding a total reflection coefficient of zero (this is due to the fact that the round-trip path difference in the film introduces a 180° phase difference between the two reflected waves).
A useful equation for appropriate selection of quarter-wave film materials is the following [1]:

$$R = \frac{n_1^2 - n_0 n_2}{n_0 n_2 + n_1^2} \qquad \text{(D.44)}$$

This equation gives the reflection coefficient (R) as a function of the refraction indices of air, film and target material (i.e., n_0, n_1 and n_2 respectively). Forcing the reflection coefficient to zero requires a film refraction index of $n_1 = \sqrt{n_0 n_2}$.

Antireflection coatings can be used in conjunction with shaping. However, particularly for airborne applications, the successful application of films to the reduction of LCS requires a delicate trade-off between electrical, mechanical, and thermal performance. Material properties of primary concern are strength, elasticity, hardness, thermal conductivity, finishing characteristics and durability.

D.7 References

1. Jenn D. C., "Radar amd Laser Cross Section Engineering". American Institute of Aeronautics and astronautics (AIAA) Education Series. 1995.
2. Stover J.C., "Optical Scattering – Measurement and Analysis". Second Edition. SPIE Optical Engineering Press. 1990.
3. Davies H., "The Reflection of Electromagnetic waves from a rough surface". Proceedings of the I.E.E. – Vol. 101 (Pt. III) (pp. 209-214). 1954.
4. Gu Z.H., Dummer R.S., Maradudin A.A., and McGurn A.R., "Experimental Study of the Opposition Effect in the Scattering of Light From a Randomly Rough Metal Surface". Applied Optics – Vol. 28 (N° 3). 1989.